NUREG/CR--5451

TI90 017530

Crack-Arrest Behavior in SEN Wide Plates of Low-Upper-Shelf Base Metal Tested Under Nonisothermal Conditions: WP-2 Series

Manuscript Completed: July 1990
Date Published: August 1990

Prepared by
D. J. Naus, J. Keeney-Walker, B. R. Bass, G. C. Robinson, Jr.,
S. K. Iskander, R. J. Fields,[1] R. deWit,[1] S. R. Low,[1] C. W. Schwartz,[2]
D. J. Alexander, L.-B. Johansson[3]

Oak Ridge National Laboratory
Operated by Martin Marietta Energy Systems, Inc.

Oak Ridge National Laboratory
Oak Ridge, TN 37831

[1]National Institute of Standards and Technology, Gaithersburg, MD 20849
[2]Department of Mechanical Engineering, University of Maryland, College Park, MD 20742
[3]Royal Institute of Technology, 100 44 Stockholm, Sweden

Prepared for
Division of Engineering
Office of Nuclear Regulatory Research
U.S. Nuclear Regulatory Commission
Washington, DC 20555
NRC FIN B0119
Under Contract No. DE-AC05-84OR21400

DISCLAIMER

Portions of this document may be illegible in electronic image products. Images are produced from the best available original document.

ABSTRACT

Current pressure vessel safety assessment methods are based largely on Sects. III and XI of the *American Society of Mechanical Engineers Boiler and Pressure Vessel Code (ASME B&PVC)*. These documents take the position that the fracture-toughness correlations cannot be assumed for a crack-arrest toughness value >220 MPa·$\sqrt{m}$ for light-water reactor pressure vessel steels. This limit is imposed largely because until recently essentially no crack-arrest toughness (K_{Ia}) data existed at or above this level and because Charpy tests show that impact energy levels exhibit an upper-shelf behavior. Certain pressurized-thermal-shock scenarios can lead to conditions where the driving force (K_I) on a propagating crack increases to levels in excess of the ASME limit.

The Heavy-Section Steel Technology (HSST) Program at the Oak Ridge National Laboratory under the sponsorship of the Nuclear Regulatory Commission is conducting analytical and experimental studies aimed at understanding the circumstances that would initiate the growth of an existing crack in a reactor pressure vessel (RPV) and the conditions leading to arrest of a propagating crack. Objectives of these studies are to determine (1) if the material will exhibit crack-arrest behavior when the driving force on a crack exceeds the ASME limit, (2) the relationship between K_{Ia} and temperature, and (3) the interaction of fracture modes (arrest, stable crack growth, unstable crack growth, and tensile instability) when arrest occurs at high temperatures. In meeting these objectives, crack-arrest data are being developed over an expanded temperature range through tests involving large thermally shocked cylinders, pressurized thermally shocked vessels, and wide-plate specimens. The wide-plate specimens provide the opportunity for a significant number of data points to be obtained at relatively affordable costs. These tests are designed to provide fracture-toughness measurements approaching or above the onset of the Charpy upper-shelf regime in a rising toughness region and with an increasing driving force.

The HSST wide-plate crack-arrest tests are being performed at the National Institute of Standards and Technology, Gaithersburg, Maryland, in their 27-MN capacity testing machine. The third series of tests, which used a Charpy low-upper-shelf base metal, are discussed. Each test used a 1 × 1 × 0.1 m or 1 × 1 × 0.15 m thick single-edge-notched plate specimen (a/w = 0.2) that was subjected to a linear thermal gradient along the plane of crack propagation. The thermal gradient was applied to the specimen by cooling the notched edge and heating the other edge. Through selection of the crack-tip temperature and transverse temperature profile, the initiation load and depth of crack propagation was changed from test to test. During each test, strain and temperature measurements were obtained as functions of position and time. Load, crack-opening-displacement, accelerometer, dynamic displacement, and acoustic-emission data were also obtained as functions of time.

Results obtained from the WP-2 series of crack-arrest tests have produced crack-arrest toughness values well above the limit recognized by current ASME Code guidelines with arrests occurring at temperatures

up to 102°C above the material drop-weight nil-ductility transition temperature (DW_{NDT} = 60°C) and up to 12°C above the onset of Charpy upper-shelf energy (temperature onset ≃ 150°C). Crack propagation has been predominantly cleavage until arrest occurred, and even for very high driving forces, ductile tearing occurred only after arrest. The fracture data support (1) the use of current linear-elastic fracture-mechanics concepts to analyze cleavage run-arrest events, (2) the analytical treatment of cleavage run-arrest and ductile fracture modes as separate events, and (3) the fact that cleavage arrest can and does occur above the ASME limit.

CONTENTS

	Page
ABSTRACT	iii
LIST OF FIGURES	vii
LIST OF TABLES	xix
FOREWORD	xxi
ACKNOWLEDGMENTS	xxxi
EXECUTIVE SUMMARY	xxxiii
1. INTRODUCTION	1
REFERENCES	3
2. BACKGROUND	4
REFERENCES	6
3. CHARACTERIZATION OF WIDE-PLATE SERIES 2 MATERIAL	8
3.1 INTRODUCTION	8
3.2 DROP-WEIGHT TESTING	10
3.3 CVN TESTING	11
3.4 TENSILE TESTING	11
3.5 CRACK-ARREST TESTING	19
3.6 FRACTURE-TOUGHNESS TESTING	23
REFERENCES	30
4. SPECIMEN PREPARATION, INSTRUMENTATION, AND TESTING PROCEDURE	32
4.1 SPECIMEN PREPARATION	32
4.2 INSTRUMENTATION	36
4.3 HEATING-COOLING-INSULATION SYSTEMS	51
4.4 TESTING PROCEDURE	53
REFERENCES	53
5. SUMMARY OF WIDE-PLATE CRACK-ARREST TESTS WP-2.1 THROUGH WP-2.6	54
5.1 TEST WP-2.1	54
5.2 TEST WP-2.2	61
5.3 TEST WP-2.3	71
5.4 TEST WP-2.4	84
5.5 TEST WP-2.5	99

Page

5.6 TEST WP-2.6 115

REFERENCE 129

6. POSTTEST ANALYSES, CRACK-ARREST TOUGHNESS RESULTS, AND COMPARISON OF DATA WITH OTHER LARGE-SCALE TEST RESULTS 130

6.1 POSTTEST ANALYSES 130

6.1.1 Posttest 3-D Static Analyses 130

6.1.2 Posttest 2-D Static and Dynamic Analyses 133

6.2 CRACK-ARREST TOUGHNESS RESULTS 145

6.3 COMPARISON OF WIDE-PLATE CRACK-ARREST TOUGHNESS DATA WITH OTHER LARGE-SCALE TEST RESULTS 148

REFERENCES 150

7. CONCLUSIONS 153

APPENDIX A. SUMMARY OF INSTRUMENTATION RESULTS 155

APPENDIX B. EFFECTS OF LOAD-POINT BOUNDARY CONDITIONS AND ANALYSIS METHOD ON WIDE-PLATE CRACK-ARREST TEST RESULTS 241

APPENDIX C. EFFECTS OF TUNNELING 253

LIST OF FIGURES

Figure		Page
2.1	Summary of large-specimen, high-temperature crack-arrest data	5
3.1	Allocation of 2 1/4 Cr-1 Mo 159-mm-thick LUS steel plate for various tests	9
3.2	CVN test results in T-L orientation for material from halves of wide-plate specimens WP-2.1 and -2.5	13
3.3	Curve fits of CVN impact energy vs temperature for characterization block PTC1 (2 1/4 Cr-1 Mo steel) for T-L orientation and at various plate depths	15
3.4	Comparison of WP-2 material tensile strength test results with 99% confidence interval obtained from PTC1 characterization block material tests	16
3.5	Typical room-temperature stress-strain curve for material obtained from characterization block PTC1 in direction transverse to material rolling orientation	18
3.6	Comparison of posttest crack-arrest toughness (K_a) values obtained for specimens fabricated from plate halves of specimens WP-2.1 and -2.5 with those obtained from PTC1 material and ASME K_{Ia} curve	19
3.7	Comparison of regression fits of crack-arrest toughness data for all PTC1 (T-L and T-S orientations) material data and for WP-2 and PTC1 materials (T-L orientation)	22
3.8	Comparison of crack-arrest toughness test results obtained from PTC1 and PTSE-2 LUS 2 1/4 Cr-1 Mo materials	23
3.9	Comparison of posttest initiation toughness (K_{Jc}) for specimens fabricated from plate halves of specimens WP-2.1 and -2.5 with range of values exhibited for specimens fabricated from PTC1 characterization block	24
3.10	Graphical output from analysis of a typical fracture toughness test at 80°C using single-specimen unloading compliance method	25
3.11	Comparison of J-integral (J_m) resistance curves at three temperatures for specimens obtained from WP-2.5 material at midthickness in T-L orientation	29
4.1	Schematic of HSST wide-plate crack-arrest specimen	32
4.2	Wide-plate test specimen undergoing hydrogen charging of an EB weld	33

Figure		Page
4.3	Schematic of chevron configuration of crack front	34
4.4	Overall specimen dimensions for (*a*) tests WP-2.1 and -2.2, (*b*) tests WP-2.3 and -2.4, and (*c*) tests WP-2.5 and -2.6	37
4.5	Out-of-plane deviation vs axial position from top load pin	40
4.6	Thermocouple locations for wide-plate, crack-arrest specimens (*a*) WP-2.1 and -2.4; (*b*) WP-2.2, -2.3, and 2.6; and (*c*) WP-2.5	41
4.7	Schematic of HSST wide-plate, crack-arrest data acquisition system	44
4.8	Strain-gage locations for wide-plate, crack-arrest specimens (*a*) WP-2.1 and -2.5, (*b*) WP-2.2, (*c*) WP-2.3, and (*d*) WP-2.4	45
4.9	Strain-gage locations for wide-plate, crack-arrest specimen WP-2.6	49
4.10	HSST wide-plate, crack-arrest test specimen installed in NIST testing machine	52
5.1	Transverse temperature profiles at approximate time of crack initiation-arrest events: WP-2 series	56
5.2	Fracture surfaces of WP-2 series specimens	57
5.3	Actual and ideal temperature distributions across specimen width (*a*) at start of test, (*b*) at 9.2-MN load, and (*c*) at ~10 s before initiation of fracture events: test WP-2.1	58
5.4	Load history for test WP-2.1	59
5.5	Fracture surface of specimen WP-2.1	60
5.6	Reduction-in-thickness contour map of specimen WP-2.1	62
5.7	Strain-gage-derived crack-front position vs time: test WP-2.1	62
5.8	Actual and ideal temperature distributions across specimen width during warm prestressing: test WP-2.2	66
5.9	Load vs (*a*) time and (*b*) front-face COD during warm prestressing: test WP-2.2	67
5.10	Actual and ideal temperature distributions across specimen width (*a*) at start of loading and (*b*) just before initiation of cleavage crack run-arrest events: test WP-2.2	68
5.11	Load history for test WP-2.2	69

Figure		Page
5.12	Fracture surface of specimen WP-2.2	70
5.13	Reduction-in-thickness contour map of specimen WP-2.2	72
5.14	Strain-gage-derived crack-front position vs time: test WP-2.2	76
5.15	Actual and ideal temperature distributions across specimen width (*a*) at start of test and (*b*) a few seconds before fracture: test WP-2.3	77
5.16	Fracture surface of specimen WP-2.3	78
5.17	Close-up of cleavage and loss-of-cleavage regions (*a*) without cleavage run-arrest events highlighted, and (*b*) with cleavage run-arrest events highlighted: test WP-2.3	79
5.18	Reduction-in-thickness contour map of specimen WP-2.3	80
5.19	Strain-gage-derived crack-front position vs time for (*a*) results for first 50 ms of test and (*b*) results for entire ~950 ms of test: test WP-2.3	83
5.20	Actual and ideal temperature distributions across specimen width at approximate time of specimen fracture: test WP-2.4	85
5.21	Load history for test WP-2.4	85
5.22	Fracture surface of specimen WP-2.4	86
5.23	Close-up of initial flaw and region of pop-in: test WP-2.4	87
5.24	Pop-in detected by strain gages 1–3 on plate front face and 13 and 14 on plate back face: test WP-2.4	88
5.25	Reduction-thickness contour map of specimen WP-2.4	89
5.26	Strain-gage-derived crack-front position vs time: test WP-2.4	89
5.27	Fracture surface of specimen WP-2.4, showing how the fracture surface was sectioned for further examination	93
5.28	A view of a portion of tip of precrack for specimen WP-2.4, Sect. 1 (Fig. 5.27)	94
5.29	Detail of ductile tearing from EB weld flaw, Sect. 1 (Fig. 5.27)	95
5.30	Apparent initiation site for first crack run-arrest event, Sect. 1 (Fig. 5.27)	96

Figure		Page
5.31	Section 2 (Fig. 5.27) showing first arrest event on part of fracture surface	97
5.32	Apparent initiation site for second crack run-arrest event, Sect. 2 (Fig. 5.27)	98
5.33	Actual and ideal temperature distributions across specimen width (*a*) at start of test, (*b*) at crack pop-in event, and (*c*) at approximate time of fracture events: test WP-2.5	100
5.34	Load history for test WP-2.5	101
5.35	Fracture surface for specimen WP-2.5	102
5.36	Close-up of fracture surface for specimen WP-2.5	103
5.37	Close-up of initial EB weld-generated crack and region of pop-in: test WP-2.5	104
5.38	Pop-in as detected by strain gages 1–3 on plate front face and 13 and 14 on plate back face: test WP-2.5	106
5.39	High-resolution strain-gage records for companion crack-line gages during pop-in event: test WP-2.5	107
5.40	High-resolution accelerometer records during the pop-in event: test WP-2.5	108
5.41	Strain-gage-derived crack-front position vs time: test WP-2.5	111
5.42	Fracture surface of specimen WP-2.5, showing how the fracture surface was sectioned for further examination	112
5.43	Precrack and initial tearing from specimen WP-2.5, Sect. A (Fig. 5.42)	113
5.44	View of apparent initiation site for first crack run-arrest event, Sect. A (Fig. 5.42)	114
5.45	First arrest location from Sect. B (Fig. 5.42)	116
5.46	Ductile tearing strip from Sect. B (Fig. 5.42) after first crack run-arrest event	117
5.47	Actual and ideal temperature distribution across specimen width during warm prestressing: test WP-2.6	118
5.48	Load vs (*a*) time, (*b*) front-face COD, and (*c*) back-face COD during warm prestressing: test WP-2.6	119
5.49	Actual and ideal temperature distributions across specimen width (*a*) at start of loading and (*b*) just before initiation of cleavage crack run-arrest events: test WP-2.6	120

Figure		Page
5.50	Load history for test WP-2.6	121
5.51	Fracture surfaces of bottom and top plate halves of specimen WP-2.6	122
5.52	Close-up of cleavage and loss-of-cleavage regions (*a*) without and (*b*) with arrest locations highlighted: test WP-2.6	123
5.53	Reduction-in-thickness contour map of specimen WP-2.6	124
5.54	Strain-gage-derived crack-front position vs time: test WP-2.6	128
6.1	Example of finite-element model used for dynamic analysis of wide-plate crack-arrest tests	131
6.2	Detail of crack-tip region from 3-D finite-element model of 102-mm-thick wide-plate specimen	132
6.3	Statically calculated crack lengths: test WP-2.4	134
6.4	Determination of arrest toughness at initiation load of 8.85 MN: test WP-2.4	135
6.5	Complete static and stability analyses for initiation load of 8.85 MN: test WP-2.4	136
6.6	Dynamic-analysis, crack-depth history: test WP-2.4	137
6.7	Dynamic factor, static toughness, quasi-static displacement-controlled factor, and crack velocity vs instantaneous crack length: test WP-2.4	138
6.8	Crack-depth history from front-face strain gages: test WP-2.4	140
6.9	Calculated stress-intensity factor vs time from generation-mode dynamic analysis (fixed-load case): test WP-2.4	140
6.10	Actual and computed strain histories for front-face crack-line gages 1–4: test WP-2.4	142
6.11	Actual and computed strain histories for crack-line gages 5, 17, 7, and 8: test WP-2.4	143
6.12	Actual and computed strain histories for front-face crack-line gages 9–12: test WP-2.4	144
6.13	Actual and generation-mode dynamic analysis computed COD at a/w = 0.15 for front-face gage (fixed-load case): test WP-2.4	145
6.14	Fixed-load, generation-mode, dynamic finite-element crack-arrest toughness results for HSST wide-plate tests	148

Figure		Page
6.15	Relationship of WP-2 series initiation and arrest events to CVN energy vs temperature curve	149
6.16	HSST wide-plate crack-arrest data (fixed-load, generation-mode dynamic finite-element calculations) show trend consistent with other large-specimen crack-arrest test results	149
A.1	Strain histories for companion crack-line gages: test WP-2.1 (gages 1–4 and 13–15)	156
A.2	Strain histories for companion crack-line gages: test WP-2.1 (gages 5–8 and 16–19)	157
A.3	Strain histories for companion crack-line gages: test WP-2.1 (gages 9–12 and 20–22)	158
A.4	Near- and far-field strain histories: test WP-2.1 (gages 23, 24, 26, and 27)	159
A.5	Strain histories for gages 1–4 showing crack passing under strain gage 1 and arresting before reaching strain gage 2: test WP-2.1	160
A.6	Strain histories for gages 2–5 showing crack passing under strain gages 2 and 3, arresting momentarily before passing under strain gage 4, and arresting before passing under gage 5: test WP-2.1	161
A.7	Strain histories for gages 2–5 showing momentary arrest between gages 3 and 4: test WP-2.1	162
A.8	Twenty-millisecond records of strain gages 4–7 showing previous crack run-arrest events and crack passing under gage 5 and arresting before reaching gages 6 and 7: test WP-2.1	163
A.9	Fifty-millisecond records of strain gages 5–8 showing fibrous tearing after a cleavage arrest just past gage 5, followed by cleavage fracture, reinitiation just past gage 6, another arrest, and cleavage fracture reinitiation that passes under gage 8 and arrests: test WP-2.1	164
A.10	Strain histories of gages 9–12 showing fibrous tearing past these gages: test WP-2.1	165
A.11	Strain histories for gages 13–16 showing crack passing under gages 13 and 14 before arresting before gage 15: test WP-2.1	166
A.12	Strain histories for gages 15–18 showing crack passing under gage 15, reinitiating, passing under gage 16, arresting, reinitiating, passing under gage 17, arresting, reinitiating, and passing under gage 18: test WP-2.1	167

Figure		Page
A.13	Strain histories for gages 19–22 showing fibrous tearing past these gages: test WP-2.1	168
A.14	AE results for various time resolutions: test WP-2.1	169
A.15	Longitudinal acceleration results at various time resolutions measured by top and bottom "damped" accelerometers mounted 3.653 m above and 3.655 m below crack plane, respectively: test WP-2.1	171
A.16	Front and back COD histories obtained from gages mounted at a/w = 0.15: test WP-2.1	172
A.17	Strain histories for companion crack-line gages showing cleavage crack passing these gages: test WP-2.2 (gages 1, 2, and 13)	173
A.18	Strain histories for companion crack-line gages showing cleavage crack passing these gages: test WP-2.2 (gages 3, 4, 15, and 16)	174
A.19	Strain histories for companion crack-line gages showing cleavage crack propogating past gages 5 and 17 and arresting just past gages 6 and 18: test WP-2.2	175
A.20	Strain histories for companion crack-line gages showing cleavage crack passing these gages followed by cleavage crack run-arrest events: test WP-2.2 (gages 7, 8, 19, and 20)	176
A.21	Strain histories for front-face crack-line gages showing arrest of cleavage crack propagation past gage 9 with subsequent fibrous crack propagation past gages 10–12: test WP-2.2	177
A.22	Strain history for near-field gage 21 (*a*) during cleavage run-arrest events and (*b*) during entire fracture process: test WP-2.2	178
A.23	Strain histories for far-field gages 22–25 during cleavage run-arrest events: test WP-2.2	179
A.24	Strain histories for far-field gages 22–25 during entire fracture process: test WP-2.2	180
A.25	Front- and back-face COD histories at two time resolutions: test WP-2.2	181
A.26	Dynamic displacement and longitudinal acceleration histories at two time resolutions: test WP-2.2	182
A.27	Strain histories for companion crack-line gages: test WP-2.3 (gages 1–4 and 13–15)	184
A.28	Strain histories for companion crack-line gages: test WP-2.3 (gages 5–8 and 16–19)	185

Figure		Page
A.29	Strain histories for companion crack-line gages: test WP-2.3 (gages 9-12 and 20-22)	186
A.30	Crack run-arrest events as detected by near- and far-field strain gages: test WP-2.3 (gages 24, 26, and 27)	187
A.31	Strain histories for gages 1-4 showing crack passing under gages 1 and 2 and arresting before reaching gages 3 and 4: test WP-2.3	188
A.32	Strain histories for gages 1-4 showing reinitiation of crack propagation as detected by gages 1 and 2 and crack passing gage 3 with a subsequent arrest before reaching gage 4: test WP-2.3	189
A.33	Strain histories for gages 5-8 showing propagation of the crack past gage 5, a subsequent arrest before reaching gage 6, and reinitiation with the crack propagating past gages 6-8: test WP-2.3	190
A.34	Strain histories for gages 5-8 showing crack passing gages 6-8: test WP-2.3	191
A.35	Strain histories for gages 9-12 showing crack passing these gages: test WP-2.3	192
A.36	Strain histories for back-face gages 13-15 showing crack passing gages 13 and 14 and then arresting before reaching gage 15: test WP-2.3	193
A.37	Strain histories for back-face gages 13-15 showing multiple crack run-arrest events: test WP-2.3	194
A.38	Strain histories for back-face gages 17 and 18 showing early crack run-arrest events followed much later by crack passing gage 18: test WP-2.3	195
A.39	Strain histories for back-face gages 19-22 showing propagation of crack past these gages: test WP-2.3	196
A.40	Longitudinal acceleration results at two levels of time resolution measured by top and bottom "damped" accelerometers mounted 3.585 m above and 3.589 m below the crack plane, respectively: test WP-2.3	197
A.41	Bottom displacement gage results (*a*) during initial crack run-arrest events and (*b*) during entire test: test WP-2.3	198
A.42	COD gage results during initial crack run-arrest events: test WP-2.3	199
A.43	AE results for various time resolutions: test WP-2.3	200

Figure		Page
A.44	Strain histories for companion crack-line gages: test WP-2.4 (gages 1-4 and 13-15)	202
A.45	Strain histories for companion crack-line gages: test WP-2.4 (gages 5-8 and 16-19)	203
A.46	Strain histories for companion crack-line gages: test WP-2.4 (gages 9-12 and 20-22)	204
A.47	Initiation of first crack run-arrest event as detected by strain gage 1 for two time resolutions: test WP-2.4	205
A.48	Propagation of crack during first crack run-arrest event as detected by companion crack-line gages 2 and 3 and 13 and 14: test WP-2.4	206
A.49	Arrest and reinitiation of crack propagation as detected by companion crack-line gages 4 and 15 at two levels of time resolution: test WP-2.4	207
A.50	Additional crack run-arrest events as detected by companion crack-line gages 5 and 6 and 16 and 17: test WP-2.4	208
A.51	Additional crack run-arrest events as detected by companion crack-line gages 7 and 8 and 18 and 19: test WP-2.4	209
A.52	Ductile tearing as detected by companion crack-line gages 9 and 10 and 20 and 21: test WP-2.4	210
A.53	Ductile tearing as detected by crack-line gages 11, 12, and 22: test WP-2.4	211
A.54	Crack run-arrest events as monitored by near-field strain gages 23 and 25 and far-field strain gages 26 and 27: test WP-2.4	212
A.55	AE results at different levels of time resolutions: test WP-2.4	213
A.56	Longitidual acceleration during test measured by "damped" accelerometer mounted 4.041 m below crack plane: test WP-2.4	214
A.57	Longitidual acceleration during test measured by "shock" accelerometer mounted 4.038 m below crack plane: test WP-2.4	215
A.58	Front- and back-face COD at various time spans after fracture initiation: test WP-2.4	216
A.59	Strain histories for companion crack-line gages: test WP-2.5 (gages 1-4 and 13-15)	217
A.60	Strain histories for companion crack-line gages: test WP-2.5 (gages 5-8 and 16-19)	218

Figure		Page
A.61	Strain histories for companion crack-line gages: test WP-2.5 (gages 9–12 and 20–22)	219
A.62	Near- and far-field strain histories: test WP-2.5 (gages 23, 24, 26, and 27)	220
A.63	Strain histories for front-face gages 1–3, indicating that crack passes gages 1 and 2 and arrests before reaching gage 3 ($t = 0.344$ ms): test WP-2.5	221
A.64	Strain histories for front-face gages 5, 6, 9, and 10 indicating multiple crack run-arrest events (see Table 5.6): test WP-2.5	222
A.65	Strain histories for back-face gages 13–15 indicating that crack passes gages 13 and 14 with a subsequent arrest ($t = 0.54$ ms) before reaching gage 15: test WP-2.5	223
A.66	Strain histories for back-face gages 15–18, indicating that crack passes gages 15 and 16, arrests ($t = 8.16$ ms) before reaching gage 17, reinitiates ($t = 11.16$ ms), passes under gage 17, arrests ($t = 11.49$ ms) before reaching gage 18, reinitiates ($t = 19.11$ ms), and then passes under gage 18: test WP-2.5	224
A.67	Strain histories for back-face gages 19–22 showing crack passing gage 19, arresting ($t = 27.95$ ms), converting to fibrous tearing, and then passing under gages 20–22: test WP-2.5	225
A.68	Accelerometer outputs during first crack run-arrest event: test WP-2.5	227
A.69	Front- and back-face CODs during the fracture event: test WP-2.5	228
A.70	Strain histories for front-face crack-line gages: test WP-2.6 (gages 1–4)	229
A.71	Strain histories for front-face crack-line gages: test WP-2.6 (gages 5–8)	230
A.72	Strain histories for front-face crack-line gages: test WP-2.6 (gages 9–12)	231
A.73	Strain histories for back-face crack-line gages: test WP-2.6 (gages 13–16)	232
A.74	Strain histories for back-face crack-line gages: test WP-2.6 (gages 17–20)	233
A.75	Strain history for near-field gage 21 at two time resolutions: test WP-2.6	234

Figure		Page
A.76	Strain histories for far-field gages 22–25 during entire fracture process: test WP-2.6	235
A.77	Front- and back-face COD histories at two time resolutions: test WP-2.6	237
A.78	Longitudinal acceleration (at two levels of time resolution) measured by top and bottom "damped" accelerometers mounted 3.491 m above and 3.398 m below crack plane, respectively: test WP-2.6	238
A.79	Dynamic displacement history at two levels of time resolution of a point 3.393 m below the crack plane during (*a*) cleavage crack run-arrest events and (*b*) entire fracture: test WP-2.6	239
B.1	K vs time results from linear generation-mode analyses: test WP-2.4	242
B.2	CMOD from linear generation-mode analyses: test WP-2.4	242
B.3	Acceleration vs time data measured by "damped" accelerometer near the lower load point: test WP-2.4	244
B.4	Influence of test frame inertia on computed K vs time: test WP-2.4	246
B.5	Influence of test frame inertia on computed CMOD: test WP-2.4	246
B.6	Influence of test frame inertia on computed load-point axial displacement: test WP-2.4	247
B.7	Computed nodal accelerations at "damped" accelerometer location near lower load point (linearly elastic fixed-load analysis, lumped mass at load point): test WP-2.4	247
B.8	Computed nodal accelerations at load point (linearly elastic fixed-load analysis, lumped mass at load point): test WP-2.4	248
B.9	Computed velocities at load point (linearly elastic fixed-load analysis, lumped mass at load point): test WP-2.4	248
B.10	Effect of analysis method and boundary condition on calculated crack-arrest toughness values for test WP-2.4	250
C.1	Idealization of crack tunneling in (*a*) low-toughness and (*b*) high-toughness material (Ref. C.3)	254

Figure		Page
C.2	Illustration of superposition principle for determining the stress-intensity factor (Ref. C.3)	254
C.3	Smith's model for restraining effect of ligaments (Ref. C.4)	256
C.4	Extension of Smith's approach to triangular ligament geometry	257
C.5	Comparison of Popelar's and Smith's tunneling correction approaches for parabolic and triangular ligament geometrics	259
C.6	Fracture surface of WP-1 series specimens	261
C.7	Corrected crack-arrest toughness vs temperature for WP-1 test series	262

LIST OF TABLES

Table		Page
3.1	Results of drop-weight testing on 2 1/4 Cr-1 Mo material from 1/2t depth of broken halves of specimens WP-2.1 and -2.5 (T-L orientation)	10
3.2	Charpy impact test results for 2 1/4 Cr-1 Mo material from broken halves of specimens WP-2.1 and -2.5 (T-L orientation)	12
3.3	Curve-fit parameters of CVN impact energy: WP-2 series material (T-L orientation)	14
3.4	Curve-fit parameters of CVN impact energy: PTC1 characterization block (T-L orientation)	14
3.5	Summary of results for drop-weight and CVN impact tests: broken halves of WP-2.1 and WP-2.5 specimens and PTC1 characterization block	15
3.6	Tensile properties of transverse-oriented specimens machined from broken halves of specimens WP-2.1 and -2.5	16
3.7	Tensile properties of specimens machined transverse to rolling direction of material from characterization block PTC1	17
3.8	Crack-arrest toughness data from specimens WP-2.1 and -2.5 material for both weld-embrittled and duplex specimens in T-L orientation	20
3.9	Crack-arrest (K_a) data for PTC1 material (T-L orientation)	21
3.10	Transition region fracture-toughness results from posttest characterization using 25-mm C(T) specimens (1/2t) machined from broken halves of specimens WP-2.1 and -2.5 (T-L orientation)	26
3.11	Ductile-shelf fracture-toughness results from posttest characterization using 25-mm C(T) specimens (1/2t) machined from broken half of specimen WP-2.5 (T-L orientation)	28
4.1	WP-2 series test specimen dimensions	35
4.2	Presence and location of accelerometer and dynamic displacement instrumentation used in WP-2 series tests	50
5.1	Summary of HSST wide-plate crack-arrest test conditions and results for specially heat treated 2 1/4 Cr-1 Mo steel: WP-2 series	55

Table		Page
5.2	Crack position vs time and velocity: test WP-2.1	63
5.3	Crack position vs time and velocity: test WP-2.2	73
5.4	Crack position vs time and velocity: test WP-2.3	81
5.5	Crack position vs time and velocity: test WP-2.4	90
5.6	Crack position vs time and velocity: test WP-2.5	109
5.7	Crack position vs time and velocity: test WP-2.6	125
6.1	Summary of WPSTAT results for WP-2 series tests	135
6.2	Summary of application-mode dynamic analyses for WP-2 series tests	139
6.3	Summary of generation-mode (fixed-load) dynamic analysis results for test WP-2.4	141
6.4	Summary of HSST wide-plate crack-arrest test conditions and crack-arrest toughness values for specially heat-treated 2 1/4 Cr-1 Mo steel: WP-2 series	146
B.1	Summary of computed results for test WP-2.4	243
B.2	Computed crack-arrest toughness values for wide-plate crack-arrest test WP-2.4	249
C.1	Ligament geometry parameters for WP-1 test series specimens	260
C.2	Corrections for tunneling effects in WP-1 test series	260

FOREWORD

The work reported here was performed at Oak Ridge National Laboratory under the Heavy-Section Steel Technology (HSST) Program, W. E. Pennell, Program Manager. The program is sponsored by the Office of Nuclear Regulatory Research of the U.S. Nuclear Regulatory Commission (NRC). The technical monitor for the NRC is M. E. Mayfield.

This report is designated HSST Report 103. Prior and future reports in this series are listed below.

1. S. Yukawa, *Evaluation of Periodic Proof Testing and Warm Prestressing Procedures for Nuclear Reactor Vessels*, HSSTP-TR-1, General Electric Company, Schenectady, N.Y. (July 1, 1969).
2. L. W. Loechel, *The Effect of Testing Variables on the Transition Temperature in Steel*, MCR-69-189, Martin Marietta Corporation, Denver, Colo. (November 20, 1969).
3. P. N. Randall, *Gross Strain Measure of Fracture Toughness of Steels*, HSSTP-TR-3, TRW Systems Group, Redondo Beach, Calif. (November 1, 1969).
4. C. Visser, S. E. Gabrielse, and W. VanBuren, *A Two-Dimensional Elastic-Plastic Analysis of Fracture Test Specimens*, WCAP-7368, Westinghouse Electric Corporation, PWR Systems Division, Pittsburgh, Pa. (October 1969).
5. T. R. Mager and F. O. Thomas, *Evaluation by Linear Elastic Fracture Mechanics of Radiation Damage to Pressure Vessel Steels*, WCAP-7328 (Rev.), Westinghouse Electric Corporation, PWR Systems Division, Pittsburgh, Pa. (October 1969).
6. W. O. Shabbits, W. H. Pryle, and E. T. Wessel, *Heavy-Section Fracture Toughness Properties of A533 Grade B Class 1 Steel Plate and Submerged Arc Weldment*, WCAP-7414, Westinghouse Electric Corporation, PWR Systems Division, Pittsburgh, Pa. (December 1969).
7. F. J. Loss, *Dynamic Tear Test Investigations of the Fracture Toughness of Thick-Section Steel*, NRL-7056, Naval Research Laboratory, Washington, D.C. (May 14, 1970).
8. P. B. Crosley and E. J. Ripling, *Crack Arrest Fracture Toughness of A533 Grade B Class 1 Pressure Vessel Steel*, HSSTP-TR-8, Materials Research Laboratory, Inc., Glenwood, Ill. (March 1970).
9. T. R. Mager, *Post-Irradiation Testing of 2T Compact Tension Specimens*, WCAP-7561, Westinghouse Electric Corporation, PWR Systems Division, Pittsburgh, Pa. (August 1970).
10. T. R. Mager, *Fracture Toughness Characterization Study of A533, Grade B, Class 1 Steel*, WCAP-7578, Westinghouse Electric Corporation, PWR Systems Division, Pittsburgh, Pa. (October 1970).
11. T. R. Mager, *Notch Preparation in Compact Tension Specimens*, WCAP-7579, Westinghouse Electric Corporation, PWR Systems Division, Pittsburgh, Pa. (November 1970).

12. N. Levy and P. V. Marcal, *Three-Dimensional Elastic-Plastic Stress and Strain Analysis for Fracture Mechanics, Phase I: Simple Flawed Specimens*, HSSTP-TR-12, Brown University, Providence, R.I. (December 1970).

13. W. O. Shabbits, *Dynamic Fracture Toughness Properties of Heavy Section A533 Grade B Class 1 Steel Plate*, WCAP-7623, Westinghouse Electric Corporation, PWR Systems Division, Pittsburgh, Pa. (December 1970).

14. P. N. Randall, *Gross Strain Crack Tolerance of A 533-B Steel*, HSSTP-TR-14, TRW Systems Group, Redondo Beach, Calif. (May 1, 1971).

15. H. T. Corten and R. H. Sailors, *Relationship Between Material Fracture Toughness Using Fracture Mechanics and Transition Temperature Tests*, T&AM Report 346, University of Illinois, Urbana, Ill. (August 1, 1971).

16. T. R. Mager and V. J. McLaughlin, *The Effect of an Environment of High Temperature Primary Grade Nuclear Reactor Water on the Fatigue Crack Growth Characteristics of A533 Grade B Class 1 Plate and Weldment Material*, WCAP-7776, Westinghouse Electric Corporation, PWR Systems Division, Pittsburgh, Pa. (October 1971).

17. N. Levy and P. V. Marcal, *Three-Dimensional Elastic-Plastic Stress and Strain Analysis for Fracture Mechanics, Phase II: Improved Modelling*, HSSTP-TR-17, Brown University, Providence, R.I. (November 1971).

18. S. C. Grigory, *Tests of 6-in.-Thick Flawed Tensile Specimens, First Technical Summary Report, Longitudinal Specimens Numbers 1 Through 7*, HSSTP-TR-18, Southwest Research Institute, San Antonio, Tex. (June 1972).

19. P. N. Randall, *Effects of Strain Gradients on the Gross Strain Crack Tolerance of A533-B Steel*, HSSTP-TR-19, TRW Systems Group, Redondo Beach, Calif. (June 15, 1972).

20. S. C. Grigory, *Tests of 6-Inch-Thick Flawed Tensile Specimens, Second Technical Summary Report, Transverse Specimens Numbers 8 Through 10, Welded Specimens Numbers 11 Through 13*, HSSTP-TR-20, Southwest Research Institute, San Antonio, Tex. (June 1972).

21. L. A. James and J. A. Williams, *Heavy Section Steel Technology Program Technical Report No. 21, The Effect of Temperature and Neutron Irradiation Upon the Fatigue-Crack Propagation Behavior of ASTM A533 Grade B, Class 1 Steel*, HEDL-TME 72-132, Hanford Engineering Development Laboratory, Richland, Wash. (September 1972).

22. S. C. Grigory, *Tests of 6-Inch-Thick Flawed Tensile Specimens, Third Technical Summary Report, Longitudinal Specimens Numbers 14 Through 16, Unflawed Specimen Number 17*, HSSTP-TR-22, Southwest Research Institute, San Antonio, Tex. (October 1972).

23. S. C. Grigory, *Tests of 6-Inch-Thick Tensile Specimens, Fourth Technical Summary Report, Tests of 1-Inch-Thick Flawed Tensile*

Specimens for Size Effect Evaluation, HSSTP-TR-23, Southwest Research Institute, San Antonio, Tex. (June 1973).

24. S. P. Ying and S. C. Grigory, *Tests of 6-Inch-Thick Tensile Specimens, Fifth Technical Summary Report, Acoustic Emission Monitoring of One-Inch and Six-Inch-Thick Tensile Specimens*, HSSTP-TR-24, Southwest Research Institute, San Antonio, Tex. (November 1972).

25. R. W. Derby, J. G. Merkle, G. C. Robinson, G. D. Whitman, and F. J. Witt, *Test of 6-Inch-Thick Pressure Vessels. Series 1: Intermediate Test Vessels V-1 and V-2*, ORNL-4895, Oak Ridge National Laboratory, Oak Ridge, Tenn. (February 1974).

26. W. J. Stelzman and R. G. Berggren, *Radiation Strengthening and Embrittlement in Heavy Section Steel Plates and Welds*, ORNL-4871, Oak Ridge National Laboratory, Oak Ridge, Tenn. (June 1973).

27. P. B. Crosley and E. J. Ripling, *Crack Arrest in an Increasing K-Field*, HSSTP-TR-27, Materials Research Laboratory, Inc., Glenwood, Ill. (January 1973).

28. P. V. Marcal, P. M. Stuart, and R. S. Bettes, *Elastic-Plastic Behavior of a Longitudinal Semi-Elliptic Crack in a Thick Pressure Vessel*, HSSTP-TR-28, Brown University, Providence, R.I. (June 1973).

29. W. J. Stelzman, R. G. Berggren, and T. N. Jones, *ORNL Characterization of Heavy-Section Steel Technology Program Plates 01, 02 and 03*, NUREG/CR-4092 (ORNL/TM-9491), Oak Ridge National Laboratory, Oak Ridge, Tenn. (April 1985).

30. Canceled.

31. J. A. Williams, *The Irradiation and Temperature Dependence of Tensile and Fracture Properties of ASTM A533, Grade B, Class 1 Steel Plate and Weldment*, HEDL-TME 73-75, Hanford Engineering Development Laboratory, Richland, Wash. (August 1973).

32. J. M. Steichen and J. A. Williams, *High Strain Rate Tensile Properties of Irradiated ASTM A533 Grade B Class 1 Pressure Vessel Steel*, Hanford Engineering Development Laboratory, Richland, Wash. (July 1973).

33. P. C. Riccardella and J. L. Swedlow, *A Combined Analytical-Experimental Fracture Study of the Two Leading Theories of Elastic-Plastic Fracture (J-Integral and Equivalent Energy)*, WCAP-8224, Westinghouse Electric Corporation, Pittsburgh, Pa. (October 1973).

34. R. J. Podlasek and R. J. Eiber, *Final Report on Investigation of Mode III Crack Extension in Reactor Piping*, Battelle Columbus Laboratories, Columbus, Ohio (December 14, 1973).

35. T. R. Mager, J. D. Landes, D. M. Moon, and V. J. McLaughlin, *Interim Report on the Effect of Low Frequencies on the Fatigue Crack Growth Characteristics of A533 Grade B Class 1 Plate in an Environment of High-Temperature Primary Grade Nuclear Reactor Water*, WCAP-8256, Westinghouse Electric Corporation, Pittsburgh, Pa. (December 1973).

36. J. A. Williams, *The Irradiated Fracture Toughness of ASTM A533, Grade B, Class 1 Steel Measured with a Four-Inch-Thick Compact Tension Specimen*, HEDL-TME 75-10, Hanford Engineering Development Laboratory, Richland, Wash. (January 1975).

37. R. H. Bryan, J. G. Merkle, M. N. Raftenberg, G. C. Robinson, and J. E. Smith, *Test of 6-Inch-Thick Pressure Vessels. Series 2: Intermediate Test Vessels V-3, V-4, and V-6*, ORNL-5059, Oak Ridge National Laboratory, Oak Ridge, Tenn. (November 1975).

38. T. R. Mager, S. E. Yanichko, and L. R. Singer, *Fracture Toughness Characterization of HSST Intermediate Pressure Vessel Material*, WCAP-8456, Westinghouse Electric Corporation, Pittsburgh, Pa. (December 1974).

39. J. G. Merkle, G. D. Whitman, and R. H. Bryan, *An Evaluation of the HSST Program Intermediate Pressure Vessel Tests in Terms of Light-Water-Reactor Pressure Vessel Safety*, ORNL/TM-5090, Oak Ridge National Laboratory, Oak Ridge, Tenn. (November 1975).

40. J. G. Merkle, G. C. Robinson, P. P. Holz, J. E. Smith, and R. H. Bryan, *Test of 6-In.-Thick Pressure Vessels. Series 3: Intermediate Test Vessel V-7*, ORNL/NUREG-1, Oak Ridge National Laboratory, Oak Ridge, Tenn. (August 1976).

41. J. A. Davidson, L. J. Ceschini, R. P. Shogan, and G. V. Rao, *The Irradiated Dynamic Fracture Toughness of ASTM A533, Grade B, Class 1 Steel Plate and Submerged Arc Weldment*, WCAP-8775, Westinghouse Electric Corporation, Pittsburgh, Pa. (October 1976).

42. R. D. Cheverton, *Pressure Vessel Fracture Studies Pertaining to a PWR LOCA-ECC Thermal Shock: Experiments TSE-1 and TSE-2*, ORNL/NUREG/TM-31, Oak Ridge National Laboratory, Oak Ridge, Tenn. (September 1976).

43. J. G. Merkle, G. C. Robinson, P. P. Holz, and J. E. Smith, *Test of 6-In.-Thick Pressure Vessels. Series 4: Intermediate Test Vessels V-5 and V-9 with Inside Nozzle Corner Cracks*, ORNL/NUREG-7, Oak Ridge National Laboratory, Oak Ridge, Tenn. (August 1977).

44. J. A. Williams, *The Ductile Fracture Toughness of Heavy Section Steel Plate*, NUREG/CR-0859, Hanford Engineering Development Laboratory, Richland, Wash. (September 1979).

45. R. H. Bryan, T. M. Cate, P. P. Holz, T. A. King, J. G. Merkle, G. C. Robinson, G. C. Smith, J. E. Smith, and G. D. Whitman, *Test of 6-in.-Thick Pressure Vessels. Series 3: Intermediate Test Vessel V-7A Under Sustained Loading*, ORNL/NUREG-9, Oak Ridge National Laboratory, Oak Ridge, Tenn. (February 1978).

46. R. D. Cheverton and S. E. Bolt, *Pressure Vessel Fracture Studies Pertaining to a PWR LOCA-ECC Thermal Shock: Experiments TSE-3 and TSE-4 and Update of TSE-1 and TSE-2 Analysis*, ORNL/NUREG-22, Oak Ridge National Laboratory, Oak Ridge, Tenn. (December 1977).

47. D. A. Canonico, *Significance of Reheat Cracks to the Integrity of Pressure Vessels for Light-Water Reactors*, ORNL/NUREG-15, Oak Ridge National Laboratory, Oak Ridge, Tenn. (July 1977).

48. G. C. Smith and P. P. Holz, *Repair Weld Induced Residual Stresses in Thick-Walled Steel Pressure Vessels*, NUREG/CR-0093 (ORNL/NUREG/TM-153), Oak Ridge National Laboratory, Oak Ridge, Tenn. (June 1978).

49. P. P. Holz and S. W. Wismer, *Half-Bead (Temper) Repair Welding for HSST Vessels*, NUREG/CR-0113 (ORNL/NUREG/TM-177), Oak Ridge National Laboratory, Oak Ridge, Tenn. (June 1978).

50. G. C. Smith, P. P. Holz, and W. J. Stelzman, *Crack Extension and Arrest Tests of Axially Flawed Steel Model Pressure Vessels*, NUREG/CR-0126 (ORNL/NUREG/TM-196), Oak Ridge National Laboratory, Oak Ridge, Tenn. (October 1978).

51. R. H. Bryan, P. P. Holz, J. G. Merkle, G. C. Smith, J. E. Smith, and W. J. Stelzman, *Test of 6-in.-Thick Pressure Vessels. Series 3: Intermediate Test Vessel V-7B*, NUREG/CR-0309 (ORNL/NUREG-38), Oak Ridge National Laboratory, Oak Ridge, Tenn. (October 1978).

52. R. D. Cheverton, S. K. Iskander, and S. E. Bolt, *Applicability of LEFM to the Analysis of PWR Vessels Under LOCA-ECC Thermal Shock Conditions*, NUREG/CR-0107 (ORNL/NUREG-40), Oak Ridge National Laboratory, Oak Ridge, Tenn. (October 1978).

53. R. H. Bryan, D. A. Canonico, P. P. Holz, S. K. Iskander, J. G. Merkle, J. E. Smith, and W. J. Stelzman, *Test of 6-in.-Thick Pressure Vessels, Series 3: Intermediate Test Vessel V-8*, NUREG/CR-0675 (ORNL/NUREG-58), Oak Ridge National Laboratory, Oak Ridge, Tenn. (December 1979).

54. R. D. Cheverton and S. K. Iskander, *Application of Static and Dynamic Crack Arrest Theory to TSE-4*, NUREG/CR-0767 (ORNL/NUREG-57), Oak Ridge National Laboratory, Oak Ridge, Tenn. (June 1979).

55. J. A. Williams, *Tensile Properties of Irradiated and Unirradiated Welds of A533 Steel Plate and A508 Forgings*, NUREG/CR-1158 (ORNL/Sub/79-50917/2), Hanford Engineering Development Laboratory, Richland, Wash. (July 1979).

56. K. W. Carlson and J. A. Williams, *The Effect of Crack Length and Side Grooves on the Ductile Fracture Toughness Properties of ASTM A533 Steel*, NUREG/CR-1171 (ORNL/Sub/79-50917/3), Hanford Engineering Development Laboratory, Richland, Wash. (October 1979).

57. P. P. Holz, *Flaw Preparations for HSST Program Vessel Fracture Mechanics Testing; Mechanical-Cyclic Pumping and Electron-Beam Weld-Hydrogen Charge Cracking Schemes*, NUREG/CR-1274 (ORNL/NUREG/TM-369), Oak Ridge National Laboratory, Oak Ridge, Tenn. (May 1980).

58. S. K. Iskander, *Two Finite Element Techniques for Computing Mode I Stress Intensity Factors in Two- or Three-Dimensional Problems*, NUREG/CR-1499 (ORNL/NUREG/CSD/TM-14), Computer Sciences Division, Union Carbide Corp. Nuclear Division, Oak Ridge, Tenn. (February 1981).

59. P. B. Crosley and E. J. Ripling, *Development of a Standard Test for Measuring K_{Ia} with a Modified Compact Specimen*, NUREG/CR-2294 (ORNL/Sub/81-7755/1), Materials Research Laboratory, Glenwood, Ill. (August 1981).

60. S. N. Atluri, B. R. Bass, J. W. Bryson, and K. Kathiresan, *NOZ-FLAW: A Finite Element Program for Direct Evaluation of Stress Intensity Factors for Pressure Vessel Nozzle-Corner Flaws*, NUREG/CR-1843 (ORNL/NUREG/CSD/TM-18), Computer Sciences Division, Oak Ridge Gaseous Diffusion Plant, Oak Ridge, Tenn. (March 1981).

61. A. Shukla, W. L. Fourney, and G. R. Irwin, *Study of Energy Loss and Its Mechanisms in Homalite 100 During Crack Propagation and Arrest*, NUREG/CR-2150 (ORNL/Sub/79-7778/1), University of Maryland, College Park, Md. (August 1981).

62. S. K. Iskander, R. D. Cheverton, and D. G. Ball, *OCA-I, A Code for Calculating the Behavior of Flaws on the Inner Surface of a Pressure Vessel Subjected to Temperature and Pressure Transients*, NUREG/CR-2113 (ORNL/NUREG-84), Oak Ridge National Laboratory, Oak Ridge, Tenn. (August 1981).

63. R. J. Sanford, R. Chona, W. L. Fourney, and G. R. Irwin, *A Photoelastic Study of the Influence of Non-Singular Stresses in Fracture Test Specimens*, NUREG/CR-2179 (ORNL/Sub/79-7778/2), University of Maryland, College Park, Md. (August 1981).

64. B. R. Bass, S. N. Atluri, J. W. Bryson, and K. Kathiresan, *OR-FLAW: A Finite Element Program for Direct Evaluation of K-Factors for User-Defined Flaws in Plate, Cylinders, and Pressure-Vessel Nozzle Corners*, NUREG/CR-2494 (ORNL/CSD/TM-165), Oak Ridge National Laboratory, Oak Ridge, Tenn. (April 1982).

65. B. R. Bass and J. W. Bryson, *ORMGEN-3D: A Finite Element Mesh Generator for 3-Dimensional Crack Geometries*, NUREG/CR-2997, Vol. 1 (ORNL/TM-8527/V1), Oak Ridge National Laboratory, Oak Ridge, Tenn. (December 1982).

66. B. R. Bass and J. W. Bryson, *ORVIRT: A Finite Element Program for Energy Release Rate Calculations for 2-Dimensional and 3-Dimensional Crack Models*, NUREG/CR-2997, Vol. 2 (ORNL/TM-8527/V2), Oak Ridge National Laboratory, Oak Ridge, Tenn. (February 1983).

67. R. D. Cheverton, S. K. Iskander, and D. G. Ball, *PWR Pressure Vessel Integrity During Overcooling Accidents: A Parametric Analysis*, NUREG/CR-2895 (ORNL/TM-7931), Oak Ridge National Laboratory, Oak Ridge, Tenn. (February 1983).

68. D. G. Ball, R. D. Cheverton, J. B. Drake, and S. K. Iskander, *OCA-II, A Code for Calculating Behavior of 2-D and 3-D Surface Flaws in a Pressure Vessel Subjected to Temperature and Pressure Transients*, NUREG/CR-3491 (ORNL-5934), Oak Ridge National Laboratory, Oak Ridge, Tenn. (February 1984).

69. A. Sauter, R. D. Cheverton, and S. K. Iskander, *Modification of OCA-I for Application to a Reactor Pressure Vessel with Cladding on the Inner Surface*, NUREG/CR-3155 (ORNL/TM-8649), Oak Ridge National Laboratory, Oak Ridge, Tenn. (May 1983).

70. R. D. Cheverton and D. G. Ball, *OCA-P, A Deterministic and Probabilistic Fracture-Mechanics Code for Application to Pressure Vessels*, NUREG/CR-3618 (ORNL-5991), Oak Ridge National Laboratory, Oak Ridge, Tenn. (May 1984).

71. J. G. Merkle, *An Examination of the Size Effects and Data Scatter Observed in Small Specimen Cleavage Fracture Toughness Testing*, NUREG/CR-3672 (ORNL/TM-9088), Oak Ridge National Laboratory, Oak Ridge, Tenn. (April 1984).

72. C. E. Pugh et al., *Heavy-Section Steel Technology Program — Five-Year Plan FY 1983–1987*, NUREG/CR-3595 (ORNL/TM-9008), Oak Ridge National Laboratory, Oak Ridge, Tenn. (April 1984).

73. D. G. Ball, B. R. Bass, J. W. Bryson, R. D. Cheverton, and J. B. Drake, *Stress Intensity Factor Influence Coefficients for Surface Flaws in Pressure Vessels*, NUREG/CR-3723 (ORNL/CSD/TM-216), Oak Ridge National Laboratory, Oak Ridge, Tenn. (February 1985).

74. W. R. Corwin, R. G. Berggren, and R. K. Nanstad, *Charpy Toughness and Tensile Properties of Neutron Irradiated Stainless Steel Submerged-Arc Weld Cladding Overlay*, NUREG/CR-3927 (ORNL/TM-9309), Oak Ridge National Laboratory, Oak Ridge, Tenn. (September 1984).

75. C. W. Schwartz, R. Chona, W. L. Fourney, and G. R. Irwin, *SAMCR: A Two-Dimensional Dynamic Finite Element Code for the Stress Analysis of Moving CRacks*, NUREG/CR-3891 (ORNL/Sub/79-7778/3), University of Maryland, College Park, Md. (November 1984).

76. W. R. Corwin, G. C. Robinson, R. K. Nanstad, J. G. Merkle, R. G. Berggren, G. M. Goodwin, R. L. Swain, and T. D. Owings, *Effects of Stainless Steel Weld Overlay Cladding on the Structural Integrity of Flawed Steel Plates in Bending, Series 1*, NUREG/CR-4015 (ORNL/TM-9390), Oak Ridge National Laboratory, Oak Ridge, Tenn. (April 1985).

77. R. H. Bryan, B. R. Bass, S. E. Bolt, J. W. Bryson, D. P. Edmonds, R. W. McCulloch, J. G. Merkle, R. K. Nanstad, G. C. Robinson, K. R. Thoms, and G. D. Whitman, *Pressurized-Thermal-Shock Test of 6-in.-Thick Pressure Vessels. PTSE-1: Investigation of Warm Prestressing and Upper-Shelf Arrest*, NUREG/CR-4106 (ORNL-6135), Oak Ridge National Laboratory, Oak Ridge, Tenn. (April 1985).

78. R. D. Cheverton, D. G. Ball, S. E. Bolt, S. K. Iskander, and R. K. Nanstad, *Pressure Vessel Fracture Studies Pertaining to the PWR Thermal-Shock Issue: Experiments TSE-5, TSE-5A, and TSE-6*, NUREG/CR-4249 (ORNL-6163), Martin Marietta Energy Systems, Inc., Oak Ridge National Laboratory, Oak Ridge, Tenn. (June 1985).

79. R. D. Cheverton, D. G. Ball, S. E. Bolt, S. K. Iskander, and R. K. Nanstad, *Pressure Vessel Fracture Studies Pertaining to the PWR Thermal-Shock Issue: Experiment TSE-7*, NUREG/CR-4304 (ORNL-6177), Martin Marietta Energy Systems, Inc., Oak Ridge National Laboratory, Oak Ridge, Tenn. (August 1985).

80. R. H. Bryan, B. R. Bass, S. E. Bolt, J. W. Bryson, J. G. Merkle, R. K. Nanstad, and G. C. Robinson, *Test of 6-in.-Thick Pressure Vessels. Series 3: Intermediate Test Vessel V-8A — Tearing*

Behavior of Low Upper-Shelf Material, NUREG/CR-4760 (ORNL-6187), Martin Marietta Energy Systems, Inc., Oak Ridge National Laboratory, Oak Ridge, Tenn. (May 1987).

81. R. D. Cheverton and D. G. Ball, *A Parametric Study of PWR Pressure Vessel Integrity During Overcooling Accidents, Considering Both 2-D and 3-D Flaws*, NUREG/CR-4325 (ORNL/TM-9682), Martin Marietta Energy Systems, Inc., Oak Ridge National Laboratory, Oak Ridge, Tenn. (August 1985).

82. E. C. Rodabaugh, *Comments on the Leak-Before-Break Concept for Nuclear Power Plant Piping Systems,* NUREG/CR-4305 (ORNL/Sub/82-22252/3), E. C. Rodabaugh Associates, Inc., Hilliard, Ohio (August 1985).

83. J. W. Bryson, *ORVIRT.PC: A 2-D Finite Element Fracture Analysis Program for a Microcomputer*, NUREG/CR-4367 (ORNL-6208), Martin Marietta Energy Systems, Inc., Oak Ridge National Laboratory, Oak Ridge, Tenn. (October 1985).

84. D. G. Ball and R. D. Cheverton, *Adaptation of OCA-P, a Probabilistic Fracture-Mechanics Code, to a Personal Computer*, NUREG/CR-4468 (ORNL/CSD/TM-233), Martin Marietta Energy Systems, Inc., Oak Ridge National Laboratory, Oak Ridge, Tenn. (January 1986).

85. J. W. Bryson and B. R. Bass, *ORMGEN.PC: A Microcomputer Program for Automatic Mesh Generation of 2-D Crack Geometries*, NUREG/CR-4475 (ORNL-6250), Martin Marietta Energy Systems, Inc., Oak Ridge National Laboratory, Oak Ridge, Tenn. (March 1986).

86. G. D. Whitman, *Historical Summary of the Heavy-Section Steel Technology Program and Some Related Activities in Light-Water Reactor Pressure Vessel Safety Research*, NUREG/CR-4489 (ORNL-6259), Martin Marietta Energy Systems, Inc., Oak Ridge National Laboratory, Oak Ridge, Tenn. (March 1986).

87. C. Inversini and J. W. Bryson, *ORPLOT.PC: A Graphic Utility for ORMGEN.PC and ORVIRT.PC*, NUREG/CR-4633 (ORNL-6291), Martin Marietta Energy Systems, Inc., Oak Ridge National Laboratory, Oak Ridge, Tenn. (June 1986).

88. J. J. McGowan, R. K. Nanstad, and K. R. Thoms, *Characterization of Irradiated Current-Practice Welds and A533 Grade B Class 1 Plate for Nuclear Pressure Vessel Service*, NUREG/CR-4880 (ORNL/TM-10387), Martin Marietta Energy Systems, Inc., Oak Ridge National Laboratory, Oak Ridge Tenn. (July 1988).

89. K. V. Cook and R. W. McClung, *Flaw Density Examinations of a Clad Boiling Water Reactor Pressure Vessel Segment*, NUREG/CR-4860 (ORNL/TM-10364), Martin Marietta Energy Systems, Inc., Oak Ridge National Laboratory, Oak Ridge, Tenn. (April 1987).

90. D. J. Naus et al., *Crack-Arrest Behavior in SEN Wide Plates of Quenched and Tempered A 533 Grade B Steel Tested Under Nonisothermal Conditions*, NUREG/CR-4930 (ORNL-6388), Martin Marietta Energy Systems, Inc., Oak Ridge National Laboratory, Oak Ridge, Tenn. (August 1987).

91. D. B. Barker et al., *A Report on the Round Robin Program Conducted to Evaluate the Proposed ASTM Standard Test Method for Determining the Plane Strain Crack Arrest Fracture Toughness, K_{Ia}, of Ferritic Materials*, NUREG/CR-4966 (ORNL/Sub/79-7778/4), University of Maryland, College Park, Md. (January 1988).

92. W. H. Bamford, *A Summary of Environmentally Assisted Crack-Growth Studies Performed at Westinghouse Electric Corporation Under Funding from the Heavy-Section Steel Technology Program*, NUREG/CR-5020 (ORNL/Sub/82-21598/1), Westinghouse Electric Corp., Pittsburgh, Pa. (May 1988).

93. R. H. Bryan et al., *Pressurized-Thermal-Shock Test of 6-in.-Thick Pressure Vessels. PTSE-2: Investigation of Low Tearing Resistance and Warm Prestressing*, NUREG/CR-4888 (ORNL-6377), Martin Marietta Energy Systems, Inc., Oak Ridge National Laboratory, Oak Ridge, Tenn. (December 1987).

94. J. H. Giovanola and R. W. Klopp, *Viscoplastic Stress-Strain Characterization of A533B Class 1 Steel*, NUREG/CR-5066 (ORNL/Sub/87-SA193/1), SRI International, Menlo Park, Calif. (to be published).

95. L. F. Miller et al., *Neutron Exposure Parameters for the Metallurgical Test Specimens in the Fifth Heavy-Section Steel Technology Irradiation Series Capsules*, NUREG/CR-5019 (ORNL/TM-10582), Martin Marietta Energy Systems, Inc., Oak Ridge National Laboratory, Oak Ridge, Tenn. (March 1988).

96. Canceled.

97. D. J. Naus, J. Keeney-Walker, B. R. Bass, S. E. Bolt, R. J. Fields, R. deWit, and S. R. Low III, *High-Temperature Crack-Arrest Behavior in 152-mm-Thick SEN Wide Plates of Quenched and Tempered A 533 Grade B Class 1 Steel*, NUREG/CR-5330 (ORNL/TM-11083), Martin Marietta Energy Systems, Inc., Oak Ridge National Laboratory, Oak Ridge, Tenn. (April 1989).

98. K. V. Cook, R. A. Cunningham, Jr., and R. W. McClung, *Detection and Characterization of Indications in Segments of Reactor Pressure Vessels*, NUREG/CR-5322 (ORNL/TM-11072), Martin Marietta Energy Systems, Inc., Oak Ridge National Laboratory, Oak Ridge, Tenn. (August 1989).

99. R. D. Cheverton, W. E. Pennell, G. C. Robinson, and R. K. Nanstad, *Impact of Radiation Embrittlement on Integrity of Pressure Vessel Supports for Two PWR Plants*, NUREG/CR-5320 (ORNL/TM-10966), Martin Marietta Energy Systems, Inc., Oak Ridge National Laboratory, Oak Ridge, Tenn. (February 1989).

100. D. J. Naus et al., *SEN Wide-Plate Crack-Arrest Tests Utilizing A 533 Grade B Class 1 Material: WP-CE Test Series,* NUREG/CR-5408 (ORNL/TM-11269), Martin Marietta Energy Systems, Inc., Oak Ridge National Laboratory, Oak Ridge, Tenn. (November 1989).

101. D. J. Naus et al., High-Temperature Crack-Arrest Tests Using 152-mm-Thick SEN Wide Plates of Low-Upper-Shelf Base Material: Tests WP-2.2 and WP-2.6, NUREG/CR-5450 (ORNL/TM-11352), Martin

Marietta Energy Systems, Inc., Oak Ridge, National Laboratory, Oak Ridge, Tenn. (March 1989).

102. L. F. Miller et al., Neutron Exposure Parameters for the Metallurgical Test Specimens in the Sixth Heavy-Section Steel Technology Irradiation Series Capsules, NUREG/CR-5409 (ORNL/TM-11267), Oak Ridge National Laboratory, Oak Ridge, Tenn. (to be published).

103. This report.

ACKNOWLEDGMENTS

The authors wish to acknowledge the significant contributions made to this testing program by those who are not otherwise referred to in this report: D. E. Harne at the National Institute of Standards and Technology (performance of tests); G. R. Irwin, D. B. Barker, J. W. Dally, and W. L. Fourney at the University of Maryland (assistance in development of specimen design, instrumentation and testing techniques, and analysis of test results); R. K. Nanstad and E. T. Manneschmidt of the Metals and Ceramics (M&C) Division at Oak Ridge National Laboratory (ORNL) (material characterization); S. E. Bolt and W. F. Jackson of the Engineering Technology Division (ETD) at ORNL (specimen preparation, special test fixturing design, and fabrication); and C. E. Pugh and J. G. Merkle of the ETD at ORNL (test program definition).

EXECUTIVE SUMMARY

The pressurized-thermal-shock (PTS) issue for pressurized-water reactors (PWRs) involves a broad range of fracture phenomena. In PTS scenarios, flaws in the inner surface of the reactor pressure vessel (RPV) have a high propensity to propagate because they are located in the region of highest stress and lowest fracture toughness (lowest temperature and greatest irradiation damage). If such flaws begin to propagate radially through the vessel wall, they will extend into regions of higher fracture toughness because of the higher temperatures and less irradiation damage. Certain PTS scenarios lead to conditions where the driving force on a propagating crack increases to levels well in excess of the ASME crack-arrest fracture-toughness limit (220 $MPa\cdot\sqrt{m}$) contained in the *American Society of Mechanical Engineers Boiler and Pressure Vessel Code (ASME B&PVC)*. Assessment of the integrity of an RPV under such a postulated crack run-arrest condition requires prediction of the arrest potential; the potential for reinitiation including stable and unstable ductile crack growth; and structural instability of the remaining vessel-wall ligament.

Work being conducted under Task H.5 of the Heavy-Section Steel Technology (HSST) Program at Oak Ridge National Laboratory is concerned with understanding the ability of RPV materials to arrest running cracks as they propagate into regions of higher toughness and conditions of increasing values for the stress-intensity factor. As a part of this task, the HSST Program in late FY 1984 initiated an investigation of the run-arrest behavior of cracks in large plates that possess steep toughness gradients. These tests use wide-plate ($1 \times 1 \times 0.1$ m or $1 \times 1 \times 0.15$ m) specimens that possess a single-edge notch (crack) that initiates cleavage propagation at low temperature and arrests in a region of increased fracture toughness. The toughness gradient is achieved through a linear transverse temperature profile across the plate. The experiments require the application of large tensile loads and are being conducted at the National Institute of Standards and Technology in Gaithersburg, Maryland. The overall objectives of these tests are to determine (1) if RPV materials will exhibit crack-arrest behavior when the driving force on a crack exceeds the ASME limit (220 $MPa\cdot\sqrt{m}$); (2) the relationship between crack-arrest toughness and temperature for $K_{Ia} > 220$ $MPa\cdot\sqrt{m}$; and (3) the interaction of fracture modes (arrest, stable crack growth, unstable crack growth, and tensile instability) when arrest occurs at high temperatures.

In meeting these objectives, three series of wide-plate tests have been conducted: WP-1 (A 533 grade B class 1 steel), WP-CE (second heat of A 533 grade B class 1 steel), and WP-2 [low-upper-shelf (LUS) base material]. This report contains results for the six tests that comprised the WP-2 series, which utilized a Charpy LUS base material (specially heat treated 2 1/4 Cr-1 Mo steel). Following are highlights of each chapter to aid readers who are interested only in certain aspects of the report.

1. INTRODUCTION

Limitations imposed by the *ASME B&PVC* are discussed. Objectives of the crack-arrest studies and program goals are presented.

2. Background

Prior crack-arrest studies and their limitations are discussed. A summary of large-specimen crack-arrest toughness data is presented in Fig. 2.1.

3. MATERIAL CHARACTERIZATION

A description of the Charpy LUS material used in the WP-2 test series is provided. Drop-weight (Table 3.1), Charpy V-notch (Table 3.2), tensile (Table 3.6), crack-arrest toughness (Table 3.8), and transition-region (Table 3.10) and ductile shelf (Table 3.11) fracture toughness properties are provided. Equations (3.2) and (3.5) present the relations for K_a and K_{Ic}, respectively, that were used in the analysis of the test results.

4. SPECIMEN PREPARATION, INSTRUMENTATION, AND TESTING PROCEDURE

Procedures used for precracking and assembling the test articles are outlined. Instrumentation used to obtain pertinent data during a test (load, strain, temperature, crack-opening-displacement, dynamic displacement), as well as the data acquisition system, are described. The heating, cooling, and insulation systems used to produce the desired specimen transverse temperature profile are delineated. The technique used to conduct a wide-plate crack-arrest test (Fig. 4.9) is presented.

5. SUMMARY OF WIDE-PLATE CRACK-ARREST TESTS WP-2.1 THROUGH WP-2.6

General test conditions (Table 5.1) for each wide-plate test are delineated, and transverse temperature profiles for each test are summarized (Fig. 5.1). The highlights for each test, as well as pertinent test data, are reiterated. Fracture surfaces for each test specimen are presented (Fig. 5.2).

6. POSTTEST ANALYSES, CRACK-ARREST TOUGHNESS RESULTS, AND COMPARISON OF DATA WITH OTHER LARGE-SCALE TEST RESULTS

Posttest static and dynamic fracture analyses conducted for each wide-plate crack-arrest test are described. The development and use of dynamic analysis methods were required to incorporate the significant dynamic effects exhibited by the wide-plate specimens; that is, multiple crack run-arrest events occurred in each test over a relatively short time (up to seven crack run-arrest events in <7 ms). Crack-arrest toughness results determined by dynamic analyses (fixed-load and generation-mode) are presented (Table 6.4). The relationship between fixed-load, generation-mode, crack-arrest toughness values for tests in the WP-2 series, as well as for other wide-plate crack-arrest tests (WP-1 and WP-CE test series), and the K_{IR} curve of the *ASME B&PVC* is shown (Fig. 6.14). The HSST wide-plate crack-arrest test results are compared with other large-scale test results (Fig. 6.16).

7. CONCLUSIONS

Results of the investigation are summarized. Wide-plate tests demonstrate that crack-arrest values above the 220 $MPa\cdot\sqrt{m}$ limit in the *ASME Code* are achievable and that crack arrest can and does occur at temperatures up to and slightly above those that correspond to the onset of Charpy upper-shelf behavior.

CRACK-ARREST BEHAVIOR IN SEN WIDE PLATES OF LOW-UPPER-SHELF BASE METAL TESTED UNDER NONISOTHERMAL CONDITIONS: WP-2 SERIES

D. J. Naus, R. J. Fields
J. Keeney-Walker, R. DeWit
B. R. Bass, S. R. Low
G. C. Robinson, Jr., C. W. Schwartz
S. K. Iskander, D. J. Alexander
I.-B. Johansson

1. INTRODUCTION

In pressurized-thermal-shock (PTS) scenarios, flaws on the inner surface of a reactor pressure vessel (RPV) have a high propensity to propagate because they are in the region of highest thermal stress and lowest fracture toughness (i.e., lowest temperature and greatest irradiation damage). If such flaws begin to propagate radially through the vessel wall, they will extend into regions of higher fracture toughness because of the higher temperatures and less irradiation damage. Assessment of the integrity of an RPV under such a postulated crack run-arrest scenario requires prediction of the arrest potential; the potential for reinitiation, including stable and unstable ductile crack growth; and structural instability of the remaining vessel-wall ligament.

Current light-water reactor (LWR) pressure-vessel safety assessment methods are based largely on Sects. III and XI of the *American Society of Mechanical Engineers Boiler and Pressure Vessel Code (ASME B&PVC)*. The fracture-toughness correlations contained in the *ASME B&PVC* embody the position that one cannot assume a crack-arrest toughness value (K_{Ia}) >220 MPa·$\sqrt{m}$ for LWR pressure-vessel steels. The imposition of this limit is based partly on the fact that no K_{Ia} data existed at or above this level and because Charpy and "small" C(T)-specimens exhibit an upper-shelf behavior. Therefore, the nature of crack-arrest behavior and K_{Ia} extrapolations to temperatures higher than that at which this limit occurred could not be presumed.

The ASME limit does not impose difficulties in making assessments for LWR pressure vessels undergoing thermal shock transients with very low accompanying pressure levels. However, PTS scenarios could lead to conditions under which the driving force on a propagating crack increases to levels well in excess of the current ASME limit. Thus, safety assessment methods for this type of condition would require an understanding of the following points.

1. If the driving force on a crack exceeds 220 MPa·$\sqrt{m}$ by a significant margin, can the material exhibit crack-arrest behavior?
2. If the material exhibits high K_{Ia} values with increasing temperature, what is the relationship between K_{Ia} and temperature? That

is, does a temperature limit exist above which cleavage crack propagation cannot continue regardless of how high the driving force?

3. If crack arrest occurs at high temperatures where the material behavior is typically dominated by ductile behavior, then what interactions exist between the various fracture modes, including arrest, stable crack growth, unstable crack growth, and tensile instability?

The pressurized-water reactor (PWR) PTS issue has been under intensive investigation at Oak Ridge National Laboratory (ORNL) since 1973 in the form of two Nuclear Regulatory Commission (NRC)-sponsored programs: Integrated Pressurized Thermal Shock (IPTS) and Heavy-Section Steel Technology (HSST). The IPTS Program is primarily concerned with an overall estimate of the frequency of vessel failure for specific PWR plants and thus included the identification of dominant transients, as well as the contributions of design and operating features of these plants. One important component of the IPTS study is a probabilistic fracture-mechanics analysis of the reactor vessel and, in particular, the role of crack-arrest in mitigating the consequences of the postulated PTS transients. Results of the IPTS studies[1,2] indicated that crack arrest in the probabilistic fracture-mechanics model does not substantially influence the calculated frequency of vessel failure. However, the influence could be different if $K_{Ia}(T)$ was significantly different than that assumed for $K_{Ia} > 220$ MPa$\cdot\sqrt{m}$. Furthermore, there are still significant questions regarding flaw behavior for low-upper-shelf (LUS) materials. Thus, the HSST Program is continuing to pursue these areas of uncertainty.

The primary objective of the wide-plate crack-arrest studies under the HSST Program is to generate data for understanding the crack-arrest behavior of prototypical RPV steels at temperatures near and above the onset of the Charpy upper-shelf region. Program goals include (1) extending the existing K_{Ia} data bases to values above those associated with the upper limit in the *ASME B&PVC*; (2) clearly establishing that cleavage crack arrest occurs before fracture-mode conversion; (3) observing the relationship between arrest data and machine/specimen compliance behavior; and (4) validating the predictability of crack arrest, stable tearing, and/or unstable tearing sequences for ductile materials. In the present study, the program objectives and goals were investigated for a material that met the American Society of Testing Materials (ASTM) A 387 grade 22 chemical composition (2 1/4 Cr-1 Mo) but was specially heat treated to produce a base metal having a low Charpy upper-shelf toughness and a high transition temperature.

REFERENCES

1. R. D. Cheverton and D. G. Ball, "The Role of Crack Arrest in the Evaluation of PWR Pressure Vessel Integrity During PTS Transients," Eng. Fract. Mech. 23(1), 71–80, 1986.*

2. R. D. Cheverton and D. G. Ball, "A Reassessment of PWR Pressure Vessel Integrity During Overcooling Accidents, Considering 3-D Flaws," *J. Pressure Vessel Technology* **106**, November 1984.*

---

*Available in public technical libraries.

2. BACKGROUND

Under the HSST Program, crack-arrest data have been generated over an expanded temperature range in tests involving large thermally shocked cylinders[1,2] (TSCs), pressurized thermally shocked vessels[3,4] (PTSVs), stub-panel specimens,[5] and wide-plate specimens.[6-8] The TSCs and PTSVs also provide data under multiaxial transient and high-restraint loadings for validation of fracture models and analysis methods. A thermal-shock experiment (TSE) has also been conducted in France.[9] While the HSST and French TSEs have generated a significant number of data points, the driving force in these experiments has been thermal stress only, and, consequently, crack-arrest data have not ranged above ~150 MPa·$\sqrt{m}$. An important conclusion of the TSEs is that the K_{Ia} data from these highly restrained propagations fall well within the range of K_{Ia} data from the small laboratory specimens and above the ASME reference toughness (K_{IR}) curve, which provides a lower bound of crack arrest (K_{Ia}) and dynamic fracture toughness (K_{Id}) as a function of the temperature relative to the reference nil-ductility temperature (RT_{NDT}). The HSST pressurized-thermal-shock experiments (PTSEs) can provide higher K_{Ia} values under similar highly restrained conditions, as evidenced by the first two PTSEs, which produced K_{Ia} data as high as ~420 MPa·$\sqrt{m}$ at temperatures up to ~90°C above the drop-weight NDT for the vessel insert material (~75°C). Although the stub-panel test series has just begun, early indications are that those tests can be used to provide crack-arrest toughness values at temperatures up to those corresponding to the Charpy upper-transition region. Crack-arrest tests that used wide-plate specimens fabricated from A 533 grade B class 1 material have produced K_{Ia} data >500 MPa·$\sqrt{m}$ (fixed-load, generation-mode analysis) at temperatures up to 115°C above the material RT_{NDT} (−23°C).

Crack-arrest data for RPV-grade materials were also developed under an Electric Power Research Institute (EPRI) Program (EPRI Research Program RP-2180-3) conducted by Combustion Engineering, Inc. (CE).[10] The analytical/experimental program was conducted to determine the response of precracked specimens subjected to thermal and mechanical loadings in the range of temperature and pressure conditions that might occur in PWR primary coolant systems during extreme cooldown/depressurization/repressurization situations. The test specimen used to study the effects of a crack running from a brittle material into a ductile material was a moment-modified compact-tension specimen (MMCT). Material toughness was varied in the direction of crack propagation by cooling one edge by liquid nitrogen chill blocks and heating the other edge with electrical resistance heaters. A rising stress-intensity factor was achieved by imposing an initial high tensile stress across the specimen test section. Thermal gradient stresses were simulated by wedge-loading a fatigue precrack. The wedge-loading was applied in small increments until a crack-propagation event occurred. The MMCT tests produced K_{Ia} data as high as ~150 MPa·$\sqrt{m}$ at temperatures up to ~51°C above RT_{NDT}.

Recently, considerable testing of wide-plate specimens has been done in Japan.[11-16] Some of the specimens are referred to as double-tension specimens[14] because they used a notched tensile-loaded tab attached to the edge of the specimen as an auxiliary crack-starting device. Other Japanese tests employed ESSO specimens[17] and produced K_{Ia} data as high as ~380 MPa·$\sqrt{m}$ at temperatures up to ~90°C above RT_{NDT}.

Figure 2.1 presents a summary of K_{Ia} data for the HSST Program TSEs, PTSEs, stub-panel experiments, and wide-plate tests (WP-1 series); the French TSE; the CE/EPRI MMCT tests; and the Japanese tests. As shown in the figure, few crack-arrest toughness measurements were made above 150 MPa·$\sqrt{m}$, except for data produced in the HSST Program PTSEs and wide-plate tests and the Japanese wide-plate specimens. To meet the HSST Program objective of understanding the crack-arrest behavior of prototypical RPV steels at temperatures near and above the onset of the Charpy upper-shelf region, either PTSEs or wide-plate tests were required. Because the wide-plate tests have the ability to provide a significant number of data points (K_{Ia} > 220 MPa·$\sqrt{m}$) at relatively reasonable cost, they were selected for use in the investigation.

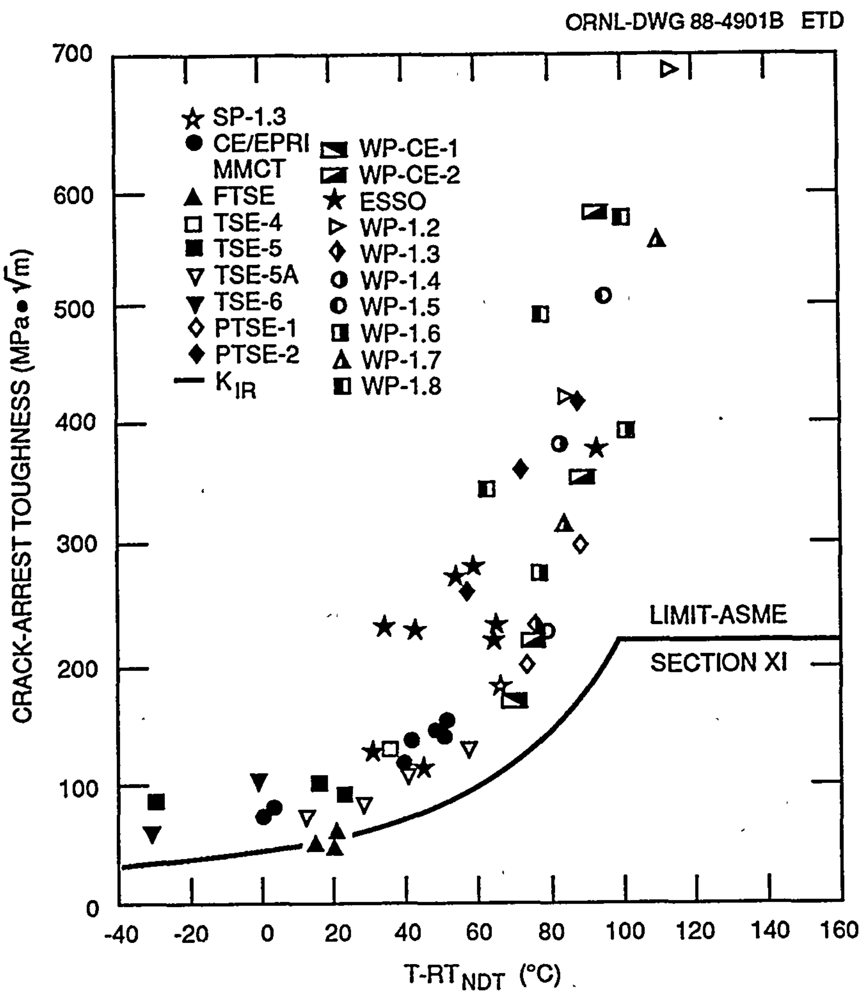

Fig. 2.1. Summary of large-specimen, high-temperature crack-arrest data.

REFERENCES

1. R. D. Cheverton et al., Martin Marietta Energy Systems, Inc., Oak Ridge Natl. Lab., *Pressure Vessel Fracture Studies Pertaining to the PWR Thermal-Shock Issue: Experiments TSE-5, TSE-5A, and TSE-6*, USNRC Report NUREG/CR-4249 (ORNL-6163), June 1985.*

2. R. D. Cheverton et al., Martin Marietta Energy Systems, Inc., Oak Ridge Natl. Lab., *Pressure Vessel Fracture Studies Pertaining to the PWR Thermal-Shock Issue: Experiment TSE-7*, USNRC Report NUREG/CR-4304 (ORNL-6177), August 1985.*

3. R. H. Bryan et al., Martin Marietta Energy Systems, Inc., Oak Ridge Natl. Lab., *Pressurized-Thermal-Shock Test of 6-in.-Thick Pressure Vessels. PTSE-1: Investigation of Warm Prestressing and Upper-Shelf Arrest*, USNRC Report NUREG/CR-4106 (ORNL-6135), April 1985.*

4. R. H. Bryan et al., Martin Marietta Energy Systems, Inc., Oak Ridge Natl. Lab., *Pressurized-Thermal-Shock Test of 6-in.-Thick Pressure Vessels. PTSE-2: Investigation of Low Tearing Resistance and Warm Prestressing*, USNRC Report NUREG/CR-4888 (ORNL-6377), December 1987.*

5. C. E. Pugh et al., "Crack-Arrest Toughness Determination from Stub-Panel Specimen Tests," Vol. F, pp. 37–42 in *Transactions of the 10th International Conference on Structural Mechanics in Reactor Technology, Anaheim, Calif., August 14–18, 1989*, American Association for Structural Mechanics in Reactor Technology, Los Angeles, 1989.†

6. D. J. Naus et al., Martin Marietta Energy Systems, Inc., Oak Ridge Natl. Lab., *Crack-Arrest Behavior in SEN Wide Plates of Quenched and Tempered A 533 Grade B Steel Tested Under Nonisothermal Conditions*, USNRC Report NUREG/CR-4930 (ORNL-6388), August 1987.*

7. D. J. Naus et al., Martin Marietta Energy Systems, Inc., Oak Ridge Natl. Lab., *High-Temperature Crack-Arrest Behavior in 152-mm-Thick SEN Wide Plates of Quenched and Tempered A 533 Grade B Class 1 Steel*, USNRC Report NUREG/CR-5330 (ORNL/TM-11083), April 1989.*

8. D. J. Naus et al., Martin Marietta Energy Systems, Inc., Oak Ridge Natl. Lab., *SEN Wide-Plate Crack-Arrest Tests Utilizing A 533 Grade B Class 1 Material: WP-CE Test Series*, USNRC Report NUREG/CR-5408 (ORNL/TM-11269), October 1989.*

9. A. Pellissier-Tanon, P. Sollogoub, and B. Houssin, "Crack Initiation and Arrest in an SA 508 Class-3 Cylinder Under Liquid Nitrogen Thermal-Shock," Paper G/F 1/8, Vol. G/H, pp. 137-42 in *Transactions of the 7th International Conference on Structural Mechanics in Reactor Technology, August 1983*, Elsevier Publishing Co., Inc., New York, 1983.†

10. R. Y. Schonenberg and D. M. Norris, "Moment Modified Compact Tension Specimen for Measuring Crack Arrest Toughness," *Nucl. Eng. and Des.* **96**, 277–86 (1986).†

11. Japan Welding Council, *Structural Integrity of Very Thick Steel Plate for Nuclear Reactor Pressure Vessels*, JWES-AE-7806, 1977 (in Japanese).

12. T. Kanazawa, S. Machida, and T. Teramoto, "Preliminary Approaches to Experimental and Numerical Study of Fast Crack Propagation and Crack Arrest," pp. 39–58 in *Fast Fracture and Crack Arrest*, ASTM STP 627, American Society for Testing and Materials, Philadelphia, Pa., 1977.*

13. N. Ohashi et al., "Fracture Toughness of Heavy Section LWR Pressure Vessel Steel Plate Produced by Basic Oxygen Furnace and Ladle Refining Process," pp. 391-96 in *Proceedings of the Fourth International Conference on Pressure Vessel Technology*, Vol. 1, *I. Mech. E.*, 1980.†

14. T. Kanazawa et al., "Study on Fast Fracture and Crack Arrest," *Experimental Mechanics* 21(2), 77–88 (February 1981).†

15. S. Machida, Y. Kawaguchi, and M. Tsukamoto, "An Evaluation of the Crack Arrestability of 9% Ni Steel Plate to an Extremely Long Brittle Crack," *Journal of the Society of Naval Architects of Japan* **150**, 511–17 (1981) (translation ORNL-tr-5052).†

16. T. Kanazawa, S. Machida, and H. Yajima, "Recent Studies on Brittle Crack Propagation and Arrest in Japan," in *Fracture Mechanics Technology Applied to Material and Structure Design*, G. C. Sih, N. E. Ryan, and R. Jones, Eds. (Martinua Nijhoff, The Hague, 1983), pp. 81–100.

17. Y. Nakano, "Stress Intensity Factor During Brittle Crack Propagation and Arrest in ESSO Specimen," in *Proceedings of the 18th National Symposium in X-Ray Study on Deformation and Fracture Solids, July 13–14, 1981*, The Society of Materials Science, Japan.†

---

*Available for purchase from National Technical Information Service, Springfield, VA 22161.

†Available in public technical libraries.

3. CHARACTERIZATION OF WIDE-PLATE SERIES 2 MATERIAL

3.1 INTRODUCTION

The chemical composition of the material used in the WP-2 series of wide-plate experiments is in accordance with ASTM Standard Specification for Pressure Vessel Plates, Alloy Steel, Chromium-Molybdenum (A 387), grade 22 (2 1/4 Cr—1 Mo). A 159-mm-thick plate was procured by Babcock and Wilcox[1] (B&W) for the HSST Program to provide material for the second series of wide-plate tests (WP-2) and the second pressurized-thermal-shock experiment (PTSE-2).[2] It was specially heat treated to produce LUS toughness and a high transition temperature.

Allocation of the material is shown in Fig. 3.1. Material characterization for pretest analyses of PTSE-2 and WP-2 has been conducted with the characterization piece PTC1. Charpy V-notch (CVN), tensile, drop weight, hardness, fracture-toughness, crack-arrest toughness, and metallographic results have been reported previously.[3-5] The pretest characterization and the physical properties also have been included in the final report on the PTSE-2 experiments.[2]

The purpose of posttest characterization is to determine (using a smaller number of specimens than would normally be used to fully characterize the material) if the wide-plate properties are significantly different from those inferred from characterization block PTC1. PTC1 received a stress-relief heat treatment of 524 ± 14°C for 7.25 h. The wide plates and a characterization block WPQ1 were stress-relieved as one piece at 552 ± 14°C for 7 h. The plate stock used for PTSE-2 and the wide-plate tests was found to exhibit anomalous variations in properties thought to be associated with the primary heat treatment process. The properties of the WP-2 series material have been determined to be similar to those of PTC1, although PTC1 received a stress-relief heat treatment, which differed slightly from that of the wide plates and WPQ1. Block WPQ1 was not representative of the wide-plate material and is mentioned solely for completeness (the results of tests on WPQ1 are given in Ref. 1).

The posttest characterization of the WP-2 series material was conducted with specimens machined from the broken halves of plates WP-2.1 and -2.5. All characterization was performed in the T-L orientation; that is, the fracture plane of the test specimens was parallel to the fracture plane of the wide plates. Drop-weight NDT temperature, CVN, tensile, initiation fracture toughness, J-R, and crack-arrest tests have been performed. The results of the posttest characterization are compared with those from block PTC1. For purposes of analyzing the results of the wide-plate structural tests, the differences between the PTC1 and wide-plate material found in the CVN, tensile, and crack-arrest tests may be considered insignificant. However, for material from the wide plates, the NDT temperatures are higher by ~10 K, and the initiation fracture toughness K_{Jc} is noticeably lower than for PTC1.

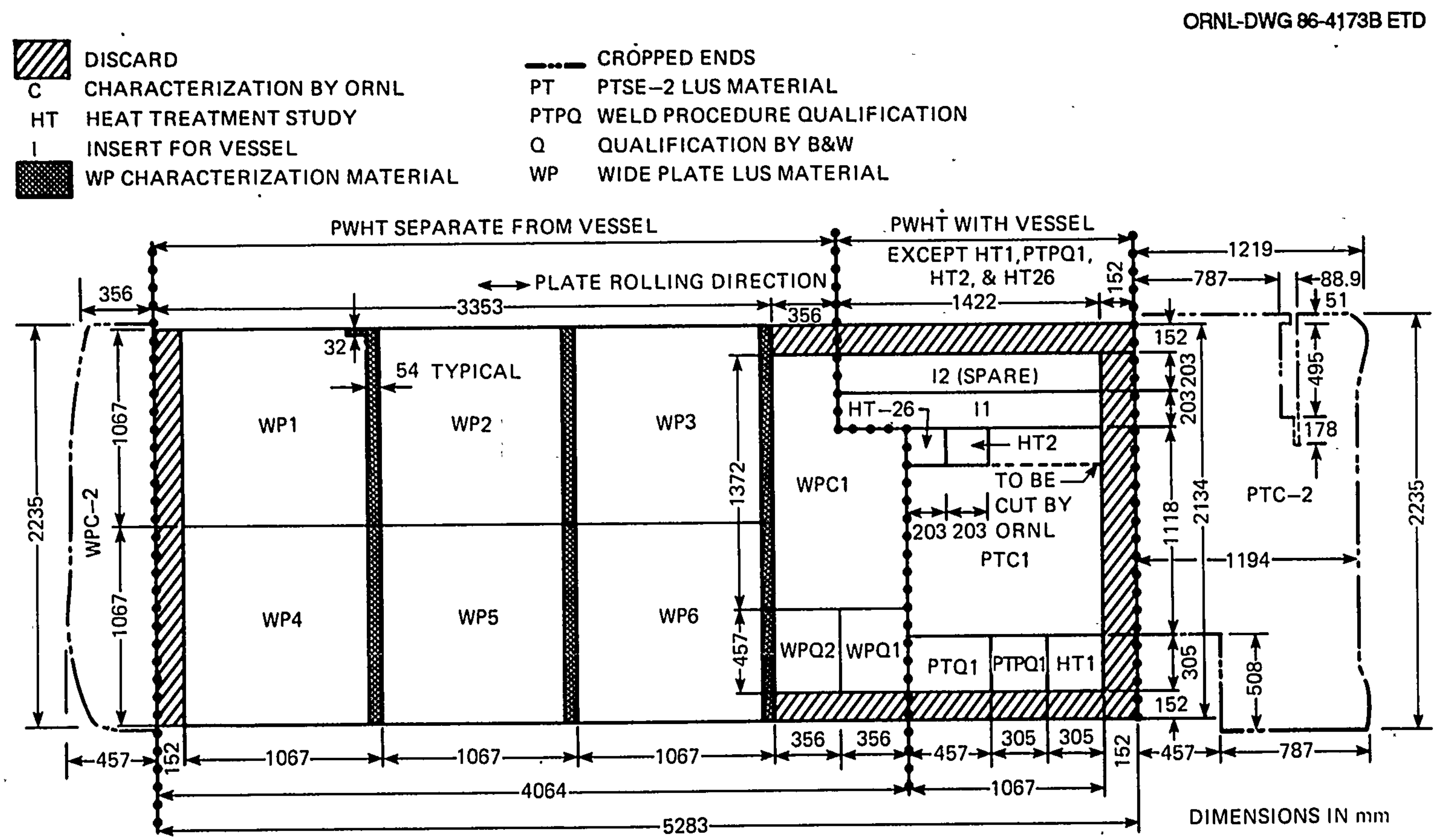

Fig. 3.1. Allocation of 2 1/4 Cr-1 Mo 159-mm-thick LUS steel plate for various tests.

3.2 DROP-WEIGHT TESTING

Drop-weight testing was conducted with standard P-3 specimens per ASTM Standard Method for Conducting Drop-Weight Test to Determine Nil-Ductility Transition Temperature of Ferritic Steels (E 208-85). In accordance with E-208-85, a single-pass-weld crack starter bead was used to prepare the drop-weight specimens. This standard explicitly states that, although the drop-weight test is insensitive to specimen orientation, all specimens should be of a single orientation, which must be noted in the test report. The specimen orientation used was T-L (for a crack propagating along the surface on either side of the crack starter bead).

The results of individual specimens for material from midthickness (1/2t) of each of the two plates are given in Table 3.1. The NDT temperature was determined to be 60 and 55°C for material from plates WP-2.1 and -2.5, respectively. Note that NDT for material from characterization block PTC1 at 1/4t was 49°C; although there was insufficient material for a full determination, a tentative pretest NDT for specimens machined from a portion of WP-2.4 was estimated to be 60°C (see p. 62 of Ref. 5). This value agrees with the posttest value obtained for WP-2.1 material. The 5°C difference between NDT for plates WP-2.1 and -2.5 may not be significant, considering the variability that this material has exhibited; an NDT of 60°C is used in this report.

Table 3.1. Results of drop-weight testing on 2 1/4 Cr-1 Mo material from 1/2t depth of broken halves of specimens WP-2.1 and -2.5 (T-L orientation)

Specimen	Test temperature (°C)	Test results		
		Break	No break	NDT
	WP-2.1 material			
WP2.101	65		✓	
WP2.110	60	✓		
WP2.112	65		✓	60
	WP-2.5 material			
WP2.505	65		✓	
WP2.503	60		✓	
WP2.502	55		✓	
WP2.506	50		✓	
WP2.512	45	✓		
WP2.508	50	✓		
WP2.509	55	✓		
WP2.501	60		✓	55

3.3 CVN TESTING

CVN testing has been performed on 12 specimens from the 1/2t depth of each of plates WP-2.1 and -2.5. In addition, 12 specimens were tested from the 1/4t depth of plate WP-2.1. All specimens were in the T-L orientation and tested at the same temperature intervals. The temperature ranged from 25 to 250°C for comparing with previous work.[1,3]

Table 3.2 gives the data obtained during CVN testing. Figure 3.2 shows plots of the CVN test results vs temperature for all three material regions (WP-2.1 at 1/4t, WP-2.1 at 1/2t, and WP-2.5 at 1/2t depths) and hyperbolic tangent curve fits. The curve fit parameters are presented in Table 3.3. For comparison, the corresponding parameters for PTC1 are given in Table 3.4 (reproduced from Ref. 3).

If the CVN energies of material from the three regions are compared, there is a small difference in the upper-shelf-energy (USE) levels that range from 61 to 65 J, a ±3% variation about the mean. The range of variation of USE of PTC1 was approximately ±12% about a mean of 57 J. For both WP-2 and PTC1 materials, USE decreases consistently with increases in plate depth.

The WP-2 material exhibits relatively little difference in energy absorbed in the midtransition region (at 100°C). The greatest differences (±10 J) were exhibited in the lower-transition region around NDT. The knee of the upper shelf is reached at ~150°C when judged by the attainment of 100% shear fracture appearance (see Table 3.2 and Fig. 3.2). This temperature compares favorably with the results for PTC1 (Fig. 3.3). The midcurve transition temperatures, which range from 76 to 82°C, compare well with those of PTC1, 74 to 81°C (Table 3.4). The results of drop-weight and CVN testing are summarized in Table 3.5.

An RT_{NDT} (in accordance with Subarticle NB-2330 of *ASME B&PVC*, Sect. III) cannot be determined because a minimum 68-J CVN impact energy was not attained for specimens fabricated from either the WP-2.1 or the -2.5 plate materials (see Table 3.2).

3.4 TENSILE TESTING

Tensile tests were performed using 6.3-mm-diam specimens. The results are given in Table 3.6 and plotted in Fig. 3.4 together with the 99% confidence band of the tensile test results using material from characterization block PTC1. The tests on PTC1 were obtained using 4.52-, 6.35-, and 12.7-mm-diam specimens, and the results are given in Table 3.7.

The 0.2% yield strength is highly dependent on prior straining history. Figure 3.5 shows a typical stress-strain curve from a room-temperature tensile test on a 12.7-mm-diam specimen from PTC1 material and illustrates the difficulty of defining the 0.2% yield strength because of the very short linear portion of the diagram. Moreover, if the material were strained even to values <0.2% yield and then unloaded, this can increase the 0.2% yield strength. This is because the linear portion of the stress strain diagram will be extended and the 0.2% offset line will intersect the stress-strain curve at a higher stress.

Table 3.2. Charpy impact test results for 2 1/4 Cr-1 Mo material from broken halves of specimens WP-2.1 and -2.5 (T-L orientation)

Specimen	Test temperature (°C)	Energy (J)	Lateral expansion (mm)	Appearance (% shear)
		WP-2.1 (1/4t depth)		
WP2101	30	7.1	0.0508	0
WP2102	30	6.1	0.0254	0
WP2103	60	18	0.254	10
WP2104	60	26	0.343	10
WP2105	100	39	0.546	40
WP2106	100	41	0.597	40
WP2107	150	64	1.04	99
WP2108	150	63	1.08	99
WP2109	200	60	0.94	100
WP2110	200	59	1.04	100
WP2111	250	61	1.05	100
WP2112	250	60	1.09	100
		WP-2.1 (1/2t depth)		
WP2121	30	6.8	0.0254	0
WP2122	30	6.8	0.0254	0
WP2123	60	15	0.178	0
WP2124	60	14	0.178	0
WP2125	100	45	0.737	40
WP2126	100	39	0.686	50
WP2131	150	68	1.09	99
WP2132	150	65	1.09	99
WP2129	200	60	1.09	100
WP2130	200	60	0.94	100
WP2127	250	56	1.07	100
WP2128	250	57	1.02	100
		WP-2.5 (1/2t depth)		
WP2501	30	7.1	0.0508	0
WP2502	30	8.5	0.0508	10
WP2503	60	29	0.381	20
WP2504	60	23	0.305	30
WP2505	100	43	0.66	40
WP2506	100	42	0.711	50
WP2507	150	66	1.12	99
WP2508	150	69	1.12	100
WP2509	200	64	1.07	100
WP2510	200	65	1.12	100
WP2511	250	62	1.12	100
WP2512	250	59	1.04	100

ORNL-DWG 89-5007 ETD

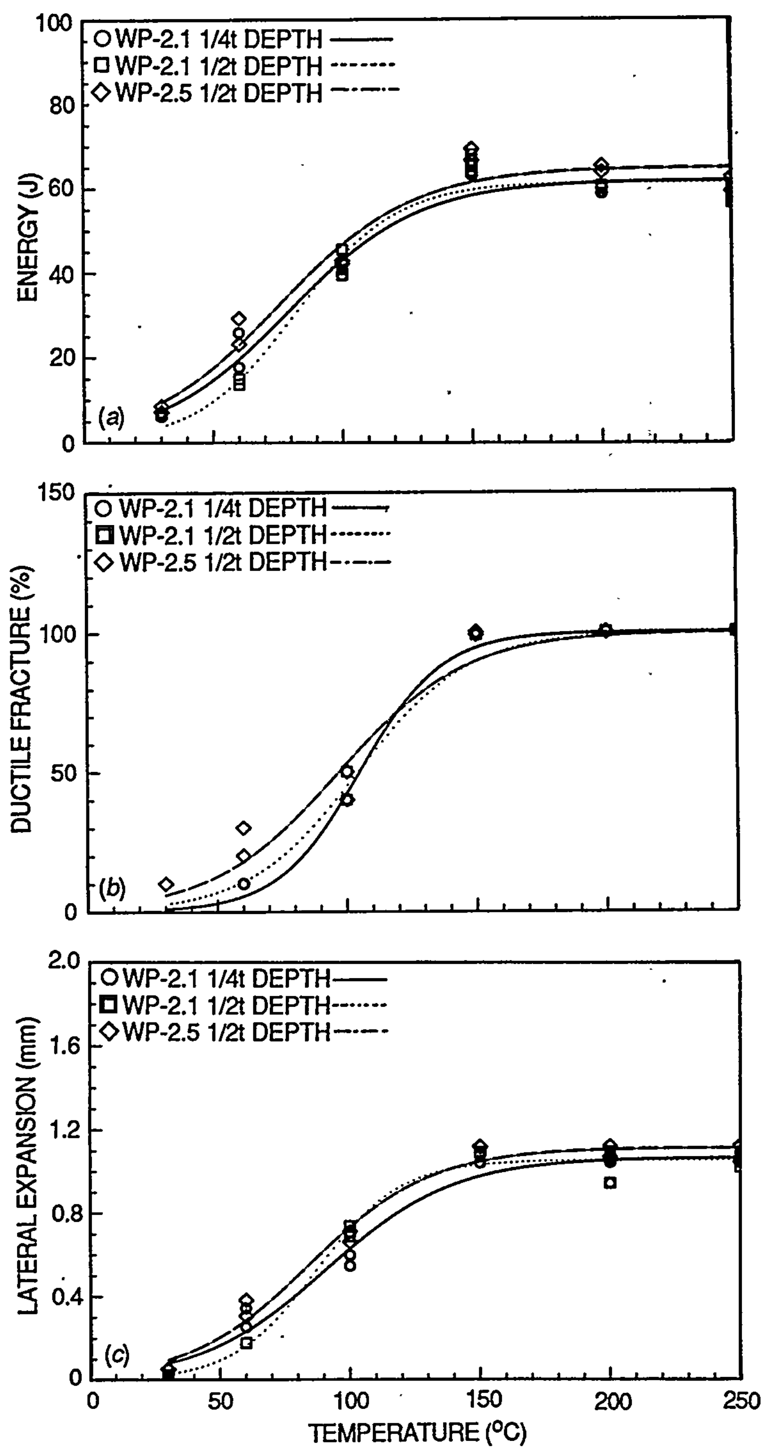

Fig. 3.2. CVN test results in T-L orientation for material from halves of wide-plate specimens WP-2.1 and -2.5. (*a*) CVN impact energy, (*b*) percent ductile fracture, and (*c*) lateral expansion.

Table 3.3. Curve-fit parameters of CVN impact energy: WP-2 series material (T-L orientation)

Region	Depth (t)	$E = (A/2)\{1+\tanh[B(T-C)]\}$[a] A (J)	B ($°C^{-1}$)	C (°C)	NDT (°C)	E at NDT (J)	Temperature at 41 J (°C)
WP2.1	1/4	62	0.01996	79	*b*	20	96
WP2.1	1/2	61	0.02595	82	60	15	96
WP2.5	1/2	65	0.01939	76	55	20	90

[a]E = CVN impact energy at temperature T in °C,
A = USE,
B = related to slope of curve in transition region,
C = temperature corresponding to energy equal to one-half USE.

[b]Not calculated; drop-weight NDT temperature was determined with specimens from 1/2t.

Table 3.4. Curve fit parameters of CVN impact energy: PTC1 characterization block (T-L orientation)

Depth (t)	$E = (A/2)\{1+\tanh[B(T-C)]\}$[a] A (J)	B ($°C^{-1}$)	C (°C)	E at NDT of 49°C (J)	Temperature at 41 J (°C)
0	60	0.02062	81	*b*	99
1/4	59	0.01998	74	16	94
1/2	50	0.01675	76	*b*	120
3/4	64	0.02255	73	*b*	87
1	63	0.02112	78	*b*	92

[a]E = CVN impact energy at temperature T in °C,
A = USE,
B = related to slope of curve in transition region,
C = temperature corresponding to energy equal to one-half USE.

[b]Not calculated; drop-weight NDT temperature was determined with specimens from 1/4t.

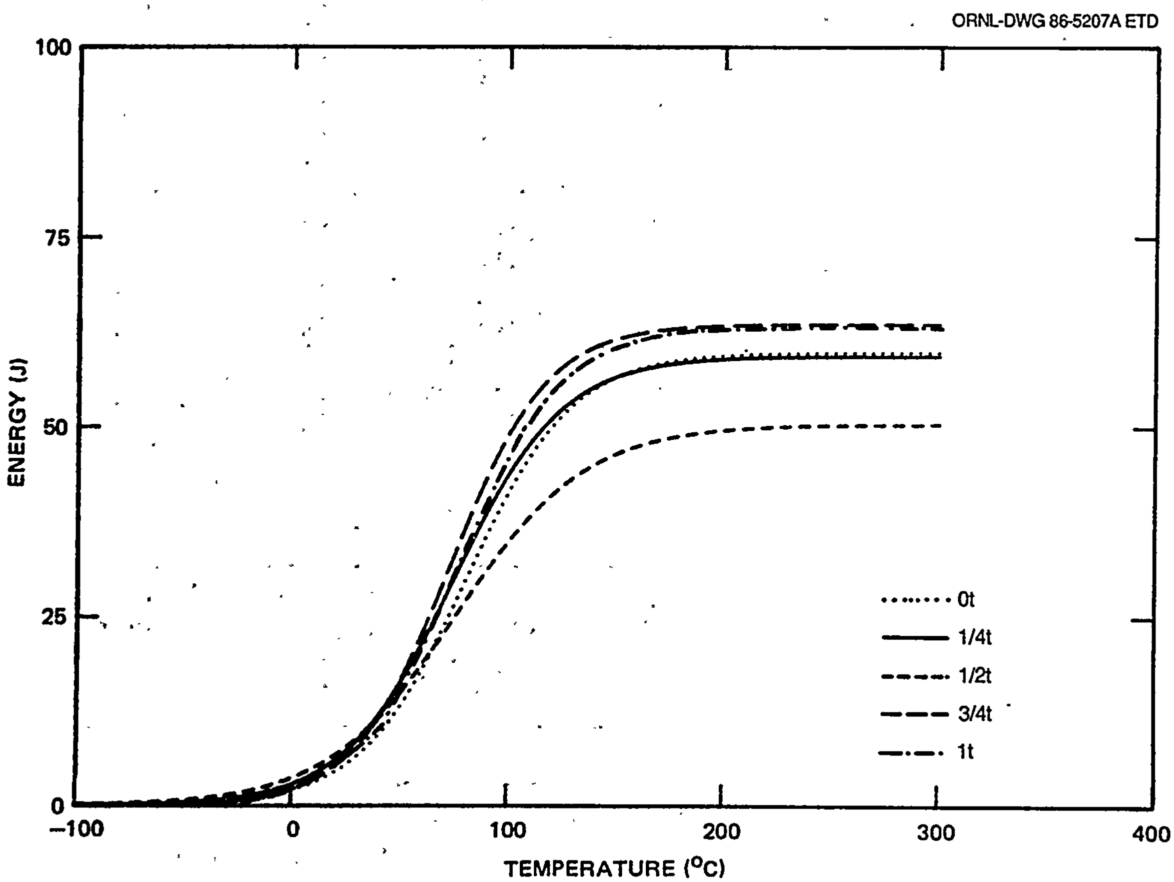

Fig. 3.3. Curve fits of CVN impact energy vs temperature for characterization block PTC1 (2 1/4 Cr-1 Mo steel) for T-L orientation and at various plate depths.

Table 3.5. Summary of results for drop-weight and CVN impact tests: broken halves of WP-2.1 and -2.5 specimens and PTC1 characterization block

	Averages[a] from WP-2.1 and -2.5	PTC1
Drop-weight NDT temperature, °C	60	49
CVN		
Energy at NDT temperature, J	15–20	16
USE, J	61–65	50–64
Temperature at 41 J, °C	90–96	87–120
Temperature at onset of 100% shear, °C	150	150
Temperature at 50% of USE, °C	76–82	73–81

[a]Averages of results for material from both plates, including tests from quarter- and half-thickness depths in plate.

Table 3.6. Tensile properties of transverse-oriented specimens machined from broken halves of specimens WP-2.1 and -2.5

Specimen	Temperature (°C)	Strength (MPa) 0.2% yield Test result	Strength (MPa) 0.2% yield [a]	Strength (MPa) Ultimate Test result	Strength (MPa) Ultimate [a]	Total elongation (%) [b]	Total elongation (%) [c]	Reduction of area (%)
				WP-2.1 material				
WP2-110	23	311		595		26	25	50
WP2-101	23	318	315	598	596	23	23	51
WP2-102	100	262		544		21	20	50
WP2-112	100	271	267	544	544	23	23	51
WP2-103	200	249		519		23	21	44
WP2-106	200	249	249	523	521	22	19	46
WP2-105	300	263		527		22	19	44
WP2-108	300	281	272	533	530	15	16	38
				WP-2.5 material				
WP2-505	23	292	292	597	597	21	20	50
WP2-508	100	287	287	554	554	19	18	46
WP2-504	200	226		472		23	21	51
WP2-506	200	222	224	472	472	22	21	50
WP2-501	300	285	285	543	543	16	16	40

[a]Averages of results at this temperature.

[b]As determined from gage length.

[c]As determined from change in total specimen length divided by length of reduced section.

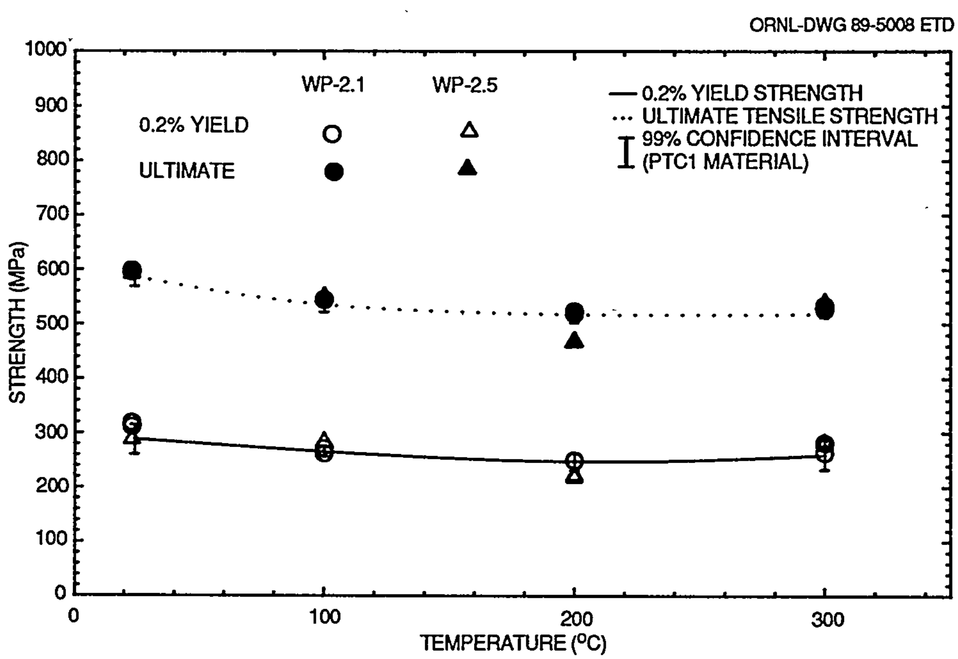

Fig. 3.4. Comparison of WP-2 material tensile strength test results with 99% confidence interval obtained from PTC1 characterization block material tests.

Table 3.7. Tensile properties of specimens machined transverse to the rolling direction of material from characterization block PTC1

Specimen[a]	Temperature (°C)	Strength (MPa) Yield [b]	Strength (MPa) Yield [c]	Strength (MPa) Ultimate	Fracture stress (MPa)	Elongation[d] (%)	Reduction of area (%)
				4.52-mm-diam specimens			
PI97	−100		512	715	573	35	50
PI93	−100		503	719	572	41	51
PI94	−50		348	664	470	28	51
PI127	0		321	603	466	26	53
PI118	0		346	599	468	25	56
PI123	100		320	537	441	21	48
PI98	200		269	493	411	20	50
PI114	300		327	533	478	15	38
				6.35-mm-diam specimens			
PI283	24	266	348	574	467	26	51
PI291	24	314	314	586	501	25	44
PI285	100	265	359	530	446	22	47
PI286	100	266	337	523	432	24	50
PI292	100	259	340	530	449	26	47
PI287	200	241	315	511	447	20	46
PI288	200	248	315	509	434	19	46
PI293	200	234	330	513	442	20	45
PI289	300	290	344	520	454	16	41
PI290	300	244	325	513	454	17	43
PI294	300	248	335	515	461	16	41
				12.7-mm-diam specimens			
PI369	24	275	336	578		26	47
PI370	25	295		603		27	50
PI371	100	256		536		23	46
PI372	100	276		554		24	46
PI374	200	263		534		23	47
PI373	300	254		524		21	42

[a]All specimen machined from 1/4t depth in plate with transverse orientation.

[b]Yield strength obtained from x-y plot of load vs strain extensometer (25.4-mm gage length).

[c]Yield strength obtained from strip-chart recording of load vs crosshead speed.

[d]Computed from strip-chart readings of elongation of specimen, corrected to a gage length of four diameters when necessary. The elongations for the 12.7-mm-diam specimens were computed from gage marks in the specimens.

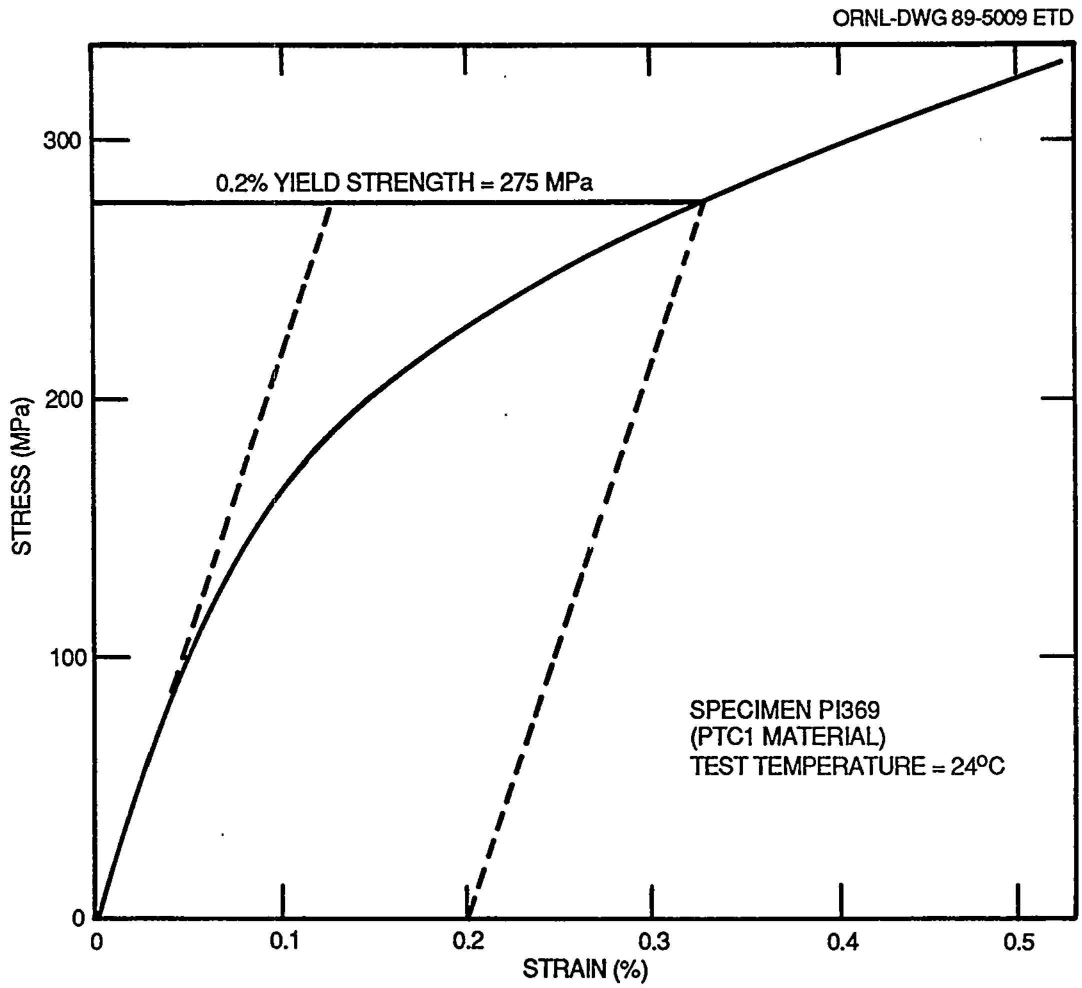

Fig. 3.5. Typical room-temperature stress-strain curve for material obtained from characterization block PTC1 in direction transverse to material rolling orientation.

As may be seen from Fig. 3.4, most results from the present tests fall within the 99% confidence interval of results obtained previously from the PTC1 material. The only deviations were two specimens using WP-2.5 material tested at 200°C, in which both the yield and ultimate strength are about 10% less than the averages obtained from WP-2.1 material. Tensile properties generally do not exhibit much scatter, and it is assumed that the cause of this deviation is experimental error. Thus, it may be concluded that the posttest material from the WP-2 plates had not been subjected to any significant strain levels, either during the fabrication or testing of the large 10-m-long, single-edge-notch (SEN) specimens.

3.5 CRACK-ARREST TESTING

Crack-arrest tests were performed according to the ASTM Test for Determining Plane-Strain Crack-Arrest Fracture Toughness, K_{Ia}, of Ferritic Steels (E 1221-88) using 33 × 150 × 150 mm specimens. From each of plates WP-2.1 and -2.5 seven specimens were fabricated; three specimens were duplex, and four were weld embrittled. The test results are given in Table 3.8 and plotted in Fig. 3.6. Also plotted in Fig. 3.6 are the results from previous T-L orientation tests on the PTC1 characterization block (given in Table 3.9). Only one specimen, WP213, from the WP-2.1 material and tested at 70°C was valid in strict accordance to ASTM E 1221 and gave a K_{Ia} of 82 MPa·$\sqrt{m}$. The ASTM E-1221 measures of validity have also been included in Table 3.8. The letters A–E refer to the corresponding criteria given in Table 2 of ASTM E 1221-88. The first row of values given for each specimen in the table are the lengths of the unbroken ligament (A and B), specimen thickness (C), and the crack jump (D and E). The values in parentheses are the minimum ones specified in ASTM E 1221-88. Some specimens are marginally invalid, and others grossly so.

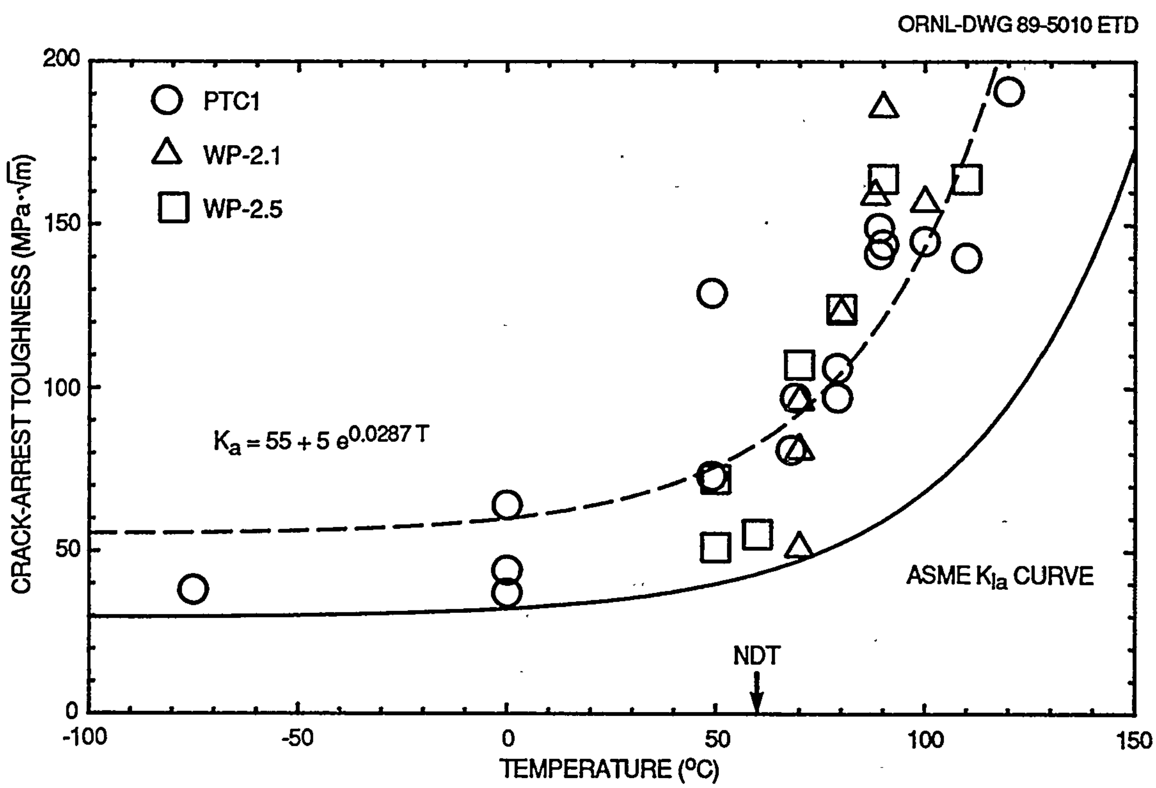

Fig. 3.6. Comparison of posttest crack-arrest toughness (K_a) values obtained for specimens fabricated from plate halves of specimens WP-2.1 and -2.5 with those obtained from PTC1 material and ASME K_{Ia} curve.

Table 3.8. Crack-arrest toughness data from WP-2.1 and -2.5 material for both weld-embrittled and duplex specimens in the T-L orientation

Specimen ID	Specimen Type[c]	Temperature (°C)	K_a (MPa·$\sqrt{m}$)	ASTM E 1221 validity criteria[a] measured and minimum values[b] (mm)				
				A	B	C	D	E
				WP-2.1 material				
WP212	WE	70	97	46 (19)	46 (49)	33 (39)	35 (23)	35 (36)
WP213	WE	70	82	37 (19)	37 (35)	33 (28)	43 (23)	43 (35)
WP214A	WE	70	52	18 (19)	18 (14)	33 (11)	63 (23)	63 (30)
WP211	WE	80	124	63 (19)	63 (81)	33 (65)	18 (23)	18 (35)
WP216	DX	88	160	45 (19)	45 (143)	33 (114)	24 (25)	
WP218	DX	90	187	62 (19)	62 (194)	29 (155)	7 (20)	
WP215	DX	100	158	53 (19)	53 (141)	29 (113)	15 (20)	
				WP-2.5 material				
WP252	WE	50	51	7 (19)	7 (13)	33 (11)	73 (23)	73 (41)
WP253	WE	50	72	24 (19)	24 (27)	33 (21)	57 (23)	57 (51)
WP254	WE	70	107	57 (19)	57 (60)	33 (48)	24 (23)	24 (33)
WP251	WE	60	55	14 (19)	14 (16)	33 (13)	67 (23)	67 (42)
WP256	DX	80	124	43 (19)	43 (86)	33 (68)	26 (24)	
WP257	DX	90	164	56 (19)	56 (148)	33 (119)	13 (24)	
WP255	DX	110	164	59 (19)	59 (156)	33 (124)	9 (24)	

[a]The letters A–E refer to the validity criteria per ASTM 1221-88 paragraph 9.3, Table 2.

[b]Minimum values are in parentheses.

[c]WE = weld-embrittled specimen; DX = duplex specimen.

Table 3.9. Crack-arrest (K_a) data for PTC1 material (T-L orientation)

Specimen	Test temperature (°C)	K_a (MPa·$\sqrt{m}$)
Weld embrittled, 33 × 152 × 152 mm		
P1320	0	44
PI321	0	37
P1313	49	73
P1318	49	129
P1314	68	81
P1316	69	97
P1317	79	106
P1319	79	97
P1315	89	149
PI322	89	141
Duplex, 33 × 152 × 152 mm		
PI308	90	144
PI310	100	145
PI311	110	140
PI312	120	191
Precracked, 33 × 152 × 152 mm		
PTC1A	−75	38
PTC1C	−75	38
PTC1B	0	64

All T-L orientation data from both PTC1 and WP-2 material were used to obtain the regression fit of the curve shown dashed in Fig. 3.6. The equation was of the form $K_a = a + b \exp(0.0287\ T)$, where T = temperature (°C), K_a is the crack-arrest toughness (MPa·$\sqrt{m}$), and a and b are constants to be determined by regression. The resulting equation is

$$K_a = 55 + 5 \exp(0.0287\ T)\ \text{MPa}\cdot\sqrt{m}\ . \qquad (3.1)$$

The constant 0.0287 was chosen for consistency with previous wide-plate test results (see p. 37, Ref. 6). Equation (3.1) may also be written in a form used in previous work as

$$K_a = 55 + 30 \exp[0.0287\ (T - \text{NDT})]\ \text{MPa}\cdot\sqrt{m}\ , \qquad (3.2)$$

where NDT = 60°C.

In the analysis of the PTSE-2 experiment,[2] the same form of equation was regression-fit to both T-L and T-S small-specimen data and gave $K_a = 34 + 11 \exp[0.02413\ T]$, which can be rewritten as

$$K_a = 34 + 36 \exp[0.02413\ (T - NDT)]\ MPa\cdot\sqrt{m}\ , \qquad (3.3)$$

where, for PTC1, NDT = 49°C. Equations (3.2) and (3.3) have been plotted together in Fig. 3.7 for comparison. Note that Eq. (3.2) is an "average" one in the least-squares sense, with the coefficient of the temperature 0.0287 chosen "*a priori*." The parameters in Eq. (3.3) were adjusted to give a better fit to the temperatures of interest. As may be seen from Fig. 3.7, the differences between K_a calculated from either Eq. (3.2) or (3.3) for temperatures above NDT are relatively small, while there are substantial differences below NDT.

The results of the crack-arrest testing, in spite of invalidity in strict accordance with ASTM E 1221-88, appear to agree reasonably well with those of PTC1. Moreover, the trends exhibited by both valid and invalid small-specimen data from PTC1, T-L and T-S orientations,* agreed

*Incidently, there seems to be no noticeable differences between the T-L and T-S orientations in the small-specimen crack-arrest data from PTC1, as can be seen from Fig. 3.7.

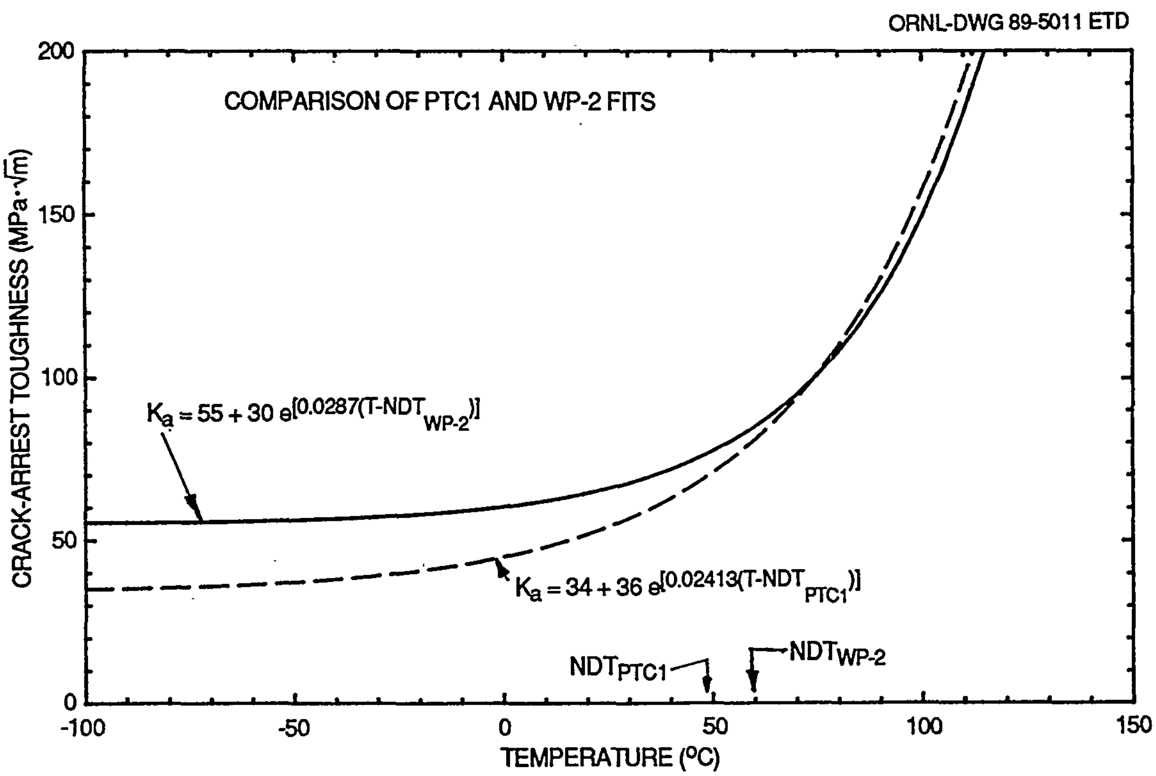

Fig. 3.7. Comparison of regression fits of crack-arrest toughness data for all PTC1 (T-L and T-S orientations) material data and for WP-2 and PTC1 materials (T-L orientation).

well with the results of PTSE-2 (Fig. 3.8). This agreement tends to further reinforce the belief that the validity criteria of ASTM E 1221-88 may be overly restrictive.

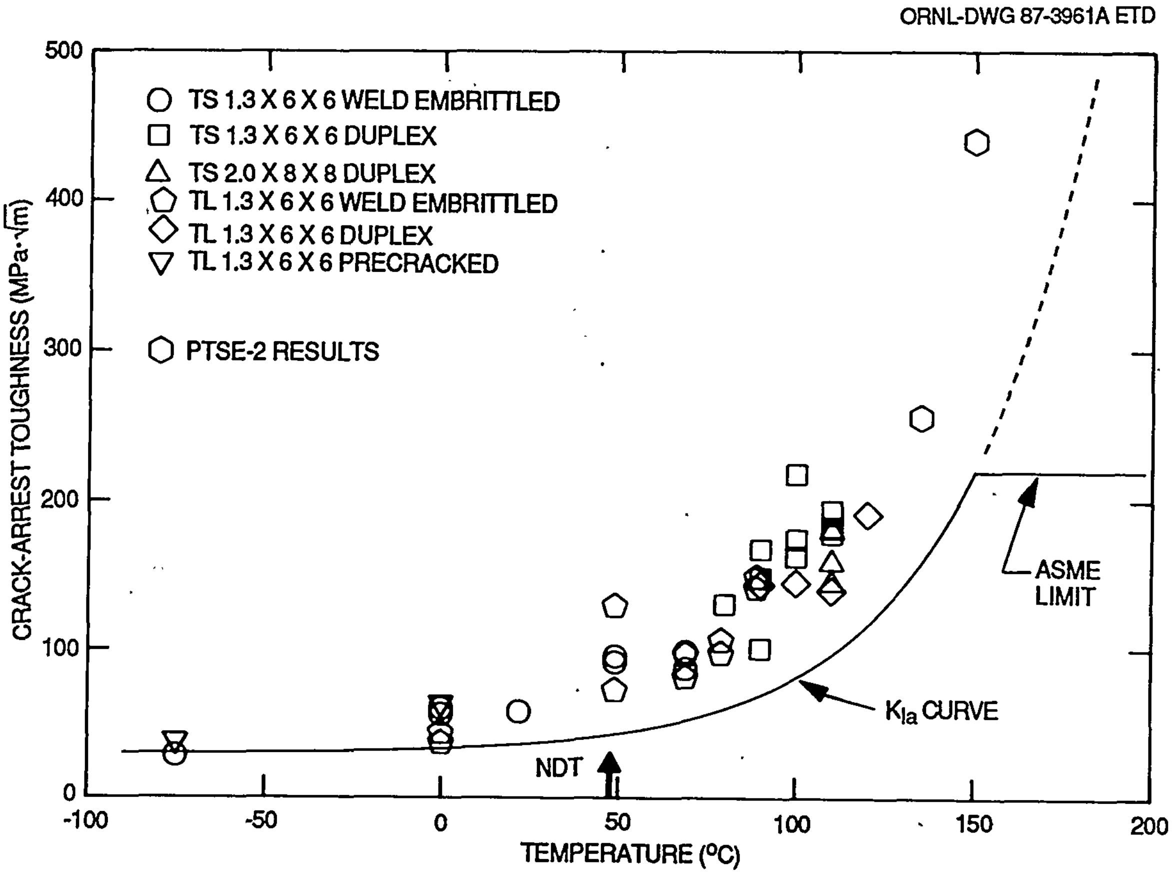

Fig. 3.8. Comparison of crack-arrest toughness test results obtained from PTCl and PTSE-2 LUS 2 1/4 Cr-1 Mo materials.

3.6 FRACTURE-TOUGHNESS TESTING

Fracture-toughness testing was conducted with 25-mm compact specimens C(T) machined from halves of plates WP-2.1 and -2.5. The same procedures and methods of analysis were used as for the characterization of PTCl. The specimens were machined from midthickness (1/2t) in the T-L orientation. In the temperature range 40 to 60°C, where cleavage was expected, the specimens were not side grooved. One trial specimen with no side grooves was tested at 80°C and did not cleave. Thus, those remaining to be tested at 80°C or higher were side grooved 20%. Because of the limited purpose of posttest characterization, only specimens from WP-2.5 material were tested at 80°C or higher.

In the 40 to 80°C transition range, a K_{Jc} value was calculated by determining the modified J-integral[7] at the point of cleavage (J_c) and using the relationship $K^2_{Jc} = EJ_c$, where E is Young's modulus (a value of 205 GPa was used). For the single specimen, WP2504, that experienced significant stable ductile tearing without final cleavage failure, a "J_c" was determined at the point of maximum load, resulting in a "K_{Jc}" of 206 MPa·√m. Specimen WP2504 also experienced a pop-in at 120 MPa·√m, and this is the value used on the plot of transition region fracture toughness given in Fig. 3.9, and not the 206-MPa·√m value, because no cleavage is associated with the latter. The unloading compliance method was used to estimate crack extension, but the test is conducted so as not to preclude a possible determination of K_{Ic} per ASTM Standard Test Method for Plane-Strain Fracture Toughness of Metallic Materials (E 399). The graphical output from the analysis of a typical test is shown in Fig. 3.10. Crack extension was determined using the nine-point averaging technique.

The results of the 40, 60, and 80°C K_{Jc} tests are shown in Table 3.10. Also given in Table 3.10 are the $K_{\beta c}$ values calculated using the

ORNL-DWG 89-5013 ETD

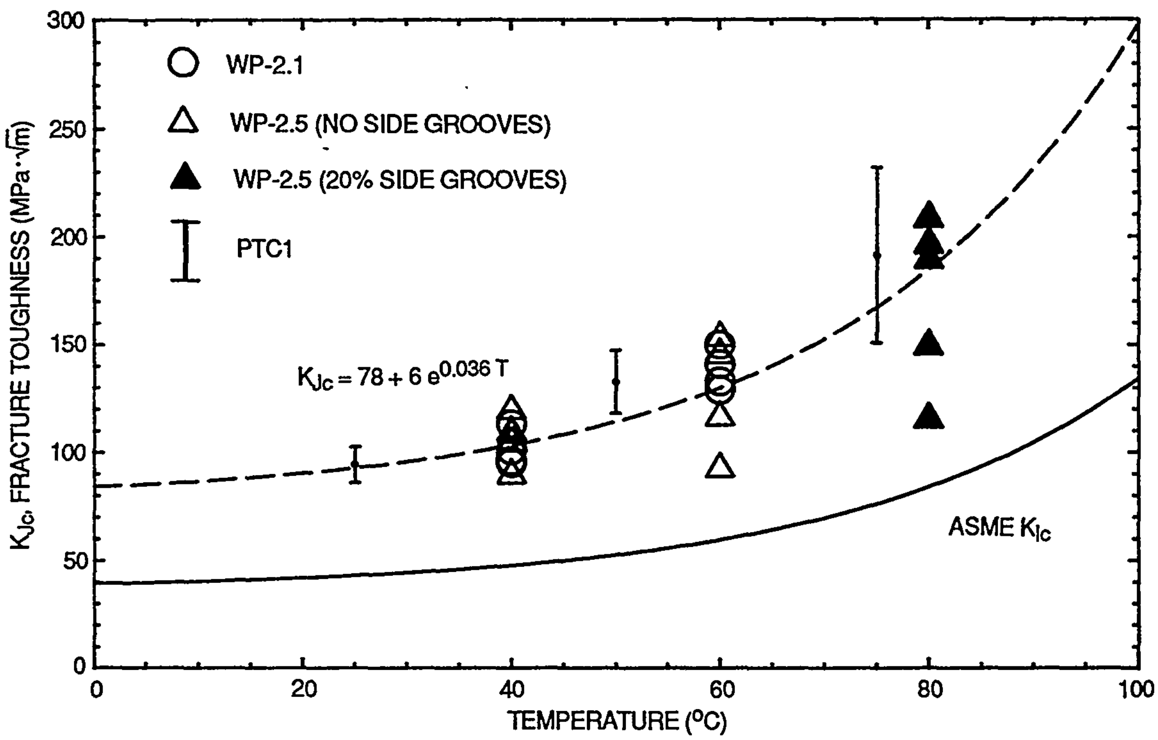

Fig. 3.9. Comparison of posttest initiation toughness (K_{Jc}) for specimens fabricated from plate halves of specimens WP-2.1 and -2.5 with range of values exhibited for specimens fabricated from PTC1 characterization block.

ORNL-DWG 89-5012 ETD

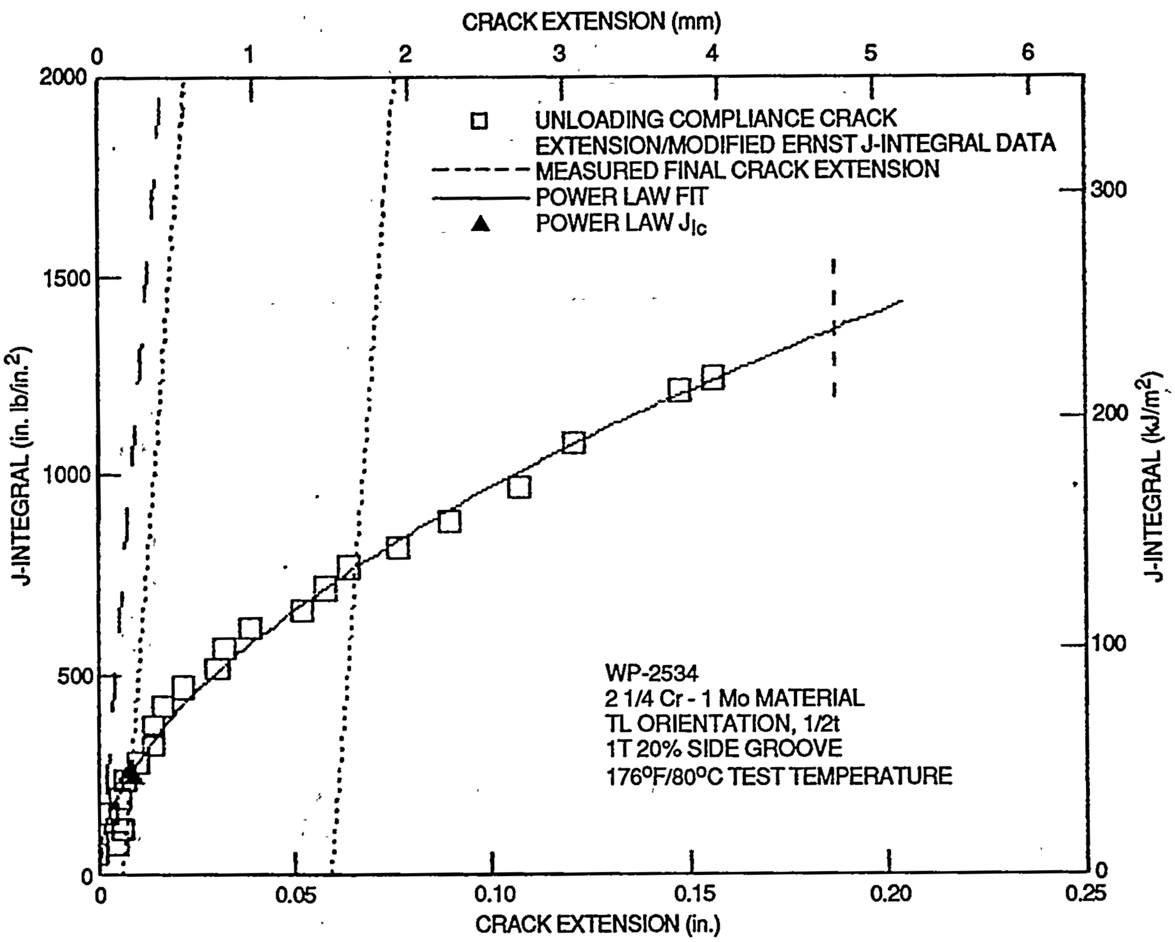

Fig. 3.10. Graphical output from analysis of a typical fracture toughness test at 80°C using single-specimen unloading compliance method.

method described by Merkle[8] and the measured stable ductile crack extension (including blunting). No valid K_{Ic} values were obtained, even at 40°C, because of the low yield strength of this material. The scatter is typical of that exhibited in the transition range. At 80°C, the upper value of K_{Jc} is about twice the lowest one, but this ratio decreases to 1.3 at 40°C. The results are also shown in Fig. 3.9, which includes the 99% confidence band of PTC1 results. There is no significant difference in results between material from WP-2.1 and that from WP-2.5, but the WP-2 material overall has noticeably lower initiation toughness than PTC1, at least >40°C.

Data from the tests at 40 and 60°C were used to obtain a regression fit to an equation of the form $K_{Jc} = a + b \exp(0.036\ T)$, where T = temperature in °C, K_{Jc} is the fracture toughness in MPa·$\sqrt{m}$, and a and b are

Table 3.10. Transition region fracture-toughness results from posttest characterization using 25-mm C(T) specimens (1/2t) machined from broken halves of specimens WP-2.1 and -2.5 (T-L orientation)

Specimen	Test temperature (°C)	Side groove (%)	K_{Jc} (MPa·$\sqrt{m}$)	$K_{\beta c}$ (MPa·$\sqrt{m}$)	Stable crack extension (mm)
		WP-2.1 material			
WP2109	40	0	95	51	0.0
WP2115	40	0	113	55	0.0
WP2108	40	0	101	53	0.0
WP2107	40	0	96	52	0.0
WP2104	60	0	141	59	0.7
WP2118	60	0	129	57	0.7
WP2106[a]	60	0	133	58	0.1
WP2101	60	0	150	61	1.0
		WP-2.5 material			
WP2506	40	0	106	54	0.0
WP2526	40	0	121	57	0.0
WP2503	40	0	110	55	0.0
WP2511	40	0	111	55	0.0
WP2521	40	0	91	51	0.0
WP2514	60	0	94	51	0.2
WP2518	60	0	118	55	0.3
WP2505	60	0	155	62	0.9
WP2508	60	0	147	60	0.9
WP2504[b]	80	20	120	52	0.4
WP2504[c]	80	20	206	63	5.9
WP2510	80	20	198	63	4.5
WP2516	80	20	191	62	3.3
WP2517	80	20	151	57	2.0
WP2534	80	20	210	64	4.7

[a]Pop-ins at 82 and 115 MPa·$\sqrt{m}$.

[b]Pop-in at cycle 13; values given are at maximum load of cycle 13.

[c]No cleavage; values are final ones when test was discontinued and are not included in Fig. 3.10.

constants to be determined by regression. The resulting equation is

$$K_{Jc} = 78 + 6 \exp (0.036\ T)\ \mathrm{MPa}\cdot\sqrt{m}\ . \tag{3.4}$$

The temperature coefficient 0.036 was chosen for consistency with previous work (WP-1 test series). Equation (3.4) may also be written in the form

$$K_{Jc} = 78 + 56 \exp [0.036\ (T - \mathrm{NDT})]\ \mathrm{MPa}\cdot\sqrt{m}\ , \tag{3.5}$$

where NDT = 60°C.

The results of toughness testing performed at 120, 160, and 200°C are given in Table 3.11. A power-law of the form $J = A(\Delta a + B)^c + D$ was fit to the J_M data, with the parameters given in Table 3.11. The intersection of the power-law fit with the 0.2-mm offset line is used to determine J_{Ic}. The table gives J-integral values calculated by deformation theory, J_D, as recommended in the ASTM Test for J_{Ic}, A Measure of Fracture Toughness (E 813 – 87), as well as modified J-integral,[7] J_M. The values of $K_{J_{Ic}}$ were determined from the respective values of J by the expression given above. The tearing modulii were obtained from the nondimensional expression

$$T = [E/(\sigma_f)^2](dJ/da)\ ,$$

where

(dJ/da) = slope of a straight line joining the intersection of the power-law fit and the 0.15- and 1.5-mm exclusion lines,
E = Young's modulus (205 GPa),
σ_f = flow stress, an average of the ultimate strength and 0.2% offset yield strength at test temperature.

The power-law curve fits to the J_M data for all seven specimens tested [120°C (three specimens), 160°C (two specimens), and 200°C (two specimens)] have been plotted in Fig. 3.11. The number of specimens tested is too small to permit statistical analysis or firm conclusions regarding comparisons with PTC1, but the scatter of the data from WP-2.5 material seems to be smaller than that exhibited by PTC1.[2] The values of J_M for WP-2.5 material seem to fall in the scatter band exhibited by PTC1. The averaged and interpolated tearing modulii for PTC1 at 120, 160, and 200°C were approximately 90, 80, and 67, whereas for WP-2.5 material they were 71, 70, and 66, respectively. Thus, the tearing modulii for WP-2 material at 120 and 160°C are ~80% of those for PTC1, but almost the same at 200°C. The trends exhibited by the tearing

Table 3.11. Ductile-shelf fracture-toughness results from posttest characterization using 25-mm C(T) specimens (1/2t) machined from broken half of specimen WP-2.5 (T-L orientation)

Specimen ID	Test temperature (°C)	J_{Ic} (kJ/m²)		$K_{J_{Ic}}$ (MPa·$\sqrt{m}$)		Crack[a] extension (mm)	Tearing modulus[b]	Curve fit parameters[c] $J = A(\Delta a + B)^C + D$			
		J_D	J_M	J_D	J_M			A	B	C	D
WP2515	120	61	60	111	110	6.6	70	113	0.069	0.449	−10
WP2519	120	50	47	100	97	7.5	70	101	0	0.477	−6
WP2507	120	54	53	104	103	5.9	72	111	0	0.449	−9
WP2509	160	54	52	103	101	7.6	62	92	0.035	0.467	−1
WP2532	160	50	47	99	96	7.4	77	142	0	0.349	−42
WP2523	200	49	48	98	97	7.0	57	81	0.037	0.459	1
WP2529	200	37	35	88	85	7.4	75	122	0	0.362	−38

[a]Measured final crack extension.

[b]Calculated from intersection of power-law fit and offset lines.

[c]J_M data were used.

ORNL-DWG 89-5014 ETD

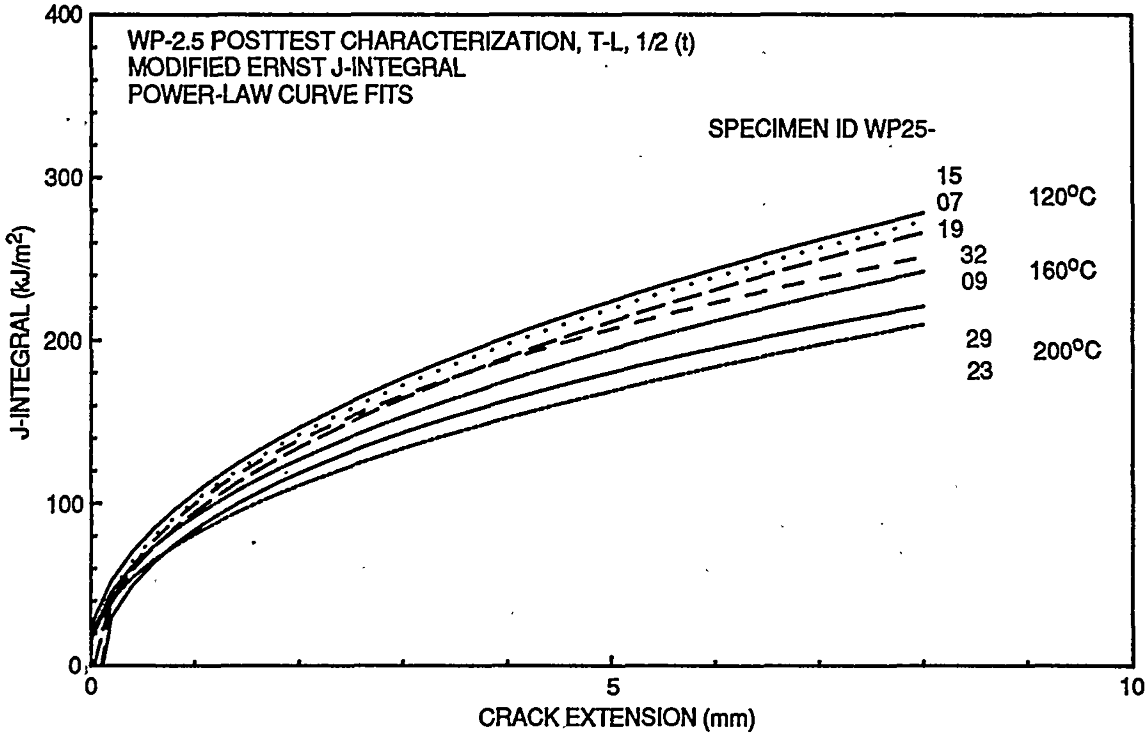

Fig. 3.11. Comparison of J-integral (J_m) resistance curves at three temperatures for specimens obtained from WP-2.5 material at midthickness in T-L orientation.

modulii for both materials are consistent because there is a decrease in modulus with increasing temperature.

The $K_{J_{Ic}}$ values for the tests that did not undergo cleavage fracture are much lower than many of the K_{Jc} values from specimens that did undergo mode conversion from stable tearing to cleavage fracture. Table 3.10 shows, for example, that specimen WP2534, tested at 80°C, experienced 4.7 mm of stable crack extension before cleavage fracture with a K_{Jc} value of 210 MPa·$\sqrt{m}$. The J-R curve for that specimen is shown in Fig. 3.9. A J_{Ic} value (using modified J) for that specimen is ~44 kJ/m², which is lower than those shown in Table 3.11 for specimens that did not cleave at 120°C. The resulting $K_{J_{Ic}}$ value is 95 MPa·$\sqrt{m}$ and compares with the K_{Jc} values at 80°C, which ranged from 120 to 210 MPa·$\sqrt{m}$. This comparison reinforces the observation that cleavage fracture-toughness values in the mid-to-upper-transition region can be substantially greater than the toughness determined at the onset of ductile tearing.

A dynamic fracture-toughness relation (see p. 38, Ref. 6) for use in analyses of the wide-plate tests is written as

$$K_{ID} = K_a + A(T)\,\dot{a}^2 , \tag{3.6}$$

where K_{Ia} is given by Eq. (3.2). For

$$T - RT_{NDT} > -13.9\ K\ ,$$

$$A(T) = [329.7 + 16.25\ (T - RT_{NDT})] \times 10^{-6}\ MPa \cdot s^2 \cdot m^{-3/2}$$

and for

$$T - RT_{NDT} \leq -13.9\ K\ ,$$

$$A(T) = [121.7 + 1.2962\ (T - RT_{NDT})] \times 10^{-6}\ MPa \cdot s^2 \cdot m^{-3/2}\ .$$

Units for K_{ID}, $\dot{a}$, and T are $MPa \cdot \sqrt{m}$, m/s, and °C, respectively. The form of the K_{ID} expression in Eq. (3.6) and relations for A(T) are derived from Ref. 9 by estimating that RT_{NDT} = −6.1°C for the material used in that study. Much of the data used in Ref. 9 are presented in Ref. 10.

REFERENCES

1. H. A. Domian, Martin Marietta Energy Systems, Inc., Oak Ridge Natl. Lab., *Low Upper-Shelf Toughness, High Transition Temperature Test Insert in HSST PTSE-2 Vessel and Wide Plate Test Specimens,* USNRC Report NUREG/CR-4711 (ORNL/Sub/85-34128/1), February 1987.*

2. R. H. Bryan et al., Martin Marietta Energy Systems, Inc., Oak Ridge Natl. Lab., *Pressurized-Thermal-Shock Test of 6-in.-Thick Pressure Vessels. PTSE-2: Investigation of Low Tearing Resistance and Warm Prestressing*, USNRC Report NUREG/CR-4888 (ORNL-6377), December 1987.*

3. R. K. Nanstad et al., Martin Marietta Energy Systems, Inc., Oak Ridge Natl. Lab., "Low-Upper-Shelf Material Characterization," pp. 75–114 in *Heavy-Section Steel Technology Program Semiann. Prog. Rep. April–September 1987*, USNRC Report NUREG/CR-4219, Vol. 4, No. 2 (ORNL/TM-9593/V4&N2), April 1988.*

4. R. K. Nanstad et al., Martin Marietta Energy Systems, Inc., Oak Ridge Natl. Lab., "Low-Upper-Shelf Material Characterization," pp. 42–55 in *Heavy-Section Steel Technology Program Semiann. Prog. Rep. October 1986–March 1987*, USNRC Report NUREG/CR-4219, Vol. 4, No. 1 (ORNL/TM-9593/V4&N1), August 1987.*

5. R. K. Nanstad et al., Martin Marietta Energy Systems, Inc., Oak Ridge Natl. Lab., "Pressurized-Thermal-Shock and Wide-Plate Crack-Arrest Characterization," pp. 55–79 in *Heavy-Section Steel Technology Program Semiann. Prog. Rep. April–September 1986*, USNRC Report NUREG/CR-4219, Vol. 3, No. 2 (ORNL/TM-9593/V3&N2), December 1986.*

6. D. J. Naus et al., Martin Marietta Energy Systems, Inc., Oak Ridge Natl. Lab., *Crack Arrest Behavior in SEN Wide Plates of Quenched and Tempered A 533 Grade B Steel Tested Under Nonisothermal Conditions*, USNRC Report NUREG/CR-4930 (ORNL-6388), August 1987.*

7. H. A. Ernst, "Material Resistance and Instability Beyond J-Controlled Crack Growth," pp. I-191–213 in *Second Symposium, Volume I – Inelastic Crack Analysis, ASTM STP 803*, American Society for Testing and Materials, Philadelphia, 1983.*

8. J. G. Merkle, Martin Marietta Energy Systems, Inc., Oak Ridge Natl. Lab., *An Examination of the Size Effects and Data Scatter Observed in Small Specimen Cleavage Fracture Toughness Testing*, USNRC Report NUREG/CR-3672 (ORNL/TM-9088), April 1984.*

9. M. F. Kanninen et al., Batelle-Columbus Laboratories for Martin Marietta Energy Systems, Inc., Oak Ridge Natl. Lab., *Preliminary Analysis of Japanese Wide-Plate Dynamic Crack Propagation Arrest Experiments*, December 1983.

10. T. Kanazawa et al., "Study on Fast Fracture and Crack Arrest," *Experimental Mechanics* 21(2), 78–88, February 1981.†

---

*Available for purchase from National Technical Information Service, Springfield, VA 22161.

†Available in public technical libraries.

4. SPECIMEN PREPARATION, INSTRUMENTATION, AND TESTING PROCEDURE

4.1 SPECIMEN PREPARATION

The 1 × 1 × 0.1 m or 1 × 1 × 0.15 m test articles, shown schematically in Fig. 4.1, were machined and precracked by ORNL before being sent to the National Institute of Standards and Technology (NIST). The precracking was done by hydrogen charging an electron-beam (EB) weld (Fig. 4.2) located at the base of a premachined notch.[1] The notch ($a/w \sim 0.2$) was composed of a 25.4-mm-wide gap that was machined to a depth of 187 mm (X in Fig. 4.1) plus the EB weld-generated crack that had a depth of ~12.7 mm at the end of the gap. Each face of the specimen was side-grooved to a depth equal to 12.5% of the plate thickness, and the grooves had a 0.25-mm-root radius. The initial crack was parallel to the rolling direction. With the exception of test specimens WP-2.3 and -2.6, the crack front of each specimen was then cut into a truncated chevron configuration (Fig. 4.3) to reduce the tensile load required to achieve crack initiation. Table 4.1 presents dimensions for each test article in the WP-2 series.

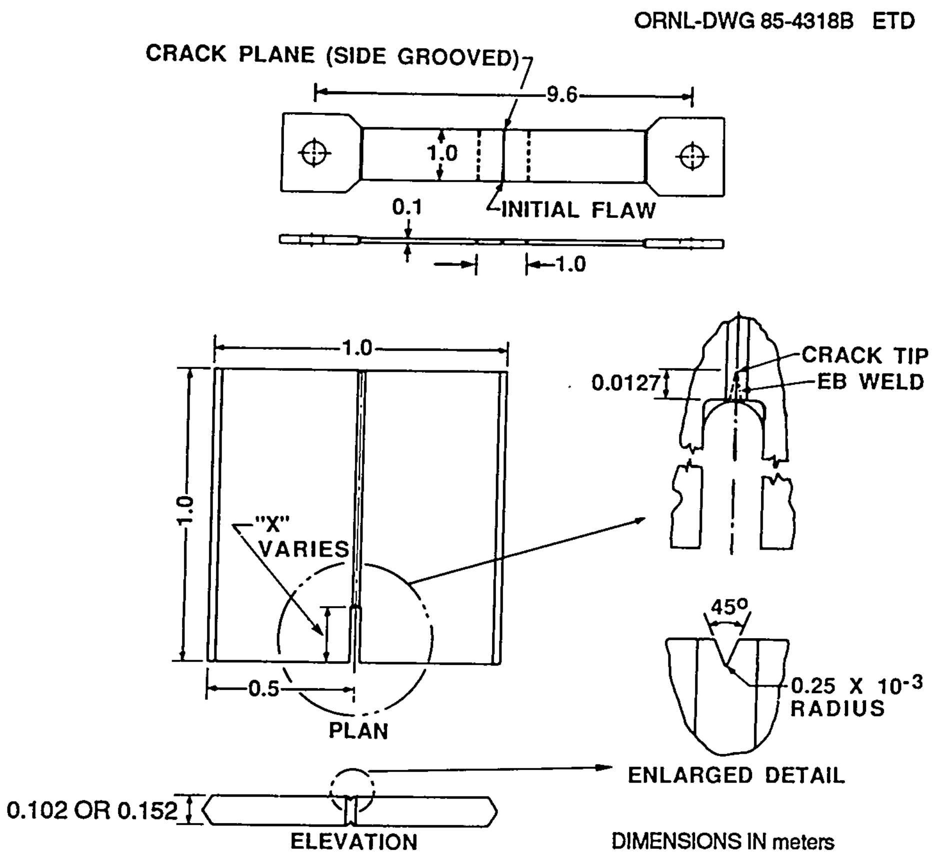

Fig. 4.1. Schematic of HSST wide-plate crack-arrest specimen.

ORNL PHOTO 7176-84

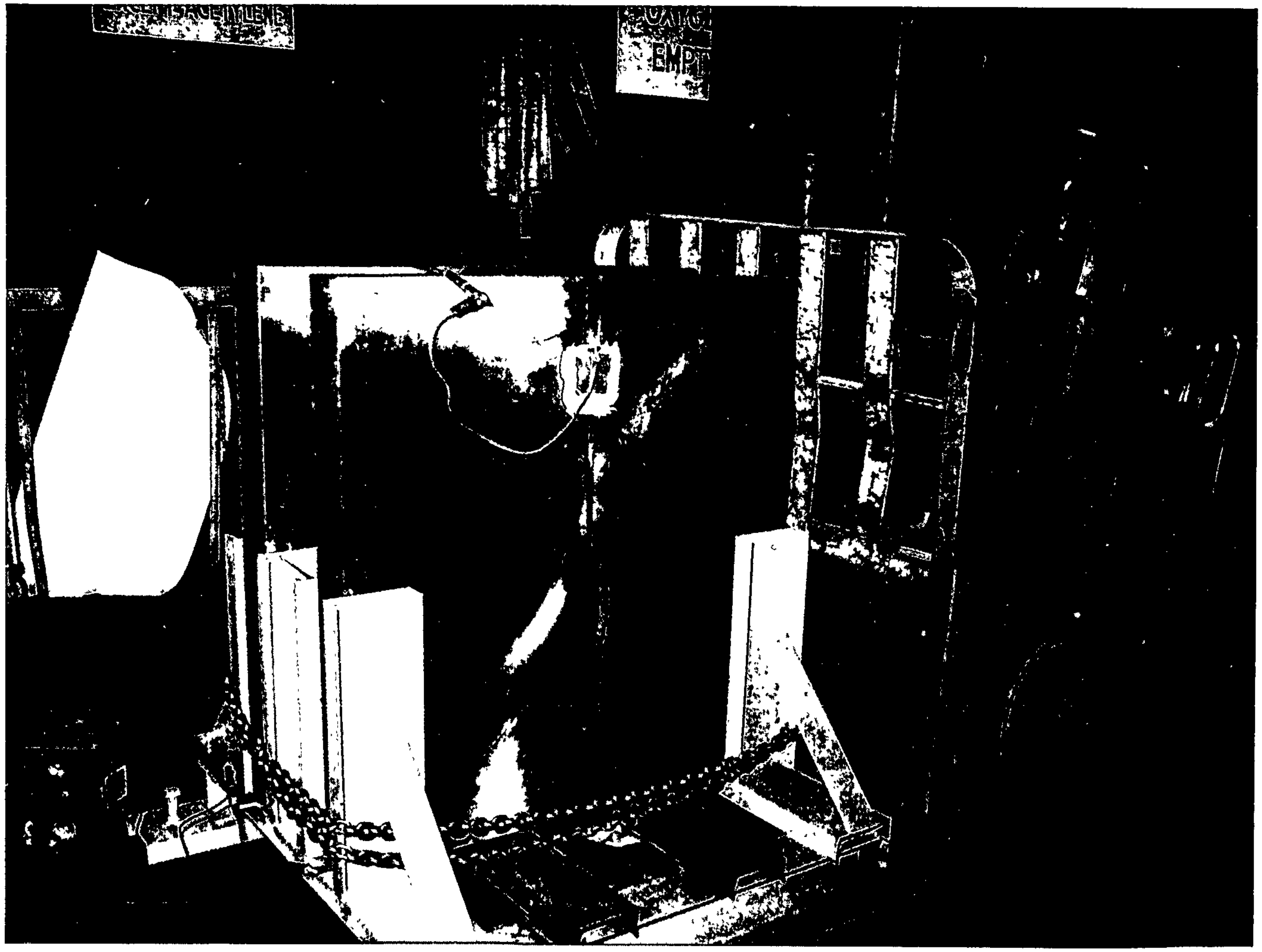

Fig. 4.2. Wide-plate test specimen undergoing hydrogen charging of an EB weld.

ORNL–DWG 86–4106 ETD

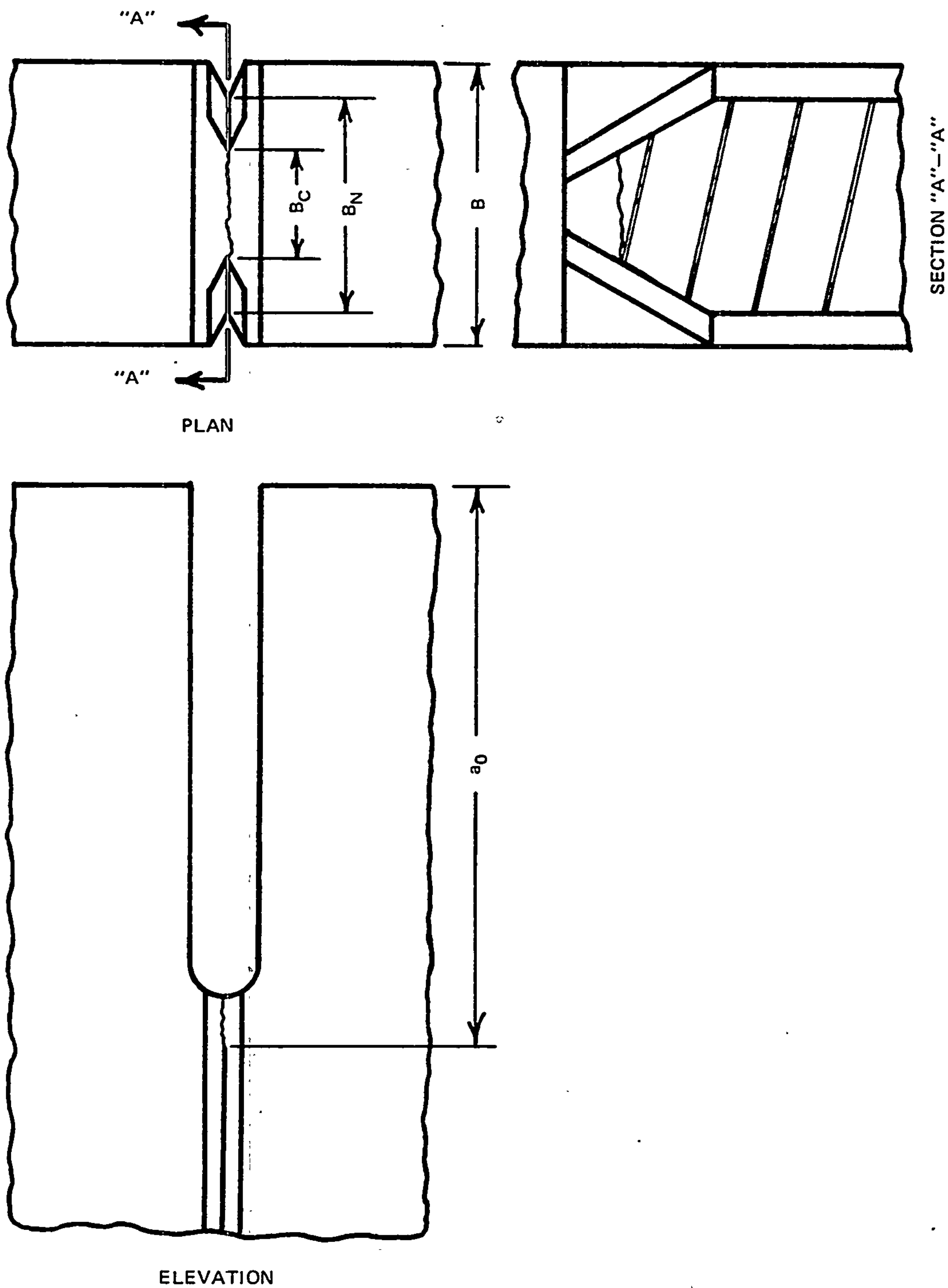

Fig. 4.3. Schematic of chevron configuration of crack front.

Table 4.1. WP-2 series test specimen dimensions

Specimen designation	Initial crack length, a_o	Thickness, B	Notched thickness, B_N	Chevron thickness at a_o, B_c	Width, W	Pop-in crack length, a_o'	Thickness at a_o', B_c'
WP-2.1	199	152.3	113.9	61.5	1000	*a*	*a*
WP-2.2	211	152.4	113.9	71.9	1000	*a*	*a*
WP-2.3	200	152.4	113.8	*a*	1000	*a*	*a*
WP-2.4	203	101.7	76.3	40.5	1000	251	75.5
WP-2.5	199	101.6	76.2	40.7	999	264	76.2[b]
WP-2.6	224	152.4	113.9	*a*	1000	*a*	*a*

[a]Not applicable.

[b]Crack length after pop-in was past the region of the plate where crack front had been cut into a truncated-chevron configuration.

Upon receipt of the test article from ORNL, NIST welded it to pull plates,* which were nominally 103 mm thick for the 102-mm-thick test articles and 153 mm thick for the 152-mm-thick test articles. The pull tabs at the end of the pull plates were strengthened by being 152 mm thick for the 103-mm-thick test articles and 162 mm thick for the 152-mm-thick test articles. (Chapter 2 of Ref. 2 presents a discussion of the development of the test specimen geometry.) Figure 4.4 gives the dimensions for each of the WP-2 test assemblies. Note that the specimen lengths changed from test to test because of removal of the test article and adjoining weldment from the pull plates after each test. Before application of axial load, the out-of-plane deviation of each of the wide-plate assemblies was determined as a function of axial position from the top load pin; the results are shown in Fig. 4.5.

4.2 INSTRUMENTATION

To obtain pertinent data during each test, the specimens were instrumented with five types of devices: thermocouples, strain gages, crack-opening-displacement (COD) gages, accelerometers, and a displacement transducer. Reference 3 gives more detailed information on specimen instrumentation than that presented below.

Up to 40 thermocouples were positioned on each specimen, as shown in Fig. 4.6. The thermocouples were attached by inserting and gluing them into 1.5-mm-diam by 3-mm-deep holes that had been drilled in each specimen. The hole and thermocouple were then covered with a protective silicone coating. Additional thermocouples, not indicated in Fig. 4.6, were used to control heating and cooling of the wide-plate specimen. The thermocouples were sequentially monitored on a periodic basis and corrected for room temperature, and the results were both recorded on magnetic tape and displayed on the computer screen (Fig. 4.7). During the heating and cooling processes, the thermocouples adjacent to the crack plane [Nos. 0–10 in Fig. 4.6(*a*) and Nos. 0–19 in Fig. 4.6(*b*) and (*c*)] were displayed graphically in real time to indicate the relationship between the actual and desired thermal gradient across the specimen width. The other thermocouples were used to indicate the temperature distribution at other positions on the specimen and pull plates during a test for use in posttest analysis.

The total number of strain gages, as well as positioning on the specimen, has varied from test to test. Up to 29 strain gages have been used in a test to provide dynamic strain-field measurments for determination of crack velocity and to provide far-field strain measurements for assessing boundary conditions. Strain gage locations used for the WP-2 series tests are presented in Figs. 4.8 and 4.9. The crack-line gages [gages 1–22 in Fig. 4.8(*a*), (*c*), and (*d*); and gages 1–20 in. Fig. 4.8(*b*) and Fig. 4.9] were two-element, 90° stacked, 350-Ω Karma alloy (nickel-chromium alloy) gages on a polyimide backing. The gages had a coefficient of thermal expansion similar to that of the test specimens.

*Automated, dual-shielded metal insert gas (MIG) process used to join test articles WP-2.1, -2.3, -2.4, and -2.5 to pull plates. Electroslag process used to join test articles WP-2.2 and -2.6 to pull plates.

ORNL-DWG 90M-3557 (Part A) ETD

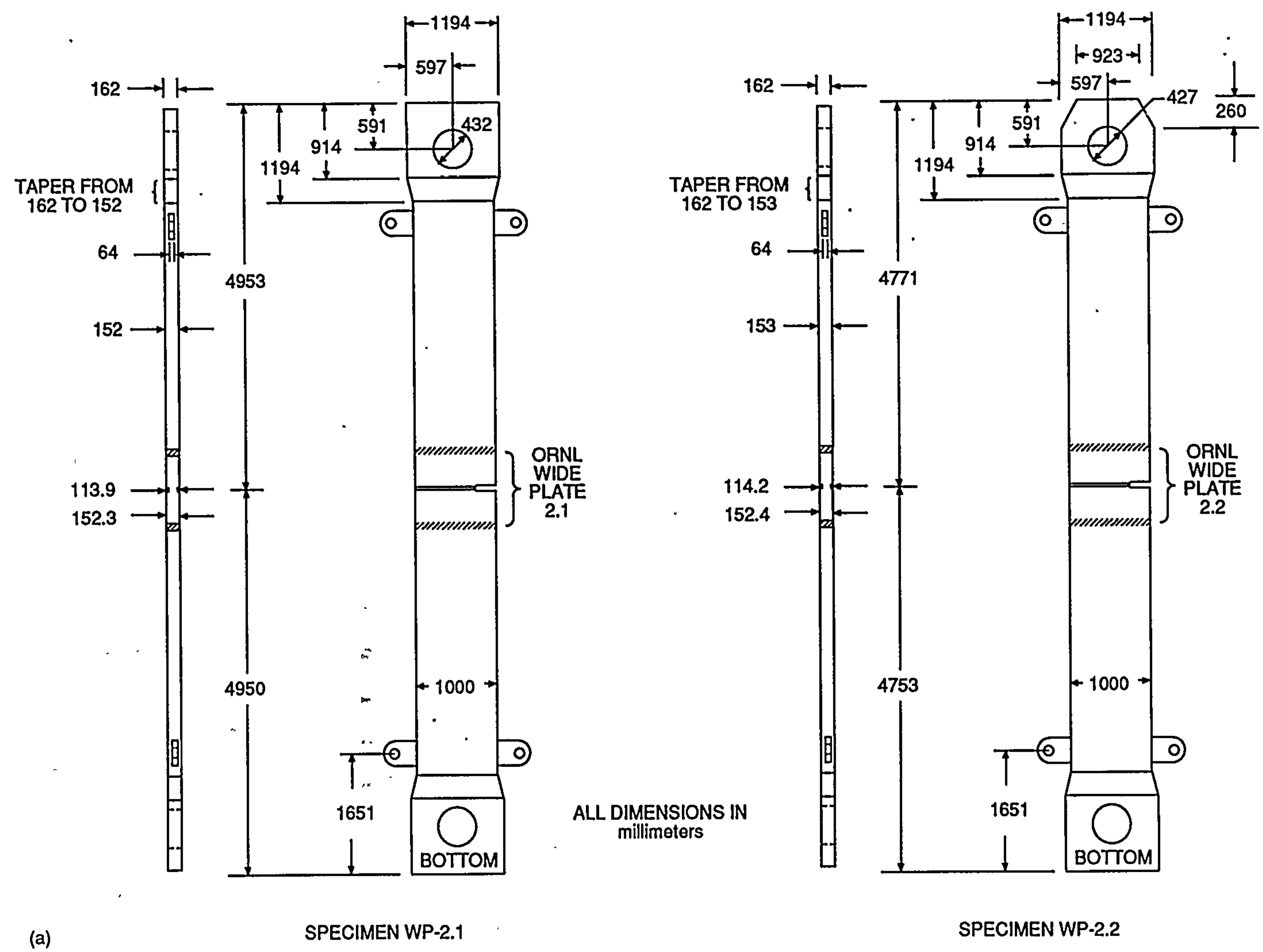

(a)

Fig. 4.4. Overall specimen dimensions for (*a*) tests WP-2.1 and -2.2, (*b*) tests WP-2.3 and -2.4, and (*c*) tests WP-2.5 and -2.6.

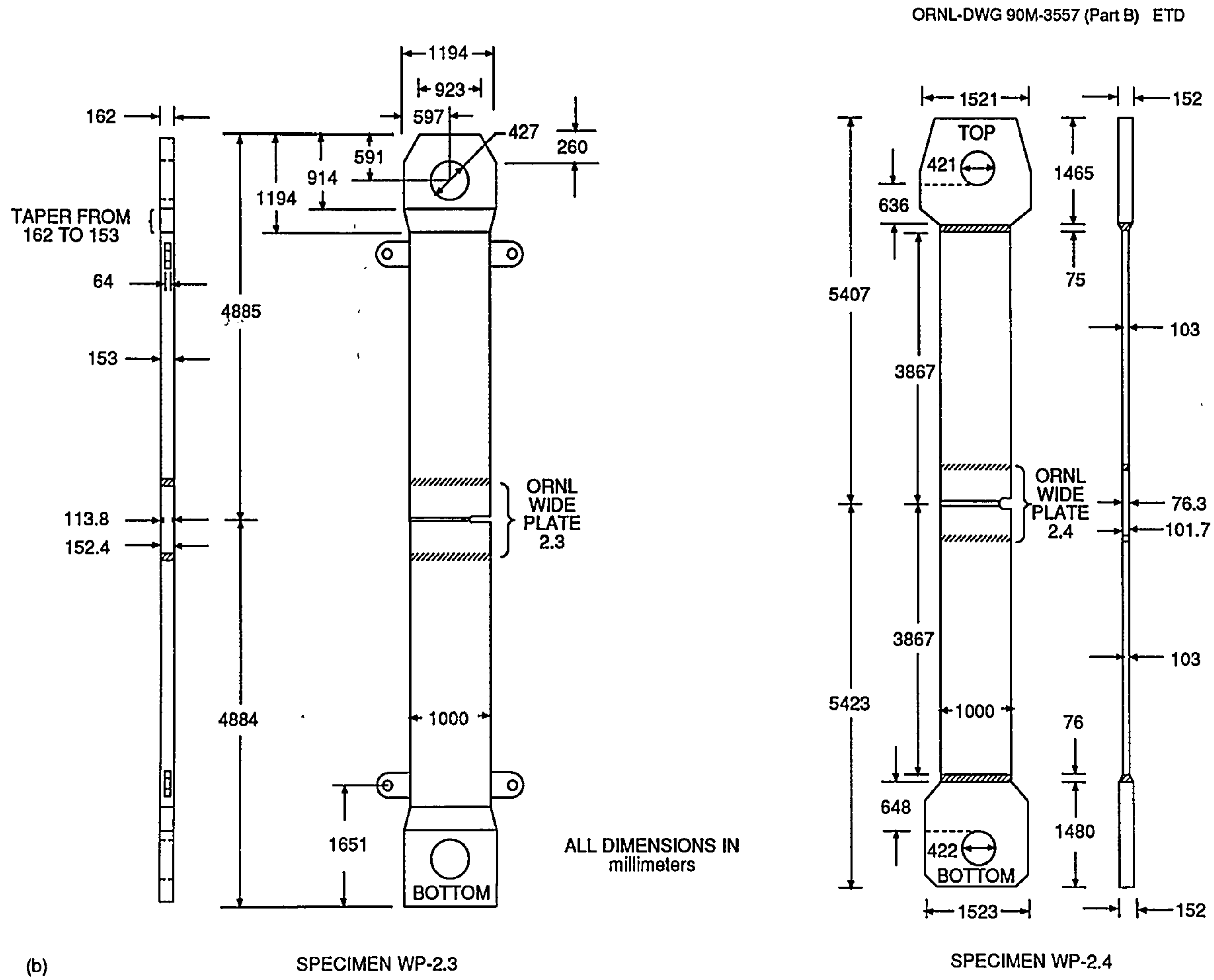

Fig. 4.4 (continued)

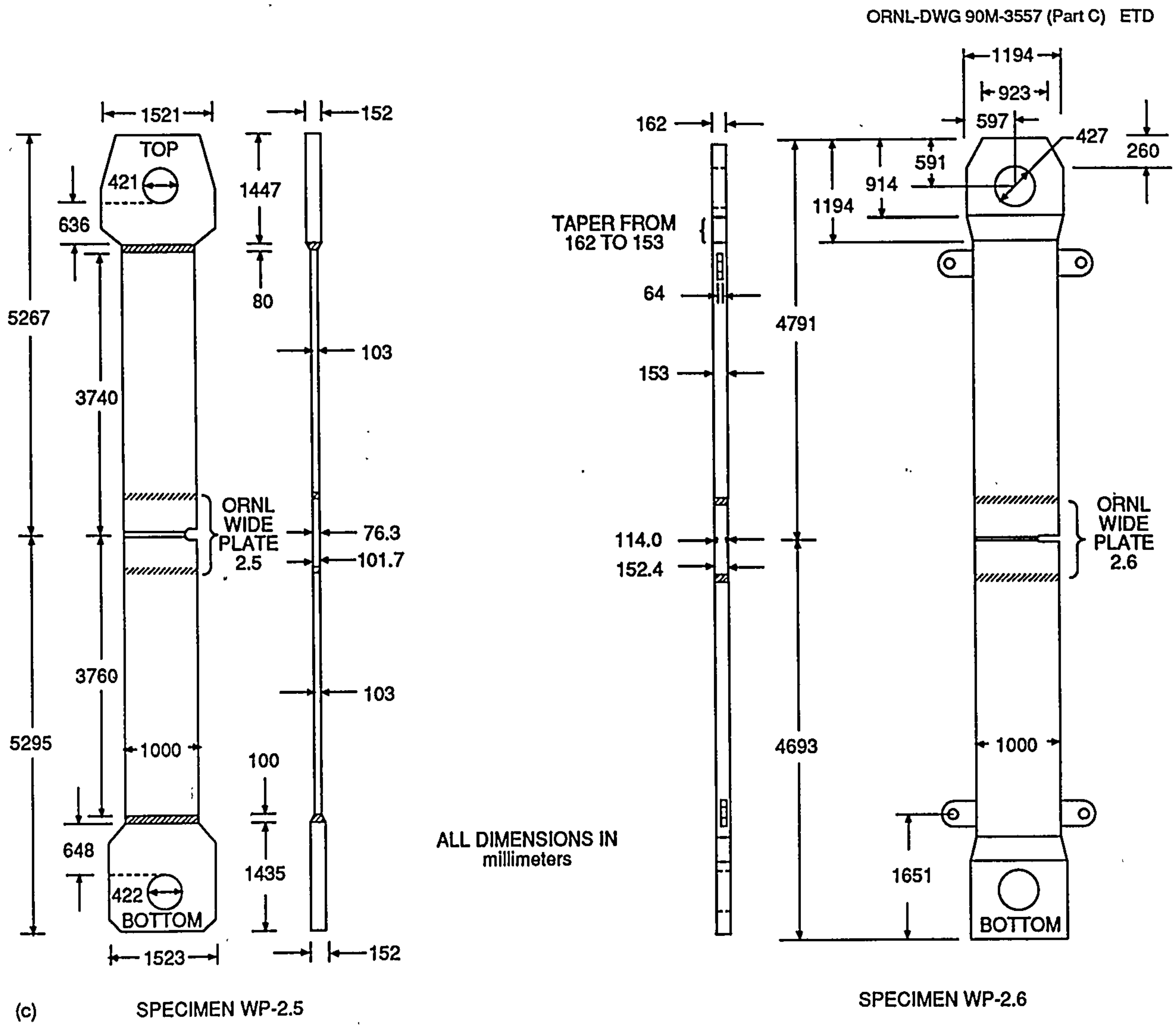

Fig. 4.4 (continued)

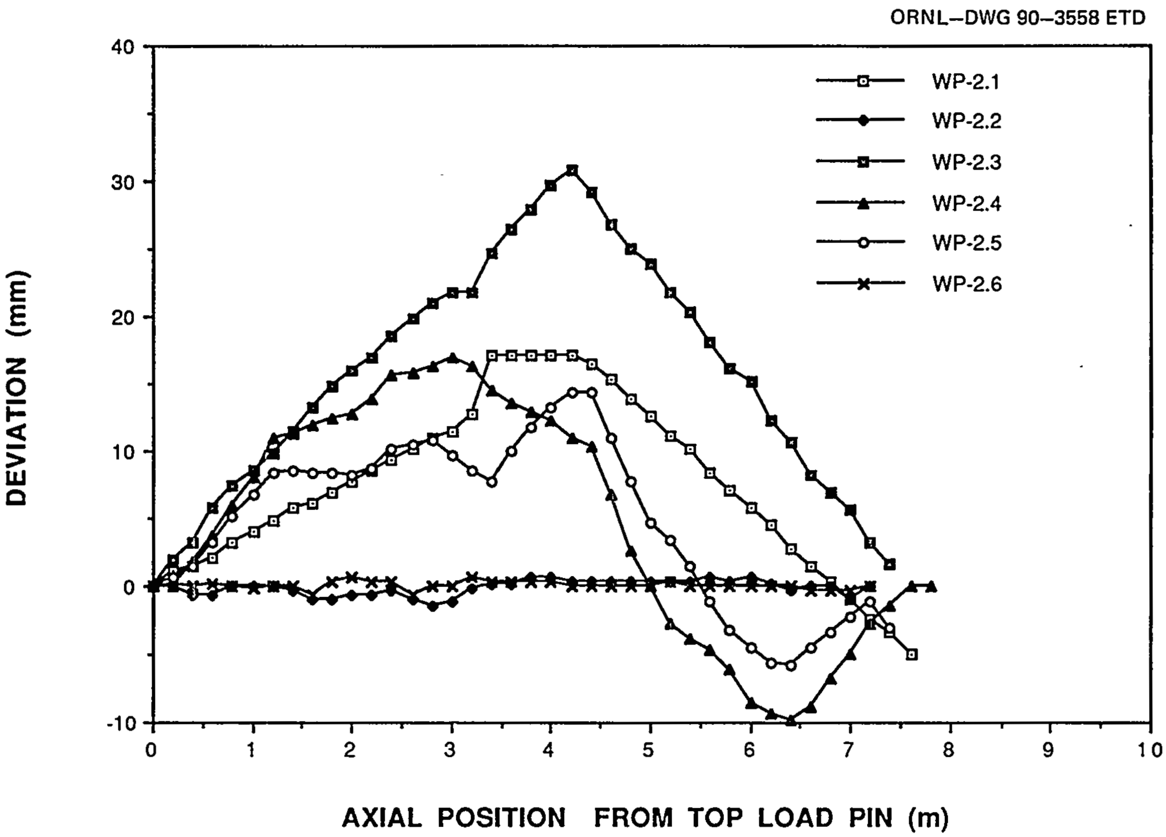

Fig. 4.5. Out-of-plane deviation vs axial position from top load pin.

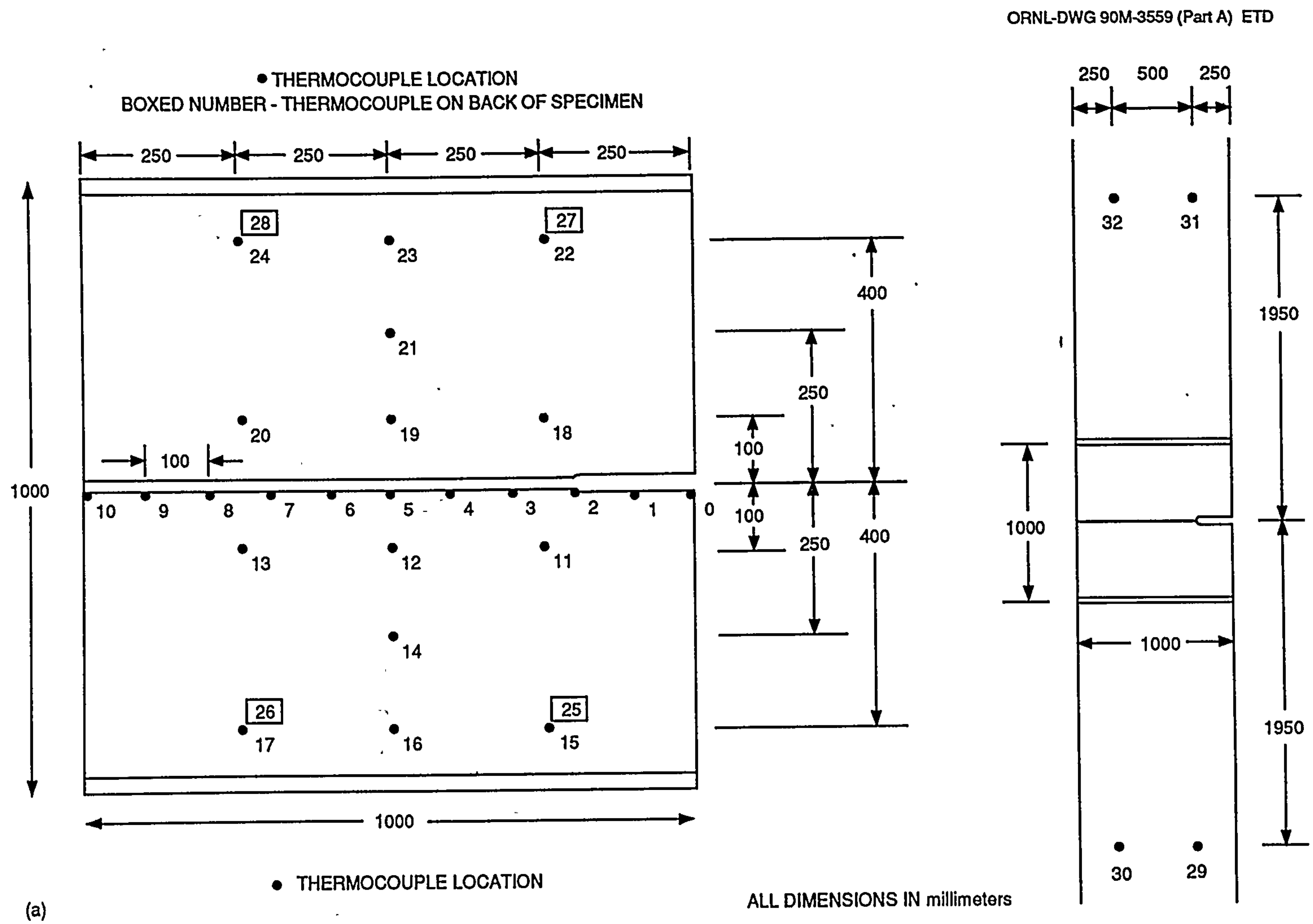

Fig. 4.6. Thermocouple locations for wide-plate, crack-arrest specimens (*a*) WP-2.1 and -2.4; (*b*) WP-2.2, -2.3, and 2.6; and (*c*) WP-2.5.

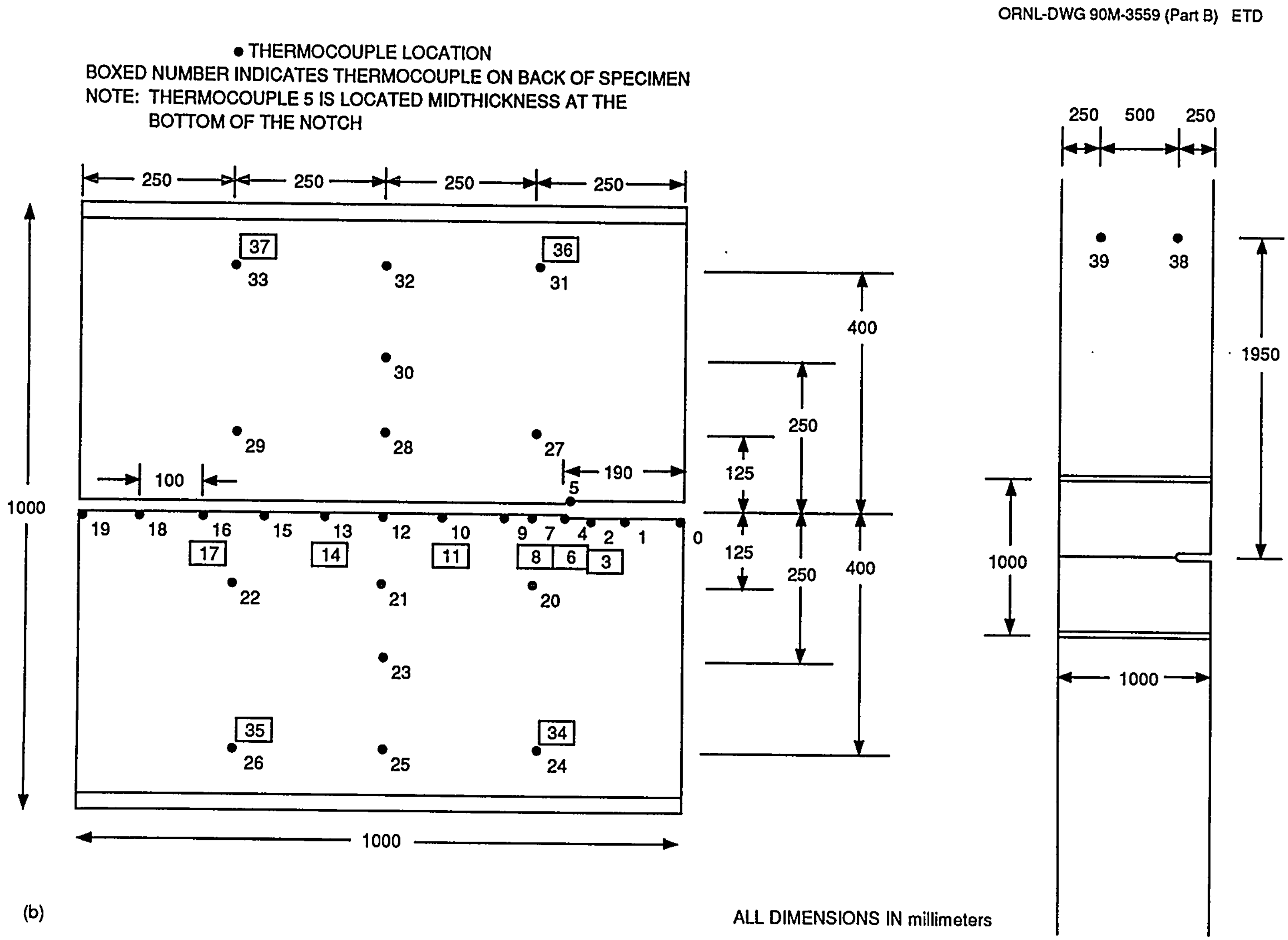

Fig. 4.6 (continued)

ORNL-DWG 90M-3559 (Part C) ETD

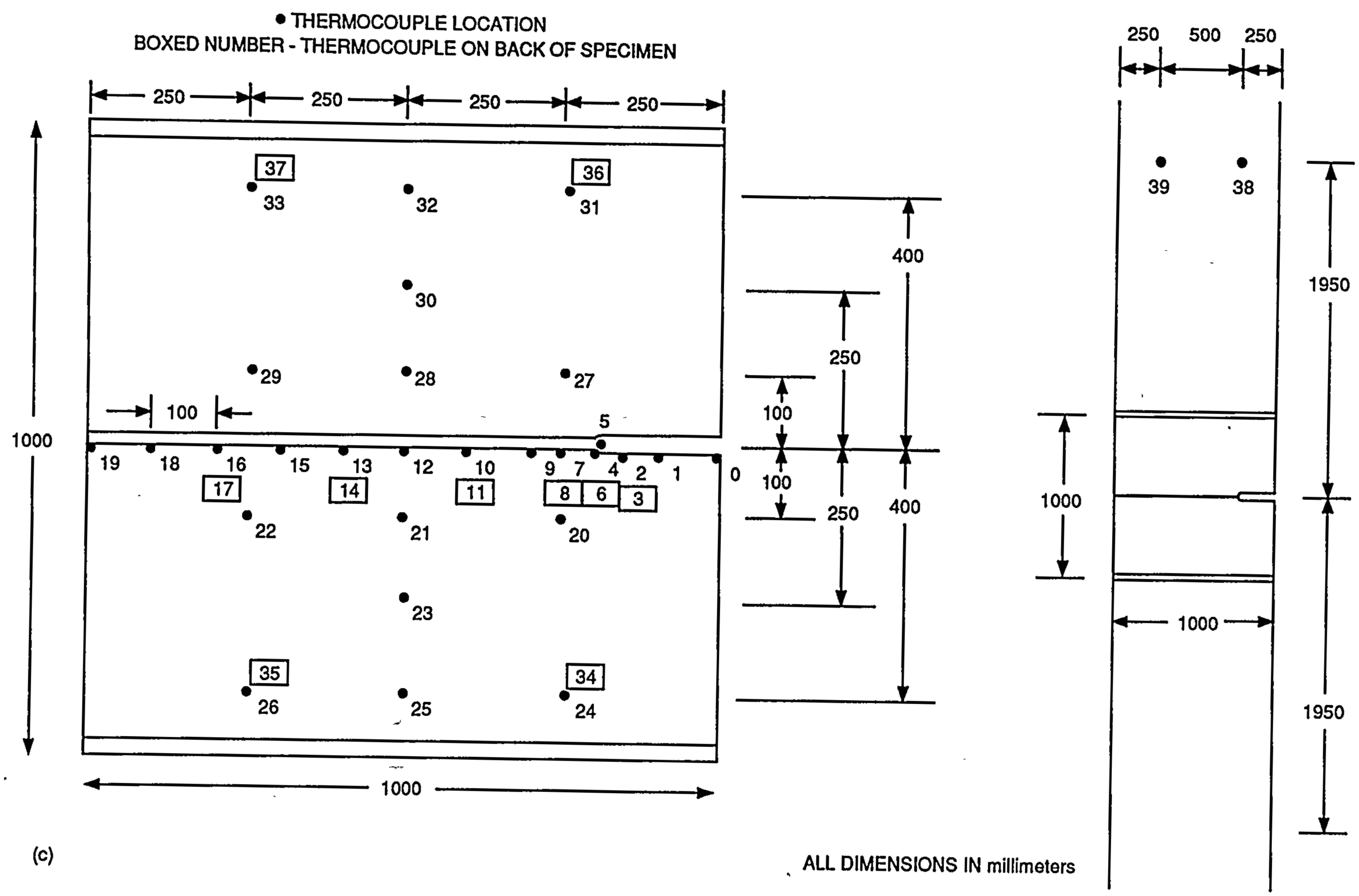

Fig. 4.6 (continued)

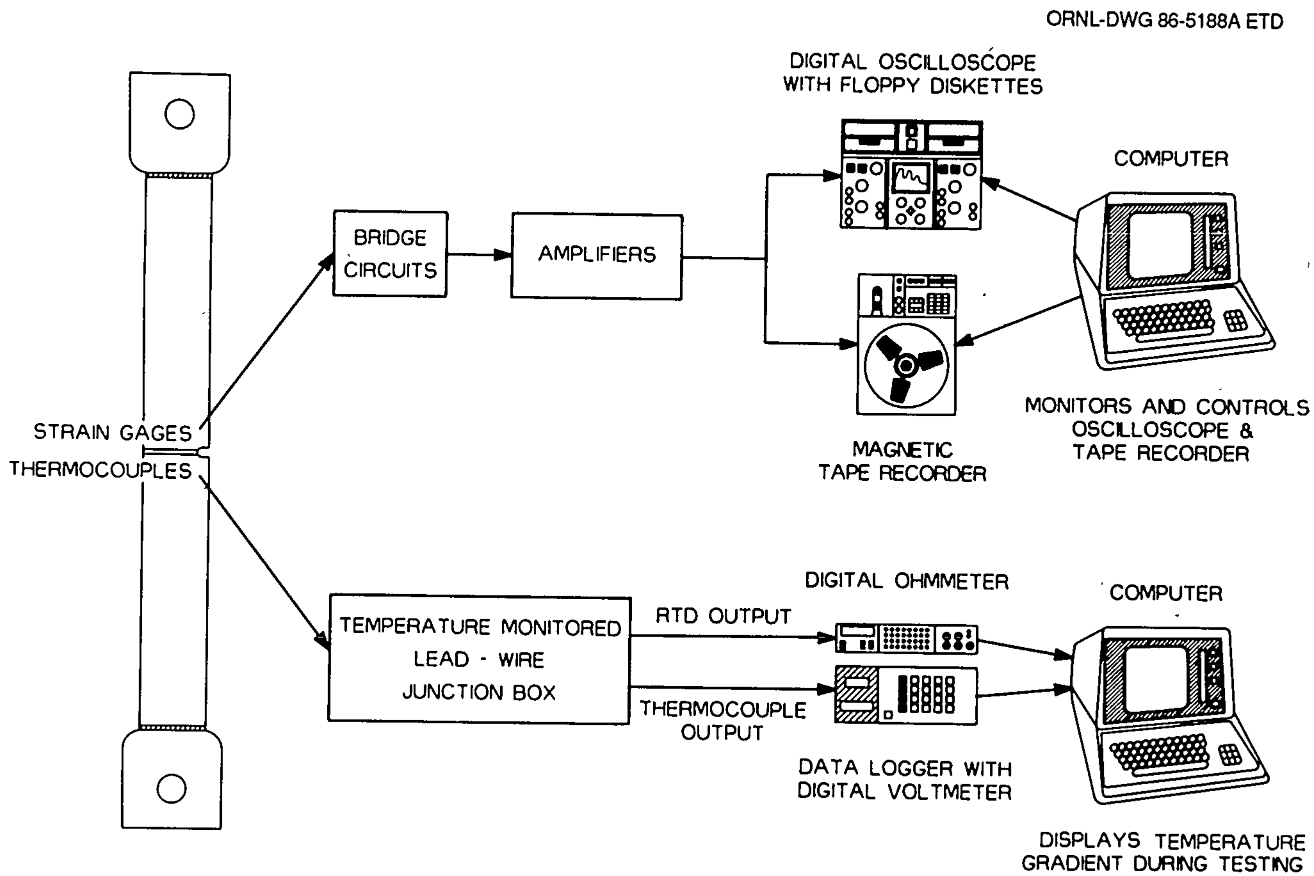

Fig. 4.7. Schematic of HSST wide-plate, crack-arrest data acquisition system.

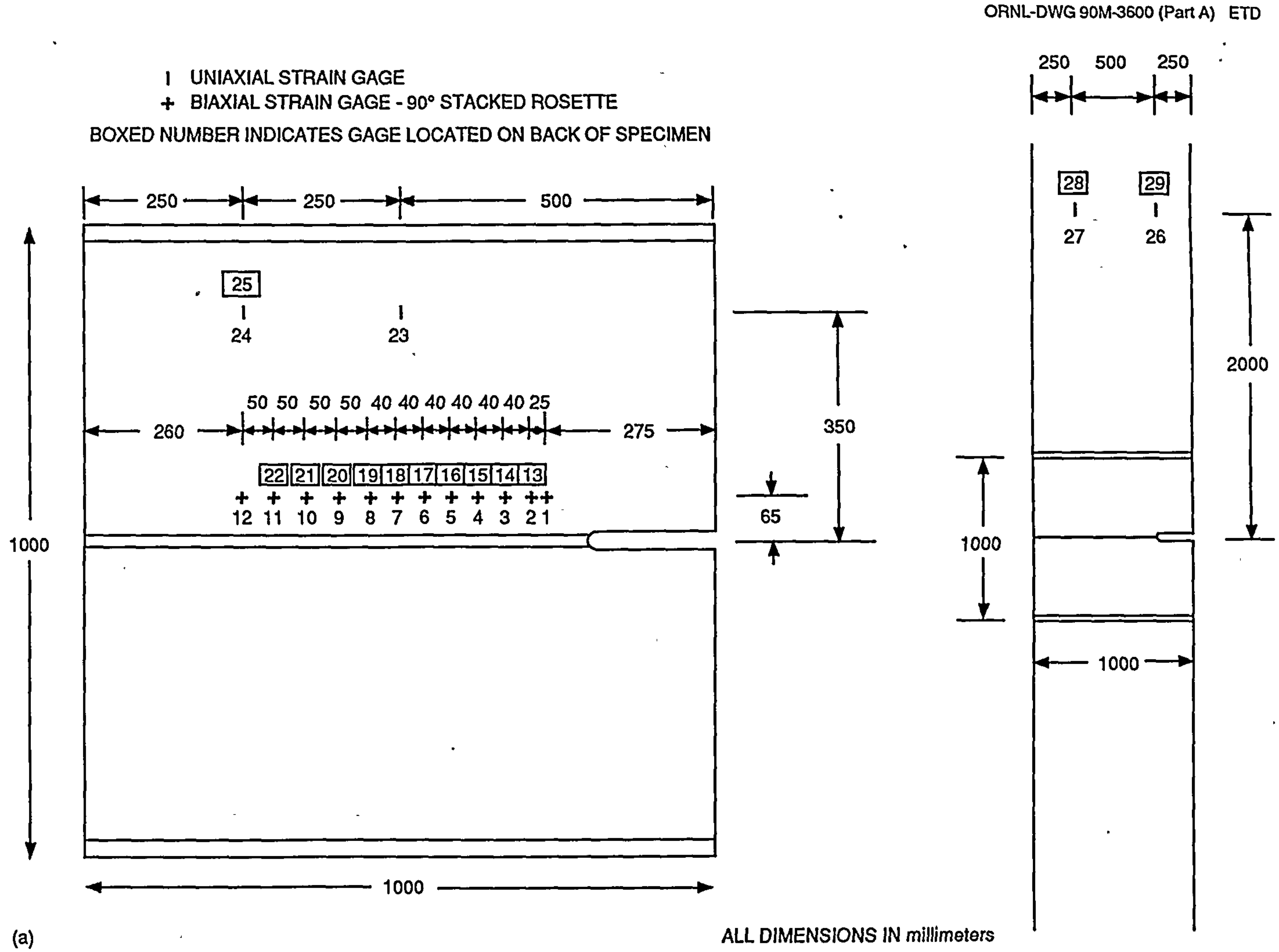

Fig. 4.8. Strain-gage locations for wide-plate, crack-arrest specimens (*a*) WP-2.1 and -2.5, (*b*) WP-2.2, (*c*) WP-2.3, and (*d*) WP-2.4.

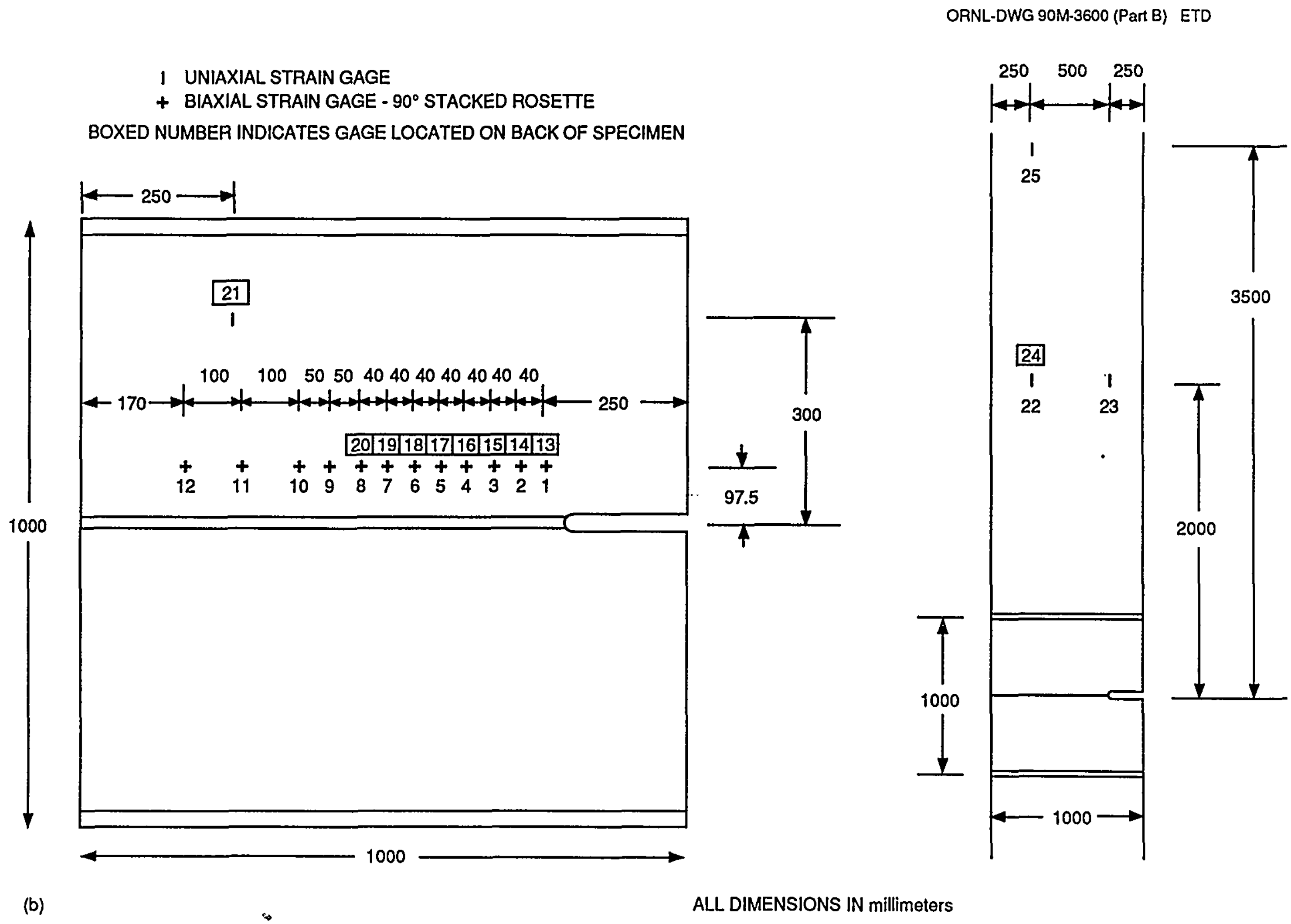

Fig. 4.8 (continued)

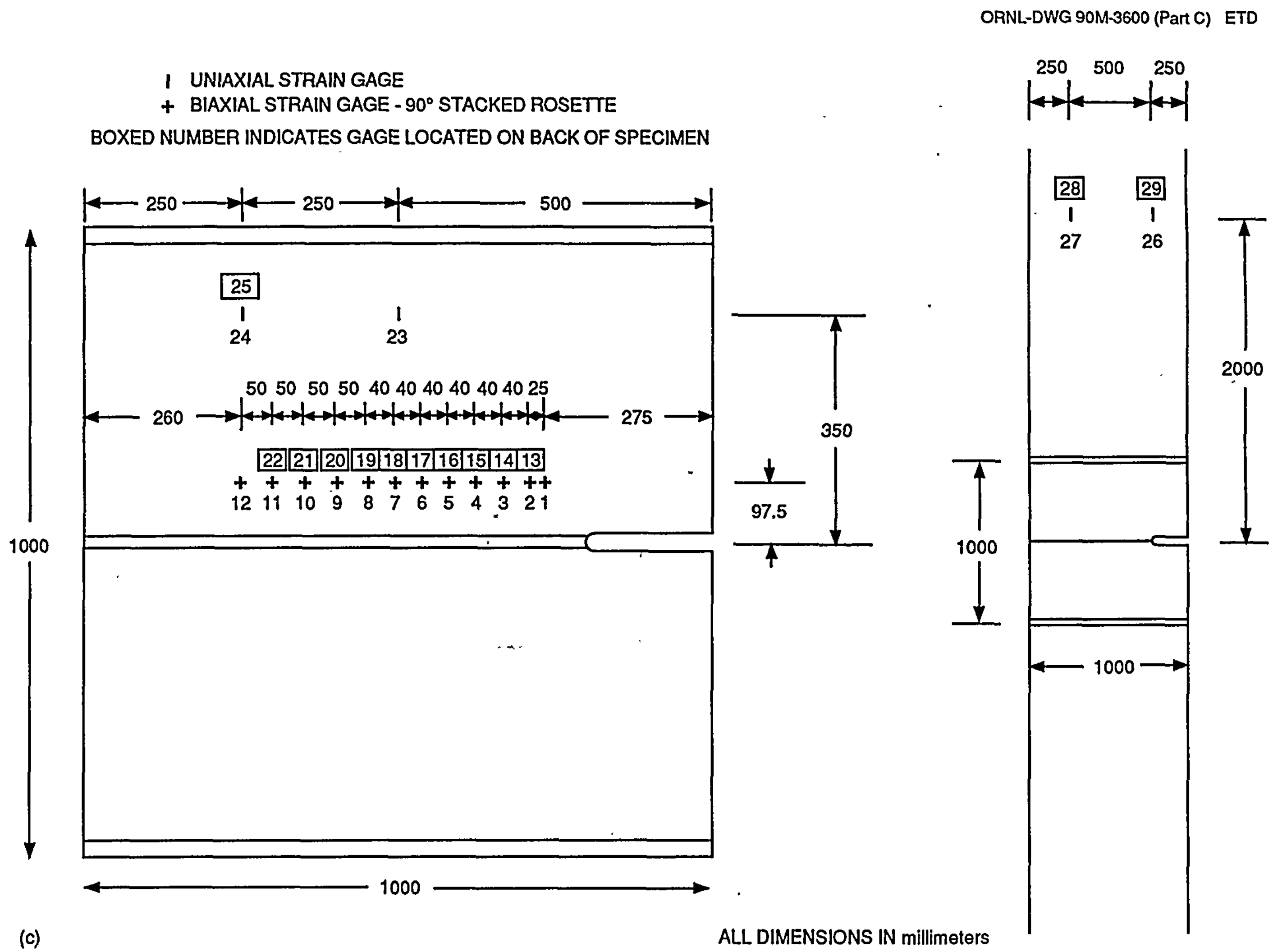

Fig. 4.8 (continued)

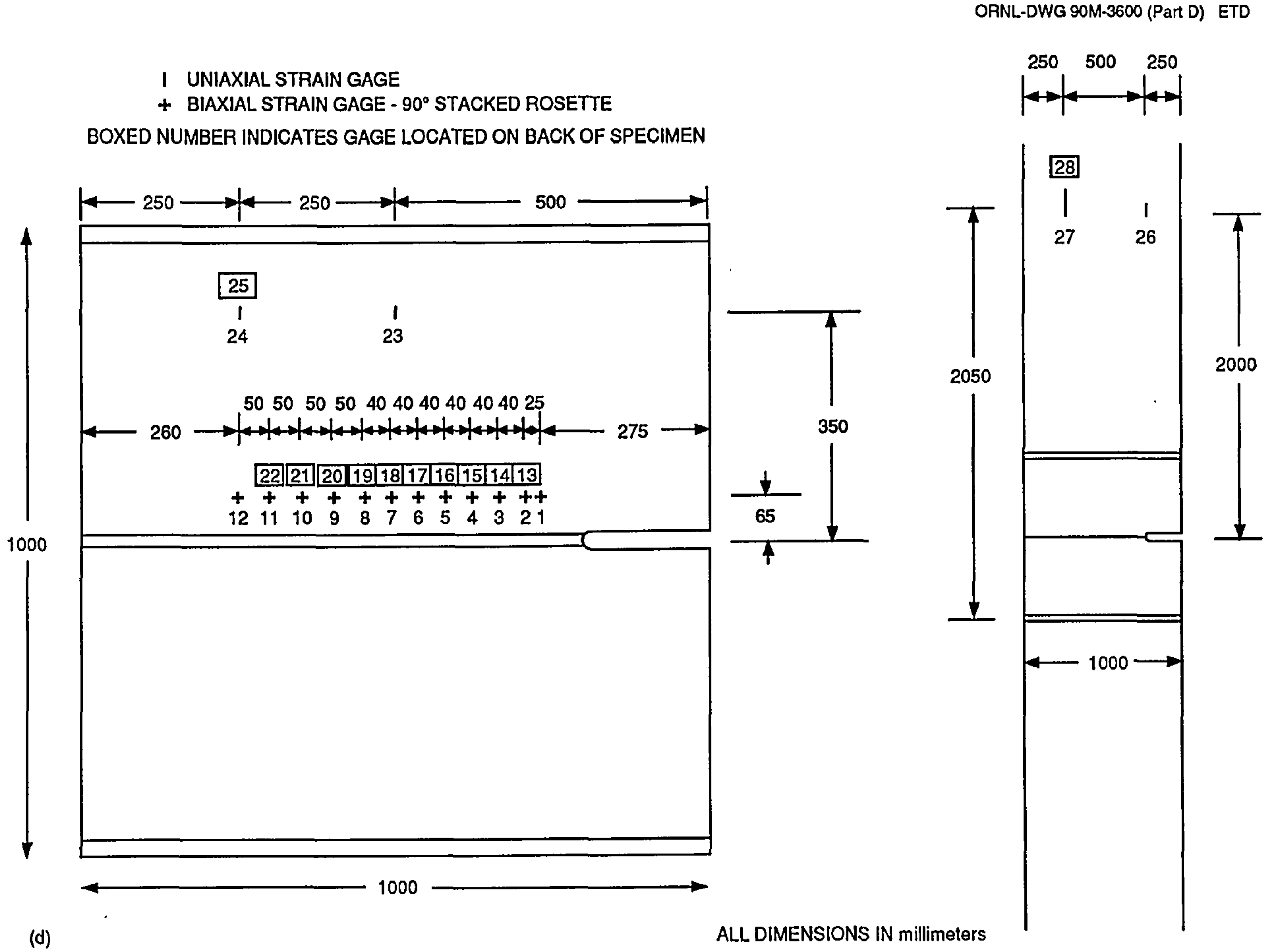

Fig. 4.8 (continued)

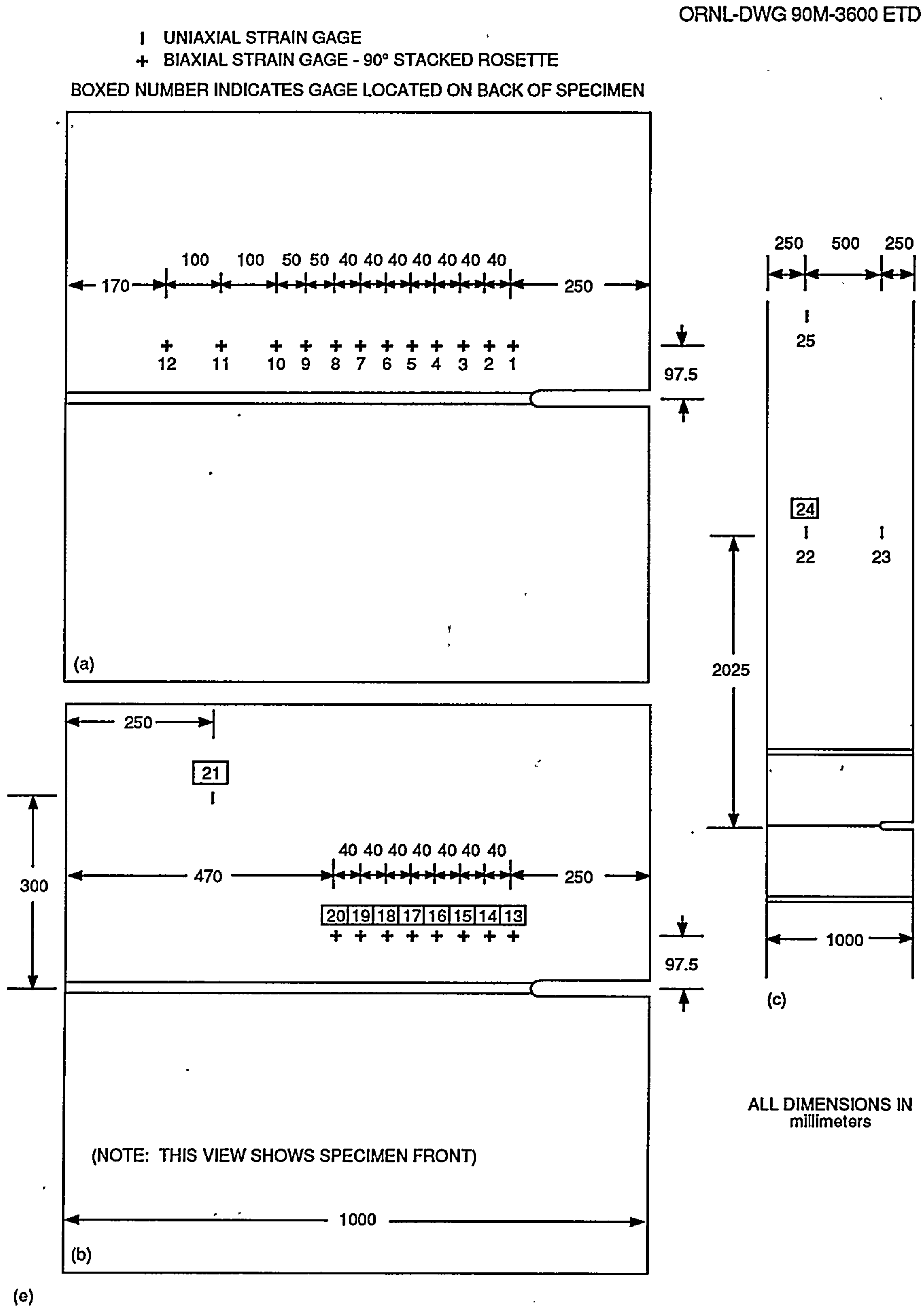

Fig. 4.9 Strain-gage locations for wide-plate specimen WP-2.6. (*a*) Plate front face, (*b*) plate back face viewed from front, and (*c*) far-field locations.

Outputs of the crack-line gages for tests WP-2.1 through -2.5 were proportional to the difference between the longitudinal and transverse strains. Outputs of crack-line gages positioned on the front face of specimen WP-2.6 were also proportional to the difference between the longitudinal and transverse strains; however, crack-line gages 13–20 positioned on the back-face of specimen WP-2.6 were rotated 45° relative to the orientation of that used for other crack-line gages (Fig. 4.9). This change in strain gage orientation was used to increase the sensitivity of the gages to the effects of the crack. Near- and far-field strain gages were uniaxial 350-Ω Constantan alloy gages on a polyimide backing. The strain gages were attached to the plates with an elevated-temperature cured epoxy. All gages were connected to low-reactance bridges (half-bridge configuration for crack-line gages), the imbalances of which were amplified by wide-band differential amplifiers. The strain-gage signals were recorded by a multichannel, wide-band, frequency-modulated, magnetic tape recorder, shown schematically in Fig. 4.7.

Additional instrumentation included capacitance-based COD gages mounted on the front and back faces of each specimen at a/w = 0.15. The gages measured the displacement between points 30 mm above and 30 mm below the crack plane. Accelerometers were located on the specimen's centerline near the upper and lower pull pins. In addition, specimens WP-2.1 and -2.3 were instrumented with an acoustic emission (AE) transducer located on the specimen's lower pull plate, and specimens WP-2.2, -2.3, and -2.6 were instrumented with a dynamic displacement transducer mounted on the specimen centerline near the bottom accelerometer. The displacement gage measured the movement of the point on the specimen where it was attached relative to that of the large columns of the testing machine. Table 4.2 indicates the presence and location of the accelerometer and dynamic displacement instrumentation for each test.

Table 4.2. Presence and location of accelerometer and dynamic displacement instrumentation used in WP-2 series tests

Test specimen	Accelerometer location[a]		Dynamic displacement gage location[b]
	Top	Bottom	
WP-2.1	3.653	3.655	
WP-2.2		3.458	3.453
WP-2.3	3.585	3.589	3.589
WP-2.4	4.038	4.041	
WP-2.5	3.911	3.934	
WP-2.6	3.491	3.398	3.393

[a]Distance in meters above (top) or below (bottom) the crack plane.

[b]Distance in meters below the crack plane.

4.3 HEATING-COOLING-INSULATION SYSTEMS*

After being instrumented, the specimen was placed into the NIST testing machine (Fig. 4.10), and eight individual electric-resistance strip heaters were attached to the back edge of the plate. Each heater was 2.8 cm wide with a heating element 61 cm long and rated at 1.9 W/cm^2. The heaters were attached to the plate in pairs and backed with 1.3-cm-thick sheets of insulating board (Marinite I) to hold them against the plate surface and to provide insulation. The heating level during a test was controlled by two means: (1) a variac transformer, which adjusted the power level or heat output of each heater, and (2) separate on/off temperature controllers, which interacted with thermocouples at the edge of the plate to regulate two zones of heating. The primary heating zone was formed by two pairs of heaters attached to the specimen edge above and below the fracture plane. The second heating zone, consisting of two areas on either side of the first zone, was heated by two outward pairs of heaters. Temperature levels in the two zones were independently controlled to better achieve and maintain a linear thermal gradient across the specimen.

The cold edge of the specimen was cooled by spraying liquid nitrogen (LN_2) onto the notched edge of the specimen. A 2.6-m-long insulated chamber was affixed to the specimen edge, equally spanning both sides of the notch. The LN_2 was pumped into the chamber and sprayed directly onto the specimen surface with a copper-tube manifold consisting of sprayers at 18-cm increments. The cooling level could be controlled by two methods. Initially, when establishing a linear thermal gradient, the temperature was controlled by adjusting the LN_2 flow rate by manually setting a hand valve. When the desired temperature was achieved, that level was maintained by controlling the LN_2 flow with an on/off temperature controller interface with a thermocouple at the cold edge of the specimen. The temperature controller powered an electric solenoid gas valve that could stop or allow the flow of LN_2 into the cold chamber.

Two types of thermal insulation were used to insulate the front and back faces of the specimen. (1) On the hot side of the plate, 5-cm-thick by 61-cm-wide mineral wool bats were used. The bats were positioned on the specimen face at the vertical centerline of the specimen and extended beyond the heated edge and the strip heaters. (2) The cold side of the plate was insulated with 61-cm-wide by 5-cm-thick styrofoam sheets, which butt up against the mineral wool at the specimen centerline and extend beyond the cooled edge or to the cold chamber. The cold chamber was insulated with 2.5-cm-thick styrofoam sheets. All insulation was held tight against the plate surface and, in total, covered an area 3 m above and 3 m below the fracture plane on both the front and

---

*Appendix B of Ref. 2 presents more details on development and checkout of the temperature gradients system and also contains a discussion of the effect of the temperature gradient on the specimen thermal strain and stress state.

ORNL PHOTO 6718-85

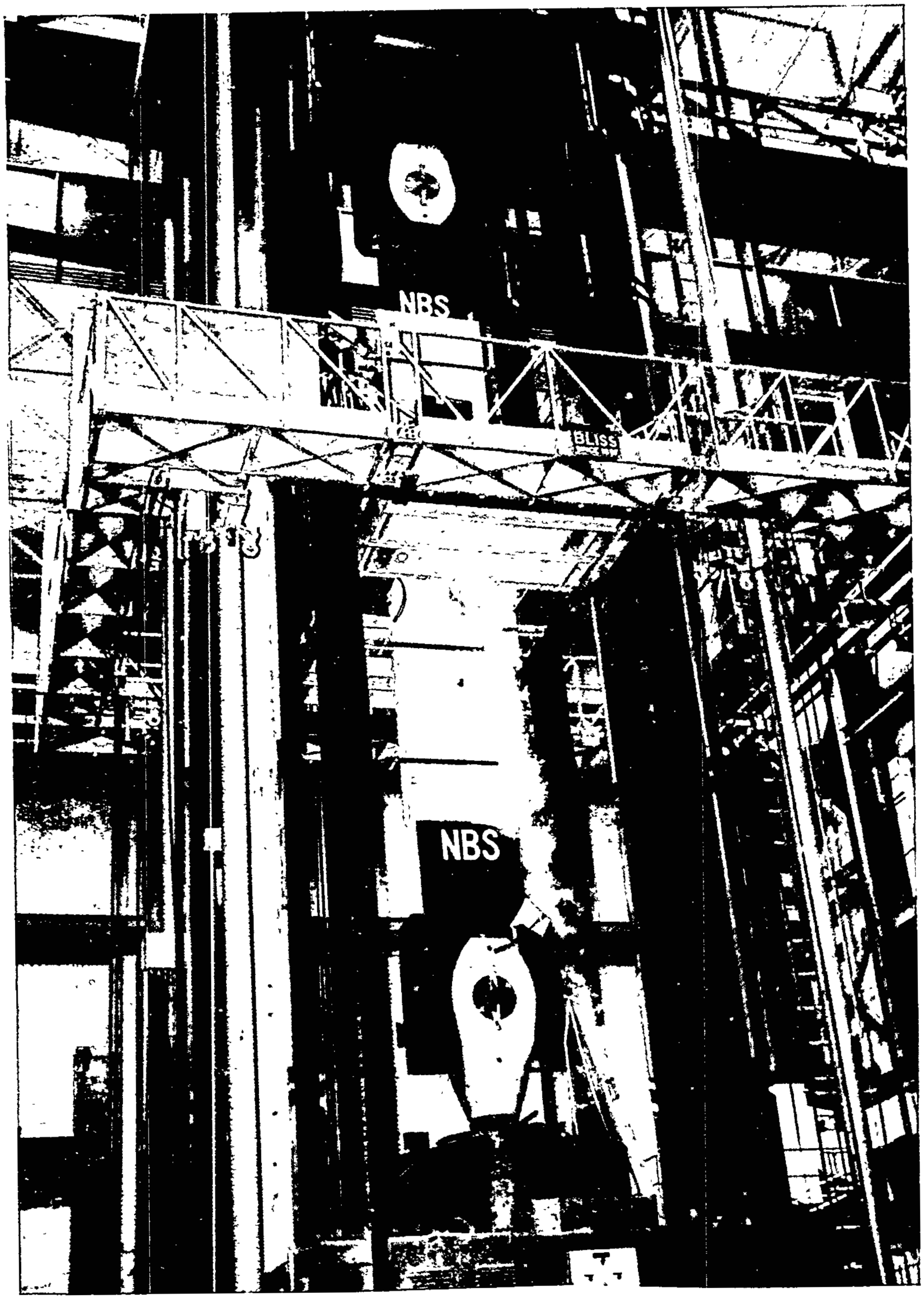

Fig. 4.10. HSST wide-plate, crack-arrest test specimen installed in NIST testing machine.

back surfaces. Additional mineral wool and styrofoam insulation were placed on the specimen edges above and below the heaters and cold chamber to cover the same length on the specimen as the back- and front-face insulation.

4.4 TESTING PROCEDURE

After completion of specimen insulation, all instrumentation was attached to the data acquisition systems. Checkout was conducted to demonstrate that all instrumentation systems were operational. A temperature gradient was imposed across the plate by LN_2 cooling of the notched edge while heating the other edge.* LN_2 flow and power to the heaters were continuously adjusted to obtain the desired thermal gradient. Final check out of strain gages, COD gages, and the load cell were completed just before initiation of specimen testing. Tensile load was then applied to the specimen at a rate of 10–25 kN/s (range for WP-2 test series) until fracture occurred. Details of each test are presented in Chap. 5.

---

*Before establishing the thermal gradient, specimens WP-2.2 and -2.6 were warm prestressed (WPS). Details of the WPS procedure used for these specimens are presented in Chap. 5.

REFERENCES

1. P. P. Holz, Union Carbide Corp. Nuclear Div., Oak Ridge Natl. Lab., *Flaw Preparations for HSST Program Vessel Fracture Mechanics Testing: Mechanical-Cycle Pumping and Electron-Beam Weld-Hydrogen-Charge Cracking Schemes*, USNRC Report NUREG/CR-1274 (ORNL/NUREG/TM-369), May 1980.*

2. D. J. Naus et al., Martin Marietta Energy Systems, Inc., Oak Ridge Natl. Lab., *Crack-Arrest Behavior in SEN Wide Plates of Qenched and Tempered A 533 Grade B Steel Tested Under Nonisothermal Conditions*, USNRC Report NUREG/CR-4930 (ORNL-6388), August 1987.*

3. G. A. Danko et al., *Wide Plate Crack Arrest Tests Instrumentation for Dynamic Strain Measurements*, NBSIR 85-3289, National Bureau of Standards, December 1985.†

---

*Available for purchase from National Technical Information Service, Springfield, VA 22161.

†Available from National Institute of Standards and Technology, Gaithersburg, Maryland.

5. SUMMARY OF WIDE-PLATE CRACK-ARREST TESTS WP-2.1 THROUGH -2.6

Table 5.1 presents a summary of the general conditions for tests that have been conducted under the WP-2 series of wide-plate crack-arrest tests. Test specimen dimensions were presented previously in Table 4.1. Transverse temperature profiles at the approximate time of the crack-initiation events are summarized in Fig. 5.1. Figure 5.2 presents the fracture surfaces of each test specimen. The remainder of this chapter contains a brief summary of each test, including presentation of pertinent results.

5.1 TEST WP-2.1

The purpose of test WP-2.1 was to initiate crack propagation in cleavage with arrest occurring in the central portion of the plate width at a temperature (~150°C) that approximates the onset of Charpy USE energy (see Sect. 3.3). After obtaining a satisfactory thermal gradient [Fig. 5.3(*a*)], specimen loading was initiated at a rate of 15.5 kN/s. As the specimen loading increased from 9.2 to 11.4 MN, the temperature at the crack tip decreased from 59 to 55°C [20-cm location in Fig. 5.3(*b*) and (*c*)]. The cause of this change is unknown. At a load of 11.9 MN, the fracture event initiated. The complete fracture event (cleavage and ductile tearing) lasted ~100 ms, with the cleavage run-arrest events occurring over an ~35-ms interval before the onset of tearing. A small (23-mm) ligament remained intact after fracture. Complete separation of the plate was obtained by reloading the specimen to 850 kN. Figure 5.4 shows the load vs time relationship that occurred during test WP-2.1.

The fracture surface of specimen WP-2.1 is shown in Fig. 5.5(*a*). Figure 5.5(*b*) gives a closeup of the fracture surface and shows more clearly the cleavage crack propagation-arrest events. Each cleavage arrest was delineated by a small line of fibrous fracture. The width of this line increased as the arrests occurred at higher temperatures; that is, at the first arrest the width of the fibrous fracture region was a fraction of a millimeter; however, at $a/w \sim 0.5$ the width of the fibrous fracture region had increased to several millimeters.* Small (1-mm-diam) islands of cleavage were visible at $a/w \approx 0.58$, which is beyond the final cleavage-arrest position. The fibrous fracture extending from

*The width of the fibrous fracture region increased with each subsequent arrest of cleavage crack propagation because of increasing dominance of tearing fracture. Reinitiation of cleavage crack propagation after the first crack run-arrest event resulted because of the dynamic nature of the stress-intensity factor resulting from the test setup, that is, reflected stress waves and specimen compliance. The process of tearing, reinitiation of cleavage crack propagation, and arrest continued until ductile fracture dominated and the specimen tore.

Table 5.1. Summary of HSST wide-plate crack-arrest test conditions and results for specially heat-treated 2 1/4 Cr-1 Mo steel: WP-2 Series

Test No.	Crack-tip location (cm)	Crack-tip temperature (°C)	Initiation load (MN)	Arrest location (cm)	Arrest temperature (°C)	Arrest $T - DW_{NDT}$ (°C)
WP-2.1A[a]	19.9	55	11.90	27.5	80	20
WP-2.1B	27.5	80	11.90	33.5	96	36
WP-2.1D	33.5	96	11.90	37.0	105	45
WP-2.1E	37.0	105	11.90	40.0	112	52
WP-2.1F	40.0	112	11.90	45.0	125	65
WP-2.1H	45.0	125	11.90	49.0	135	75
WP-2.1I	49.0	135	11.90	52.7	145	85
WP-2.1J	52.7	145	11.90	55.5	152	92
WP-2.2A[a,b]	21.1	58	17.0	43.5	120	60
WP-2.2B	43.5	120	17.0	46.5	129	69
WP-2.2C	46.5	129	17.0	47.8	133	73
WP-2.2D	47.8	133	17.0	49.9	139	79
WP-2.2E	49.9	139	17.0	51.0	142	82
WP-2.2F	51.0	142	17.0	53.8	150	90
WP-2.2G	53.8	150	17.0	58.2	162	102
WP-2.3A	20.0	66	15.3	34.0	97	37
WP-2.3B	34.0	97	15.3	37.5	106	46
WP-2.3D	37.5	106	15.3	39.7	111	51
WP-2.3F	39.7	111	15.3	45.7	126	66
WP-2.4A[a]	20.3	45	7.52	25.1	61	1
WP-2.4B	25.1[c]	61	8.85	33.8	86	26
WP-2.4C	33.8	86	8.85	39.7	102	42
WP-2.4D	39.7	102	8.85	41.3	107	47
WP-2.4E	41.3	107	8.85	46.2	121	61
WP-2.4F	46.2	121	8.85	48.4	127	67
WP-2.4G	48.4	127	8.85	51.5	137	77
WP-2.4H	51.5	137	8.85	55.5	149	89
WP-2.5A[a]	19.9	66	7.53	27.2	86	26
WP-2.5B	27.2[c]	86	8.90	35.0	104	44
WP-2.5C	35.0	104	8.90	43.5	124	64
WP-2.5D	43.5	124	8.90	47.8	135	75
WP-2.5E	47.8	135	8.90	51.6	144	84
WP-2.5F	51.6	144	8.90	56.0	154	94
WP-2.6A[d]	22.4	65	19.3	35.7	104	44
WP-2.6B	35.7	104	19.3	39.7	115	55
WP-2.6C	39.7	115	19.3	41.0	119	59
WP-2.6D	41.0	119	19.3	43.0	125	65
WP-2.6F	43.0	125	19.3	46.0	133	73
WP-2.6G	46.0	133	19.3	48.0	139	79
WP-2.6H	48.0	139	19.3	54.0	156	96

[a]Crack front cut to truncated chevron configuration.

[b]Specimen was WPS by loading to 16 MN at 124°C.

[c]After pop-in event.

[d]Specimen was WPS by loading to 15.6 MN at 110°C.

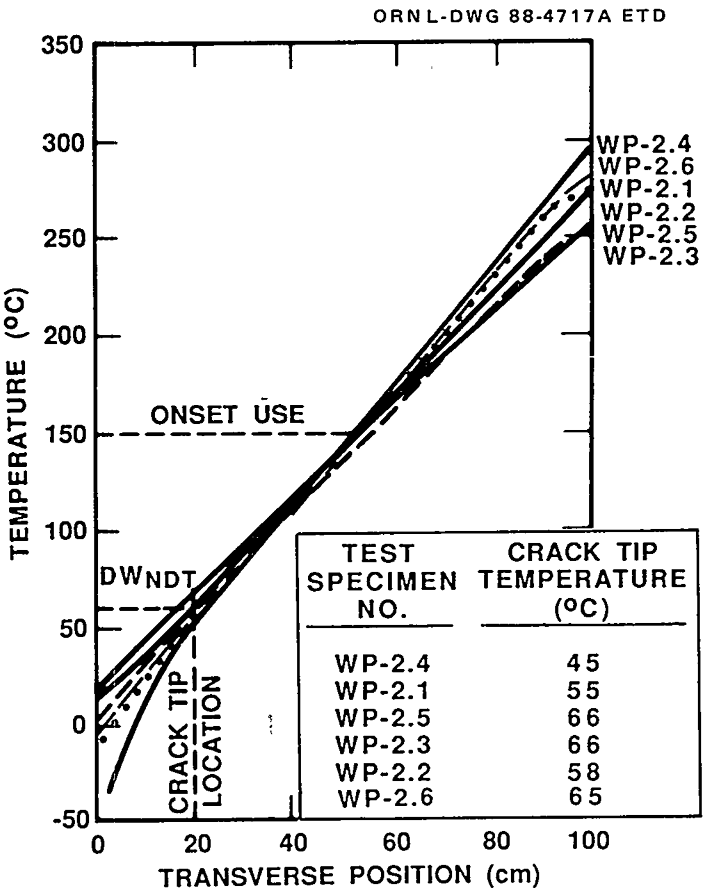

Fig. 5.1. Transverse temperature profiles at approximate time of crack initiation-arrest events: WP-2 series.

ORNL PHOTO 6810–88A

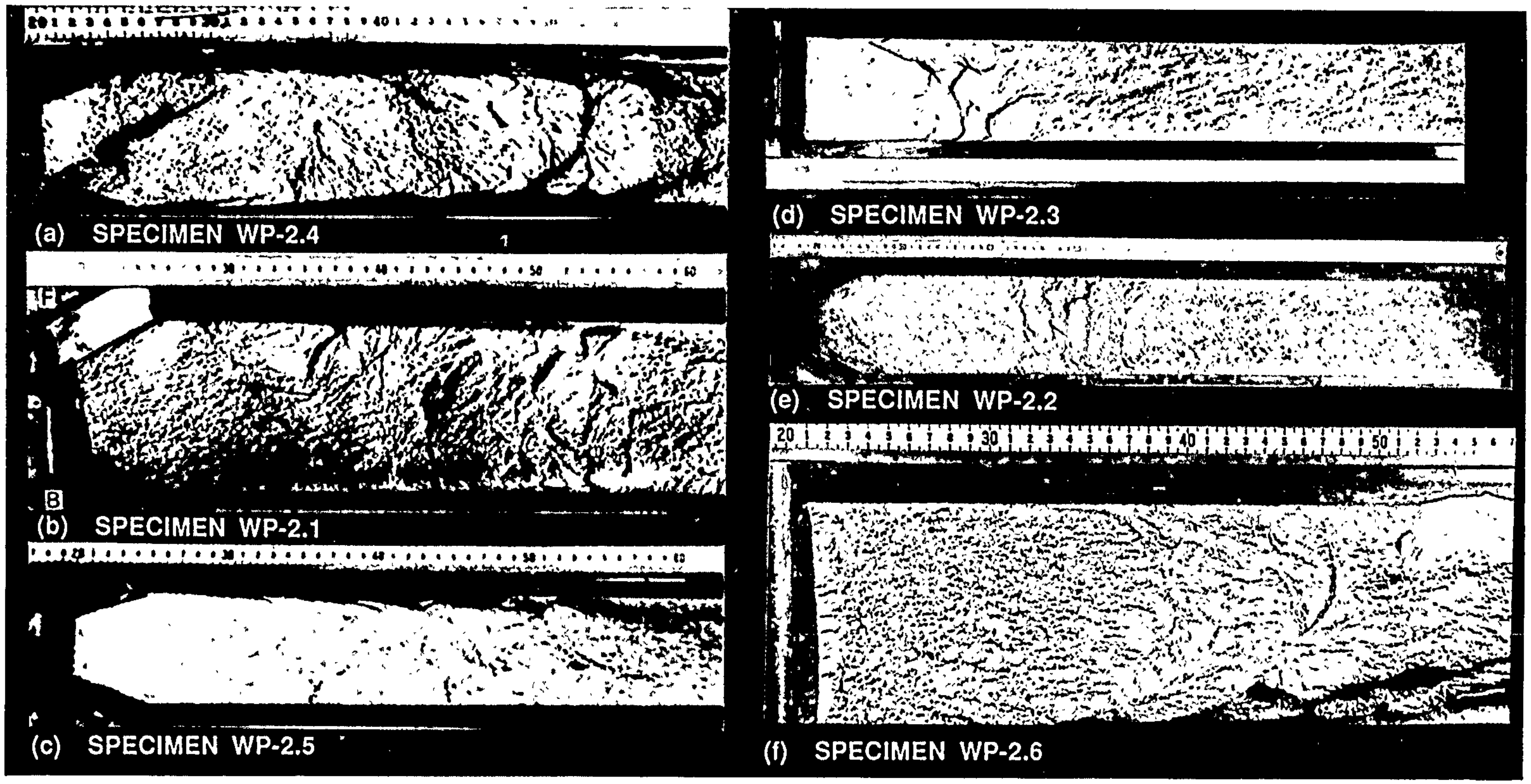

Fig. 5.2. Fracture surfaces of WP-2 series specimens.

ORNL-DWG 90M-3601 ETD

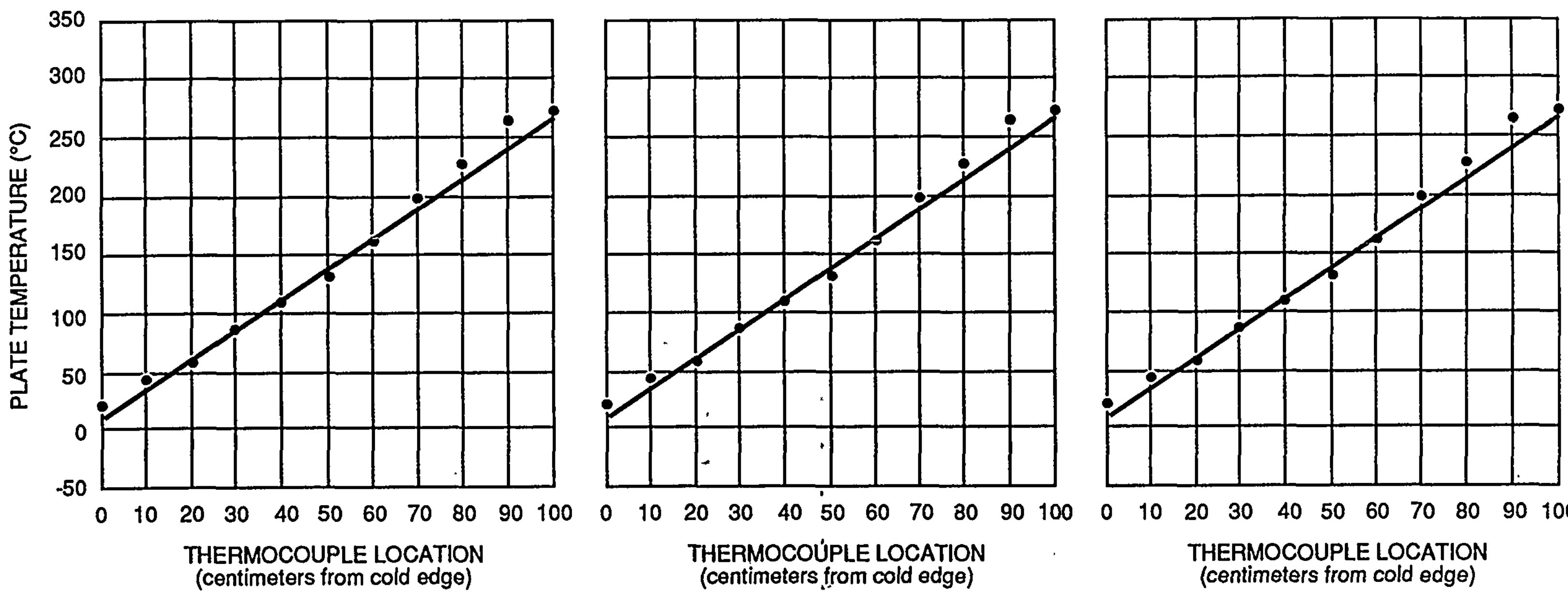

(a)

TEMPERATURE (°C)		
CENTIMETERS	REAL	IDEAL
0	14	6
10	40	33
20	59	60
30	88	86
40	111	113
50	136	139
60	164	166
70	194	193
80	226	219
90	259	246
100	280	273

(b)

TEMPERATURE (°C)		
CENTIMETERS	REAL	IDEAL
0	0	6
10	41	33
20	59	60
30	88	86
40	112	113
50.	137	139
60	165	166
70	195	193
80	227	219
90	260	246
100	280	273

(c)

TEMPERATURE (°C)		
CENTIMETERS	REAL	IDEAL
0	12	6
10	40	33
20	55	60
30	88	86
40	112	113
50	137	139
60	165	166
70	195	193
80	227	219
90	260	246
100	280	273

Fig. 5.3. Actual and ideal temperature distributions across specimen width (*a*) at start of test, (*b*) at 9.2-MN load, and (*c*) at ~10 s before initiation of fracture events: test WP-2.1.

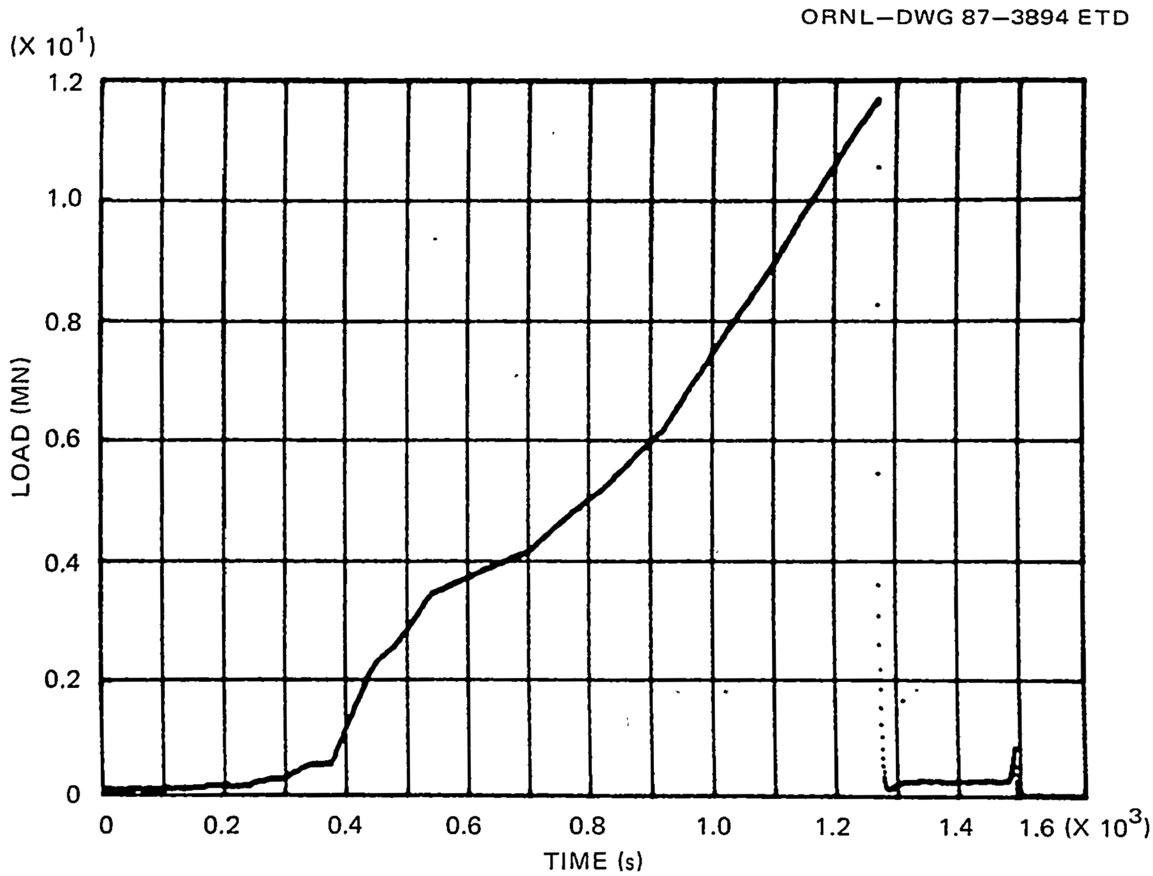

Fig. 5.4. Load history for test WP-2.1.

ORNL–PHOTO 2013–90

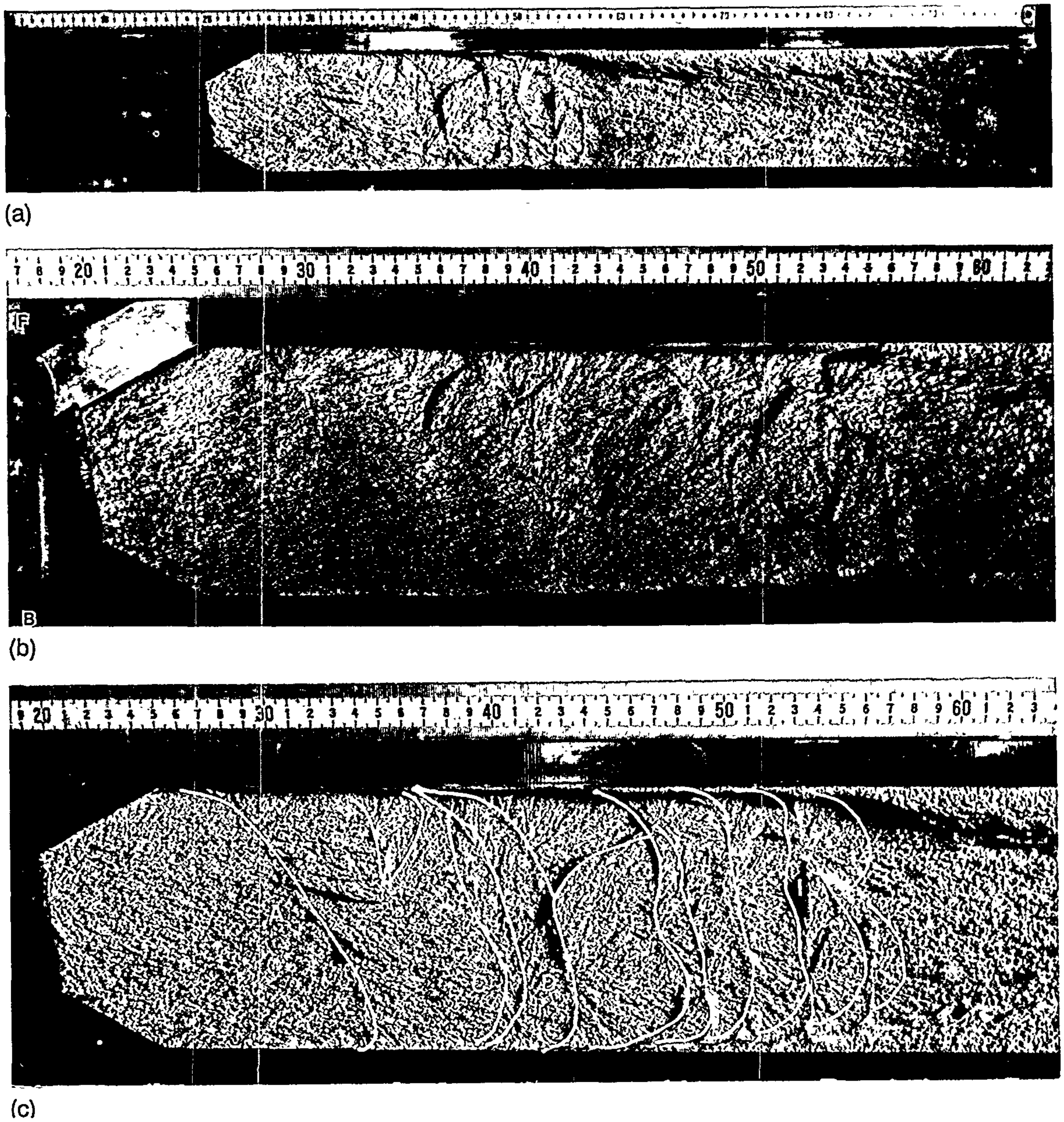

Fig. 5.5. Fracture surface of specimen WP-2.1. (*a*) Overall fracture surface, (*b*) close-up of initial crack and cleavage crack-run-arrest region, and (*c*) close-up of initial crack and cleavage crack run-arrest region with arrest location highlighted.

a/w = 0.55 to the end of the plate was extremely fine, or flat, compared with the fibrous fracture regions in the WP-1 test series[1] (A 533 grade B class 1 material).

Examination of the fracture surface indicates that initiation of cleavage crack growth was in the plane of the side grooves, but as the crack extended, it gradually deviated from this plane. By the loss-of-cleavage location (a/w ~ 0.58), the crack was 14 mm below the plane of the side grooves. Once fibrous fracture took over, the crack returned to the side-grooved plane. Reduction-in-thickness contours surrounding the crack plane are shown in Fig. 5.6.*

Evaluations of strain-gage records† and the fracture surface were used to deduce the crack length (position of the crack front) vs time, and the results are presented in Table 5.2. These strain-gage positions have been modified from those shown in Fig. 4.8(*a*) because the peak strain occurs at an angle of 72° in front of the crack tip. A plot of crack-front position vs time derived from the front-face and back-face strain gage outputs is presented in Fig. 5.7. The strain-gage-derived apparent crack position as a function of time indicates that for about the first 27.5 ms, the crack front advance was greater at the back face of the plate than at the front face. At elapsed times >27.5 ms, the crack front advance at comparable elapsed times was fairly consistent at the front and back faces.

5.2 TEST WP-2.2

Before testing, specimen WP-2.2 was WPS at a crack-tip temperature of 124°C (Fig. 5.8) by slowly loading it to 16 MN, holding the load constant at this value for 5 min, and slowly reducing the load to 3 MN. The load history and load vs front-face COD results during warm prestressing are shown in Fig. 5.9. While maintaining the load constant at 3 MN, the thermal gradient was developed.

After obtaining a satisfactory temperature profile (Fig. 5.10), the specimen was loaded at an average rate of 16.2 kN/s. At a load of 17 MN, cleavage crack propagation initiated, and within ~9 ms seven crack run-arrest events occurred. After the seventh crack run-arrest event, tearing fracture reinitiated with complete separation of the plate occurring ~34.5 ms after first initiation of cleavage crack propagation. Figure 5.11 presents the load history for test WP-2.2.

Figure 5.12 presents overall and close-up views of the fracture surface of specimen WP-2.2. The entire fracture took place in the plane

---

*Reduction-in-thickness measurements are performed using a deep-throated micrometer with a resolution of ±0.025 mm. The measurements are of total thickness with no differentiation between front and back deformation.

†Detailed presentation and discussion of the instrumentation results for each test are contained in Appendix A.

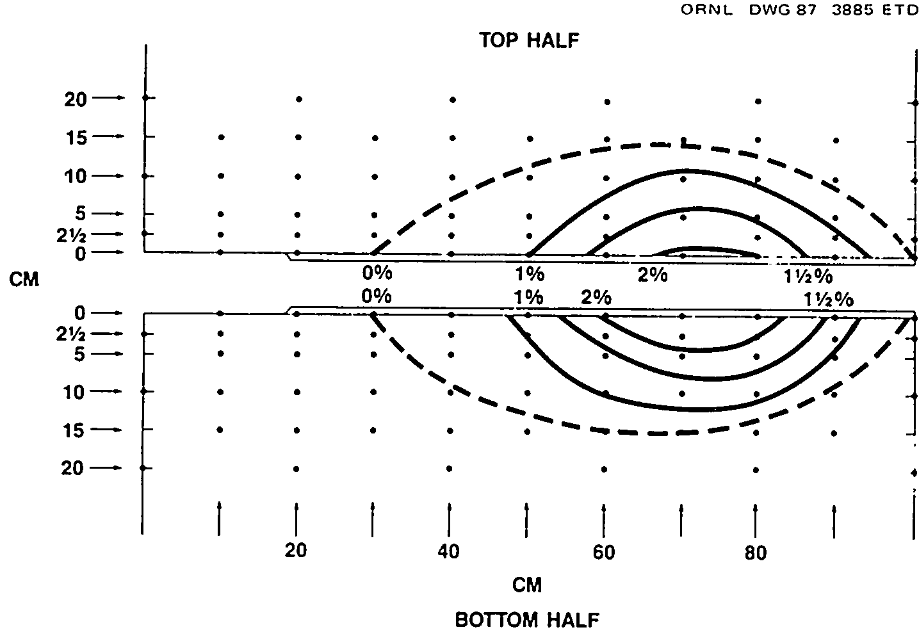

Fig. 5.6. Reduction-in-thickness contour map of specimen WP-2.1.

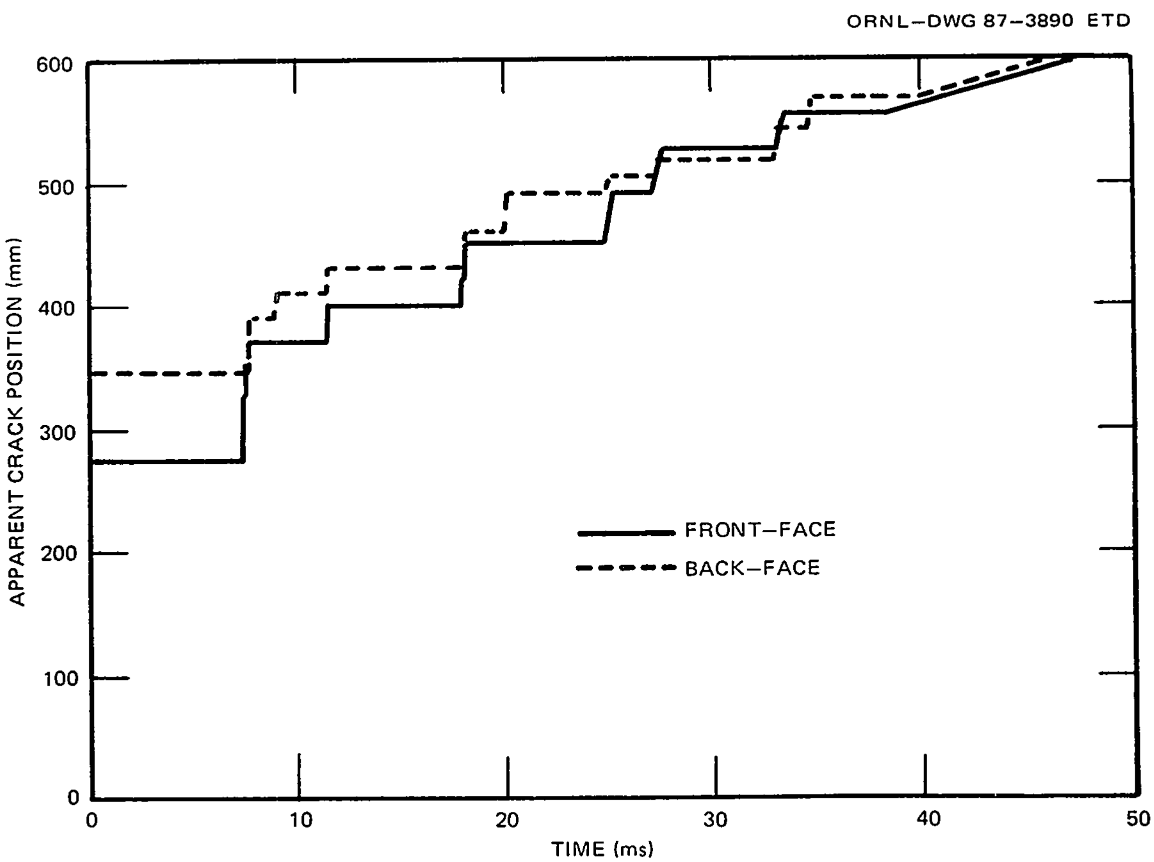

Fig. 5.7. Strain-gage-derived crack-front position vs time: test WP-2.1.

Table 5.2 (continued)

Indicator[a]	Position (mm)	Time (ms)	Velocity[b] (m/s)
Front-face measurements (continued)			
SG10	619	51.35	
			7
SG11	669	58.30	
			6
SG12	719	66.00	
			7
Remaining ligament	980	101.50	
Back-face measurements			
a_o	207	0	
			783
SG13	279	0.092	
			435
SG14	319	0.184	
			448
Arrest A	345	0.242	
Reinitiation	345	7.55	
			175
SG15	359	7.63	
			258
Arrest C	390	7.75	
Reinitiation	390	8.86	
			90
SG16	399	8.96	
			138
Arrest D	410	9.04	
Reinitiation	410	11.42	
			333
Arrest E	430	11.48	
Reinitiation	430	17.96	
			450
SG17	439	17.98	
			150
Arrest F	460	18.12	
Reinitiation	460	20.04	
			950
SG18	479	20.06	
			92
Arrest G	490	20.18	
Reinitiation	490	24.78	
			75
Arrest H	505	24.98	
Reinitiation	505	27.04	
			93

Table 5.2. Crack position vs time and velocity: test WP-2.1

Indicator[a]	Position (mm)	Time (ms)	Velocity[b] (m/s)
Front-face measurements			
a_o	199	0	
			458
SG1	254	0.120	
			284
Arrest A	275	0.194	
Reinitiation	275	7.23	
			16
SG2	279	7.48	
			200
SG3	319	7.50	
			133
Arrest B	335	7.62	
Reinitiation	335	7.68	
			600
SG4	359	7.72	
			220
Arrest D	370	7.77	
Reinitiation	370	11.48	
			1450
SG5	399	11.50	
			5
Arrest E	400	11.70	
Reinitiation	400	17.96	
			488
SG6	439	18.04	
			110
Arrest F	450	18.14	
Reinitiation	450	24.68	
			104
SG7	479	24.96	
			69
Arrest H	490	25.12	
Reinitiation	490	27.04	
			69
SG8	519	27.46	
			50
Arrest I	527	27.62	
Reinitiation	527	33.18	
			156
Arrest J	555	33.36	
Reinitiation	555	37.94	
			4
SG9	569	41.15	
			5

Table 5.2 (continued)

Indicator[a]	Position (mm)	Time (ms)	Velocity[a] (m/s)
Back-face measurements (continued)			
Arrest I	518	27.18	
Reinitiation	518	32.94	
			17
SG19	519	33.00	
			433
Arrest J	545	33.06	
Reinitiation	545	34.62	
			164
Arrest K	568	34.76	
Reinitiation	568	34.76	
			0.2
SG20	569	39.66	
			5
SG21	619	50.15	
			6
SG22	669	58.35	
			7
Remaining ligament	974	101.50	

[a]These strain-gage positions have been modified because the peak strain occurs at an angle of 72° in front of the crack tip. Also, the crack-arrest locations are averages of the quarter-thickness crack length and the crack length at the side groove.

[b]Velocity is an average calculated velocity of crack propagation between the corresponding indicator positions.

ORNL-DWG 89-5021 ETD

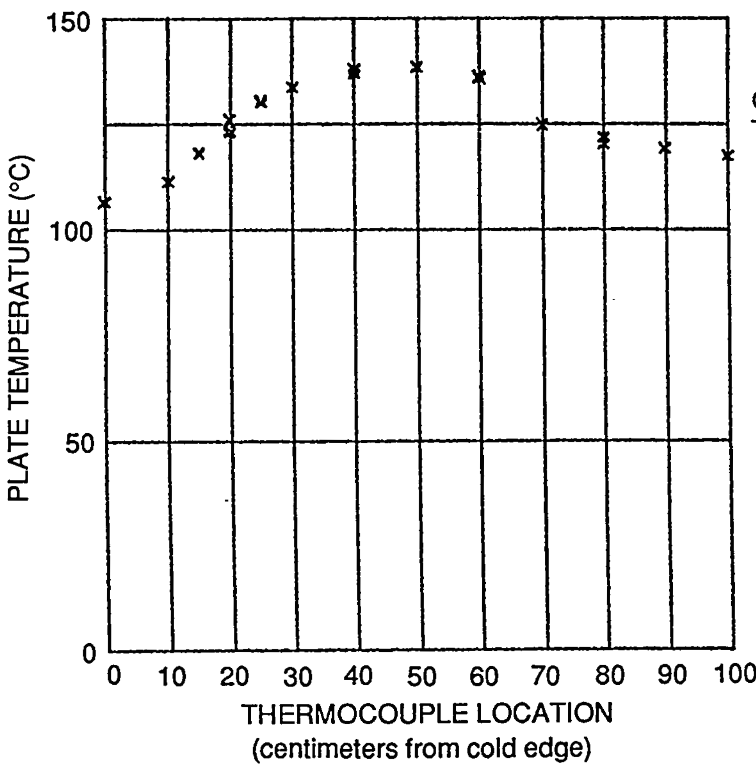

	TEMPERATURE (°C)	
CENTIMETERS	REAL	IDEAL
0	107	125
10	112	125
15	118	125
15	118	125
20	123	125
20	124	125
20	126	125
25	130	125
25	130	125
30	134	125
40	137	125
40	138	125
50	138	125
60	136	125
60	136	125
70	125	125
80	120	125
80	122	125
90	120	125
100	118	125

Fig. 5.8. Actual and ideal temperature distributions across specimen width during warm prestressing: test WP-2.2.

ORNL-DWG 89-5022 ETD

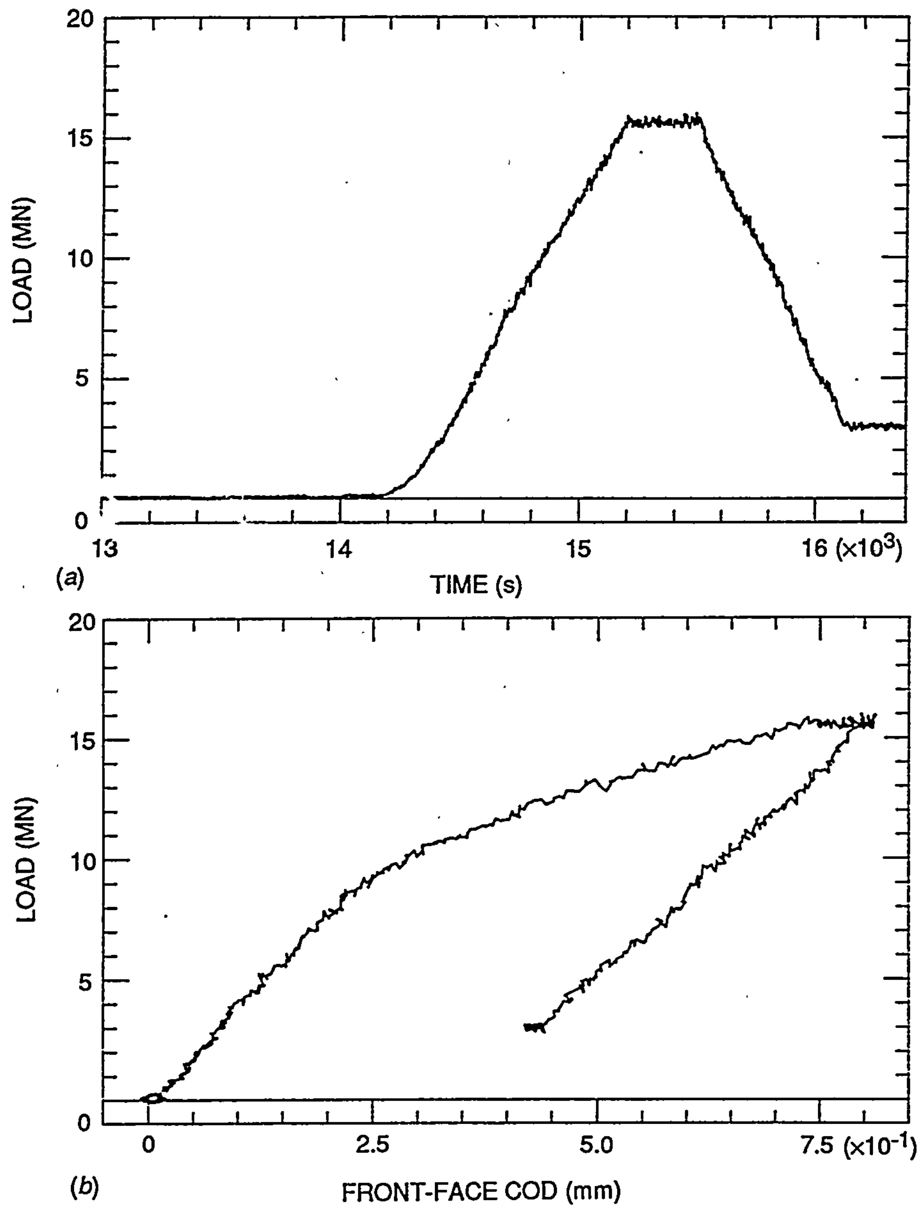

Fig. 5.9. Load vs (*a*) time and (*b*) front-face COD during warm prestressing: test WP-2.2.

ORNL-DWG 89-5023 ETD

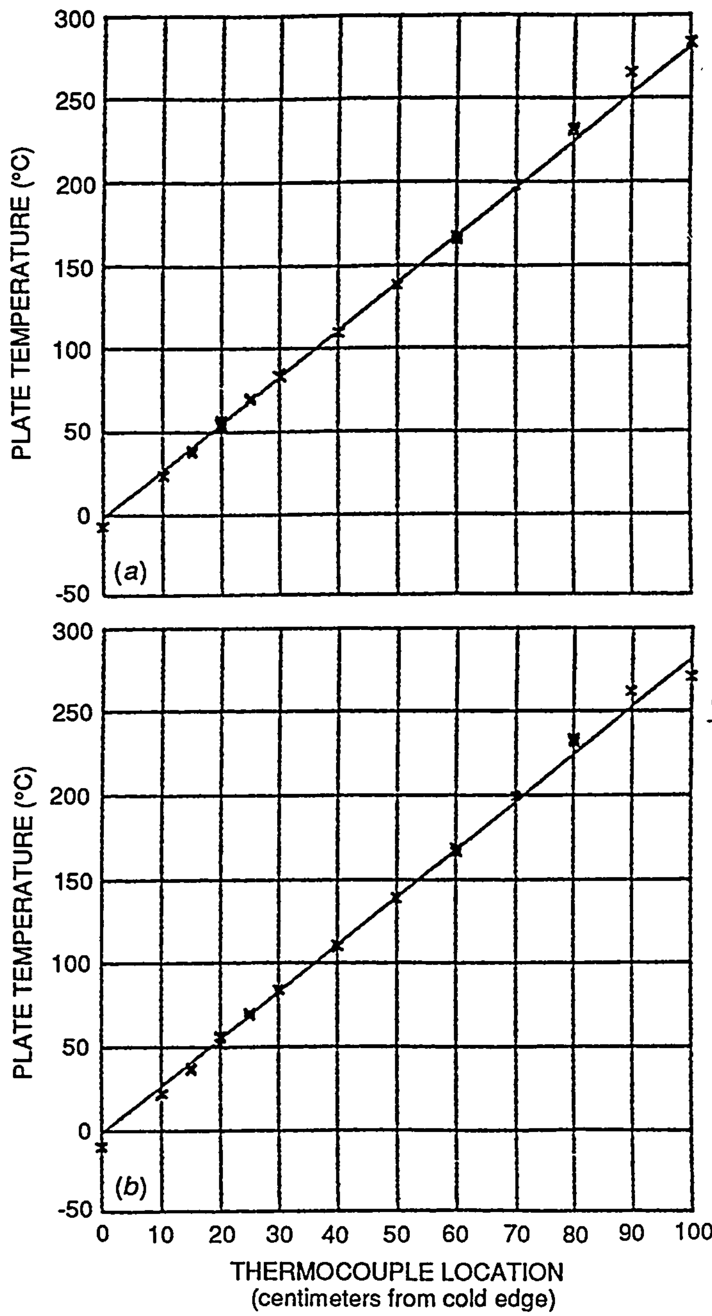

(a)

CENTIMETERS	TEMPERATURE (°C) REAL	TEMPERATURE (°C) IDEAL
0	-7	-2
10	24	26
15	37	40
15	39	40
20	55	54
20	57	54
20	53	54
25	70	69
25	69	69
30	83	83
40	110	111
40	110	111
50	138	139
60	167	168
60	165	168
70	198	196
80	231	225
80	232	225
90	266	253
100	284	281

(b)

CENTIMETERS	TEMPERATURE (°C) REAL	TEMPERATURE (°C) IDEAL
0	-9	-2
10	22	26
15	36	40
15	37	40
20	55	54
20	56	54
20	52	54
25	70	69
25	68	69
30	84	83
40	110	111
40	110	111
50	139	139
60	168	168
60	166	168
70	200	196
80	232	225
80	234	225
90	262	253
100	271	281

Fig. 5.10. Actual and ideal temperature distributions across specimen width (*a*) at start of loading and (*b*) just before initiation of cleavage crack run-arrest events: test WP-2.2.

ORNL-DWG 89-5024 ETD

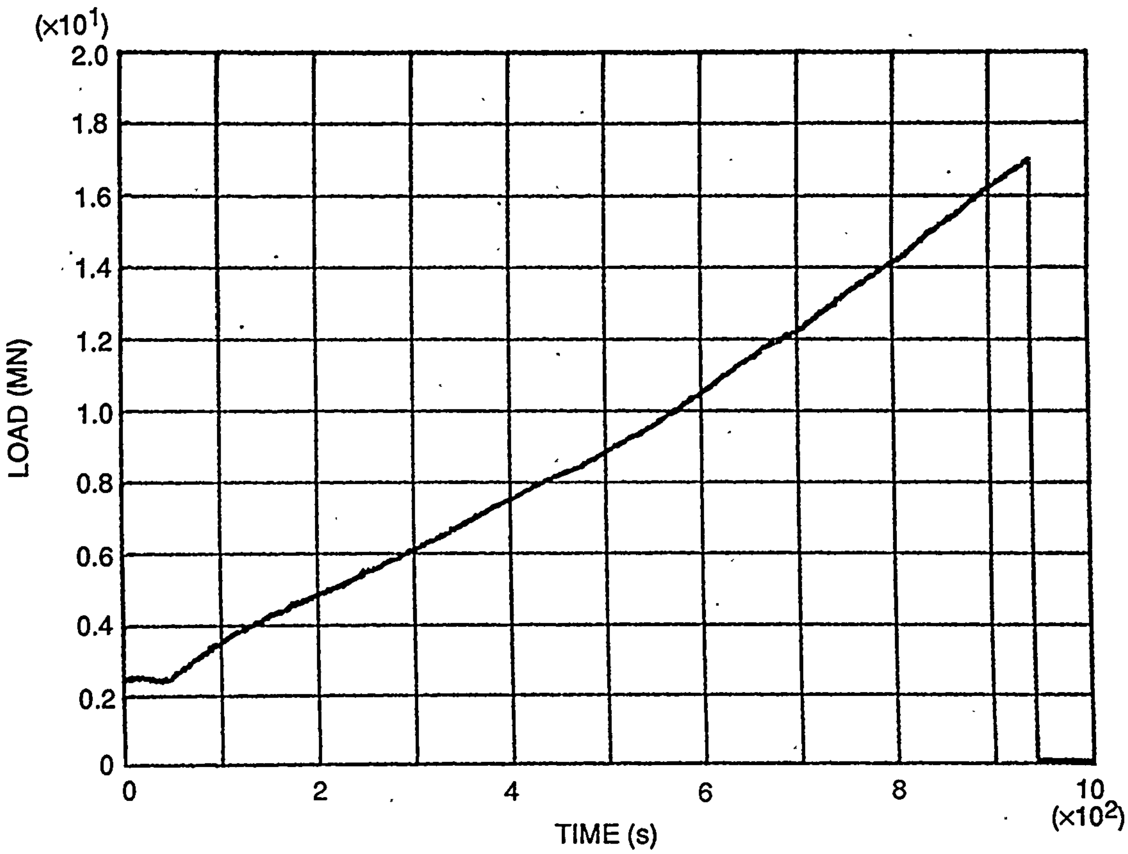

Fig. 5.11. Load history for test WP-2.2.

ORNL PHOTO 7004-89

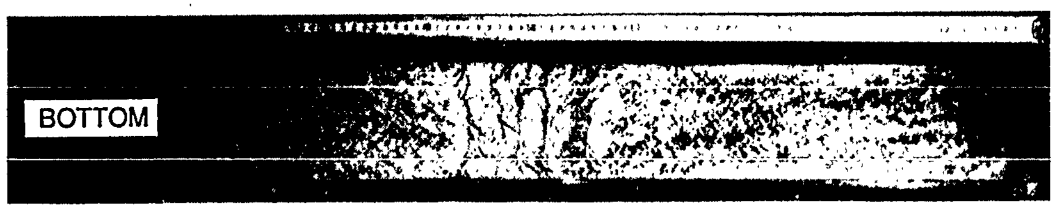

(a)

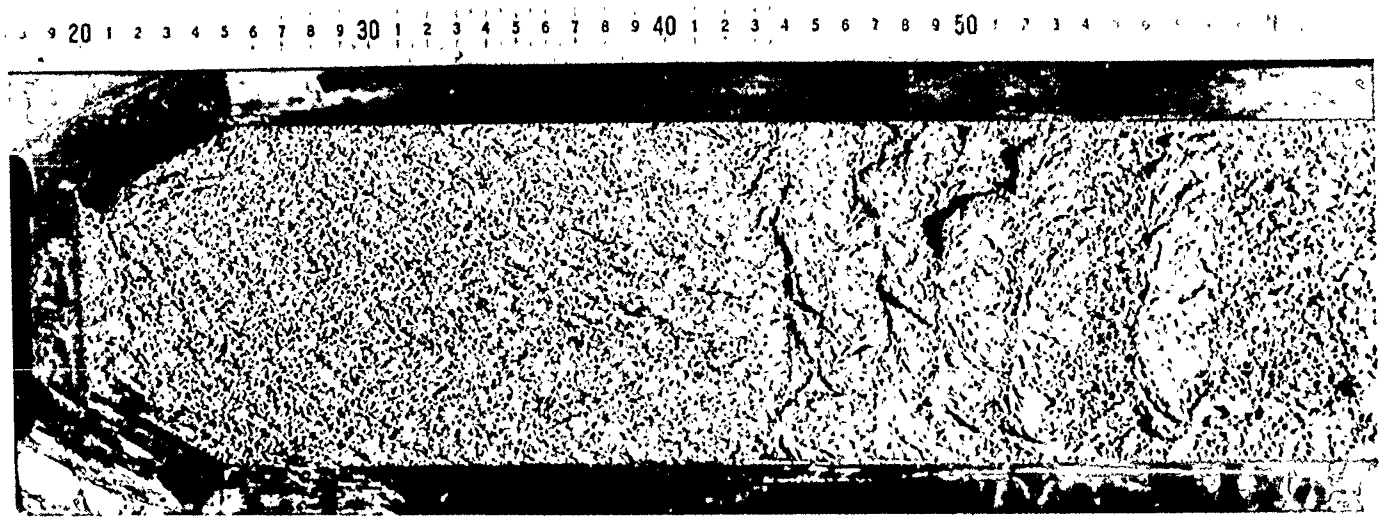

(b)

Fig. 5.12. Fracture surface of specimen WP-2.2. (*a*) Complete plate width and (*b*) close-up of cleavage arrests and ductile tearing associated with warm prestressing and reinitiation events. The scale is positioned along the plate front face.

of the side grooves. Examination of the fracture surface indicates that multiple (six to seven) crack run-arrest events occurred before the onset of ductile fracture. The reduction-in-thickness contour map for the specimen is presented in Fig. 5.13. Note that significant reductions in thickness occurred only after the location corresponding to the initial arrest; that is, $a/w \sim 0.44$.

The strain-gage records (Appendix A) and fracture surface were used to deduce the crack lengths (apparent position of the crack front) during the fracture process, and the results are summarized in Table 5.3. The crack-line strain-gage positions have been modified from those shown in Fig. 4.8(*b*) because the peak strain occurs at an angle of 72° in front of the crack tip. Figure 5.14 presents a plot of strain-gage-derived crack-front position vs time from the front- and back-face strain-gage results. Crack propagation at comparable elapsed times during the test was fairly consistent at the plate front and back faces.

5.3 TEST WP-2.3

Test WP-2.3 was the first test in the WP-2 series that did not have the crack front cut into a truncated chevron configuration. After obtaining a satisfactory thermal gradient (Fig. 5.15), specimen loading was initiated at a rate of 14 kN/s. At a load of 15.3 MN, the fracture event began and lasted about 950 ms (crack run-arrest events plus ductile tearing). Figure 5.16 shows the overall fracture surface for test specimen WP-2.3. A close-up of the cleavage and loss-of-cleavage regions with the cleavage run-arrest events highlighted is shown in Fig. 5.17. As noted in these figures, three cleavage run-arrest events occurred at the front face of the plate and four at the back face. The run-arrest events in Fig. 5.17(*b*) have been labeled A through F according to the apparent order in which they occurred. Examination of the fracture surface also indicates that initiation of crack growth in cleavage was in the plane of the side grooves, but as the crack extended, it deviated from this plane at several places. The maximum deviation was 6 mm below the plane of the side grooves on the lower half of the fracture surface. Once fibrous fracture took over, the crack returned to the plane of the side grooves. Reduction-in-thickness contours surrounding the crack plane are presented in Fig. 5.18.

Evaluation of the strain-gage records (Appendix A) and the fracture surface were used to deduce the crack length (position of the crack front) during the fracture process, and the results are summarized in Table 5.4. The strain-gage positions have been modified from those shown in Fig. 4.8(*c*) because the peak strain occurs at an angle of 72° in front of the crack tip. A plot of the strain-gage-derived crack-front position vs time from the front-face and back-face strain gage results for the first 50 ms of the test is presented in Fig. 5.19(*a*). The crack front advance at comparable elapsed times during the cleavage crack run-arrest events was more rapid near the back face of the plate than near the front face. An expanded scale plot of the crack-front position vs time derived from the front- and back-face strain gage results over the ≈950-ms duration of the test is presented in

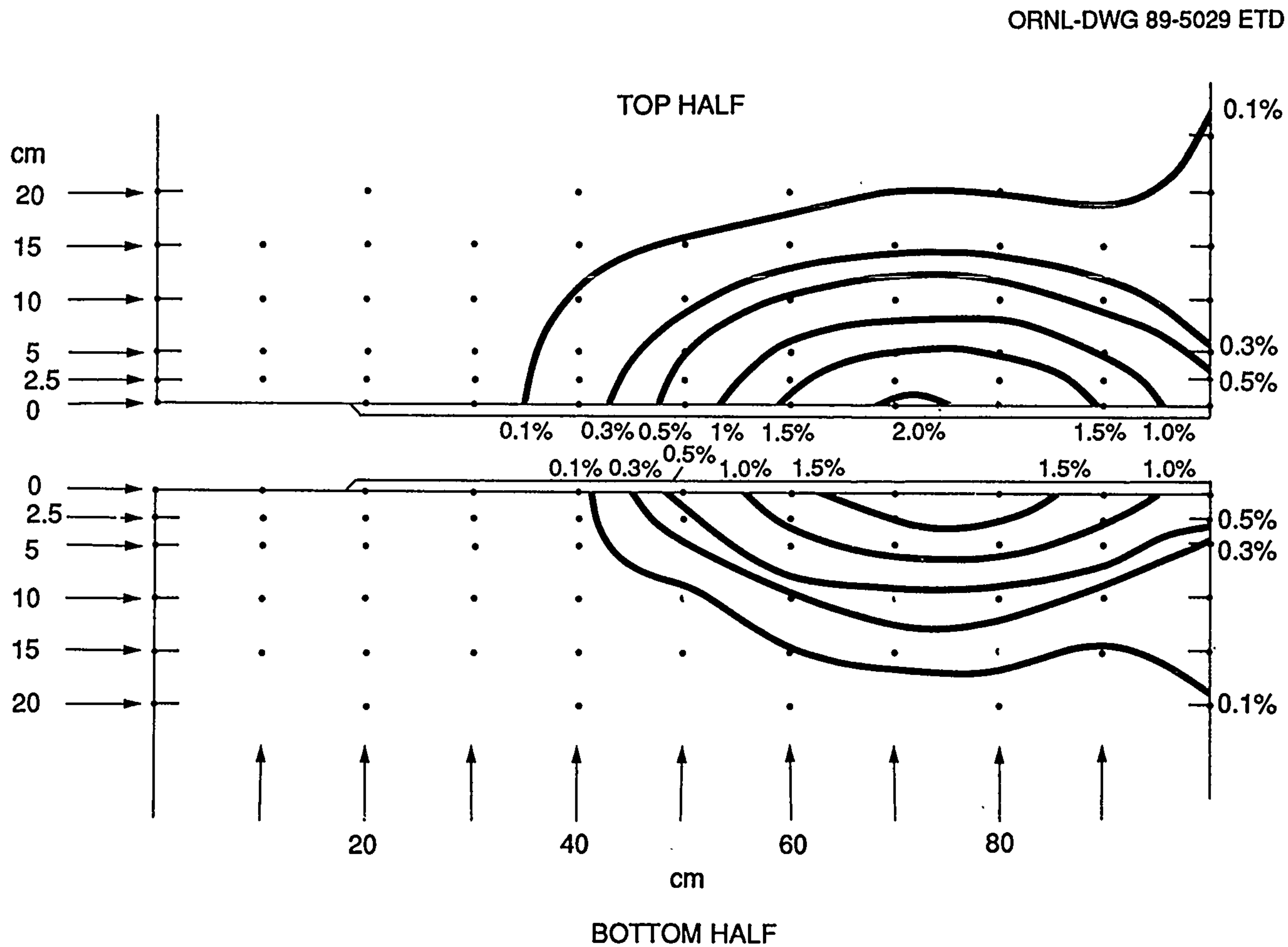

Fig. 5.13. Reduction-in-thickness contour map of specimen WP-2.2.

Table 5.3. Crack position vs time and velocity: test WP-2.2

Indicator[a]	Position (mm)	Time (ms)	Velocity[b] (m/s)
Front-face measurements			
Initial crack	211	0	
			875
SG1	218	0.008	
			870
SG2	258	0.054	
			1538
SG3	298	0.080	
			541
SG4	338	0.154	
			500
SG5	378	0.234	
			476
SG6	418	0.318	
			213
Arrest A	435	0.398	
Reinitiation	435	0.870	
			411
SG7	458	0.926	
			66
Arrest B	465	1.032	
Reinitiation	465	1.546	
			232
Arrest C	478	1.602	
Reinitiation	478	1.946	
			1111
SG8	498	1.964	
			500
Arrest D	499	1.966	
Reinitiation	499	2.266	
			204
Arrest E	510	2.320	
Reinitiation	510	3.628	
			2333

Table 5.3 (continued)

Indicator[a]	Position (mm)	Time (ms)	Velocity[b] (m/s)
Front-face measurements			
Arrest F	538	3.640	
Reinitiation	538	7.830	
(tearing)			11
SG9	548	8.77	
			317
Reinitiation	567	8.83	
(cleavage)			188
Arrest G	582	8.91	
Reinitiation	582	9.46	
(tearing)			7
SG10	598	11.91	
			20
SG11	698	16.81	
			28
SG12	798	20.39	
			14
End of plate	1000	34.48	
Back-face measurements			
Initial crack	215	0	
			150
SG13	218	0.020	
			1429
SG14	258	0.048	
			690
SG15	298	0.106	
			500
SG16	338	0.186	
			667
SG17	378	0.246	
			588
SG18	418	0.314	
			257
Arrest A	436	0.384	
Reinitiation	436	1.248	
			239

Table 5.3 (continued)

Indicator[a]	Position (mm)	Time (ms)	Velocity[b] (m/s)
	Back-face measurements		
SG19	458	1.340	
			600
Arrest B	470	1.360	
Reinitiation	470	1.934	
			417
Arrest C	490	1.982	
Reinitiation	490	2.242	
			1000
SG20	498	2.250	
			105
Arrest D	506	2.326	
Reinitiation	519	3.516	
(cleavage)			159
Arrest E	532	3.598	
Reinitiation	561	7.780	
(ductile)			6
Reinitiation	567	8.830	
(cleavage)			63
Arrest F	572	8.910	
Reinitiation	572	9.460	
(ductile)			17
End of plate	1000	34.48	

[a]These strain-gage positions are all reduced by 32 mm from the actual gage position shown in Fig. 4.8(*b*) because peak strain occurs at an angle of 72° in front of the crack tip.

[b]Velocity is an average calculated velocity for crack propagation between indicator points.

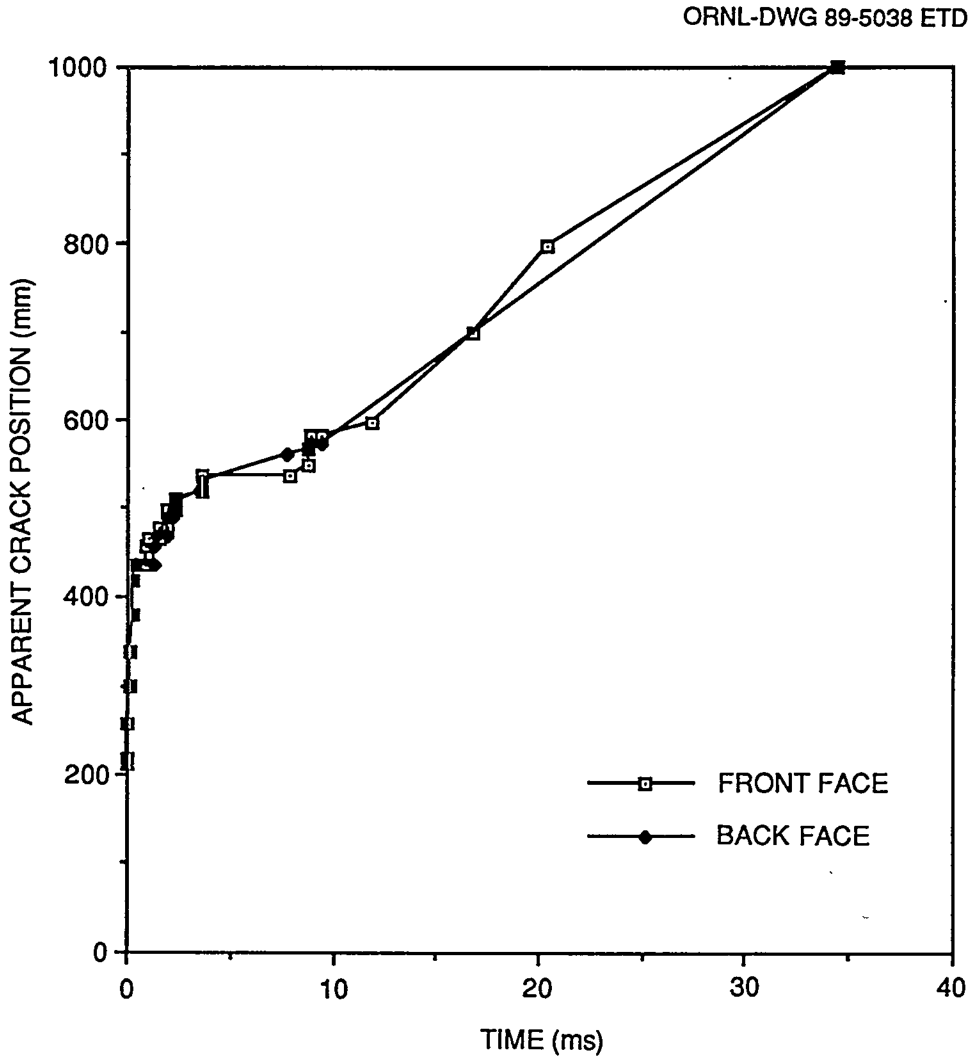

Fig. 5.14. Strain-gage-derived crack-front position vs time: test WP-2.2.

ORNL-DWG 90M-3602 ETD

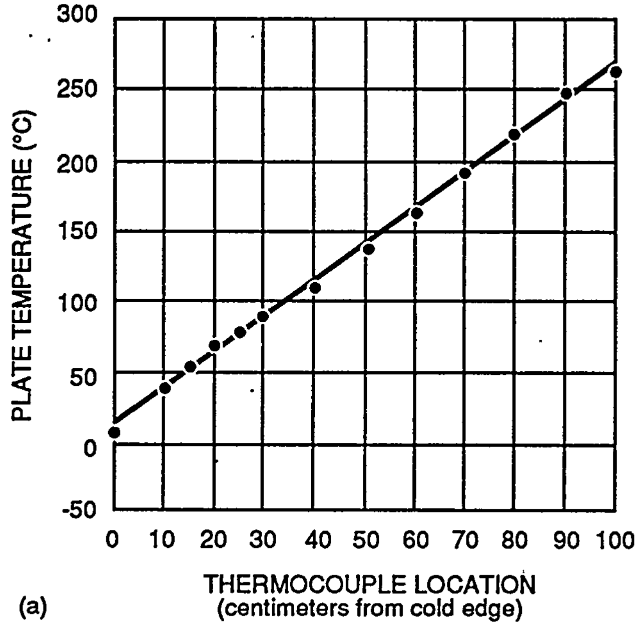

(a)

TEMPERATURE (°C)		
CENTIMETERS	REAL	IDEAL
0	5	15
10	37	39
15	51	52
15	51	52
20	66	64
20	68	64
20	66	64
25	78	77
25	78	77
30	89	89
40	112	114
40	112	114
50	136	140
60	160	164
60	161	164
70	188	189
80	214	214
80	215	214
90	242	239
100	258	265

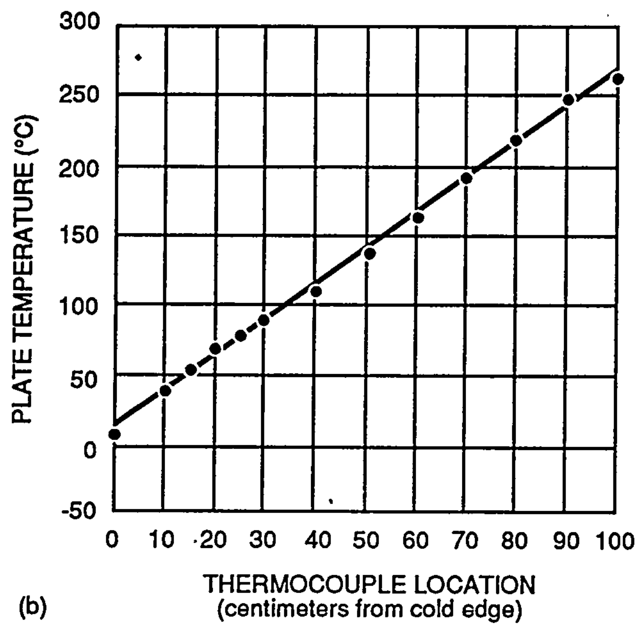

(b)

TEMPERATURE (°C)		
CENTIMETERS	REAL	IDEAL
0	4	15
10	37	39
15	51	52
15	51	52
20	65	64
20	67	64
20	66	64
25	77	77
25	77	77
30	88	89
40	111	114
40	112	114
50	136	140
60	160	164
60	160	164
70	188	189
80	214	214
80	214	214
90	242	239
100	255	265

Fig. 5.15. Actual and ideal temperature distributions across specimen width (*a*) at start of test and (*b*) a few seconds before fracture: test WP-2.3.

ORNL PHOTO 9835-87

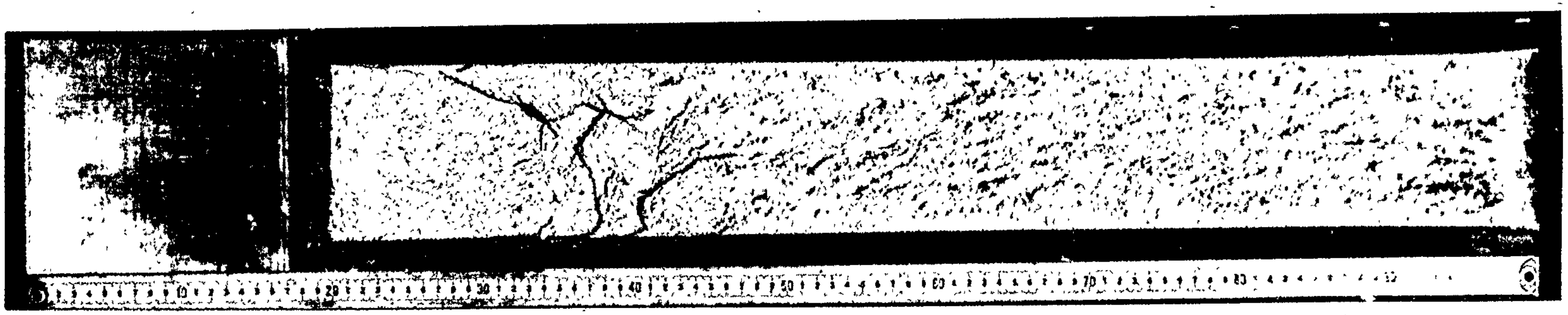

Fig. 5.16. Fracture surface of specimen WP-2.3.

ORNL–PHOTO 9836–87

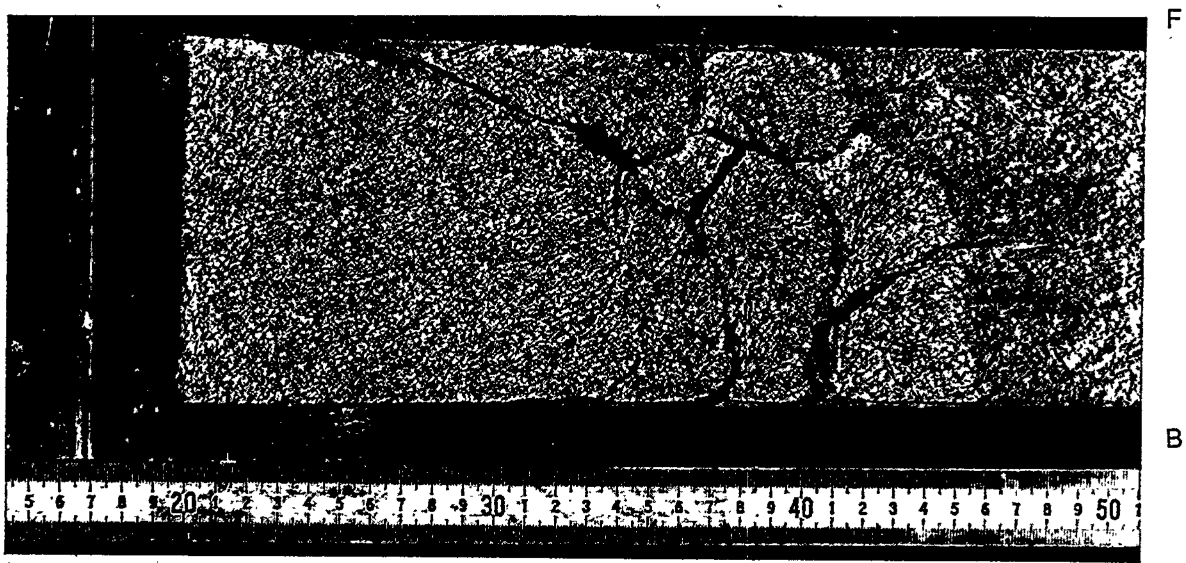

(a)

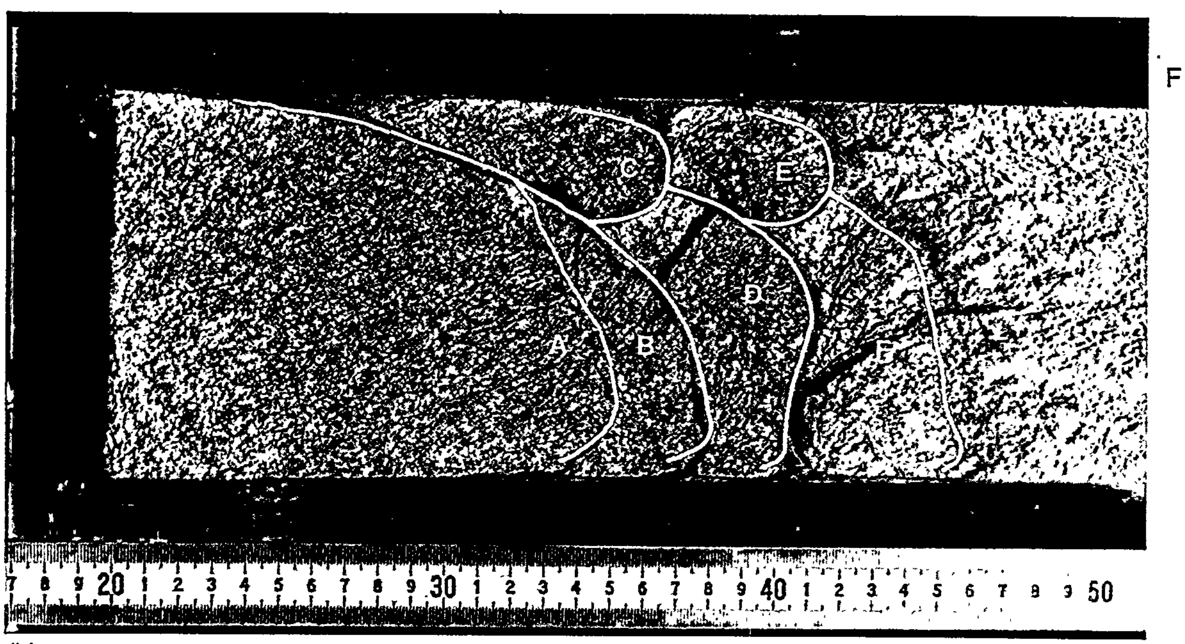

(b)

Fig. 5.17. Close-up of cleavage and loss-of-cleavage regions (*a*) without cleavage run-arrest events highlighted, and (*b*) with cleavage run-arrest events highlighted: test WP-2.3.

ORNL-DWG 87-4846 ETD

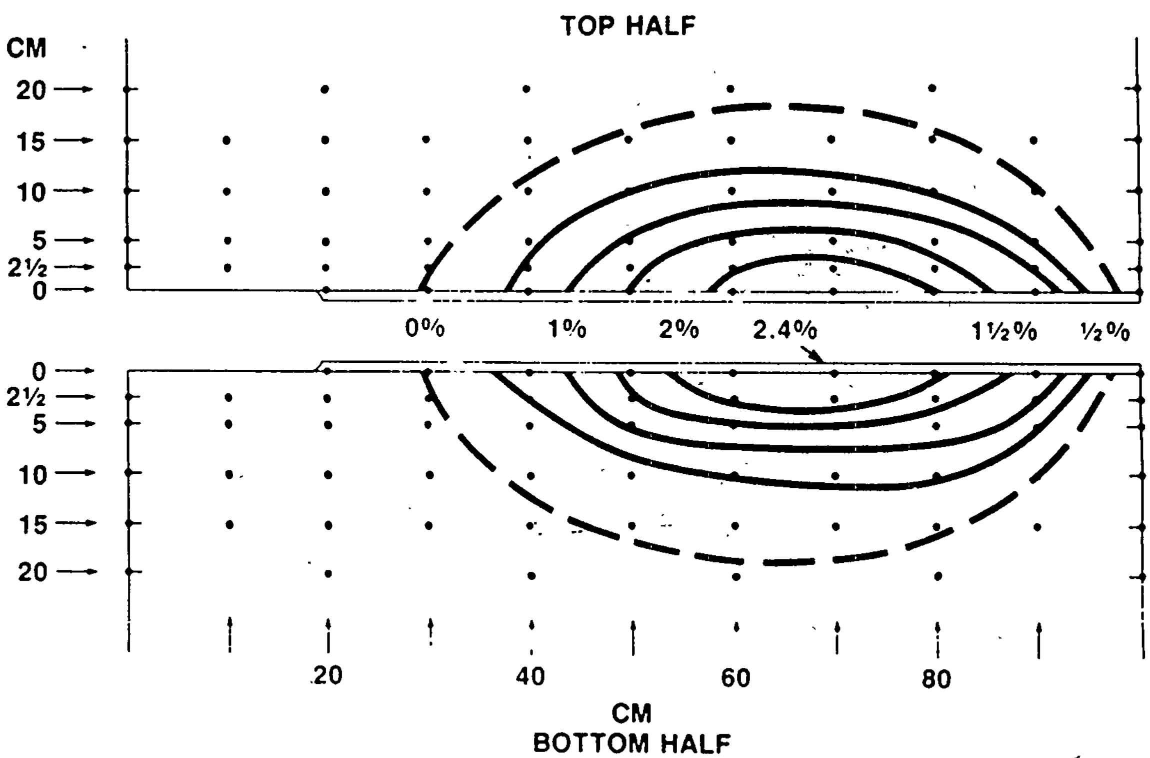

Fig. 5.18. Reduction-in-thickness contour map of specimen WP-2.3.

Table 5.4. Crack position vs time and velocity: test WP-2.3

Indicator[a]	Position (mm)	Time (ms)	Velocity[b] (m/s)
	Front-face measurements		
a_o	200	0	
			729
SG1	243	0.059	
			1667
SG2	268	0.074	
			47
Arrest A	275	0.222	
Reinitiation	275	12.489	
			388
SG3	308	12.574	
			211
Arrest C	345	12.749	
Reinitiation	345	37.344	
			150
SG4	348	37.364	
			2000
SG5	388	37.384	
			86
Arrest E	400	37.524	
Reinitiation	400	43.324	
			0.3
SG6	428	136	
			0.06
SG7	468	812	
			0.9
SG8	508	856	
			2.6
SG9	558	875	
			6.7
SG10	608	882.5	
			(8.3)
SG11[c]	658	(888.5)	
			(14.3)
SG12[c]	708	(892)	
			(11.4)
Ligament	(993)	917.0	
			0.3
End of plate	1000	942.5	

Table 5.4 (continued)

Indicator[a]	Position (mm)	Time (ms)	Velocity[b] (m/s)
	Back-face measurements		
a_o	200	0	
			1700
SG13	268	0.040	
			541
SG14	308	0.114	
			327
Arrest A	340	0.212	
Reinitiation	340	3.160	
			98
SG15	348	3.242	
			338
Arrest B	375	3.322	
Reinitiation	375	13.004	
SG16	388	Not working	314
Arrest D	397	13.074	
Reinitiation	397	38.464	
SG17	428	Too noisy	500
Arrest F	457	38.584	
Reinitiation	457	44.304	
			0.02
SG18	468	688	
			0.26
SG19	508	842	
			2.17
SG20	558	865	
			2.94
SG21	608	882	
			6
SG22	650	889	
			12
Ligament	993	917	
			0.27
End of plate	1000	942.5	

[a]These strain-gage positions are all reduced by 32 mm from the actual gage position because the peak strain occurs at an angle of 72° in front of the crack tip.

[b]Velocity is an average calculated velocity for crack propagation.

[c]Gage broke before peak formed.

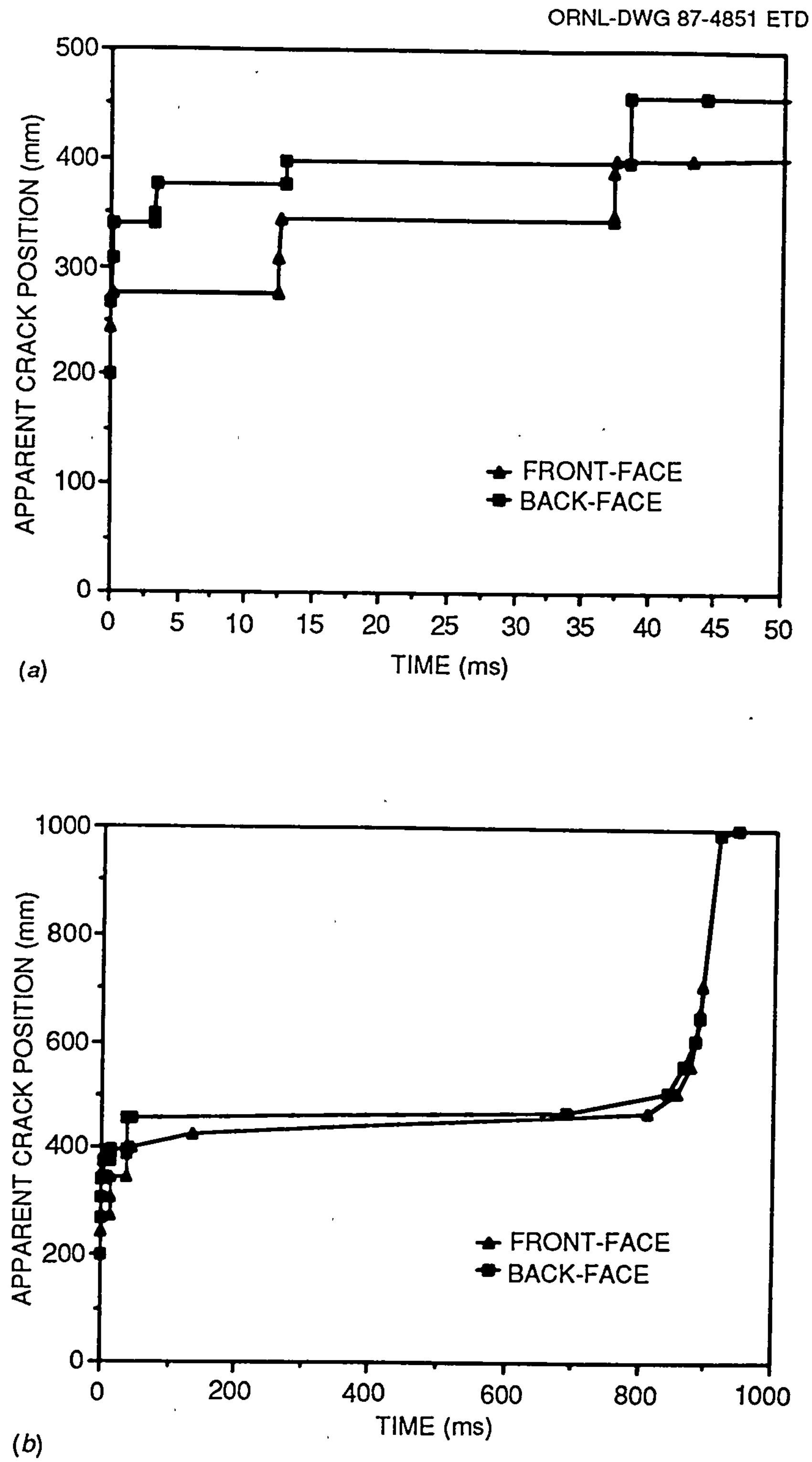

Fig. 5.19. Strain-gage-derived crack-front position vs time for (*a*) results for first 50 ms of test and (*b*) results for entire ~950 ms of test: test WP-2.3.

Fig. 5.19(*b*). As presented in this plot, the crack-front advance across the plate width did not become fairly uniform until the crack advance had reached an a/w ~ 0.6, while ductile tearing was occurring.

5.4 TEST WP-2.4

Loading of test specimen WP-2.4 at 11 kN/s was initiated after obtaining a satisfactory thermal gradient (Fig. 5.20). At 7.52 MN, or ~85% of the final peak load, a pop-in event occurred. When the load reached 8.85 MN (Fig. 5.21), the fracture event began and lasted about 90 ms (crack run-arrest events plus ductile tearing). The strain-gage records and fracture surface indicated that up to seven crack run-arrest events had occurred over an ≈29-ms interval before the onset of tearing. A small (7-mm) ligament remained intact after the main fracture events. Complete separation of the plate was achieved by applying a 254-kN load. With the exception of strain gage 6 and the top accelerometer, all gages functioned during the test. Some data, however, from strain gages 19–22, were lost late in the test because of saturation of amplifiers.

An overall view and a close-up of the fracture surface of specimen WP-2.4 is shown in Fig. 5.22. Examination of the fracture surface in the chevron region (Fig. 5.23) revealed that a crack pop-in had occurred to a crack depth of ~251 mm before initiation of the main crack run-arrest events. This pop-in is substantiated by examining records for strain gages 1–3 on the front face of the specimen and strain gages 13 and 14 on the back face of the specimen, which all show a sudden increase in strain at ~500 s into the test (Fig. 5.24). Following the sudden increase in strain, each of these gages exhibited an increase in strain rate even though no change in loading rate had occurred. (This suggests that the crack had suddenly advanced or popped-in.) As noted in Fig. 5.24, the strain and strain rate increases were less pronounced for the front-face gages than for the back-face gages, suggesting that the crack advance was less at the front-face than at the back-face of the specimen.

Examination of the fracture surface indicates that initiation of crack growth in cleavage was in the plane of the side grooves, but as it extended, it gradually deviated from this plane. By the time the crack had reached the depth at which tearing instability initiated, the crack was 8 mm below the plane of the side grooves. Once fibrous fracture took over, the crack returned to the side-grooved plane. Reduction-in-thickness contours surrounding the crack plane are shown in Fig. 5.25.

Examination of the strain-gage records (Appendix A) and the fracture surface were also used to deduce the crack length (position of the crack front) during the fracture process, and the results are presented in Table 5.5. In the table the strain gage positions have been modified from those shown in Fig. 4.8(*d*) to account for the fact that the peak strain occurs at an angle of 72° in front of the crack tip. Also, the crack lengths listed in the table are averages of the quarter-thickness crack lengths and the crack lengths at the side groove. Plots of the crack-front position vs time, derived from the front-face and back-face strain-gage results, are presented in Fig. 5.26.

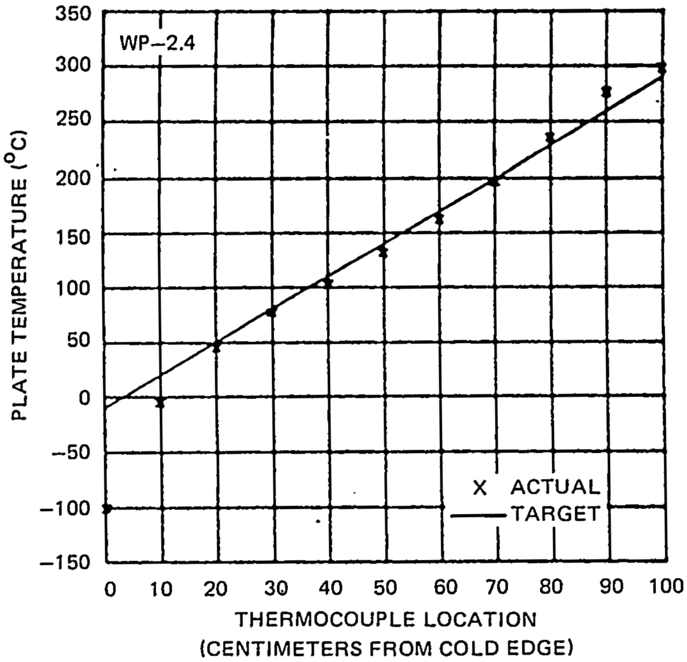

ORNL–DWG 86–5110 ETD

CENTIMETERS	TEMPERATURE (°C) ACTUAL	TEMPERATURE (°C) DESIRED
0	–101	–10
10	–5	19
20	45	49
30	76	79
40	103	109
50	132	140
60	163	169
70	197	199
80	236	229
90	276	259
100	297	290

Fig. 5.20. Actual and ideal temperature distributions across specimen width at approximate time of specimen fracture: test WP-2.4.

ORNL–DWG 86–5122 ETD

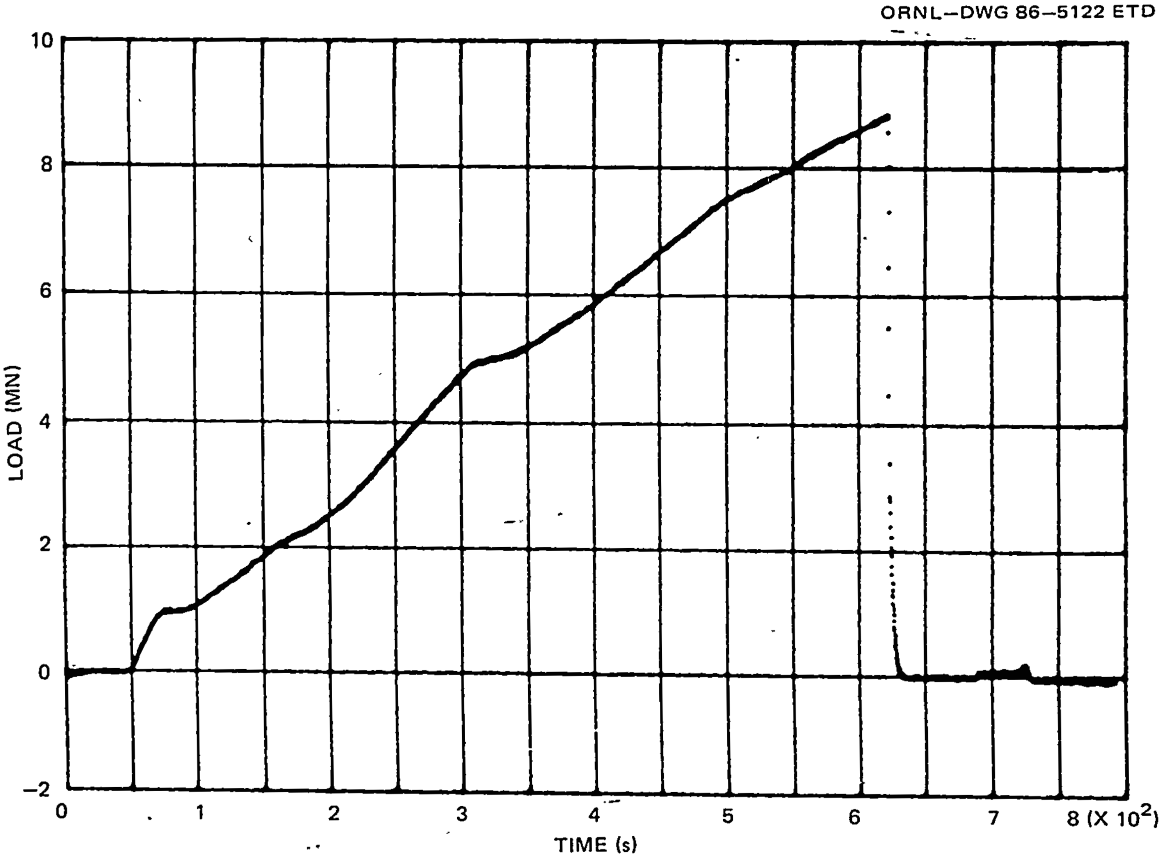

Fig. 5.21. Load history for test WP-2.4.

ORNL–PHOTO 2014–90

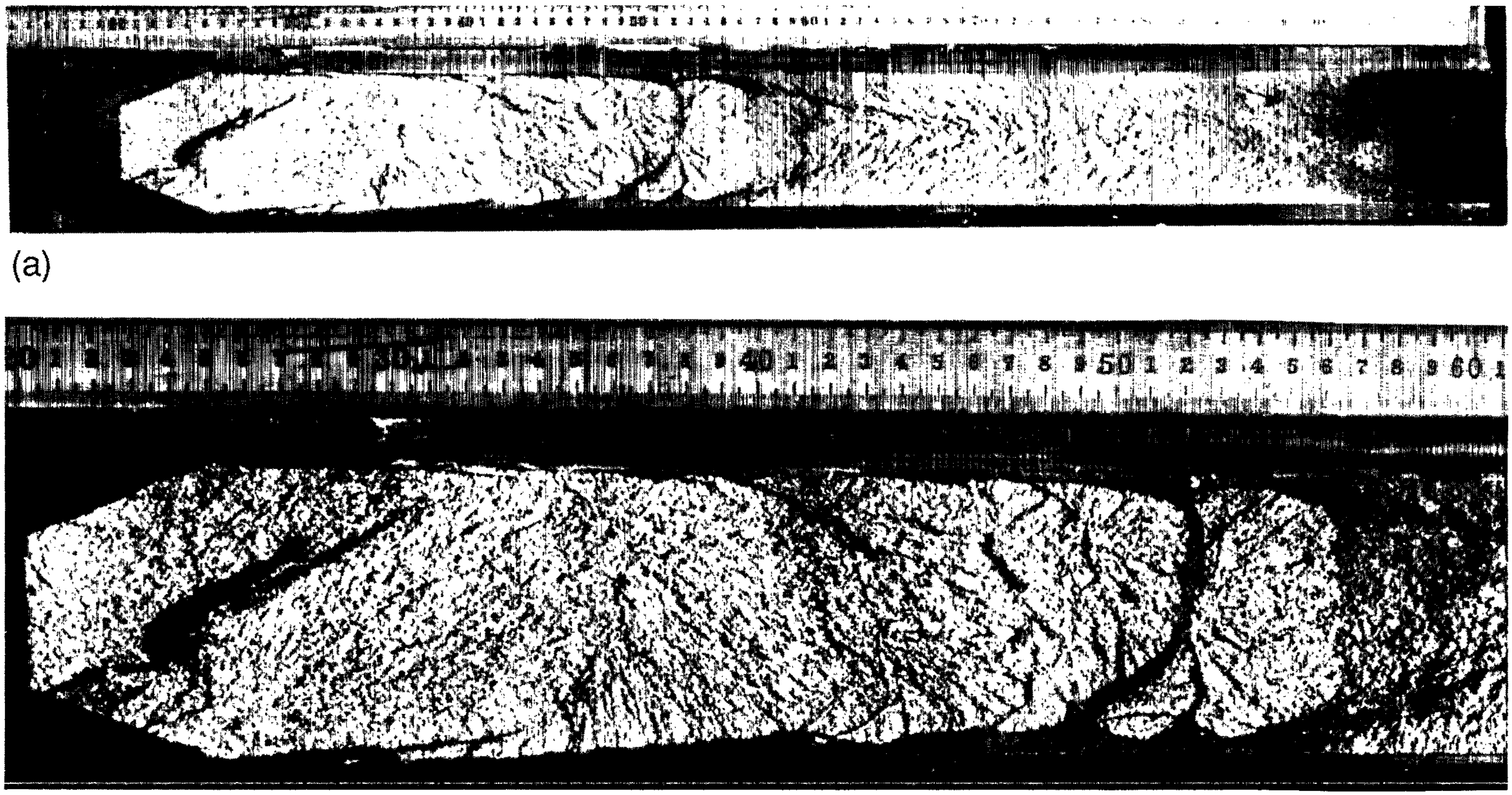

(a)

(b)

Fig. 5.22. Fracture surface of specimen WP-2.4. (*a*) Overall fracture surface and (*b*) close-up of region where crack run-arrest events occurred.

ORNL PHOTO 5728-86

Fig. 5.23. Close-up of initial flaw and region of pop-in: test WP-2.4.

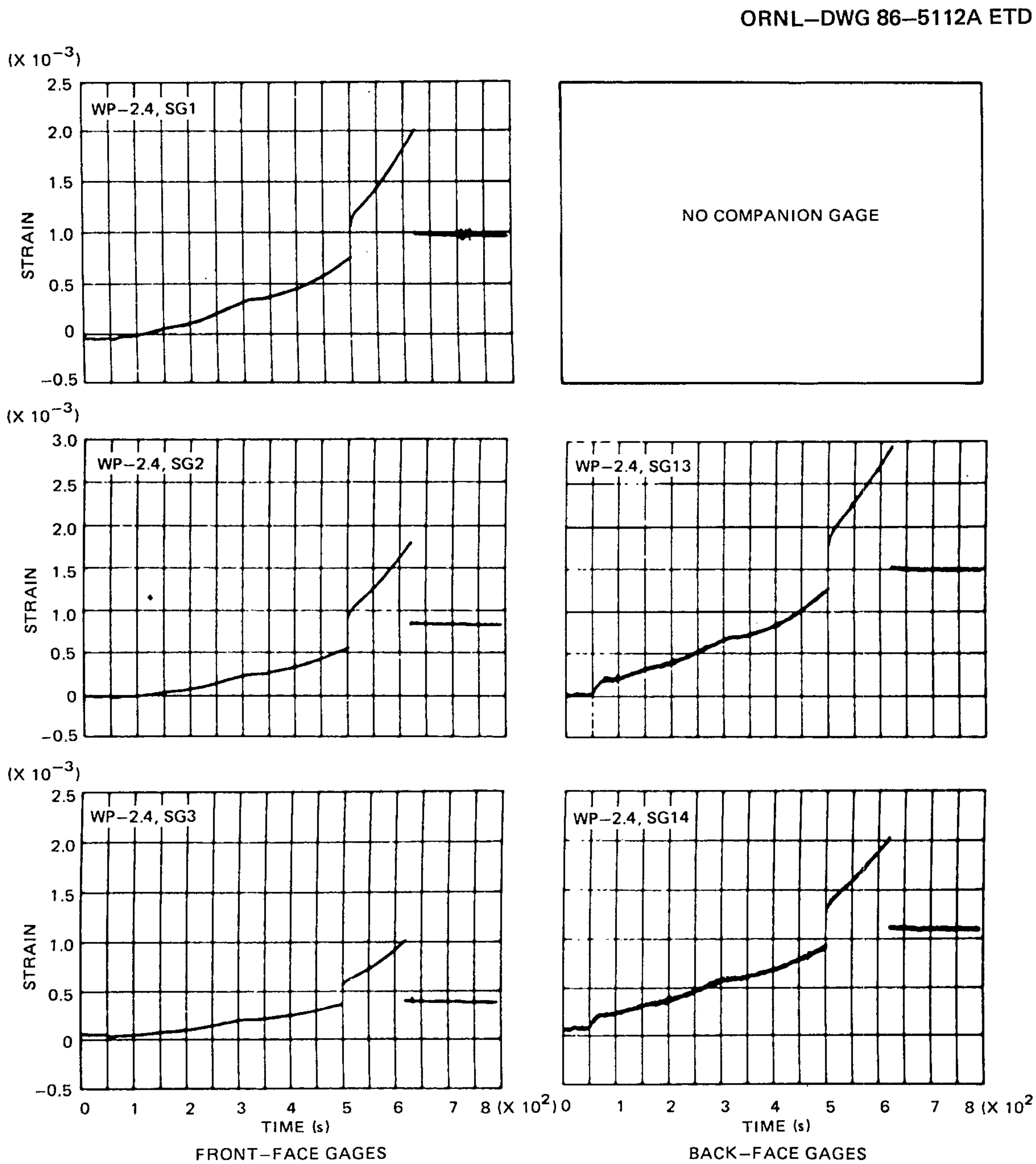

Fig. 5.24. Pop-in detected by strain gages 1–3 on plate front face and 13 and 14 on plate back face: test WP-2.4.

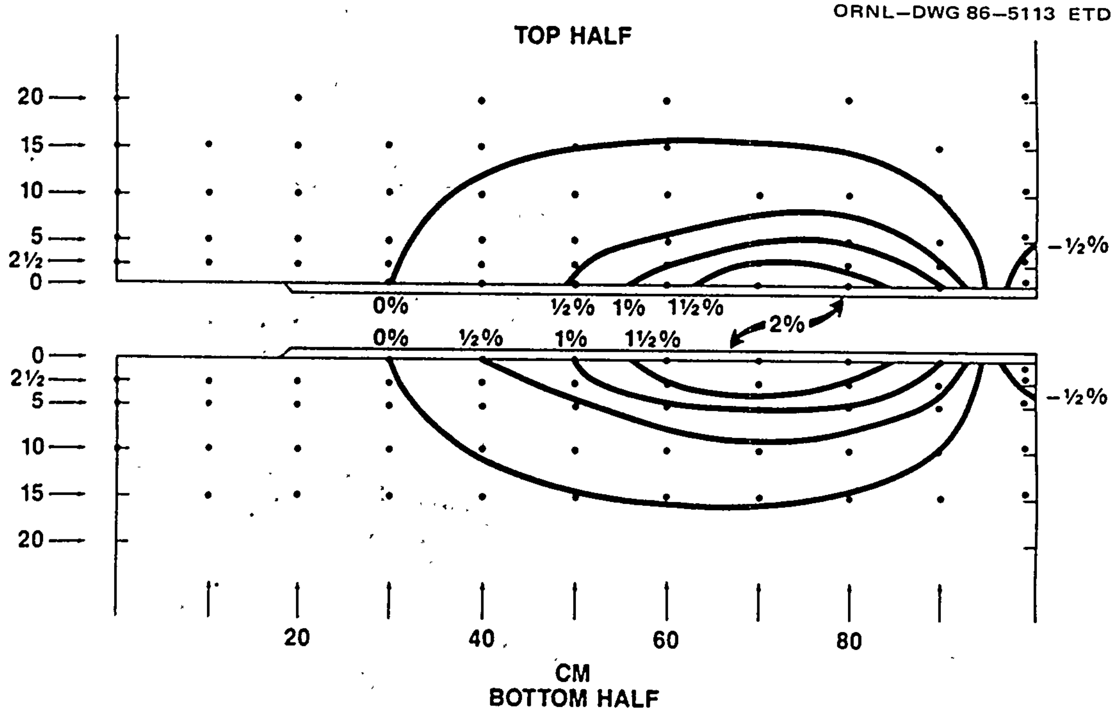

Fig. 5.25. Reduction-in-thickness contour map of specimen WP-2.4.

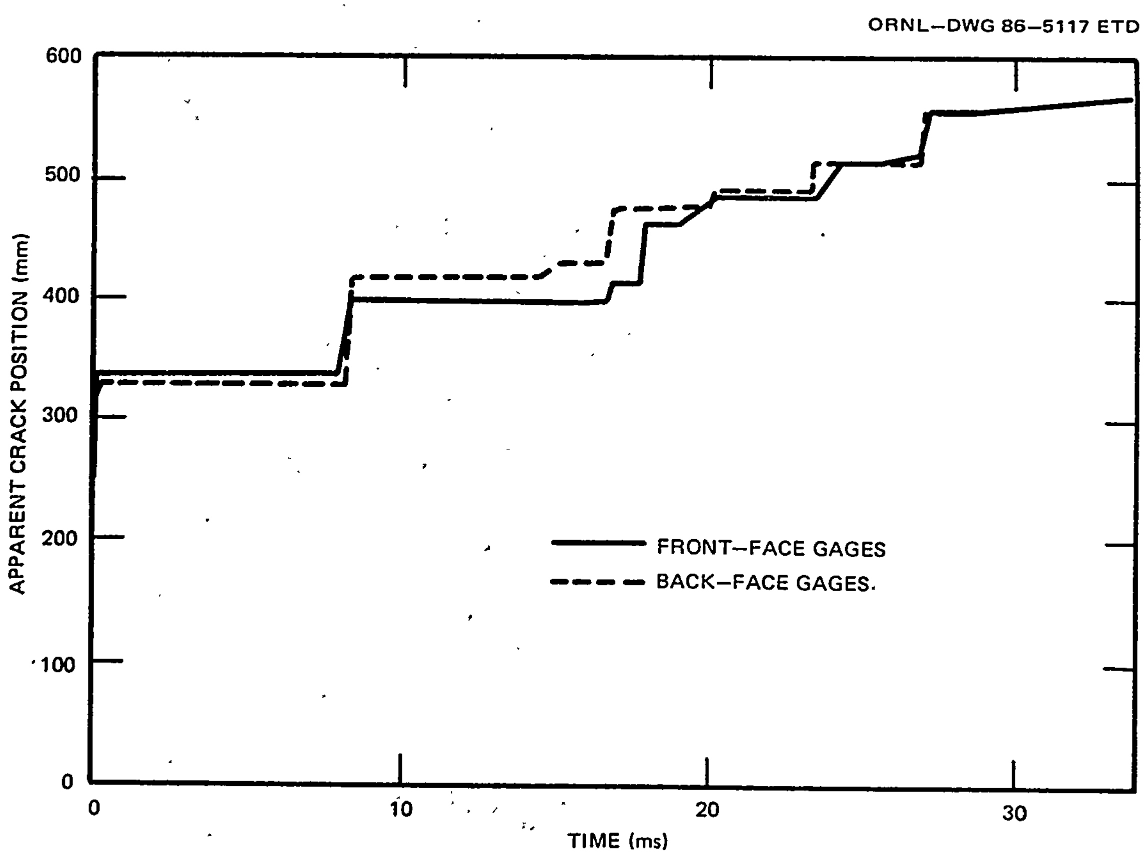

Fig. 5.26. Strain-gage-derived crack-front position vs time: test WP-2.4.

Table 5.5. Crack position vs time and velocity: test WP-2.4

Indicator[a]	Position (mm)	Time (ms)	Velocity[b] (m/s)
Front-face measurements			
Pop-in (Arrest A)	251	0	
SG1	254	0	
			1250
SG2	279	0.02	
			667
SG3	319	0.08	
			950
Arrest B	338	0.10	
Reinitiation	338	8.00	
			91
SG4	359	8.23	
			422
Arrest C	397	8.32	
Reinitiation	397	15.82	
			2
SG5	399	16.70	
			88
Arrest D	413	16.86	
Reinitiation	413	17.80	
			306
Arrest E	462	17.96	
Reinitiation	462	19.08	
			16
SG7	479	20.12	
			18
Arrest F	484	20.40	
Reinitiation	484	23.46	
			33
Arrest G	515	24.40	
Reinitiation	515	25.46	
			3
SG8	519	26.88	
			82
Arrest H	555	27.32	
Reinitiation	555	28.86	
			3
SG9	569	33.98	
			5
SG10	619	43.16	
			9
SG11	669	48.62	
			12
SG12	719	52.90	
			7
Remaining ligament	993	90.46	

Table 5.5 (continued)

Indicator[a]	Position (mm)	Time (ms)	Velocity[b] (m/s)
Back-face measurements			
Pop-in (Arrest A)	251	0	
			833
SG13	276	0.03	
			860
SG14	319	0.08	
			50
Arrest B	329	0.28	
Reinitiation	329	8.24	
			750
SG15	359	8.28	
			800
SG16	399	8.33	
			380
Arrest C	418	8.38	
Reinitiation	418	14.50	
			18
Arrest D	429	15.12	
Reinitiation	429	16.56	
			56
SG17	439	16.74	
			269
Arrest E	474	16.87	
Reinitiation	474	18.02	
			2
SG18	479	20.20	
			61
Arrest F	490	20.38	
Reinitiation	490	23.43	
			600
Arrest G	514	23.47	
Reinitiation	514	27.00	
			210
Arrest H	556	27.20	

[a]These strain-gage positions have been modified because the peak strain occurs at an angle of 72° in front of the crack tip. Also, the crack lengths listed are averages of the quarter-thickness crack lengths and the crack lengths at the side groove.

[b]Velocity is an average calculated velocity for crack propagation.

After examination of the strain-gage records and fracture surfaces to deduce the apparent crack-front position as a function of time, fractographic analyses of specimen WP-2.4 were conducted. After careful visual examination, the specimen fracture surface was cut into small pieces to allow them to be inserted into a scanning electron microscope (SEM). Figure 5.27 shows the fracture surface and indicates how it was sectioned. Section 1 in the figure was examined to determine if initial loading produced any ductile tearing from the sharp precrack produced by the EB-weld procedure. Figure 5.28 shows a portion of the fracture surface at the end of the EB-weld-generated precrack. The EB weld is on the right in the figure, and the cleavage fracture of the first crack run-arrest event is on the left. Ductile tearing was observed at the end of the welded region, and its width is given on the figure. The average width of the tearing region was ~800 μm. Figure 5.29 shows a detail of the ductile tearing from the end of the tearing strip, as indicated by the box marked on the bottom of Fig. 5.28. The EB-weld structure can be seen in the upper-right corner of Fig. 5.29(*a*), and a detail of the tearing is shown in Fig. 5.29(*b*). The apparent initiation site for the first crack run-arrest event is shown in Fig. 5.30. Figure 5.30(*a*) shows the area marked in the upper box in Fig. 5.28. Visual examination of the ridges on the fracture surface indicate that the fracture initiated in this region. Figure 5.30(*b*) presents a detail from the center of Fig. 5.30(*a*), which shows the ductile tearing that preceeded the cleavage fracture of the crack run-arrest event. Figure 5.30(*c*) presents a detail from the center of Fig. 5.30(*b*), which shows the apparent initiation site from a clump of particles at the center of the figure. Figure 5.30(*d*) presents a detail of the clump of particles.

A section was taken through section 1 in Fig. 5.27, and a surface perpendicular to the fracture was polished and examined metallographically. The heat-affected zone associated with the EB weld was noted, and from the length of this zone, it was determined that the initiation site was located in the base metal rather than in either the weld or its heat-affected zone.

Visual examination of section 2 in Fig. 5.27 suggests that an arrest event had occurred on at least part of the fracture surface of that section. Figure 5.31 shows a view of this fracture surface and reveals that an arrest event did occur. The strip of ductile tearing that is associated with the arrest event and subsequent reloading following arrest, is indicated on the figure. The width of the ductile tearing strip varies, with an average value being ~700 μm and a maximum width of ~1000 μm. The tearing strip bowed out across the surface, was not continuous across the entire specimen width, and was apparent on only about one-third the specimen width. This tearing is believed to reflect reinitiation of crack growth, before cleavage occurs, rather than the arrest process. The apparent cleavage initiation site for the second crack run-arrest event is shown in Fig. 5.32. The initiation site area, shown in Fig. 5.32(*a*), is located near the bottom of Fig. 5.31 at one end of the strip of ductile tearing. Figure 5.32(*b*) shows a view of the initiation area, located at the center top of Fig. 5.32(*a*). The apparent initiation site is shown in Fig. 5.32(*c*) and in greater detail in Fig. 5.32(*d*). The cleavage fracture appears to have initiated at a small particle near the center of Fig. 5.32(*d*).

ORNL PHOTO 2015-90

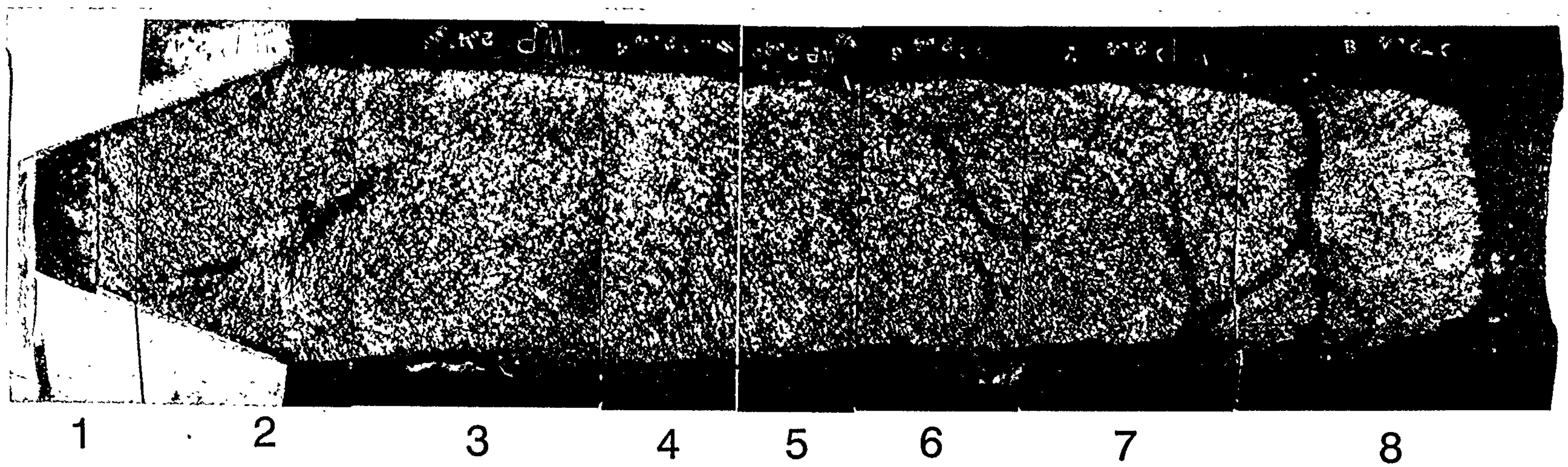

Fig. 5.27. Fracture surface of specimen WP-2.4, showing how the fracture surface was sectioned for further examination.

ORNL PHOTO 2016-90

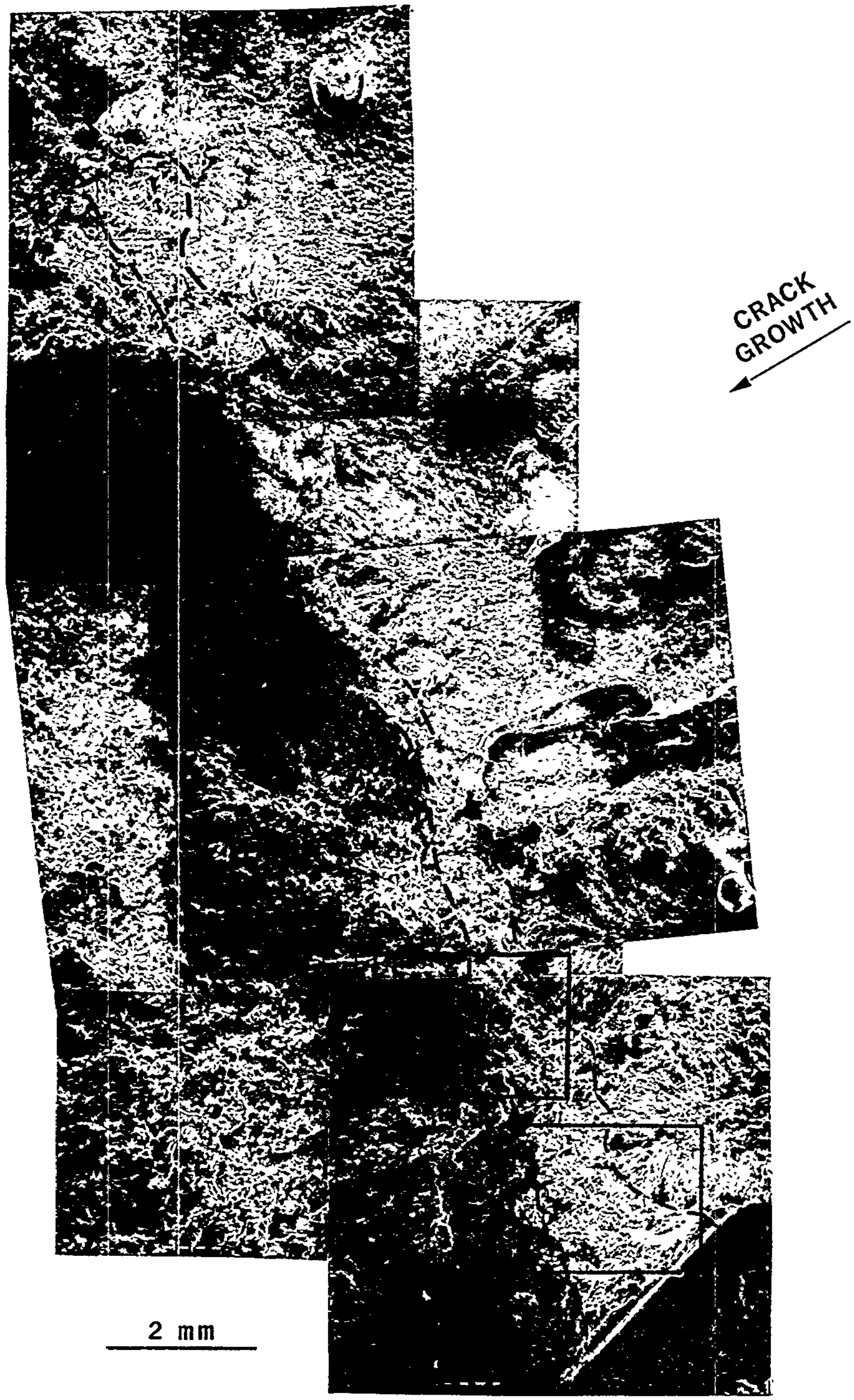

Fig. 5.28. A view of a portion of tip of precrack for specimen WP-2.4, Sect. 1 (Fig. 5.27).

ORNL PHOTO 2017-90

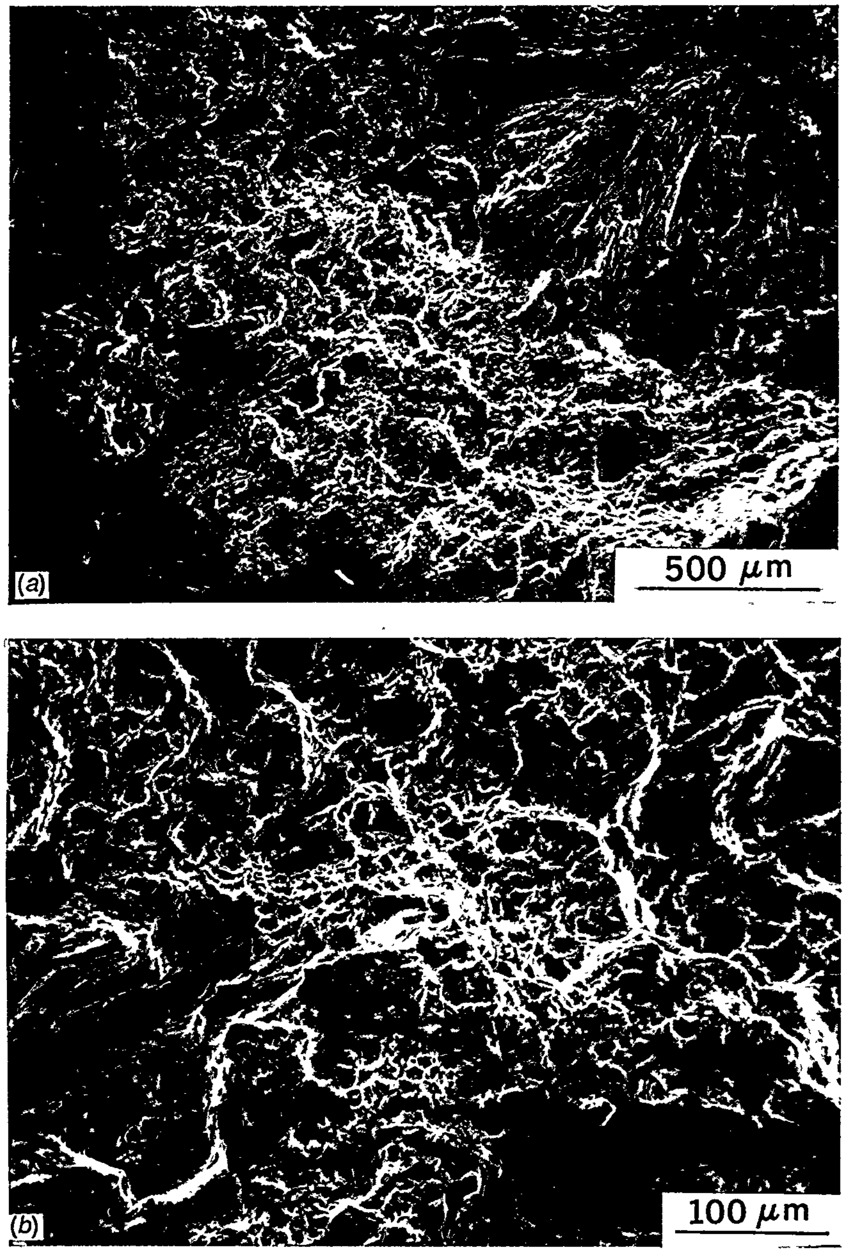

Fig. 5.29. Detail of ductile tearing from EB weld flaw, Sect. 1 (Fig. 5.27). (*a*) EB-weld structure and (*b*) detail of tearing.

ORNL PHOTO 2018-90

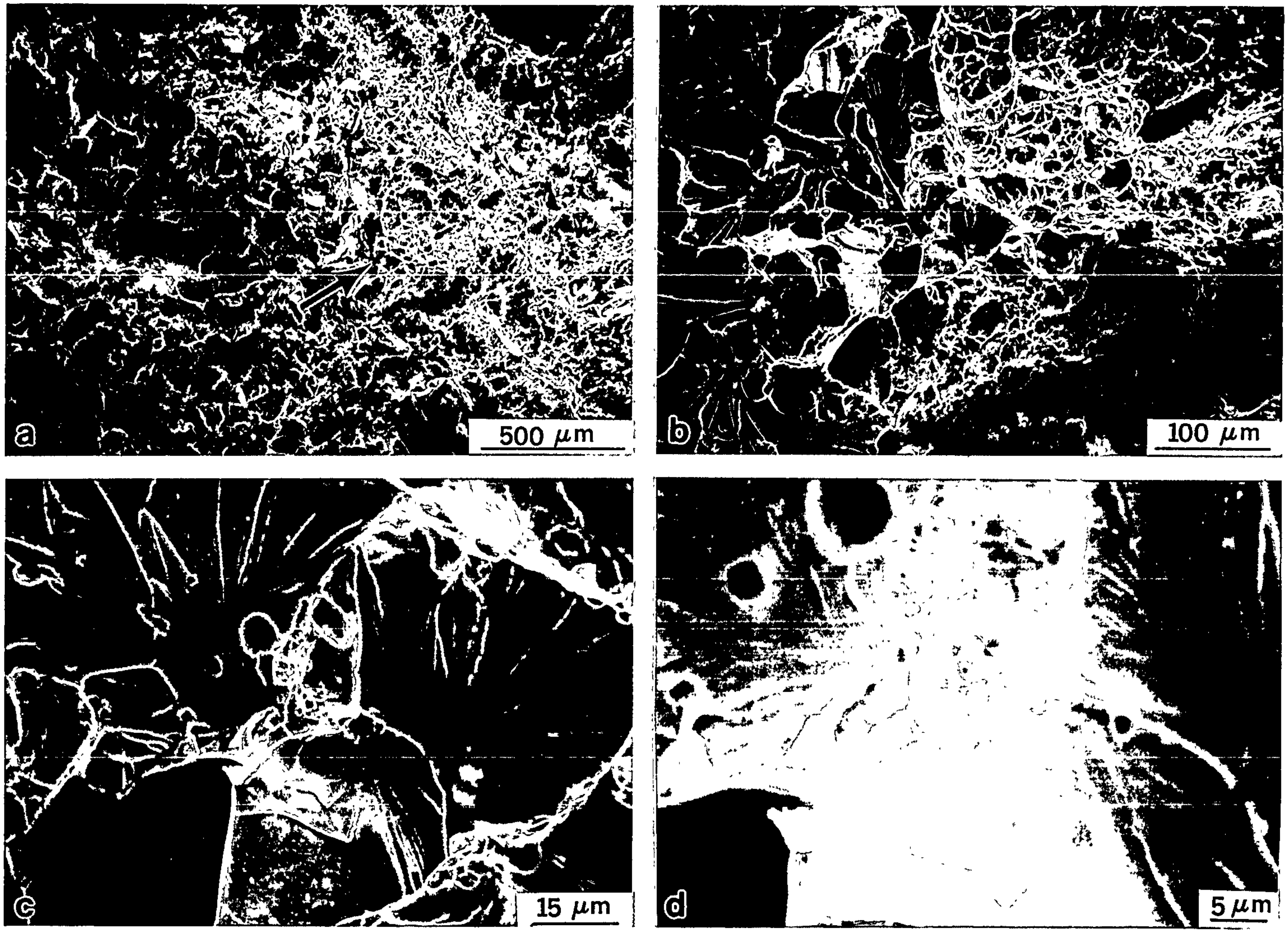

Fig. 5.30. Apparent initiation site for first crack run-arrest event, Sect. 1 (Fig. 5.27). (*a*) Low magnification view of tearing zone shown in upper box in Fig. 5.28 with apparent initiation site indicated by arrow, (*b*) detail from (*a*) showing ductile tearing and cleavage fracture, (*c*) detail of (*b*) showing initiation at a particle clump, and (*d*) detail of (*c*).

ORNL PHOTO 2019-90

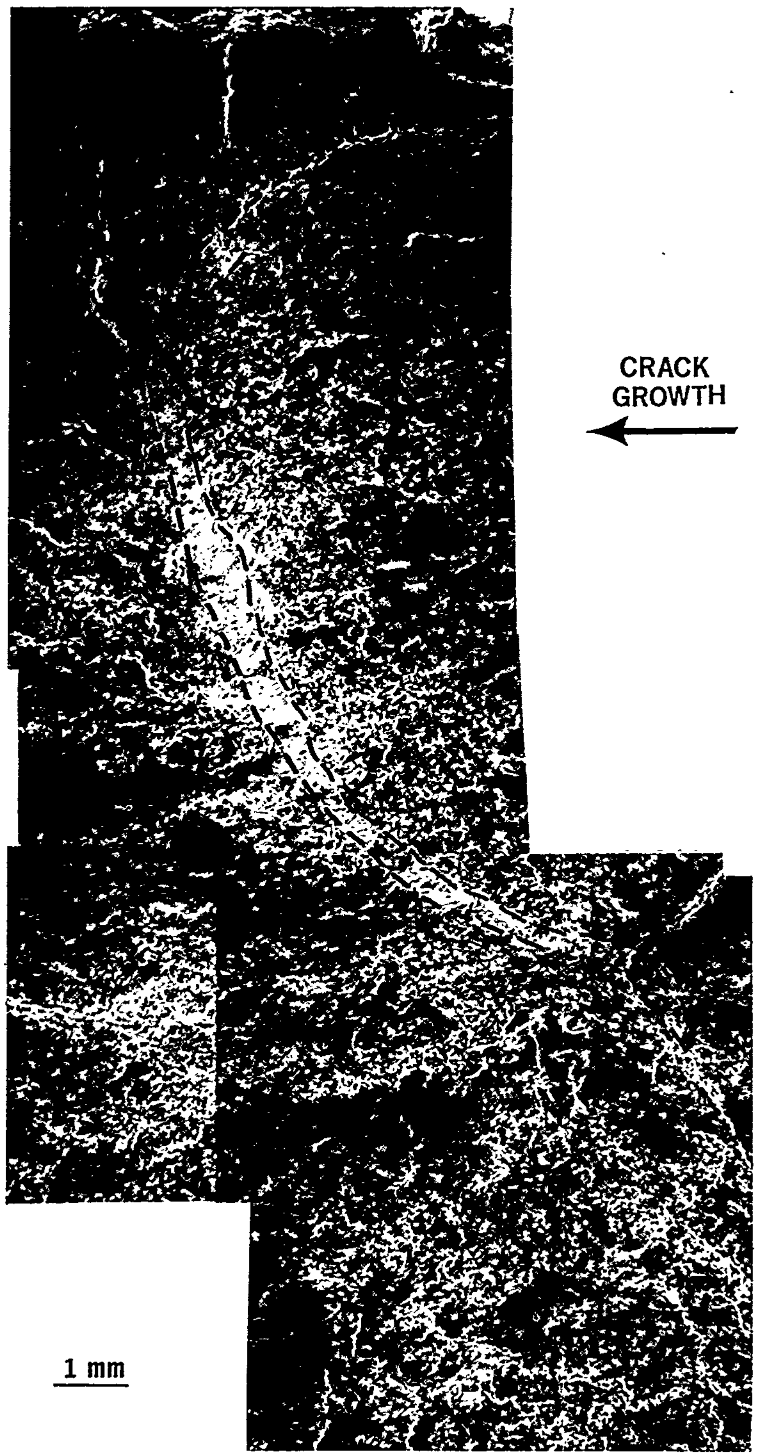

Fig. 5.31. Section 2 (Fig. 5.27) showing first arrest event on part of fracture surface.

ORNL PHOTO 2020-90

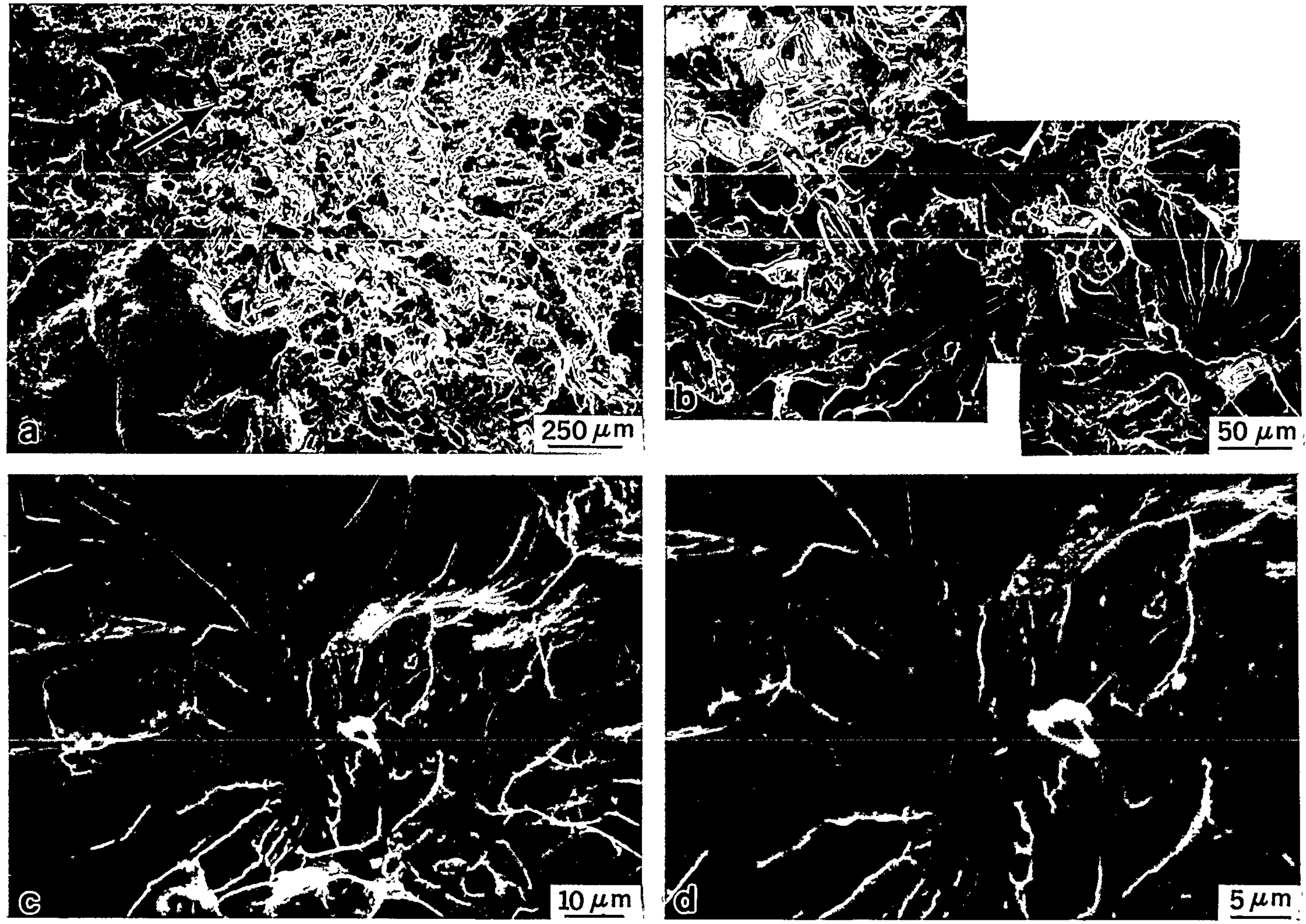

Fig. 5.32. Apparent initiation site for second crack run-arrest event, Sect. 2 (Fig. 5.27). (*a*) View of initiation area from bottom of tearing strip in Fig. 5.31 with apparent initiation site indicated by arrow, (*b*) higher magnification view of initiation region, (*c*) detail of initiation site showing initiation from a particle, and (*d*) detail of (*c*).

It is interesting to compare the extent of stable crack growth and the stress-intensity values at the initiation of cleavage fracture with fracture-toughness tests performed on material from the broken halves of specimen WP-2.5 (see Sect. 3.6). As noted in Table 3.10, tests of 25.4-mm-thick compact specimens of the TL orientation were performed at 40 and 60°C. Tests at 40°C showed no stable tearing and K_{Jc} values from 91 to 121 MPa·$\sqrt{m}$. Crack initiation for test WP-2.4 occurred at 45°C at a stress-intensity factor of 143 MPa·$\sqrt{m}$ (see Table 6.3), which is ≈18% higher than the largest value observed with the 1T compact specimens, but after ~800 μm of stable tearing. This amount of stable tearing is quite different than that observed in the 1T specimens, where no stable tearing occurred at 40°C. The second initiation for specimen WP-2.4 occurred at a location where the temperature was estimated to be 61°C. Compact specimen tests at 60°C gave final K_{Jc} values from 94 to 155 MPa·$\sqrt{m}$ with stable tearing from 200 to 900 μm. The estimated K value of 178 MPa·$\sqrt{m}$ (Table 6.3) after 700 μm of stable tearing for the second initiation event for test WP-2.4 is again ~15% greater than the highest value observed in the compact specimen tests.

5.5 TEST WP-2.5

After obtaining a satisfactory thermal gradient (Fig. 5.33), loading of test specimen WP-2.5 was initiated at 25 kN/s. At 7.53 MN, or 86% of peak load, a pop-in event was heard and was later supported by the strain-gage outputs, accelerometer readings, and examination of the fracture surface.* Specimen loading was continued, and at a load of 8.9 MN (Fig. 5.34), the fracture event began and lasted ~90 ms (cleavage fracture plus ductile tearing). A small 8.5-mm plate ligament remained intact after the fracture event. While all instrumentation was functional at the start of the test, the COD gage's responses, which for this test were recorded on a transient oscilloscope, were not complete. Because of an improper selection of triggering parameters, the first few milliseconds of COD data were not recorded (see Appendix A, Fig. A.69). In addition, strain gages 4, 7, 8, 11, and 12 became inoperative during the test.

The entire fracture surface of specimen WP-2.5 is shown in Fig. 5.35(*a*). Figure 5.35(*b*) shows the entire fracture surface with the cleavage run-arrest events highlighted. Similarly, close-ups of the cleavage and loss-of-cleavage regions without and with the cleavage run-arrest events highlighted are shown in Fig. 5.36(*a*) and (*b*), respectively. Examination of a close-up of the fracture surface in the region of the chevron (Fig. 5.37) confirmed that a pop-in event had occurred to

---

*As noted previously, specimen WP-2.4 also experienced a pop-in event before the main crack run-arrest events. Both tests WP-2.4 and -2.5 used specimens that were 102 mm thick. The remainder of the WP-2 series tests that used 152-mm-thick specimens did not experience a pop-in event.

ORNL-DWG 90M-3603 ETD

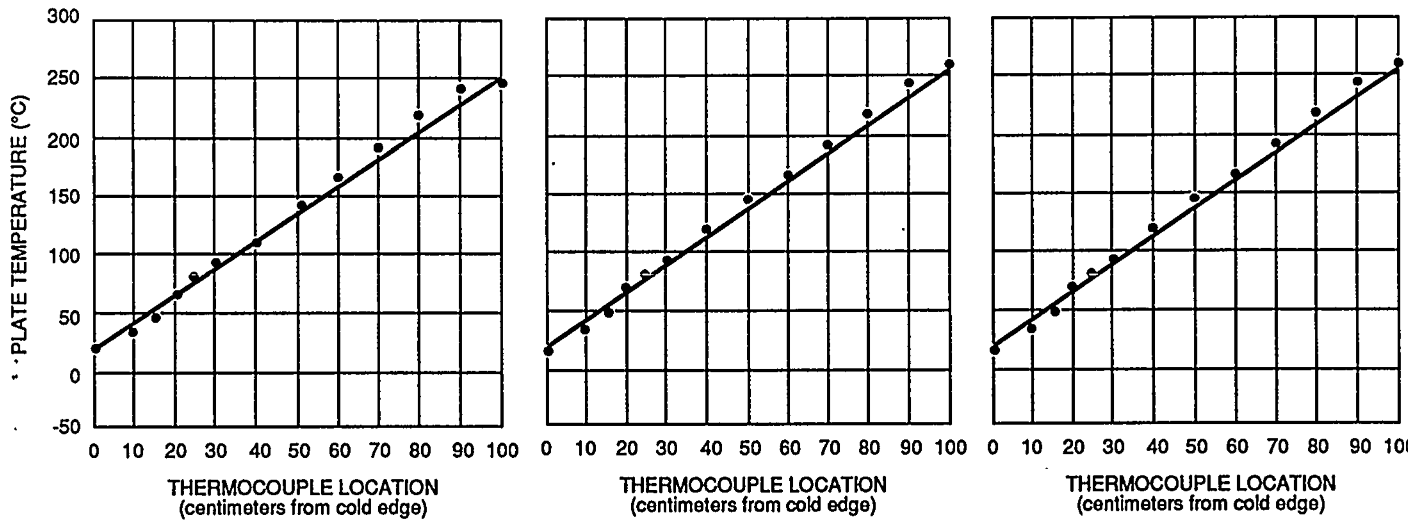

(a)

	TEMPERATURE (°C)	
CENTIMETERS	REAL	IDEAL
0	14	10
10	33	41
15	47	53
15	46	53
20	65	64
20	66	64
20	64	64
25	80	76
25	80	76
30	92	88
40	116	111
40	116	111
50	140	134
60	163	158
60	163	158
70	188	181
80	215	205
80	215	205
90	239	228
100	249	251

(b)

	TEMPERATURE (°C)	
CENTIMETERS	REAL	IDEAL
0	14	10
10	36	41
15	50	53
15	49	53
20	66	64
20	68	64
20	66	64
25	81	76
25	80	76
30	92	88
40	116	111
40	116	111
50	140	134
60	163	158
60	163	158
70	188	181
80	213	205
80	214	205
90	238	228
100	255	251

(c)

	TEMPERATURE (°C)	
CENTIMETERS	REAL	IDEAL
0	15	10
10	36	41
15	50	53
15	49	53
20	66	64
20	67	64
20	66	64
25	81	76
25	80	76
30	92	88
40	116	111
40	116	111
50	140	134
60	163	158
60	163	158
70	188	181
80	213	205
80	214	205
90	238	228
100	255	251

Fig. 5.33. Actual and ideal temperature distributions across specimen width (*a*) at start of test, (*b*) at crack pop-in event, and (*c*) at approximate time of fracture events: test WP-2.5.

ORNL-DWG 87-3902 ETD

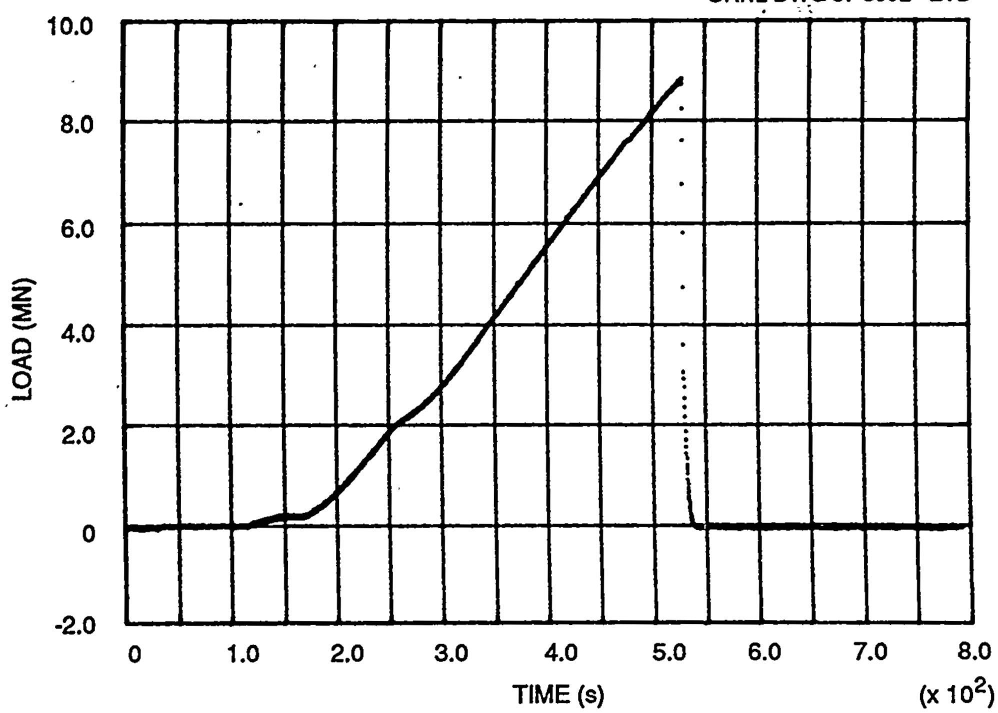

Fig. 5.34. Load history for test WP-2.5.

ORNL PHOTO 3140-87

(*a*)

(*b*)

Fig. 5.35. Fracture surface for specimen WP-2.5. (*a*) Entire fracture surface, and (*b*) entire fracture surface with cleavage run-arrest events highlighted.

ORNL PHOTO 3141-87

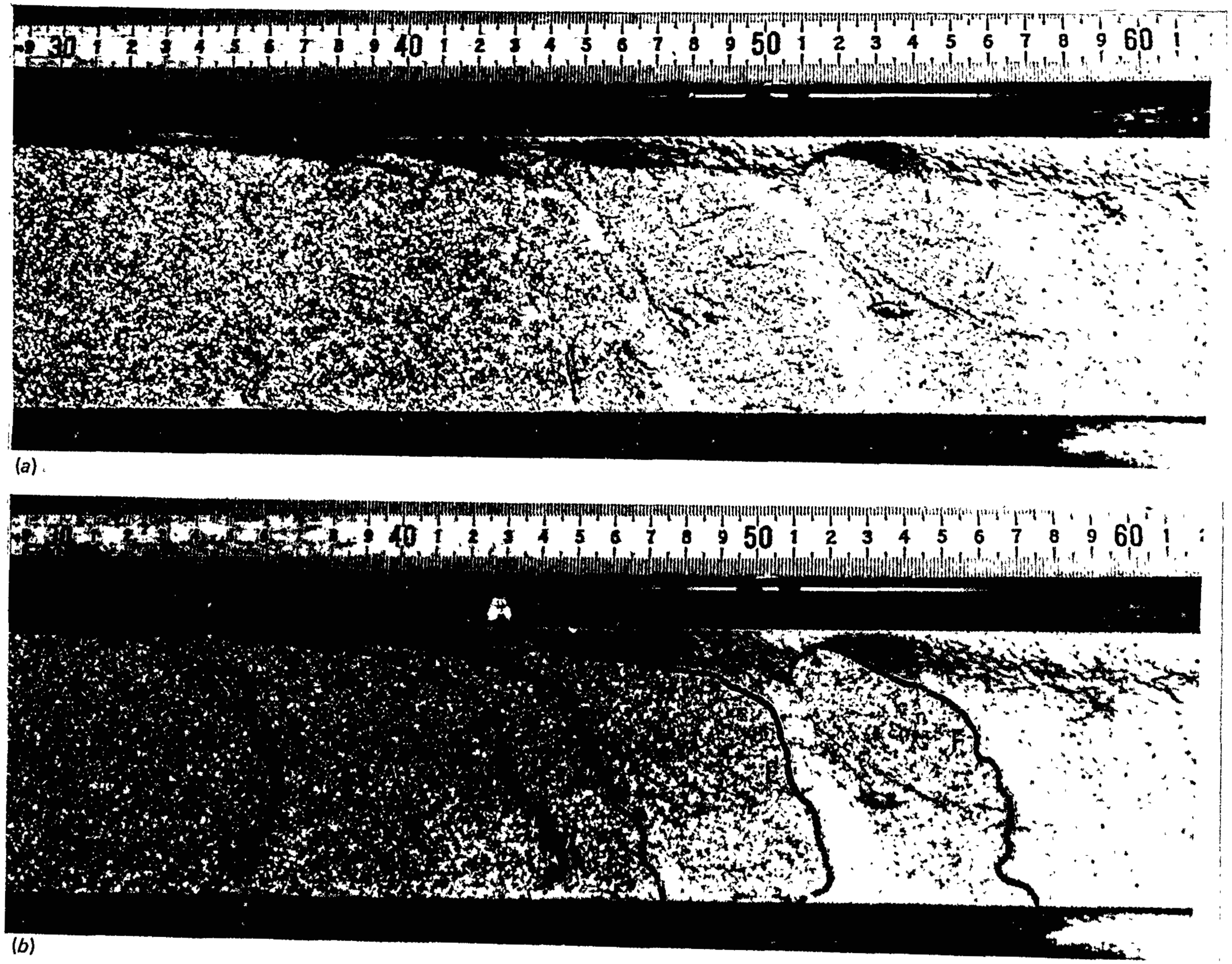

Fig. 5.36. Close-up of fracture surface for specimen WP-2.5. (*a*) Cleavage and loss-of-cleavage regions, and (*b*) cleavage and loss-of-cleavage regions with cleavage run-arrest events highlighted: test WP-2.5.

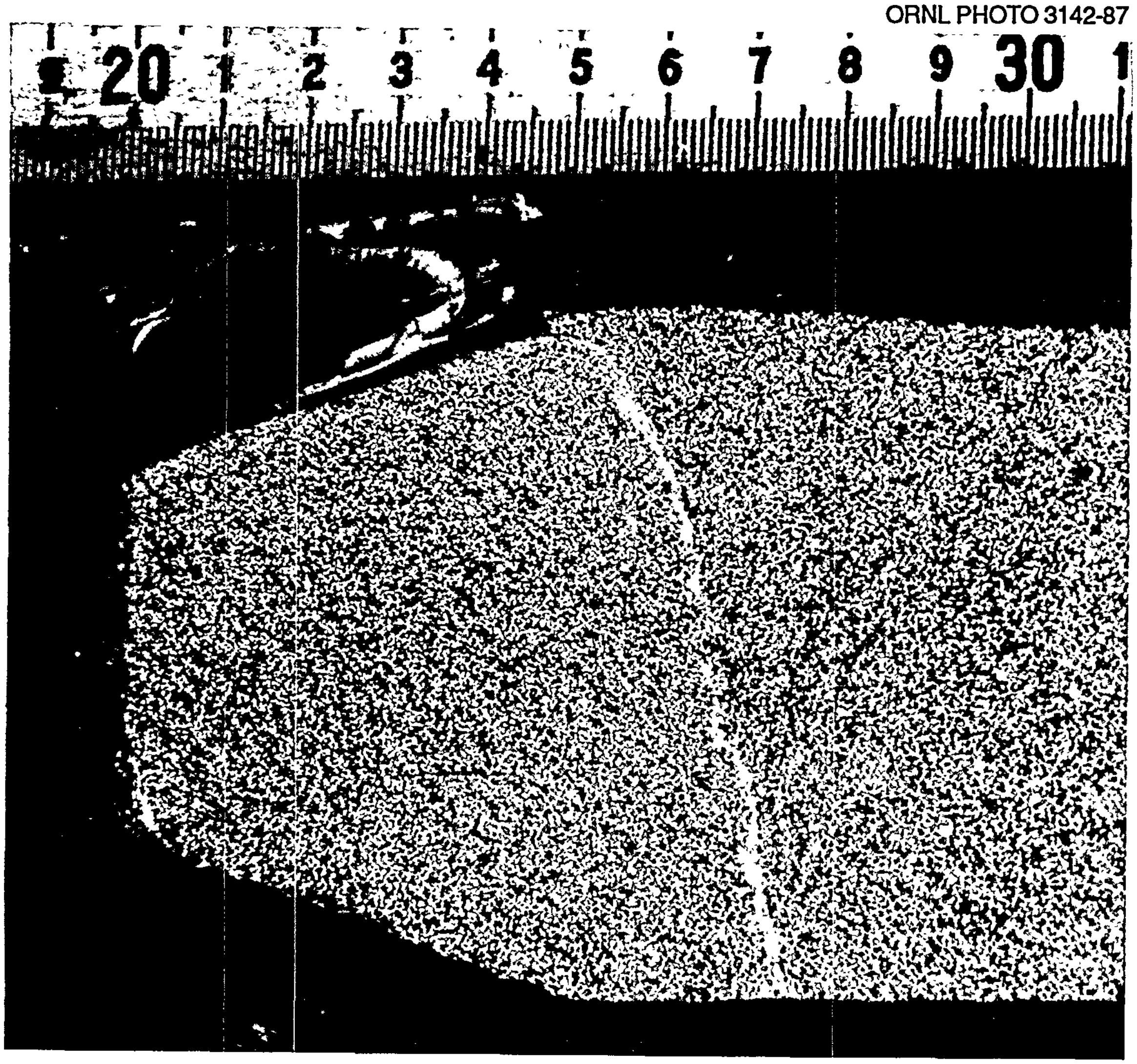

Fig. 5.37. Close-up of initial EB weld-generated crack and region of pop-in: test WP-2.5.

an estimated average crack depth of 264 mm before initiation of the main fracture event. This is further substantiated in Fig. 5.38, which presents strain-gage records for strain gages 1–3 on the front face of the specimen and strain gages 13 and 14 on the back face of the specimen; each record shows a sudden increase in strain at ~480 s into the test, followed by a sudden increase in strain and strain rate even though no change in loading rate was made by the operator. As noted in Fig. 5.38, the strain and strain rate increases were more pronounced for back-face gage 14 than its companion front-face gage 3, indicating that the crack had advanced more near the back-plate surface than the front-plate surface. A selection of high-resolution strain gage and accelerometer records during the crack pop-in are presented in Figs. 5.39 and 5.40, respectively.

Examination of the fracture surface indicates that initiation of crack growth in cleavage was in the plane of the side grooves, but as it extended, it gradually deviated from this plane. By the time the crack had reached the final cleavage-arrest location ($a/w \approx 0.56$ at plate back face) it was 8 mm below the plane of the side grooves.

Evaluation of the strain-gage records (Appendix A) and the fracture surface were also used to deduce the crack length (position of the crack front) during the fracture process, and the results are presented in Table 5.6. The strain-gage positions have been modified from those shown in Fig. 4.8(*a*) because the peak strain occurs at an angle of 72° in front of the crack tip. Also, the crack-arrest locations listed are averages of the quarter-thickness crack lengths and the crack lengths at the side groove. A plot of the strain-gage-derived crack-front position vs time using the front-face and back-face strain-gage results is presented in Fig. 5.41. Results in this figure indicate that the crack front advance at comparable elapsed times during the cleavage crack run-arrest events was more rapid near the plate back face than near the plate front face. As noted in Table 5.6, it was not until the crack advance had reached an $a/w \sim 0.669$ (while ductile tearing was occurring) that the crack front advance was fairly uniform across the plate width (as indicated by the strain gages).

After examination of the strain-gage records and fracture surfaces to deduce the apparent crack-front position as a function of time, fractographic analyses of specimen WP-2.5 were conducted. As was done for specimen WP-2.4, the fracture surface of specimen WP-2.5 was cut into smaller pieces for insertion into the SEM. Figure 5.42 shows the fracture surface and indicates how it was sectioned. Because the fracture surface of specimen WP-2.5 had not been as well preserved as that of specimen WP-2.4, which was discussed earlier, it was somewhat difficult to identify features of interest. Investigation of section A in Fig. 5.42 revealed ductile tearing at the tip of the EB weld that was followed by the cleavage area associated with the first crack run-arrest event. Figure 5.43 shows the tearing strip at the tip of the EB weld. The apparent initiation site is presented in Fig. 5.44. Figure 5.44(*a*) shows the ductile tearing strip and cleavage in the initiation area shown in the dashed box in Fig. 5.43. The average width of the tearing strip was ~1200 μm. Details of the initiation site are presented in Figs. 5.44(*b*) and (*c*). As noted earlier, damage to the fracture surface is evident in Fig. 5.44(*c*) and made it impossible to identify the exact

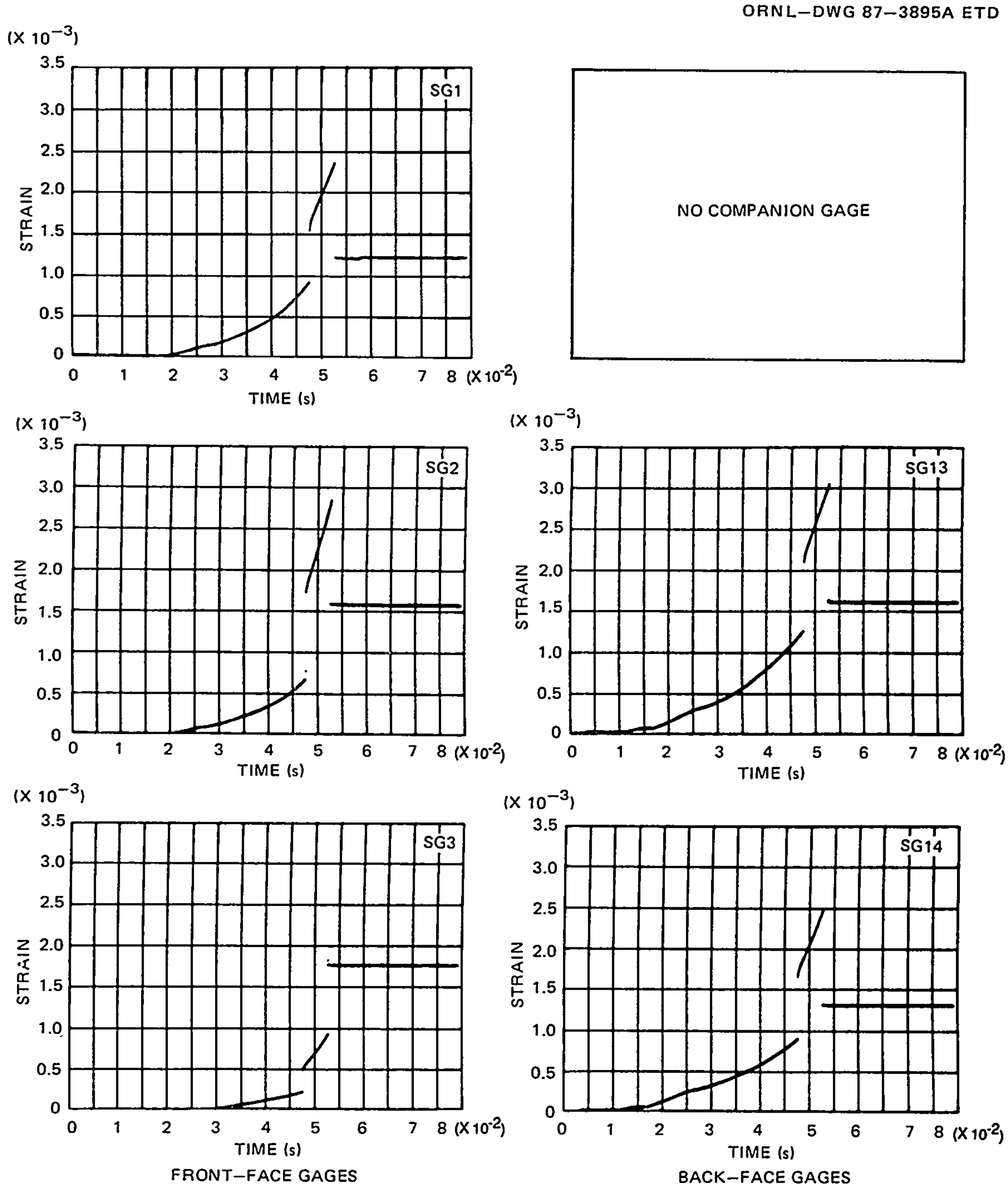

Fig. 5.38. Pop-in as detected by strain gages 1–3 on plate front face and 13 and 14 on plate back face: test WP-2.5.

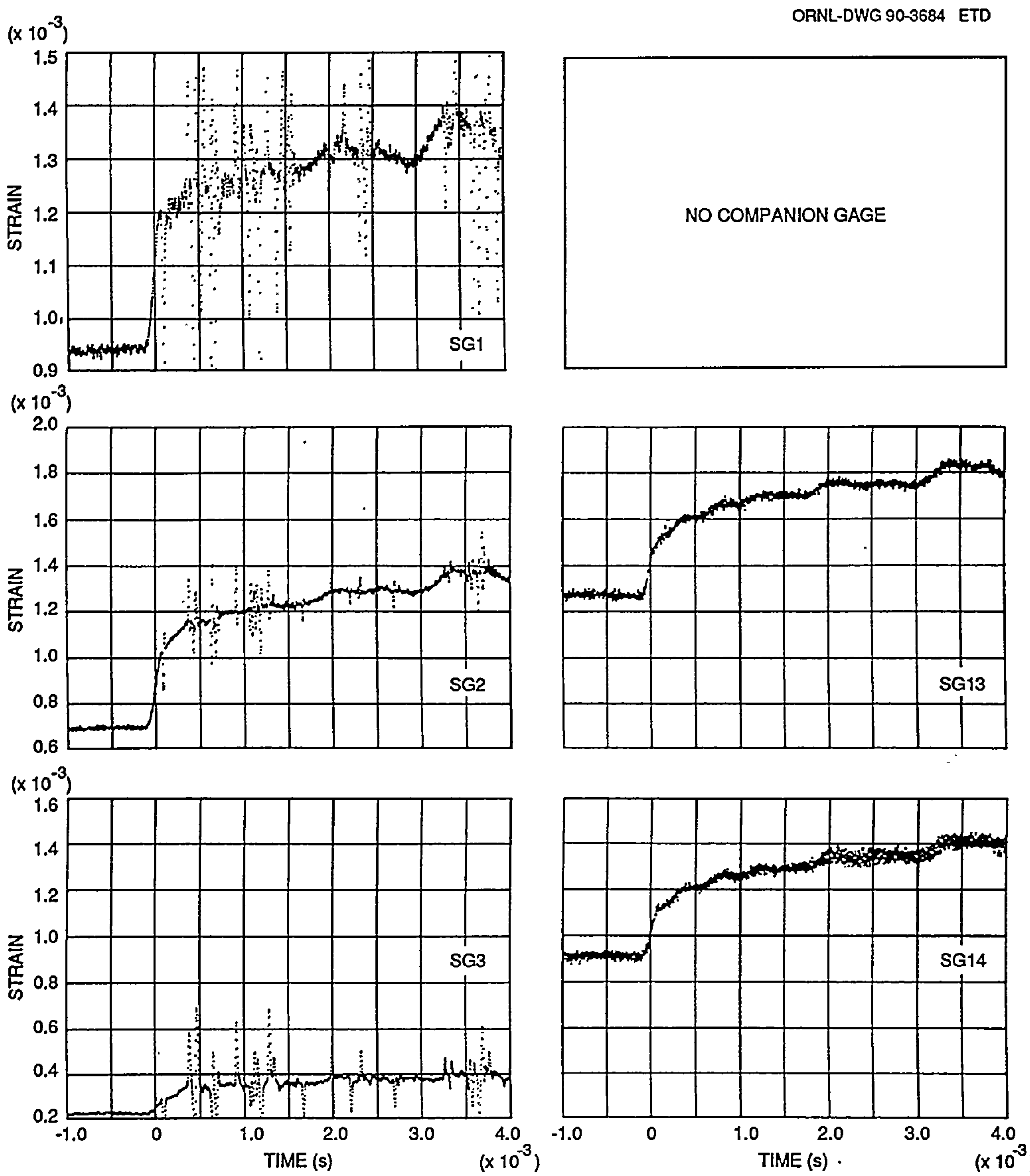

Fig. 5.39. High-resolution strain-gage records for companion crack-line gages during pop-in event: test WP-2.5.

ORNL-DWG 90-3685 ETD

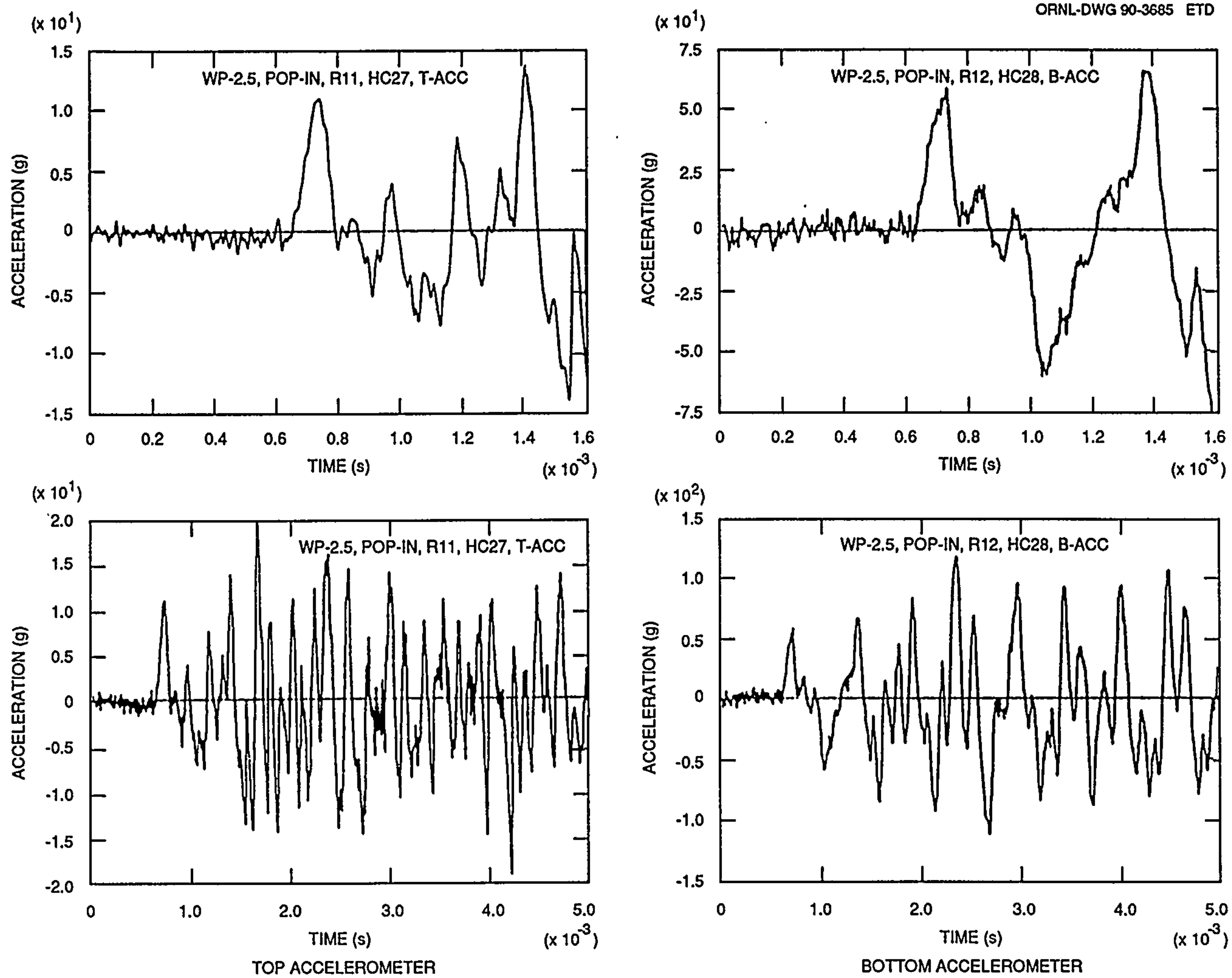

Fig. 5.40. High-resolution accelerometer records during the pop-in event: test WP-2.5.

Table 5.6. Crack position vs time and velocity: test WP-2.5

Indicator[a]	Position (mm)	Time (ms)	Velocity[b] (m/s)
Front-face measurements			
Pop-in (Arrest A)	250	0	
			133
SG1	254	0.03	
			1250
SG2	279	0.05	
			71
Arrest B	300	0.344	
Reinitiation	300	7.87	
			1900
SG3	319	7.88	
			116
Arrest C	385	8.45	
Reinitiation	385	11.33	
			140
SG5	399	11.43	
			7
Arrest D	400	11.58	
Reinitiation	400	18.39	
			51
SG6	439	19.15	
			69
Arrest E	450	19.31	
Reinitiation	450	27.79	
			183
Arrest F	523	28.19	
Reinitiation	523	33.11	
			18
SG9	569	35.67	
			6
SG10	619	43.89	
			13
SG11	669	47.85	
			9
Remaining ligament	990.5	84	
Back-face measurements			
Pop-in (Arrest A)	272	0	
SG13	276	0	
			614
SG14	319	0.07	
			66

Table 5.6 (continued)

Indicator[a]	Position (mm)	Time (ms)	Velocity[b] (m/s)
Back-face measurements (continued)			
Arrest B	350	0.54	
Reinitiation	350	7.90	
			450
SG15	359	7.92	
			800
SG16	399	7.97	
			189
Arrest C	435	8.16	
Reinitiation	435	11.16	
			80
SG17	439	11.21	
			139
Arrest D	478	11.49	
Reinitiation	478	19.11	
			10
SG18	479	19.21	
			168
Arrest E	516	19.43	
Reinitiation	516	27.63	
			21
SG19	519	27.77	
			228
Arrest F	560	27.95	
Reinitiation	560	29.01	
			10
SG20	569	29.93	
			5
SG21	619	40.29	
			7
SG22	669	47.81	
			9
Remaining ligament	990.5	84	

[a]These strain-gage positions have been modified because the peak strain occurs at an angle of 72° in front of the crack tip. Also, the crack lengths listed are averages of the quarter-thickness crack lengths and the crack lengths at the side groove.

[b]Velocity is an average calculated velocity for crack propagation.

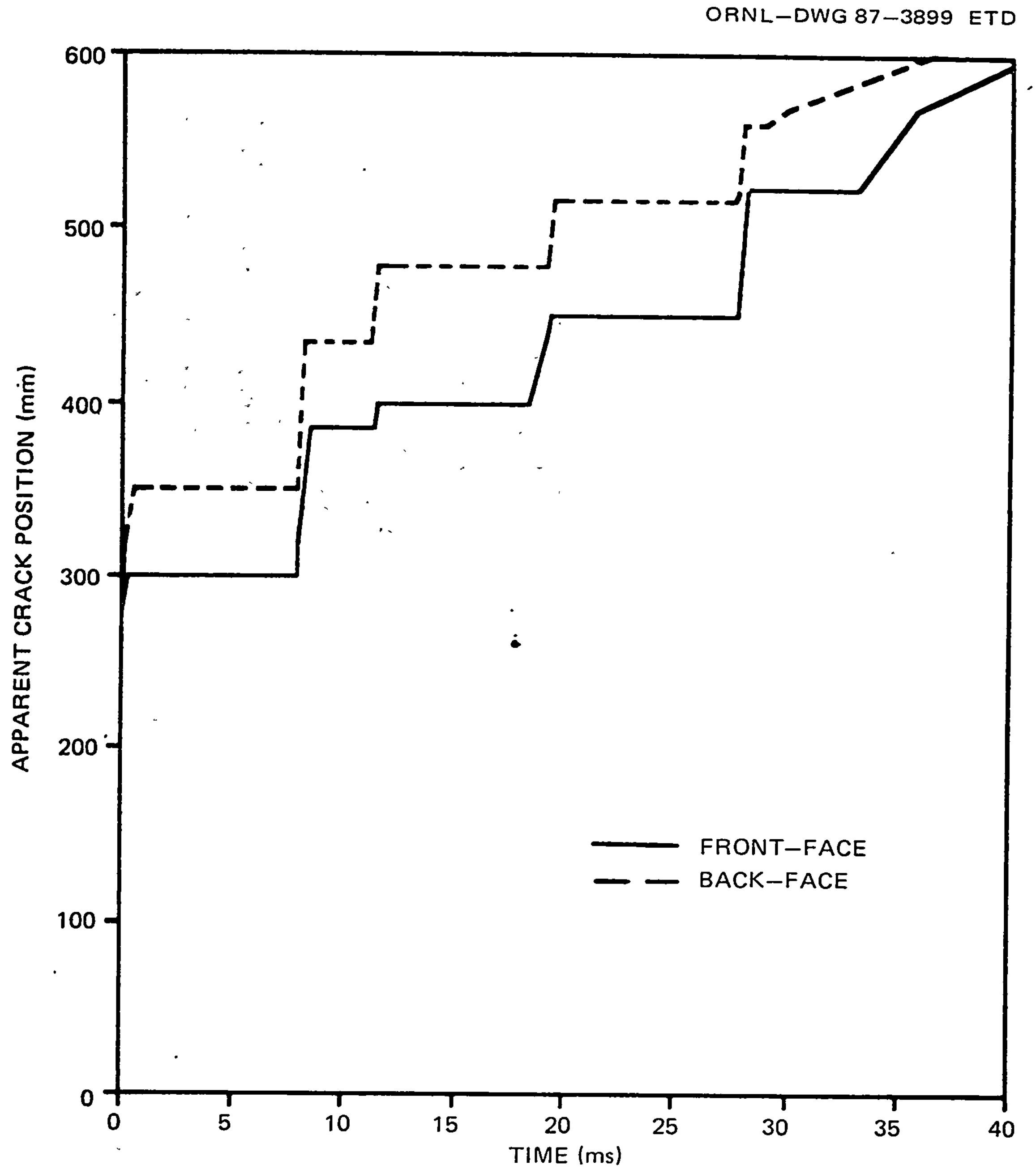

Fig. 5.41. Strain-gage-derived crack-front position vs time: test WP-2.5.

Y-12 PHOTO YP-8696

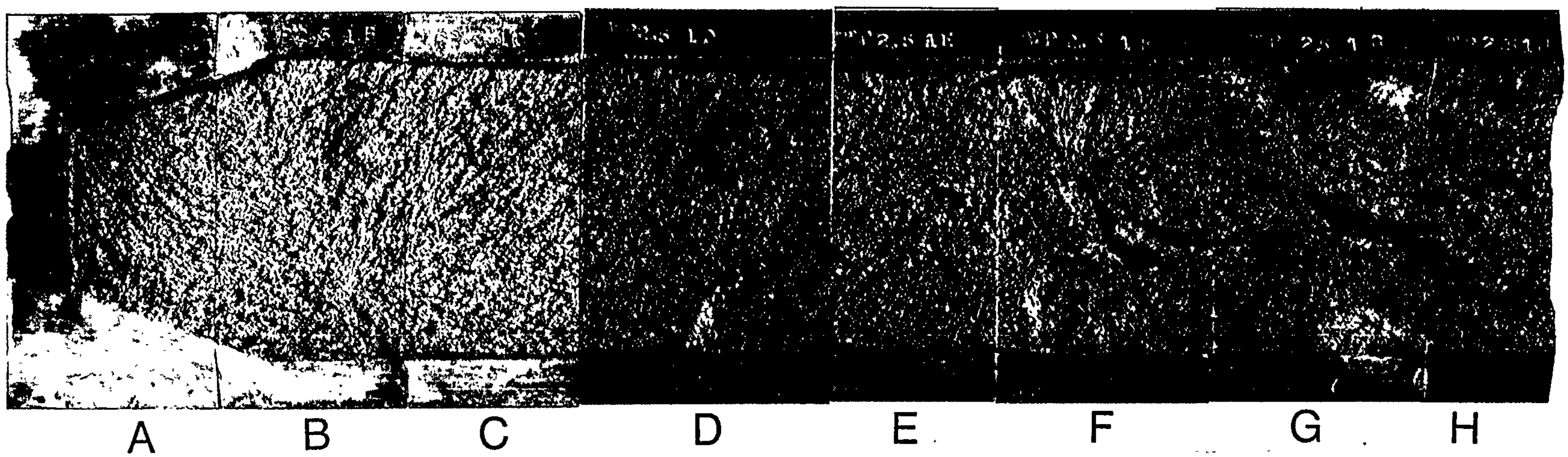

Fig. 5.42. Fracture surface of specimen WP-2.5, showing how the fracture surface was sectioned for further examination.

ORNL PHOTO 2241-90

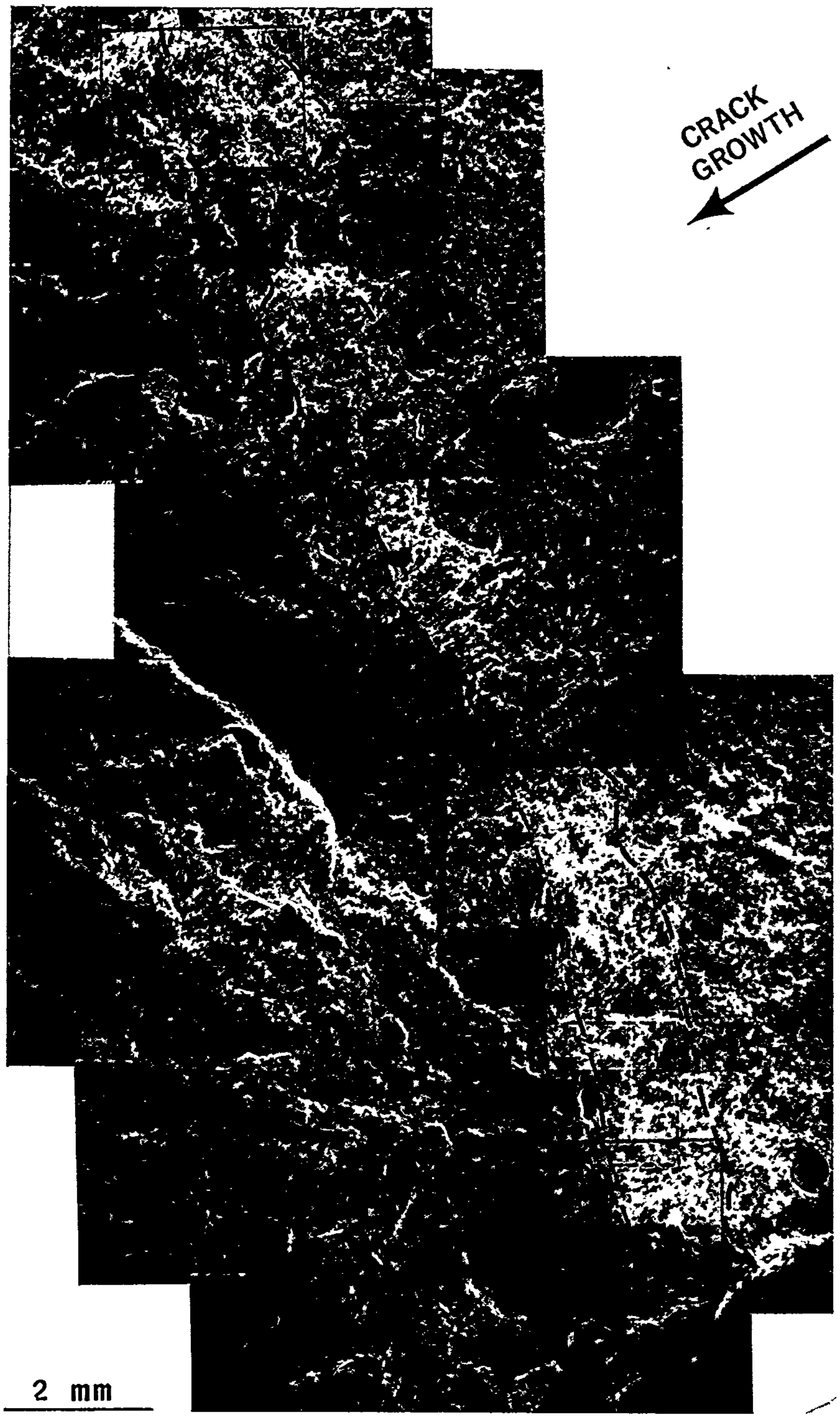

Fig. 5.43. Precrack and initial tearing from specimen WP-2.5, Sect. A (Fig. 5.42). The tearing strip from the initial loading is marked. The EB weld is to the right and the first crack run-arrest event to the left.

ORNL PHOTO 2242-90

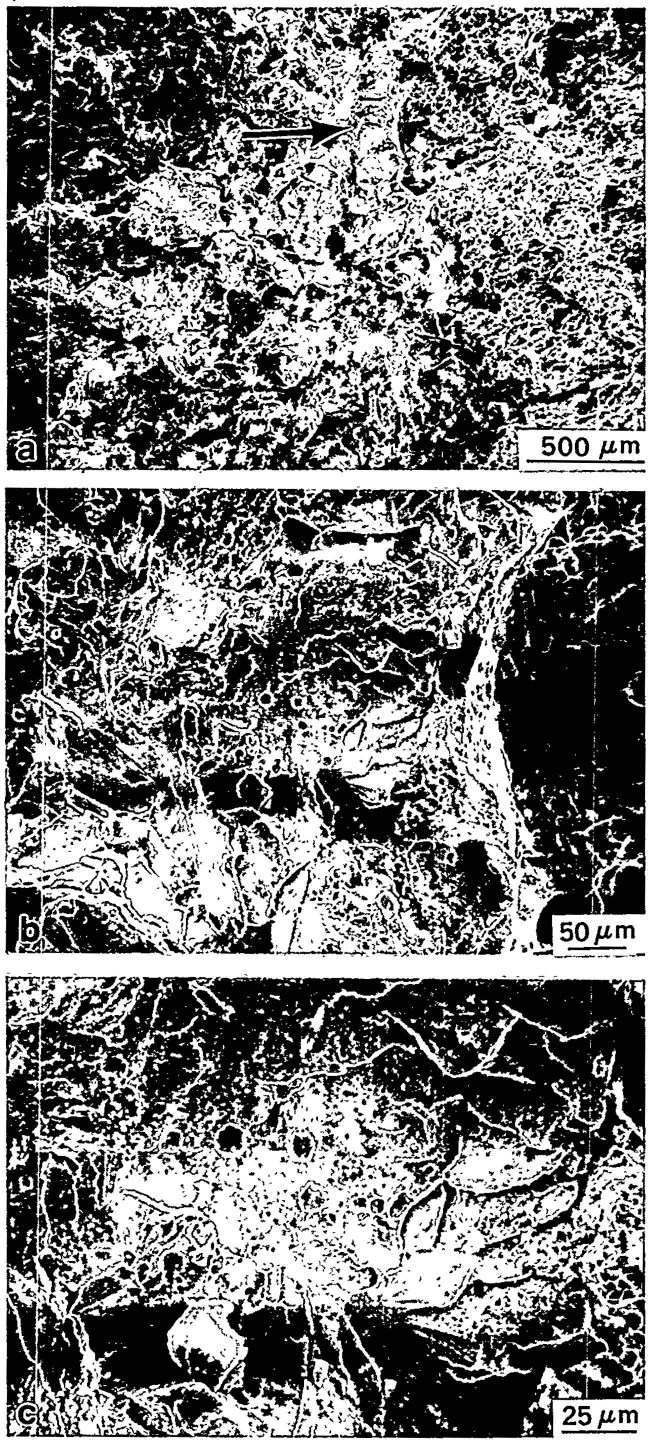

Fig. 5.44. View of apparent initiation site for first crack run-arrest event, Sect. A (Fig. 5.42). (*a*) View of ductile tearing zone and cleavage fracture from dashed box in Fig. 5.43 with apparent initiation site indicated by arrow, (*b*) detail of apparent initiation site, and (*c*) detail of (*b*).

feature associated with the initiation event. Section B of Fig. 5.42 contains the first arrest front and the second crack run-arrest event. The arrest front is marked by a band of ductile tearing, ~1500 μm wide and is shown in Fig. 5.45. The ductile tearing from a region in the center of the specimen, as indicated by a box in Fig. 5.45, is shown in greater detail in Fig. 5.46. The initiation site for the next crack run-arrest event could not be identified because of the damage noted earlier to the fracture surface.

5.6 TEST WP-2.6

Specimen WP-2.6 was the second specimen in WP-2 series to not have its crack front cut into a truncated chevron configuration. It was also the second WPS specimen in this series. The warm prestressing procedure consisted of slowly loading the specimen to 15.56 MN while maintaining the crack tip temperature at 110°C (Fig. 5.47), holding the load constant at this value for 5 min, and slowly reducing the load to 3.25 MN. The load history and load vs front- and back-face COD results during warm prestressing are shown in Fig. 5.48. While maintaining the load at 3.25 MN, the thermal gradient was developed.

After obtaining a satisfactory temperature profile (Fig. 5.49), the specimen was loaded at an average rate of 9.6 kN/s. At a load of 19.33 MN, cleavage crack propagation initiated, and within an ~10.5-ms interval seven crack run-arrest events occurred. After the seventh crack run-arrest event, tearing fracture reinitiated with complete separation of the plate occurring ~34.5 ms after first initiation of cleavage crack propagation. Figure 5.50 presents the load history for test WP-2.6.

Figure 5.51 shows the fracture surface of specimen WP-2.6. As noted in Fig. 5.52, which presents a close-up of the region where the crack run-arrest events occurred, there were numerous crack run-arrest events during this test. As the crack propagated, it deviated from the plane of the side grooves, reaching ~10 mm above the plane at the furthest extent of cleavage crack propagation. Reduction-in-thickness contours surrounding the crack plane are shown in Fig. 5.53.

The strain-gage records (Appendix A) and fracture surface were used to deduce the crack length (apparent position of the crack front) during the fracture process, and the results are summarized in Table 5.7. In the table, the strain-gage positions have been modified from those shown in Fig. 4.8(*e*) to account for the fact that the peak strain occurs at an angle of 72° in front of the crack tip. Figure 5.54 is a plot of strain-gage-derived crack-front position vs time from the front-face and back-face strain gage results during the entire fracture process.

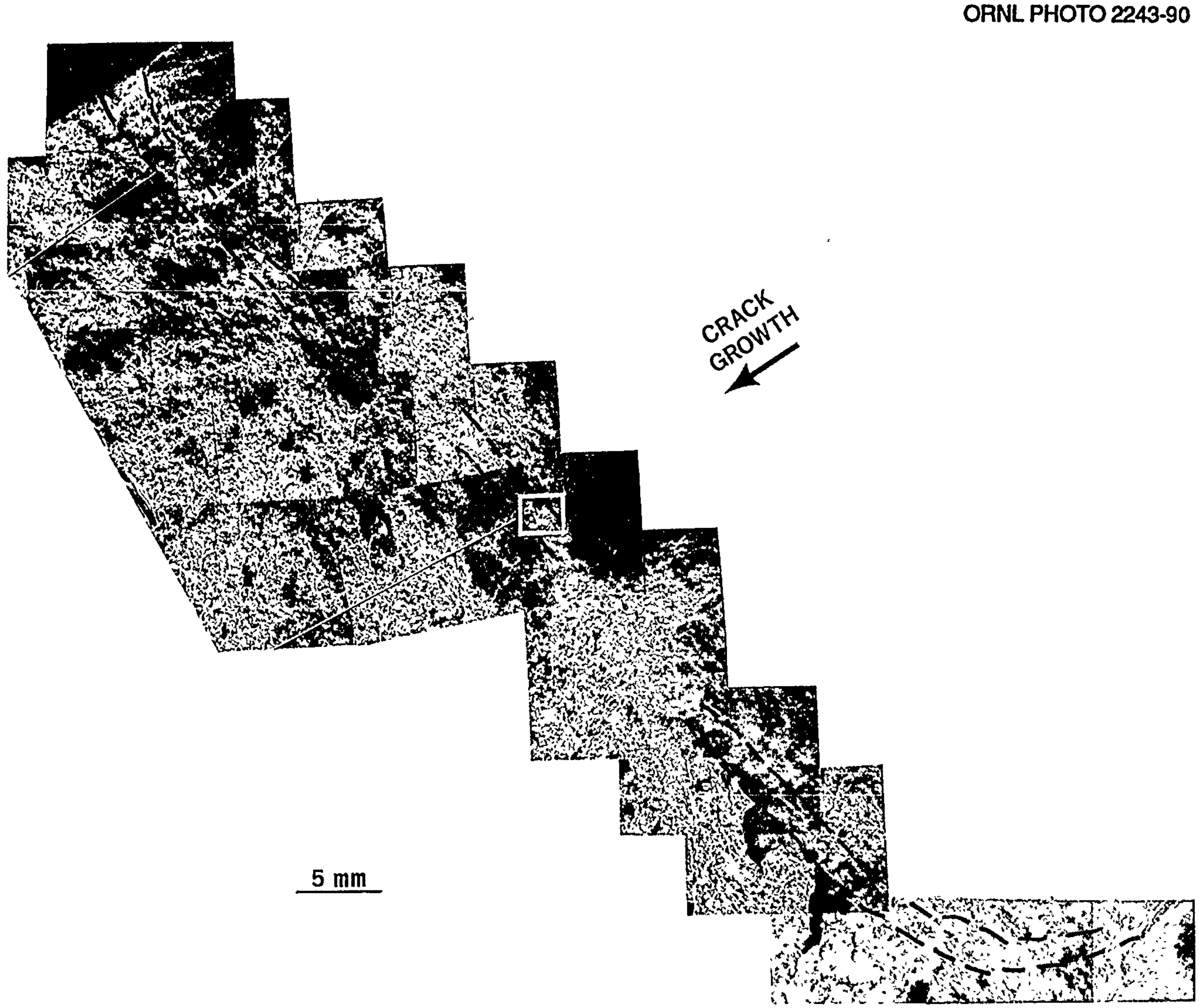

Fig. 5.45. First arrest location from Sect. B (Fig. 5.42). The tearing strip is shown by the dashed lines.

ORNL PHOTO 2244-90

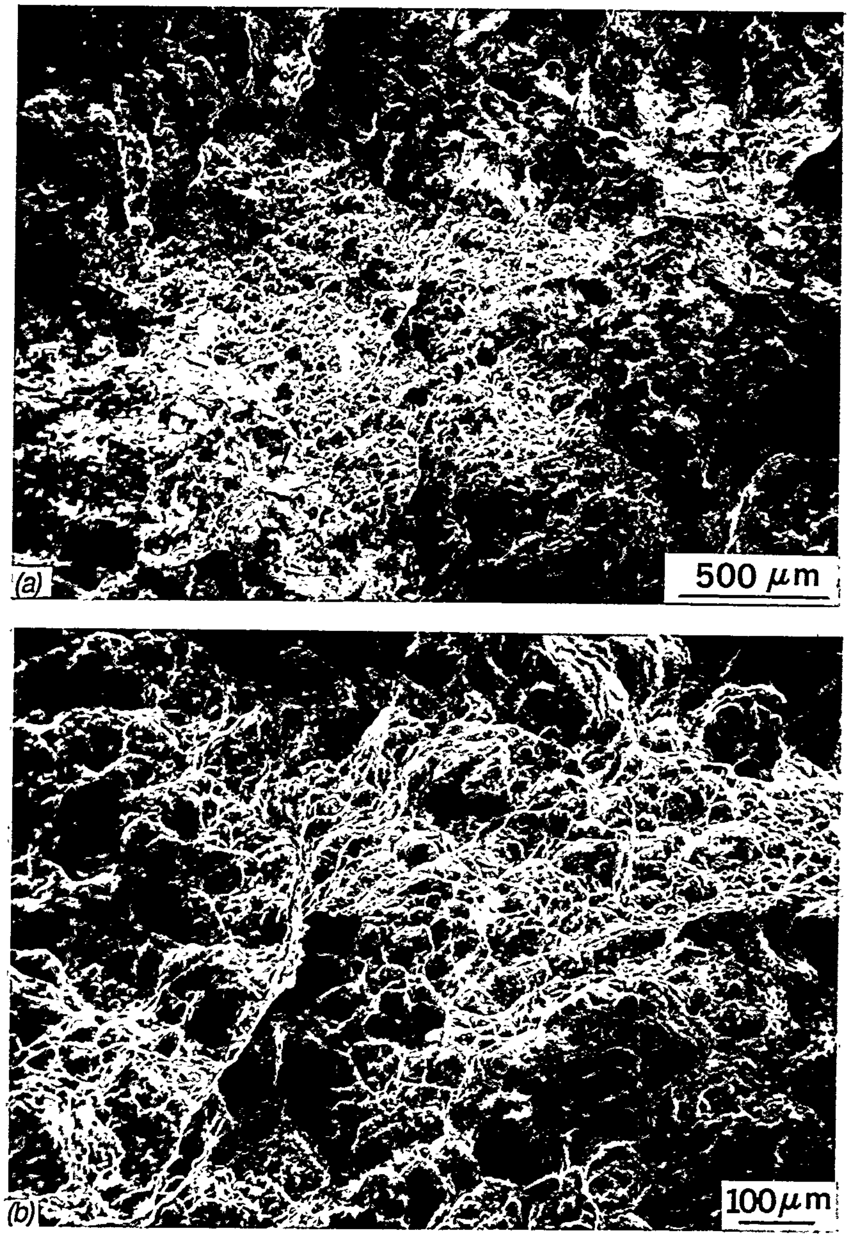

Fig. 5.46. Ductile tearing strip from Sect. B (Fig. 5.42) after first crack run-arrest event. (*a*) Detail of ductile tearing from box shown in center of Fig. 5.45, and (*b*) detail of ductile tearing.

ORNL-DWG 89-5025 ETD

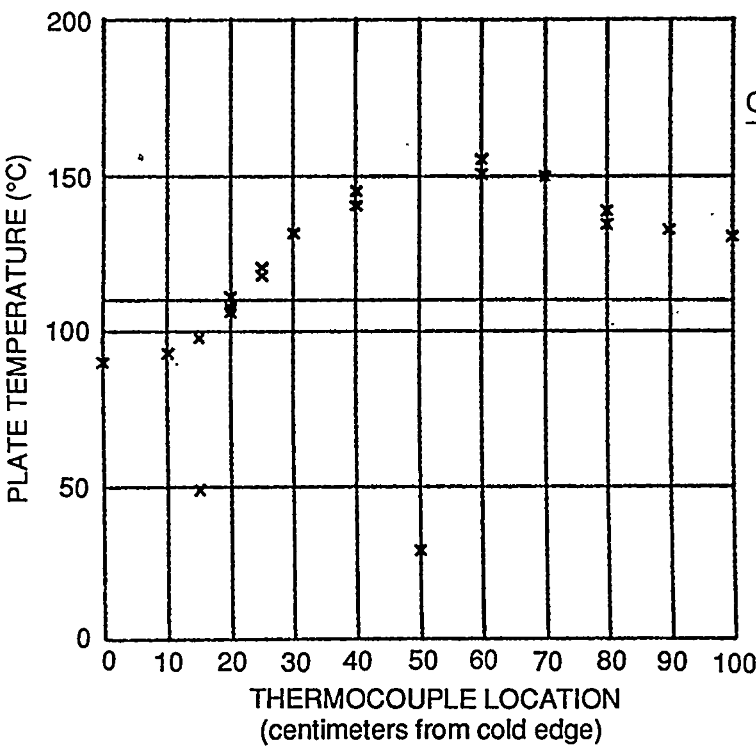

	TEMPERATURE (°C)	
CENTIMETERS	REAL	IDEAL
0	90	110
10	93	110
15	98	110
15	49	110
20	106	110
20	111	110
20	108	110
25	120	110
25	118	110
30	132	110
40	145	110
40	140	110
50	29	110
60	155	110
60	151	110
70	150	110
80	135	110
80	139	110
90	133	110
100	131	110

Fig. 5.47. Actual and ideal temperature distribution across specimen width during warm prestressing: test WP-2.6.

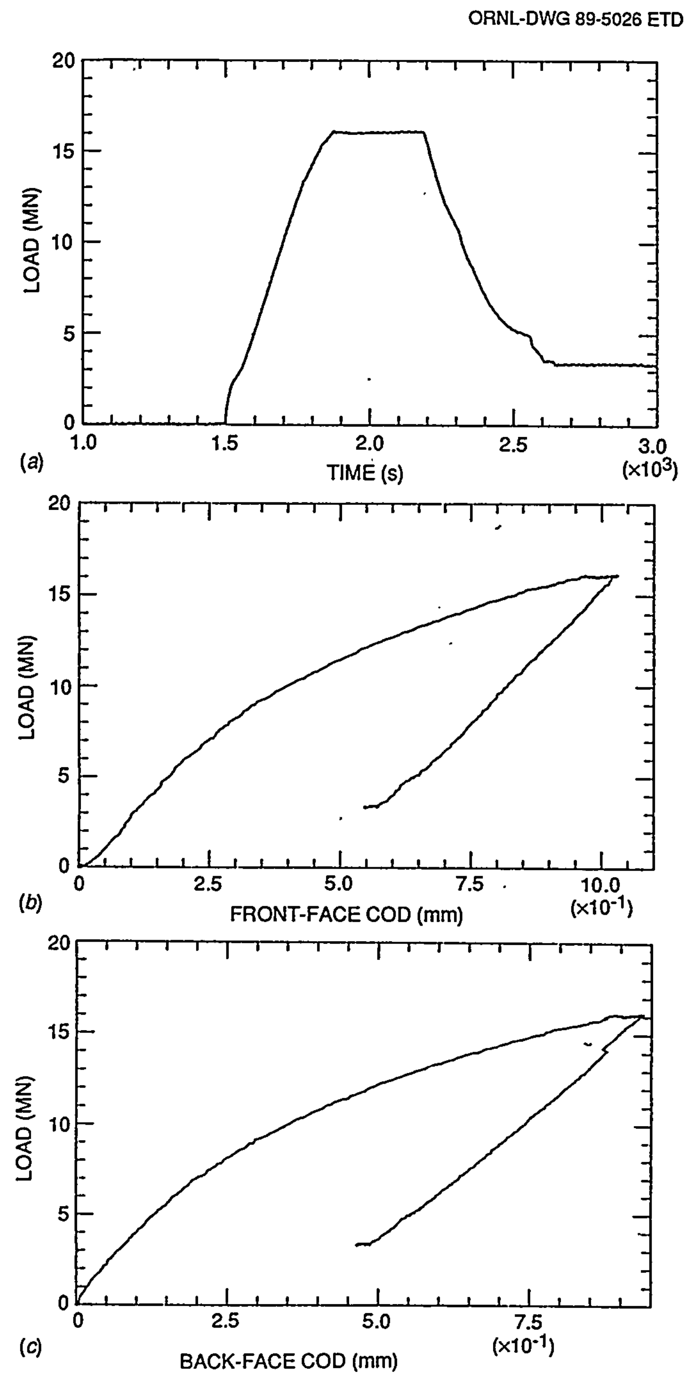

Fig. 5.48. Load vs (a) time, (b) front-face COD, and (c) back-face COD during warm prestressing: test WP-2.6.

ORNL-DWG 89-5027 ETD

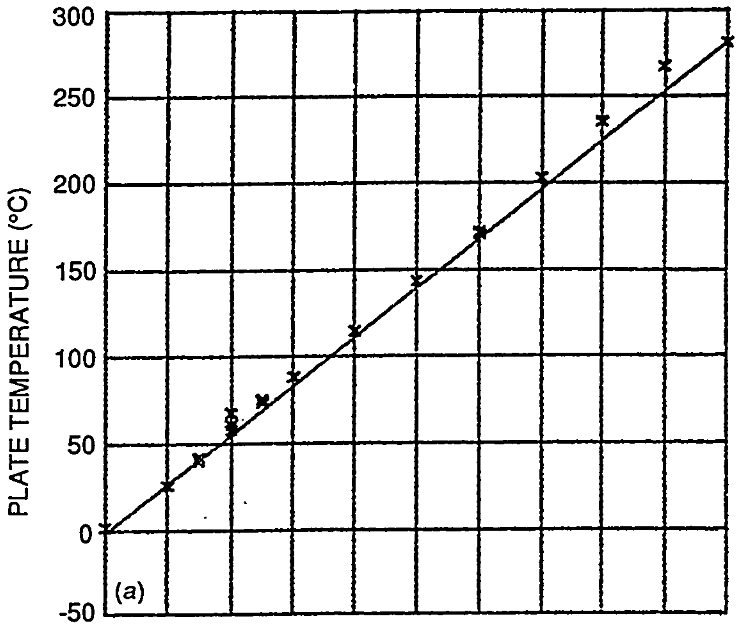

CENTIMETERS	TEMPERATURE (°C) REAL	IDEAL
0	2	-2
10	26	26
15	42	40
15	40	40
20	61	54
20	67	54
20	57	54
25	75	69
25	73	69
30	88	83
40	114	111
40	115	111
50	143	139
60	172	168
60	171	168
70	203	196
80	235	225
80	236	225
90	267	253
100	282	281

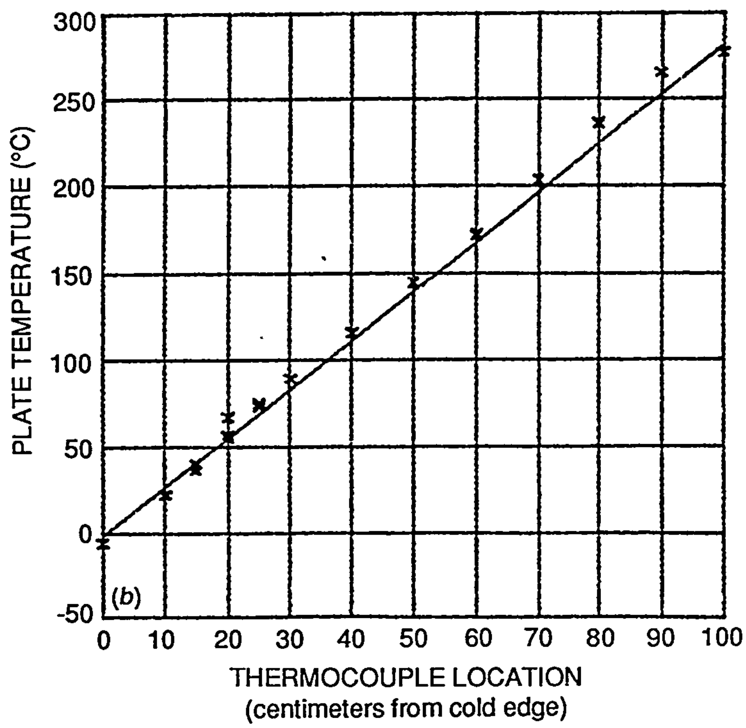

CENTIMETERS	TEMPERATURE (°C) REAL	IDEAL
0	-6	-2
10	22	26
15	40	40
15	37	40
20	57	54
20	67	54
20	55	54
25	75	69
25	73	69
30	89	83
40	116	111
40	116	111
50	145	139
60	172	168
60	172	168
70	204	196
80	236	225
80	236	225
90	265	253
100	277	281

Fig. 5.49. Actual and ideal temperature distributions across specimen width (*a*) at start of loading and (*b*) just before initiation of cleavage crack run-arrest events: test WP-2.6.

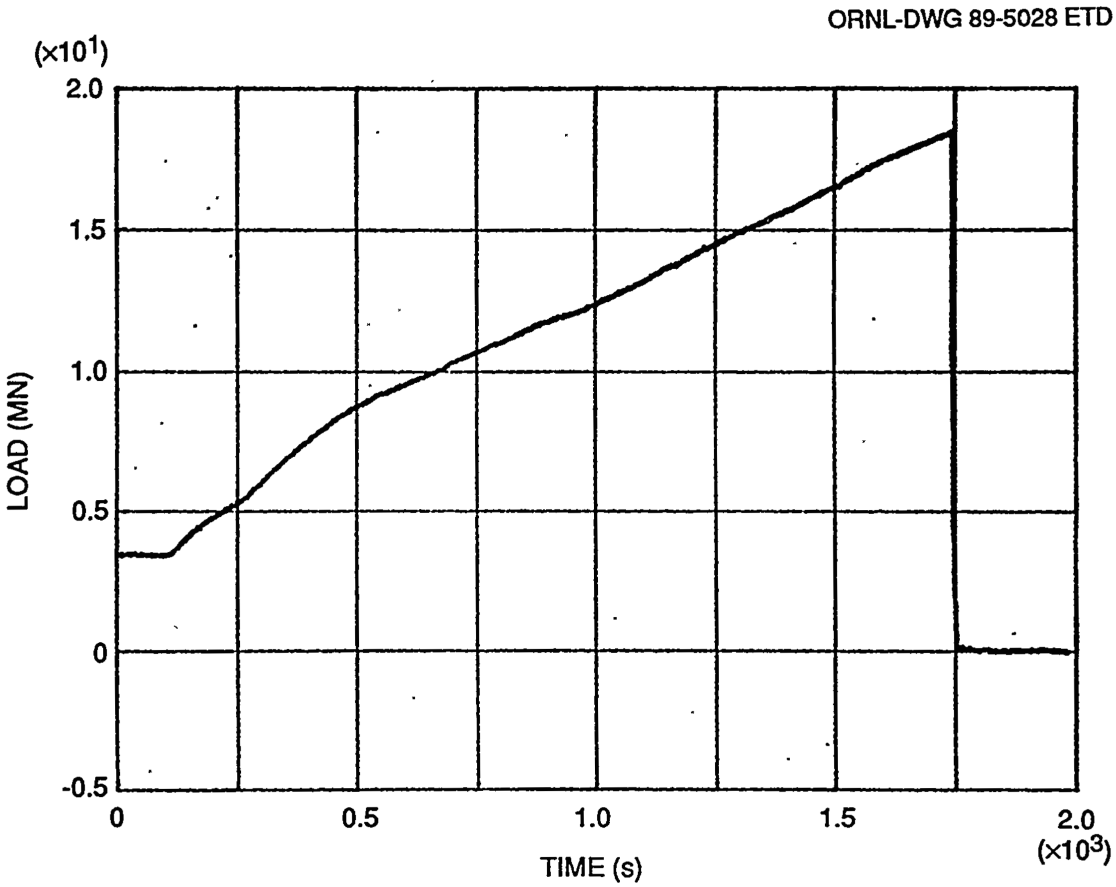

Fig. 5.50. Load history for test WP-2.6.

ORNL PHOTO 7005-89R

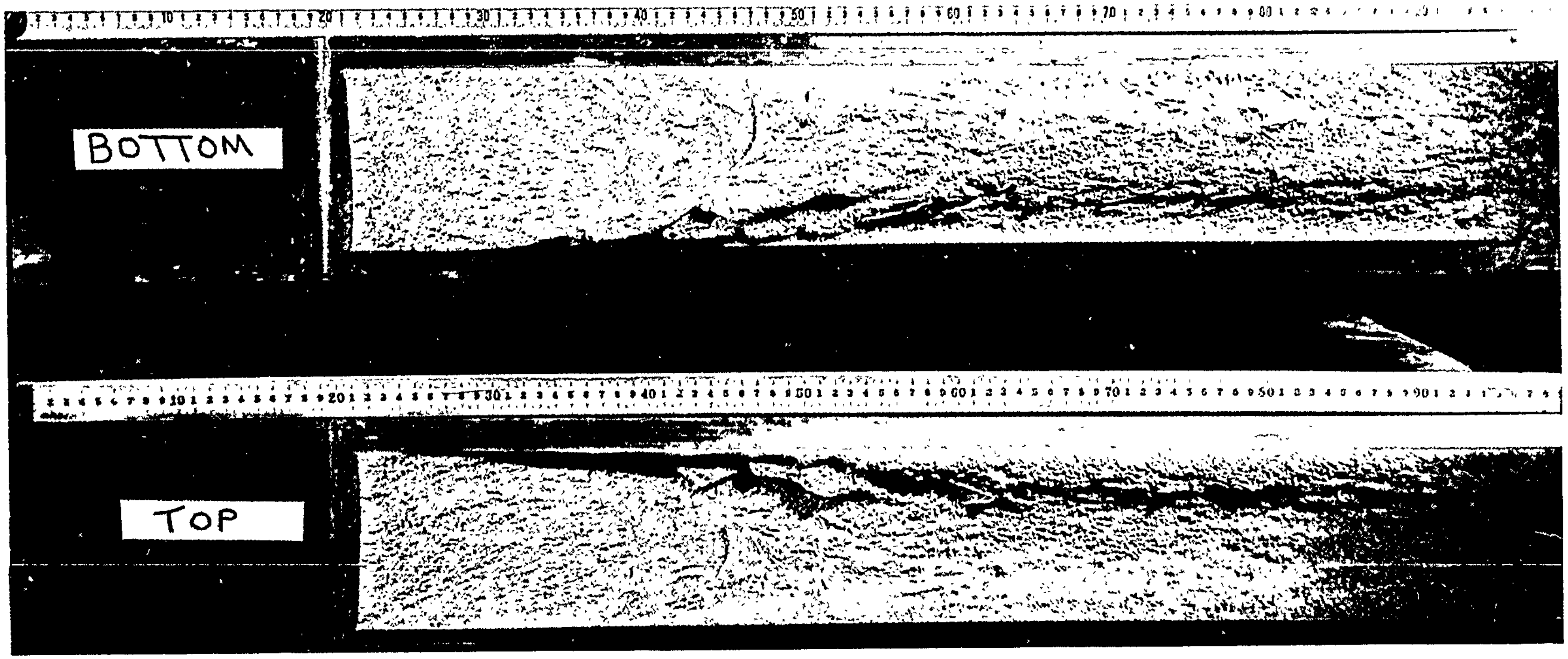

Fig. 5.51. Fracture surfaces of bottom and top plate halves of specimen WP-2.6.

ORNL PHOTO 7006-89R

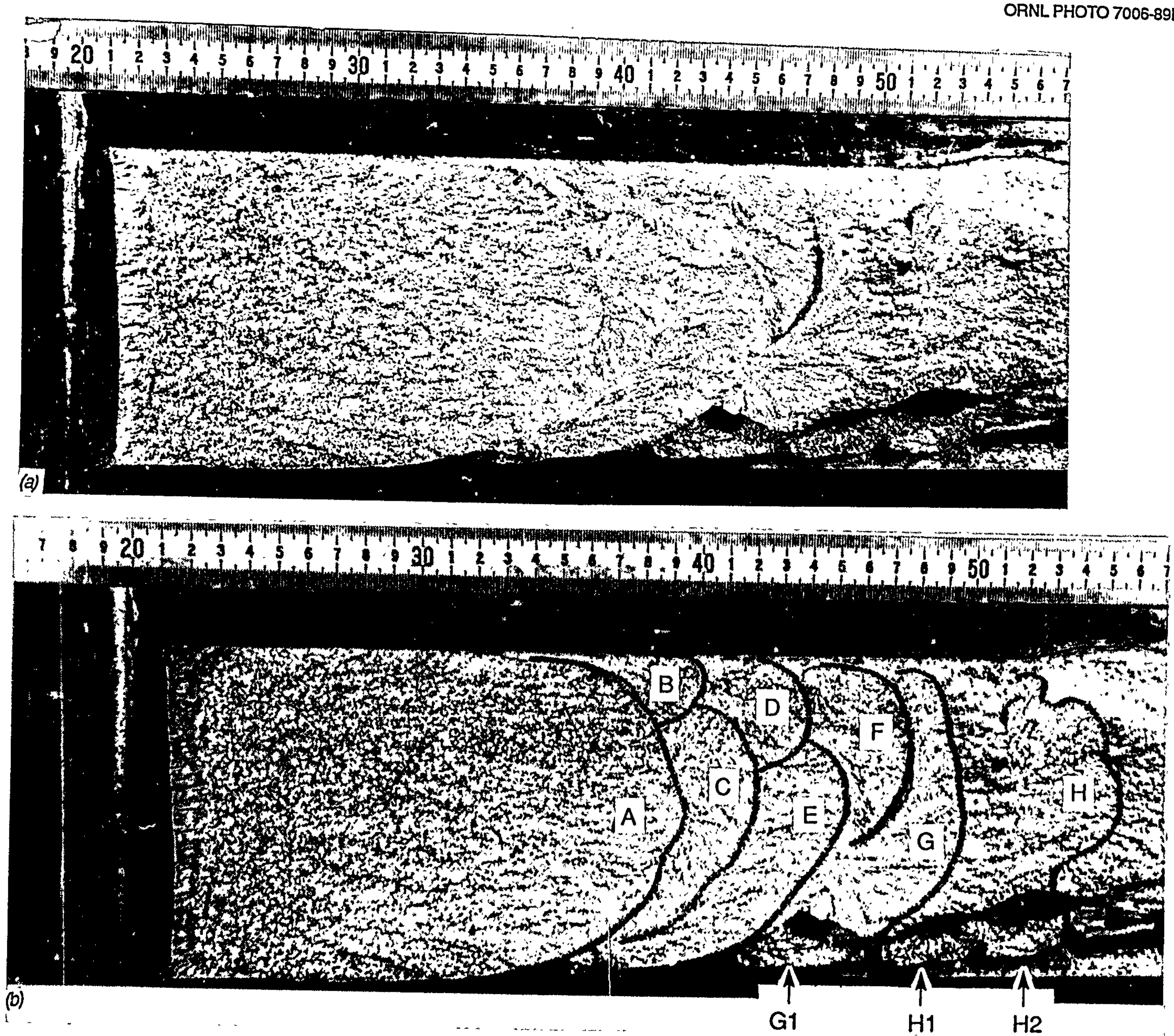

Fig. 5.52. Close-up of cleavage and loss-of-cleavage regions (*a*) without and (*b*) with arrest locations highlighted: test WP-2.6.

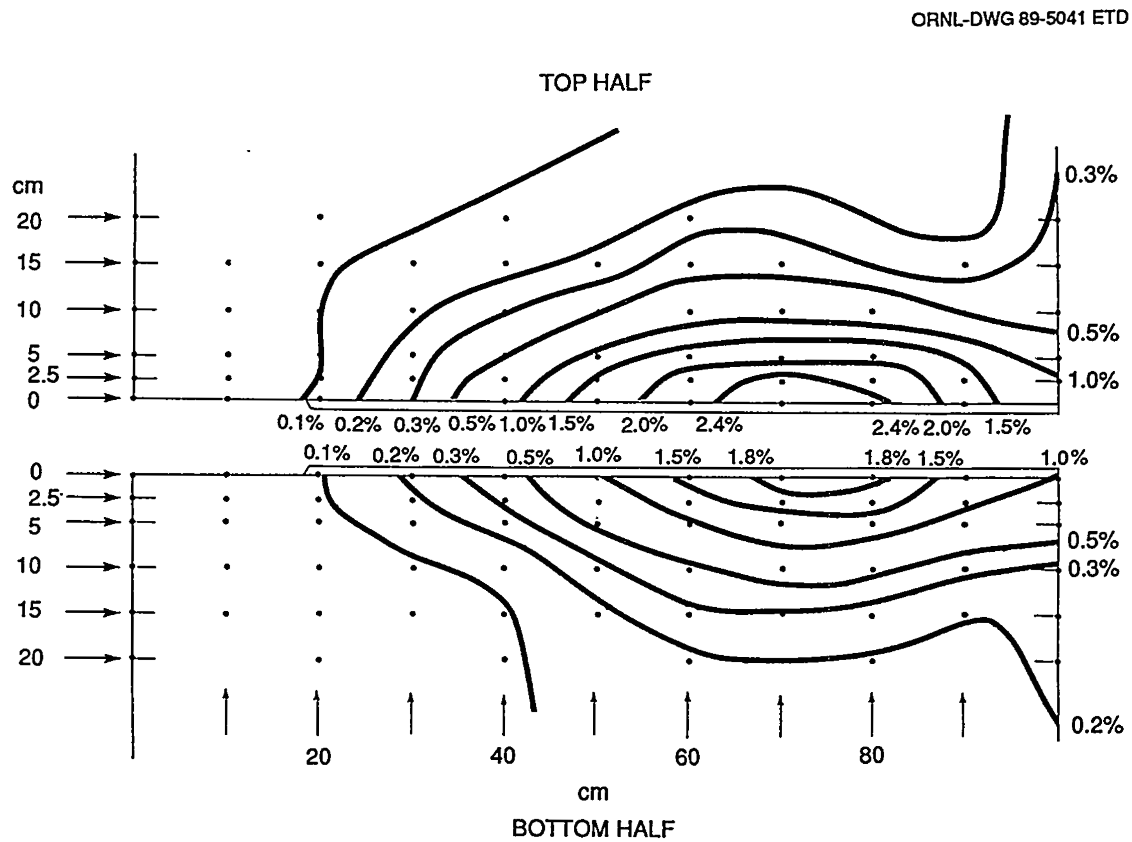

Fig. 5.53. Reduction-in-thickness contour map of specimen WP-2.6.

Table 5.7. Crack position vs time and velocity: test WP-2.6

Indicator[a]	Position (mm)	Time (ms)	Velocity[b] (m/s)
Front-face measurements			
SG1	218	0	
Initial crack[c]	225	0	
			971
SG2	258	0.034	
			625
SG3	298	0.098	
			435
SG4	338	0.190	
			232
Arrest A	357	0.272	
Reinitiation A	357	1.000	
			467
SG5	378	1.045	
			317
Arrest B	397	1.105	
Reinitiation B	397	1.405	
			108
Arrest C	410	1.525	
Reinitiation C	410	1.945	
			27
SG6	418	2.237	
			145
Arrest D	430	2.320	
Reinitiation D	430	3.255	
			49
SG7	458	3.830	
			8
Arrest F	460	4.090	
Reinitiation F	460	7.165	
			73
Arrest G	480	7.440	
Reinitiation G	480	10.380	
			1064

Table 5.7 (continued)

Indicator[a]	Position (mm)	Time (ms)	Velocity[b] (m/s)
Front-face measurements (continued)			
SG8	530	10.427	
			108
Arrest H	540	10.520	
Reinitiation H	540	12.910	
			20
SG9	580	14.900	
			114
SG10	630	15.340	
			22
SG11	730	19.790	
			20
SG12	830	24.760	
			18
End of plate	1000	34.470	
Back-face measurements			
SG13	218	0	
Initial crack[c]	223	0	
			921
SG14	258	0.038	
			952
SG15	298	0.080	
			299
SG16	338	0.214	
			465
SG17	378	0.300	
			333
Arrest A	380	0.306	
Reinitiation A	380	1.396	
			74
Arrest C	390	1.532	
Reinitiation C	390	1.854	
			103
SG18	418	2.126	
			175

Table 5.7 (continued)

Indicator[a]	Position (mm)	Time (ms)	Velocity[b] (m/s)
Back-face measurements (continued)			
Arrest E	425	2.166	
Reinitiation E	425	3.152	
			198
Arrest G1	480	3.430	
Reinitiation G1	480	7.160	
			71
SG19	490	7.300	
			167
Arrest H1	520	7.480	
Reinitiation H1 (ductile)	520	7.480	
			6
SG20 (ductile tearing past)	530	9.190	
			5
Reinitiation H1 (cleavage)	535	10.250	
			20
Arrest H2	540	10.500	
Reinitiation H2 (ductile)	540	10.500	
			19
End of plate	1000	34.47	

[a]These strain-gage positions are all reduced by 32 mm from the actual gage position shown in Fig. 4.8(*e*) because the peak strain occurs at an angle of 72° in front of the crack tip. Also note that back-face gages 13–20 have been rotated 45° relative to companion front-face gages.

[b]Velocity is an average calculated velocity for crack propagation between indicator points.

[c]During warm prestressing the crack grew past initial crack-line gages on plate front and back faces.

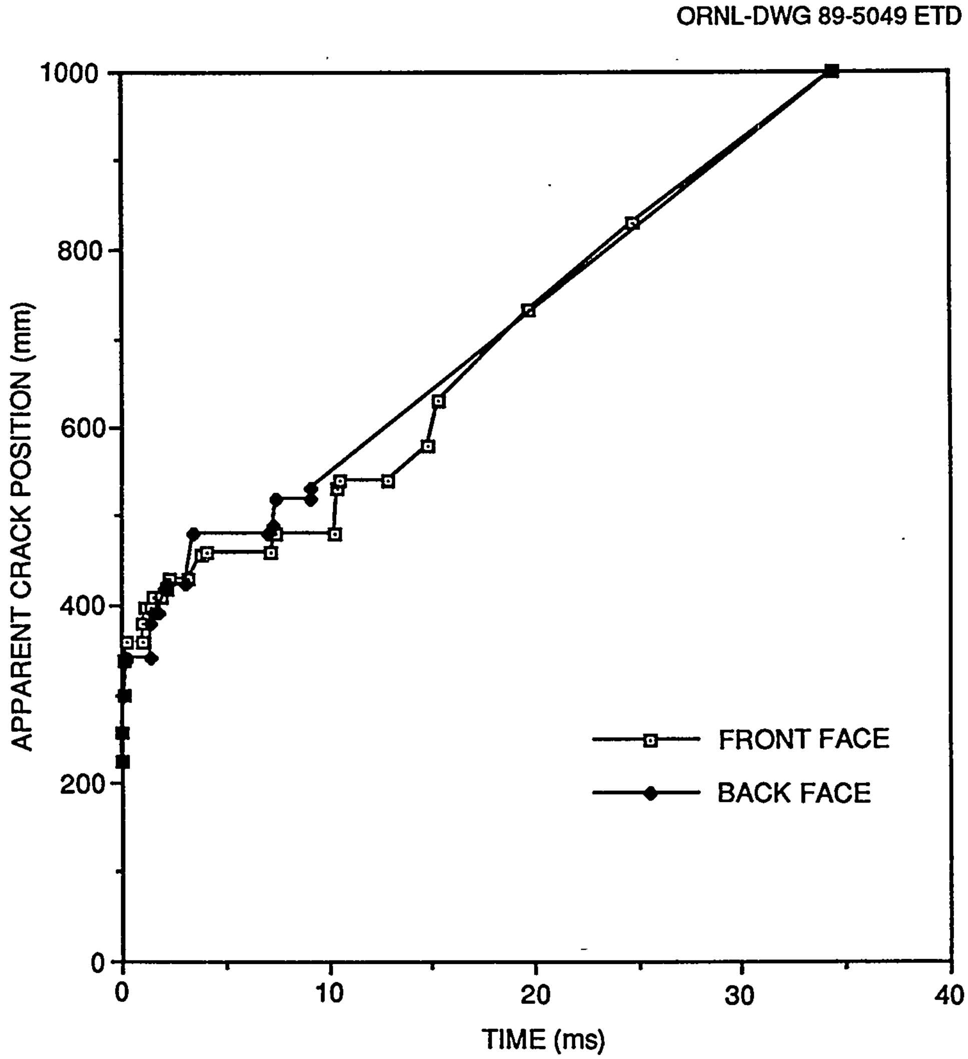

Fig. 5.54. Strain-gage-derived crack-front position vs time: test WP-2.6.

REFERENCE

1. D. J. Naus et al., Martin Marietta Energy Systems, Inc., Oak Ridge Natl. Lab., *Crack-Arrest Behavior in SEN Wide Plates of Quenched and Tempered A 533 Grade B Steel Tested Under Nonisothermal Conditions*, USNRC Report NUREG/CR-4930 (ORNL-6388), August 1987.*

---

*Available for purchase from National Technical Information Service, Springfield, VA 22161.

6. POSTTEST ANALYSES, CRACK-ARREST TOUGHNESS RESULTS, AND COMPARISON OF DATA WITH OTHER LARGE-SCALE TEST RESULTS

6.1 POSTTEST ANALYSES

Posttest analyses were conducted for each of the wide-plate, crack-arrest tests in the WP-2 series to investigate the interaction of parameters (plate geometry, material properties, temperature profile, and mechanical loading) that affect the crack run-arrest events. Three-dimensional (3-D), static, finite-element analyses were performed to determine the static stress-intensity factor at the time of crack initiation. These analyses were conducted using the ORMGEN/ORVIRT fracture analysis system[1,2] in conjunction with the ADINA-84 finite-element code.[3] Quasi-static analyses use the ORNL computer code WPSTAT[4] to evaluate static stress-intensity factors as a function of crack length and temperature differential across the plate. WPSTAT also categorizes arrested crack lengths in terms of three types of instability limits: reinitiation, tearing instability, and tensile instability.

Two-dimensional (2-D) elastodynamic analyses* were carried out using the ADINA/VPF dynamic crack analysis code[5] that is capable of performing both application- and generation-mode analyses. In the application-mode analysis, the crack tip is propagated incrementally when K_I, the dynamically computed stress-intensity factor, equals the specified dynamic fracture-toughness value K_{ID}, which depends on the crack velocity $\dot{a}$ and the temperature T [Eq. (3.6)]. In the generation-mode analysis, the crack tip is propagated incrementally according to a prescribed crack-position-vs-time relationship, and values of fracture toughness are determined from the dynamically computed K_I. For both modes of analysis, the dynamic stress-intensity factor is determined in each time step from the dynamic J-integral containing the appropriate inertial and thermal terms.

6.1.1 Posttest 3-D Static Analyses

The 3-D finite-element model used for the wide-plate analyses incorporated a segment of the plate assembly measured from the crack plane to the top of the load-pin hole† (Fig. 6.1). The crack-tip region

---

*The development and use of dynamic analysis methods was required to incorporate the significant dynamic effects exhibited by the wide-plate tests, that is, multiple crack-run-arrest events.

†The length of the segment modeled varied from test to test as a result of the cutting procedure used to remove a test article before welding the next test article to the pull plates. For wide-plate specimens WP-2.1 through -2.6 the segments modeled (dimension Y in Fig. 6.1) were 4.58, 4.38, 4.62, 5.00, 4.90, and 4.36 m, respectively.

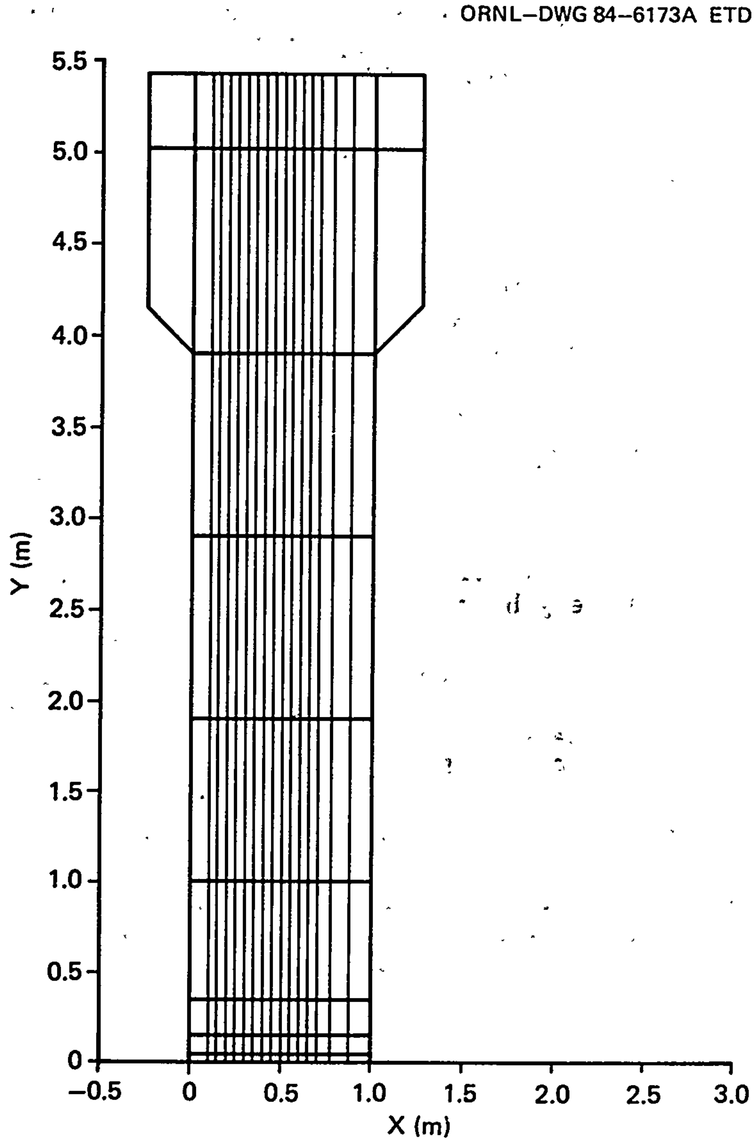

Fig. 6.1. Example of finite-element model used for dynamic analysis of wide-plate crack-arrest tests.

of the model included the chevron cutout (if present),* the side grooving, and the edge notch (Fig. 6.2). Table 4.1 and Figs. 4.1 and 4.3 present specimen dimensions. From symmetry conditions that neglected out-of-plane eccentricity, one-quarter of the partial pull-plate assembly was modeled using 3751 nodes and 720 20-noded isoparametric elements.

The thermal deformations computed from a posttest 2-D analysis were superimposed on a 3-D finite-element model to account for the in-plane

---

*Specimens WP-2.3 and -2.6 did not have their crack front cut into a truncated chevron configuration.

ORNL—DWG 85-5184 ETD

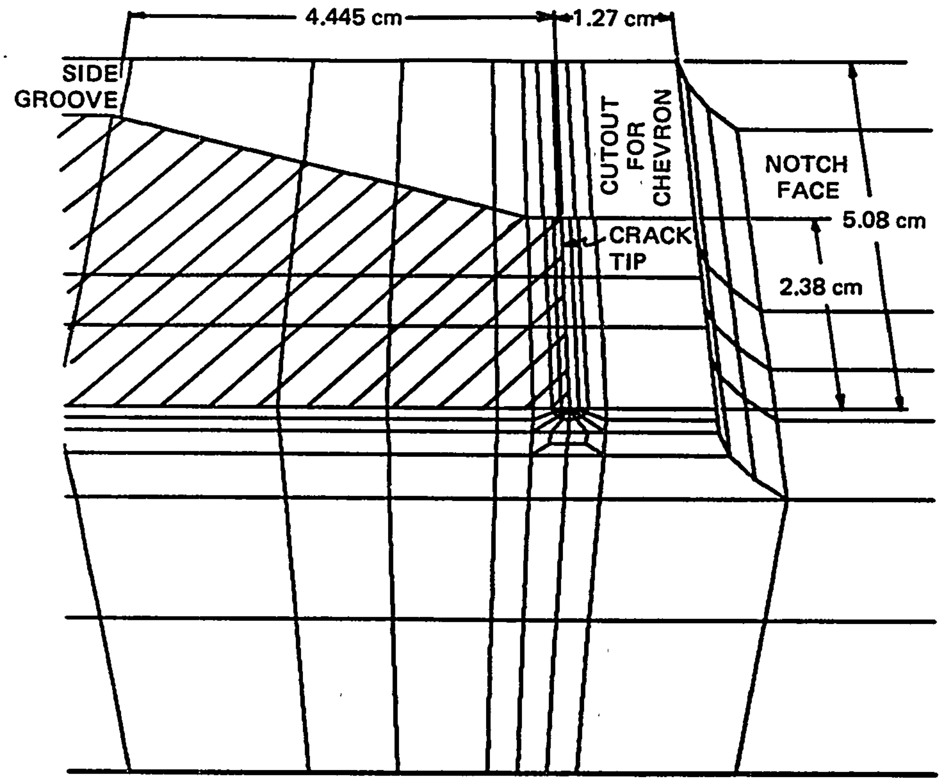

Fig. 6.2. Detail of crack-tip region from 3-D finite-element model of 102-mm-thick wide-plate specimen.

thermal bending effect in the 3-D analyses. The 2-D thermoelastic analysis used a temperature distribution from a heat-conduction analysis based on assumptions that the heated and cooled edges of the plate were fixed at T_{max} and T_{min}, respectively, along a 2.4-m length (centered relative to the crack plane) and that the pull-tab edges were maintained at T = 20.0°C.* The edge temperatures were selected to yield a temperature distribution in the crack plane ($0.2 \leq a/w \leq 0.6$) that agreed with the measured values presented in Chap. 5 for each specimen, for example, Fig. 5.20 for test WP-2.4. Computed load-line (through the top of the load-pin hole) eccentricities produced by the in-plane thermal bending in tests WP-2.1 through -2.6 were 2.01, 1.96, 1.74, 2.37, 1.97, and 2.02 cm, respectively, relative to the geometric center of the plates.

In the 3-D analysis a uniform line load, statically equivalent to the initiation load, was applied at the location corresponding to the top of the load-pin hole. The results of this analysis yielded a static stress-intensity factor (K_I) at the center of the plate. Values of K_I

---

*Values of T_{min} and T_{max} for wide-plate tests WP-2.1 through -2.6 were 0 and 274°C, −2 and 280°C, 19 and 253°C, −11 and 275°C, 17 and 263°C, and 0 and 290°C, respectively.

that were obtained for tests WP-2.1 through -2.6 were 126, 183, 136, 143, 141, and 174 MPa·$\sqrt{m}$, respectively. Comparison of these computed K_I values with the small-specimen static initiation values, K_{Jc}, evaluated from Eq. (3.5) using the appropriate specimen crack-tip temperature (Table 5.1) and a DW_{NDT} = 60°C, yields K_I/K_{Jc} ratios of 1.01, 1.4, 0.92, 1.07, 0.72, and 1.2, for tests WP-2.1 through -2.6, respectively.

6.1.2 Posttest 2-D Static and Dynamic Analyses

6.1.2.1 Static and Stability Analyses

Posttest quasistatic 2-D analyses for both crack arrest and crack stability were done using the ORNL computer code WPSTAT.[4] As described in Ref. 4, the WPSTAT code evaluates static stress-intensity factors as a function of crack length a and temperature differential $\Delta T = T_{max} - T_{min}$ across the plate. These factors are computed for fixed-force conditions K_I^F (a, ΔT) and for fixed load-pin displacement conditions K_I^{DSP} (a, ΔT) by superposing contributions from tension and bending finite-element and handbook solutions. Also, WPSTAT categorizes arrested crack lengths in terms of the three types of instability limits described below.

For the WP-2 series wide-plate tests the posttest WPSTAT calculations of the static factors K_I^F (a, ΔT) and K_I^{DSP} (a, ΔT) used the actual temperature profiles at the approximate time of initiation of the crack run-arrest events shown in Fig. 5.1. For these specified temperature profiles, the dependence of the arrested crack lengths and crack stabilities upon the applied initiation load F_{in} (Table 5.1) was investigated with WPSTAT, and the results are presented in Fig. 6.3 for test WP-2.4.* Figure 6.3 includes the statically calculated final crack length a_{fc} and the instability crack lengths for reinitiation a_{rein}, for tensile instability a_{I1}, and for tearing instability a_{I2}. The tensile instability calculation is based on the average stress in the remaining ligament equal to an ultimate stress σ_u = 500 MPa, which represents the lowest value for the temperature range of interest. For the tearing instability calculation, the material tearing resistance is assumed to be represented by a power-law J-resistance curve of the following form $J_R = C(\Delta a)^m$, where C = 0.1114, m = 0.3832, and the units of J_R and Δa are kJ/m² and mm, respectively. In Fig. 6.3, the statically computed arrest length corresponding to the measured initiation load F_{in} = 8.85 MN is a_{fc} = 0.432 m. This computed arrest point is between the tensile instability curve a_{I1} and the tearing instability curve a_{I2}, implying an unstable condition. The measured initial arrest point a_{fm_1} = 0.338 m is below the tearing instability curve.

*Only the results for test WP-2.4 are presented in the remainder of this section. Posttest static and stability analyses for tests WP-2.1, -2.2, -2.3, -2.5, and -2.6 are contained in Refs. 6, 7, 8, 8, and 7, respectively.

ORNL-DWG 90M-3634 ETD

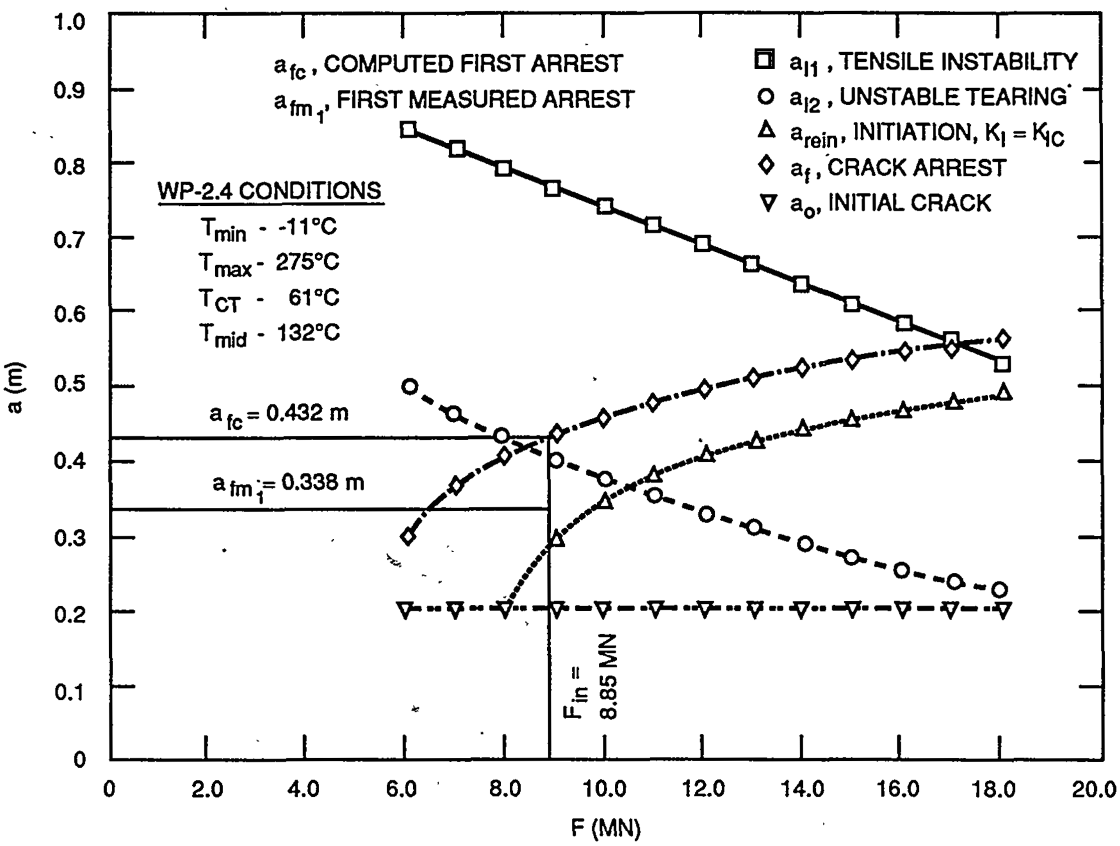

Fig. 6.3. Statically calculated crack lengths: test WP-2.4.

In Fig. 6.4, the K_{Ia} function presented in Eq. (3.2) is evaluated on the arrest crack-length curve a_f, on the incipient tearing-instability curve a_{I2}, and on the cleavage-reinitiation curve a_{rein}. The K_{Ic} function presented in Eq. (3.5) is evaluated on the curve $a_{rein}(F)$. Evaluation of the K_{Ia} curve at the initiation load F_{in} = 8.85 MN yields an arrest toughness of K_{Ia} = 190 MPa·$\sqrt{m}$ at the computed arrest point a_{fc} = 0.432 m where the crack-tip temperature would be 112°C (see Table 6.1*).

The complete static fracture-mechanics and stability analyses are depicted in Fig. 6.5 for the initiation load F_{in} = 8.85 MN. Included in the figure are curves for initiation toughness K_{Ic}, arrest toughness K_{Ia}, displacement-controlled stress-intensity factor K_I^{DISP}, and force-controlled stress-intensity factor K_I^F. The regions of tearing and

*Although only the results for test WP-2.4 are discussed in this section, Table 6.1 presents a summary of WPSTAT results for each of the tests in the WP-2 series. More detailed information on the analyses for each test can be obtained from the references noted previously.

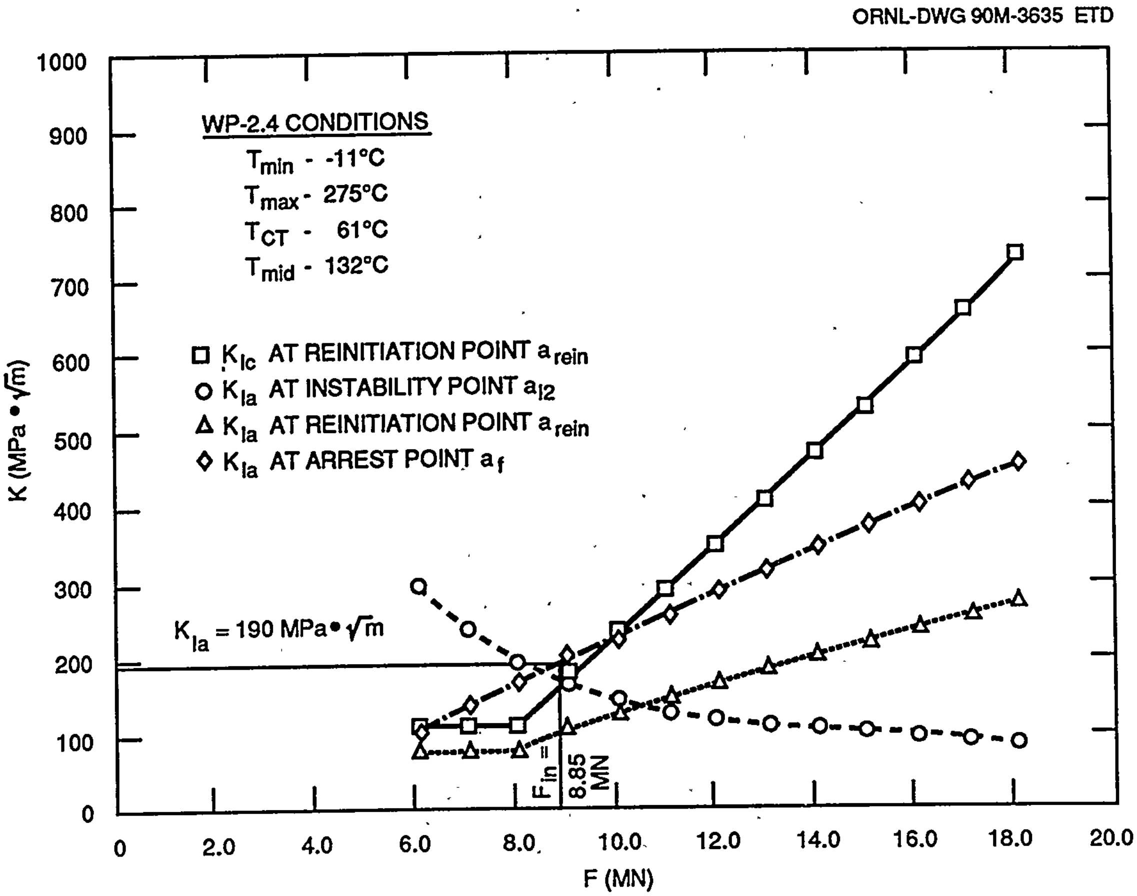

Fig. 6.4. Determination of arrest toughness at initiation load of 8.85 MN: test WP-2.4.

Table 6.1. Summary of WPSTAT results for WP-2 series tests

Test specimen	Initiation load, F_{in} (MN)	Predicted arrest crack length, a_f (m)	Temperature at arrest point, T_f (°C)	Crack-arrest toughness, K_{Ia} (MPa·√m)
WP-2.1	11.9	0.347	99	148
WP-2.2	17.0	0.452	125	250
WP-2.3	15.3	0.427	118	215
WP-2.4	8.9	0.432	112	190
WP-2.5	8.9	0.358	106	167
WP-2.6	19.3	0.451	131	284

ORNL-DWG 90M-3636 ETD

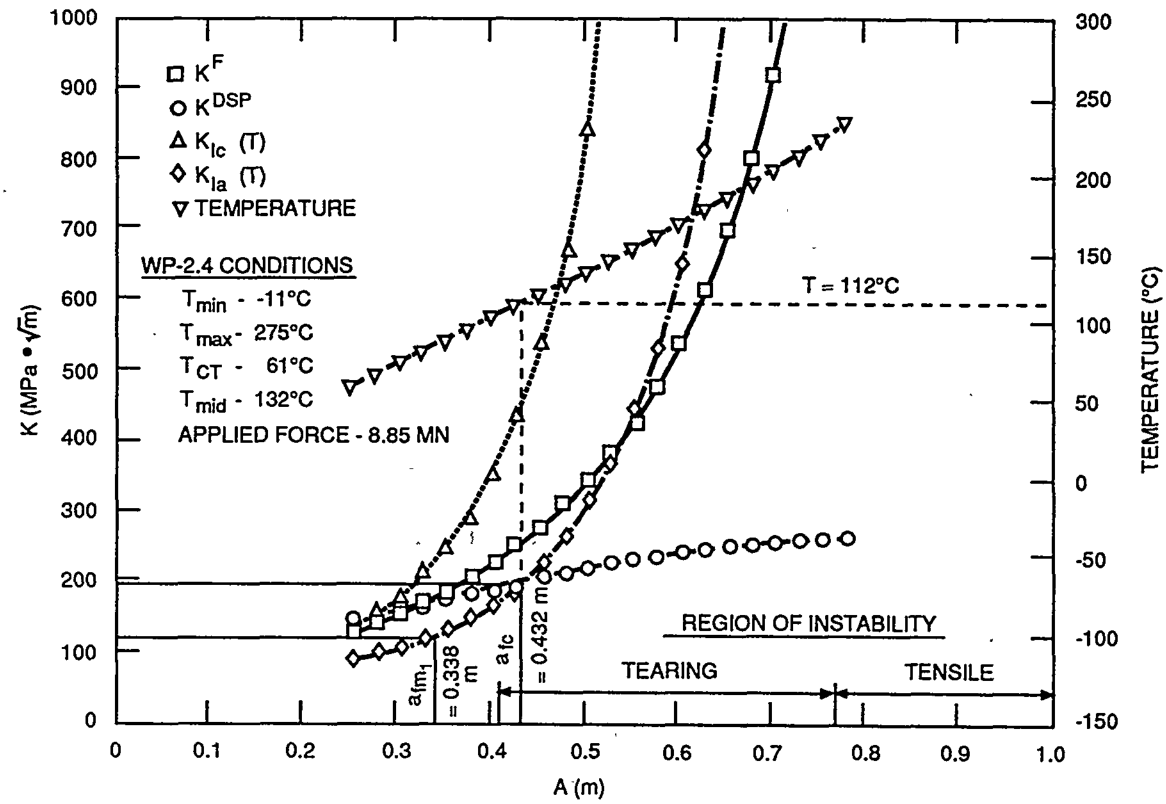

Fig. 6.5. Complete static and stability analyses for initiation load of 8.85 MN: test WP-2.4.

tensile instability and the computed initial arrest point a_{fc} are also identified in Fig. 6.5.

6.1.2.2 Application-Mode Dynamic Analysis (Fixed-Load Boundary Condition)

Elastodynamic fracture analysis was performed using the finite-element method and the implicit Newmark-Beta scheme for the time integration. The dynamic stress-intensity factor K_I is determined in each time step from the dynamic J-integral containing the appropriate inertial and thermal terms. The crack-growth modeling technique of these codes uses a scheme in which crack-plane nodes, initially restrained normal to the crack plane by stiff springs, are released incrementally according to the selected analysis mode.

Elastodynamic analyses of wide-plate test WP-2.4 were carried out with the ADINA/VPF (Ref. 5) dynamic crack analysis code. The 2-D plane-stress finite-element model of the wide-plate configuration used in the analyses consists of 894 nodes and 264 eight-noded isoparametric elements. Thirty-one spring elements are used in the crack plane to model propagation of the crack tip. Side grooves are taken into account by adjusting the resulting stress-intensity factor calculated in each time step of the analysis, that is, multiplying by $\sqrt{B/B_N}$.

A posttest application-mode analysis of wide-plate test WP-2.4 was performed using the material properties given in Chap. 3. The global deformation of the assembly caused by thermal strains was incorporated into the analyses. For finite-element applications, static thermoelastic analyses were performed with the ADINA/ADINAT finite-element codes[3] to determine the thermal deformation of the plate assembly. The thermal displacements were added to the nodal coordinates. The temperature distribution for the analyses was interpolated from the data measured along the crack plane (Fig. 5.20) and used only for determination of dynamic fracture toughness. For the dynamic analysis, the load was fixed at the value of the measured fracture load, 8.85 MN, as a prescribed concentrated load. The time step was set at $\Delta t = 5$ μs.

The calculated crack-depth history (plate front face) from this analysis is presented in Fig. 6.6. Figure 6.7 shows the dynamic stress-intensity factor K_I^{DYN}, the static toughness K_{Ia}, and the crack velocity $\dot{a}$ as a function of instantaneous crack depth. In Fig. 6.7, the crack velocity decreases smoothly, and crack propagation continues at

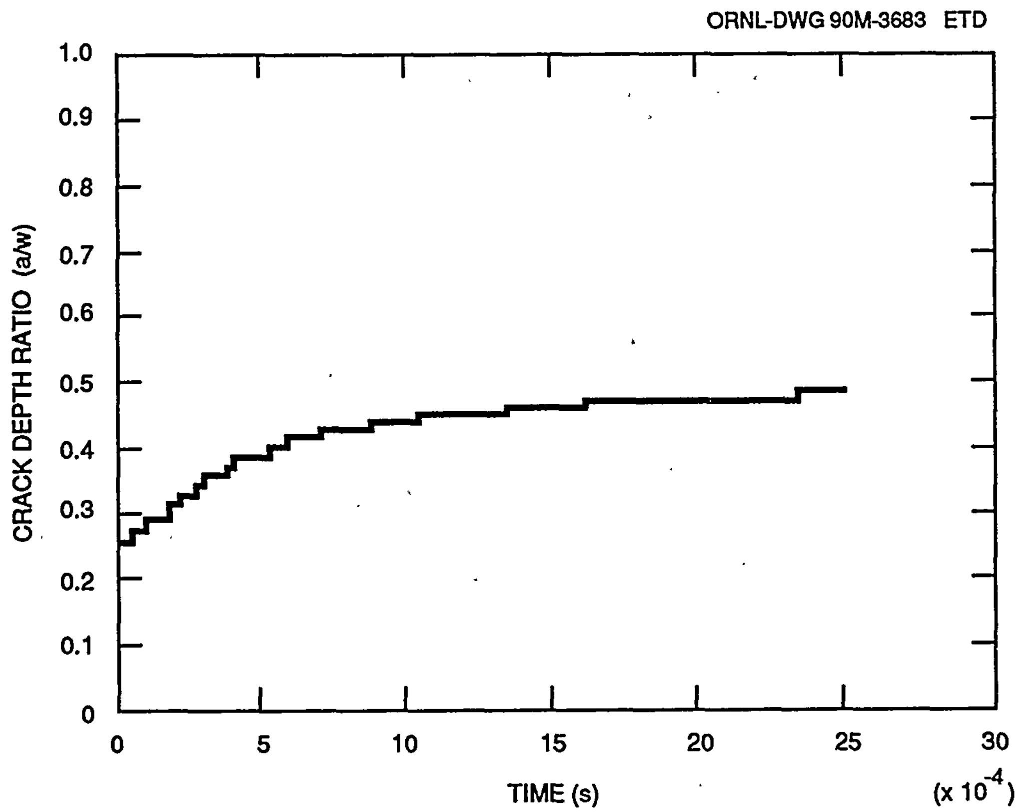

Fig. 6.6. Dynamic-analysis, crack-depth history: test WP-2.4.

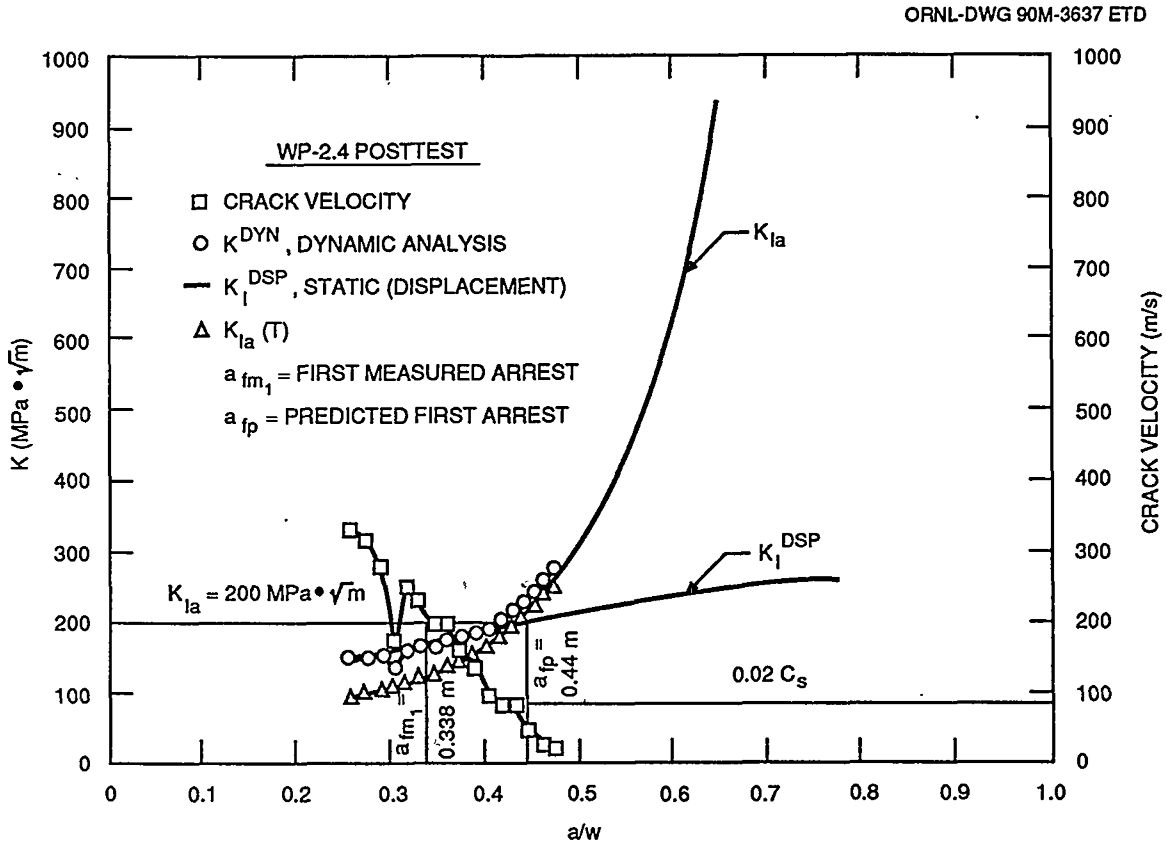

Fig. 6.7. Dynamic factor, static toughness, quasi-static displacement-controlled factor, and crack velocity vs instantaneous crack length: test WP-2.4.

small velocities for values of a/w > ~0.43. Because it is unlikely that a real crack would propagate at these low velocities for an extended period of time, arrest has been arbitrarily defined to occur when the crack velocity drops below a threshold velocity of 2% of the shear wave velocity (C_s); that is, 0.02 C_s = 64 m/s. Based on this assumption, an arrest is predicted from the application-mode analysis at a_{fp} = 0.44 m, where the crack-tip temperature would be T = 118°C and the arrest toughness would be K_{Ia} = 200 MPa·$\sqrt{m}$. The predicted arrest point exceeds the first measured arrest point, a_{fm_1} = 0.338 m, where T = 86.3°C and K_{Ia} = 122 MPa·$\sqrt{m}$. The analyses were terminated at time t = 3 ms (see Table 6.2*).

---

*Table 6.2 presents a summary of application-mode dynamic analysis results for each of the tests in the WP-2 series. More detailed information on the analyses for each test can be obtained from the references noted previously.

Table 6.2. Summary of application-mode dynamic analyses for WP-2 series tests

Test specimen	Initiation load, F_{in} (MN)	Predicted arrest crack length, a_{fp}[a] (m)	Temperature at arrest point, T (°C)	Crack-arrest toughness, K_{Ia} (MPa·$\sqrt{m}$)
WP-2.1	11.9	0.371	102	143
WP-2.2	17.0	0.452	124	251
WP-2.3	15.3	0.429	118	220
WP-2.4	8.9	0.439	118	200
WP-2.5	8.9	0.371	109	181
WP-2.6	19.3	0.430	125	253

[a]Arrest has been defined to occur when the crack velocity drops below a threshold velocity of 2% of the shear wave velocity (C_s); that is, 0.02 C_s = 64 m/s. The value given is for the first crack run-arrest event.

6.1.2.3 Generation-Mode Dynamic Analysis (Fixed Load Boundary Condition

From the output of the crack-line gages and from an inspection of the fracture surface, estimates of the crack position as a function of time were constructed and listed in Table 5.5 for the plate front and back faces for test WP-2.4.* Figure 6.8 depicts the apparent crack position vs time that was derived from Table 5.5 and used as input for the posttest generation-mode elastodynamic analysis of test WP-2.4. For these analyses, the load point was fixed at the value of the initiation load, 8.85 MN, as a prescribed concentrated load, and the time step was set at Δt = 10 µs. From these calculations, the stress-intensity factor as a function of time is given in Fig. 6.9. The generation-mode analysis (fixed-load-point boundary condition)† results for the seven crack run-arrest events (plate front face) of test WP-2.4 are given in Table 6.3.

The computed strain histories corresponding to selected points close to the front-side gage 1–12‡ [see Fig. 4.8(*d*) for gage locations]

*Only the results for test WP-2.4 are presented in this section. Generation-mode dynamic results for the other tests in the WP-2 series are summarized in Sect. 6.2. More details on each test can be obtained by consulting the appropriate references noted earlier.

†Appendix B discusses the importance of the analysis method (static vs dynamic) and boundary condition (fixed-load or fixed-load-pin displacement) used to interpret the wide-plate crack-arrest tests.

‡Note that because strain gage 6 did not function during the test, computed and actual strain histories for its companion back-face gage (17) are presented.

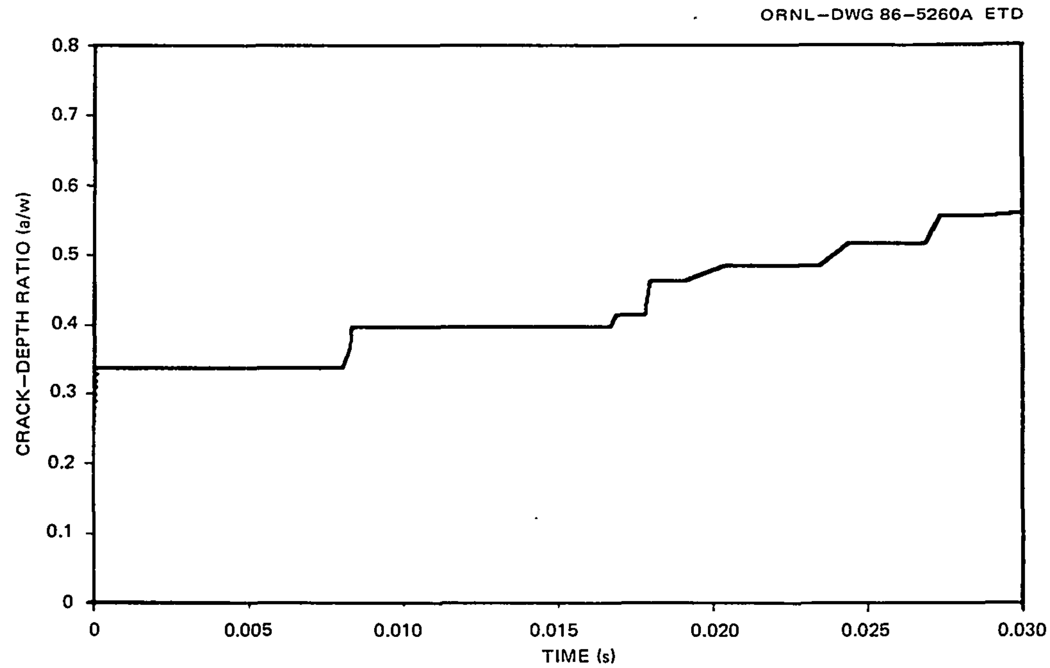

Fig. 6.8. Crack-depth history from front-face strain gages: test WP-2.4.

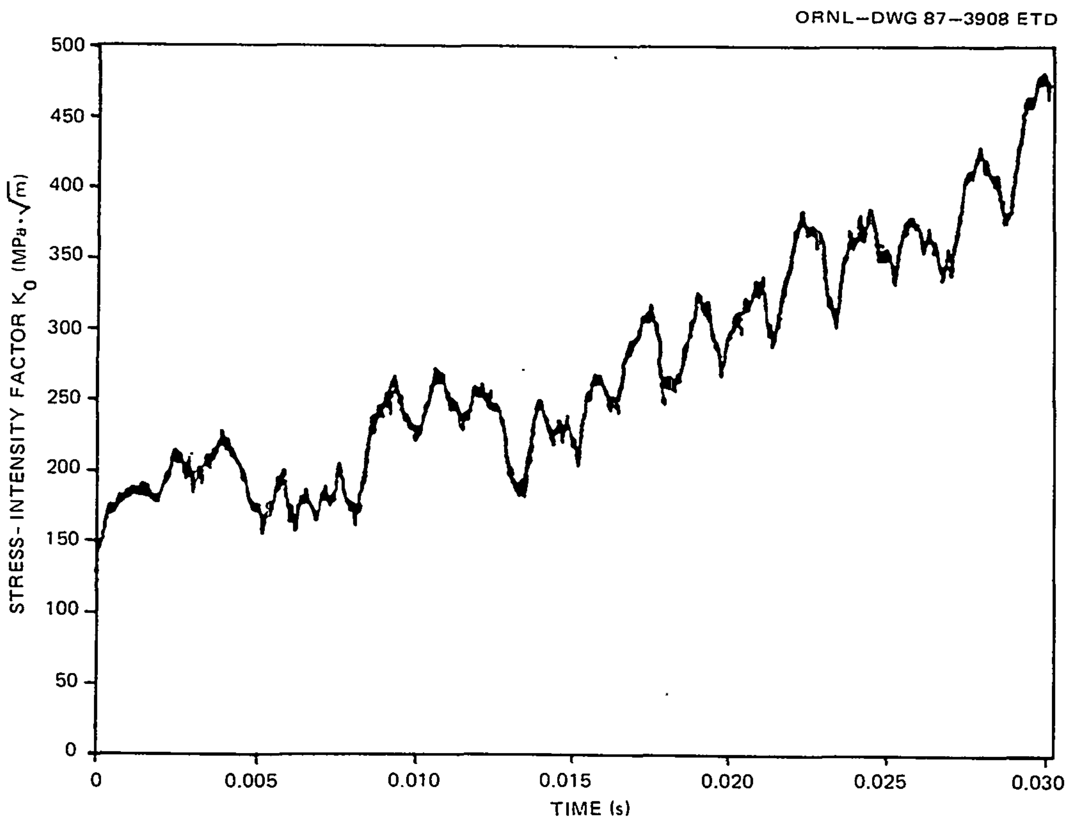

Fig. 6.9. Calculated stress-intensity factor vs time from generation-mode dynamic analysis (fixed-load case): test WP-2.4.

Table 6.3. Summary of generation-mode (fixed-load) dynamic analysis results for test WP-2.4

Event	Time (ms)	A (m)	K (MPa·$\sqrt{m}$)
Initiation	0.0	0.251	143
First arrest	0.10	0.338	137
Reinitiation	8.00	0.338	178
Second arrest	8.32	0.397	188
Reinitiation	15.82	0.397	281
Third arrest	16.86	0.413	281
Reinitiation	17.80	0.413	281
Fourth arrest	17.96	0.462	249
Reinitiation	19.08	0.462	318
Fifth arrest	20.40	0.484	307
Reinitiation	23.46	0.484	322
Sixth arrest	24.40	0.515	381
Reinitiation	25.46	0.515	355
Seventh arrest	27.32	0.555	397
Reinitiation	28.86	0.555	389

are depicted in Figs. 6.10 to 6.12 for test WP-2.4. Also shown in the figures are the actual strain histories derived from the gages. The sharply defined strain peaks in the figures correspond to the point in time when the fast-running crack passes under a gage point. As crack propagation slows, the peaks are transformed into more blunted curves. Pertinent events during a test (arrests, reinitiations, etc.), as detected by the strain gages, are noted on selected strain histories in Appendix A.

In Fig. 6.13 the COD calculated at $a/w = 0.15$ (from the plate cold edge) using the generation-mode analysis is compared with measured data from the front-face gage.

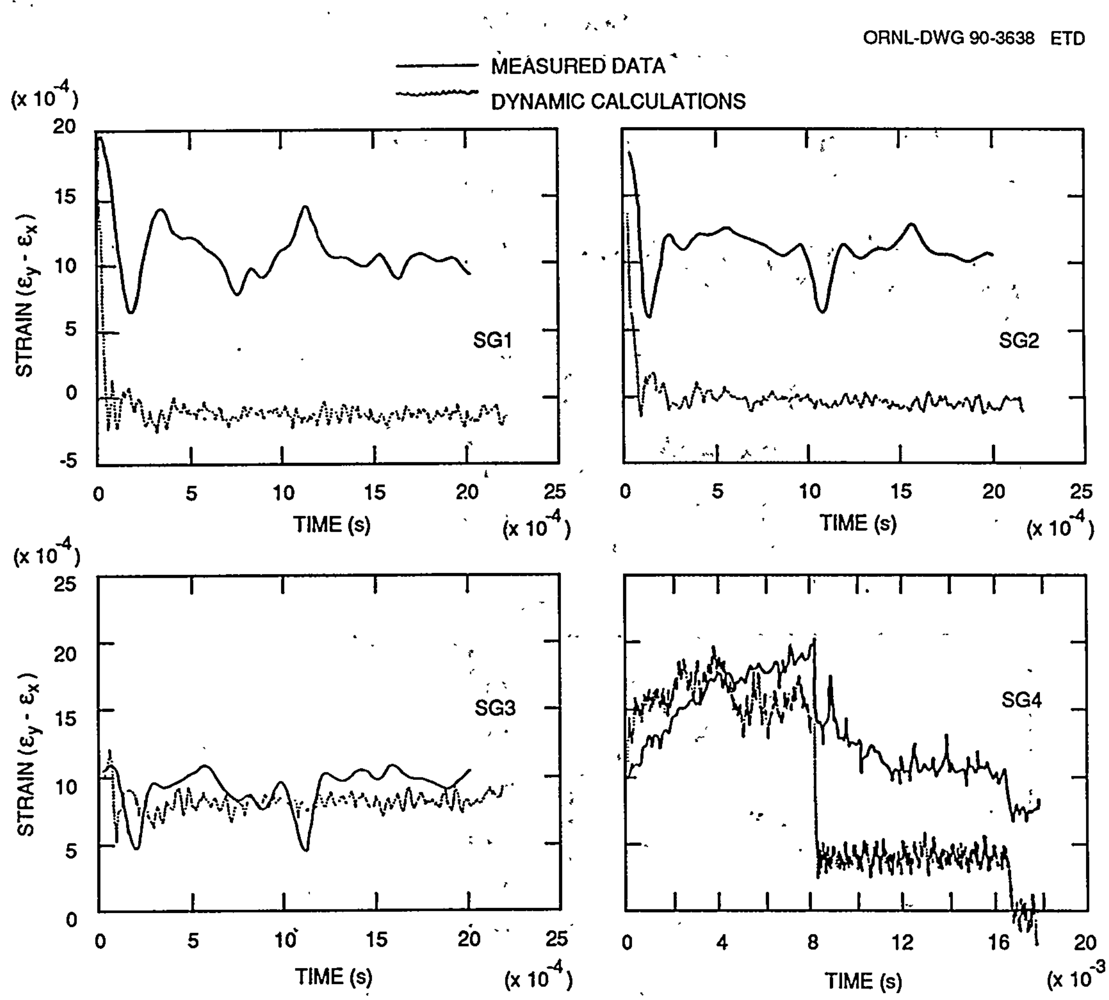

Fig. 6.10. Actual and computed strain histories for front-face crack-line gages 1–4: test WP-2.4.

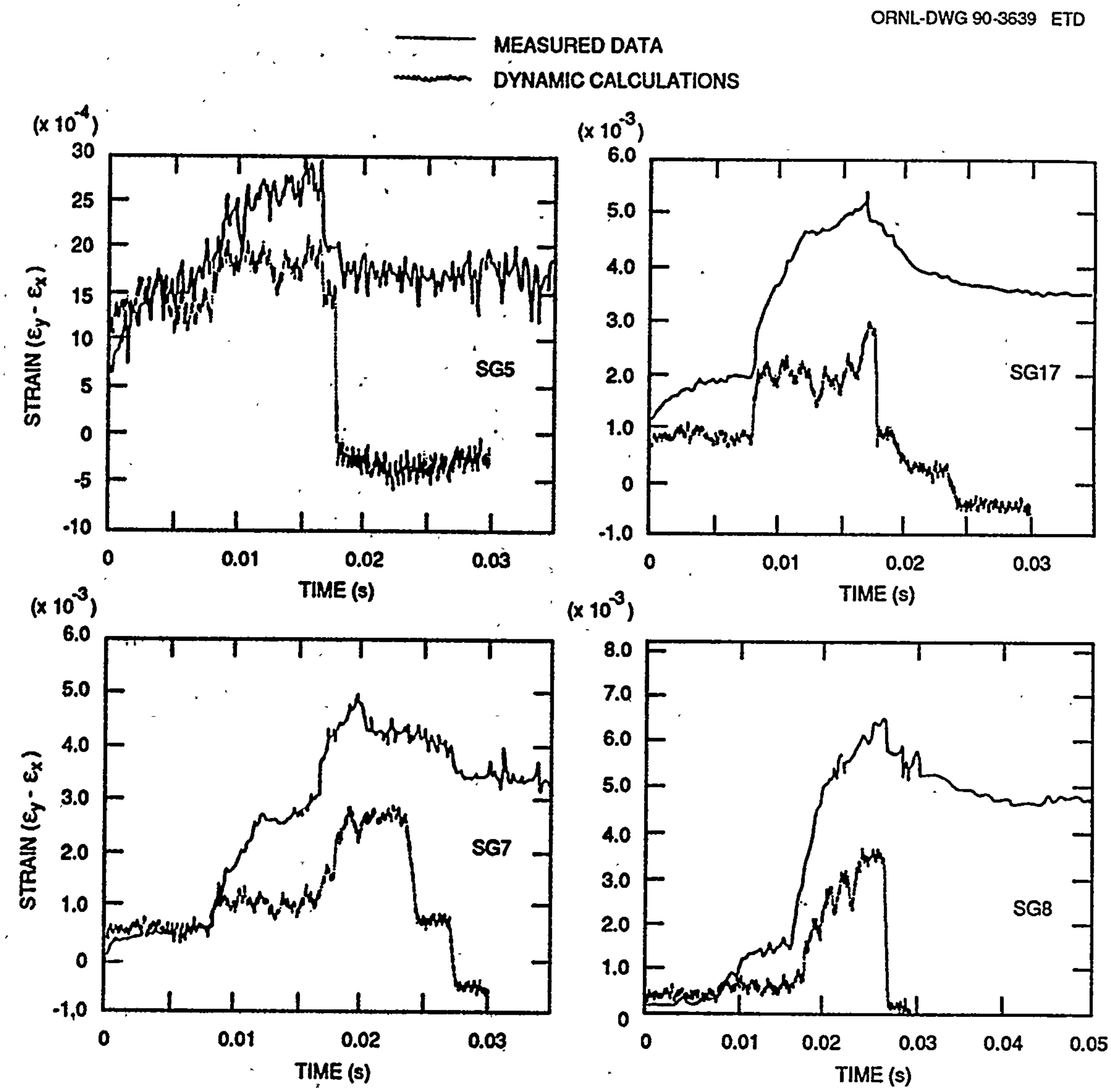

Fig. 6.11. Actual and computed strain histories for crack-line gages 5, 17, 7, and 8: test WP-2.4.

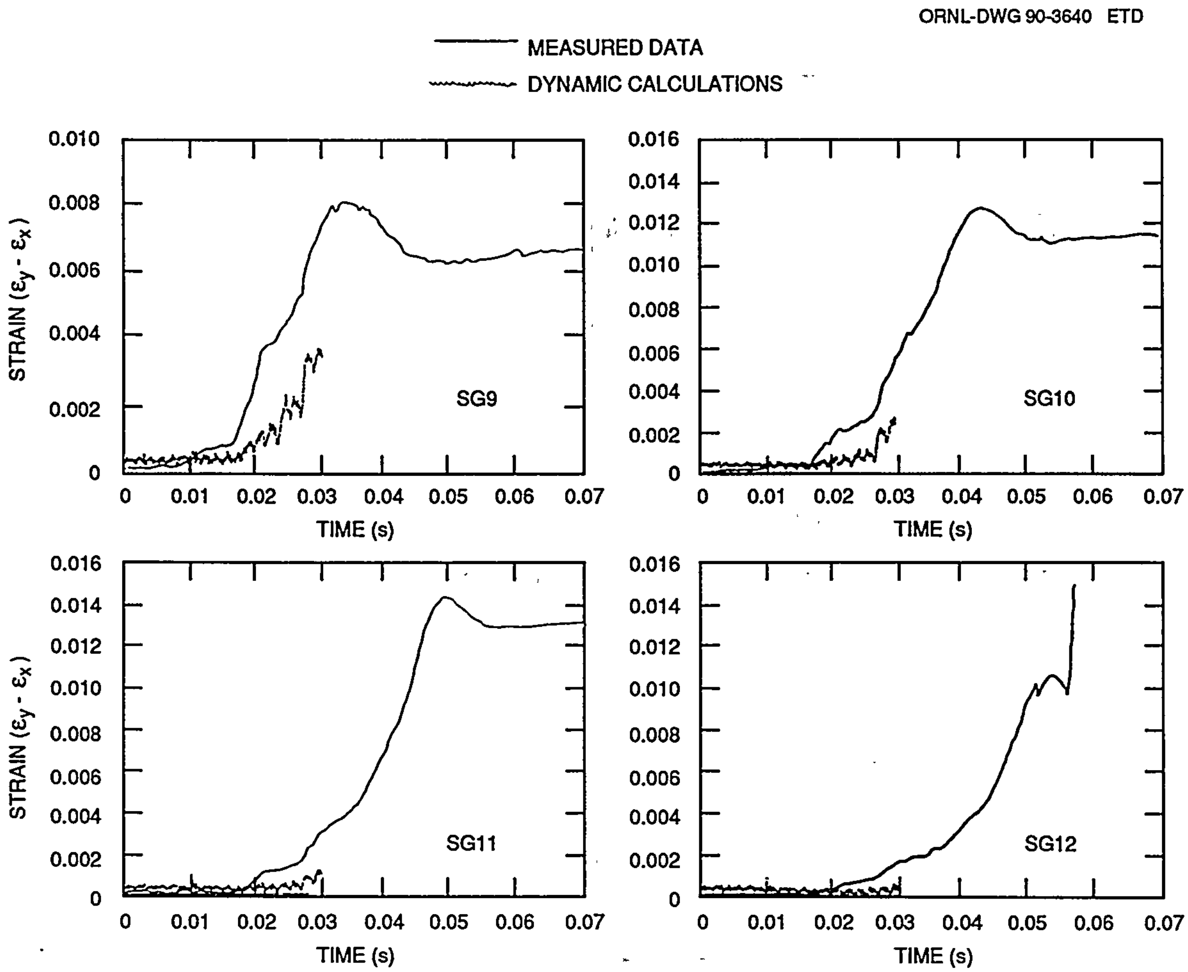

Fig. 6.12. Actual and computed strain histories for front-face crack-line gages 9–12: test WP-2.4.

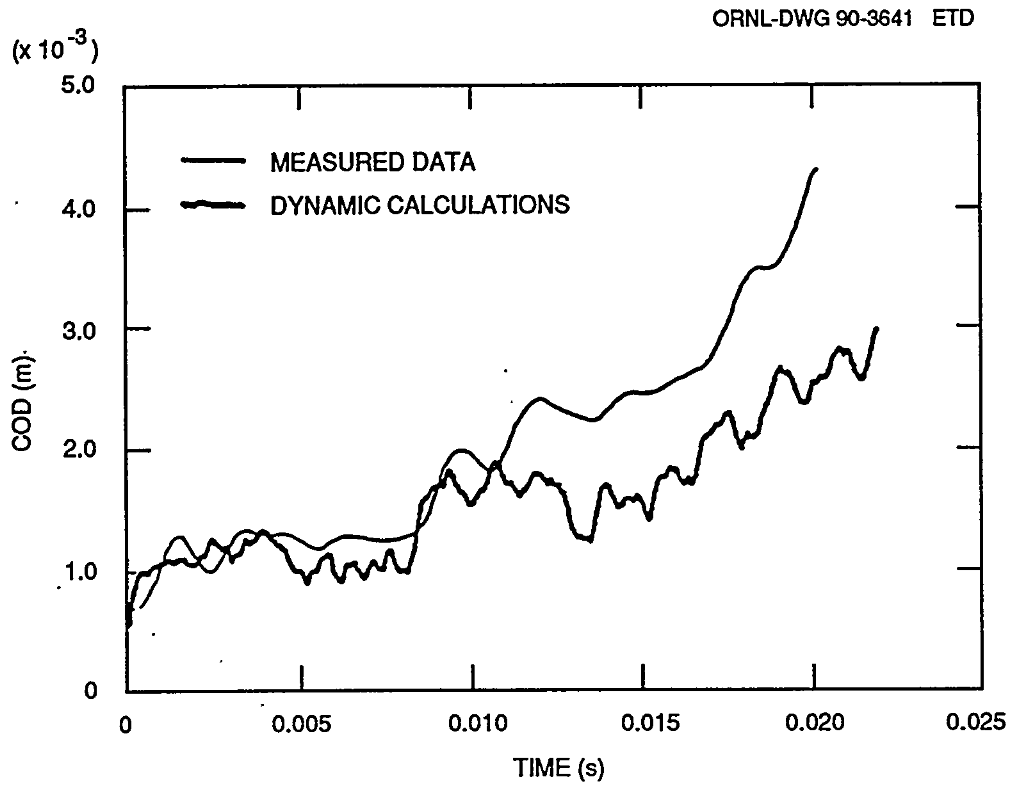

Fig. 6.13. Actual and generation-mode dynamic analysis computed COD at $a/w = 0.15$ for front-face gage (fixed-load case): test WP-2.4.

6.2 CRACK-ARREST TOUGHNESS RESULTS

Crack-arrest toughness values for the WP-2 series wide-plate tests have been determined by static and dynamic analyses, as well as by handbook techniques. Appendix B presents a discussion of the importance of the analysis method (static vs dynamic) and boundary conditions (fixed-load or fixed-load-pin displacement) used to interpret the wide-plate crack-arrest tests. For reasons discussed in Appendix B and because of the long durations of the crack run-arrest events ($t > 9$ ms) observed for the LUS WP-2 series materials, considerable load adjustment can take place as a result of specimen/pull-plate compliance. Therefore, the most meaningful calculations of crack-arrest toughness values for such conditions should take these factors into account through the use of a dynamic finite-element analysis. As shown in Appendix B, the long fracture durations of these tests lead to dynamic results that approach those predicted by load-controlled static conditions. Fixed-load, generation-mode, dynamic finite-element determinations of crack-arrest toughness values as well as test conditions for the WP-2 series tests are summarized in Table 6.4. Figure 6.14 presents a plot of crack-arrest toughness values against the arrest-toughness temperature minus DW_{NDT} (60°C) for the WP-2 series tests. Also included in the figure are previous wide-plate crack-arrest tests that used A 533 grade B class 1

Table 6.4. Summary of HSST wide-plate crack-arrest test conditions and crack-arrest toughness values for specially heat-treated 2 1/4 Cr-1 Mo steel: WP-2 Series

Test	Crack location (cm)	Crack temperature (°C)	Initiation load (MN)	Arrest location (cm)	Arrest temperature (°C)	Arrest $T - DW_{NDT}$ (°C)	Crack-arrest toughness[a] ($MPa \cdot \sqrt{m}$)
WP-2.1A[b]	19.9	55	11.90	27.5	80	20	106
WP-2.1B	27.5	80	11.90	33.5	96	36	153
WP-2.1D	33.5	96	11.90	37.0	105	45	158
WP-2.1E	37.0	105	11.90	40.0	112	52	170
WP-2.1F	40.0	112	11.90	45.0	125	65	201
WP-2.1H	45.0	125	11.90	49.0	135	75	293
WP-2.1I	49.0	135	11.90	52.7	145	85	371
WP-2.1J	52.7	145	11.90	55.5	152	92	406
WP-2.2A[b,c]	21.1	58	17.0	43.5	120	60	201
WP-2.2B	43.5	120	17.0	46.5	129	69	259
WP-2.2C	46.5	129	17.0	47.8	133	73	281
WP-2.2D	47.8	133	17.0	49.9	139	79	277
WP-2.2E	49.9	139	17.0	51.0	142	82	380
WP-2.2F	51.0	142	17.0	53.8	150	90	364
WP-2.2G	53.8	150	17.0	58.2	162	102	446
WP-2.3A	20.0	66	15.3	34.0	97	37	144
WP-2.3B	34.0	97	15.3	37.5	106	46	232
WP-2.3D	37.5	106	15.3	39.7	111	51	255
WP-2.3F	39.7	111	15.3	45.7	126	66	258
WP-2.4A[b]	20.3	45	7.52	25.1	61	1	
WP-2.4B	25.1[d]	61	8.85	33.8	86	26	137
WP-2.4C	33.8	86	8.85	39.7	102	42	188
WP-2.4D	39.7	102	8.85	41.3	107	47	281
WP-2.4E	41.3	107	8.85	46.2	121	61	249
WP-2.4F	46.2	121	8.85	48.4	127	67	307
WP-2.4G	48.4	127	8.85	51.5	137	77	381
WP-2.4H	51.5	137	8.85	55.5	149	89	397

Table 6.4 (continued)

Test	Crack location (cm)	Crack temperature (°C)	Initiation load (MN)	Arrest location (cm)	Arrest temperature (°C)	Arrest $T - DW_{NDT}$ (°C)	Crack-arrest toughness[a] ($MPa \cdot \sqrt{m}$)
WP-2.5A[b]	19.9	66	7.53	27.2	86	26	
WP-2.5B	27.2[d]	86	8.90	35.0	104	44	171
WP-2.5C	35.0	104	8.90	43.5	124	64	190
WP-2.5D	43.5	124	8.90	47.8	135	75	268
WP-2.5E	47.8	135	8.90	51.6	144	84	306
WP-2.5F	51.6	144	8.90	56.0	154	94	366
WP-2.6A[e]	22.4	65	19.3	35.7	104	44	204
WP-2.6B	35.7	104	19.3	39.7	115	55	259
WP-2.6C	39.7	115	19.3	41.0	119	59	286
WP-2.6D	41.0	119	19.3	43.0	125	65	350
WP-2.6F	43.0	125	19.3	46.0	133	73	328
WP-2.6G	46.0	133	19.3	48.0	139	79	411
WP-2.6H	48.0	139	19.3	54.0	156	96	413

[a]Dynamic finite-element analyses (fixed load) using ORNL program ADINA/VPF (Ref. 5). K_{Ia} values are presently being reassessed to incorporate tunneling effects and should therefore not be considered as final. Incorporation of tunneling effects will result in a slight reduction in K_{Ia} valves presented (i.e., ≤10–20%) as noted in Appendix C.

[b]Crack front cut to truncated chevron configuration.

[c]Specimen was warm prestressed by loading to 16 MN at 124°C.

[d]After pop-in event.

[e]Specimen was warm prestressed by loading to 15.6 MN at 110°C.

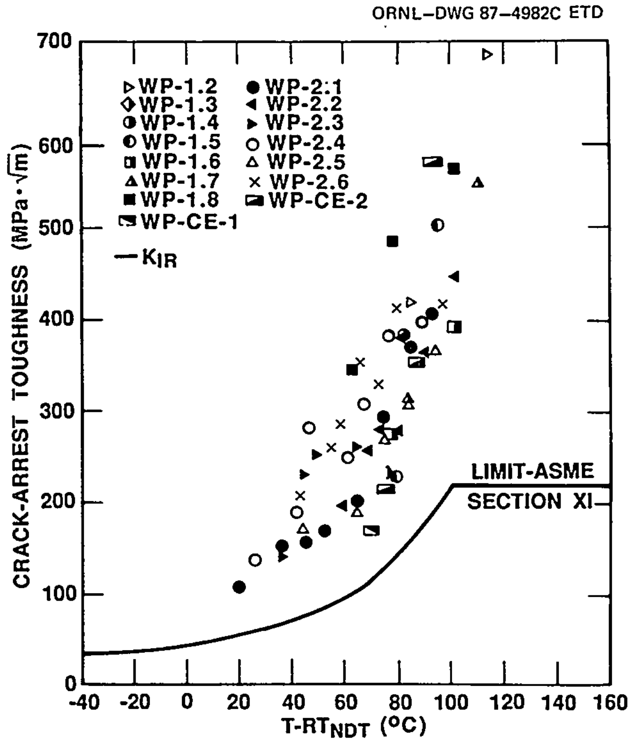

Fig. 6.14. Fixed-load, generation-mode, dynamic finite-element crack-arrest toughness results for HSST wide-plate tests.

materials (WP-1 and WP-CE series)[9-11] and the K_{IR} curve from Sect. XI of the *ASME B&PVC*. The crack-arrest toughness results obtained from the HSST wide-plate crack-arrest tests consistently extend above the reference fracture-toughness curve. At temperatures near and above the onset of Charpy USE ($T - RT_{NDT}$ = 78, 85, and 90°C* for the WP-1, WP-CE, and WP-2 series materials, respectively), the K_{Ia} values increase with temperature at an accelerating rate. Also, as noted in Fig. 6.15, crack arrests in the WP-2 test series have occurred at temperatures up to 102°C above the DW_{NDT} (60°C) and up to 12°C above the temperature corresponding to the onset of Charpy USE (150°C).

6.3 COMPARISON OF WIDE-PLATE CRACK-ARREST TOUGHNESS DATA WITH OTHER LARGE-SCALE TEST RESULTS

The trend for K_{Ia} values to extend above the limit proposed in *ASME B&PVC* Sect. XI, as shown in Fig. 6.14, is further substantiated in Fig. 6.16. Included in the figure are K_{Ia} data from several large-scale tests[12-23] plus the wide-plate results. The rate of K_{Ia} increase in these tests appears to increase significantly at $T - RT_{NDT}$* above ~90°C.

*$T - DW_{NDT}$ value for WP-2 series material.

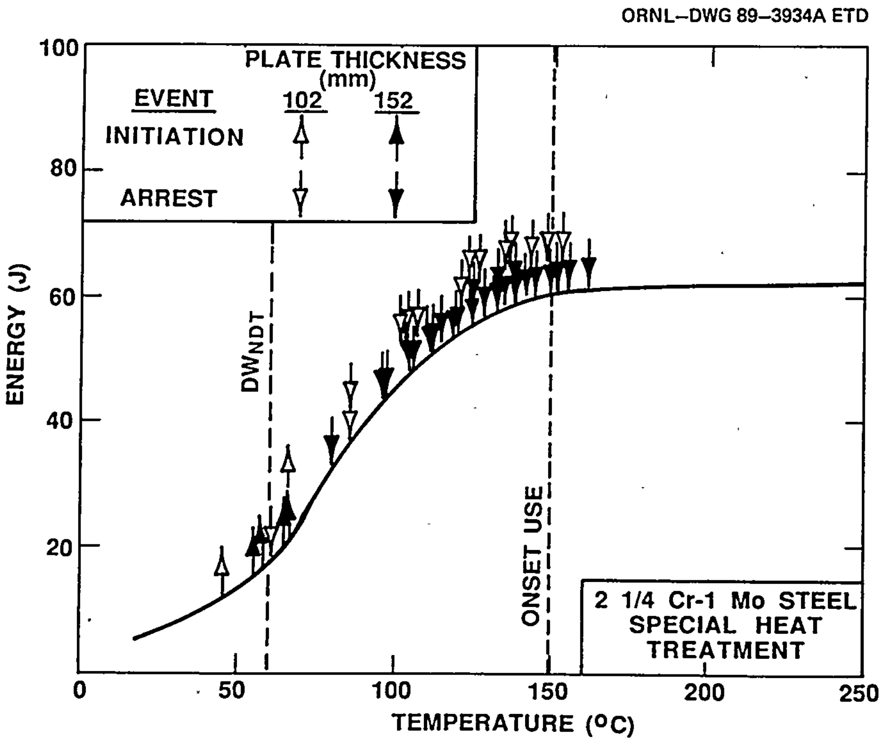

Fig. 6.15. Relationship of WP-2 series initiation and arrest events to CVN energy vs temperature curve.

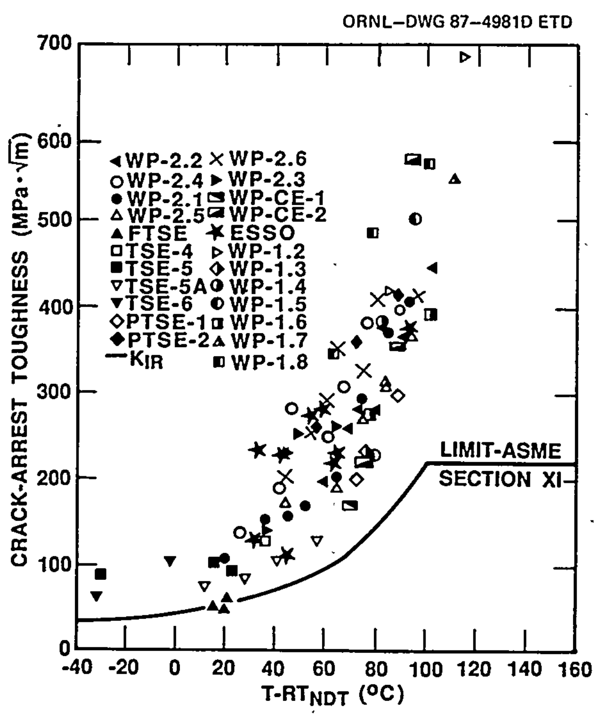

Fig. 6.16. HSST wide-plate crack-arrest data (fixed-load, generation-mode dynamic finite-element calculations) show trend consistent with other large-specimen crack-arrest test results.

REFERENCES

1. B. R. Bass and J. W. Bryson, Union Carbide Corp. Nuclear Div., Oak Ridge Natl. Lab., *Application of Energy Release Rate Technique to Part-Through Cracks in Plates and Cylinders, Volume 1, ORMGEN-3D: A Finite Element Mesh Generator for 3-Dimensional Crack Geometries*, USNRC Report NUREG/CR-2997/V1 (ORNL/TM-8527/V1), December 1982.*

2. B. R. Bass and J. W. Bryson, Union Carbide Corp. Nuclear Div., Oak Ridge Natl. Lab., *Applications of Energy Release Rate Technique to Part-Through Cracks in Plates and Cylinders, Volume 2, ORVIRT: A Finite Element Program for Energy Release Rate Calculations for 2-D and 3-D Crack Models*, USNRC Report NUREG/CR-2997/V2 (ORNL/TM-8527/V2), February 1983.*

3. K. J. Bathe, *ADINA — A Finite Element Program and Automatic Dynamic Incremental Nonlinear Analysis*, Report A-1, Massachusetts Institute of Technology, Cambridge, Mass., 1984.

4. B. R. Bass, C. E. Pugh, and H. K. Stamm, "Dynamic Analyses of a Crack Run-Arrest Experiment in a Nonisothermal Plate," in *Pressure Vessel Components Design and Analysis*, Vol. 4, ASME Publication PVP, Vol. 98.2, pp. 175–84, 1985.†

5. B. R. Bass and J. Keeney-Walker, Martin Marietta Energy Systems, Inc., Oak Ridge Natl. Lab., "Computer Program Development for Dynamic Fracture Analysis," in *Heavy-Section Steel Technology Program Semiann. Prog. Rep. April–September 1985*, USNRC Report NUREG/CR-4219/V2 (ORNL/TM-9593/V2), January 1986.*

6. B. R. Bass and J. Keeney-Walker, Martin Marietta Energy Systems, Inc., Oak Ridge Natl. Lab., "Wide-Plate Analyses at ORNL," pp. 111–31 in *Heavy-Section Steel Technology Program Semiann. Prog. Rep. October 1986–March 1987*, USNRC Report NUREG/CR-4219, Vol. 4, No. 1 (ORNL/TM-9593/V4&N1), August 1987.*

7. D. J. Naus et al., Martin Marietta Energy Systems, Inc., Oak Ridge Natl. Lab., "High-Temperature Crack Arrest Tests Using 152-mm-Thick SEN Wide Plates of Low-Upper-Shelf Base Material: Test WP-2.2 and WP-2.6," USNRC Report NUREG/CR-5450 (ORNL/TM-11352), February 1990.*

8. B. R. Bass and J. Keeney-Walker, Martin Marietta Energy Systems, Inc., Oak Ridge Natl. Lab., "Wide-Plate Analyses at ORNL," pp. 156–91 in *Heavy-Section Steel Technology Program Semiann. Prog. Rep. April–September 1987*, USNRC Report NUREG/CR-4219, Vol. 4, No. 2 (ORNL/TM-9593/V4&N2), April 1988.*

9. D. J. Naus et al., Martin Marietta Energy Systems, Inc., Oak Ridge Natl. Lab., *Crack-Arrest Behavior in SEN Wide Plates of Quenched and Tempered A 533 Grade B Steel Tested Under Nonisothermal Conditions*, USNRC Report NUREG/CR-4930 (ORNL-6388), August 1987.*

10. D. J. Naus et al., Martin Marietta Energy Systems, Inc., Oak Ridge Natl. Lab., *High-Temperature Crack-Arrest Behavior in 152-mm-Thick SEN Wide Plates of Quenched and Tempered A 533 Grade B Class 1 Steel*, USNRC Report NUREG/CR-5330 (ORNL/TM-11083), April 1989.*

11. D. J. Naus et al., Martin Marietta Energy Systems, Inc., Oak Ridge Natl. Lab., *SEN Wide-Plate Crack-Arrest Tests Utilizing A 533 Grade B Class 1 Material: WP-CE Test Series*, USNRC Report NUREG/CR-5408 (ORNL/TM-11269), November 1989.*

12. R. D. Cheverton et al., Martin Marietta Energy Systems, Inc., Oak Ridge Natl. Lab., *Pressure Vessel Fracture Studies Pertaining to the PWR Thermal-Shock Issue: Experiments TSE-5, TSE-5A, and TSE-6*, USNRC Report NUREG/CR-4249 (ORNL-6163), June 1985.*

13. R. D. Cheverton et al., Martin Marietta Energy Systems, Inc., Oak Ridge Natl. Lab., *Pressure Vessel Fracture Studies Pertaining to the PWR Thermal-Shock Issue: Experiment TSE-7*, USNRC Report NUREG/CR-4304 (ORNL-6177), August 1985.*

14. R. H. Bryan et al., Martin Marietta Energy Systems, Inc., Oak Ridge Natl. Lab., *Pressurized-Thermal-Shock Test of 6-in.-Thick Pressure Vessels. PTSE-1: Investigation of Warm Prestressing and Upper-Shelf Arrest*, USNRC Report NUREG/CR-4106 (ORNL-6135), April 1985.*

15. R. H. Bryan et al., Martin Marietta Energy Systems, Inc., Oak Ridge Natl. Lab., *Pressurized-Thermal-Shock Test of 6-in.-Thick Pressure Vessels. PTSE-2: Investigation of Low Tearing Resistance and Warm Prestressing*, USNRC Report NUREG/CR-4888 (ORNL-6377), December 1987.*

16. Japan Welding Council, *Structural Integrity of Very Thick Steel Plate for Nuclear Reactor Pressure Vessels*, JWES-AE-7806, 1977 (in Japanese).

17. T. Kanazawa, S. Machida, and T. Teramoto, "Preliminary Approaches to Experimental and Numerical Study of Fast Crack Propagation and Crack Arrest," in *Fast Fracture and Crack Arrest*, ASTM STP 627, American Society for Testing and Materials, Philadelphia, Pa., 1977, pp. 39–58.†

18. N. Ohashi et al., "Fracture Toughness of Heavy Section LWR Pressure Vessel Steel Plate Produced by Basic Oxygen Furnace and Ladle Refining Process," Vol. 1, pp. 391–96 in *Proceedings of the Fourth International Conference on Pressure Vessel Technology, I. Mech. E.*, 1980.†

19. T. Kanazawa et al., "Study on Fast Fracture and Crack Arrest," *Experimental Mechanics* 21(2), 77–88, February 1981.†

20. S. Machida, Y. Kawaguchi, and M. Tsukamoto, "An Evaluation of the Crack Arrestability of 9% Ni Steel Plate to an Extremely Long Brittle Crack," *Journal of the Society of Naval Architect of Japan* 150, 511-17 (1981), translation ORNL-tr-5052.

21. T. Kanazawa, S. Machida, and H. Yajima, "Recent Studies on Brittle Crack Propagation and Arrest in Japan," in *Fracture Mechanics Technology Applied to Material and Structure Design*, G. C. Sih, N. E. Ryan, and R. Jones, Eds. (Martinua Nijhoff, The Hague, 1983), pp. 81–100.

22. Y. Nakano, "Stress Intensity Factor During Brittle Crack Propagation and Arrest in ESSO Specimens," in *Proceedings of the 18th National Symposium on X-Ray Study on Deformation and Fracture Solids, The Society of Materials Science, Japan, July 13-14*, 1981.

23. A. Pellissier-Tanon, P. Sollogoub, and B. Houssin, "Crack Initiation and Arrest in an SA 508 Class-3 Cylinder Under Liquid Nitrogen Thermal-Shock," Paper G/F 1/8, Vol. G/H, pp. 137-42 in *Transactions of the 7th International Conference on Structural Mechanics in Reactor Technology, August 22–26, 1983, Chicago, Illinois*, Elsevier Science Publishing Co., Inc., New York, 1983.†

---

*Available for purchase from National Technical Information Service, Springfield, VA 22161

†Available in public technical libraries.

7. CONCLUSIONS

The HSST Program has an integrated effort under way to extend the range of applicability of current state-of-the-art crack-arrest practices and to develop alternatives where improvements are needed. A consistent trend is formed when the crack-arrest data now available from the three types of HSST large-specimen tests are combined on a plot of K_{Ia} vs $T - RT_{NDT}$. Collectively, these data, along with other large-specimen test results, show that arrest can and does occur at temperatures up to and above those that correspond to the onset of Charpy upper-shelf behavior, and the measured K_{Ia} values extend above the limit included in Sect. XI of the *ASME B&PVC*. Results obtained from the present study further substantiate this trend and indicate that even a degraded (simulated) material (Charpy USE ~65 J, DW_{NDT} = 60°C) will exhibit high crack-arrest toughness (K_{Ia} values >400 $MPa \cdot \sqrt{m}$). Furthermore, cleavage crack propagation and arrests for this material have occurred at temperatures up to and slightly above that corresponding to the onset of its Charpy USE (150°C). Although some tearing fracture followed arrest events in each test, the results indicate that arrest occurred before conversion to ductility tearing and that these fracture modes can be treated analytically as independent events.

In summary, the results obtained from the three series of wide-plate crack-arrest tests support (1) the use of fracture-mechanics concepts to analyze cleavage run-arrest events, (2) the treatment of cleavage- and ductile-fracture modes as separate events, and (3) the fact that cleavage arrest can occur at toughness levels well above the ASME limit and at temperatures above those that correspond to the onset of CVN USE for good-quality A 533 grade B class 1 material (WP-1 and WP-CE test series) as well as for a degraded (simulated) material (WP-2 test series).

Appendix A

SUMMARY OF INSTRUMENTATION RESULTS

A.1 TEST WP-2.1

A.1.1 Strain Gages

Strain-gage records [see Fig. 4.8(a) for strain-gage locations] for companion front- and back-face gages adjacent to the crack propagation plane are shown in Figs. A.1 to A.3. Available near- and far-field strain-gage results are presented in Fig. A.4. Evaluation of the strain-gage records and examination of the fracture surface indicate that multiple (eight to ten) crack run-arrest events occurred during the test. More details of these crack run-arrest events followed by fibrous tearing are presented in Figs. A.5 to A.13. Figure A.5 shows the crack passing under strain gage 1 and arresting (t = 0.194 ms) before reaching strain gages 2–4. The crack passing under strain gages 2 and 3, momentarily arresting (t = 7.62 ms) before passing under strain gage 4, and a major arrest (t = 7.77 ms) occurring before reaching strain gage 5 are illustrated in Fig. A.6. The momentary crack arrest (t = 7.62–7.68 ms) that occurred between strain gages 3 and 4 is depicted in Fig. A.7. The 20-ms records for strain gages 4–7 are shown in Fig. A.8 and reveal that the crack passed under strain gage 5 and arrested again (t = 11.70 ms) before reaching strain gages 6 and 7. The 50-ms records of strain gages 5–8 are shown in Fig. A.9 and cover the period for the cleavage arrest (t = 11.70 ms) just past strain gage 5 and subsequent arrests that occurred between strain gages 6 and 7 (t = 18.14 ms), strain gages 7 and 8 (t = 25.12 ms), and after strain gage 8 (t = 27.62 and 33.76 ms). Fibrous tearing occurred as the crack passed strain gages 9–12 (Fig. A.10). Outputs for strain gages 13–16, located on the back face of the plate adjacent to the crack propagation plane, are presented in Fig. A.11 and show the crack running past strain gages 13 and 14 prior to arresting (t = 0.242 ms) before strain gage 15. Thirty-five- to fifty-millisecond records of strain gages 15–18 (Fig. A.12) cover the period for the arrest (t = 7.75 ms) just past strain gage 15 and subsequent crack run-arrest events, with arrests occurring between strain gages 16 and 17 (t = 9.04 and 11.48 ms) and strain gages 17 and 18 (t = 18.12). Outputs of strain gages 19–22 for an 80-ms period are presented in Fig. A.13, which covers the time interval in which the arrest events occurred between gages 18 and 19 (t = 20.18, 24.98, and 27.18 ms) and gages 19 and 20 (t = 33.06 and 34.76 ms), followed by fibrous tearing.

A.1.2 Additional Instrumentation

Output from the AE transducer mounted on the lower pull plate 3.6 m below the crack plane is presented in Fig. A.14. Longitudinal accelerations recorded by "damped" accelerometers mounted 3.653 m above (top accelerometer) and 3.655 m below (bottom accelerometer) the crack plane

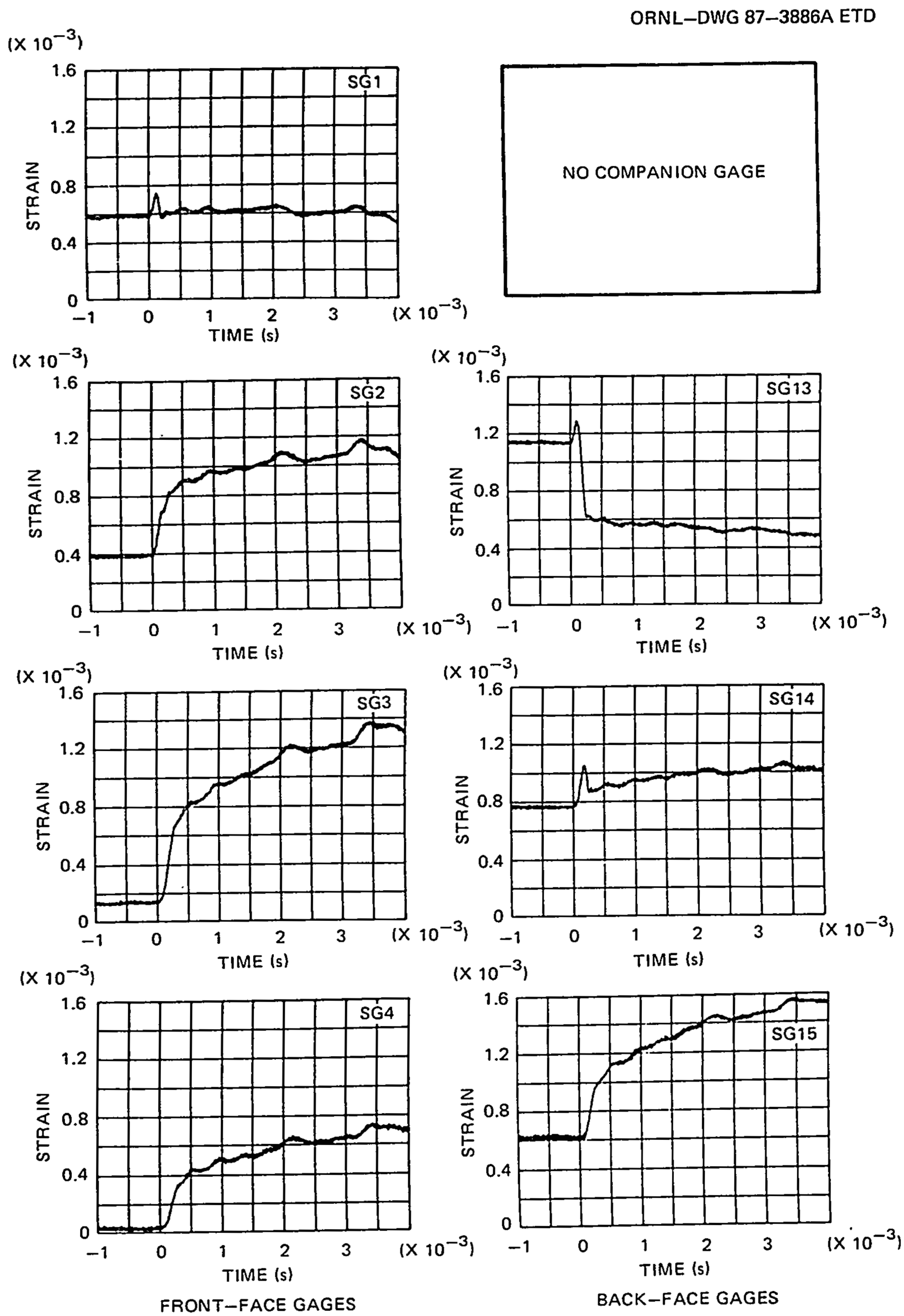

Fig. A.1. Strain histories for companion crack-line gages: test WP-2.1 (gages 1–4 and 13–15).

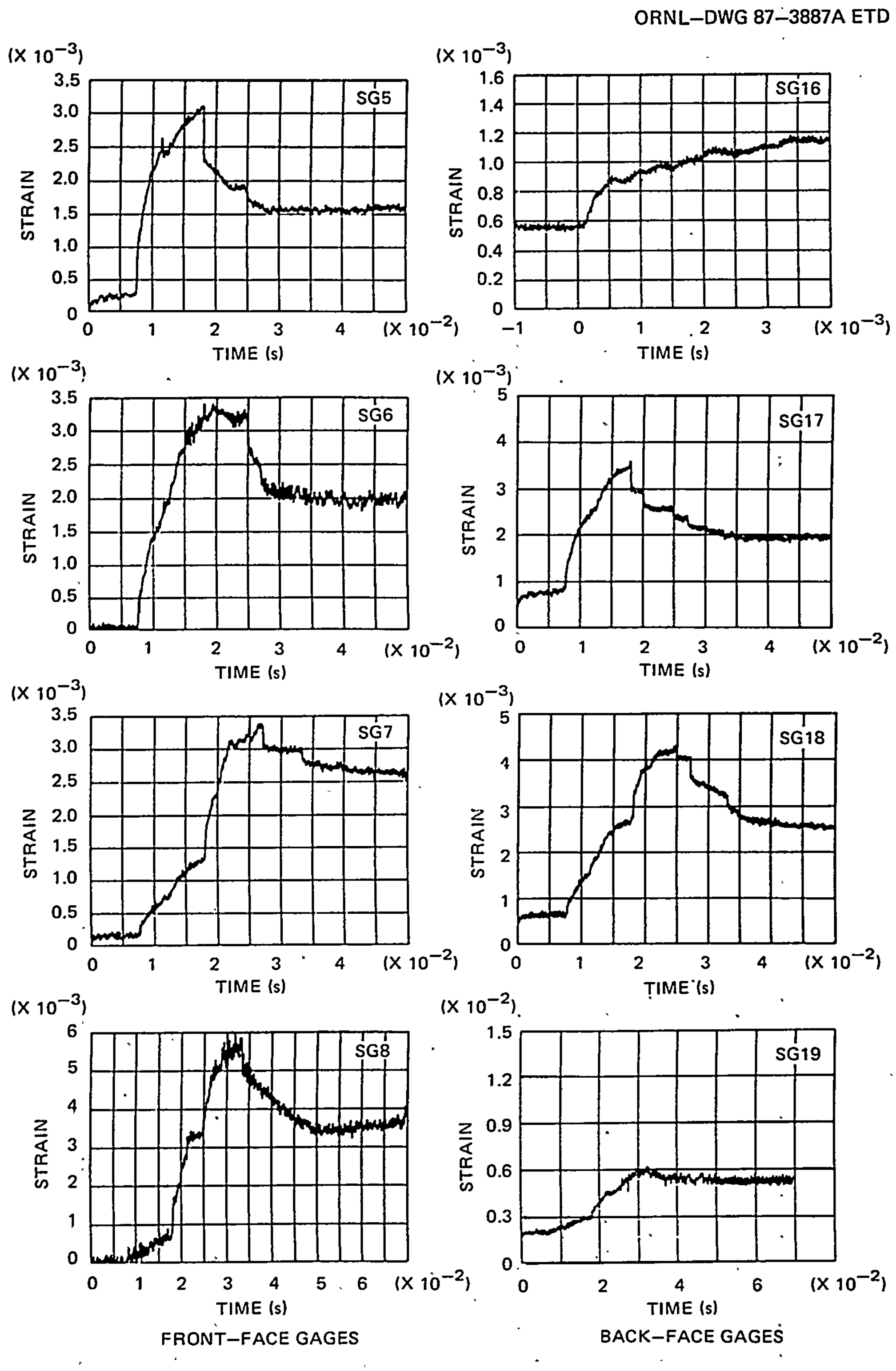

Fig. A.2. Strain histories for companion crack-line gages: test WP-2.1 (gages 5–8 and 16–19).

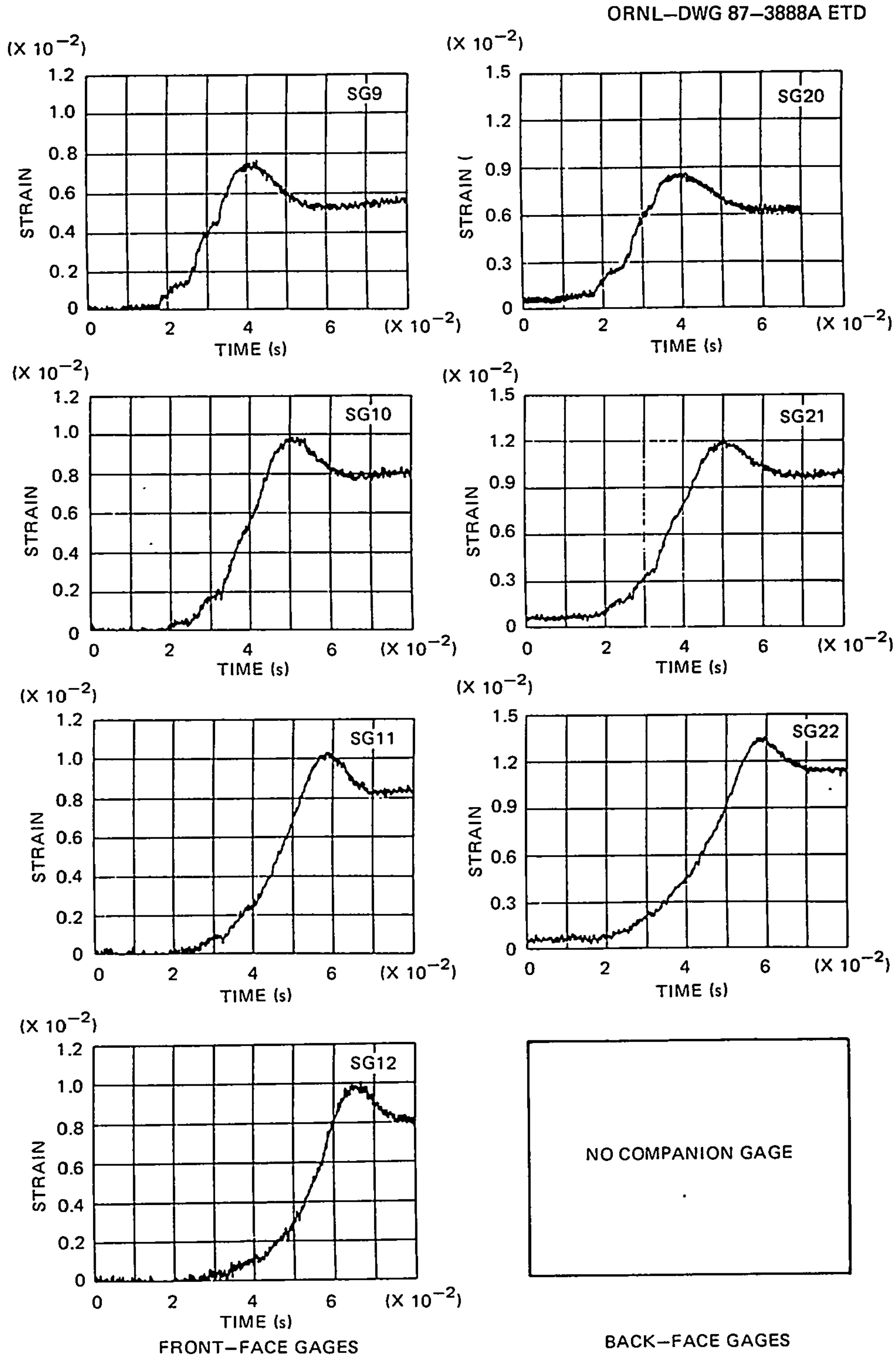

Fig. A.3. Strain histories for companion crack-line gages: test WP-2.1 (gages 9–12 and 20–22).

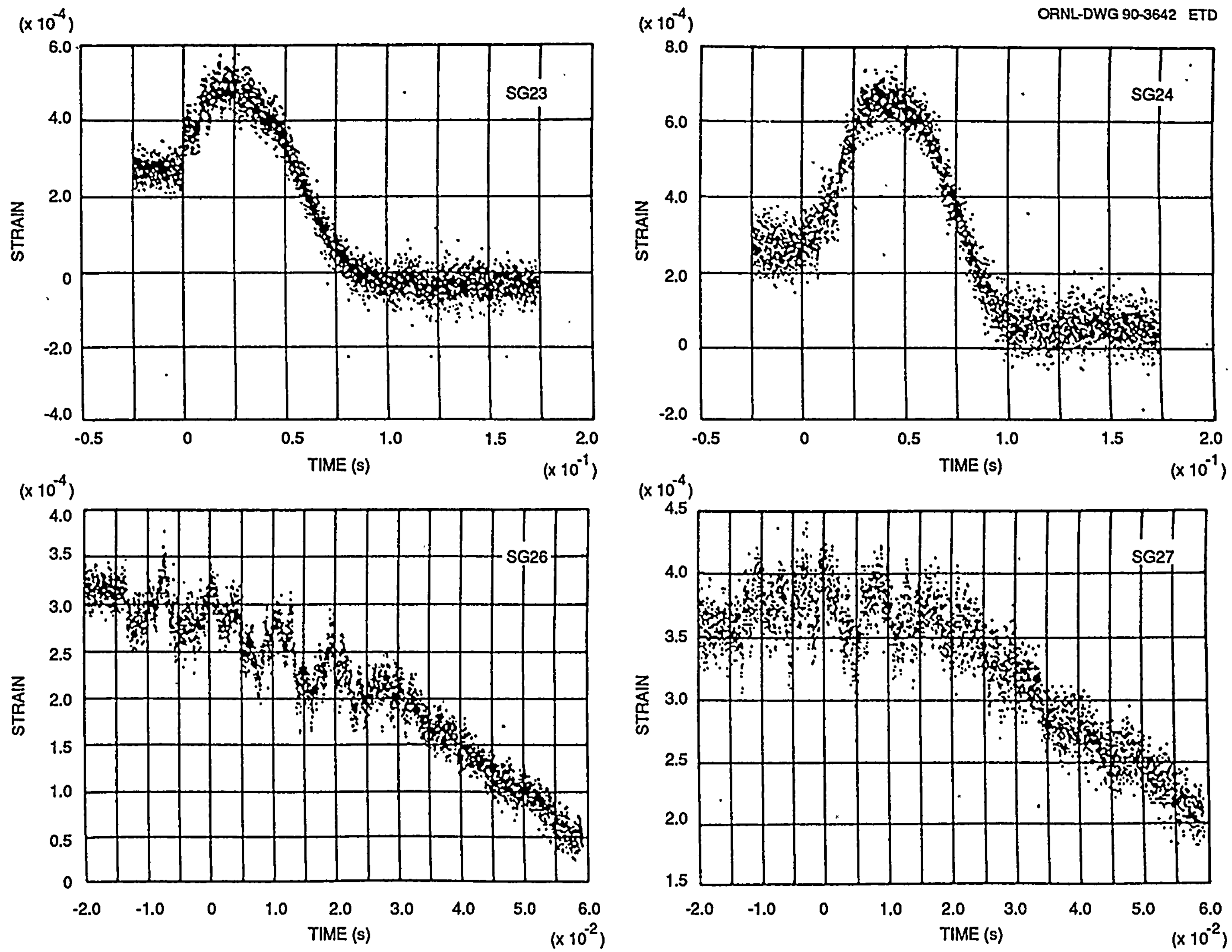

Fig. A.4. Near- and far-field strain histories: test WP-2.1 (gages 23, 24, 26, and 27).

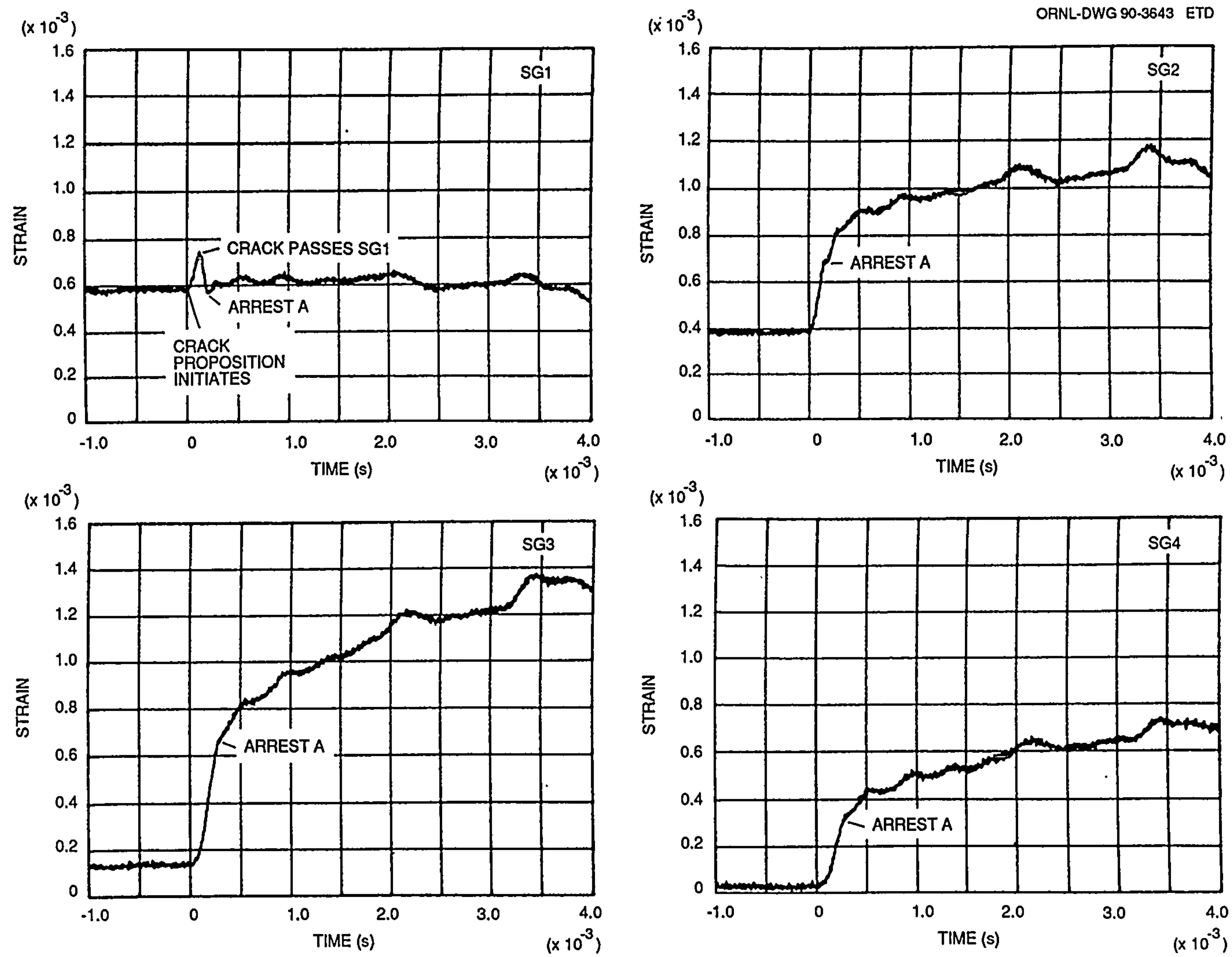

Fig. A.5. Strain histories for gages 1–4 showing crack passing under strain gage 1 and arresting before reaching strain gage 2: test WP-2.1.

ORNL-DWG 90-3644 ETD

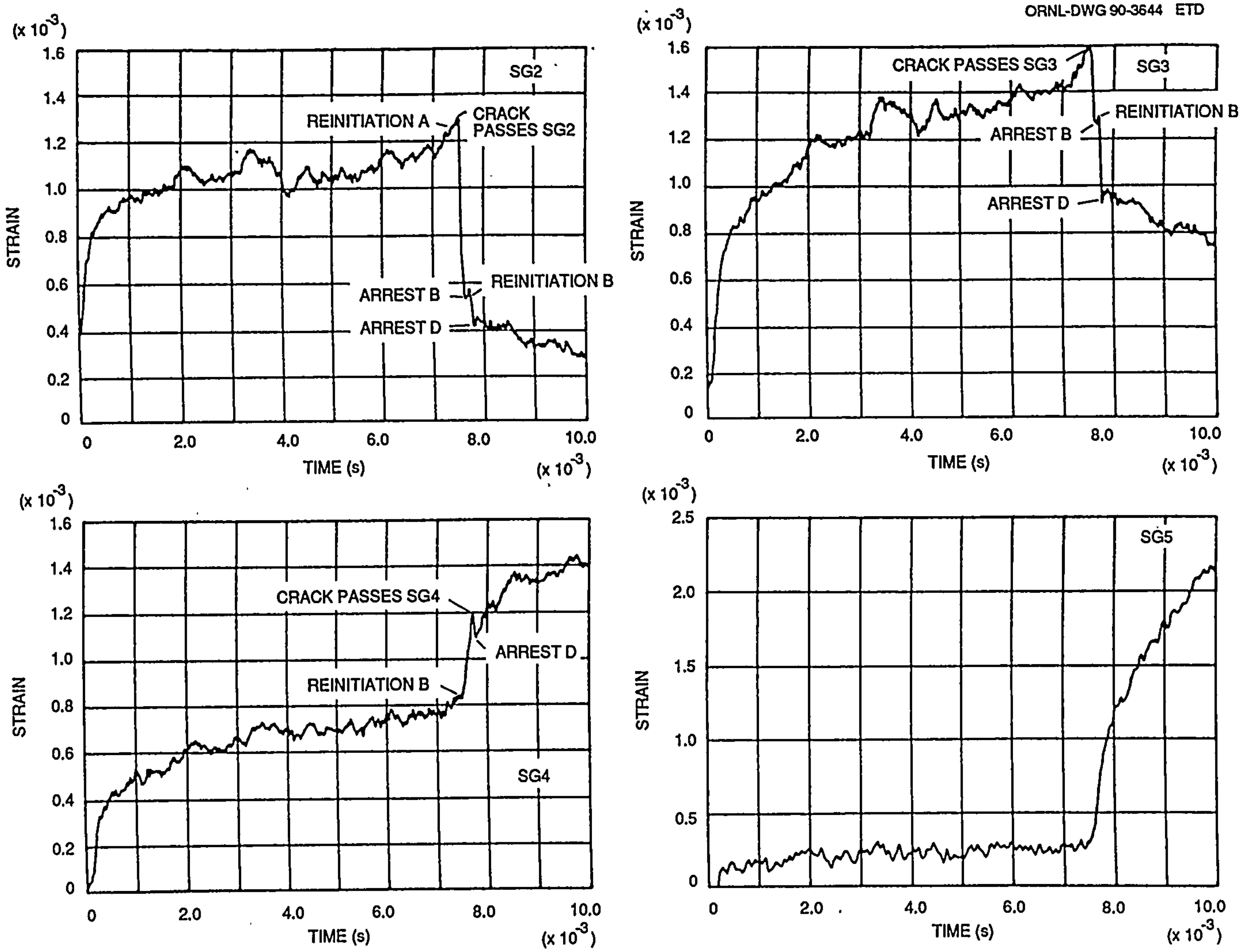

Fig. A.6. Strain histories for gages 2–5 showing crack passing under strain gages 2 and 3, arresting momentarily before passing under strain gage 4, and arresting before passing under gage 5: test WP-2.1.

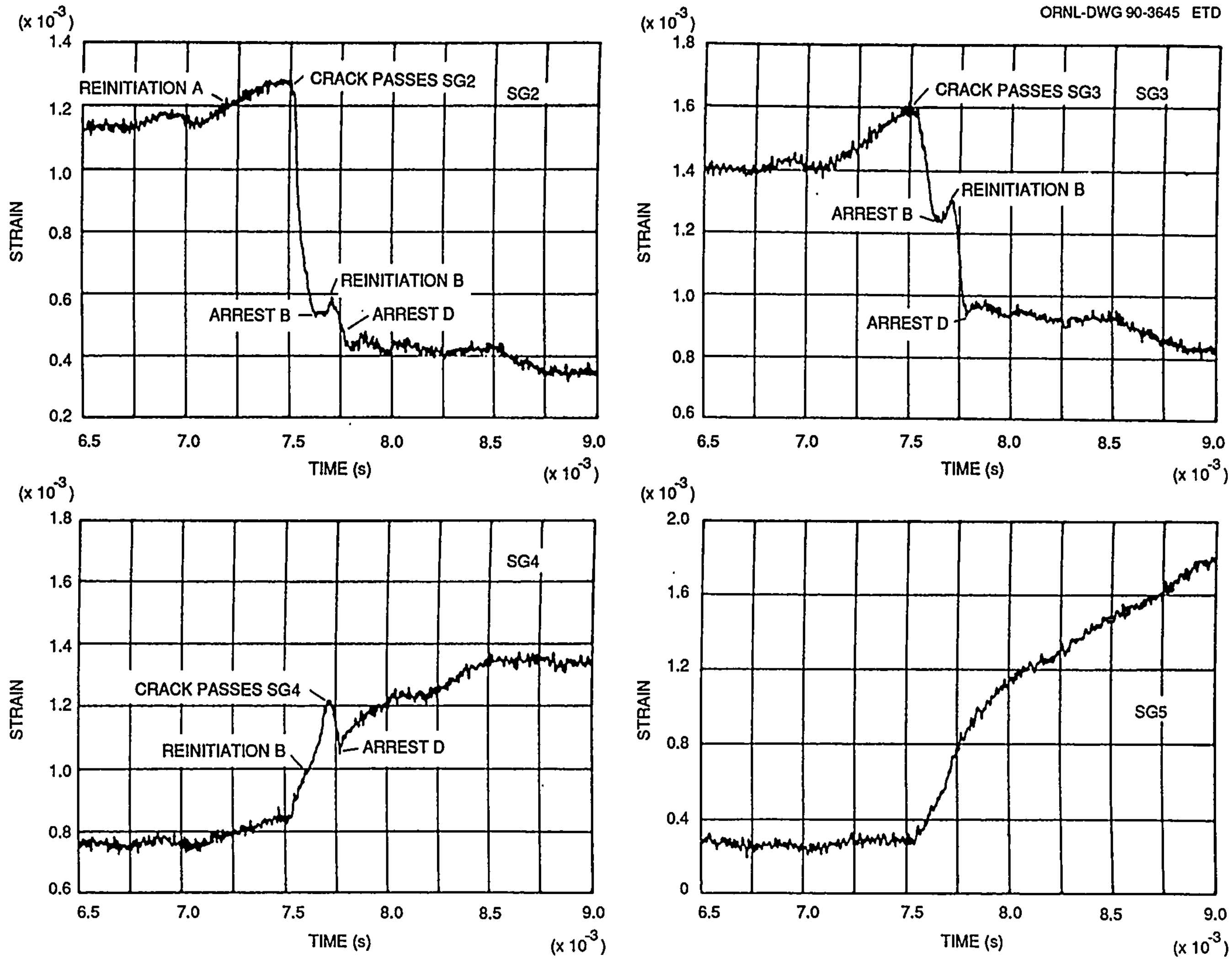

Fig. A.7. Strain histories for gages 2–5 showing momentary arrest between gages 3 and 4: test WP-2.1.

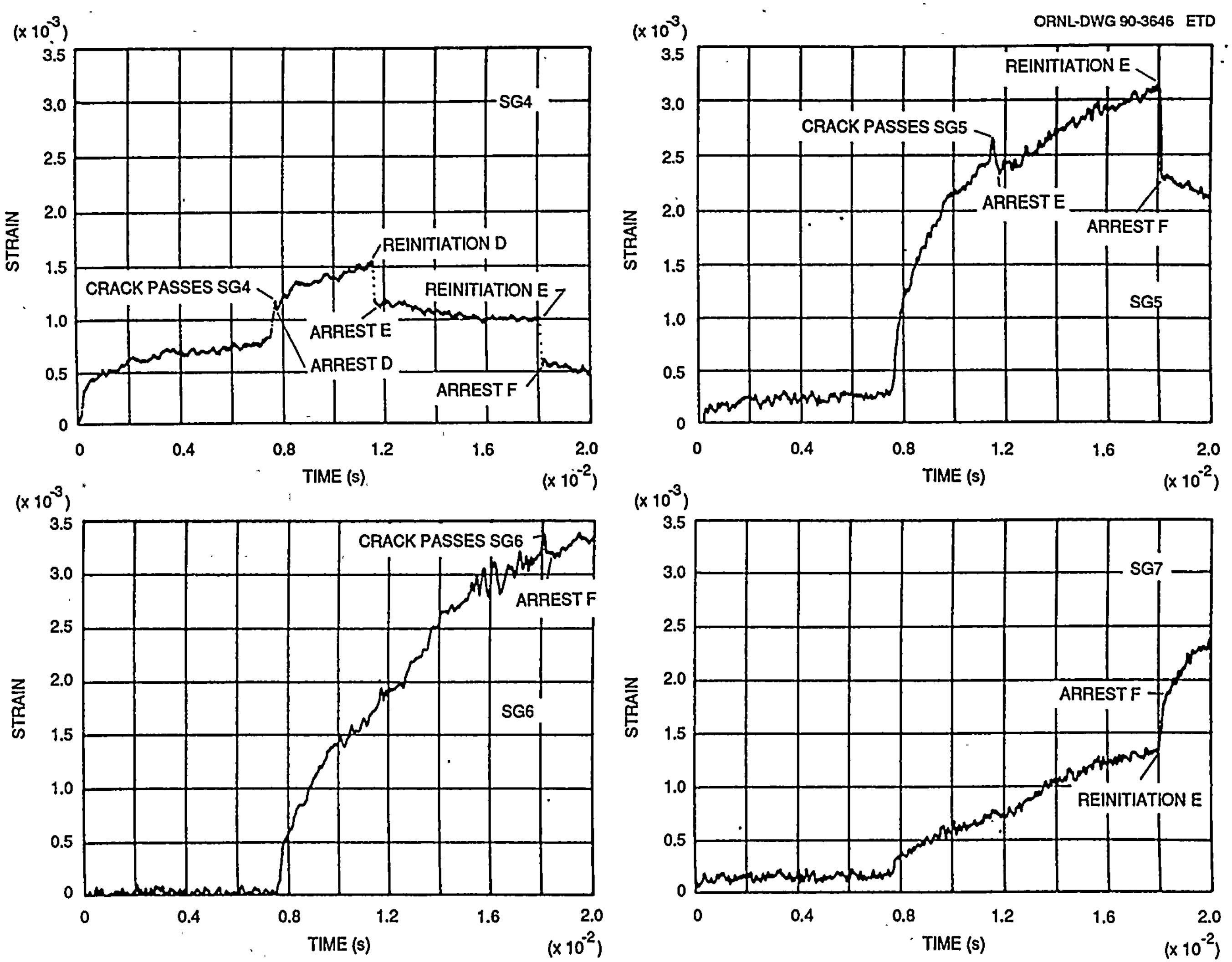

Fig. A.8. Twenty-millisecond records of strain gages 4–7 showing previous crack run-arrest events and crack passing under gage 5 and arresting before reaching gages 6 and 7: test WP-2.1.

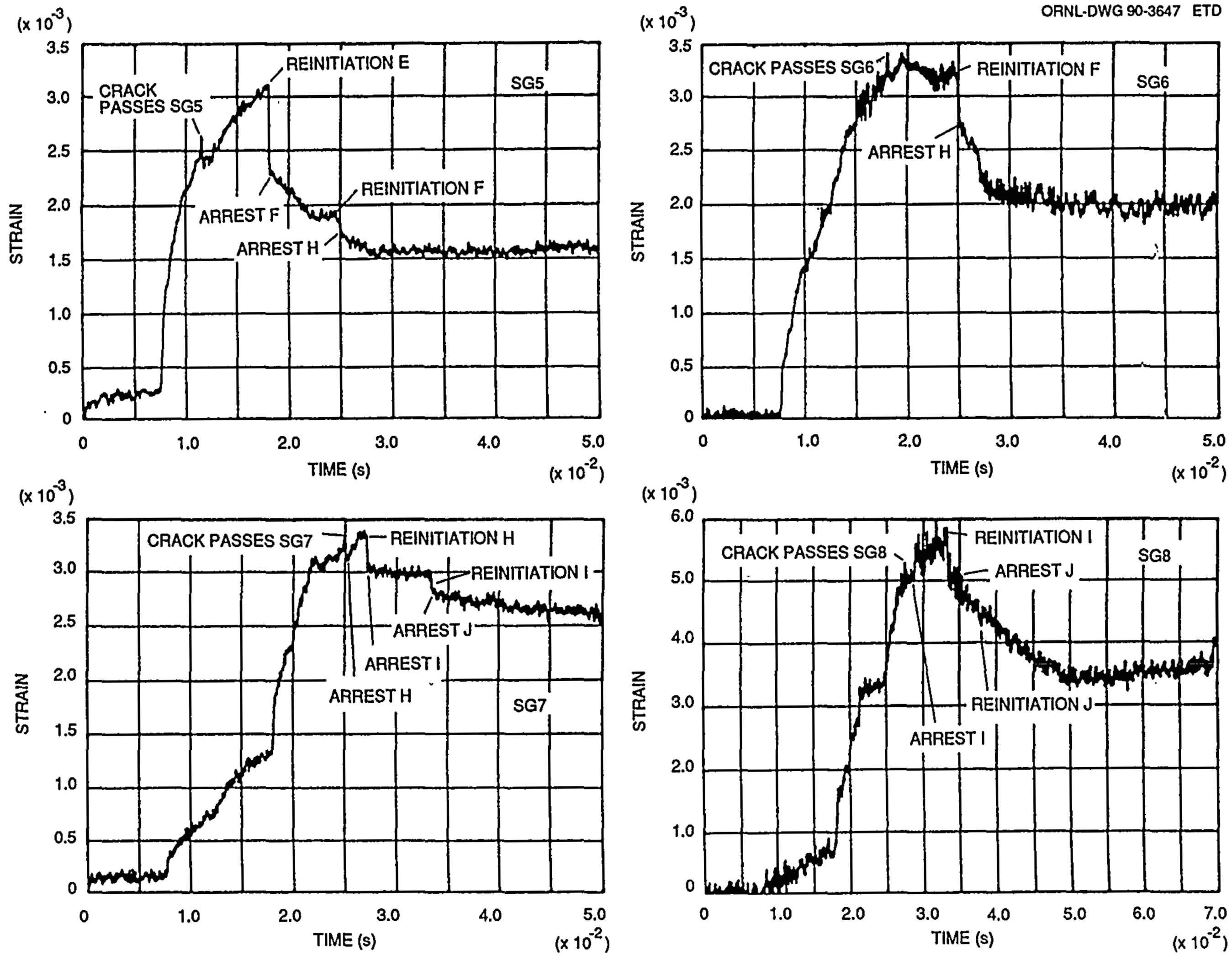

Fig. A.9. Fifty-millisecond records of strain gages 5–8 showing fibrous tearing after a cleavage arrest just past gage 5, followed by cleavage fracture, reinitiation just past gage 6, another arrest, and cleavage fracture reinitiation that passes under gage 8 and arrests: test WP-2.1.

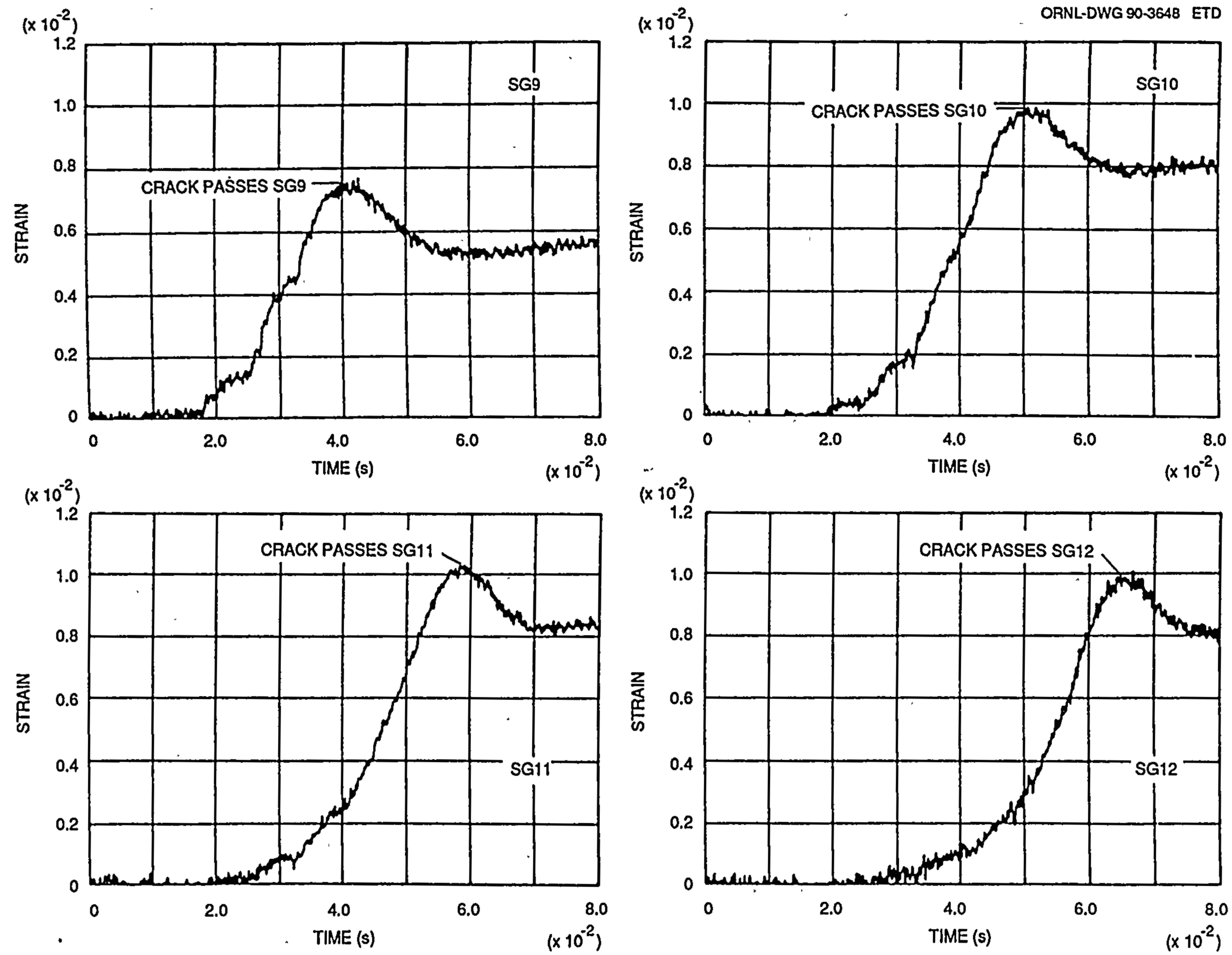

Fig. A.10. Strain histories of gages 9–12 showing fibrous tearing past these gages: test WP-2.1.

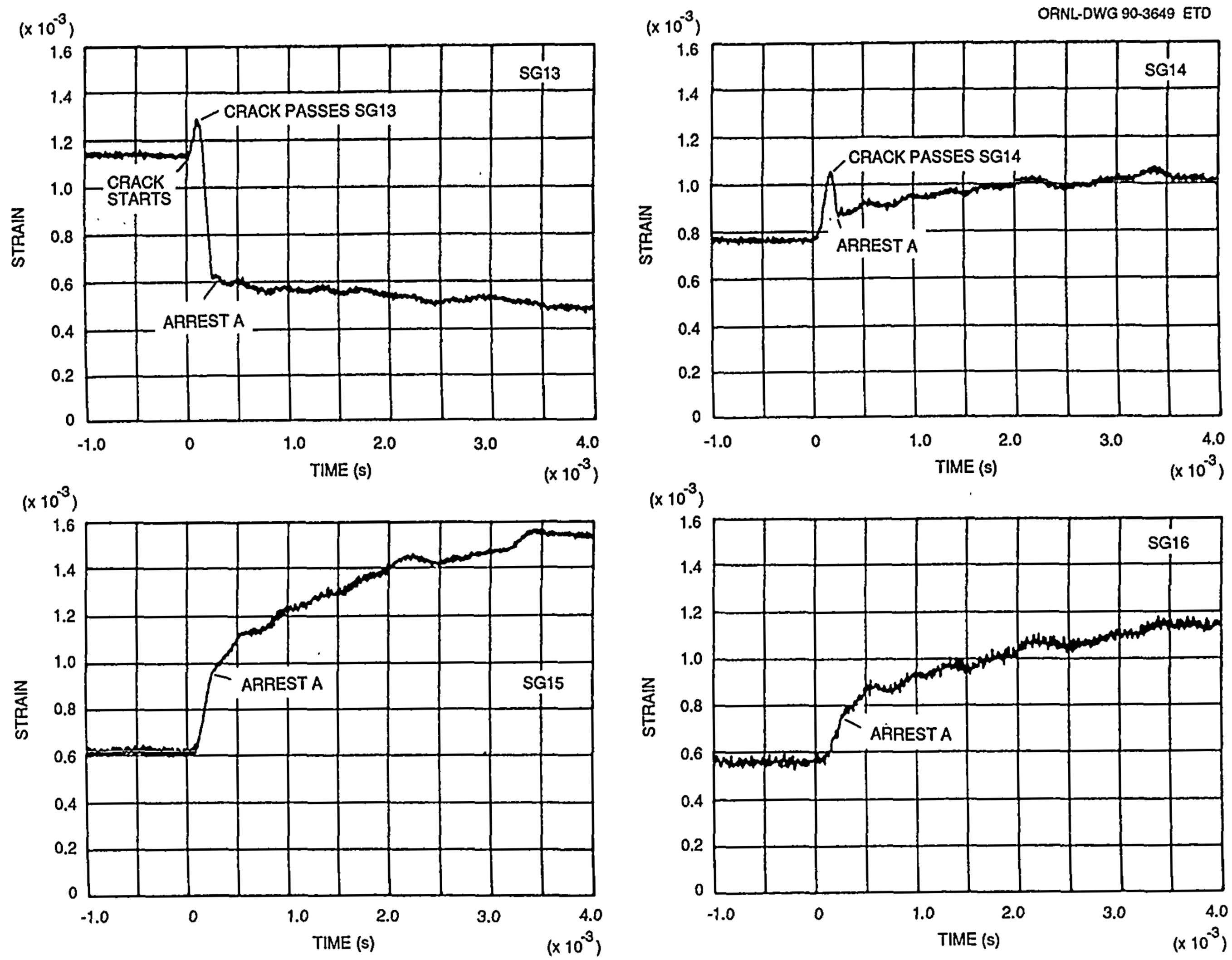

Fig. A.11. Strain histories for gages 13–16 showing crack passing under gages 13 and 14 before arresting before gage 15: test WP-2.1.

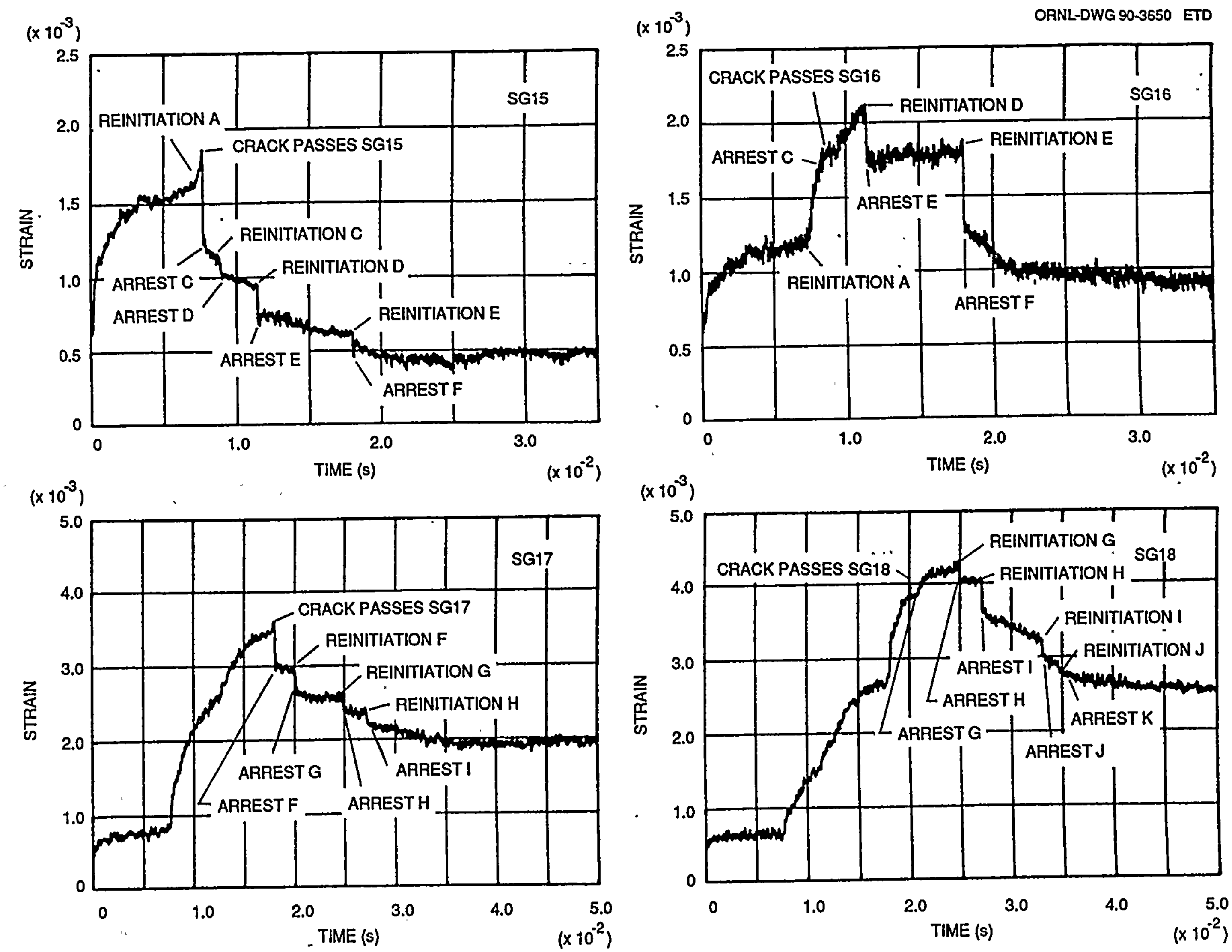

Fig. A.12. Strain histories for gages 15–18 showing crack passing under gage 15, reinitiating, passing under gage 16, arresting, reinitiating, passing under gage 17, arresting, reinitiating, and passing under gage 18: test WP-2.1.

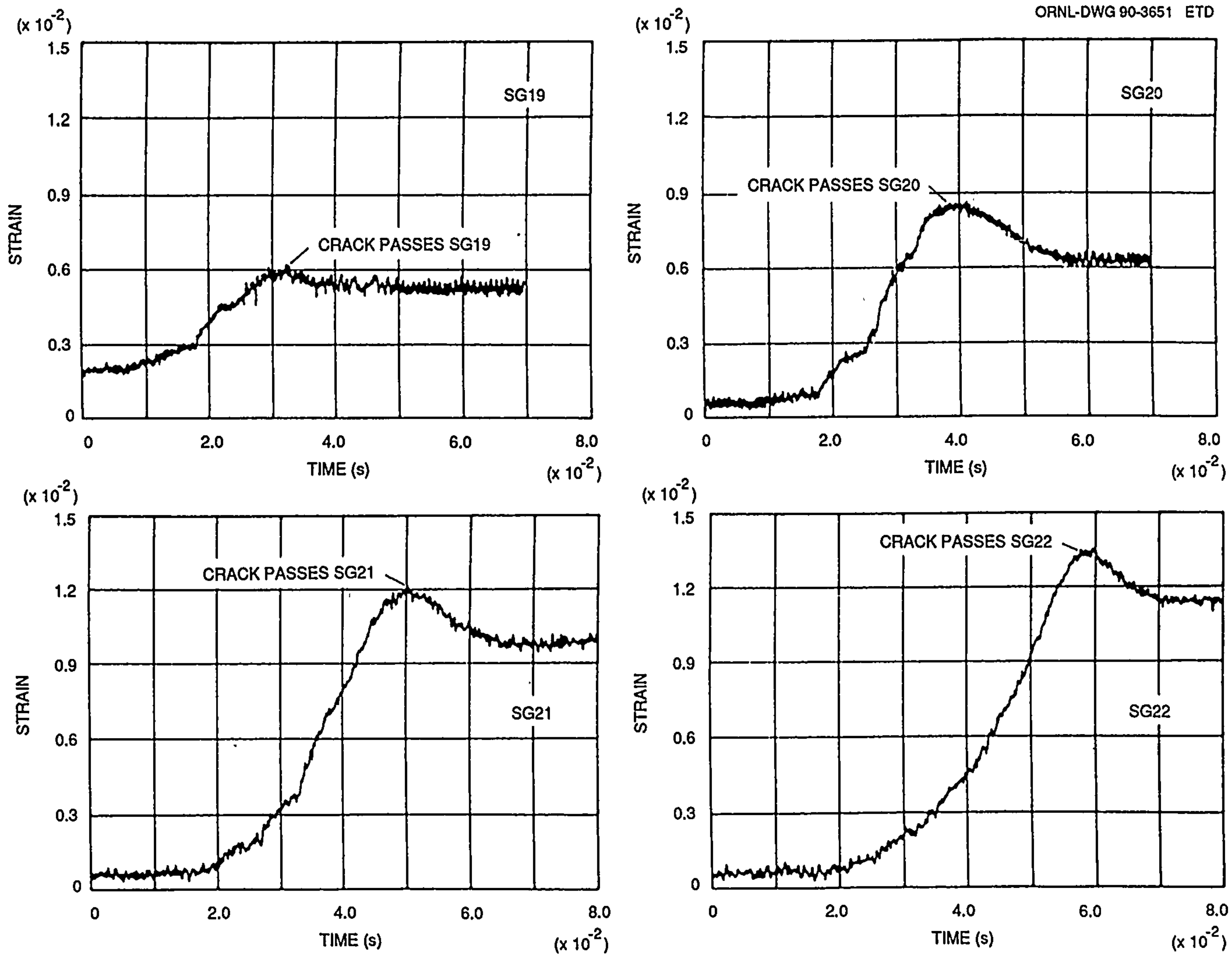

Fig. A.13. Strain histories for gages 19–22 showing fibrous tearing past these gages: test WP-2.1.

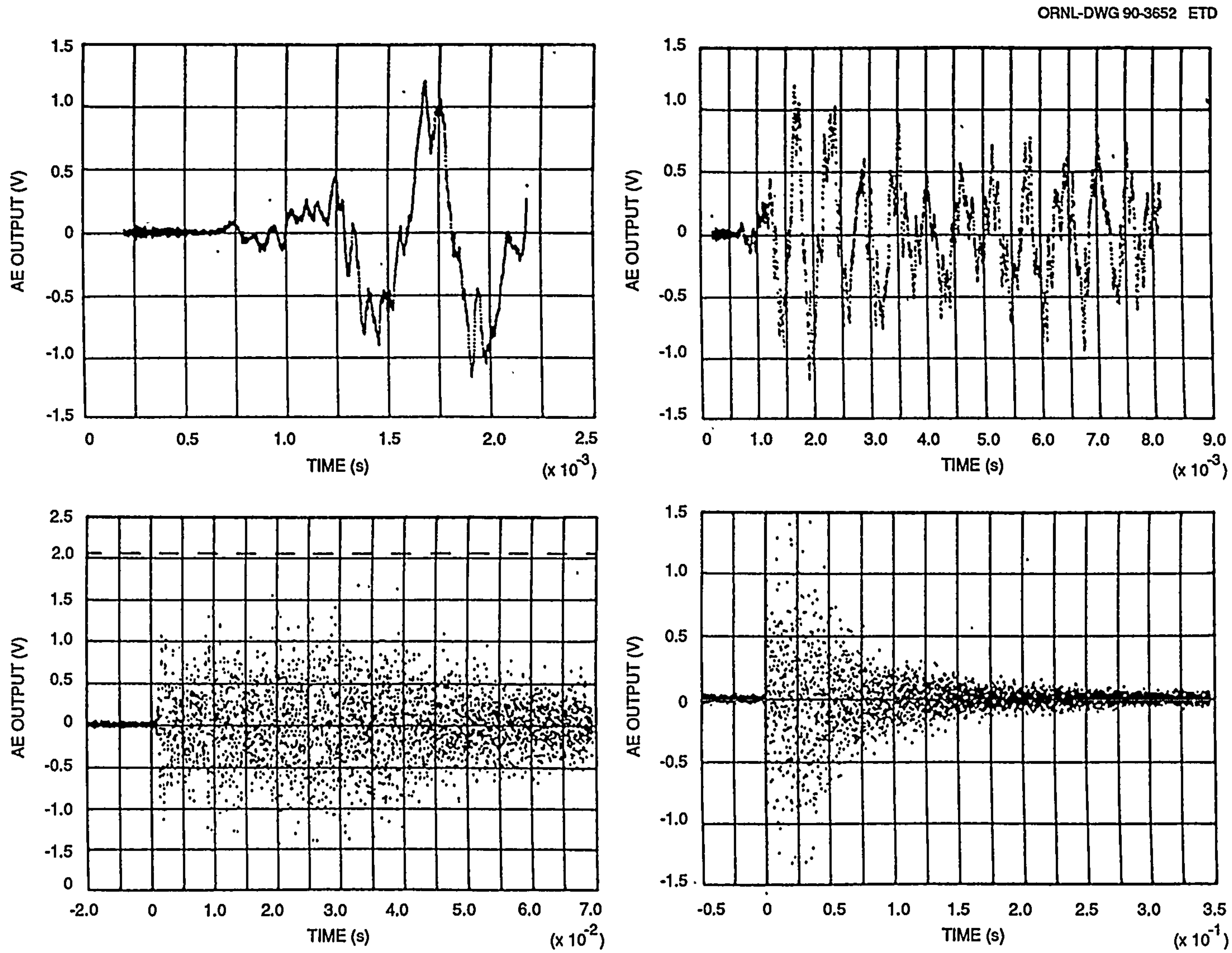

Fig. A.14. AE results for various time resolutions: test WP-2.1.

are shown in Fig. A.15. Front- and back-face COD results for gages located at a/w = 0.150 are presented in Fig. A.16. COD values obtained from the back-face COD gage, at comparable times during the fracture event, were consistently higher than values obtained from the front-face COD gage. This correlates with the results presented previously in Fig. 5.7, which indicated that for the time period monitored by the COD gages, the apparent crack front advance was more rapid at the back-face of the plate. As shown in Fig. A.16, the measurement capacities of the front- and back-face COD gages were exceeded ~36 and 31 ms, respectively, into the fracture event.

A.2 TEST WP-2.2

A.2.1 Strain Gages

Figures A.17 to A.20 present strain histories [see Fig. 4.8(*b*) for strain-gage locations] for companion front- and back-face crack-line gages. Figure A.17 shows the cleavage crack propagating past gages 1 and 2 on the plate front face and gage 13 on the plate back face (strain gage 14 did not operate correctly). Propagation of the cleavage crack past gages 3 and 4 on the plate front face and gages 15 and 16 on the plate back face is shown in Fig. A.18. Continued propagation of the cleavage crack past gages 5 and 6 on the plate front face and gages 17 and 18 on the plate back face is presented in Fig. A.19. Also shown in Fig. A.19 are arrest of cleavage crack propagation just past strain gages 6 (plate front face) and 18 (plate back face) and multiple reinitiations and arrests of cleavage crack propagation. Cleavage crack propagation past gages 7 and 8 on the plate front face and gages 19 and 20 on the plate back face, with subsequent arrests and reinitiations of cleavage crack propagation, are shown in Fig. A.20. Strain histories for front-face crack-line gages 9–12 (Fig. A.21) show arrest of cleavage crack propagation just past gage 9 with subsequent fibrous crack propagation past gages 10–12. Figure A.22 presents the strain history for near-field gage 21 (*a*) during the cleavage crack run-arrest events and (*b*) during the entire fracture process. Far-field strain histories for gages 22–25 during the cleavage crack run-arrest events are presented in Fig. A.23. Strain histories during the entire fracture process for far-field gages 22–25 are presented in Fig. A.24.

A.2.2 Additional Instrumentation

Front- and back-face COD histories at two time resolutions are presented in Fig. A.25. Longitudinal accelerations recorded by a "damped" accelerometer mounted on the specimen's centerline at 3.458 m below the crack plane are presented in Fig. A.26 at two time resolutions. Also presented in Fig. A.26 are dynamic displacements of the specimen, relative to that of the large columns of the testing machine, as measured 3.453 m below the crack plane. The dynamic displacement results cover the same time intervals as the accelerometer data.

ORNL–DWG 87–3892 ETD

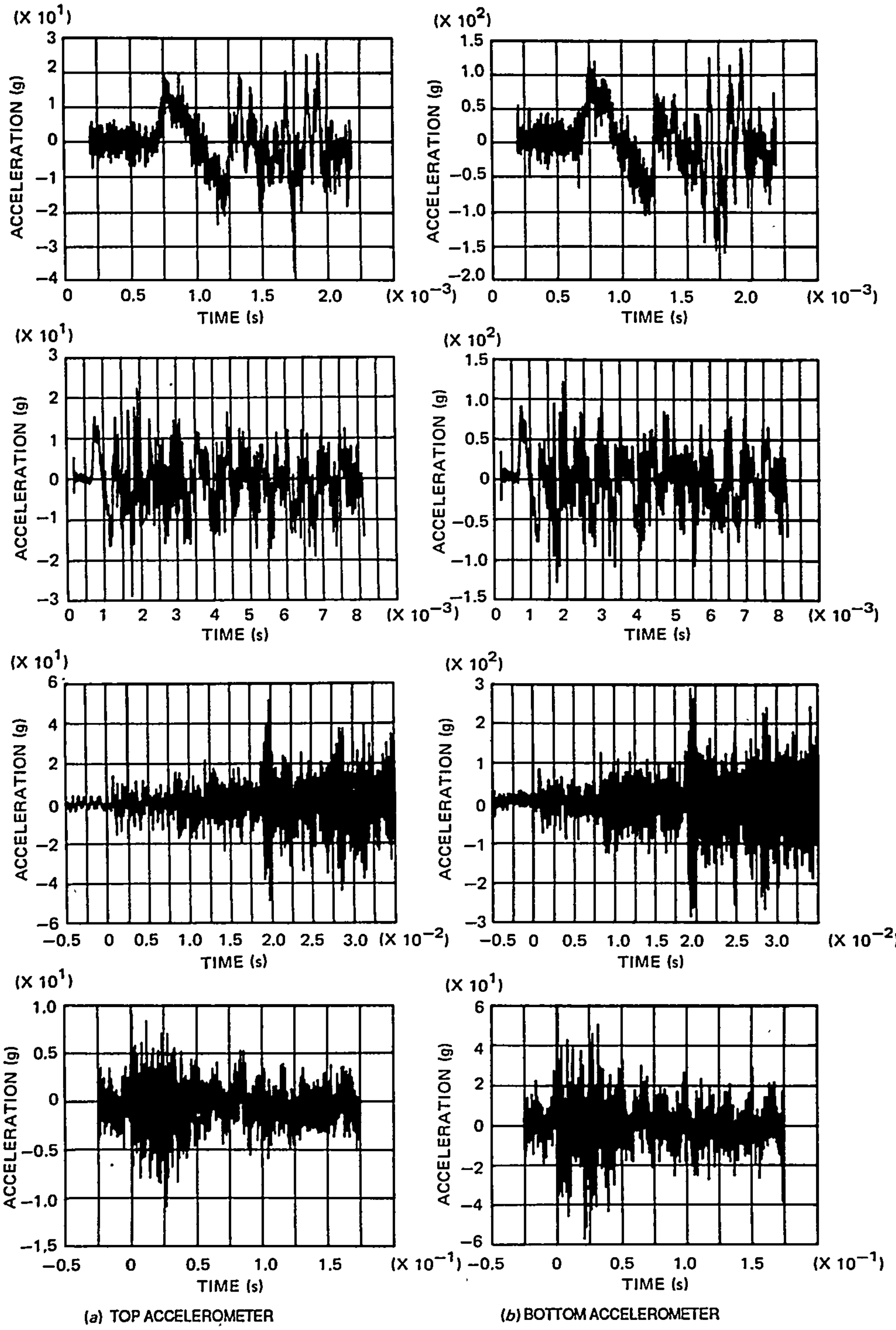

Fig. A.15. Longitudinal acceleration results at various time resolutions measured by top and bottom "damped" accelerometers mounted 3.653 m above and 3.655 m below crack plane, respectively: test WP-2.1.

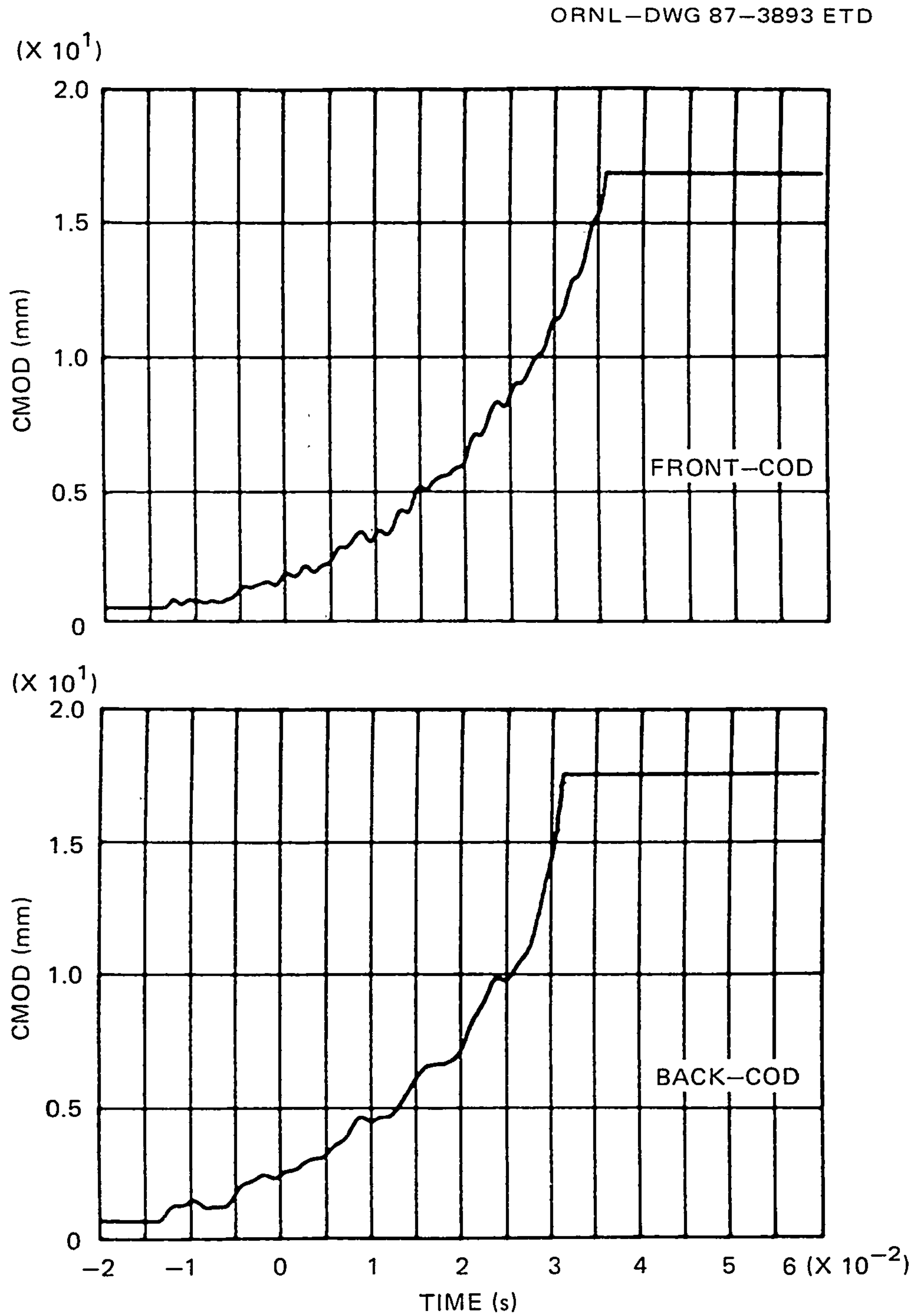

Fig. A.16. Front and back COD histories obtained from gages mounted at a/w = 0.15: test WP-2.1.

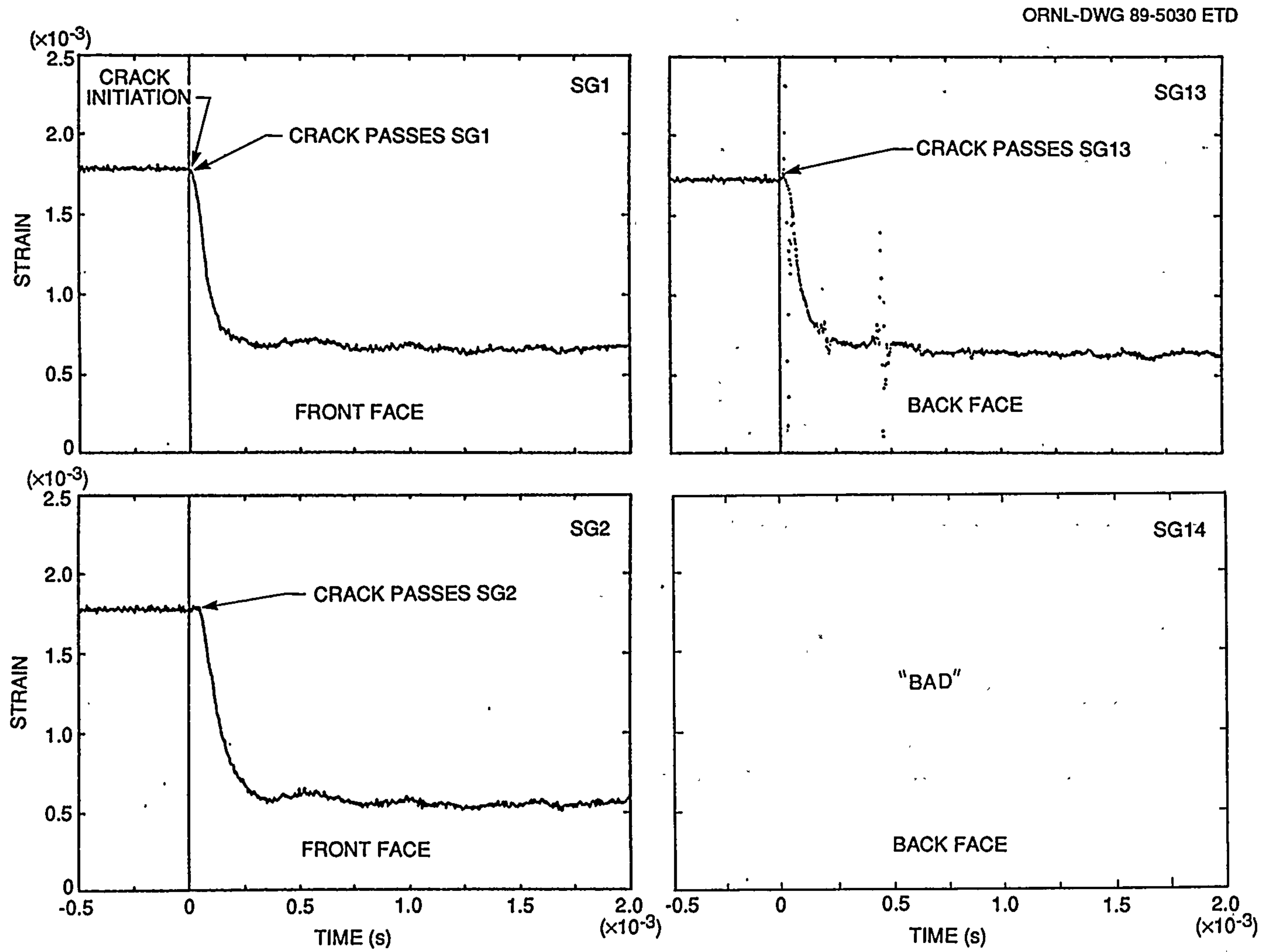

Fig. A.17. Strain histories for companion crack-line gages showing cleavage crack passing these gages: test WP-2.2 (gages 1, 2, and 13).

ORNL-DWG 89-5031 ETD

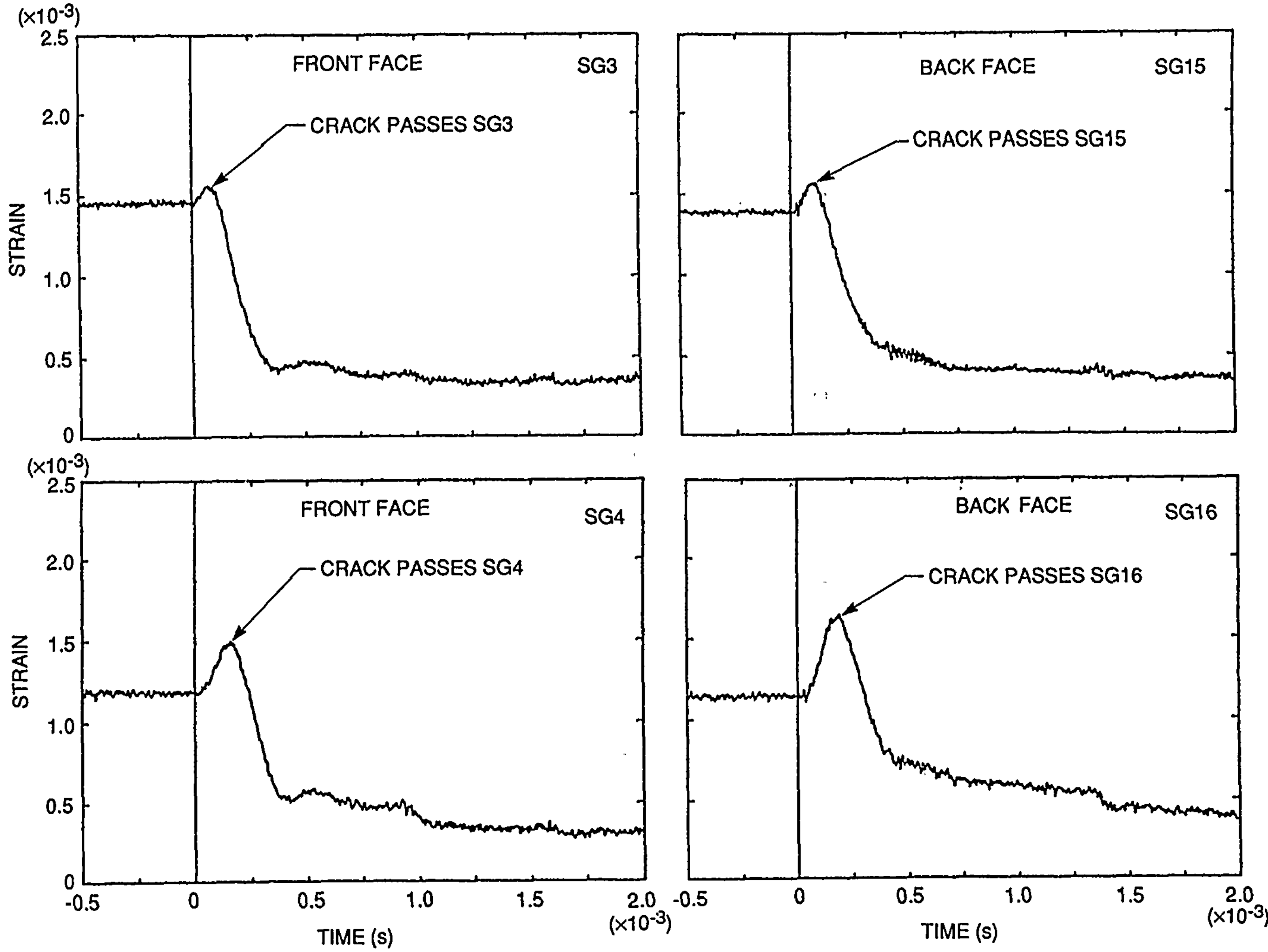

Fig. A.18. Strain histories for companion crack-line gages showing cleavage crack passing these gages: test WP-2.2 (gages 3, 4, 15, and 16).

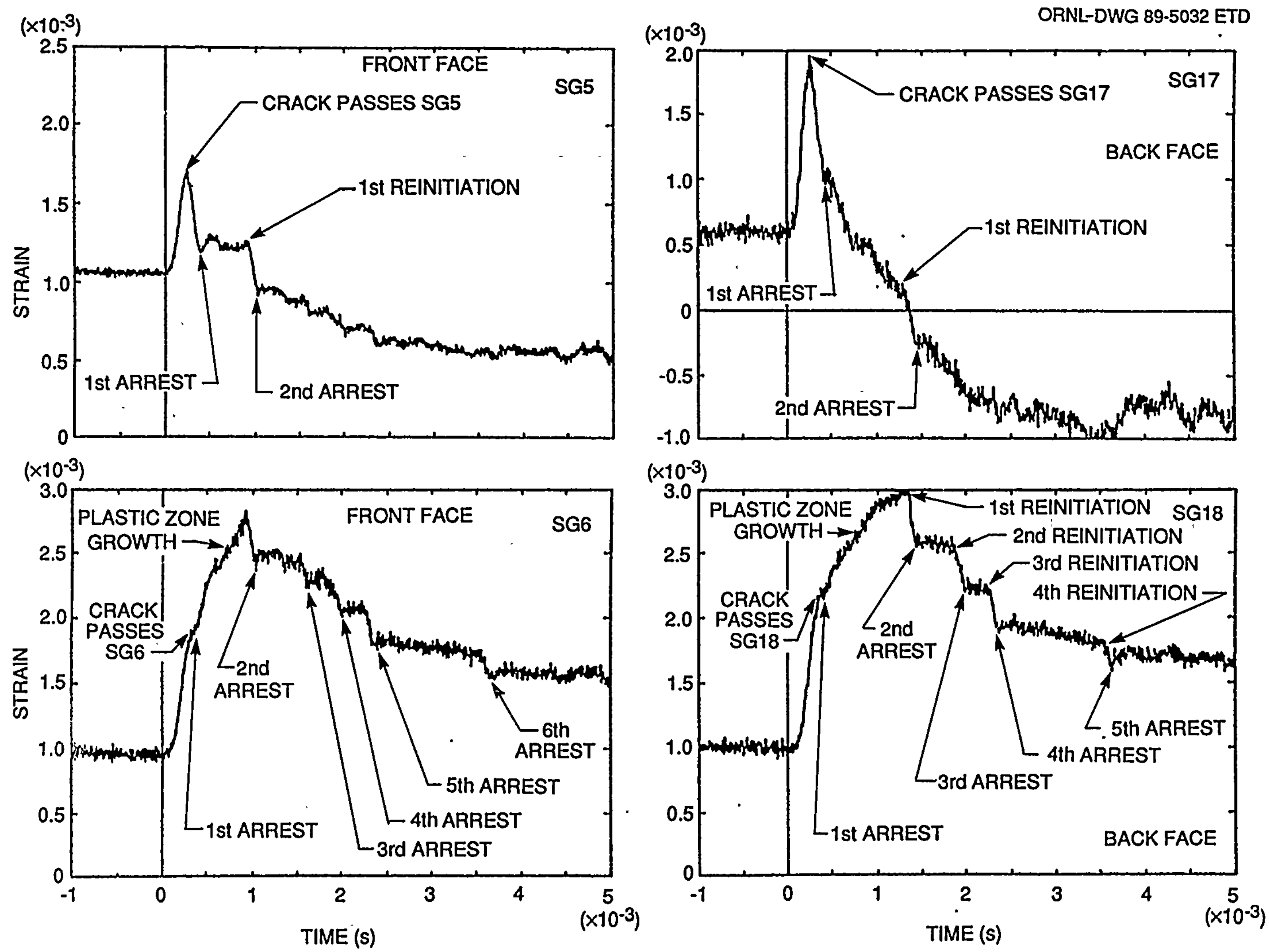

Fig. A.19. Strain histories for companion crack-line gages showing cleavage crack propagating past gages 5 and 17 and arresting just past gages 6 and 18: test WP-2.2.

ORNL-DWG 89-5033 ETD

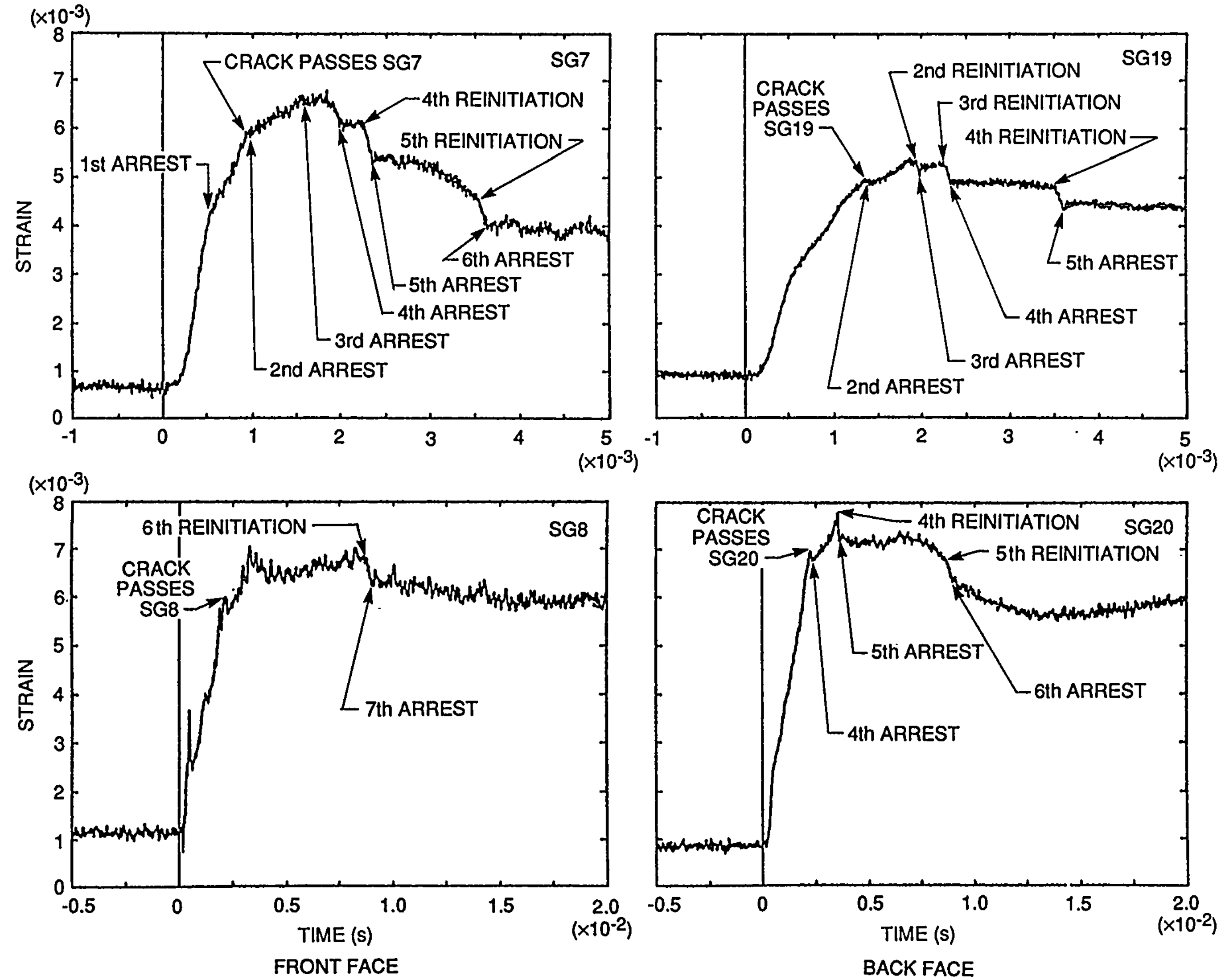

Fig. A.20. Strain histories for companion crack-line gages showing cleavage crack passing these gages followed by cleavage crack run-arrest events: test WP-2.2 (gages 7, 8, 19, and 20).

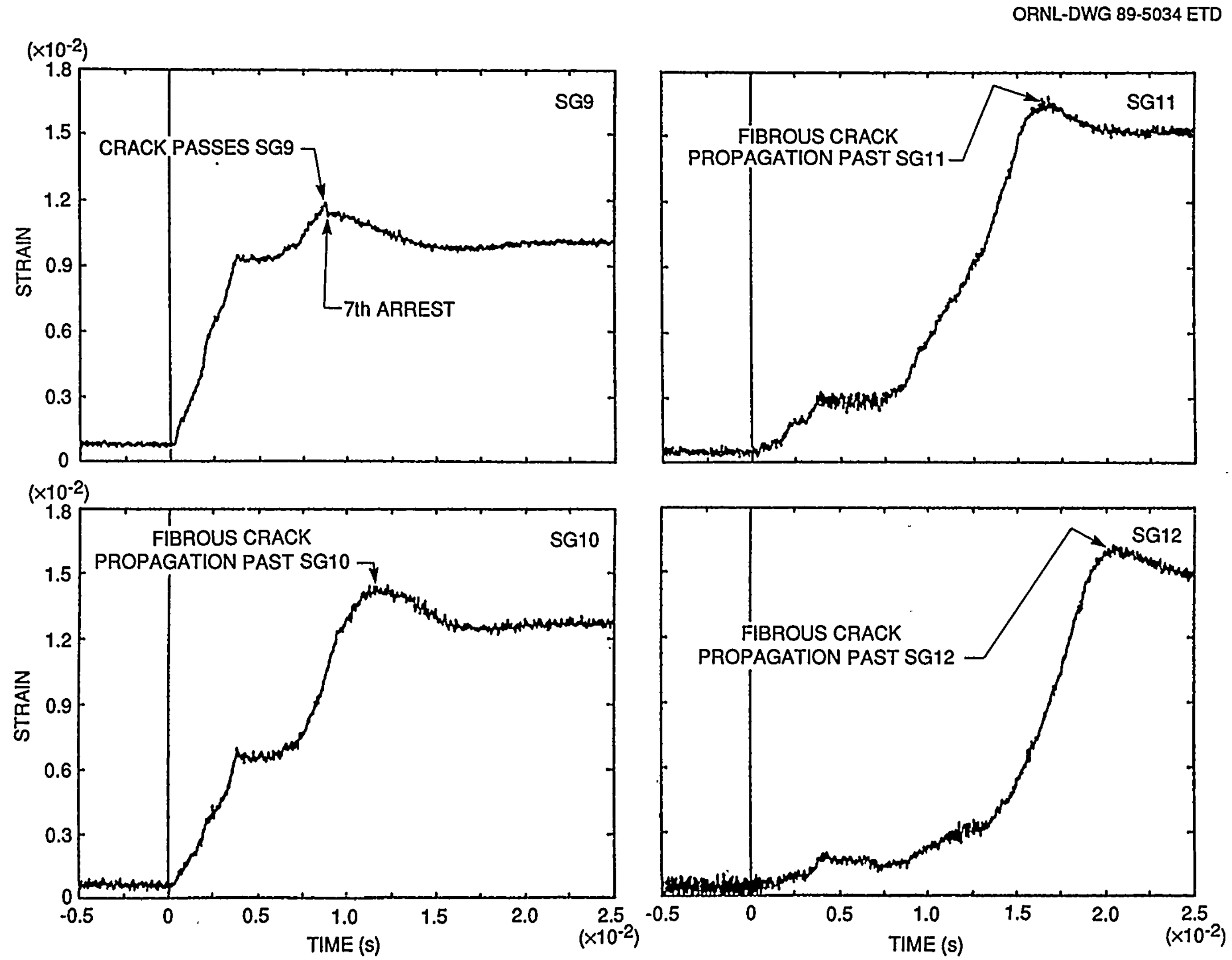

Fig. A.21. Strain histories for front-face crack-line gages showing arrest of cleavage crack propagation past gage 9 with subsequent fibrous crack propagation past gages 10–12: test WP-2.2.

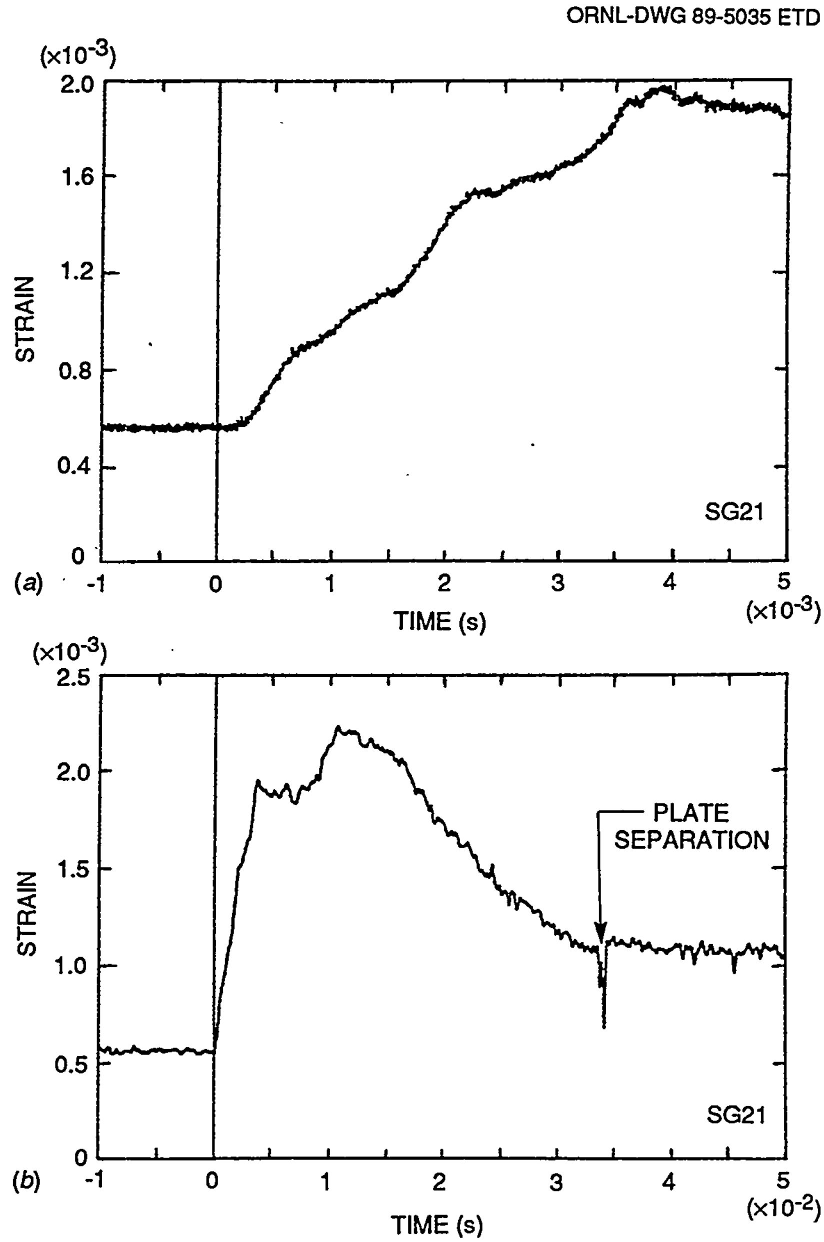

Fig. A.22. Strain history for near-field gage 21 (*a*) during cleavage run-arrest events and (*b*) during entire fracture process: test WP-2.2.

ORNL-DWG 89-5036 ETD

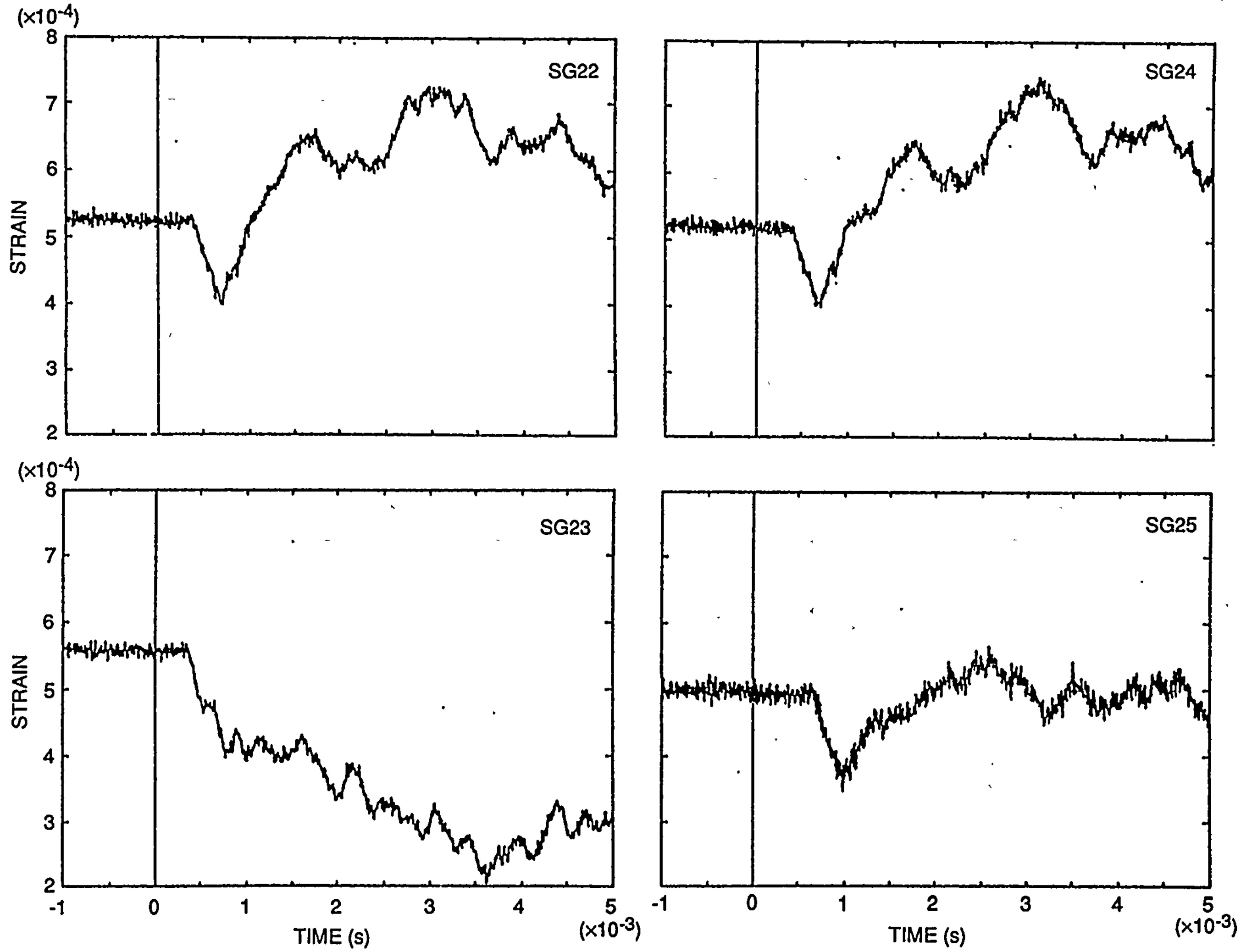

Fig. A.23. Strain histories for far-field gages 22–25 during cleavage run-arrest events: test WP-2.2.

ORNL-DWG 89-5037 ETD

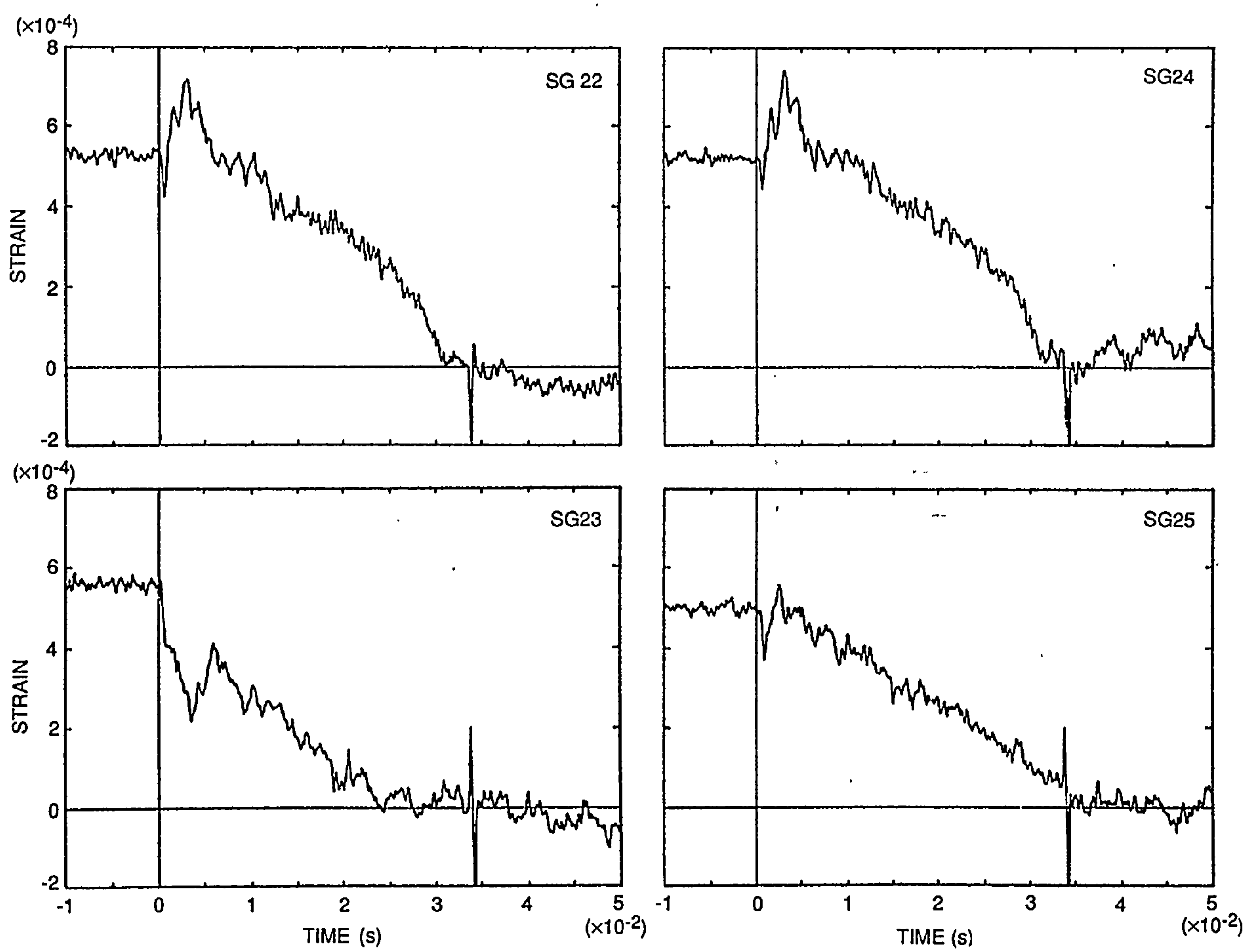

Fig. A.24. Strain histories for far-field gages 22–25 during entire fracture process: test WP-2.2.

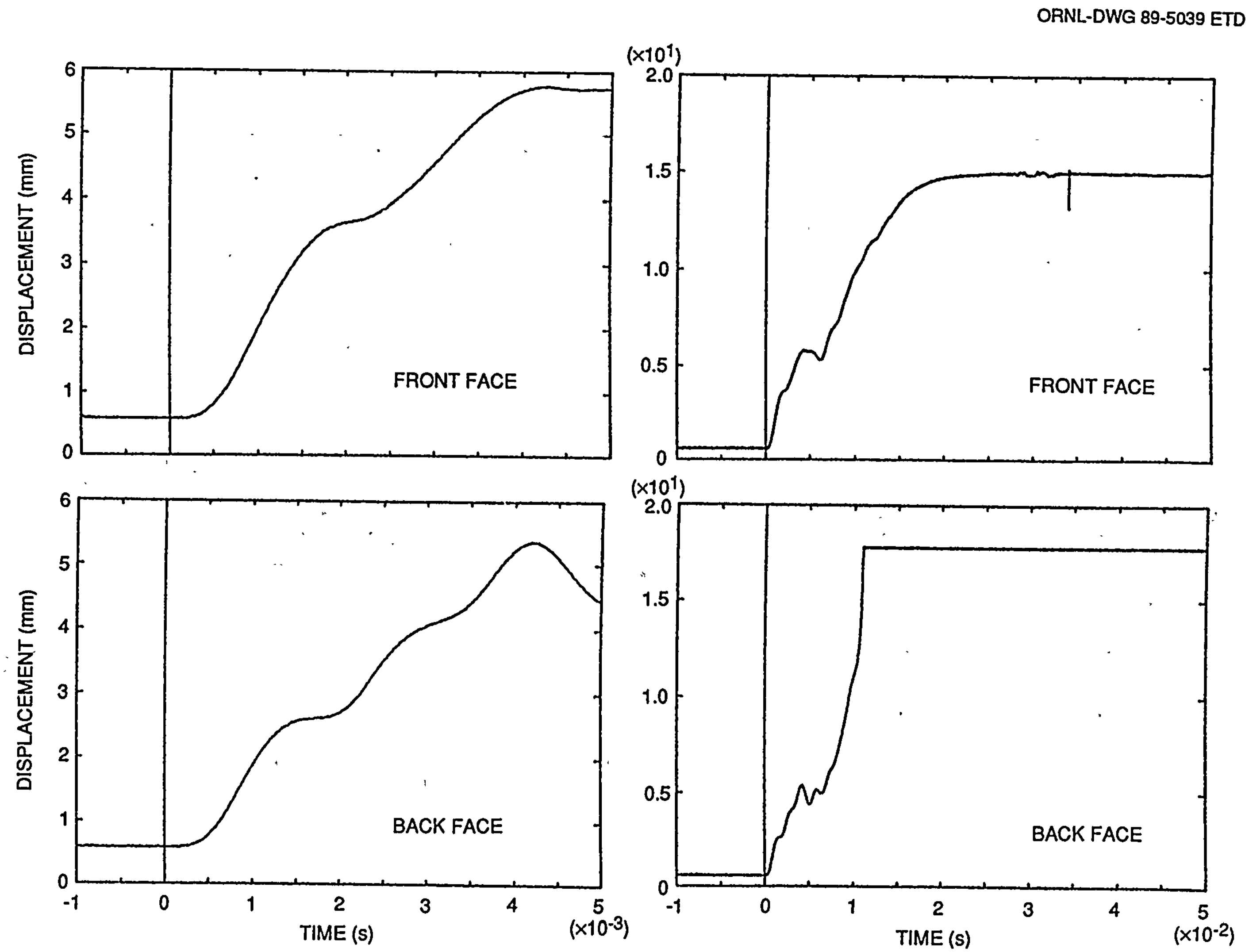

Fig. A.25. Front- and back-face COD histories at two time resolutions: test WP-2.2.

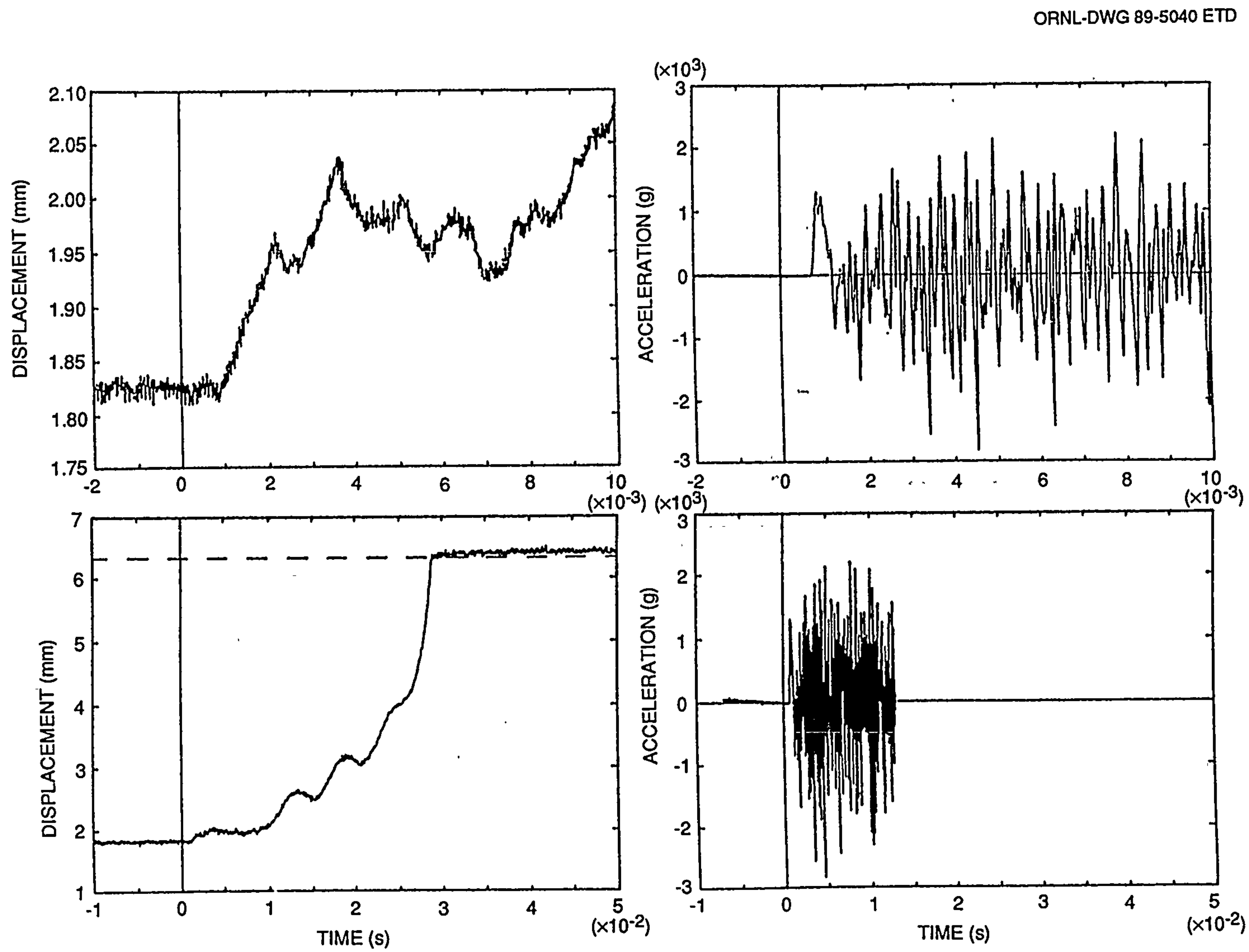

Fig. A.26. Dynamic displacement and longitudinal acceleration histories at two time resolutions: test WP-2.2.

A.3 TEST WP-2.3

A.3.1 Strain Gages

Strain-gage records, shown in Figs. A.27 to A.29 for companion crack-line gages [see Fig. 4.8(*c*) for strain-gage locations], indicate that four major cleavage crack run-arrest events occurred during the test. Near- and far-field strain-gage results are presented in Fig. A.30. More detailed information on the cleavage crack run-arrest events followed by fibrous tearing is presented in Figs. A.31 to A.39. Figure A.31 shows the crack passing under strain gages 1 and 2 and arresting (t = 0.222 ms) before reaching strain gages 3 and 4. Reinitiation of crack propagation at t = 12.489 ms, as detected by strain gages 1 and 2, and the crack passing strain gage 3 (t = 12.574) with a subsequent arrest (t = 12.749 ms) before reaching strain gage 4 are shown in Fig. A.32. Strain histories for gages 3 and 4 in the figure also show reinitiation of crack propagation at t = 37.344 ms. Propagation of the crack past strain gage 5, a subsequent arrest (t = 37.524 ms) before reaching strain gage 6, and reinitiation (t = 43.324 ms) with propagation past strain gages 6–8 are shown in Fig. A.33. An expanded time scale in Fig. A.34 for strain gages 5–8 shows the crack (now converted to fibrous tearing) passing strain gages 6–8. Propagation of the crack (fibrous tearing) past strain gages 9–12 is presented in Fig. A.35. Strain histories presented in Fig. A.36 for back-face gages 13–15 show the crack passing gages 13 (t = 0.040 ms) and 14 (t = 0.114 ms) and then arresting (t = 0.212 ms) before reaching gage 15. Multiple crack run-arrest events, as detected by strain gages 13–15, are presented in Fig. A.37. In particular, reinitiations at t = 3.160, 13.004, and 38.464 ms are evident. Although detailed interpretation of the strain output for gage 17 is not possible because of signal noise, results for strain gage 18 in Fig. A.38 indicate the early crack run-arrest events followed much later by the crack passing (t = 688 ms) the gage. Propagation of the crack (fibrous tearing) past strain gages 19–22 is shown in Fig. A.39.

A.3.2 Additional Instrumentation

Longitudinal accelerations recorded by "damped" accelerometers mounted on the specimen's centerline at 3.585 m above (top) and 3.589 m below (bottom) the crack plane are presented in Fig. A.40. Results obtained from the displacement gage mounted at the same location as the bottom accelerometer are presented in Fig. A.41. Front- and back-face-COD results obtained from gages located at a/w = 0.150 are presented in Fig. A.42. AE results obtained from a transducer mounted on the lower pull tab are presented for four levels of time resolution in Fig. A.43.

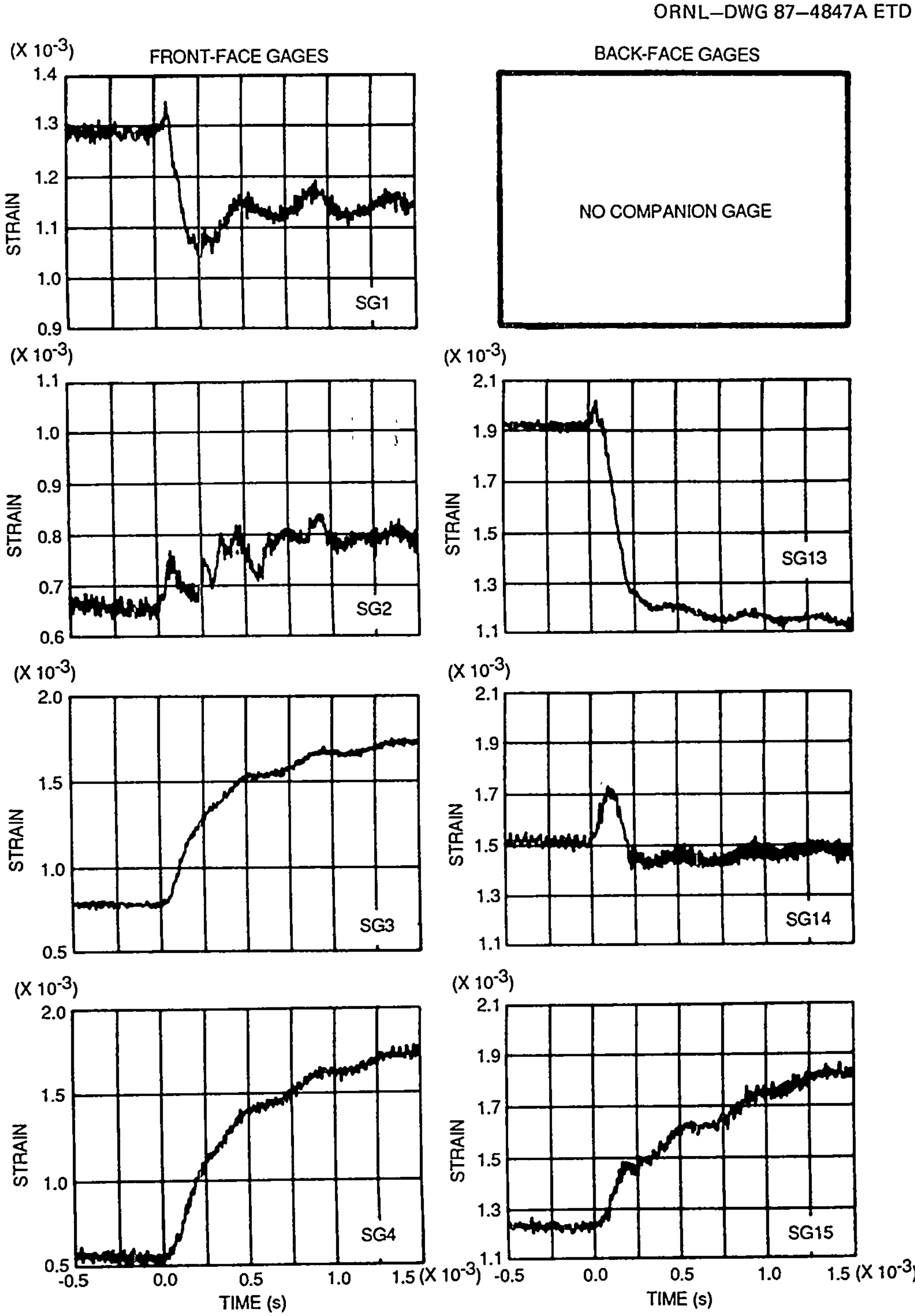

Fig. A.27. Strain histories for companion crack-line gages: test WP-2.3 (gages 1–4 and 13–15).

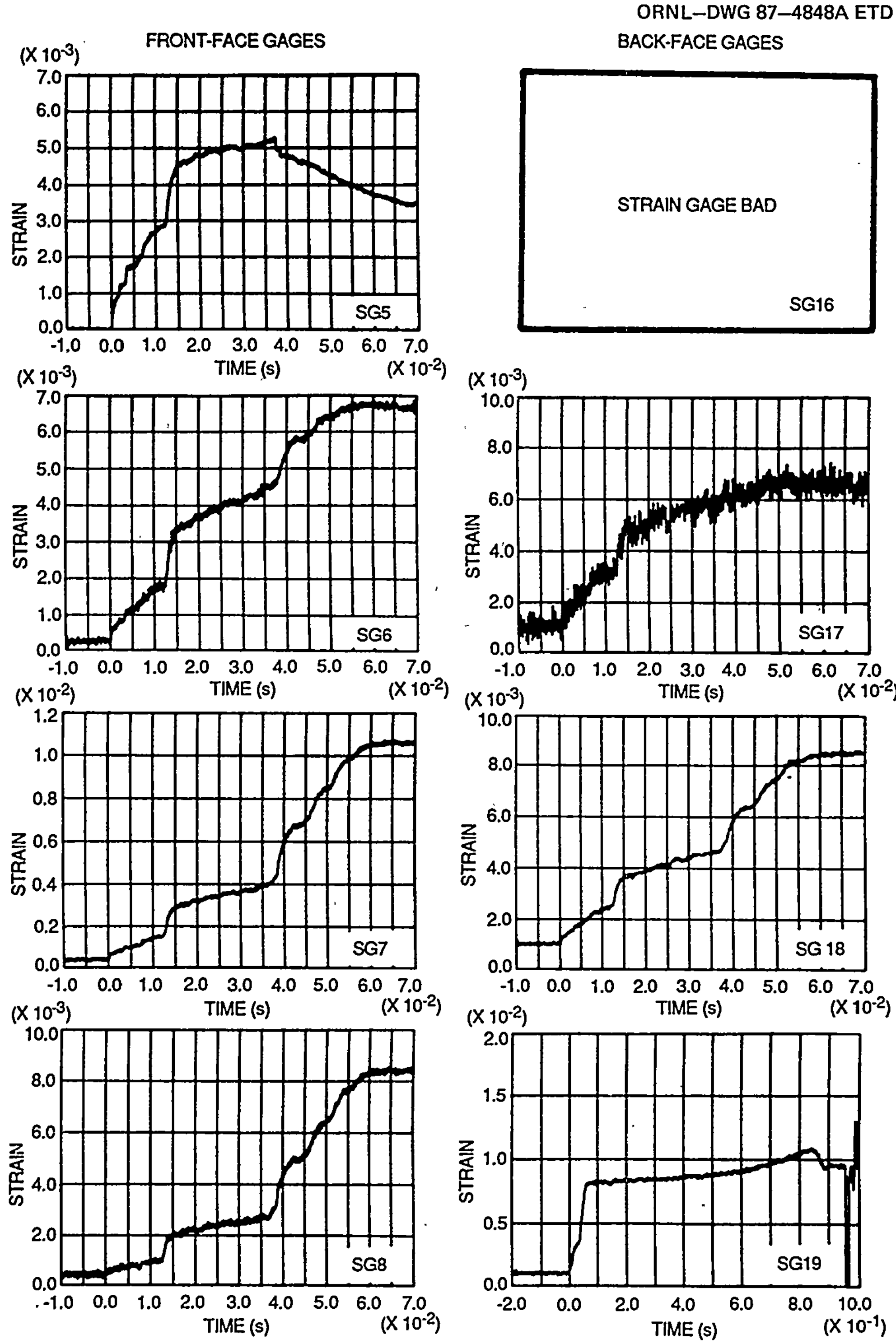

Fig. A.28. Strain histories for companion crack-line gages: test WP-2.3 (gages 5–8 and 16–19).

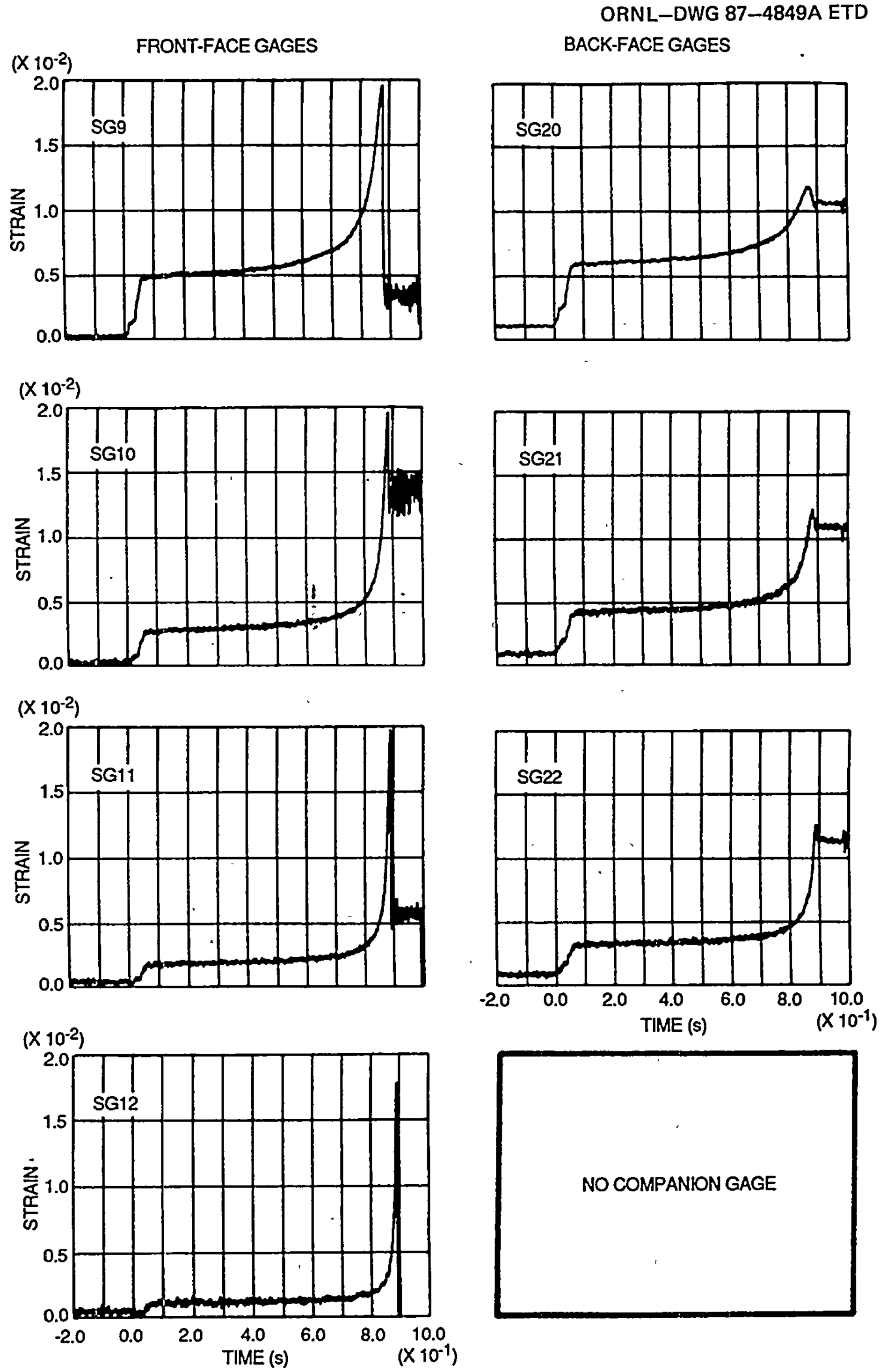

Fig. A.29. Strain histories for companion crack-line gages: test WP-2.3 (gages 9–12 and 20–22).

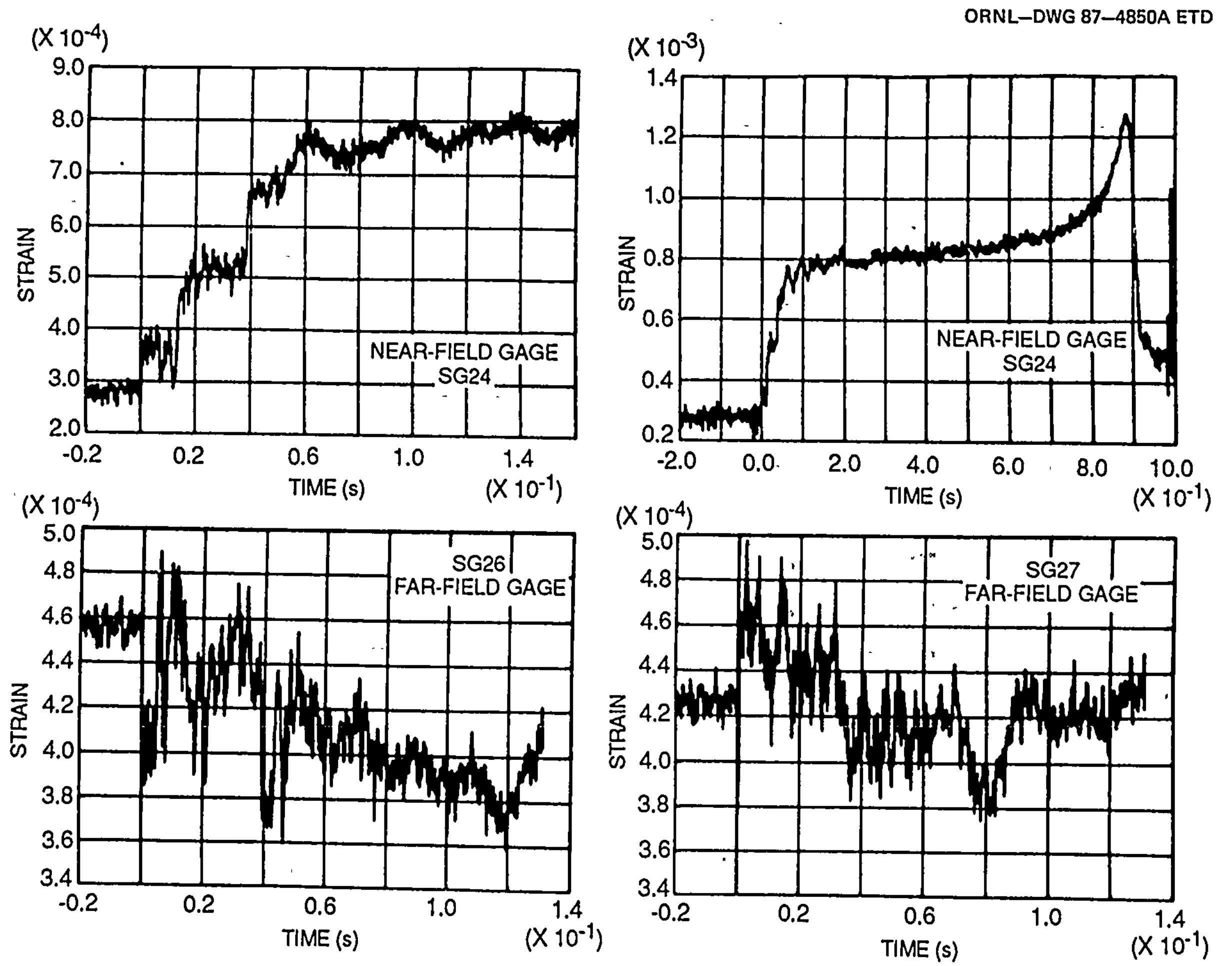

Fig. A.30. Crack run-arrest events as detected by near- and far-field strain gages: test WP-2.3 (gages 24, 26, and 27).

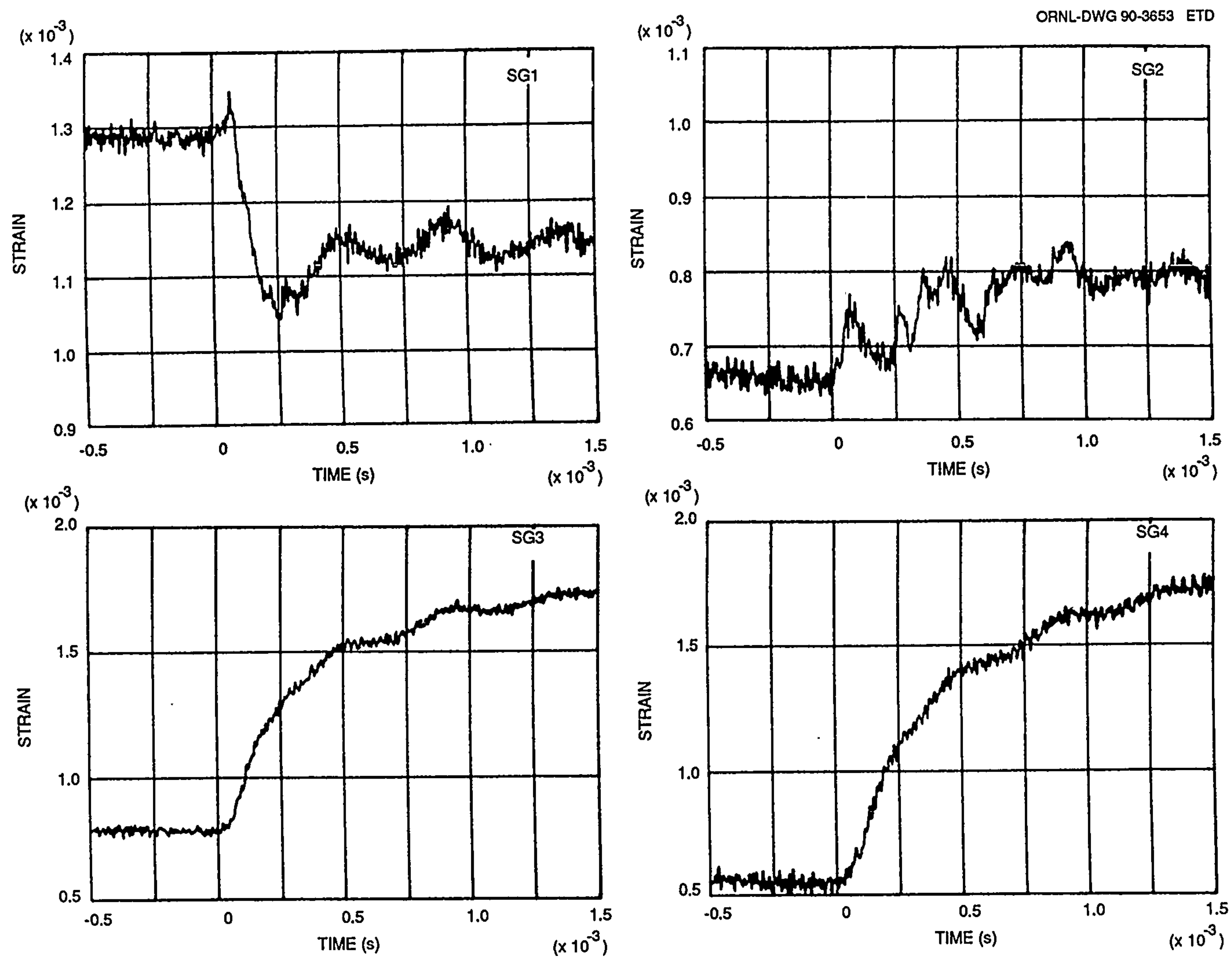

Fig. A.31. Strain histories for gages 1–4 showing crack passing under gages 1 and 2 and arresting before reaching gages 3 and 4: test WP-2.3.

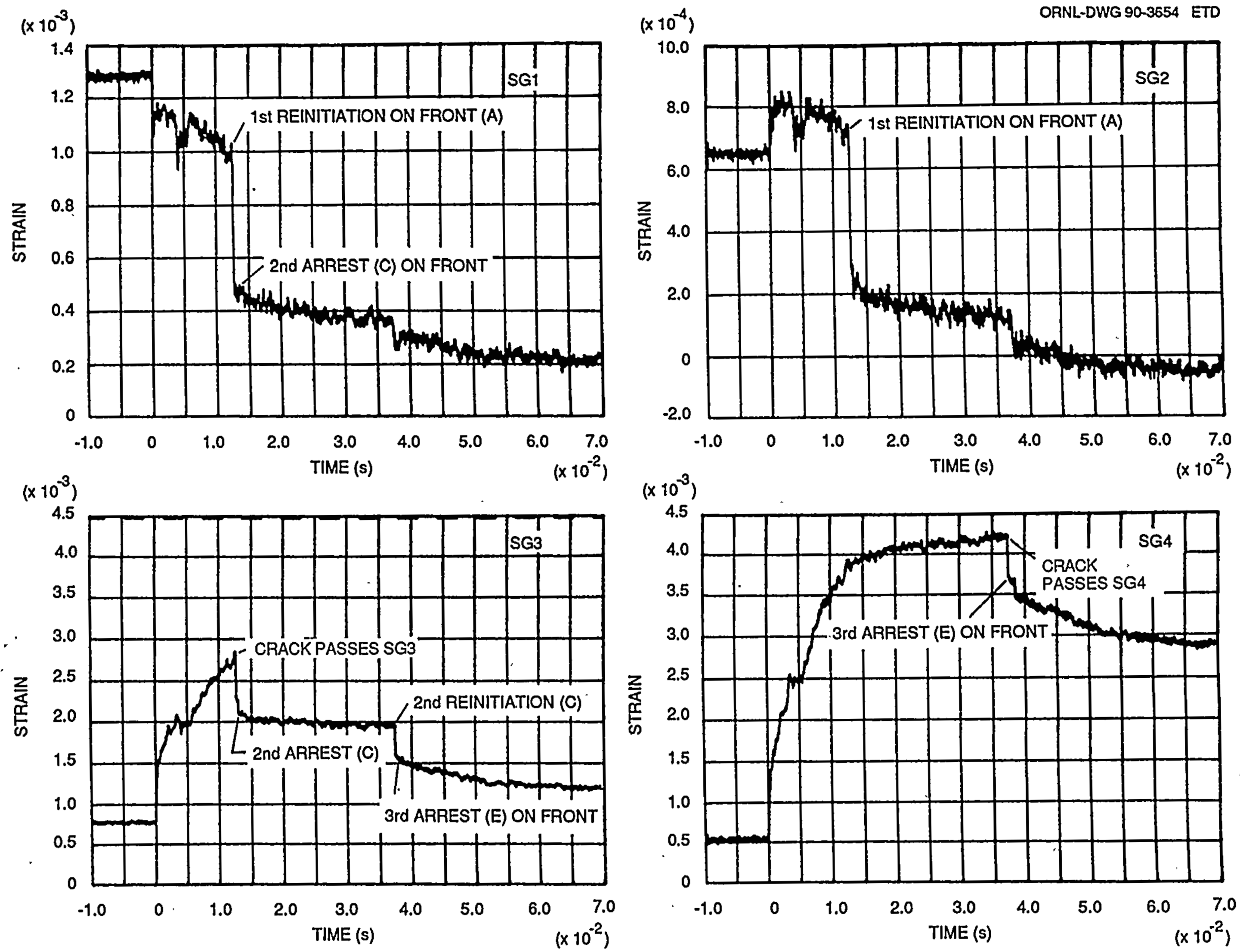

Fig. A.32. Strain histories for gages 1–4 showing reinitiation of crack propagation as detected by gages 1 and 2 and crack passing gage 3 with a subsequent arrest before reaching gage 4: test WP-2.3.

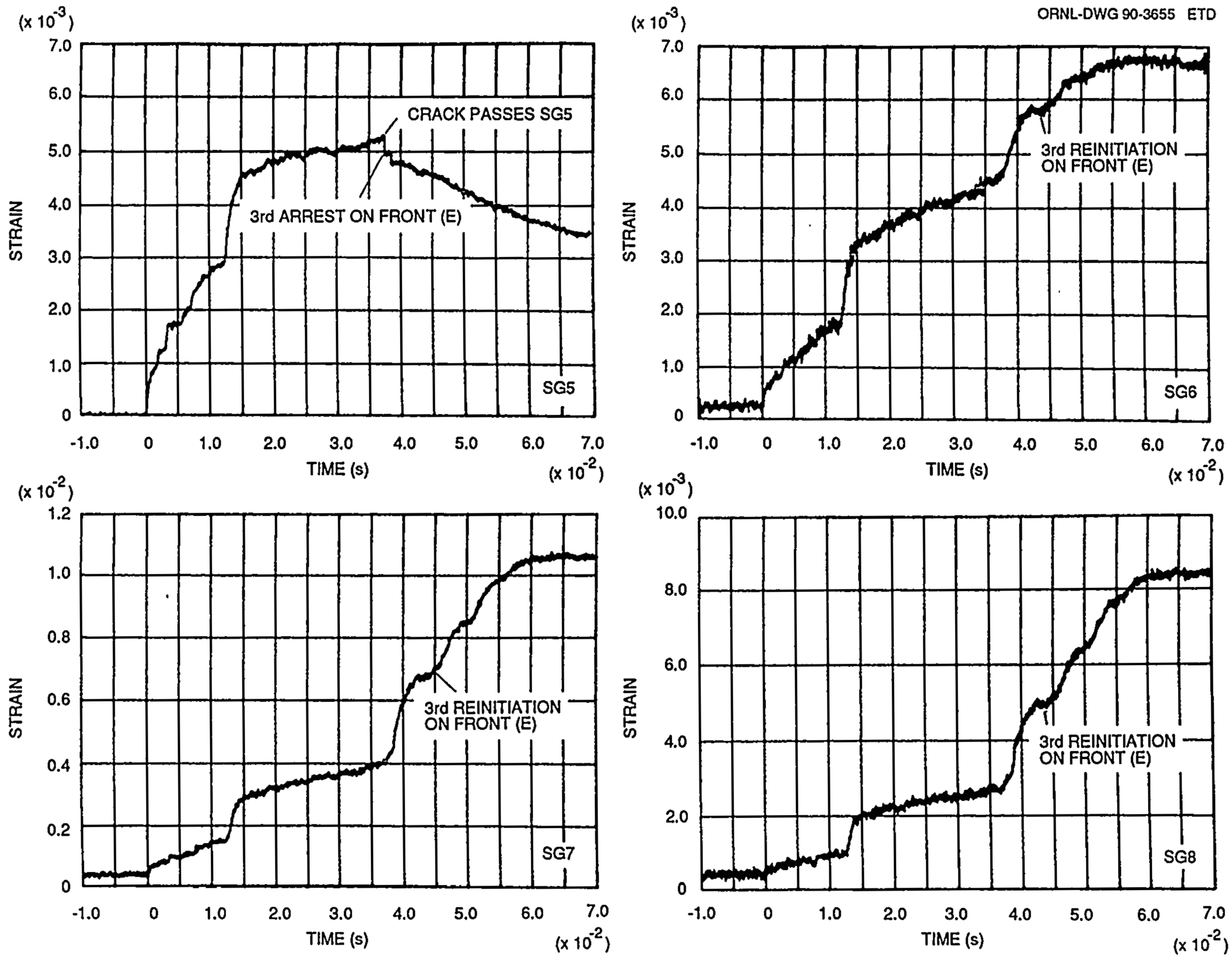

Fig. A.33. Strain histories for gages 5–8 showing propagation of the crack past gage 5, a subsequent arrest before reaching gage 6, and reinitiation with the crack propagating past gages 6–8: test WP-2.3.

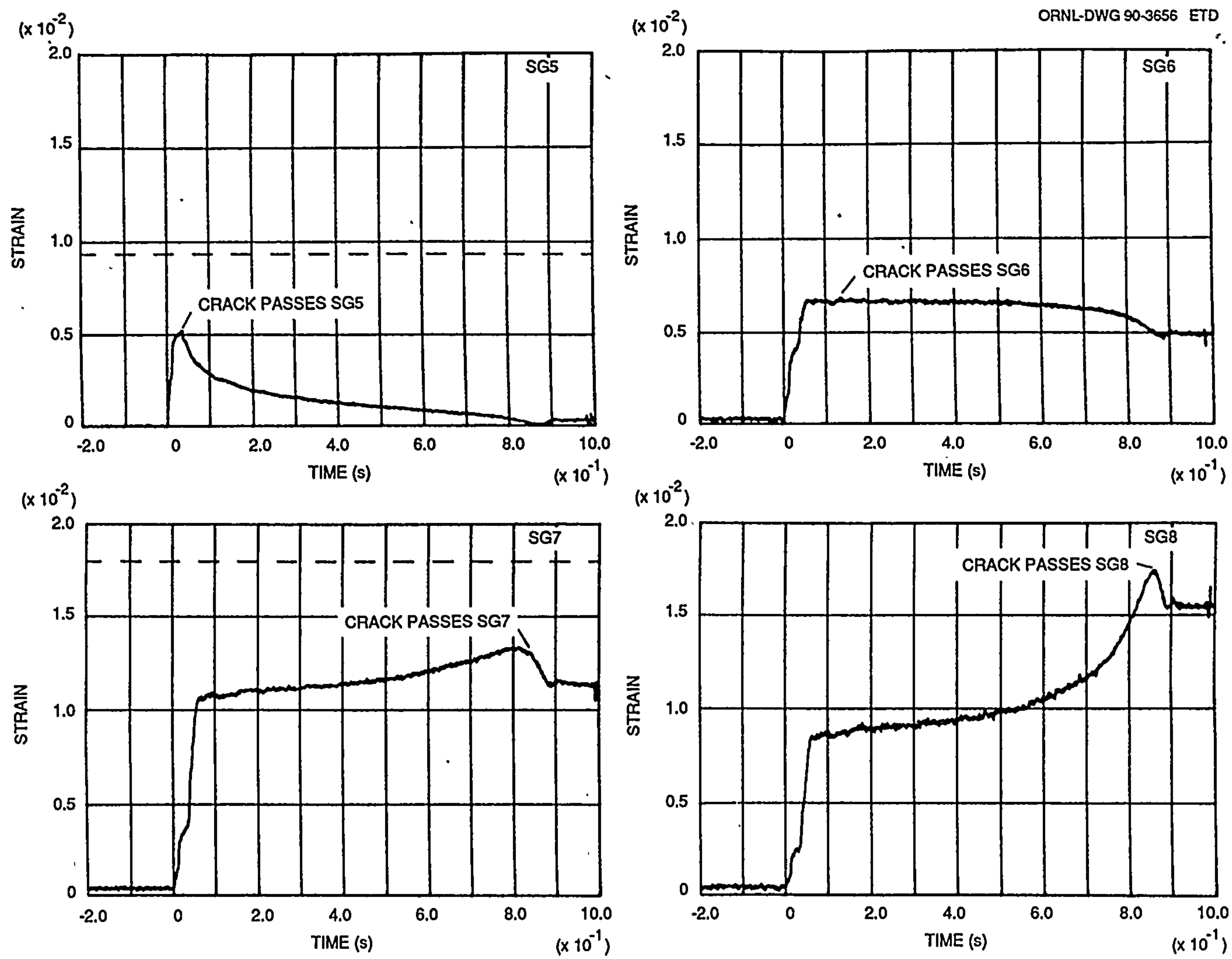

Fig. A.34. Strain histories for gages 5–8 showing crack passing gages 6–8: test WP-2.3.

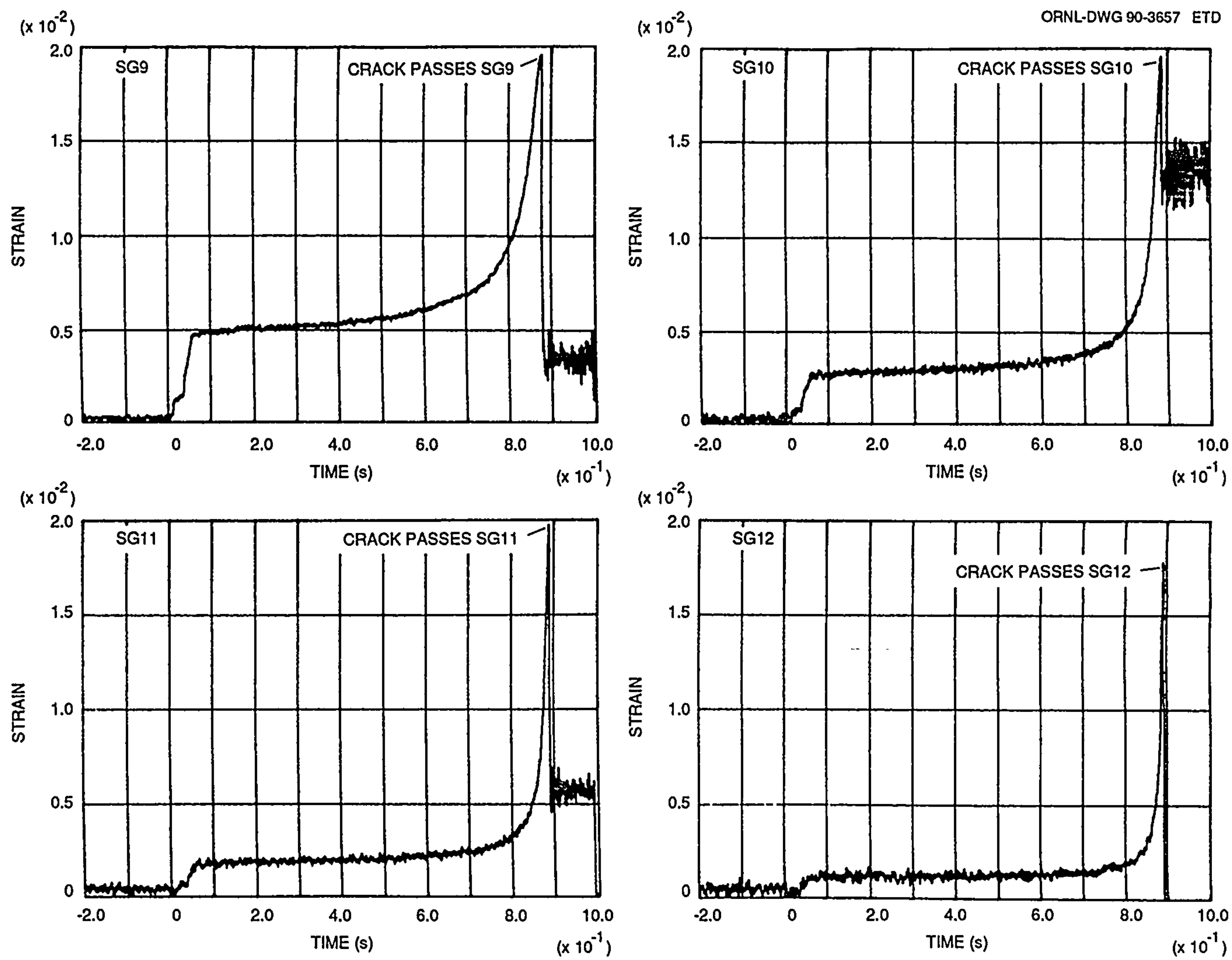

Fig. A.35. Strain histories for gages 9–12 showing crack passing these gages: test WP-2.3.

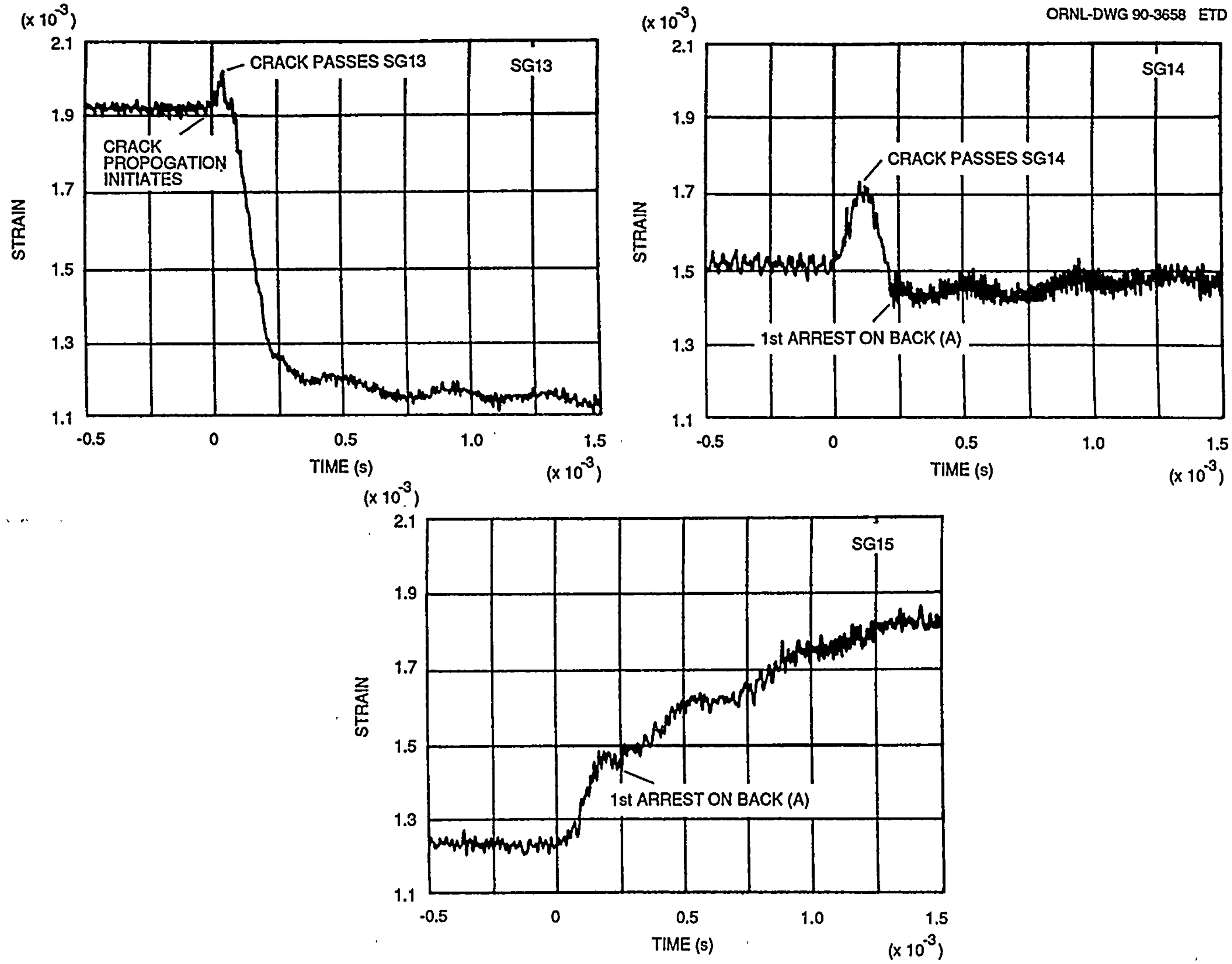

Fig. A.36. Strain histories for back-face gages 13–15 showing crack passing gages 13 and 14 and then arresting before reaching gage 15: test WP-2.3.

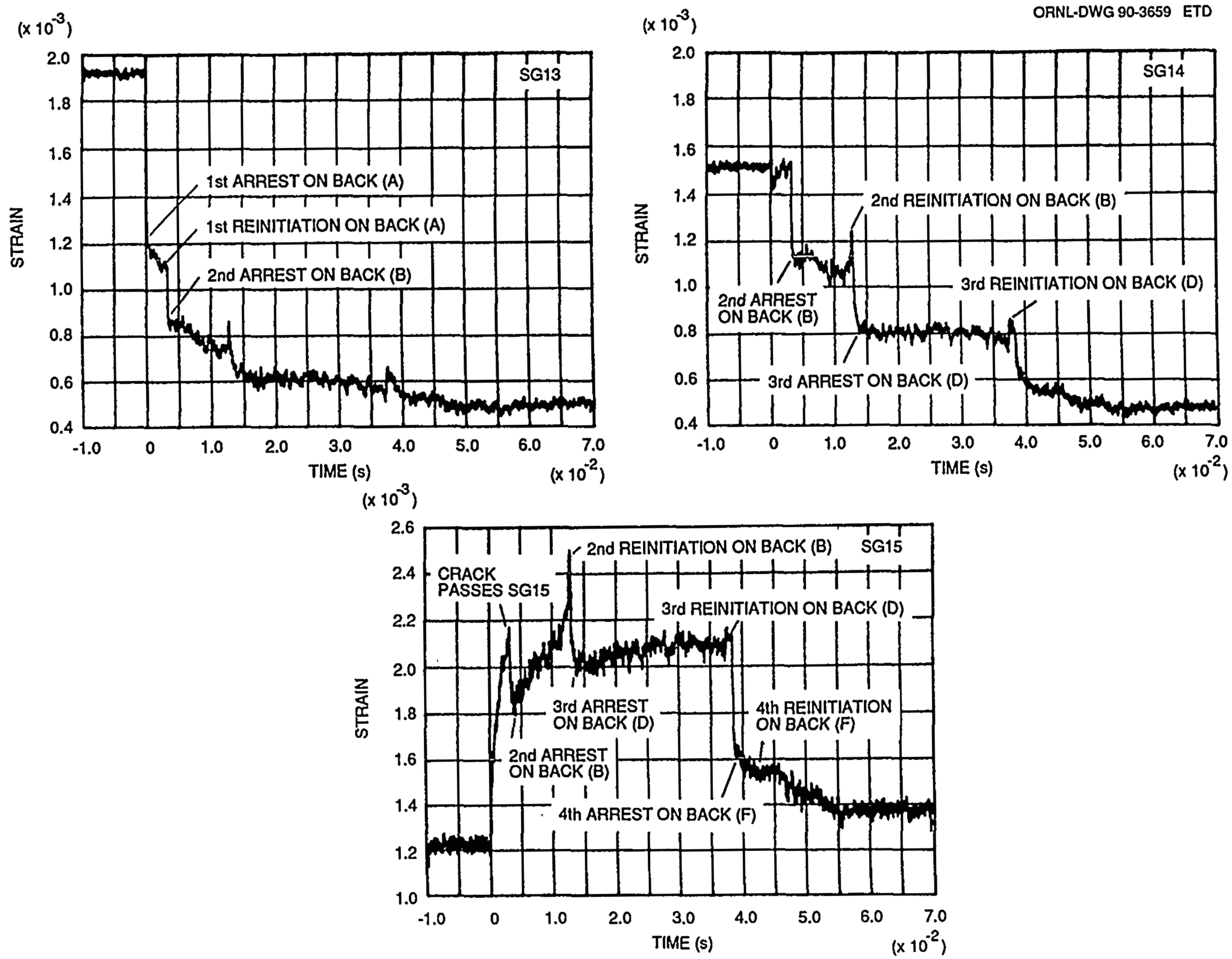

Fig. A.37. Strain histories for back-face gages 13–15 showing multiple crack run-arrest events: test WP-2.3.

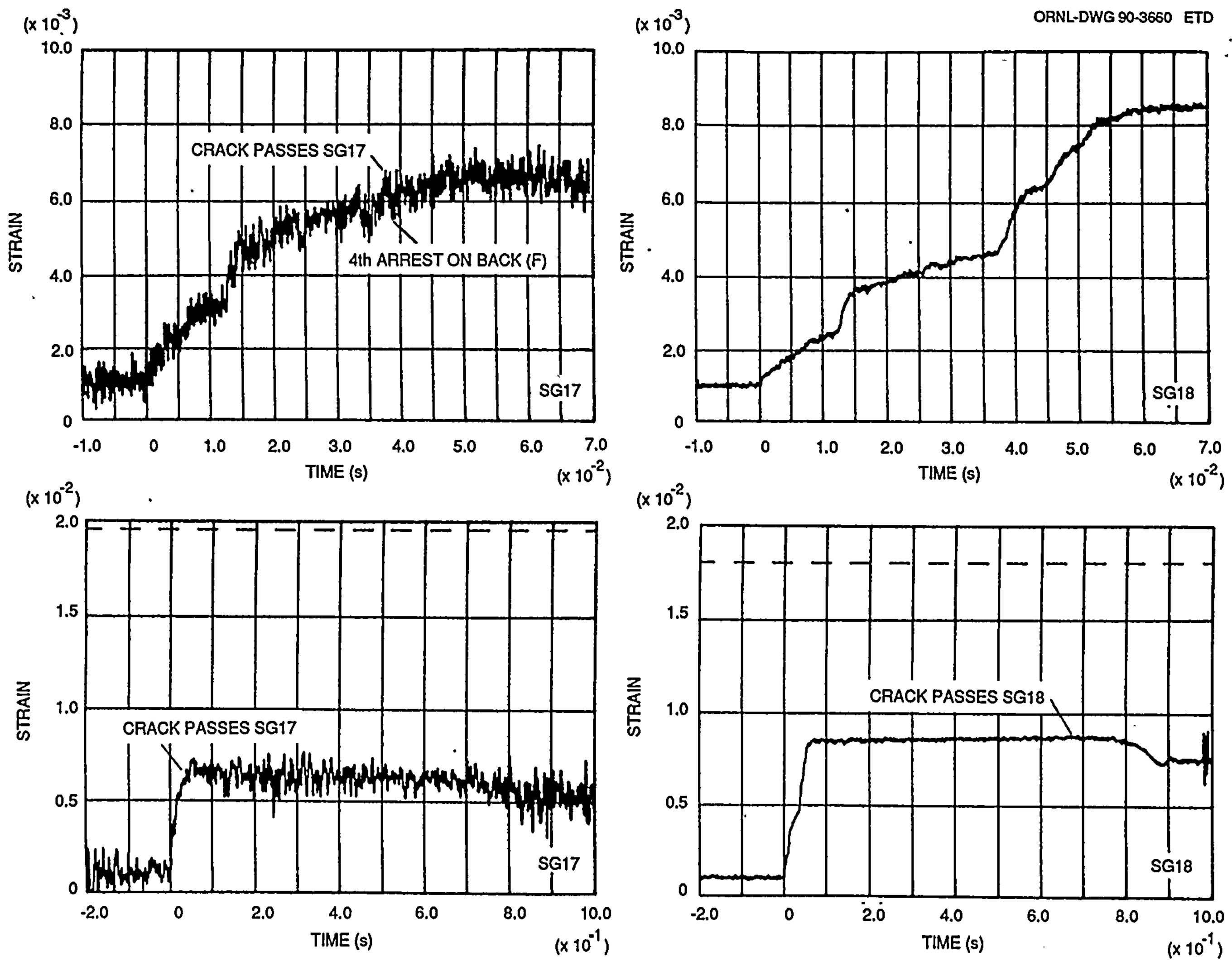

Fig. A.38. Strain histories for back-face gages 17 and 18 showing early crack run-arrest events followed much later by crack passing gage 18: test WP-2.3.

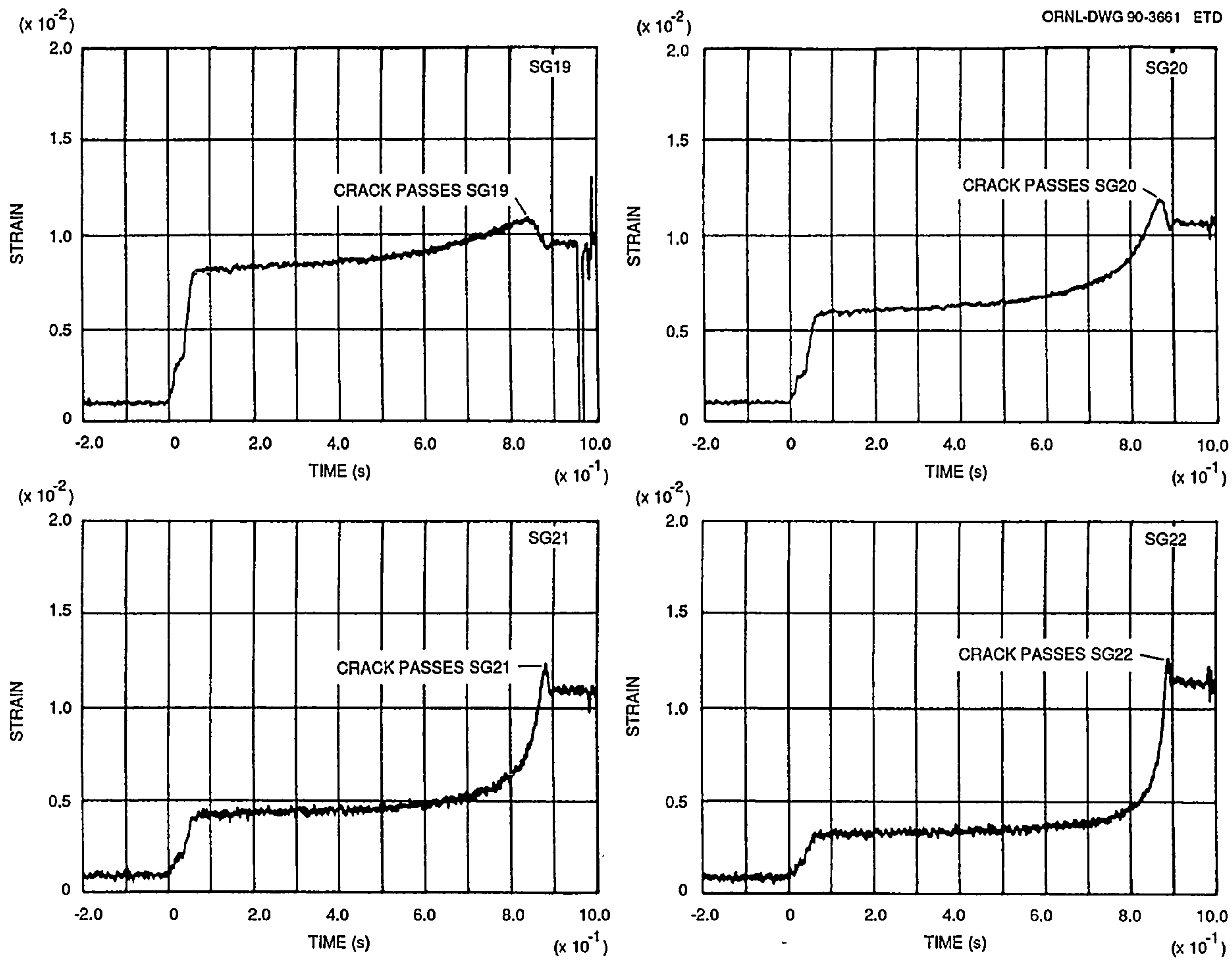

Fig. A.39. Strain histories for back-face gages 19–22 showing propagation of crack past these gages: test WP-2.3.

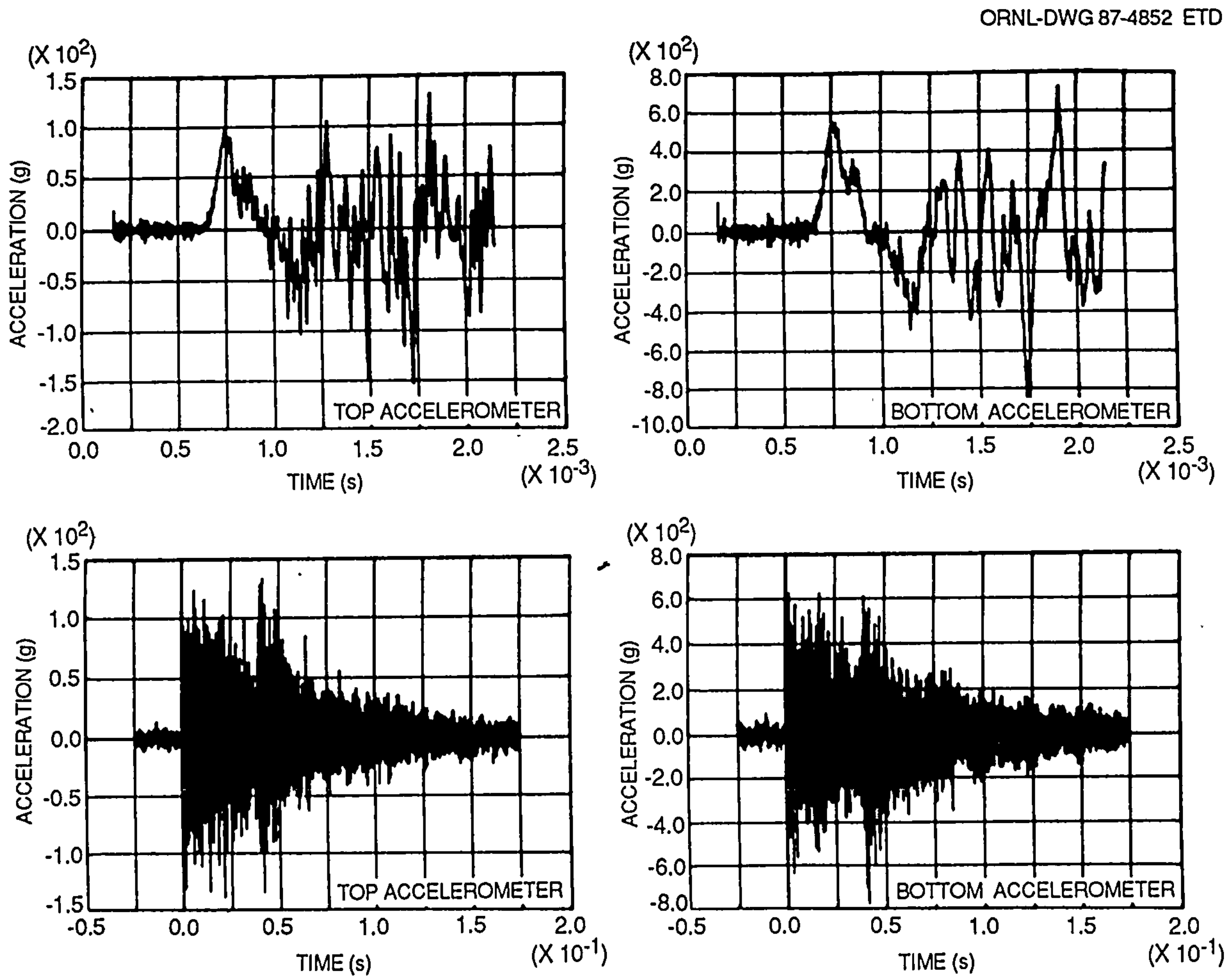

Fig. A.40. Longitudinal acceleration results at two levels of time resolution measured by top and bottom "damped" accelerometers mounted 3.585 m above and 3.589 m below the crack plane, respectively: test WP-2.3.

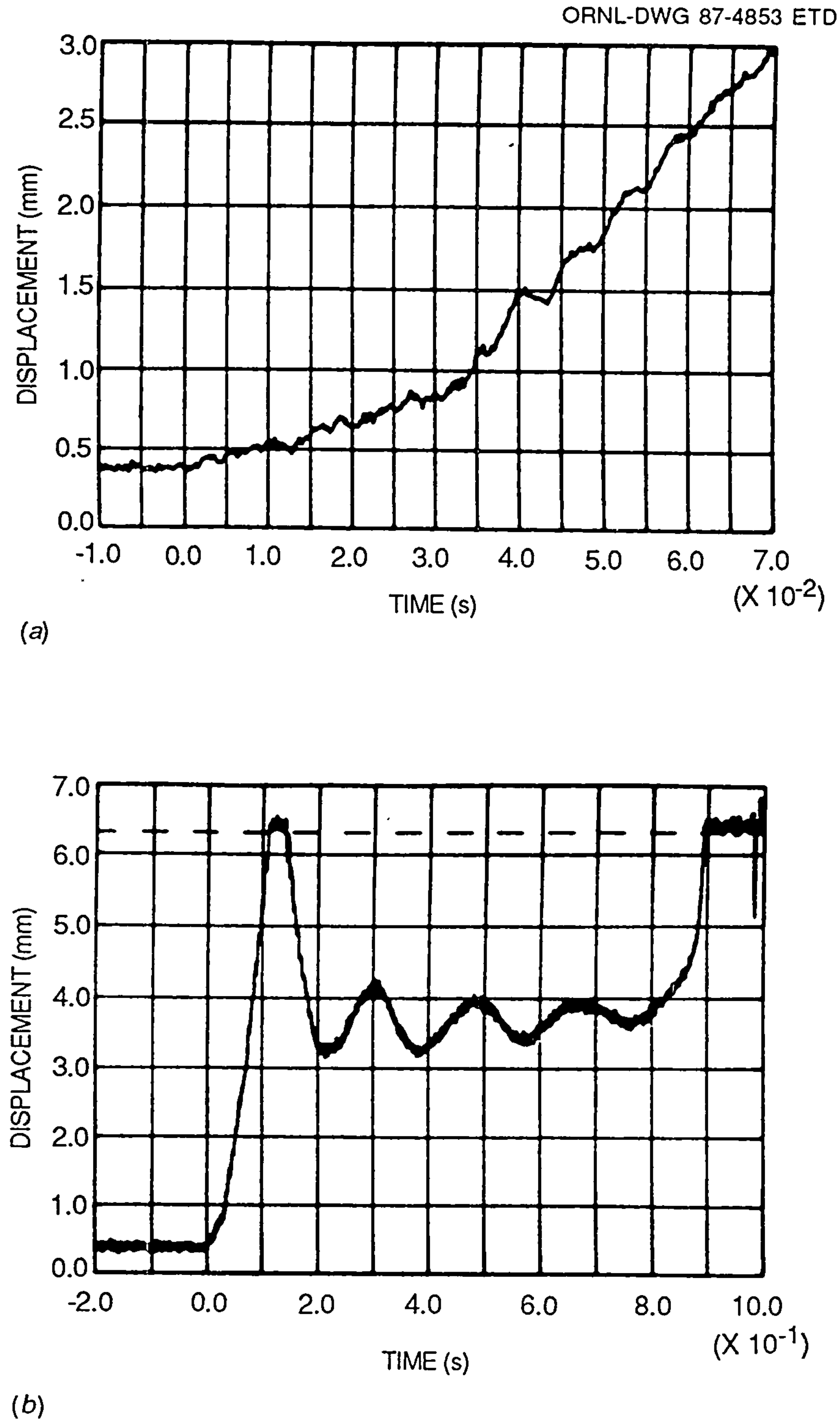

Fig. A.41. Bottom displacement gage results (*a*) during initial crack run-arrest events and (*b*) during entire test: test WP-2.3.

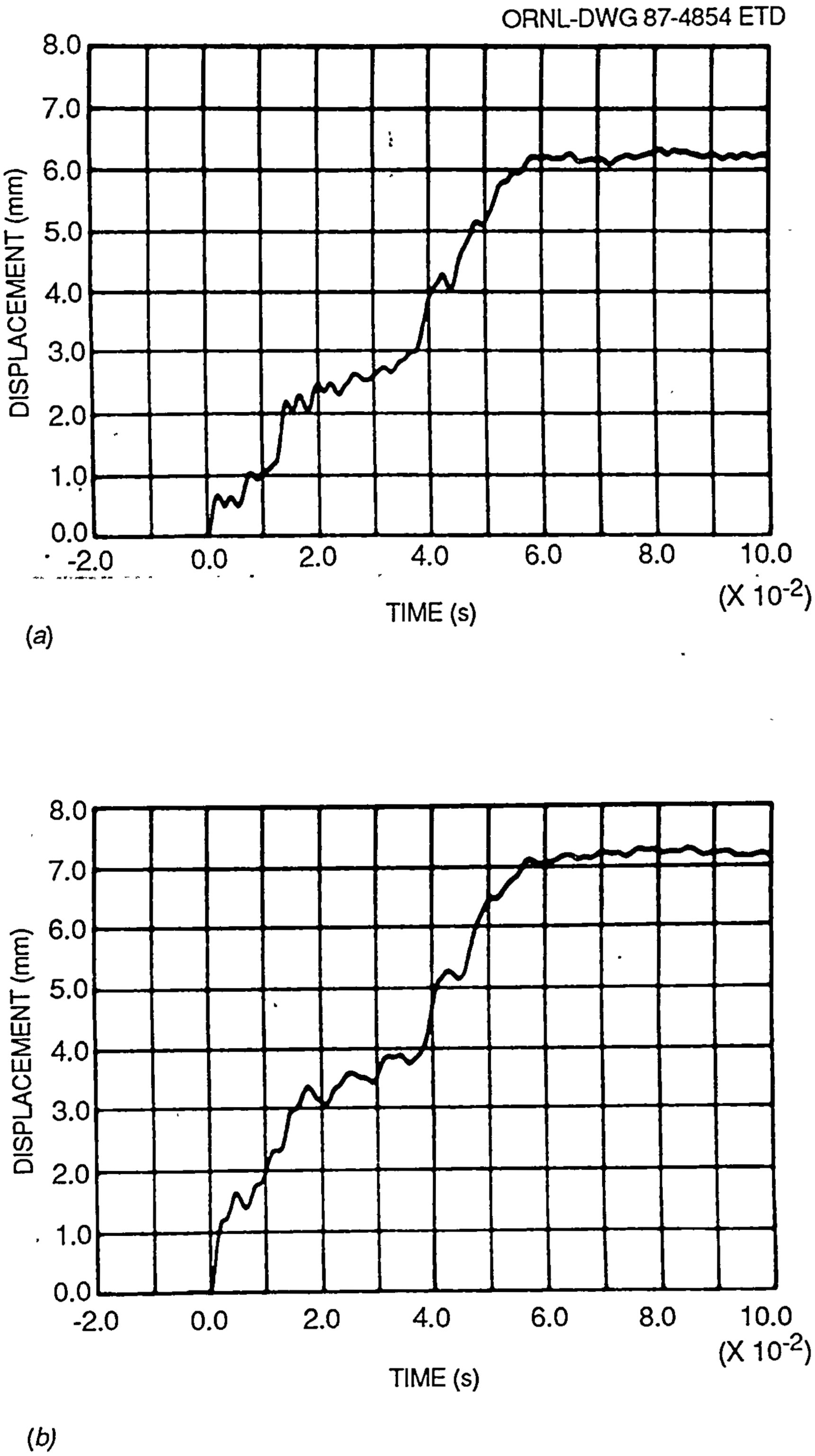

Fig. A.42. COD gage results during initial crack run-arrest events: test WP-2.3. (*a*) Front face and (*b*) back-face.

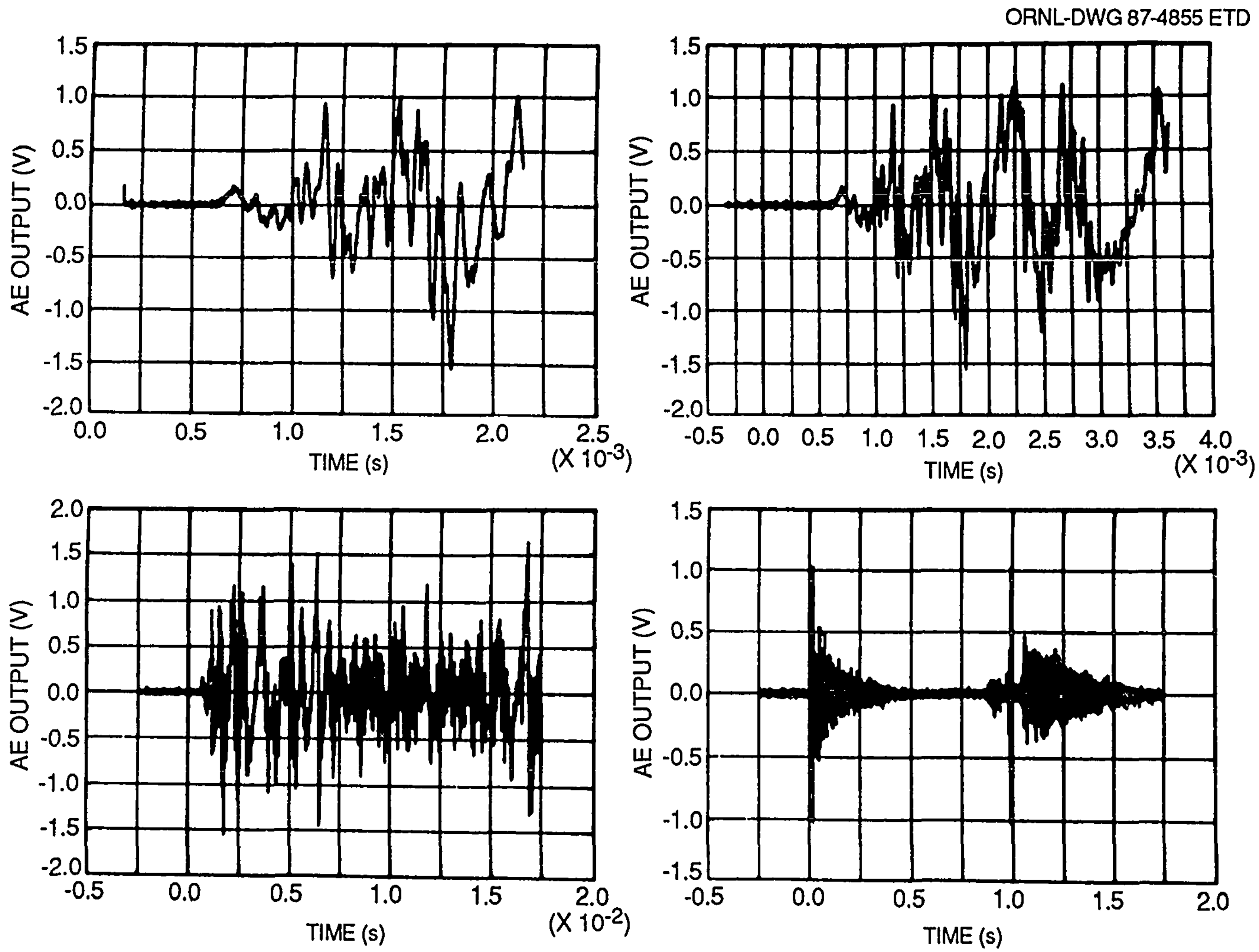

Fig. A.43. AE results for various time resolutions: test WP-2.3.

A.4 TEST WP-2.4

A.4.1 Strain Gages

Strain-gage records for companion crack-line gages [see Fig. 4.8(*d*) for strain-gage locations] are presented in Fig. A.44 to A.46. Figure A.47 shows initiation of the first crack run-arrest event as detected by strain gage 1. Propagation of the crack during the first crack run-arrest event, as detected by companion crack-line gages 2 and 3 and 13 and 14, is presented in Fig. A.48. Arrest and reinitiation of crack propagation as detected by companion crack-line gages 4 and 15 at two levels of time resolution are shown in Fig. A.49. Figure A.50 presents additional crack run-arrest events as detected by companion crack-line gages 5 and 6 and 16 and 17. Additional crack run-arrest events as detected by companion crack-line gages 7 and 8 and 18 and 19 are presented in Fig. A.51. Figure A.52 shows ductile tearing as detected by companion crack-line gages 9 and 10 and 20 and 21. Figure A.53 presents ductile tearing as detected by crack-line gages 11, 12, and 22. The fracture event, as monitored by near-field strain gages 23 and 25 and far-field strain gages 26 and 27, is shown in Fig. A.54.

A.4.2 Additional Instrumentation

Output from the AE transducer mounted on the specimen lower pull tab is presented in Fig. A.55. Longitudinal acceleration recorded by a "damped" accelerometer located 4.041 m below the crack plane is shown in Fig. A.56. Longitudinal acceleration recorded by a "shock" accelerometer located 4.038 m above the crack plane is presented in Fig. A.57. Front- and back-face COD results at various times after fracture initiation are shown in Fig. A.58.

A.5 TEST WP-2.5

A.5.1 Strain Gages

Strain records, shown in Figs. A.59 to A.61 for companion crack-line gages, indicate that six cleavage crack run-arrest events occurred during the test [gage locations are presented in Fig. 4.8(*a*)]. Near- and far-field strain-gage results are presented in Fig. A.62. More details on the crack run-arrest events followed by fibrous tearing are presented in Figs. A.63 to A.67. Figure A.63 shows the crack passing under strain gages 1 and 2 and arresting ($t = 0.344$ ms) before reaching strain gage 3. The longer strain history for gage 3 in Fig. A.63 shows reinitiation of crack propagation at $t = 7.87$ ms and the crack passing under gage 3 at $t = 7.88$ ms. Strain histories for gages 5, 6, 9, and 10 (Fig. A.64) show multiple crack run-arrest events. Figure A.65 presents strain histories for gages 13–15, indicating that the crack passes gages 13 and 14 with a subsequent arrest at $t = 0.54$ ms before reaching gage 15. The longer strain history shown in Fig. A.65 for gage 14 shows

ORNL-DWG 86-5114A ETD

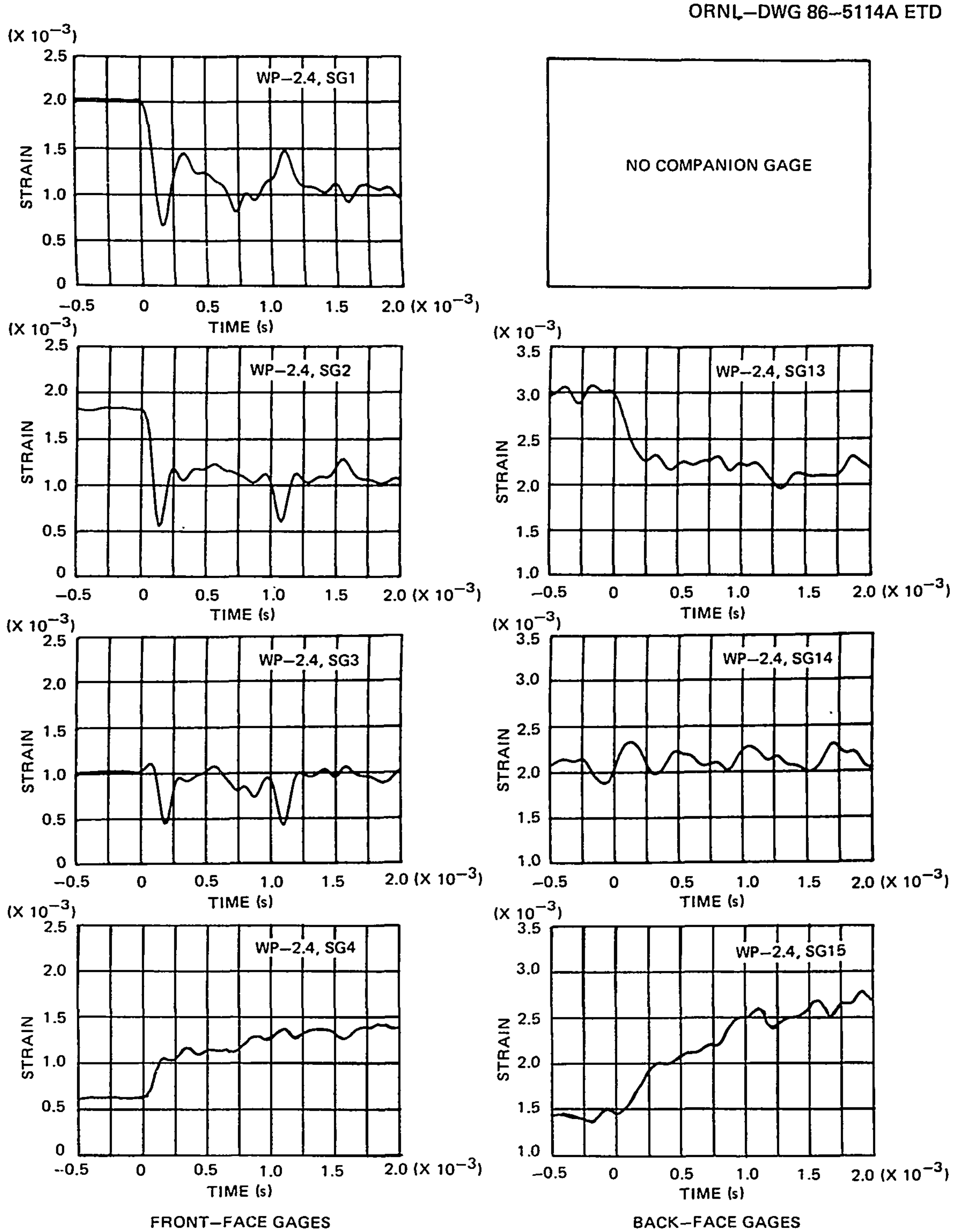

Fig. A.44. Strain histories for companion crack-line gages: test WP-2.4 (gages 1-4 and 13-15).

ORNL–DWG 86–5115A ETD

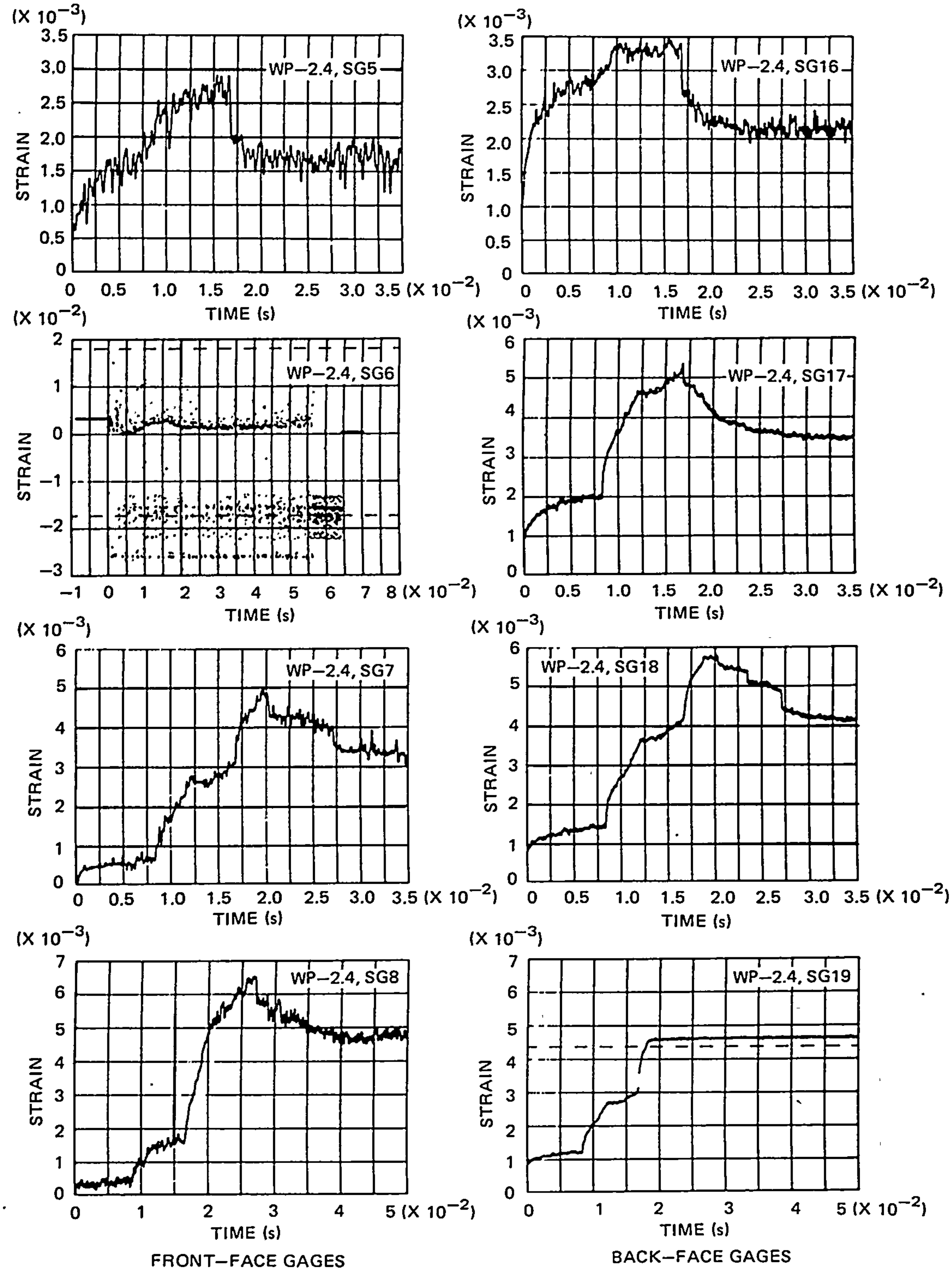

Fig. A.45. Strain histories for companion crack-line gages: test WP-2.4 (gages 5–8 and 16–19).

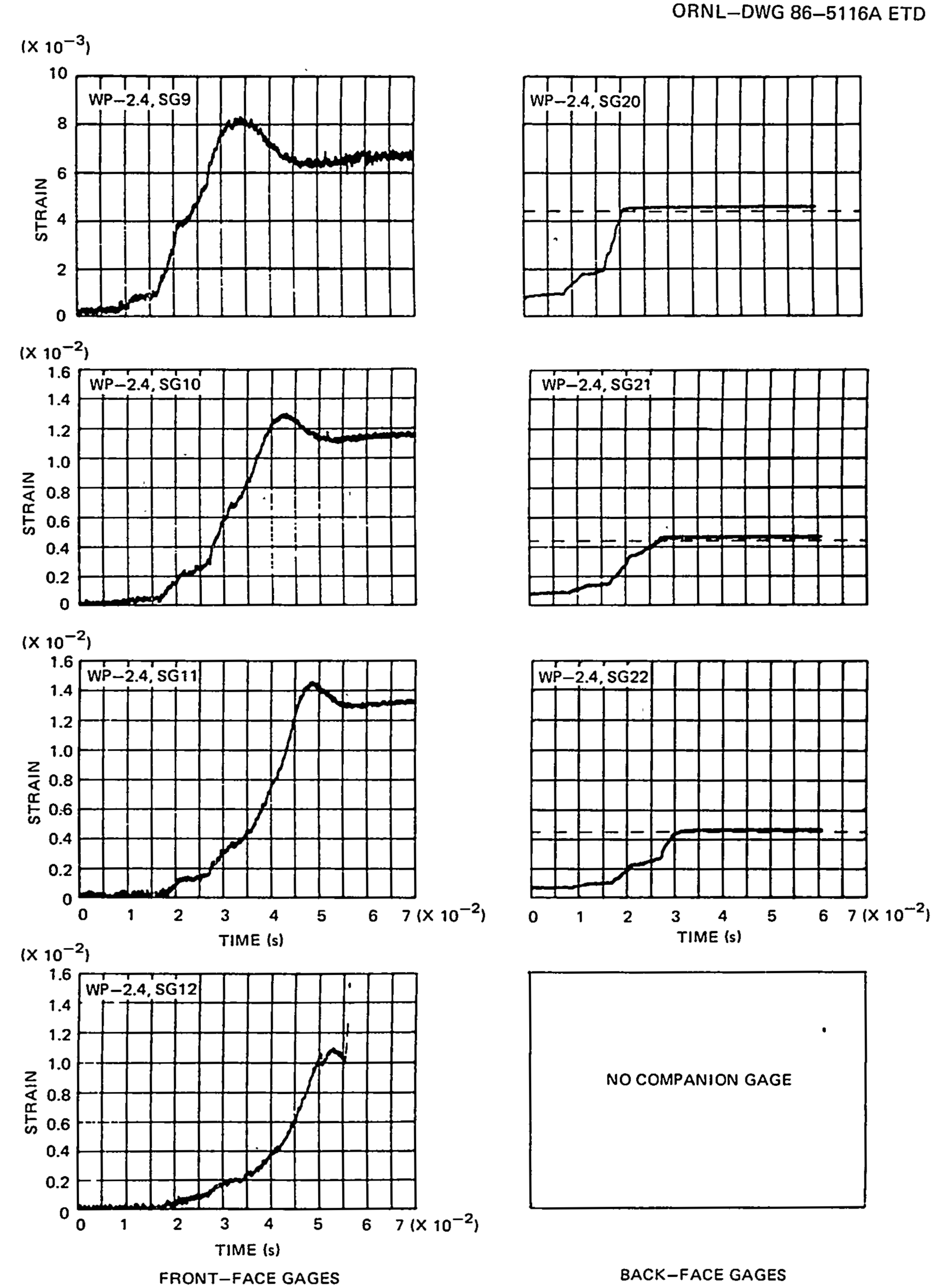

Fig. A.46. Strain histories for companion crack-line gages: test WP-2.4 (gages 9–12 and 20–22).

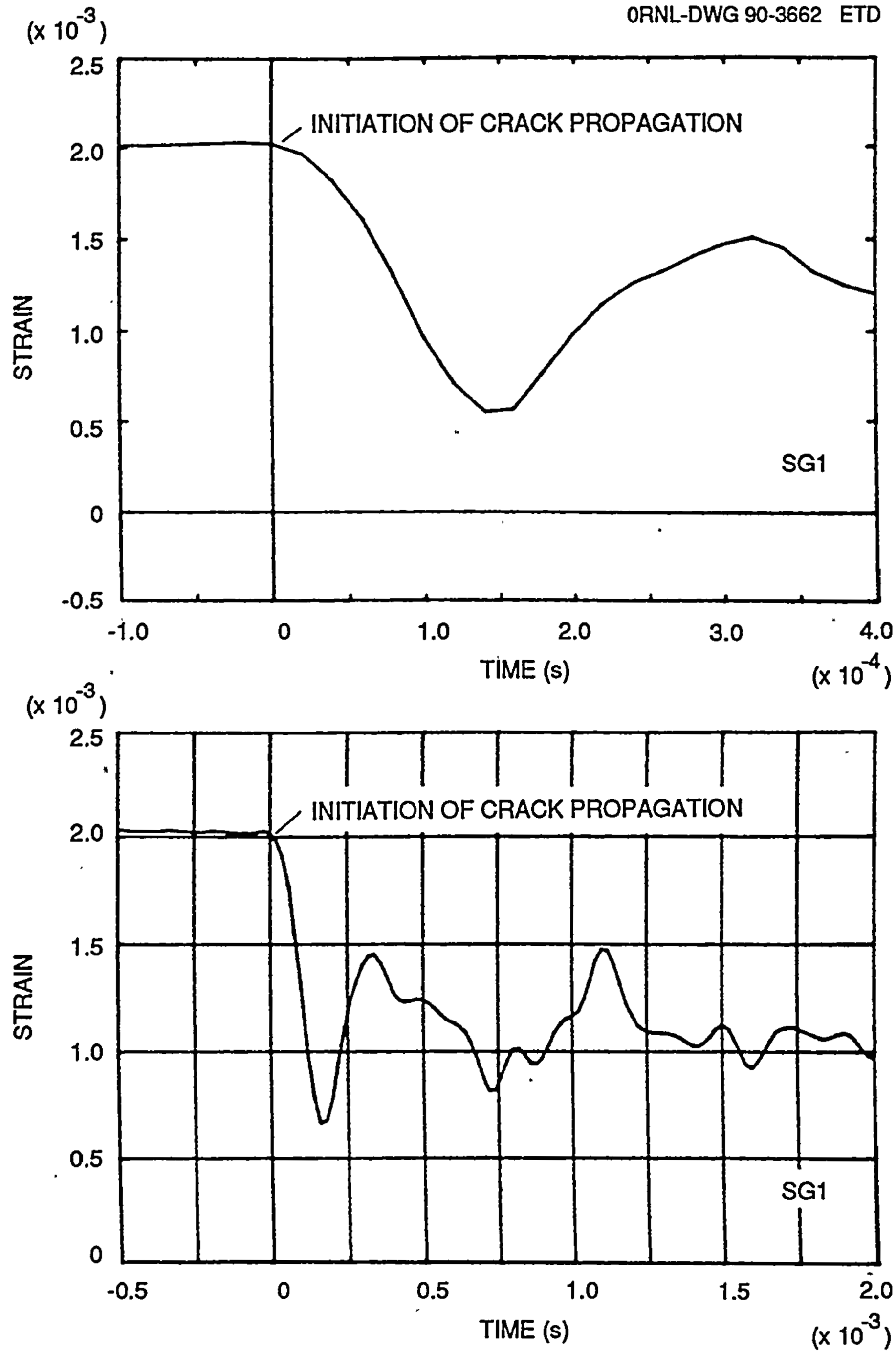

Fig. A.47. Initiation of first crack run-arrest event as detected by strain gage 1 for two time resolutions: test WP-2.4.

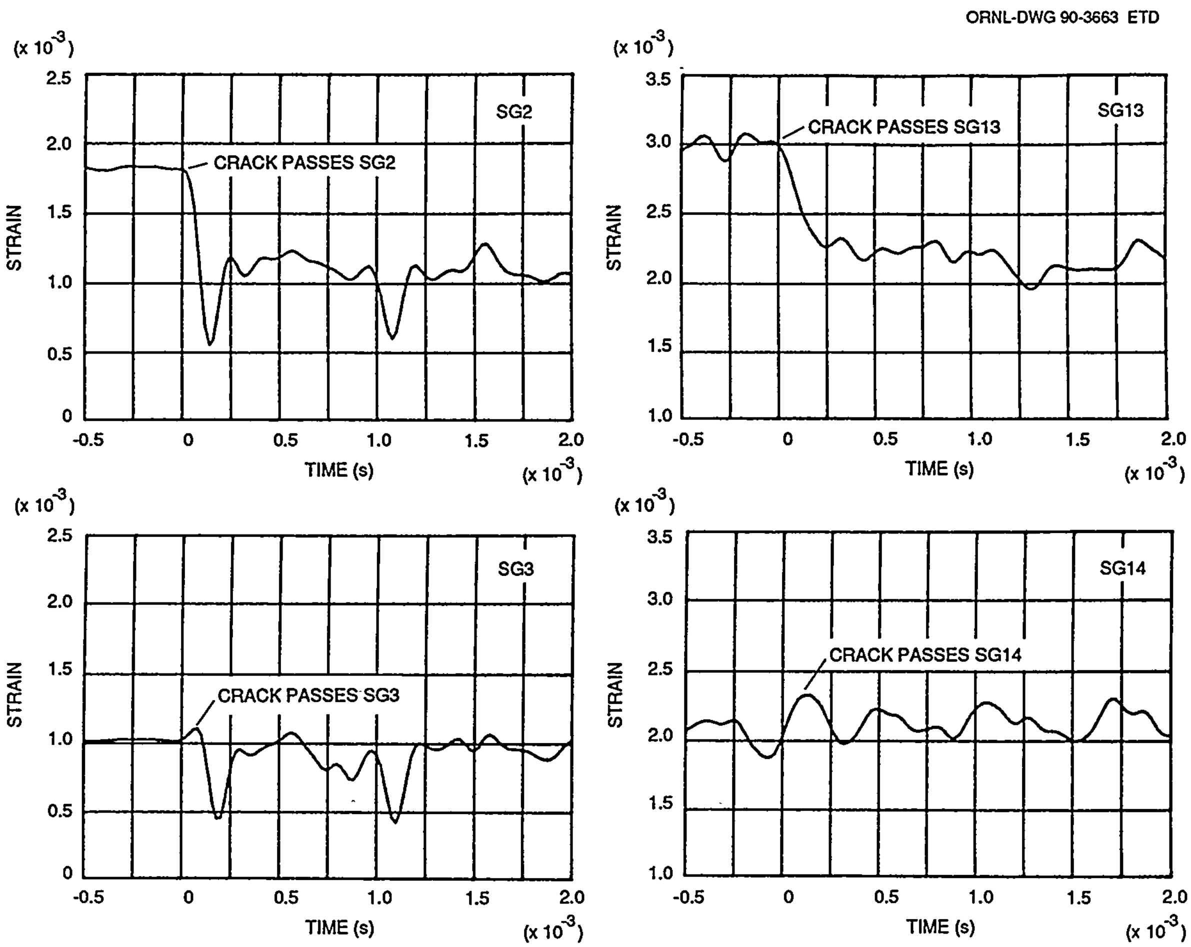

Fig. A.48. Propagation of crack during first crack run-arrest event as detected by companion crack-line gages 2 and 3 and 13 and 14: test WP-2.4.

ORNL-DWG 90-3664 ETD

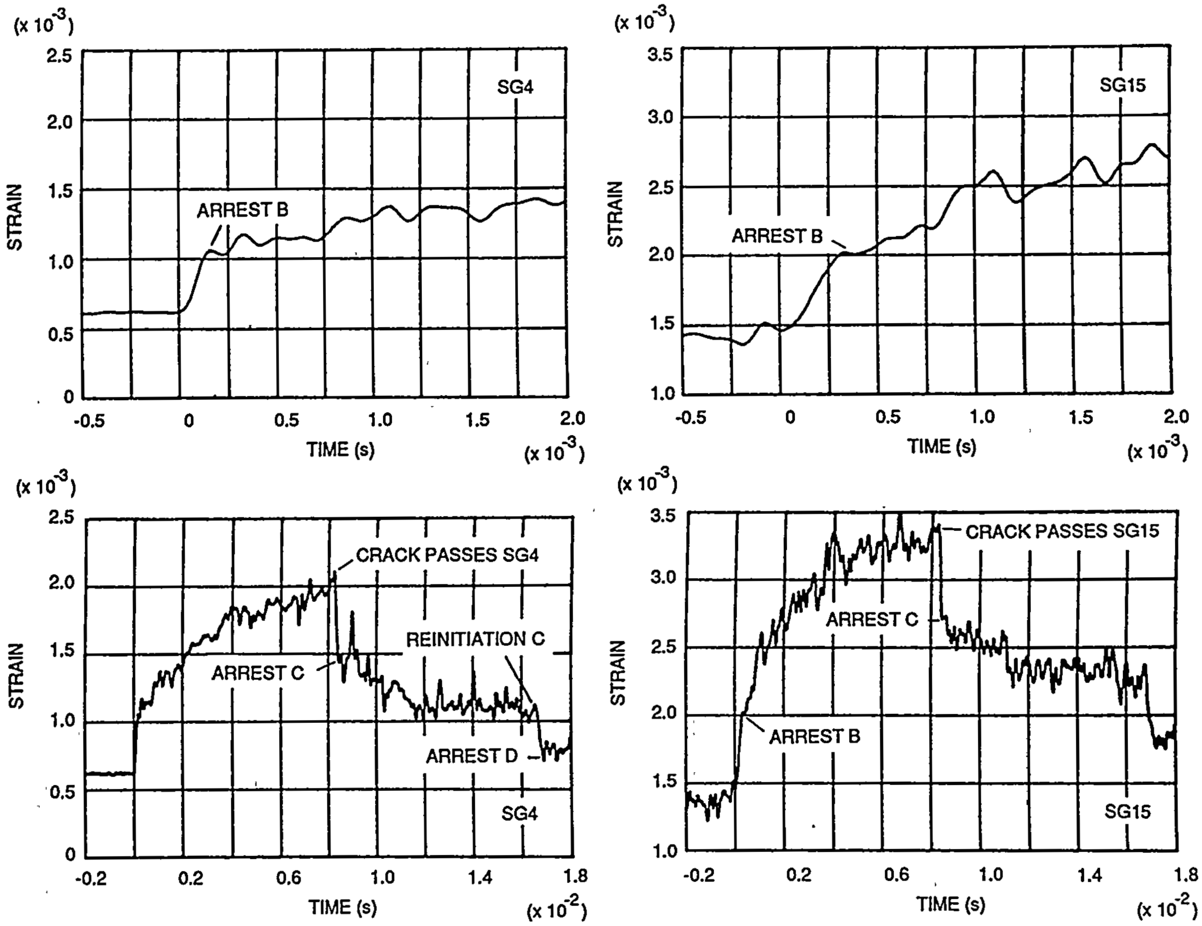

Fig. A.49. Arrest and reinitiation of crack propagation as detected by companion crack-line gages 4 and 15 at two levels of time resolution: test WP-2.4.

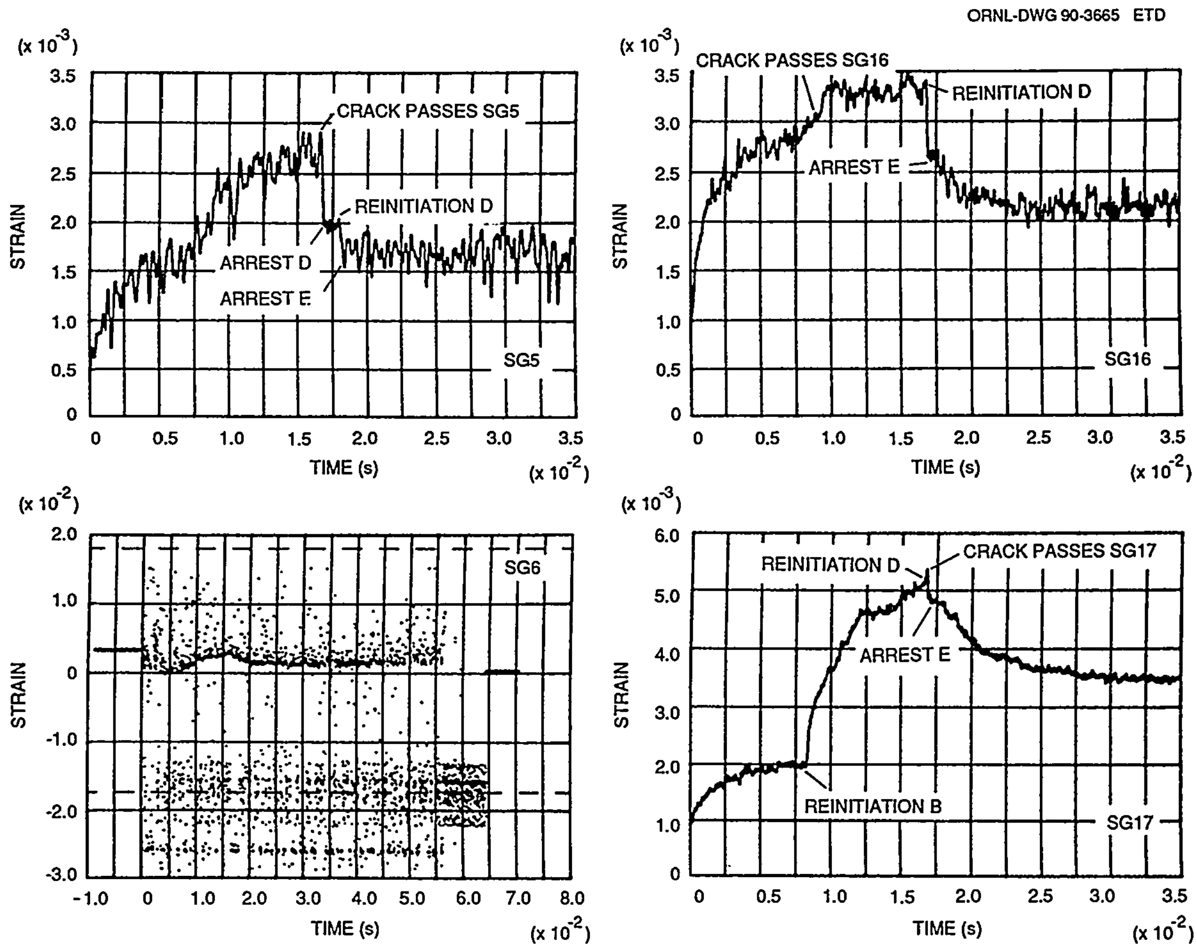

Fig. A.50. Additional crack run-arrest events as detected by companion crack-line gages 5 and 6 and 16 and 17: test WP-2.4.

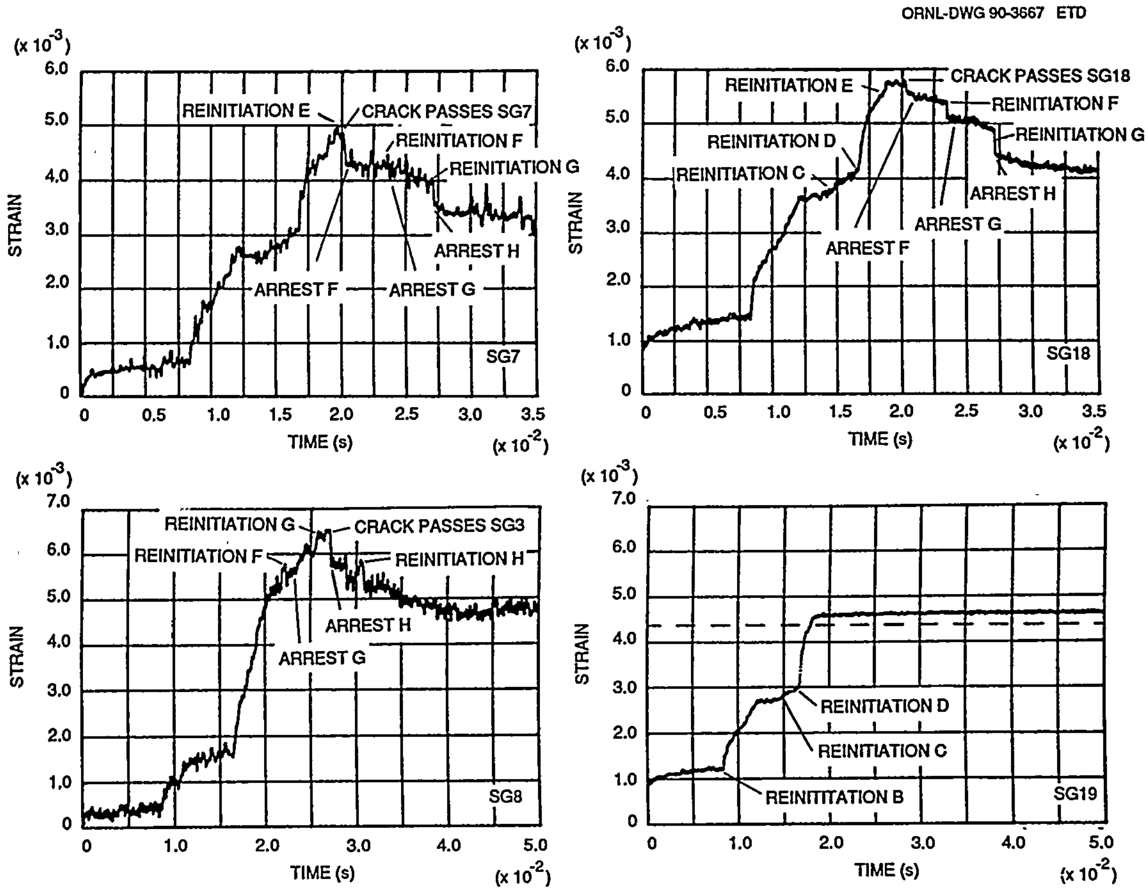

Fig. A.51. Additional crack run-arrest events as detected by companion crack-line gages 7 and 8 and 18 and 19: test WP-2.4.

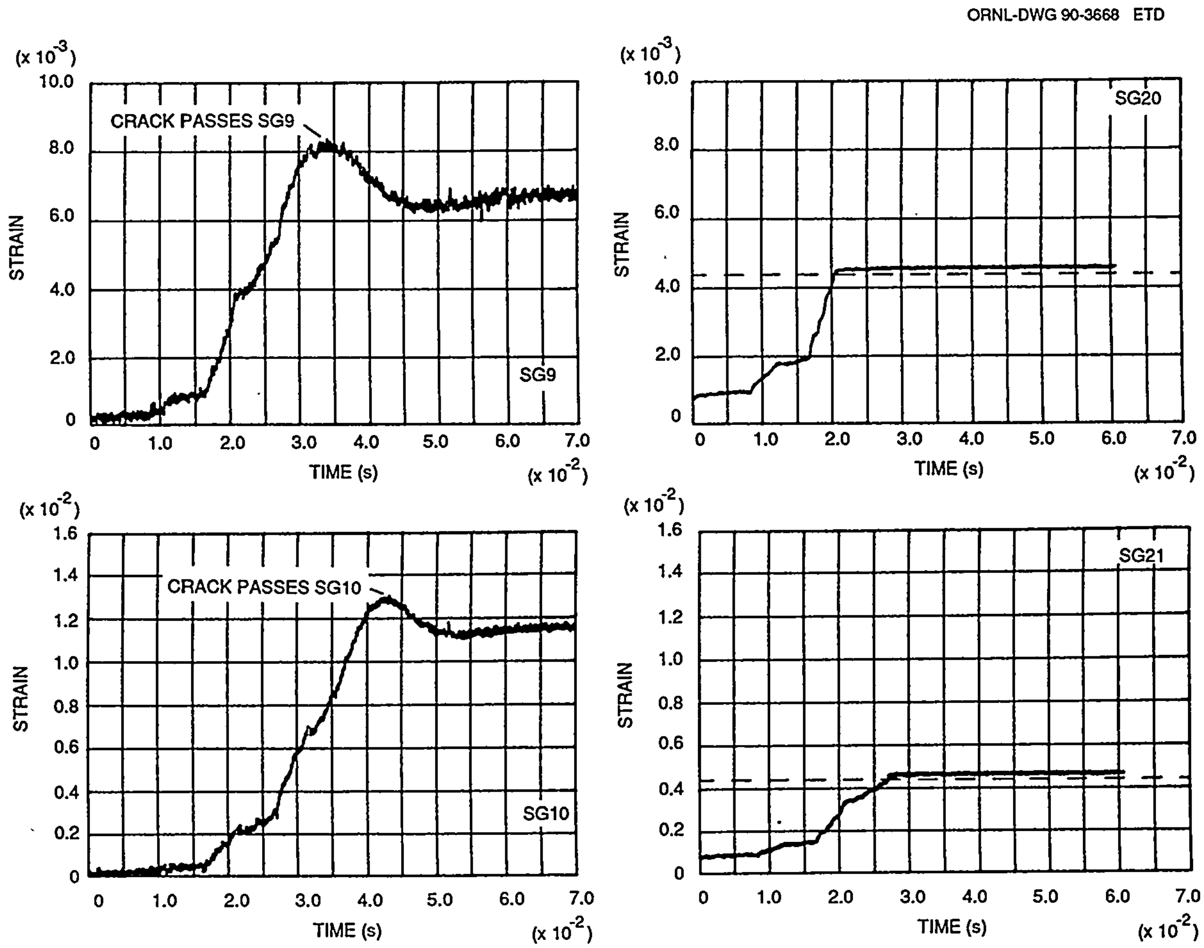

Fig. A.52. Ductile tearing as detected by companion crack-line gages 9 and 10 and 20 and 21: test WP-2.4.

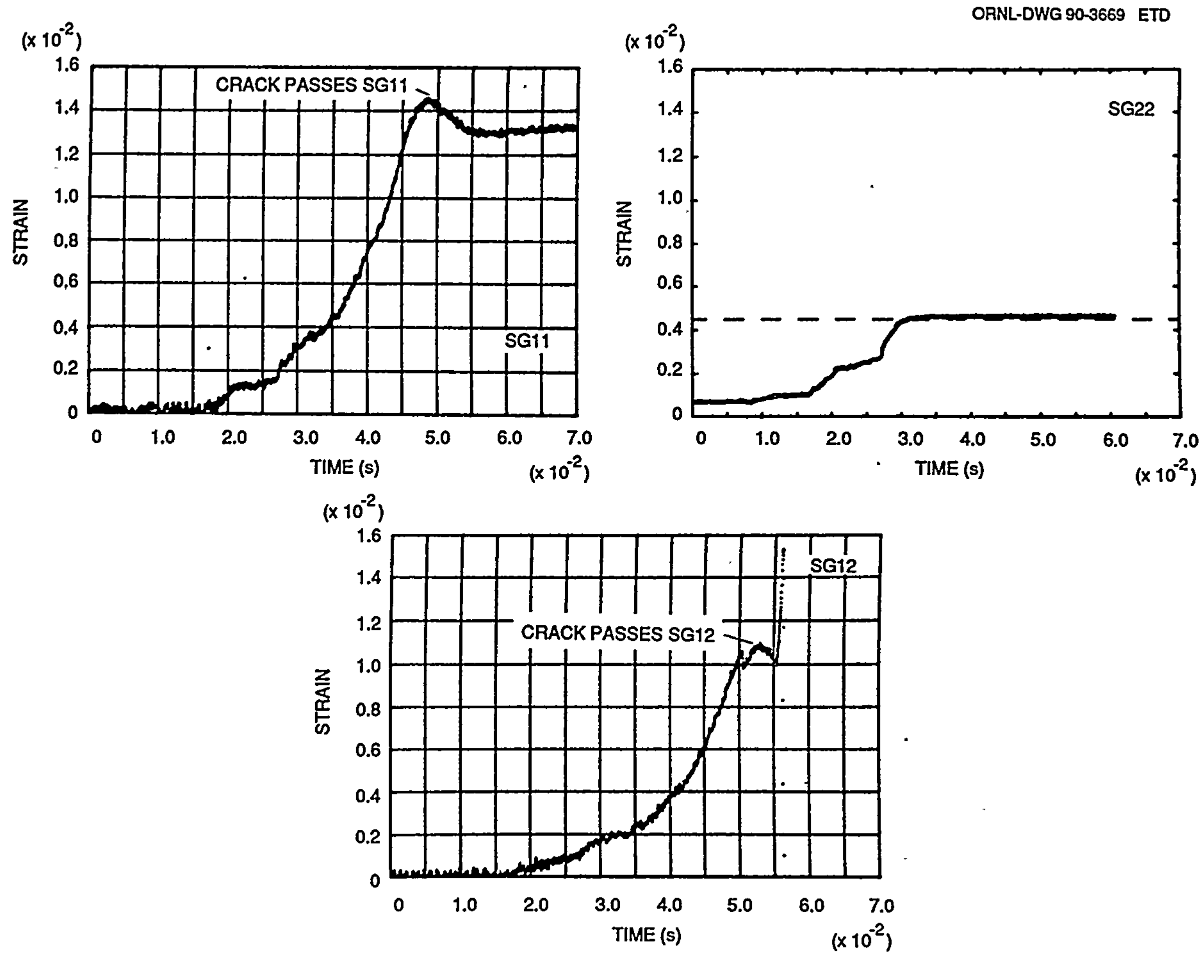

Fig. A.53. Ductile tearing as detected by crack-line gages 11, 12, and 22: test WP-2.4.

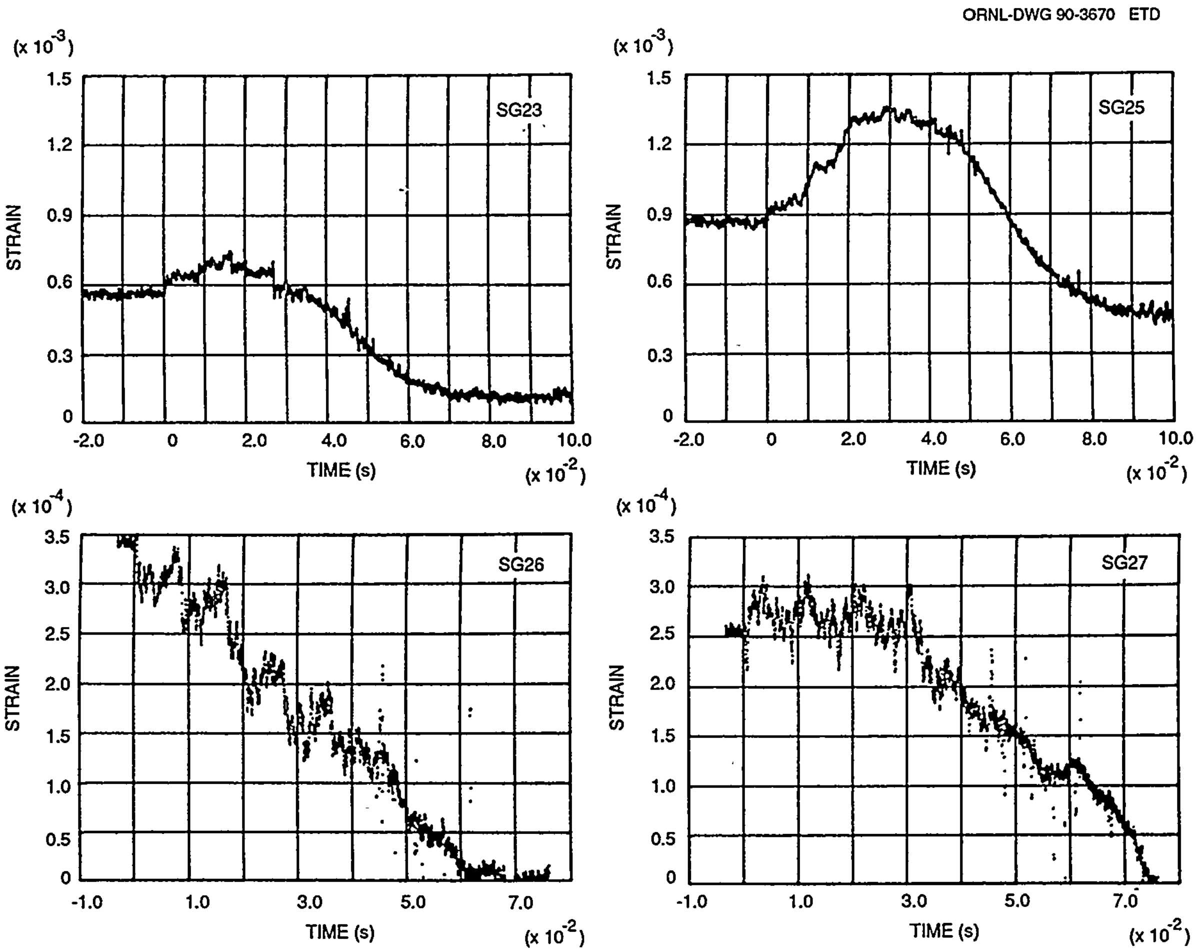

Fig. A.54. Crack run-arrest events as monitored by near-field strain gages 23 and 25 and far-field strain gages 26 and 27: test WP-2.4.

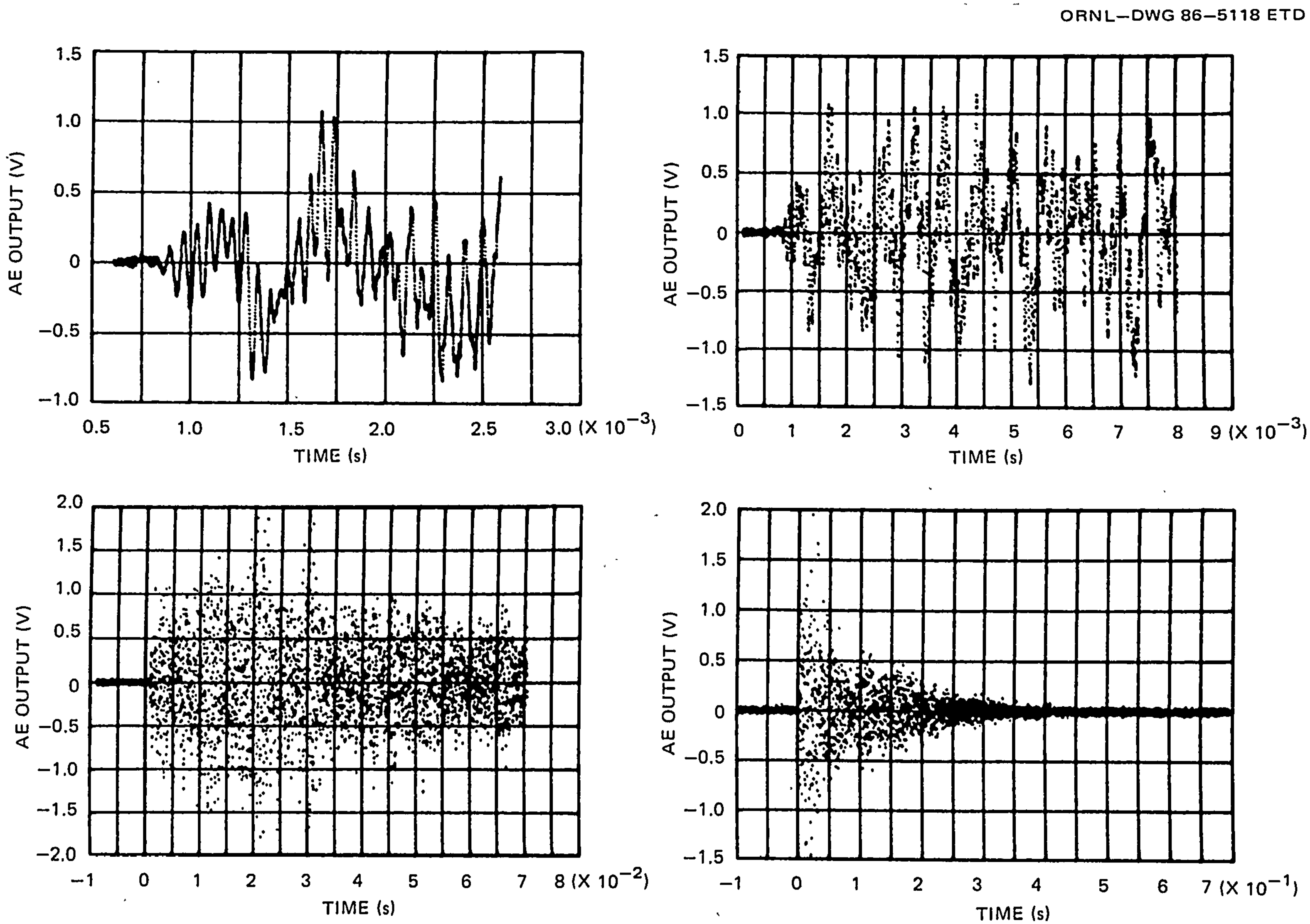

Fig. A.55. AE results at different levels of time resolutions: test WP-2.4.

ORNL-DWG 86-5119 ETD

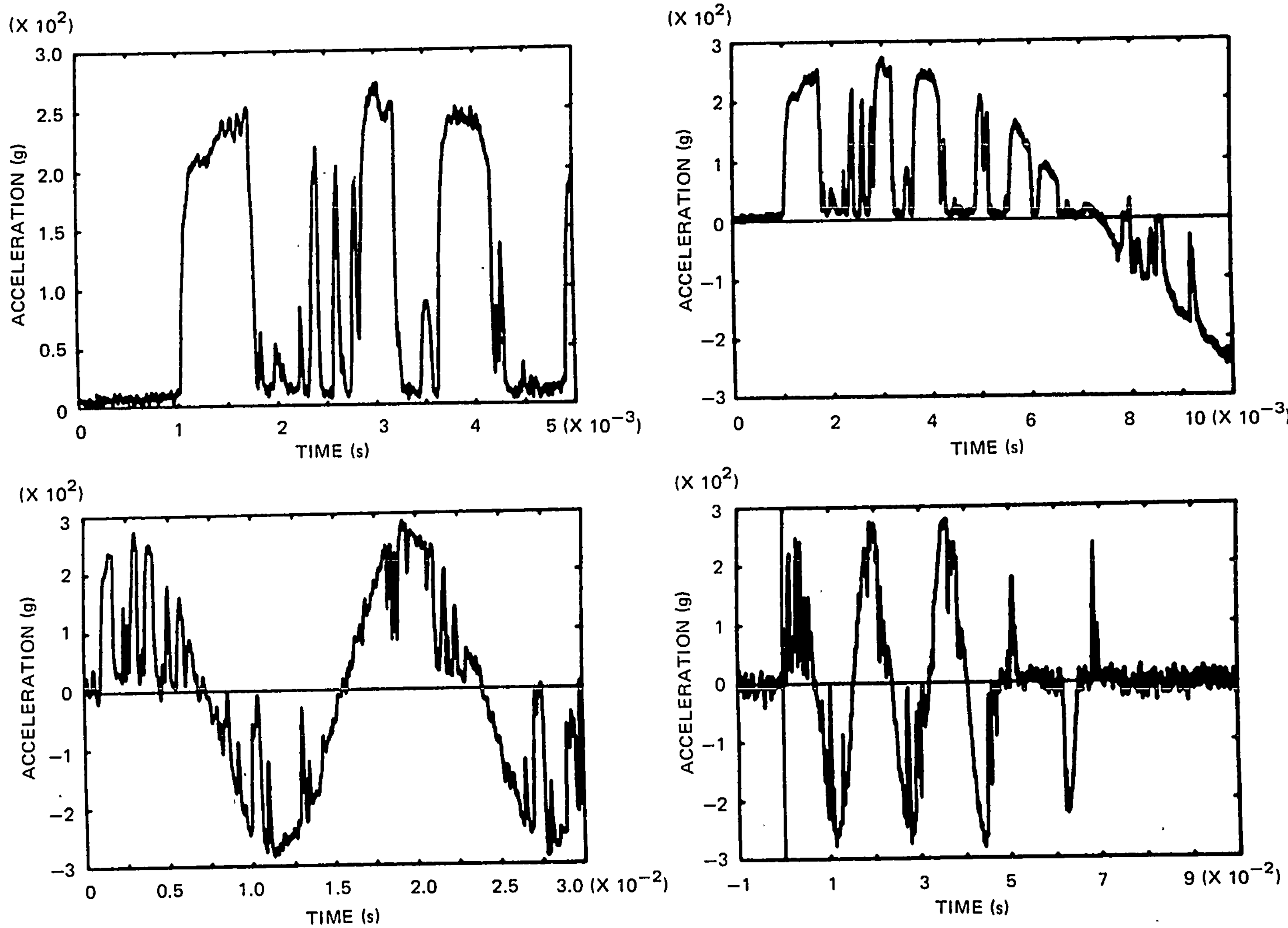

Fig. A.56. Longitidual acceleration during test measured by "damped" accelerometer mounted 4.041 m below crack plane: test WP-2.4.

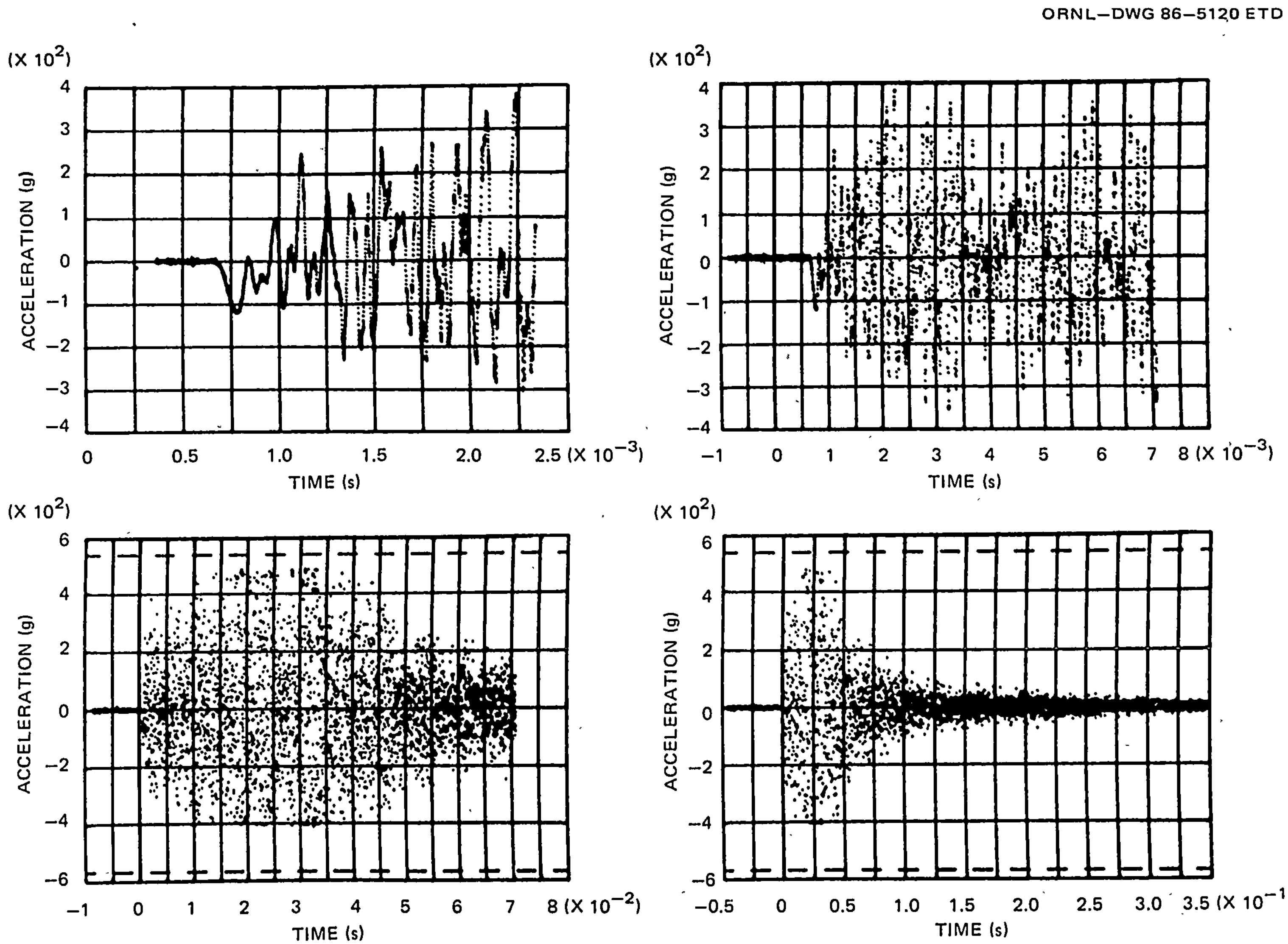

Fig. A.57. Longitidual acceleration during test measured by "shock" accelerometer mounted 4.038 m below crack plane: test WP-2.4.

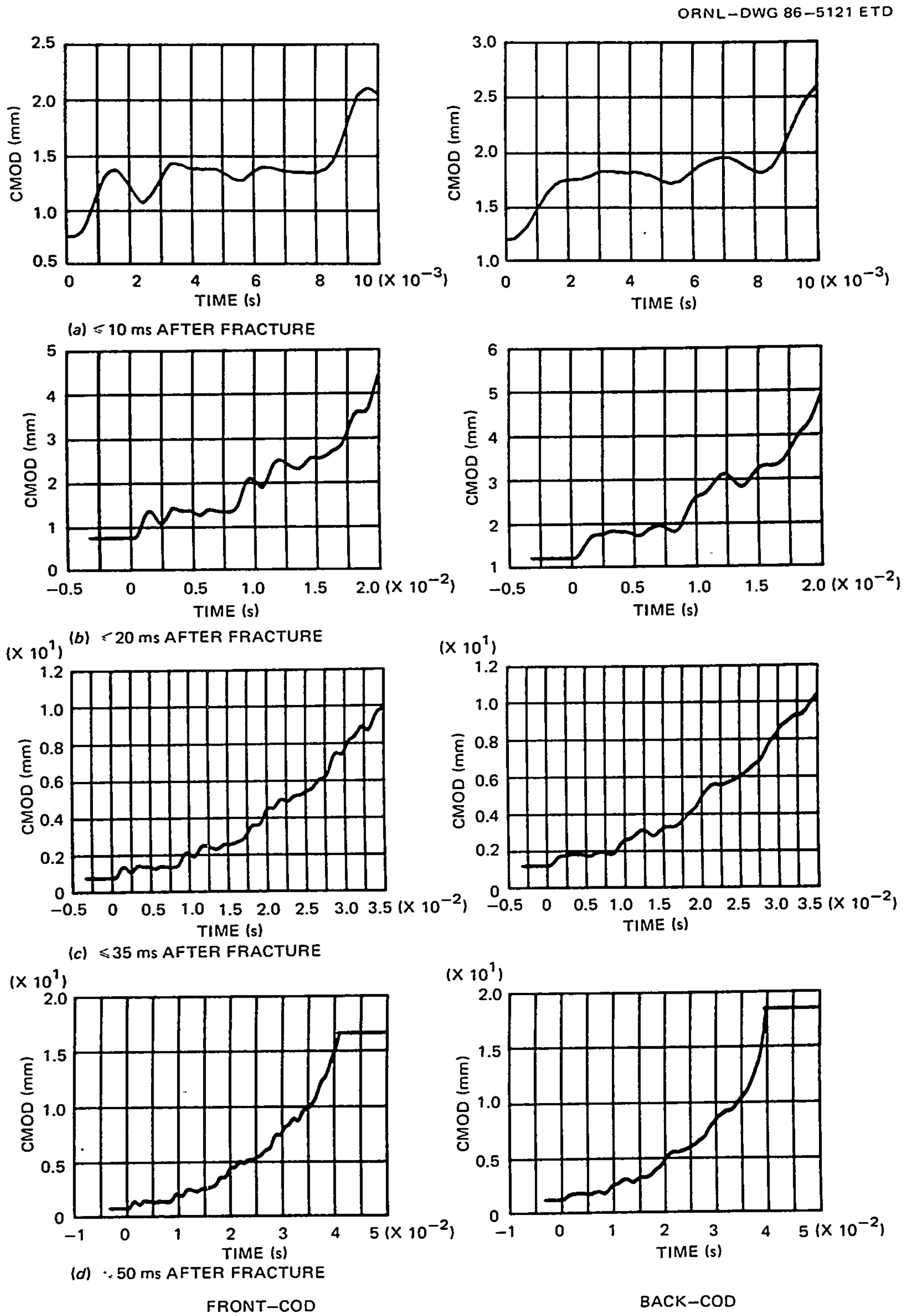

Fig. A.58. Front- and back-face COD at various time spans after fracture initiation: test WP-2.4.

ORNL–DWG 87–3896A ETD

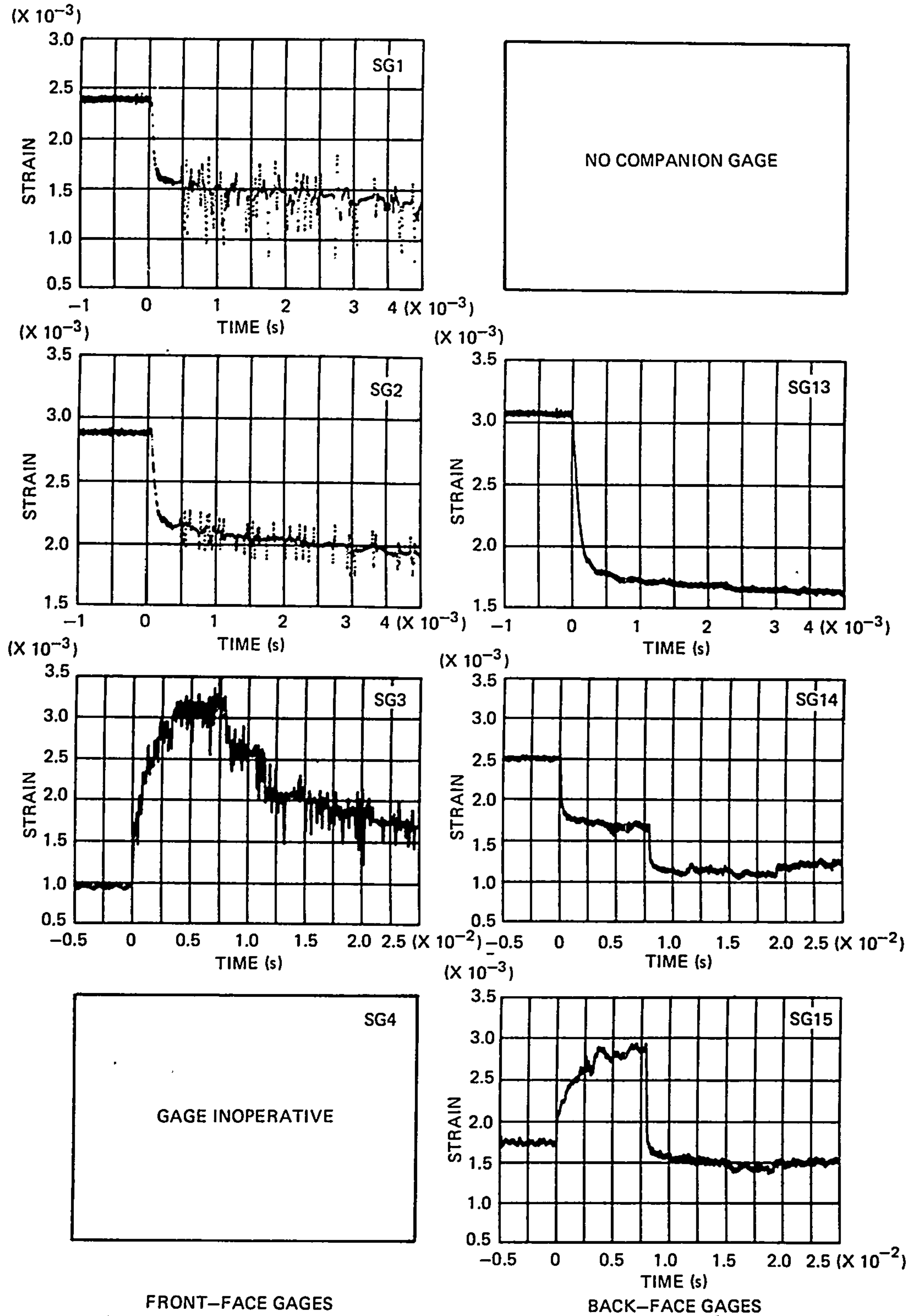

Fig. A.59. Strain histories for companion crack-line gages: test WP-2.5 (gages 1–4 and 13–15).

ORNL–DWG 87–3897A ETD

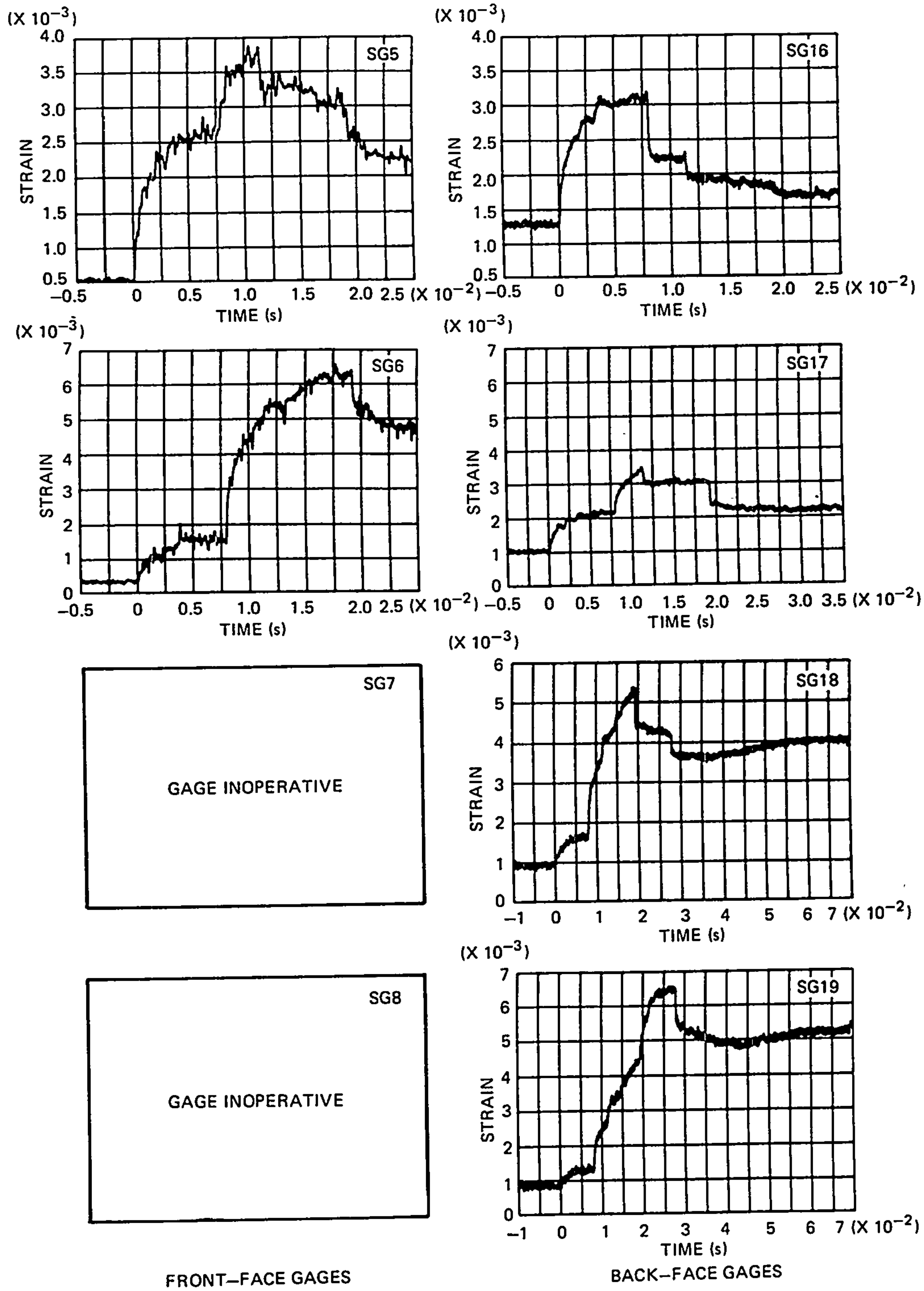

Fig. A.60. Strain histories for companion crack-line gages: test WP-2.5 (gages 5–8 and 16–19).

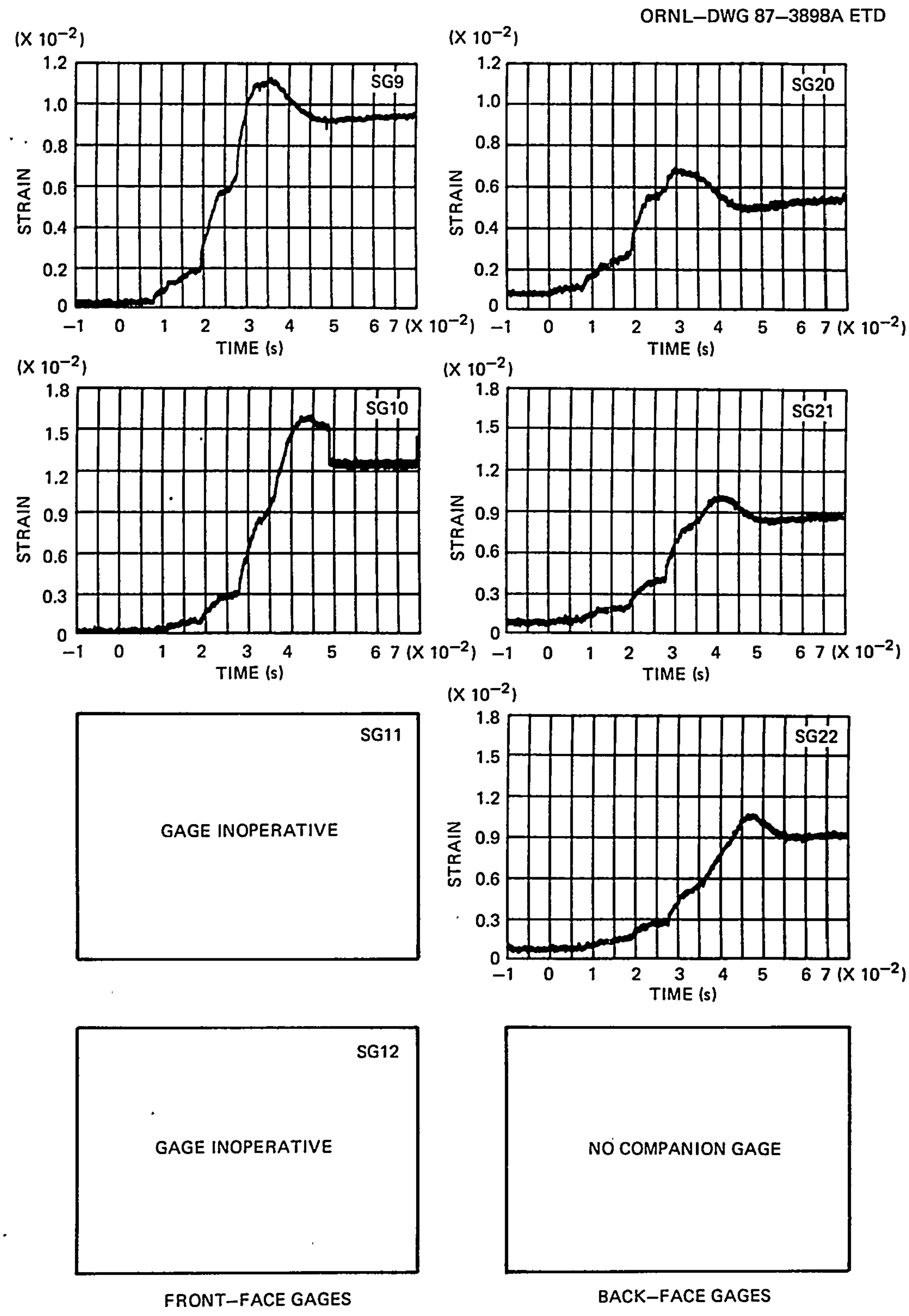

Fig. A.61. Strain histories for companion crack-line gages: test WP-2.5 (gages 9–12 and 20–22).

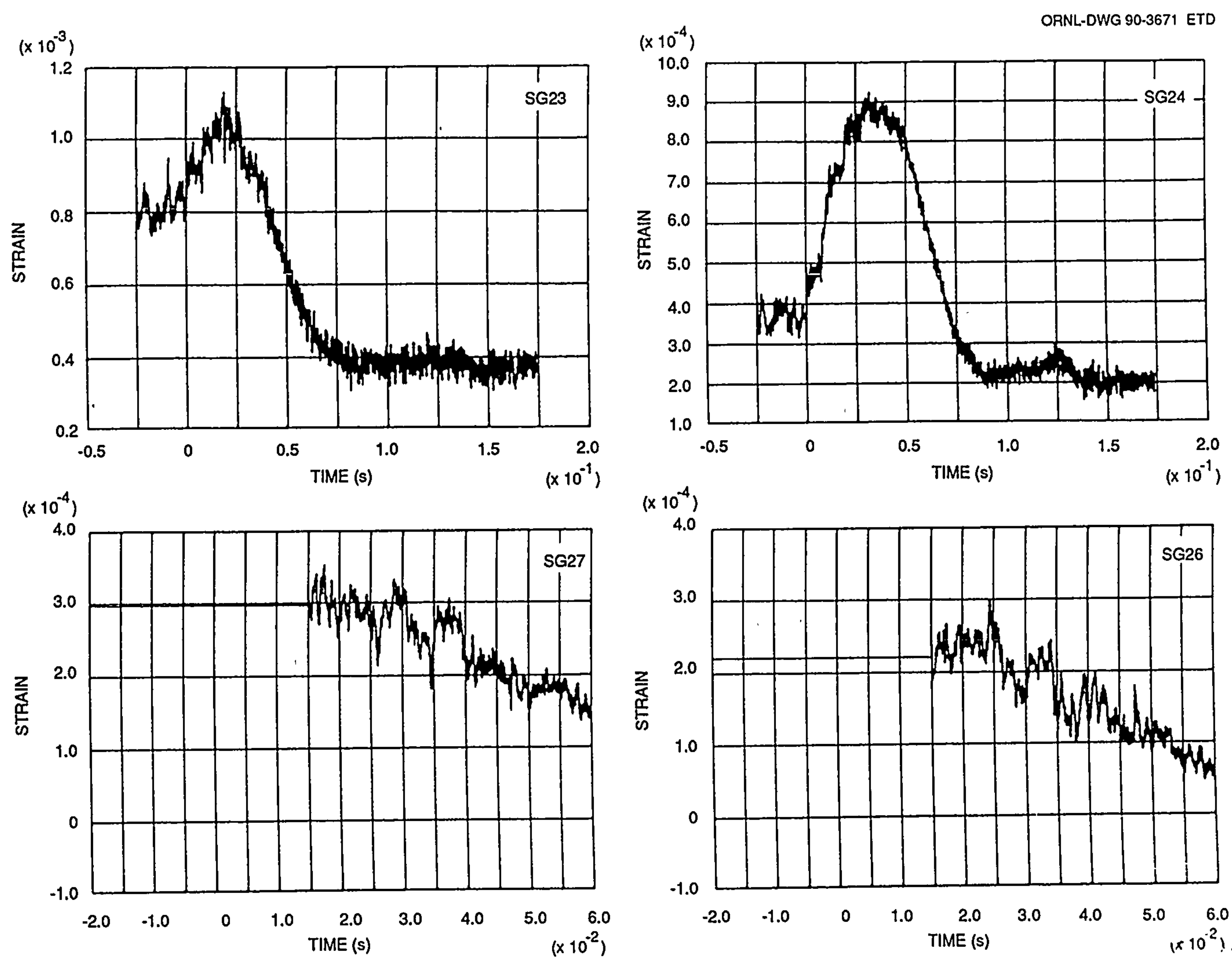

Fig. A.62. Near- and far-field strain histories: test WP-2.5 (gages 23, 24, 26, and 27).

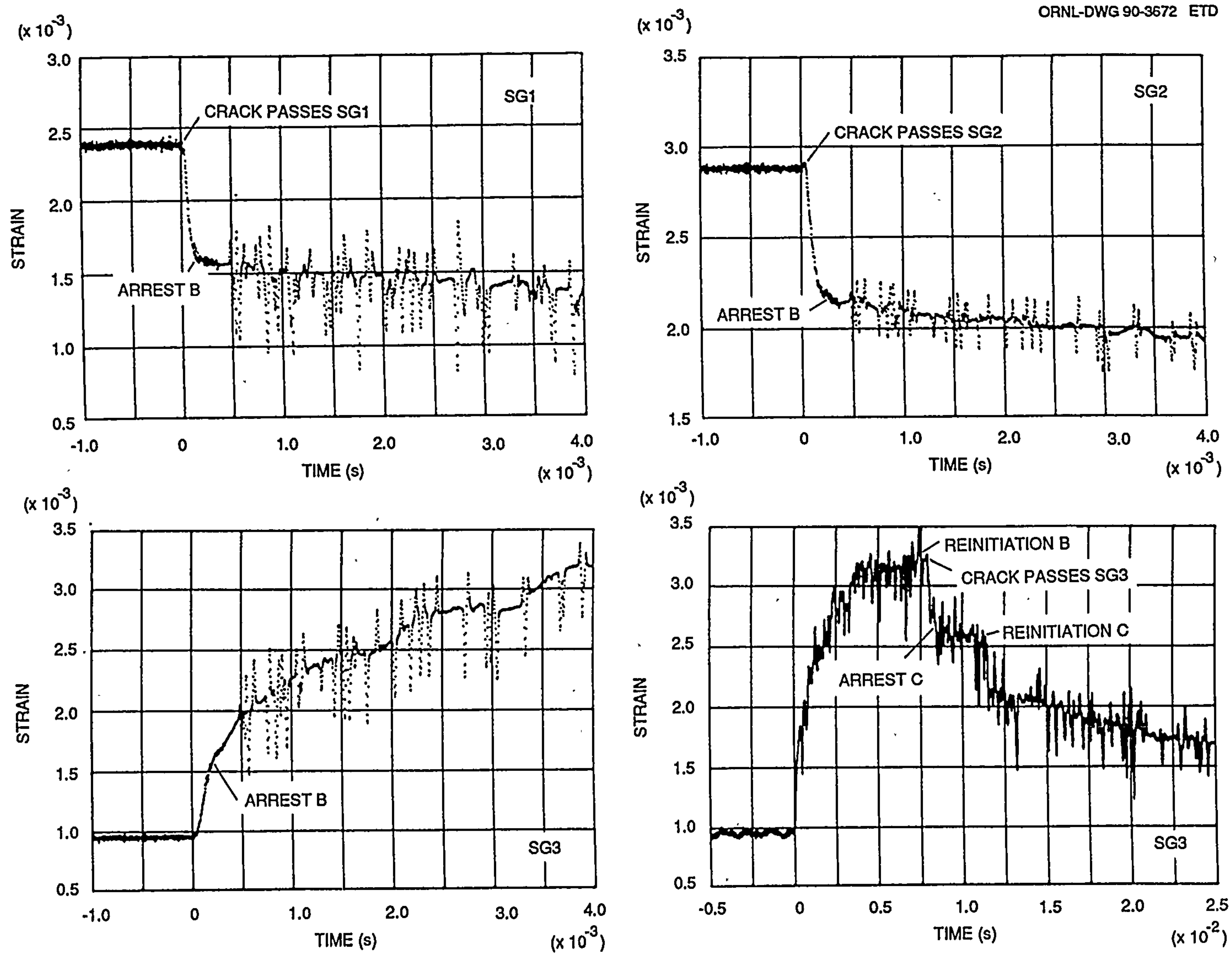

Fig. A.63. Strain histories for front-face gages 1–3, indicating that crack passes gages 1 and 2 and arrests before reaching gage 3 (t = 0.344 ms): test WP-2.5. The longer-duration strain history for gage 3 shows reinitiation (t = 7.87 ms) and the crack passing gage 3 (t = 7.88 ms).

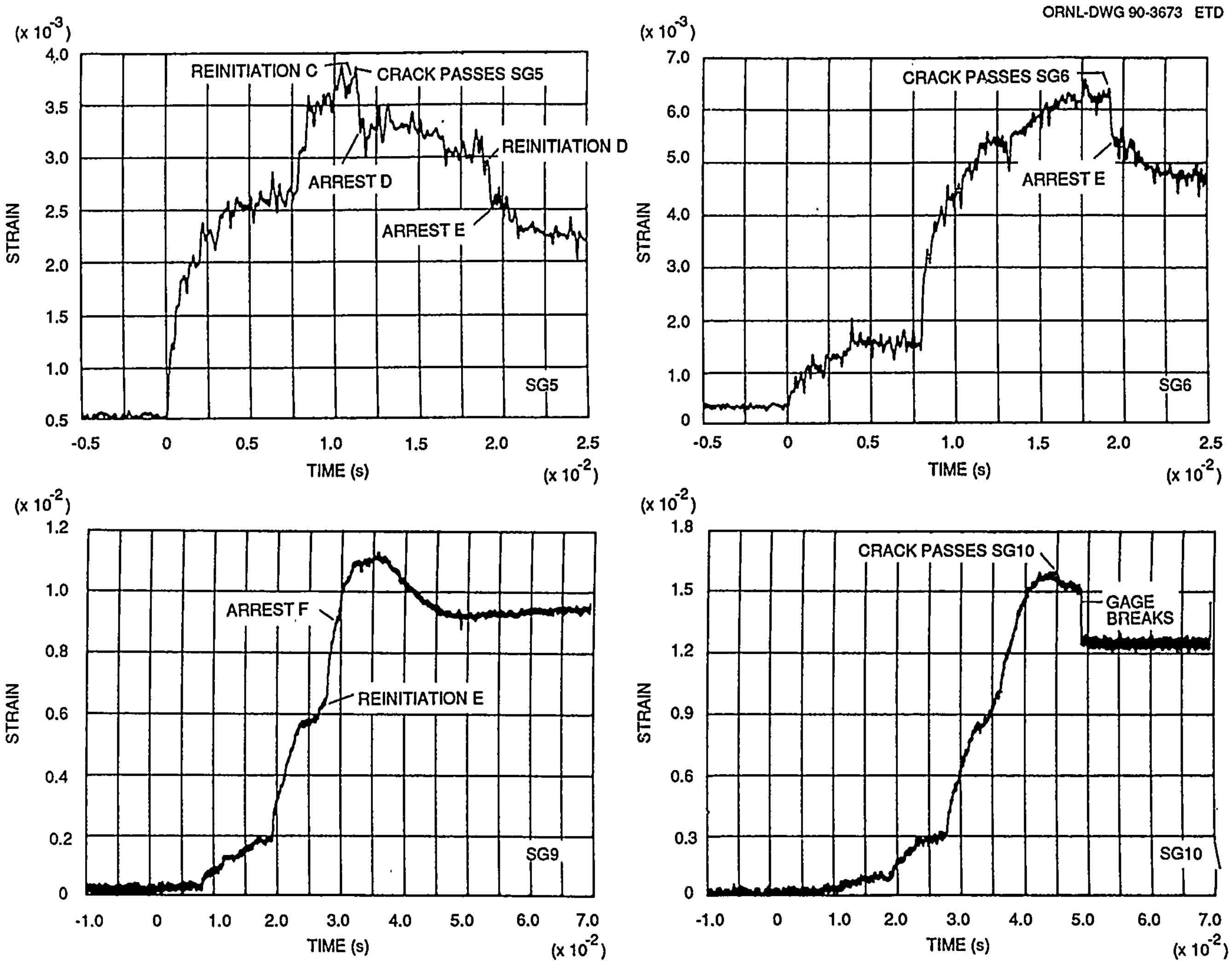

Fig. A.64. Strain histories for front-face gages 5, 6, 9, and 10 indicating multiple crack run-arrest events (see Table 5.6): test WP-2.5.

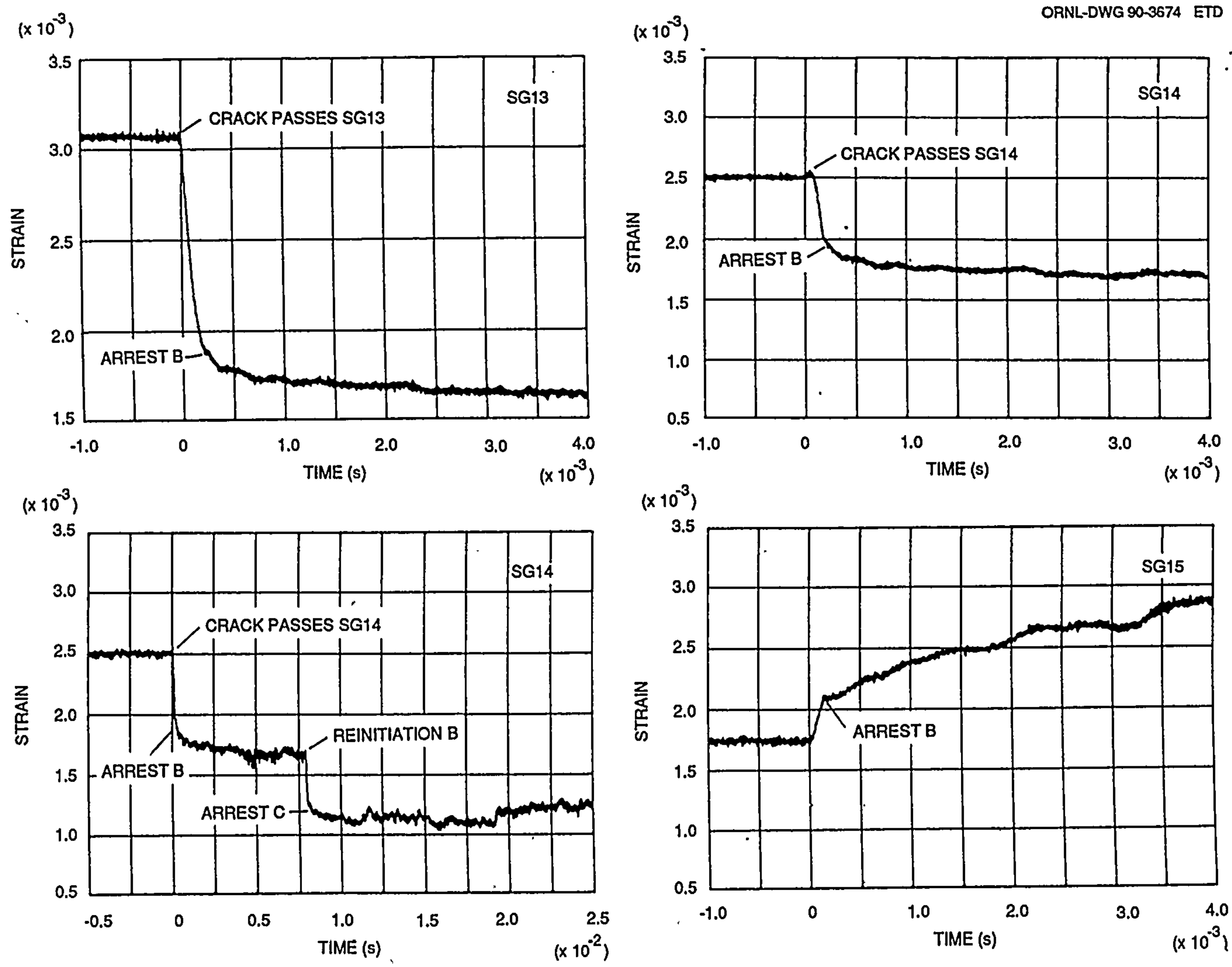

Fig. A.65. Strain histories for back-face gages 13–15 indicating that crack passes gages 13 and 14 with a subsequent arrest (t = 0.54 ms) before reaching gage 15: test WP-2.5.

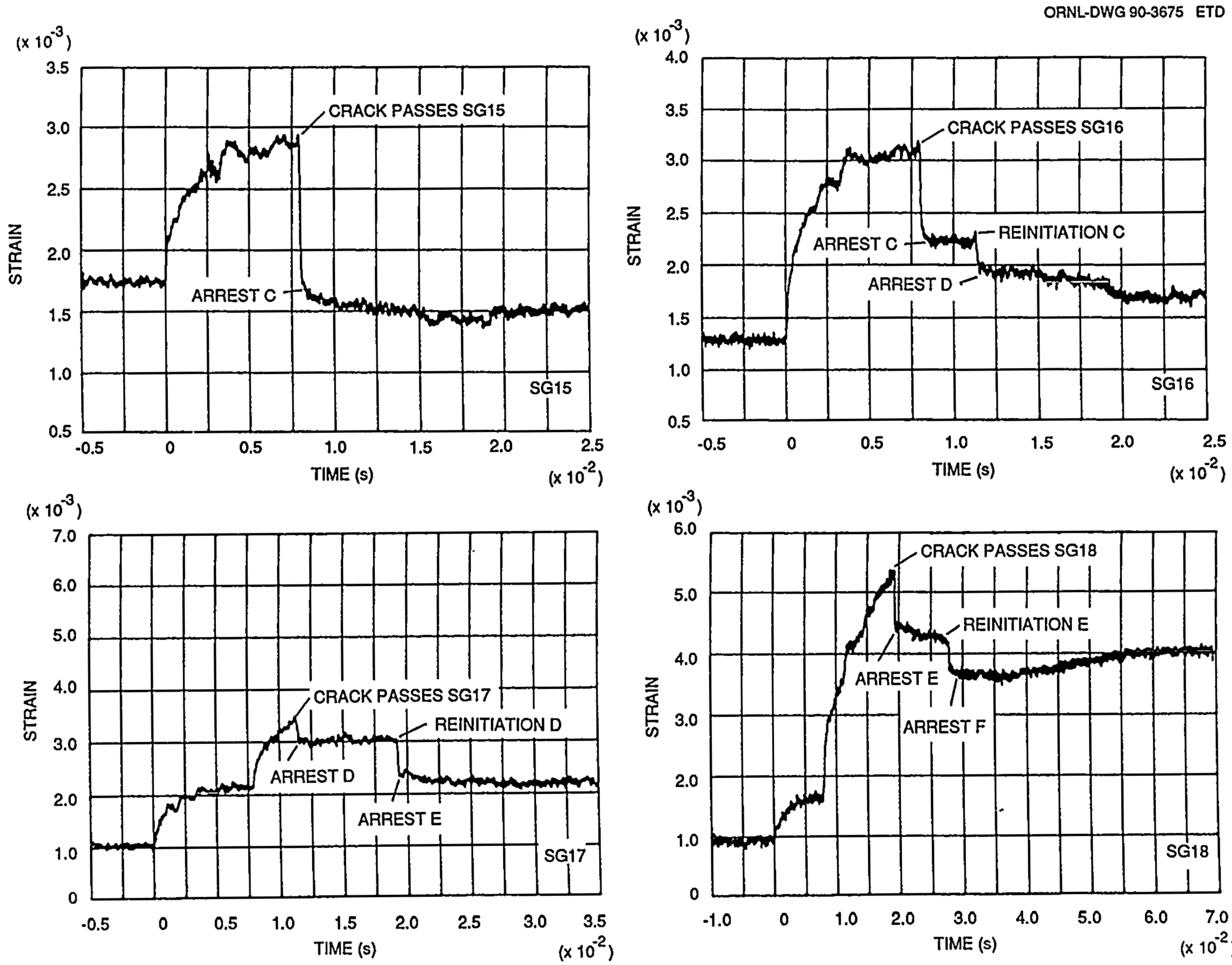

Fig. A.66. Strain histories for back-face gages 15–18, indicating that crack passes gages 15 and 16, arrests (t = 8.16 ms) before reaching gage 17, reinitiates (t = 11.16 ms), passes under gage 17, arrests (t = 11.49 ms) before reaching gage 18, reinitiates (t = 19.11 ms), and then passes under gage 18: test WP-2.5.

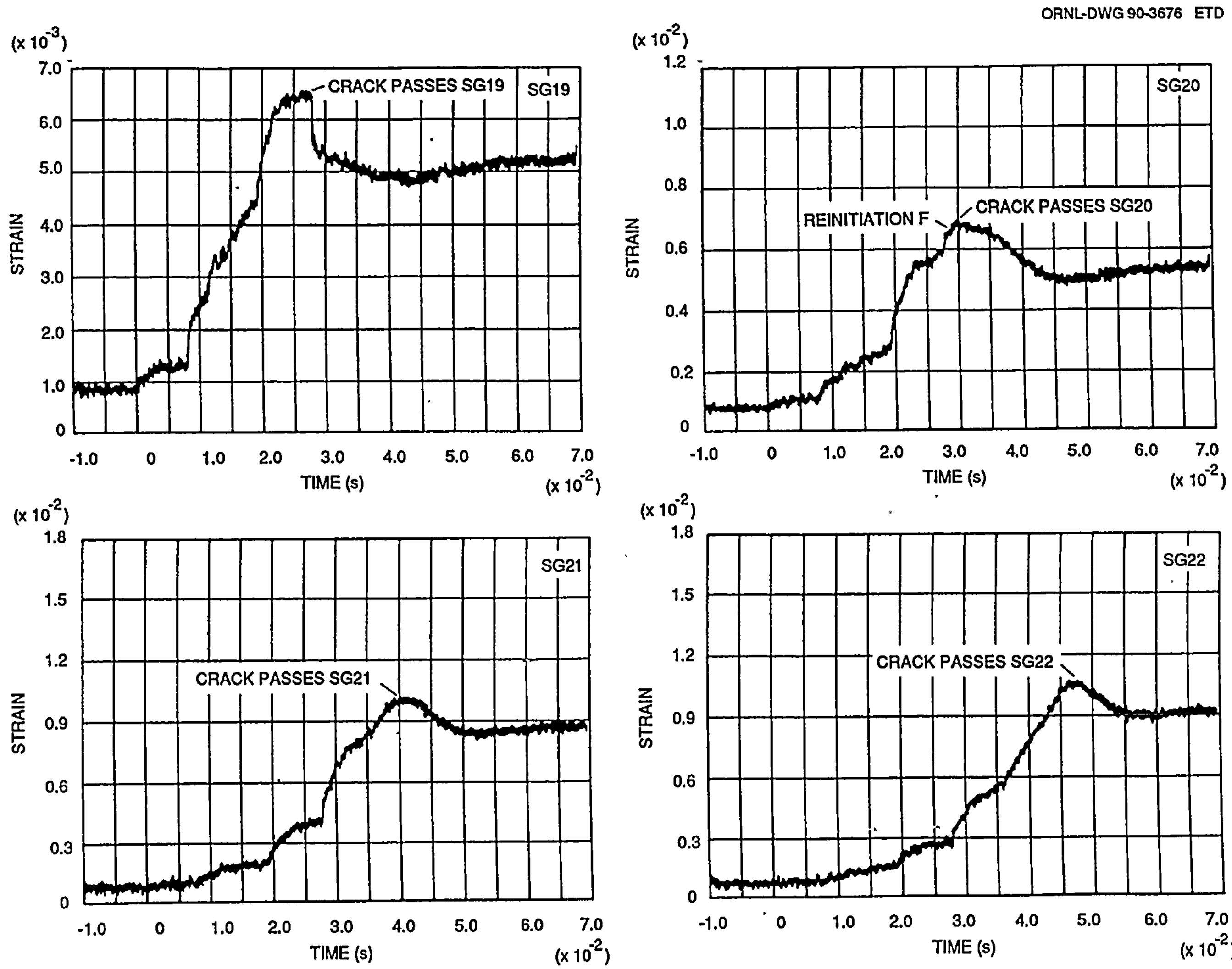

Fig. A.67. Strain histories for back-face gages 19–22 showing crack passing gage 19, arresting (t = 27.95 ms), converting to fibrous tearing, and then passing under gages 20–22: test WP-2.5.

reinitiation of crack propagation at t = 7.90 ms. Strain histories for gages 15–18, shown in Fig. A.66, indicate that the crack passes gages 15 and 16, arrests (t = 8.16 ms), reinitiates (t = 11.16 ms), passes under gage 17, arrests (t = 11.49 ms) before reaching gage 18, reinitiates (t = 19.11 ms), and then passes under gage 18. Figure A.67 shows the crack passing strain gage 19, arresting (t = 27.95 ms), converting to fibrous tearing, and then passing under strain gages 20–22.

A.5.2 Additional Instrumentation

Longitudinal accelerations recorded by "damped" accelerometers mounted 3.911 m above (top) and 3.934 m below (bottom) the crack plane during the first crack run-arrest event are shown in Fig. A.68. Front- and back-face COD results obtained from gages located at a/w = 0.150 are presented in Fig. A.69 (note that the first 15 ms of the fracture event was not recorded because of an error in the selection of triggering parameters for the gages).

A.6 TEST WP-2.6

A.6.1 Strain Gages

Figures A.70 to A.72 present strain histories for the front-face crack-line gages. (Gage locations are presented in Fig. 4.9.) Propagation of the cleavage crack past gages 1–4 with arrest of crack propagation just past gage 4 is shown in Fig. A.70. Also noted in the figure presenting the strain history of gage 4 is that a total of five crack run-arrest events occurred within ~4 ms of initiation. Examination of the strain histories for gages 5–8 (Fig. A.71) shows two additional crack run-arrest events. Strain histories for gages 9–12 (Fig. A.72) indicate fibrous crack propagation past these gages with the gages breaking as the crack approaches and passes because of high strain levels.

Strain histories for the back-face crack-line gages are presented in Figs. A.73 and A.74. Note that these gages were rotated 45° relative to the orientation of the crack-line gages positioned on the plate front face and that when the crack passes one of these gages the strain generally passes through zero. Figure A.73 shows the crack initiating near gage 13, with gage output being initially negative because the crack had been past this gage as a result of crack growth during the warm-prestressing phase. Also shown in Fig. A.73 is crack propagation past gages 14–16. Crack propagation past gages 17–20 is presented in Fig. A.74, with arrests evident by breaks or discontinuities in the strain records.

Figure A.75 presents the strain history for near-field gage 21 at two levels of time resolution. Complete separation of the plate is indicated by a leveling off of the strain output, which occurs ~34.5 ms after initiation. Far-field strain histories for gages 22–25 are presented in Fig. A.76.

ORNL–DWG 87–3900 ETD

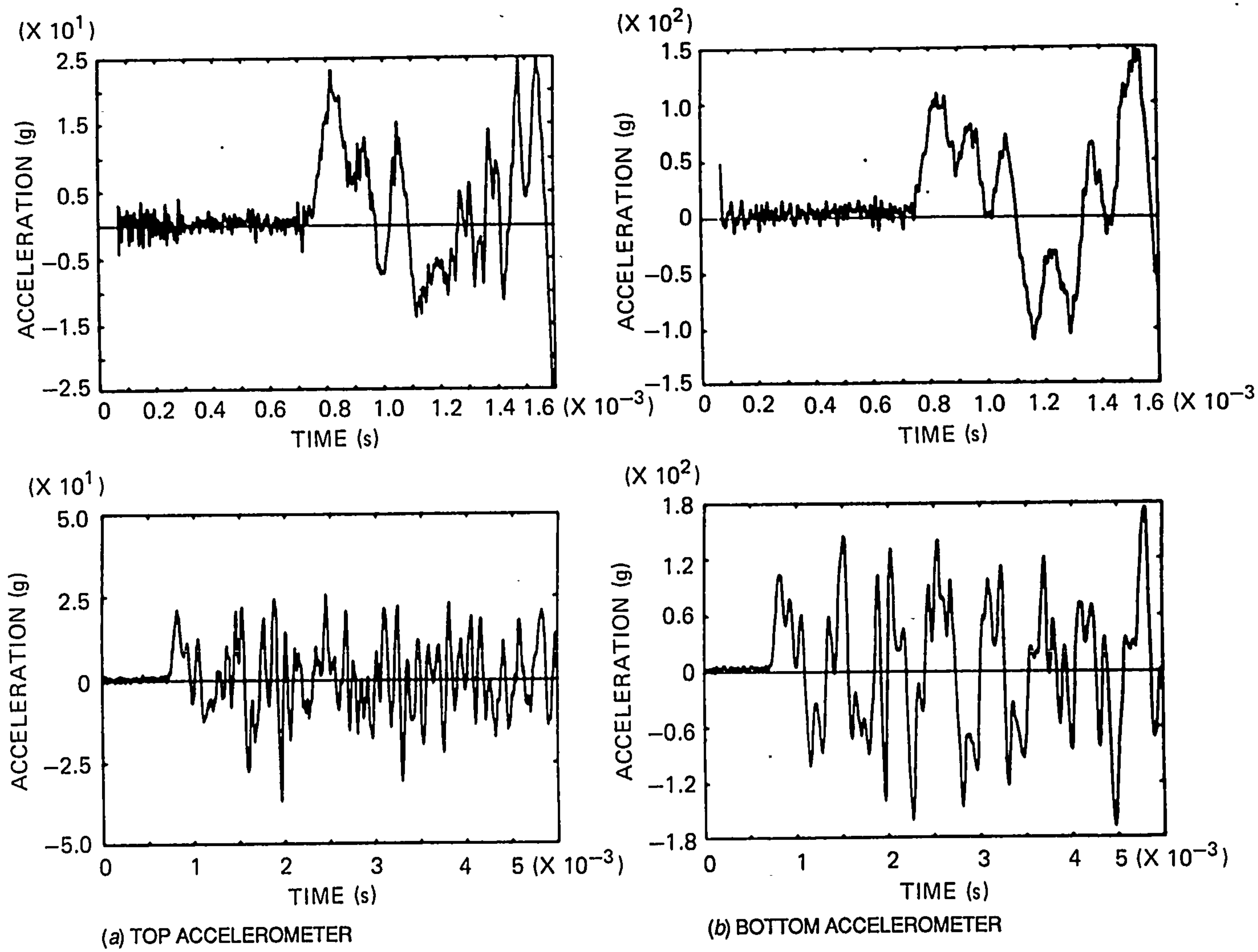

Fig. A.68. Accelerometer outputs during first crack run-arrest event: test WP-2.5.

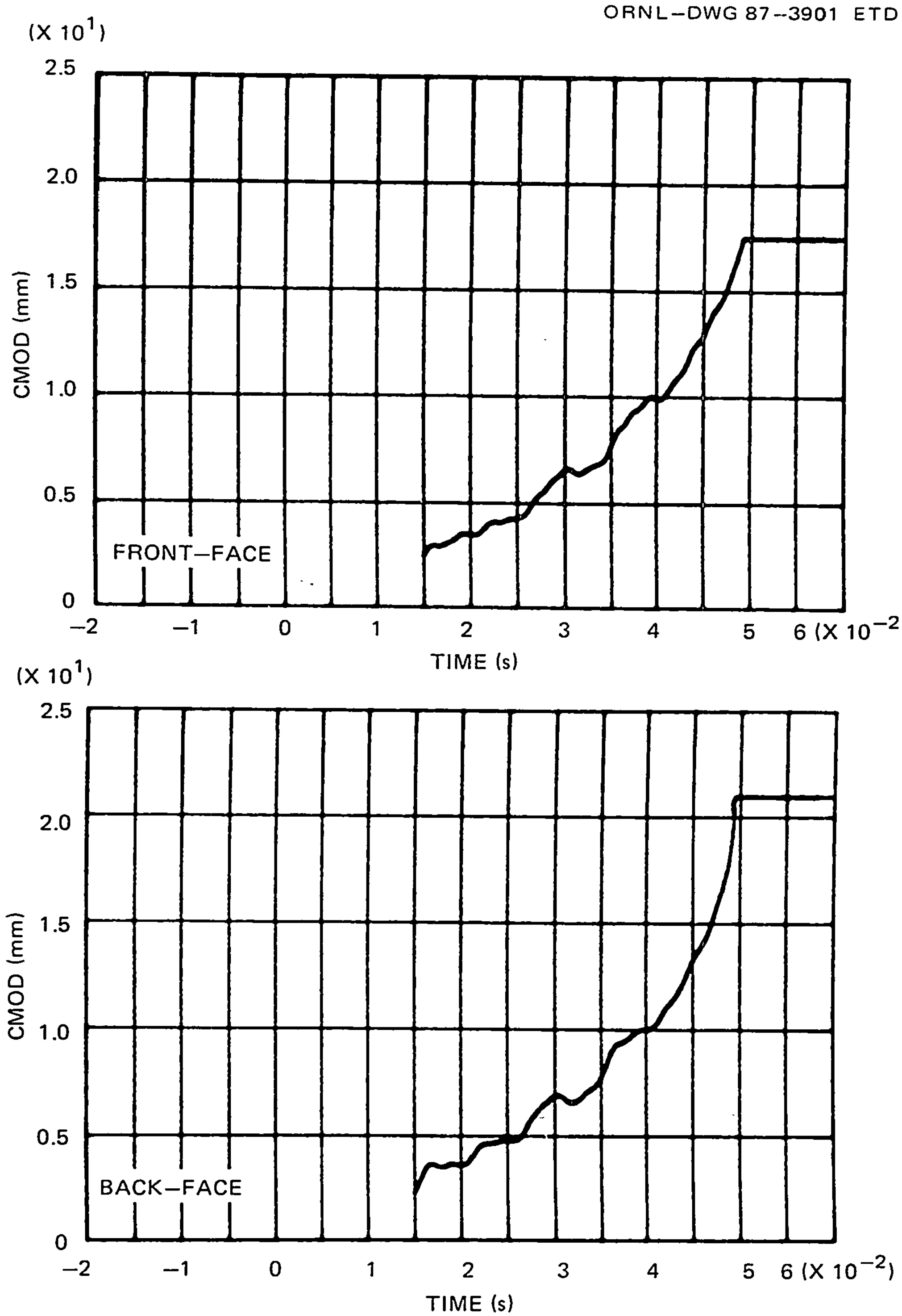

Fig. A.69. Front- and back-face CODs during the fracture event: test WP-2.5.

ORNL-DWG 89-5042 ETD

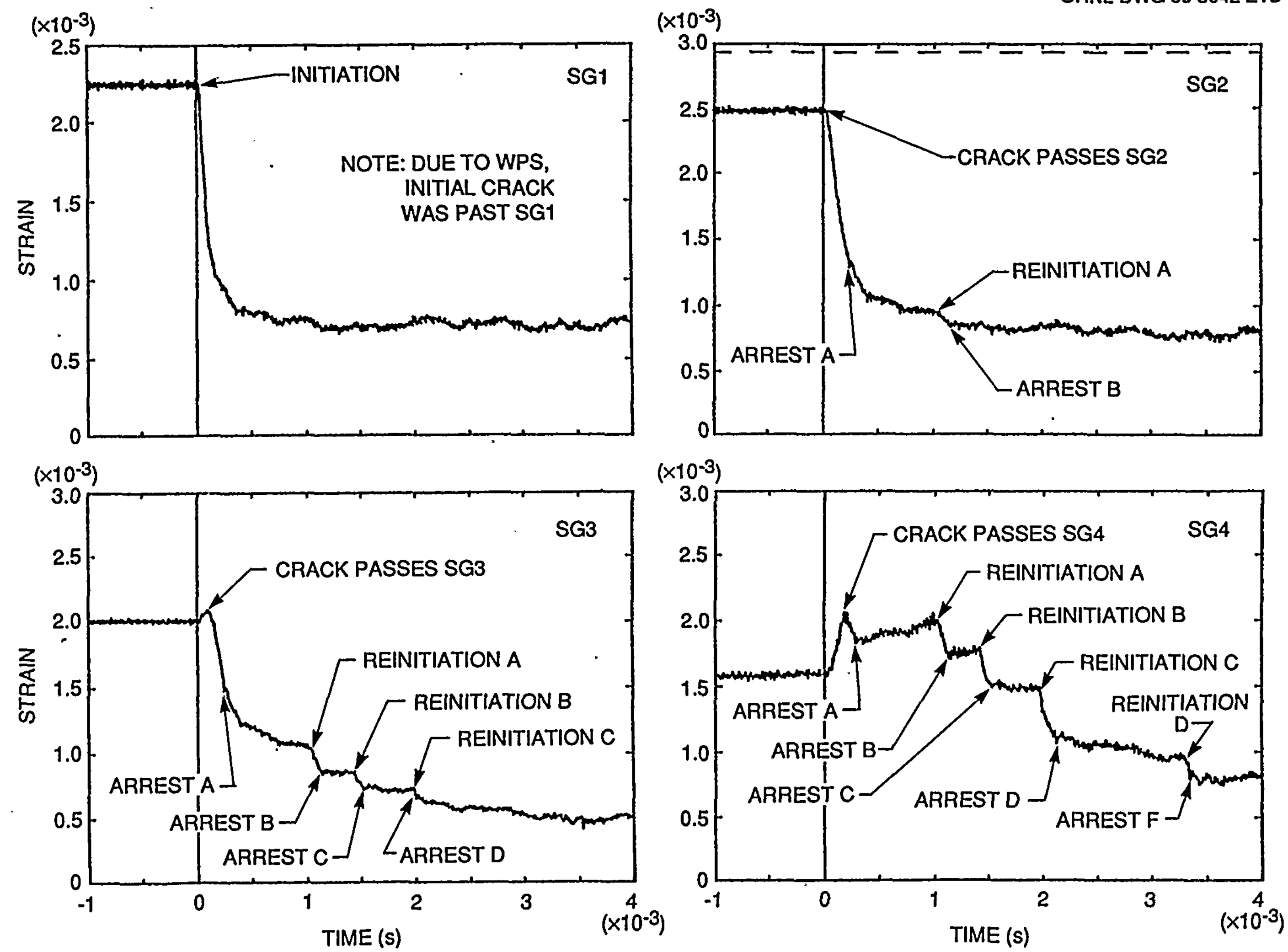

Fig. A.70. Strain histories for front-face crack-line gages: test WP-2.6 (gages 1–4).

ORNL-DWG 89-5043 ETD

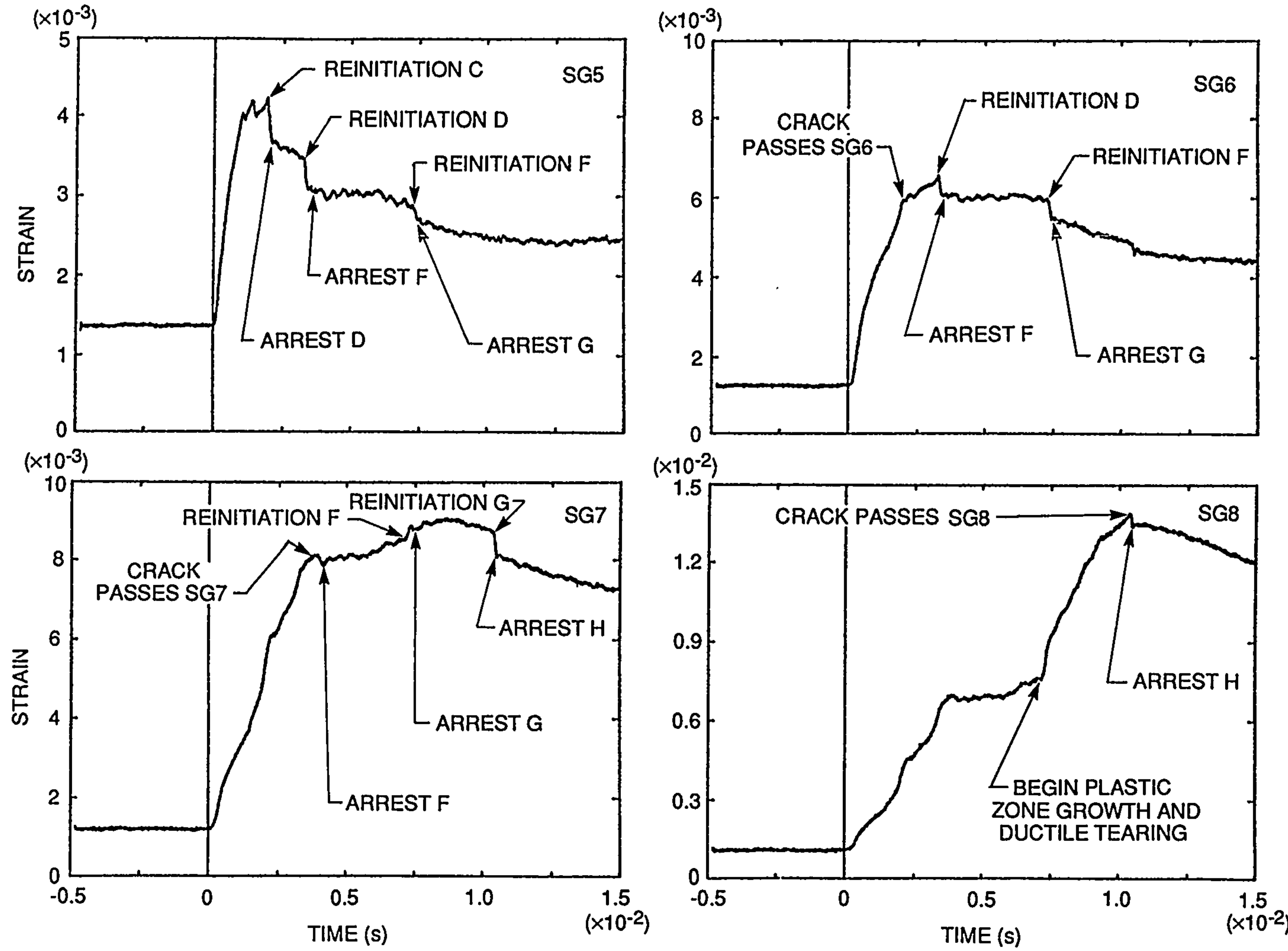

Fig. A.71. Strain histories for front-face crack-line gages: test WP-2.6 (gages 5–8).

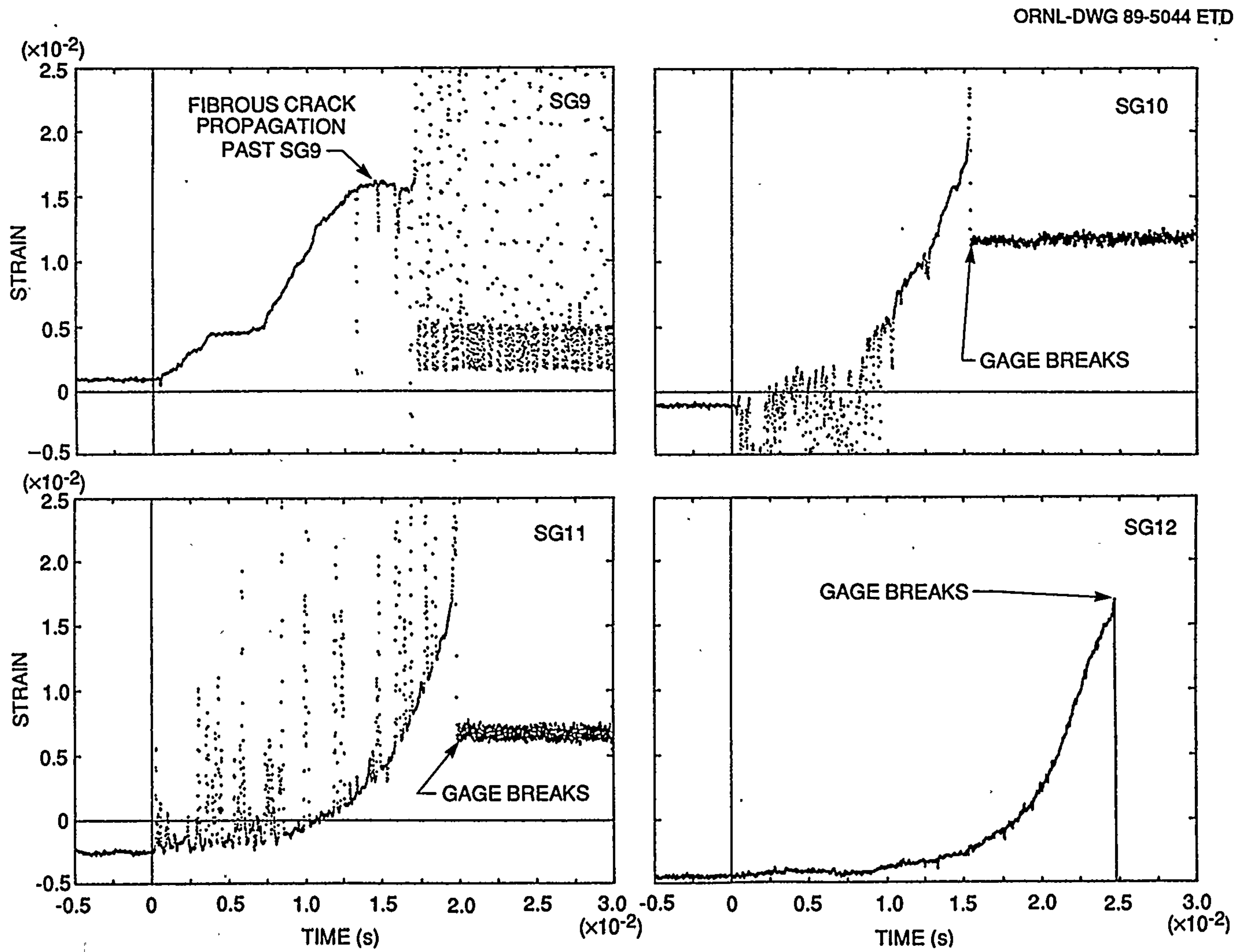

Fig. A.72. Strain histories for front-face crack-line gages: test WP-2.6 (gages 9–12).

ORNL-DWG 89-5045 ETD

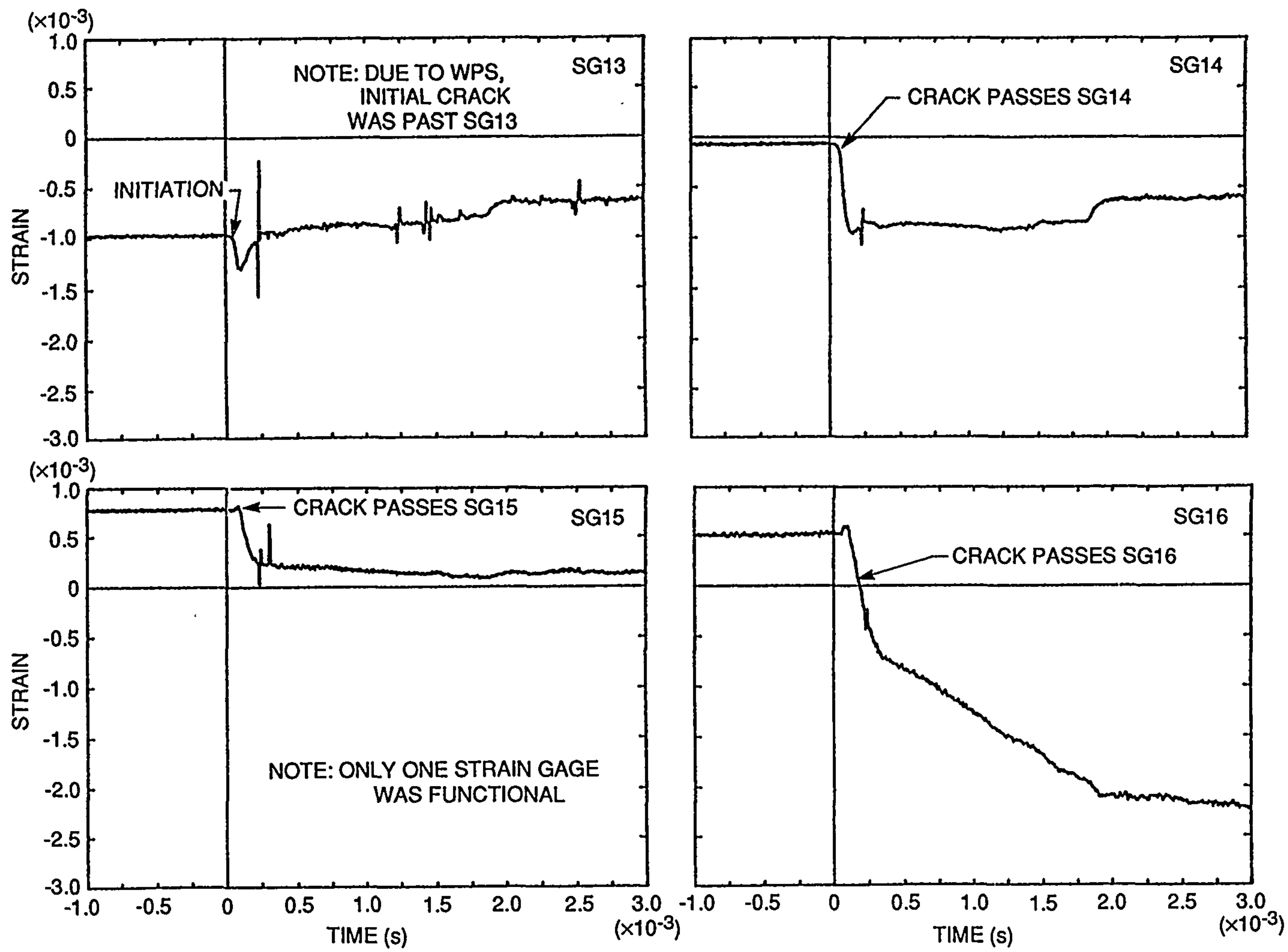

Fig. A.73. Strain histories for back-face crack-line gages: test WP-2.6 (gages 13–16).

ORNL-DWG 89-5046 ETD

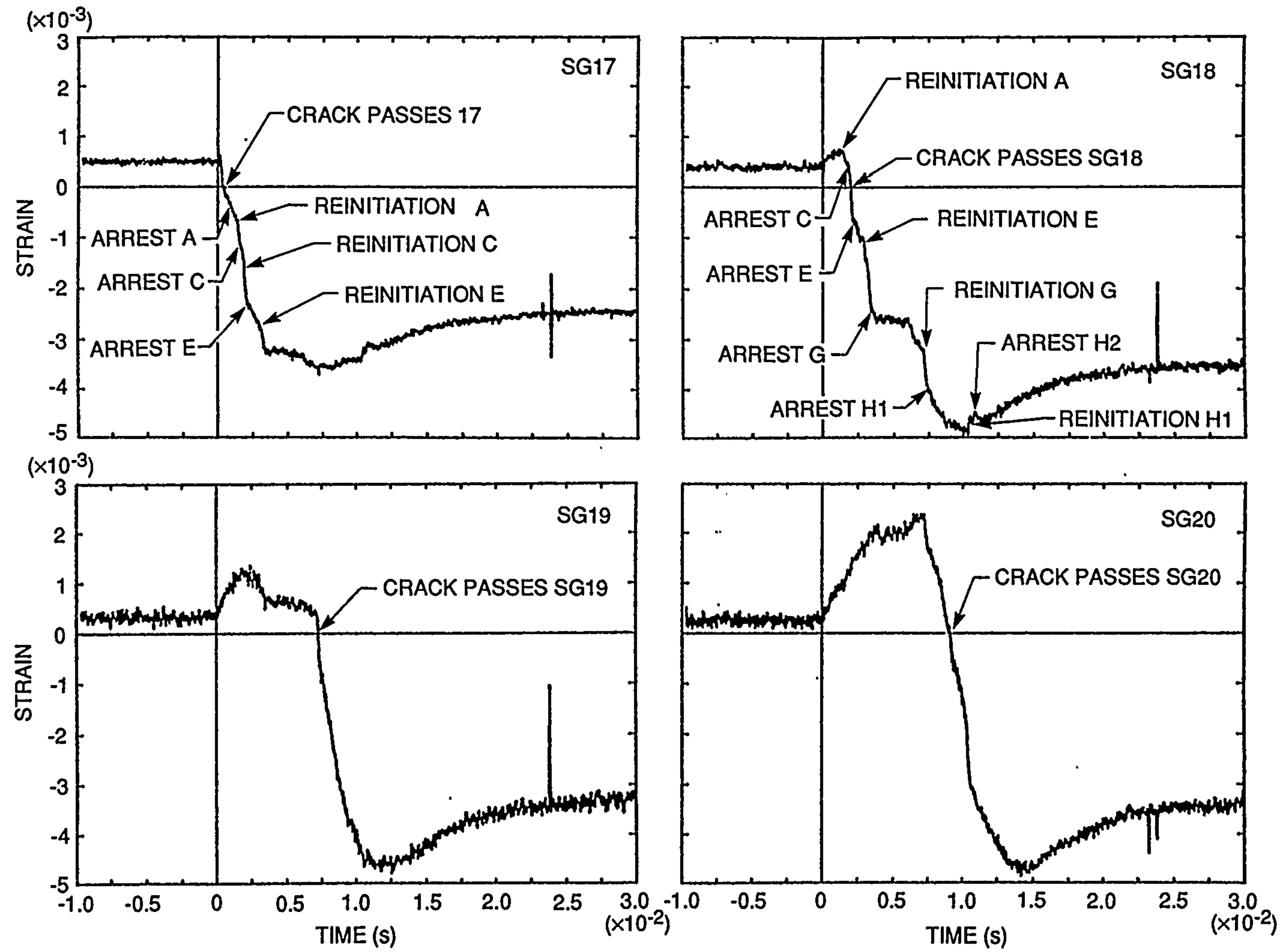

Fig. A.74. Strain histories for back-face crack-line gages: test WP-2.6 (gages 17–20).

ORNL-DWG 89-5047 ETD

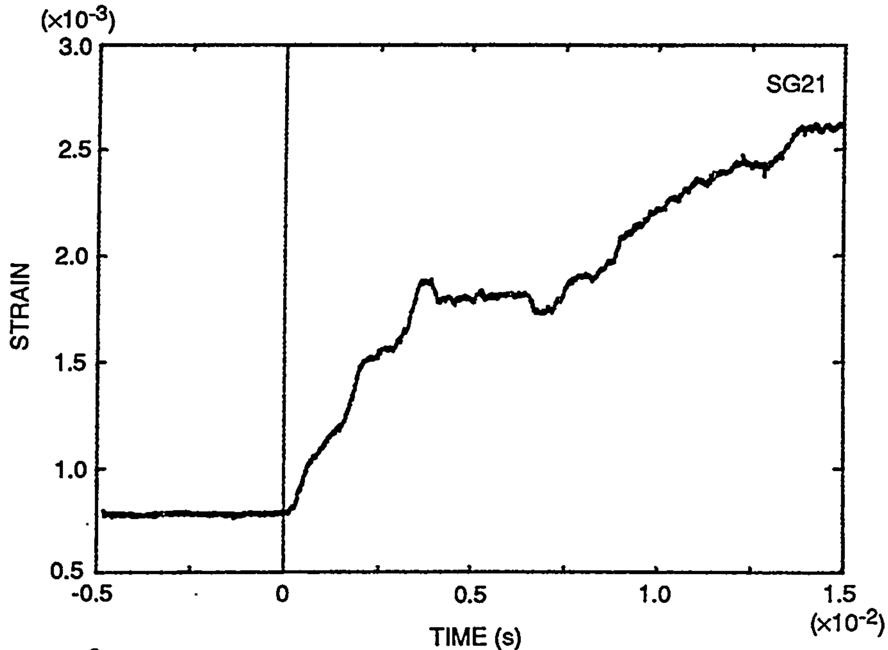

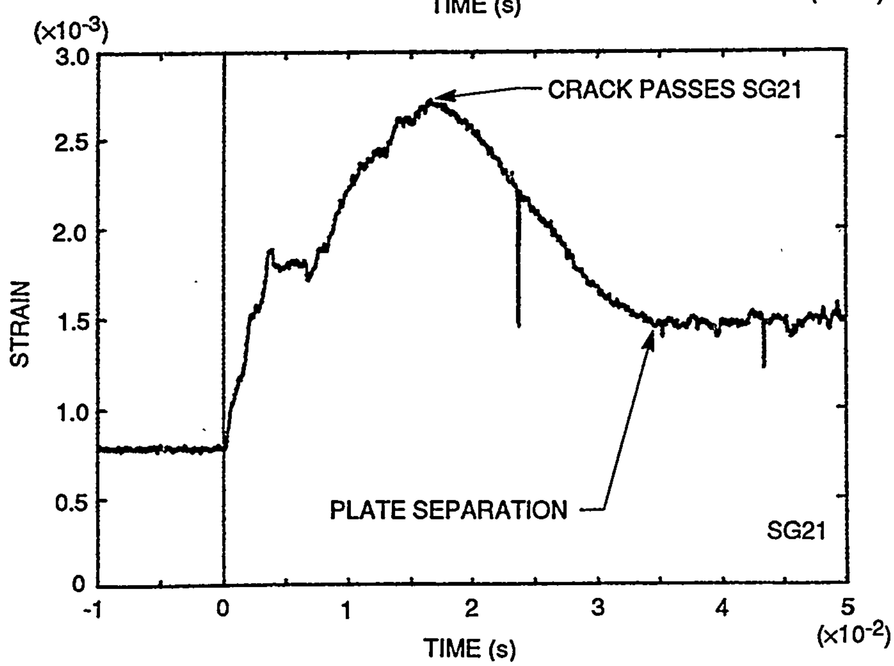

Fig. A.75. Strain history for near-field gage 21 at two time resolutions: test WP-2.6.

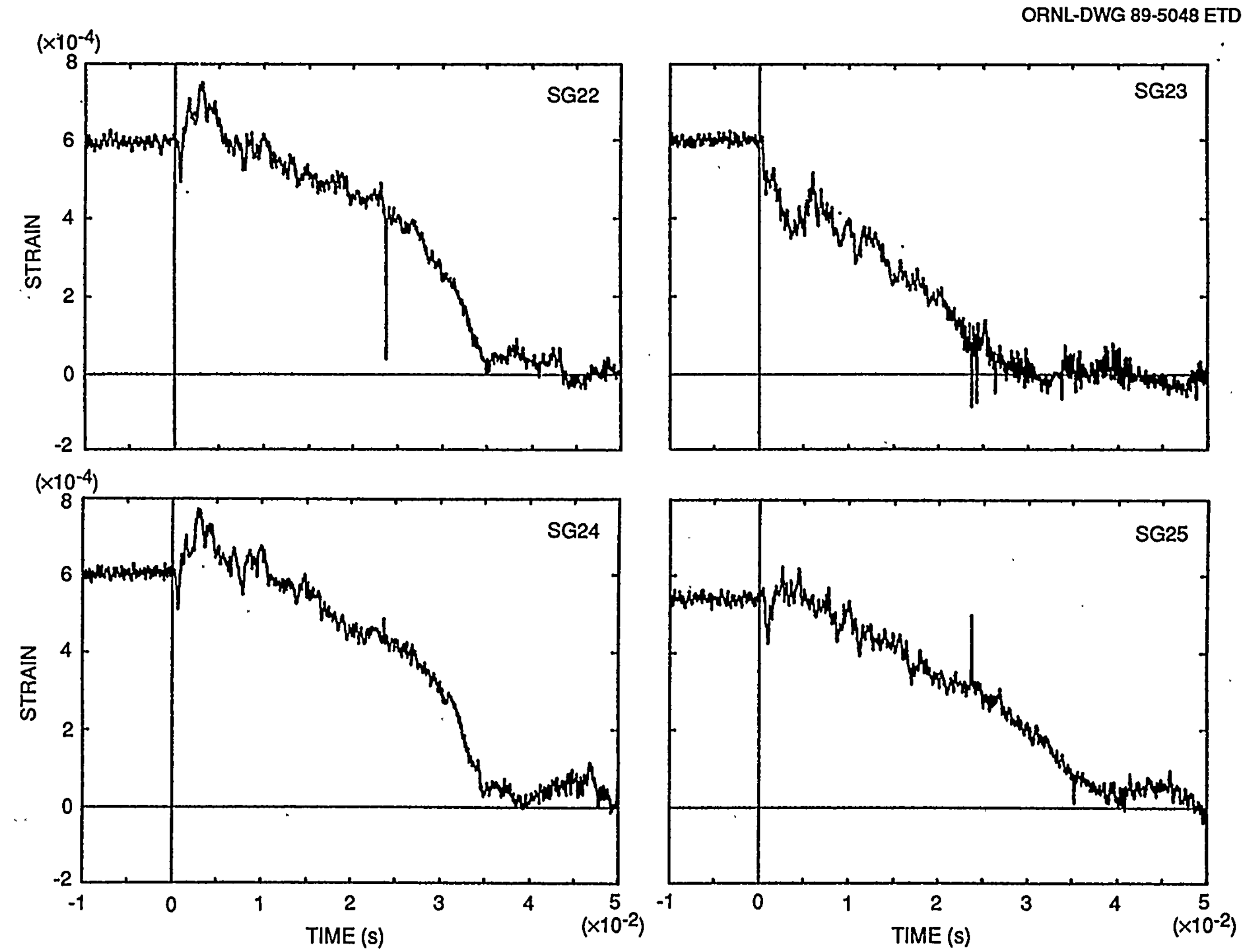

Fig. A.76. Strain histories for far-field gages 22–25 during entire fracture process: test WP-2.6.

A.6.2 Additional Instrumentation

Front- and back-face COD histories at two time resolutions are presented in Fig. A.77. Longitudinal accelerations recorded by "damped" accelerometers mounted on the specimen's centerline 3.491 m above (top) and 3.398 m below (bottom) the crack plane are presented in Fig. A.78. Dynamic displacement of the specimen, relative to that of the large columns of the testing machine, as measured 3.393 m below the crack plane, is presented in Fig. A.79 at two time scales.

ORNL-DWG 89-5050 ETD

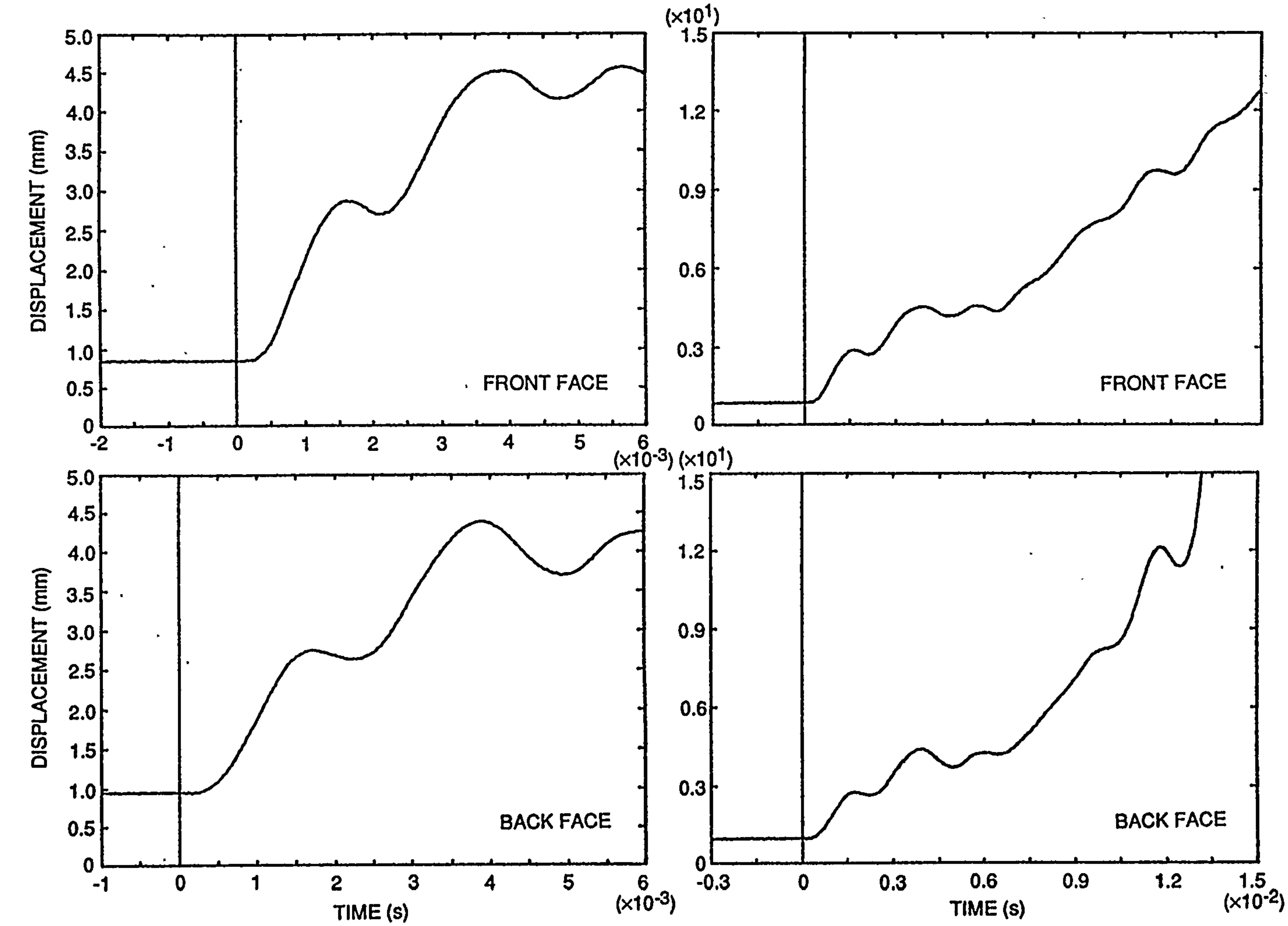

Fig. A.77. Front- and back-face COD histories at two time resolutions: test WP-2.6.

ORNL-DWG 89-5051 ETD

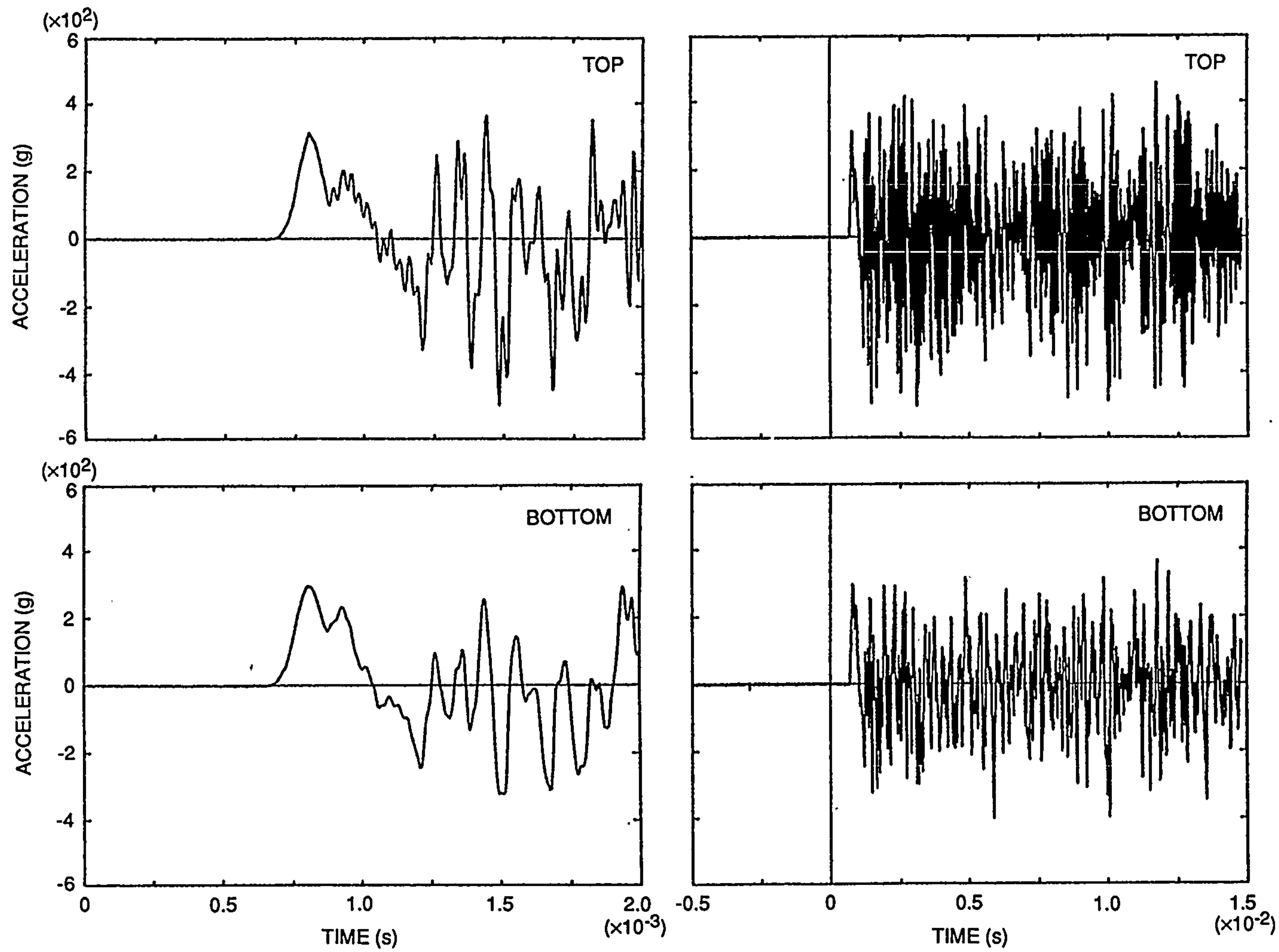

Fig. A.78. Longitudinal acceleration (at two levels of time resolution) measured by top and bottom "damped" accelerometers mounted 3.491 m above and 3.398 m below crack plane, respectively: test WP-2.6.

ORNL-DWG 89-5052 ETD

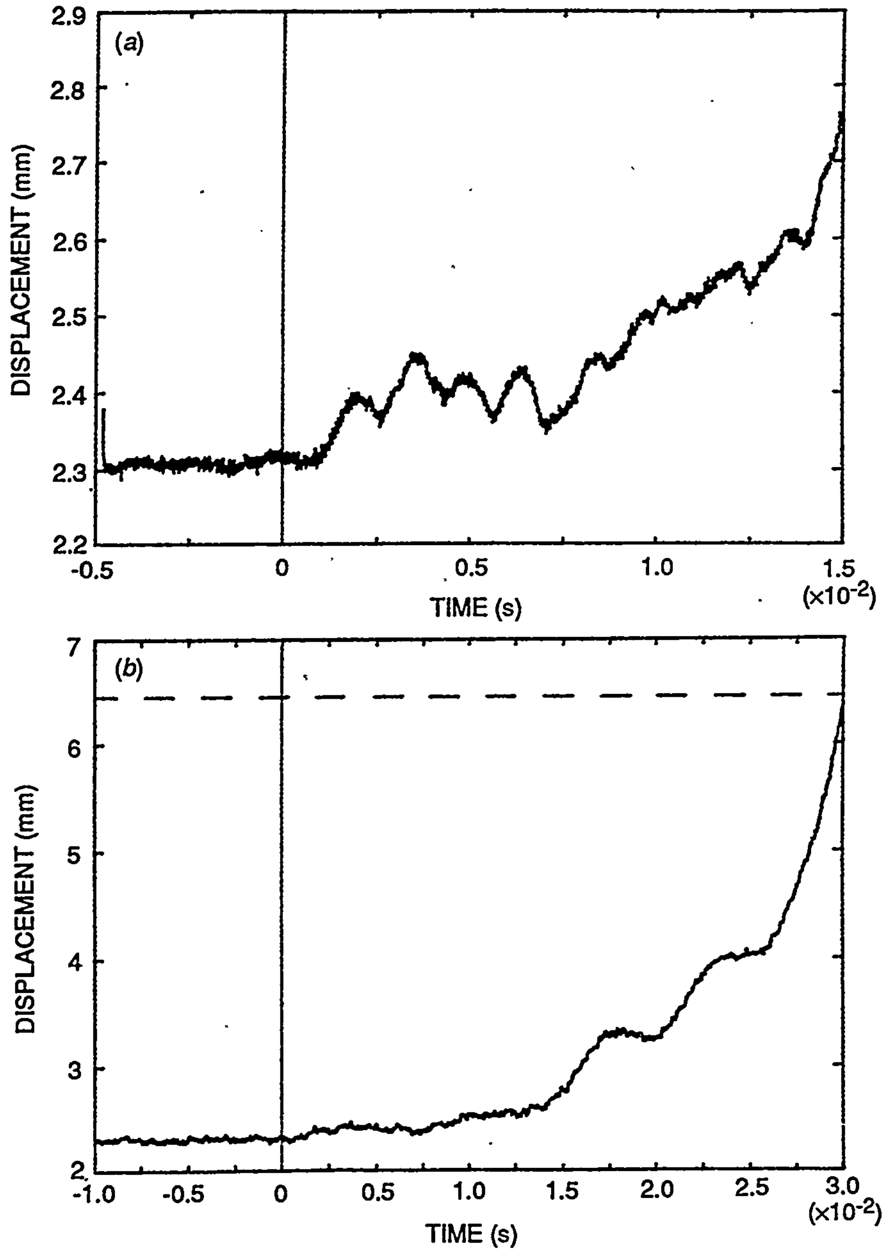

Fig. A.79. Dynamic displacement history at two levels of time resolution of a point 3.393 m below the crack plane during (*a*) cleavage crack run-arrest events and (*b*) entire fracture: test WP-2.6.

Appendix B

EFFECTS OF LOAD-POINT BOUNDARY CONDITIONS AND ANALYSIS METHOD ON WIDE-PLATE CRACK-ARREST TEST RESULTS

B.1 EFFECT OF LOAD-POINT BOUNDARY CONDITION

Long-duration (7- to 10-ms and longer) viscoplastic analyses of the wide-plate geometry will be influenced significantly by the boundary conditions imposed at the specimen load points. The two limiting cases for the load point are a fixed-load boundary condition, in which the specimen is free to stretch axially during the analysis, or a fixed-displacement boundary condition. In the fixed-displacement case, the effective axial load decreases with time as the test specimen compliance increases during crack advance.

A series of generation-mode analyses based on data measured during test WP-2.4 were conducted to investigate the influence of the load-point boundary conditions. All analyses were performed using the linearly elastic dynamic fracture code SAMCR (Ref. 1) and were carried out for 40 ms of specimen response. During this response duration, seven crack jumps were observed in the test. The computed K values for each fracture event are summarized in Table B.1.

Figure B.1 compares the computed K vs time values for the two limiting cases of fixed-load and fixed-displacement boundary conditions. The two analyses produced identical results for the first millisecond of response. After ~10 to 15 ms of response, the two cases begin to diverge significantly; at 40 ms, the fixed-load K value was 75% greater than the corresponding value for the fixed-displacement case. Similar results for the crack-mouth-opening displacement (CMOD) vs time are shown in Fig. B.2 along with the experimentally measured data from the test; in this figure, CMOD is defined as one-half of the total symmetric crack separation. Again, significant differences between the fixed-load and fixed-displacement cases appear only after ~15 ms of response. The computed CMOD values begin to diverge from the experimentally measured data at ~10 ms; at 40 ms the measured data are several times larger than the largest computed values. Recalling that the analyses assumed linearly elastic constitutive behavior, the deviations between the measured and computed CMOD values are most likely the result of plastic yielding in the test.

Although the fixed-load and fixed-displacement boundary conditions represent the upper and lower limits for the dynamic response of the specimen (assuming linear behavior), the true boundary condition for the test specimen is most probably somewhere between. There will be inertial coupling between the specimen and the test frame because of the stiffness and effective mass of the test frame at the load point. To define the actual boundary conditions during the test, accelerometers were placed near the load points of the specimen in test WP-2.4. Two types of accelerometers were installed: damped and undamped. The records from the undamped accelerometers were unfortunately plagued by a

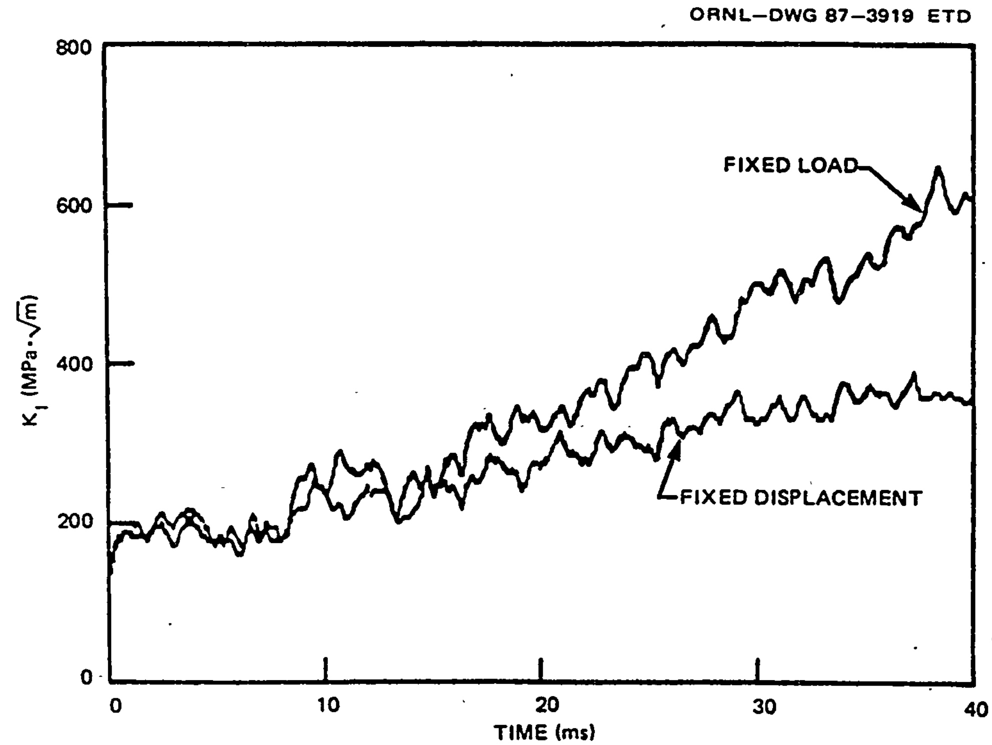

Fig. B.1. K vs time results from linear generation-mode analyses: test WP-2.4.

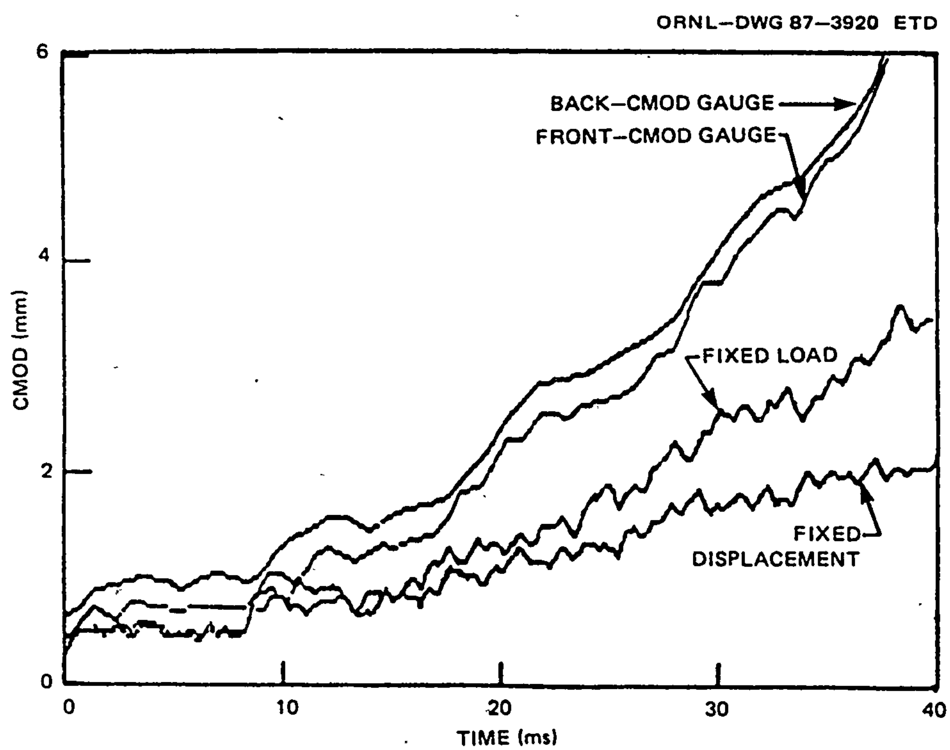

Fig. B.2. CMOD from linear generation-mode analyses: test WP-2.4.

Table B.1. Summary of computed results for test WP-2.4

Event	Time (ms)	A (m)	K (MPa·√m)		
			Fixed displacement	Fixed load	
				No mass	Lumped mass
Initiation	0.0	0.250	152.2	152.2	152.2
First arrest	0.190	0.334	145.9	145.9	156.2[a]
Reinitiation	8.121	0.334	190.2	185.7	214.4
Second arrest	8.350	0.408	187.9	193.3	207.8
Reinitiation	15.160	0.408	247.4	242.2	273.7
Third arrest	15.990	0.421	239.4	283.7	266.5
Reinitiation	17.180	0.421	257.4	326.2	302.2
Fourth arrest	17.420	0.468	263.9	320.4	296.2
Reinitiation	18.550	0.468	261.8	317.5	301.1
Fifth arrest	20.390	0.487	279.2	321.3	328.7
Reinitiation	23.440	0.487	296.9	347.6	367.7
Sixth arrest	23.940	0.514	307.0	387.6	372.0
Reinitiation	26.230	0.514	323.7	414.9	417.4
Seventh arrest	27.260	0.555	314.0	422.4	418.2
Reinitiation	28.860	0.555	352.0	441.2	472.3

[a]Differs from fixed-displacement and fixed-load/no-mass values because of minor differences in specification of crack history during first jump.

large amount of high-frequency oscillations that made interpretation difficult; in the damped accelerometers, this high-frequency component is inherently filtered from the records. Figure B.3 provides the acceleration vs time data measured by the damped accelerometer located at the bottom load point of the specimen. The peak acceleration measured during the test was ~300 g.

Some caution must be exercised in interpreting the data in Fig. B.3, however. Double integration of this acceleration record yields a final load-point displacement of 8 cm at 40 ms. This unrealistically large value implies an average elastic stress increase of >3000 MPa in the specimen; clearly, this cannot occur. The most plausible explanation for this high-displacement prediction is that it includes a large rigid body component; that is, both the top and bottom load points moved in the same direction by approximately the same amount during the test. Unfortunately, an accelerometer record for the top load point is unavailable for verifying this hypothesis.

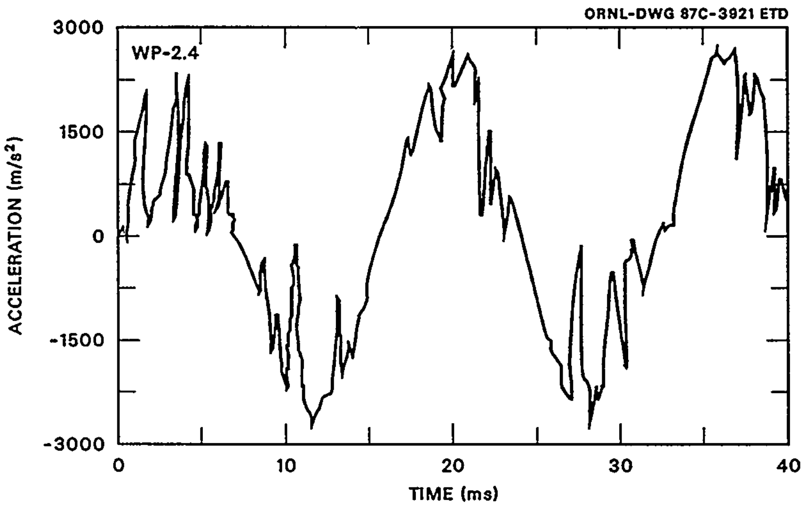

Fig. B.3. Acceleration vs time data measured by "damped" accelerometer near the lower load point: test WP-2.4.

Although the magnitudes of the accelerations and the derived displacements are suspect, the record shown in Fig. B.3 nevertheless contains valuable information regarding the natural periods of the response. Initially, there is an ~0.8-s interval during which there is no accelerometer response; this corresponds to the stress wave transit time from the crack plane to the load point. Overall, the accelerometer record suggests that the specimen vibrates in an axial fundamental mode for ~16.5 ms. Superimposed on this global vibration mode is a higher-frequency mode with a period of ~1 to 2 ms; this again appears to correspond to stress wave reflections within the specimen.

The period of the specimen vibration modes can be used to estimate the inertial coupling between the specimen and the test frame at the load point. As a first approximation, the test frame stiffness and effective mass can be treated as a simple spring and lumped mass attached to the load point. The solution for the longitudinal vibration modes for a uniform bar having a supplementary lumped mass and stiffness at its end is given by[2]

$$\xi_i \tan \xi_i = \frac{\eta \zeta_i}{\zeta_i - \eta} , \qquad \text{(B.1)}$$

in which

$$\xi_i = \frac{\rho_i \ell}{V_L} ,$$

$$\eta = \frac{m\ell}{M} ,$$

$$\zeta_i = \frac{m\ell \ \rho_i^2}{k} ,$$

and where

ρ_i = natural frequency for mode i,

m = mass per unit length of bar,

ℓ = length of bar,

V_L = longitudinal wave velocity for bar,

M = additional lumped mass at end of bar,

k = spring constant for additional stiffness at end of bar.

The test frame compliance had been estimated previously[3] as approximately five times the compliance of the specimen itself. Consequently, little error is introduced by neglecting the test frame stiffness contribution at the load point [i.e., $k = 0$ in Eq. (B.1)] and considering only the effective mass from the test frame cross arm. Equation (B.1) can then be solved for the effective mass of the test frame at the load point given the WP-2.4 test geometry and the measured fundamental period of 16.5 ms, yielding a value of 27,100 kg for the effective mass.

The fixed-load generation-mode analysis for test WP-2.4 was repeated with this additional 27,100-kg mass at the load point. As before, linearly elastic constitutive behavior was assumed for the specimen, and the analysis was performed for 40 ms of specimen response. Comparisons between the fixed-load analyses with and without the additional lumped effective mass for the test frame are given in Fig. B.4 for K vs time, Fig. B.5 for CMOD vs time, and Fig. B.6 for load-point axial displacement vs time. As is clearly shown in all three figures, the differences in the computed results between the two cases are negligible.

Unfortunately, the accelerations computed in the analyses cannot be directly compared with the measured accelerometer data. The computed nodal accelerations vs time at the accelerometer location are plotted in Fig. B.7. The computed accelerations are characterized by a very high level of high-frequency oscillations; no low-frequency periodicity can be detected in the computed record, and the peak accelerations are nearly four times the corresponding measured values. It is believed that these features of the computed accelerations are spurious products of the numerical algorithms employed in the finite-element code.

At the load point, the large added lumped mass severely damps the computed nodal accelerations, as shown in Fig. B.8. The computed peak acceleration at the load point is substantially lower than the peak value measured in the test, and any low-frequency periodicity is masked by the comparatively large amplitude high-frequency vibration modes. The period of this high-frequency vibration is on the order of 1 to 2 ms, which matches closely the period of the high-frequency component in the measured accelerometer response. Low-frequency periodicity is evident in the velocity vs time record for the load point, as shown in Fig. B.9; it is also evident to a lesser extent in the load-point displacement record shown previously in Fig. B.6. The period of this low-frequency component is ~20 ms, which is close to the target period of 16.5 ms measured during the test.

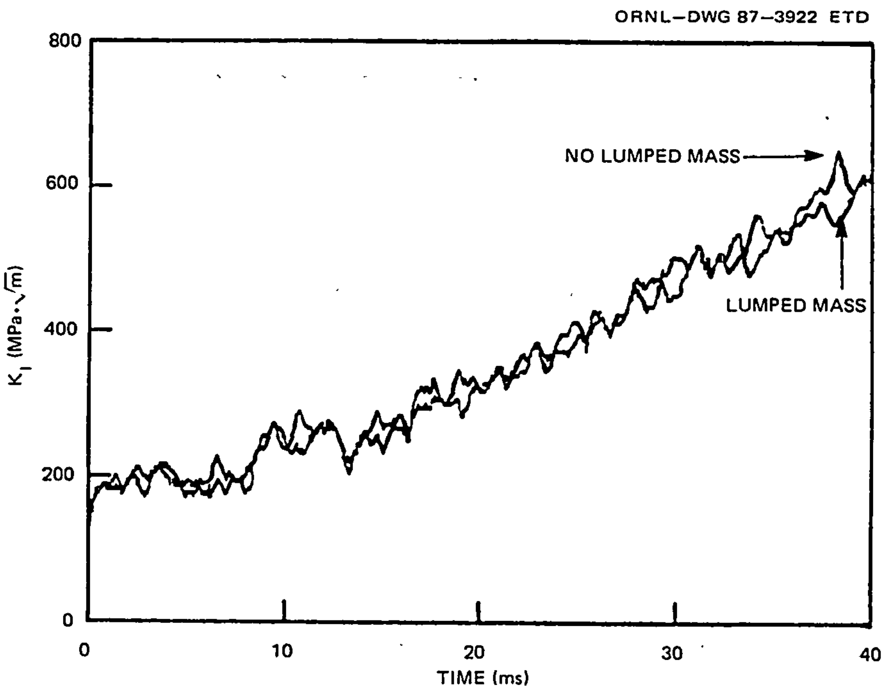

Fig. B.4. Influence of test frame inertia on computed K vs time: test WP-2.4.

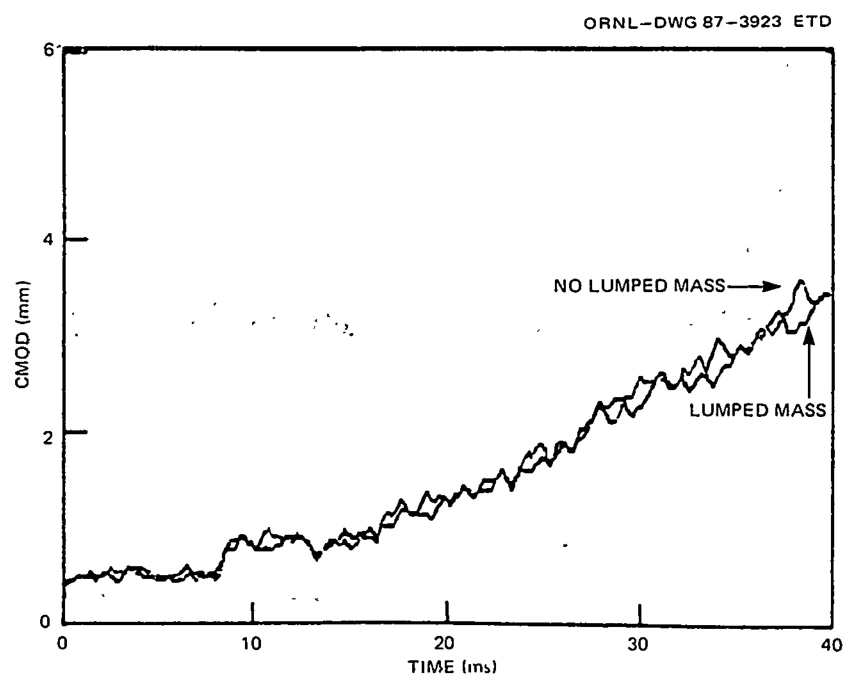

Fig. B.5. Influence of test frame inertia on computed CMOD: test WP-2.4.

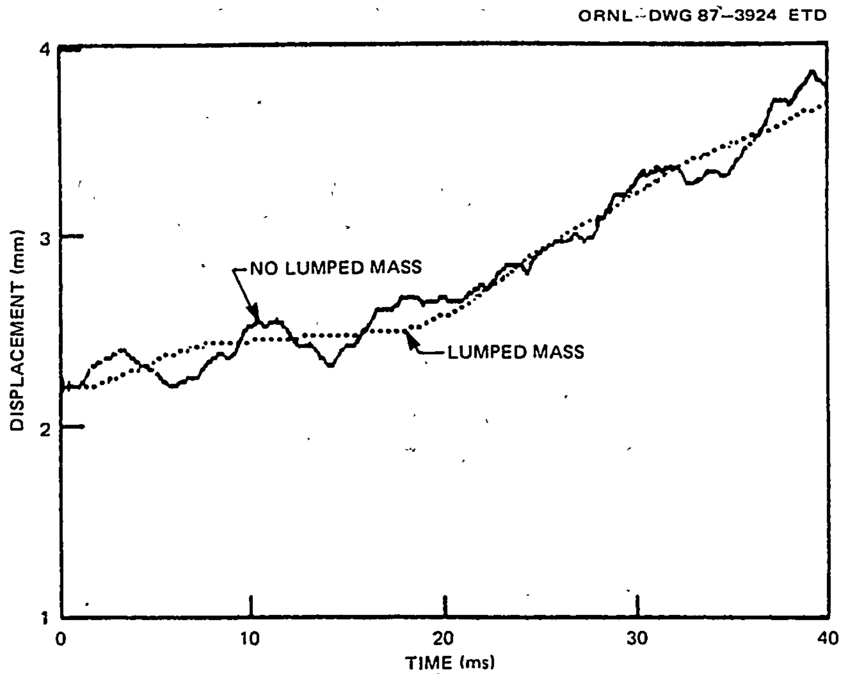

Fig. B.6. Influence of test frame inertia on computed load-point axial displacement: test WP-2.4.

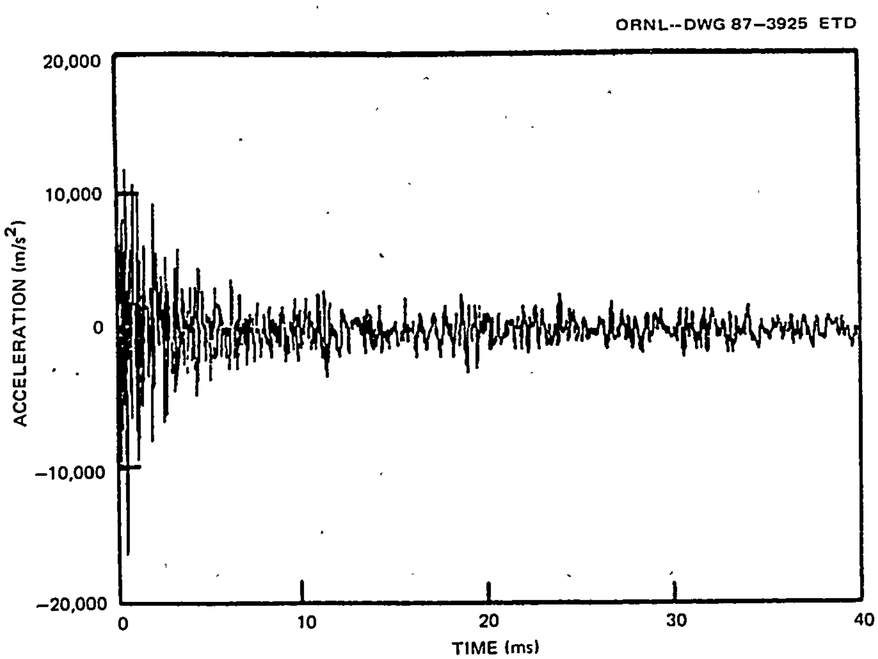

Fig. B.7. Computed nodal accelerations at "damped" accelerometer location near lower load point (linearly elastic fixed-load analysis, lumped mass at load point): test WP-2.4.

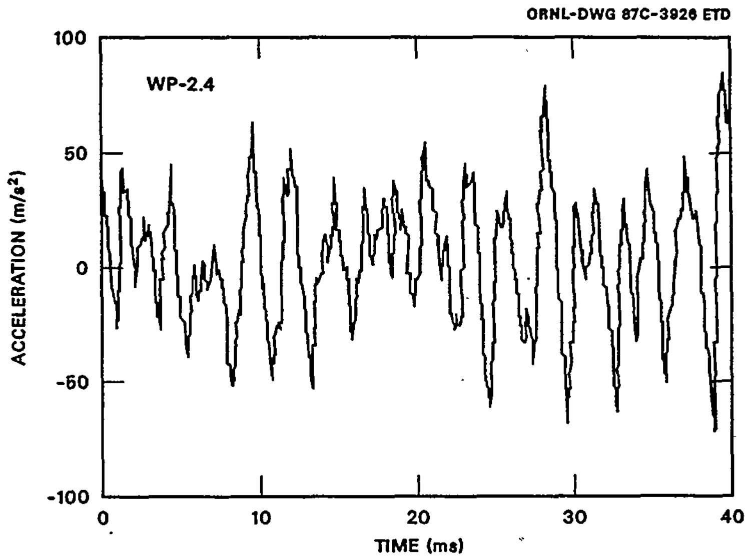

Fig. B.8. Computed nodal accelerations at load point (linearly elastic fixed-load analysis, lumped mass at load point): test WP-2.4.

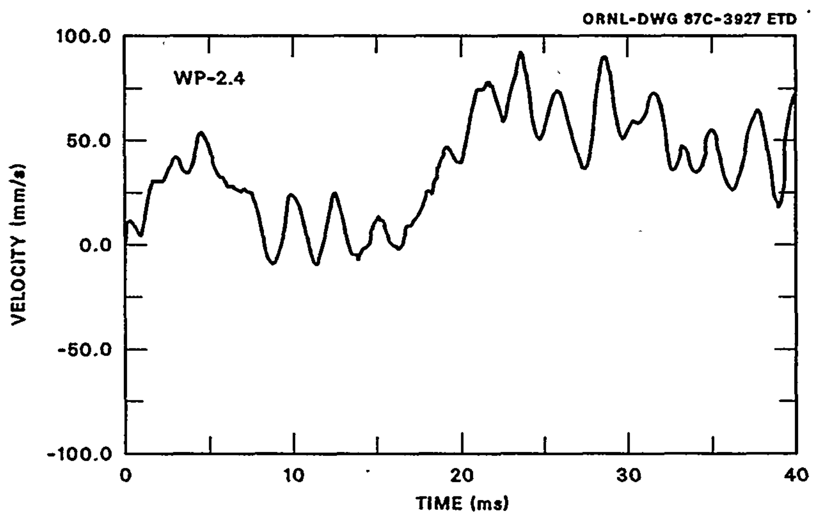

Fig. B.9. Computed velocities at load point (linearly elastic fixed-load analysis, lumped mass at load point): test WP-2.4.

These conclusions were drawn from this investigation of boundary condition effects: (1) fixed-load and fixed-displacement analyses for the wide-plate test geometry produce identical results for the first millisecond of response; (2) substantial discrepancies between fixed-load and fixed-displacement analysis results do not occur until after ~10 to 15 ms of response; (3) reasonably good agreement between computed and measured load-point behavior (at least in terms of vibration periods) can be obtained by neglecting the test frame stiffness and considering only the test frame inertia as a lumped effective mass; and (4) the influence of the test frame inertia on the computed results along the crack plane (e.g., K vs time) is negligible. These conclusions suggest that a fixed-load boundary condition without additional lumped mass is an appropriate and adequate boundary condition for medium- and long-duration dynamic viscoplastic analyses.

B.2 EFFECT OF ANALYSIS METHOD

Crack-arrest toughness values have been determined by static and dynamic analyses, as well as by handbook techniques. Table B.2 summarizes values for test WP-2.4. The effects of the analysis method (static vs dynamic) and the boundary condition (fixed load or fixed load-pin displacement) used to interpret the wide-plate crack-arrest tests are demonstrated by comparing values listed in Table B.2. These effects are illustrated in Fig. B.10, which presents selected K_{Ia} results in Table B.2 vs $T - DW_{NDT}$ for the pop-in and seven crack run-arrest events of

Table B.2. Computed crack-arrest toughness values for wide-plate crack-arrest test WP-2.4

Test	Crack-arrest toughness values (MPa·√m)					
	Static SEN		Fedderson alternate secant formula[c]	Dynamic finite element		
	Displacement control[a]	Load control[b]		Application mode	Generation mode	
					Fixed load	Fixed displacement
WP-2.4A	104	113	79			
WP-2.4B	155	186	111	122	137	137
WP-2.4C	168	234	124	155	188	193
WP-2.4D	171	249	128	166	281	249
WP-2.4E	181	303	140	207	249	232
WP-2.4F	185	332	145	229	307	276
WP-2.4G	191	378	153	269	381	257
WP-2.4H	198	451	165		–397	276

[a]From Ref. 4 (pp. 2.10–11), while assuming $a = a_f$ and no further bending occurs because of propagation of the crack.

[b]From Ref. 4 (pp. 2.10–11) while assuming $a = a_f$ and full bending according to SEN formula when the final crack depth is used.

[c]$K_I = \sigma \left[\pi a \sec\left(\frac{\pi a}{2W}\right)\right]^{1/2}$, where σ = far-field tensile stress, $a = a_f$ = final crack length, and w = full plate width.[5]

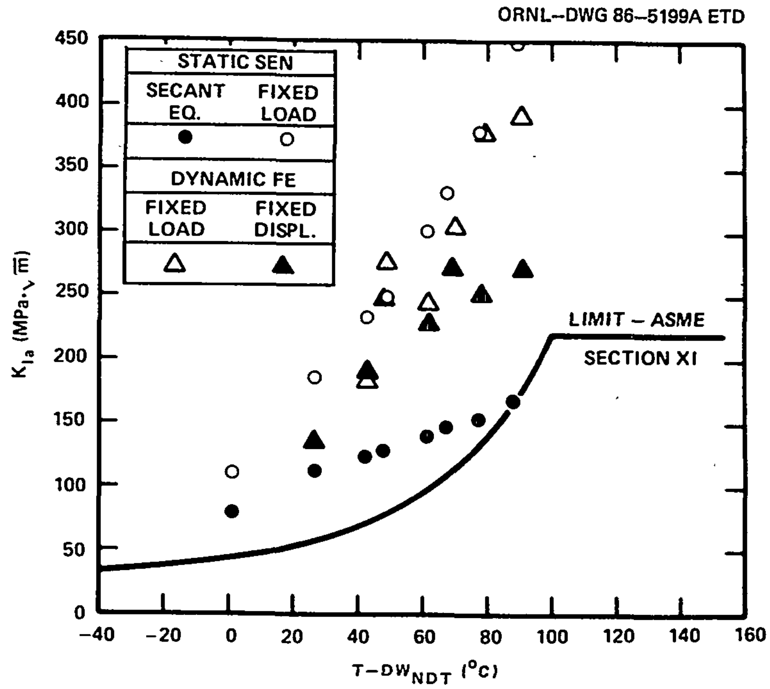

Fig. B.10. Effect of analysis method and boundary condition on calculated crack-arrest toughness values for test WP-2.4.

test WP-2.4.* As shown in the figure, values of K_{Ia} determined using the secant equation and the Tada fixed-load condition represent approximate lower and upper bounds, respectively, for the results. For long-duration crack run-arrest events (t > 10 ms), considerable load adjustment can take place as a result of specimen pull-plate compliance. Therefore, the most meaningful values of K_{Ia} should reflect this occurrence and would involve a dynamic finite-element generation-mode analysis.

---

*For test WP-2.4 the duration of the crack run-arrest events was ~27.3 ms.

REFERENCES

1. C. W. Schwartz et al., University of Maryland, College Park, *SAMCR: A Two-Dimensional Dynamic Finite Element Code for the Stress Analysis of Moving Cracks*, USNRC Report NUREG/CR-3891 (ORNL/Sub/79-7778/3), November 1984.*

2. S. Timoshenko, D. H. Young, and W. Weaver, *Vibration Problems in Engineering* (4th ed.). J. Wiley and Sons, Inc., New York, 1974.†

3. C. E. Pugh et al., Martin Marietta Energy Systems, Inc., Oak Ridge Natl. Lab., *Heavy-Section Steel Technology Program Semiann. Prog. Rep. October 1985–March 1986*, USNRC Report NUREG/CR-4219, Vol. 3, No. 1 (ORNL/TM-9593/V3&N1), June 1986.

4. R. Tada et al., *The Stress Analysis of Cracks Handbook*, Del Research Corp., Hellertown, Pa., 1973.†

5. C. F. Fedderson, "Current Status of Plane Strain Crack Toughness Testing of High-Strength Metallic Materials," *Crack Arrest Methodology and Applications*, ASTM STP-410, 77–79, 1967.‡

---

*Available for purchase from National Technical Information Service, Springfield, VA 22161.

†Available in public technical libraries.

‡Available from American Society for Testing and Materials, Philadelphia, Pa.

Appendix C

EFFECTS OF TUNNELING

Crack tunneling is commonly observed during the fracture of tough and ductile materials. The loss of constraint near the free surface of the specimen permits development of yielded ligaments that may extend for considerable distances behind the leading edge of the crack front. These yielded ligaments restrain the crack-tip displacements and alter the crack-tip stress fields. A significant portion of the apparent fracture toughness measured for a deeply tunneled crack may be caused by the restraining effects of these yielded ligaments.

Calculations by Popelar[1] suggest that correcting for the restraining effects of tunneling may substantially reduce the actual fracture toughness inferred from test data. Because considerable tunneling has been observed in several of the wide-plate tests, notably the WP-1 test series,[2] questions have been raised regarding the appropriateness of 2-D analytical models that implicitly ignore tunneling.

C.1 ANALYTICAL APPROXIMATIONS TO TUNNELING EFFECTS

Several analytical approximations have been proposed in the literature to account for the restraining effect of the yielded ligaments flanking a tunneled crack in Mode I fracture. All are based on simple superposition principles; that is, the restraining effects of the tunneling can be simply subtracted from the conditions existing at the crack front in the absence of tunneling. Superposition requires assumption of linear-elastic fracture-mechanics (LEFM) small-scale yielding conditions; that is, no shielding because yielding ahead of the crack tip is considered (small-scale, yielding assumption), and the crack tip state can be characterized by the stress-intensity factor K. The approximations all assume self-similar crack growth once the ligaments have fully developed. The ligament stresses are replaced by an equivalent set of crack-face tractions, and the stress-intensity factor as a result of these tractions represents the tunneling correction. This correction is subtracted from the stress-intensity factor for the corresponding cracked body without tunneling.

Popelar[3] considered the two cases for the ligament geometry shown in Fig. C.1: (*a*) strip ligaments, characteristic of low-toughness ductile materials, and (*b*) parabolic ligaments, characteristic of high-toughness ductile materials. The superposition approach for approximating the effects of the yielding ligaments is illustrated in Fig. C.2, where

$$K_\alpha = K_\beta - K_\gamma \ , \qquad \text{(C.1)}$$

in which K_β is the stress-intensity factor in the absence of tunneling, K_γ is the stress-intensity factor as a result of the crack-face

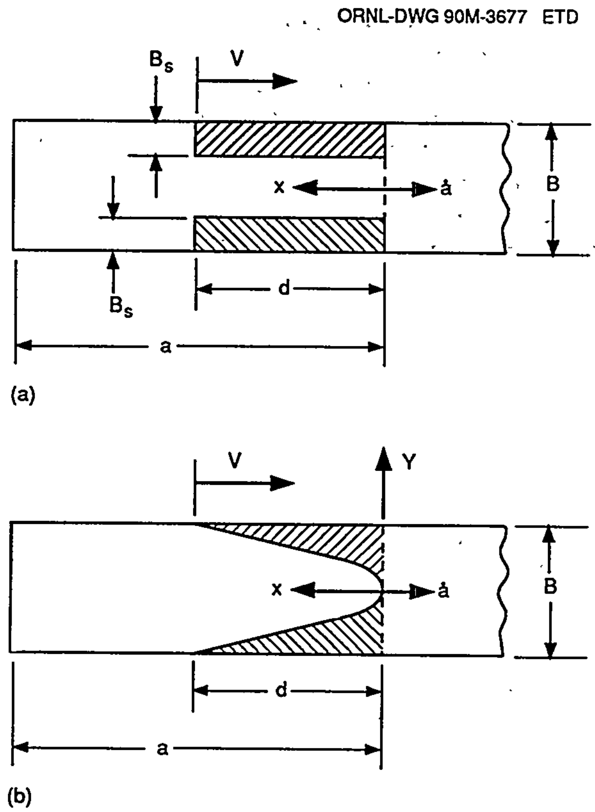

Fig. C.1. Idealization of crack tunneling in (*a*) low-toughness and (*b*) high-toughness material (Ref. C.3).

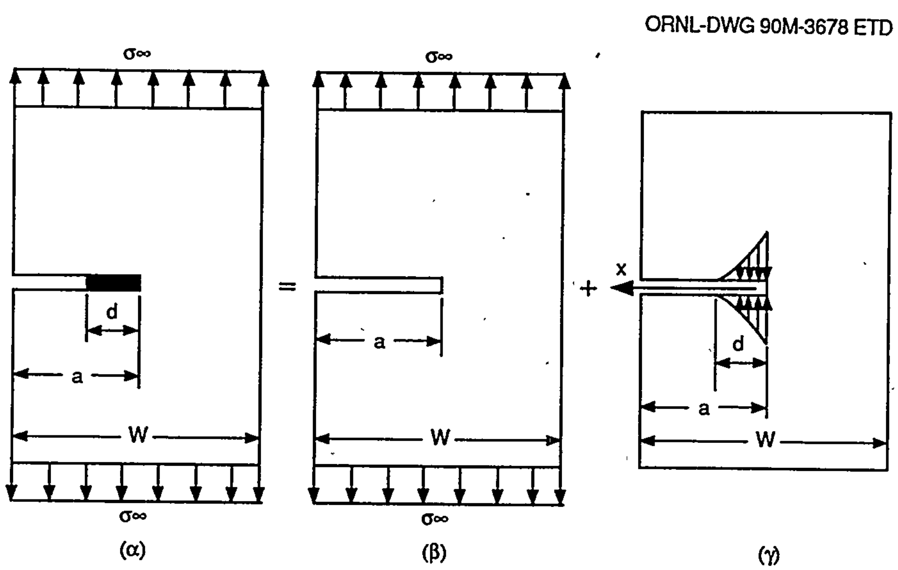

Fig. C.2. Illustration of superposition principle for determining the stress-intensity factor (Ref. C.3).

tractions (i.e., the tunneling correction), and K_α is the net or corrected stress-intensity factor.

K_β is calculated using standard 2-D LEFM solutions. K_γ is computed using a weight-function approach assuming that the stresses in the ligaments equal the plastic flow stress σ_o and that these ligament flow stresses can be averaged across the thickness. For the assumed strip and parabolic ligament geometries, respectively, these averaged or "effective" crack-face stresses σ_{eff} can be expressed as

$$\sigma_{eff} = 2 \left(\frac{B_s}{B}\right) \sigma_o , \tag{C.2}$$

and

$$\sigma_{eff} = \sigma_o \left[1 - \left(\frac{x}{d}\right)^{1/2}\right] . \tag{C.3}$$

The corresponding stress-intensity values K_γ as derived by Popelar[3] using the weight-function approach are given for the strip and parabolic ligament geometries, respectively, as

$$K_\gamma = 4\sigma_o \left(\frac{2d}{\pi}\right)^{1/2} \left(\frac{B_s}{B}\right) \left[1 + \frac{m_1}{3} \left(\frac{d}{a}\right) + \frac{m_2}{5} \left(\frac{d}{a}\right)^2\right] , \tag{C.4}$$

and

$$K_\gamma \doteq \sigma_o \left(\frac{2d}{\pi}\right)^{1/2} \left[1 + \frac{m_1}{6} \left(\frac{d}{a}\right) + \frac{m_2}{15} \left(\frac{d}{a}\right)^2\right] , \tag{C.5}$$

in which m_1 and m_2 are geometry-dependent dimensionless coefficients having values of ~5 and 2, respectively, for the wide-plate specimen geometry at the typical arrest condition of $a/w \cong 0.5$.

Smith[4] had earlier proposed a solution for the influence of tunneling based on a superposition approach similar to Popelar's but with a different formulation for the K_γ correction term. Smith considered an infinitely long crack with an infinitely long crack front that contains regularly spaced ligaments of rectangular geometry, as shown in Fig. C.3. As an approximation, a finite-width crack front under plane-strain conditions can be taken as the area between the centerlines of two neighboring ligaments. The stress in the ligaments is assumed equal to the flow stress for the material.

Smith's solution is not based on an averaging of the ligament restraining stresses across the thickness. Instead, K_γ is evaluated for the point (marked by a dot in Fig. C.3) on the crack front midway

ORNL-DWG 90M-3679 ETD

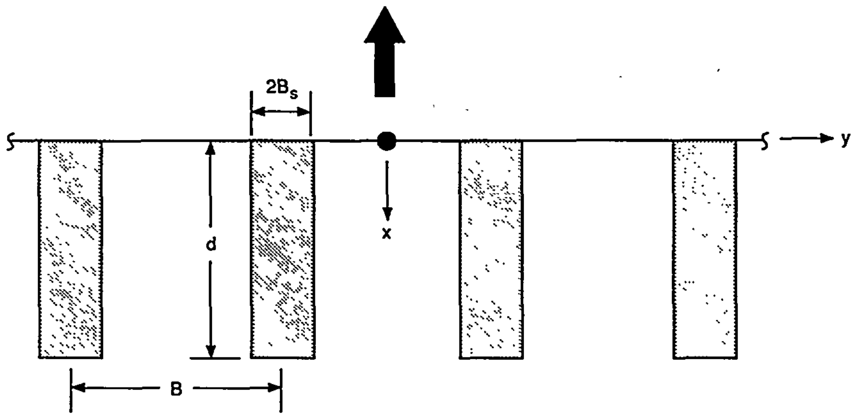

Fig. C.3. Smith's model for restraining effect of ligaments (Ref. C.4).

between two ligaments as the integral over the ligament areas of the solution for a point force applied to the crack face.[5] Using Popelar's notation, Smith's solution for the rectangular ligament geometry is expressed as

$$K_Y = \frac{2\sqrt{2}\ \sigma_o\ B_s}{\pi\ \sqrt{B}} \int_0^{\pi d/B} \frac{\tanh x}{\sqrt{x}}\, dx \ . \tag{C.6}$$

For small values of d/B (<~0.3), the integral in Eq. (C.6) can be approximated analytically as

$$K_Y \simeq \frac{4\pi}{3}\ \sigma_o \left(\frac{2d}{\pi}\right)^{1/2} \left(\frac{B_s}{B}\right) \left(\frac{d}{B}\right) . \tag{C.7}$$

For large values of d/B (>~3), Eq. (C.6) approaches Popelar's thickness-averaged solution. The integral in Eq. (C.6) must be evaluated numerically for intermediate value of d/B; for moderately deep tunneling, for example, when d/B = 1, the value of the integral is ~2. Smith observes that thickness-averaging procedures (such as Popelar's) overestimate the restraining effect of the ligaments for small-to-moderate amounts of tunneling.

As noted by Popelar, rectangular ligament geometries are characteristics of low-toughness materials. Ductile reactor steels such as A 533 grade B typically exhibit parabolic or triangular tunneling geometries, as was often observed in the WP-1 test series. We have therefore extended Smith's methodology to parabolic and triangular ligament geometries.

Consistent with Smith's approach, the crack front is treated as being infinitely long with regularly repeating ligaments of the specified geometry. Figure C.4 illustrates the assumed conditions for the triangular ligament geometry. As an approximation, a finite-thickness specimen under plane-strain conditions can be taken as the width between the centerlines of two neighboring ligaments. The restraining effect of the ligaments for both the parabolic and triangular geometries can be expressed as

$$K_\gamma = \sigma_o \sqrt{B} \sum_{n=-\infty}^{+\infty} k_n \, , \tag{C.8}$$

where n refers to the individual ligaments. The k_n terms for the parabolic ligament geometry are given as

$$k_n = \frac{1}{\pi\sqrt{\pi}} \int_{n-1/2}^{n+1/2} \left\{ \arctan\left(1 + \sqrt{2}\,\phi\right) - \arctan\left(1 - \sqrt{2}\,\phi\right) - \ln\left[\frac{1 + \sqrt{2}p + \phi^2}{(1 + \phi^4)^{1/2}}\right] \right\} \frac{d\xi}{\sqrt{\xi}} \, , \tag{C.9a}$$

where

$$\phi = \left[\frac{4\,(d/B)\,(\xi - N)^2}{\xi}\right]^{1/2} , \tag{C.9b}$$

ORNL-DWG 90M-3680 ETD

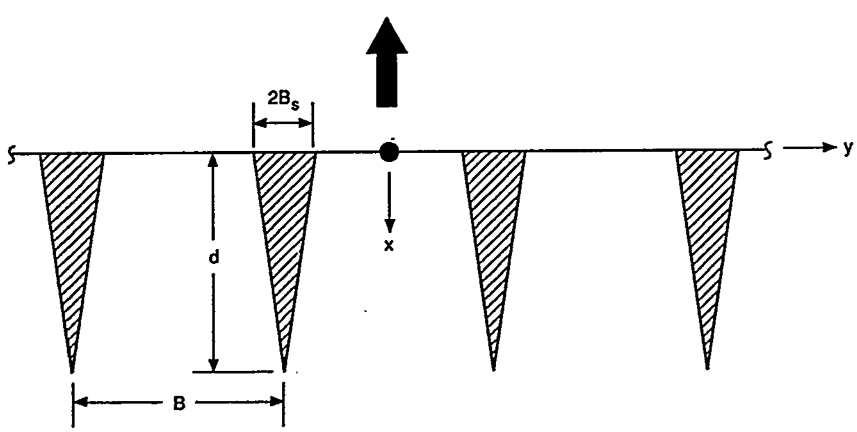

Fig. C.4. Extension of Smith's approach to triangular ligament geometry.

and for the triangular ligament geometry as

$$k_n = \frac{1}{\pi\sqrt{\pi}} \int_{n-1/2}^{n-1/2+B_s/B} \left\{ \arctan\,(1 + \sqrt{2}\,\phi) - \arctan\,(1 - \sqrt{2}\,\phi) \right.$$

$$\left. - \ln\left[\frac{1 + \sqrt{2}\,\phi + \phi^2}{(1 + \phi^4)}\right] \right\} \frac{d\xi}{\sqrt{\xi}} + \frac{1}{\pi\sqrt{\pi}} \int_{n+1/2-B_s/B}^{n+1/2} \left\{ \arctan\,(1 + \sqrt{2}\,\phi) \right.$$

$$\left. - \arctan\,(1 - \sqrt{2}\,\phi) - \ln\left[\frac{1 + \sqrt{2p} + \phi^2}{(1 + \phi^2)}\right] \right\} \frac{d\xi}{\sqrt{\xi}}\,, \qquad \text{(C.10a)}$$

where

$$\phi = \left\{ \left(\frac{d}{B_s}\right) \xi + \left[1 - (n + 1/2)\left(\frac{B}{B_s}\right)\right] \left(\frac{d}{B}\right) \right\}^{1/2} \xi^{-1/2}\,, \qquad \text{(C.10b)}$$

where

$$\xi = Y/B\,.$$

These integrals are evaluated numerically and summed to obtain the value for K_γ.

For completeness, we have also extended Popelar's approach to triangular ligament geometries

$$K_\gamma = \frac{4}{3}\,\sigma_o \left(\frac{2d}{\pi}\right)^{1/2} \left(\frac{B_s}{B}\right) \left[1 + \frac{m_1}{s}\left(\frac{d}{a}\right) + \frac{2m_2}{35}\left(\frac{d}{a}\right)^2\right]. \qquad \text{(C.11)}$$

A comparison of the solutions for parabolic and triangular ligament geometries using Popelar's and Smith's approaches is given in Fig. C.5, which plots dimensionless K_γ vs depth of tunneling for a deep crack. Popelar's approach predicts tunneling correction factors that are considerably larger than those from Smith. This difference is largest for very shallow tunneling, where Popelar's approach is much more sensitive to tunneling depth. The differences decrease as the depth of tunneling increases, but at a tunneling depth of d/B = 2 the discrepancies are still >50%. As indicated in the Fig. C.5, the ligament geometry has only a relatively minor influence on the tunneling correction factor.

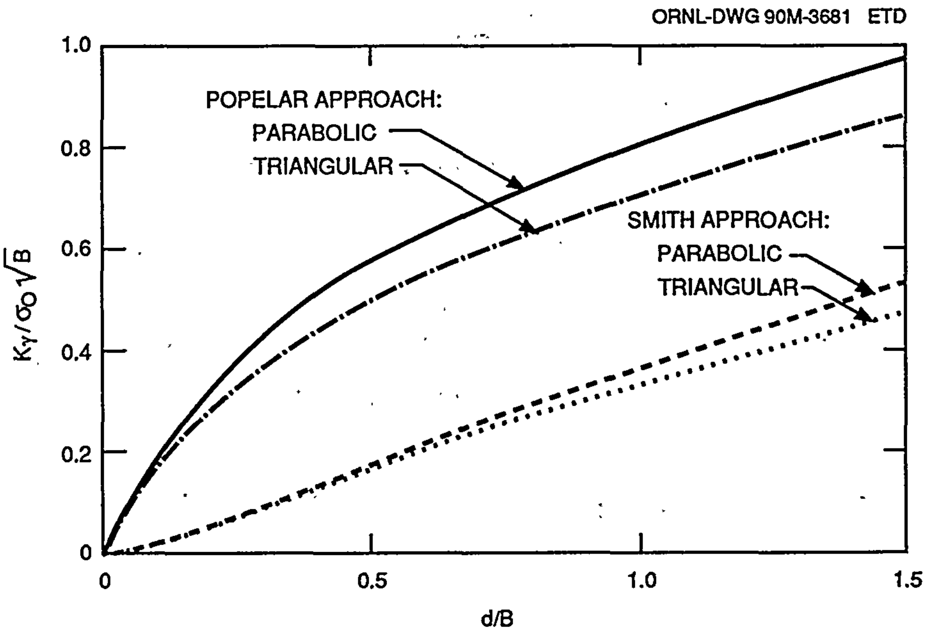

Fig. C.5. Comparison of Popelar's and Smith's tunneling correction approaches for parabolic and triangular ligament geometrics.

C.2 APPLICATIONS TO WP-1 TEST DATA*

The restraining effects of tunneling have been analyzed for 10-cm-thick WP-1 test specimens WP-1.1 through -1.6 using Popelar's and Smith's solutions and our extensions to these solutions. These analyses have been performed independently from Popelar's earlier interpretations of the WP-1 tests. The material properties, loads, arrest points, and other test conditions are as described in Ref. 1. The flow stress is taken as the average of the static yield and ultimate strengths for A 533 grade B steel at the crack tip arrest temperature. The uncorrected arrest toughness [K_β in Eq. (C.1)] is taken as the elastodynamic generation-mode value. The interpretation of the tunneled crack front geometry frequently involves subjective judgments. Our estimates of the ligament geometries are summarized in Table C.1, which was developed from Fig. C.6.

The results from our tunneling analyses are summarized in Table C.2. As previously presented by Popelar, his approach predicts a large reduction in the computed arrest toughness, particularly for events WP-1.2B and -1.4A, where the tunneling corrections are ~30 and 60%, respectively, of the uncorrected arrest toughness values. The Smith approach, however, predicts a significantly smaller correction for

*The effects of tunneling have not been applied to the WP-2 series test results; however, it is anticipated that tunneling corrections to the crack-arrest toughness results for the WP-2 test series will be less than for the WP-1 test series because of reduced tunneling.

Table C.1. Ligament geometry parameters for WP-1 test series specimens

Event	Triangular (mm) d	Triangular (mm) B_s	Parabolic d (mm)
WP-1.2A	120	28	
WP-1.2B			87
WP-1.3	10	40[a]	
WP-1.4A			50
WP-1.4B	84	24	
WP-1.5A	30	17[a]	
WP-1.5B			
WP-1.6A	15	58[a]	
WP-1.6B	47	65[a]	

[a]Assumed split symmetrically about specimen midthickness.

Table C.2. Corrections for the effects of tunneling in the WP-1 test series

Test	$T - RT_{NDT}$ (°C)	K_β[a] (MPa·$\sqrt{m}$)	Popelar approach (MPa·$\sqrt{m}$)		Smith approach (MPa·$\sqrt{m}$)	
			K_δ[b]	K_α[c]	K_δ[b]	K_α[c]
WP-1.2A	85	440	88	352	35	405
WP-1.2B	115	523	139	384	56	467
WP-1.3	77	243	29	214	23	220
WP-1.4A	52	158	99	59	32	126
WP-1.4B	83	397	56	341	21	376
WP-1.5A	79	229	22	207	5	224
WP-1.5B	95	300	56	244	N/A[d]	N/A
WP-1.6A	77	285	52	233	61	224

[a]K_β = Arrest toughness from generation-mode elastodynamic analyses.

[b]K_δ = Ligament correction.

[c]$K_\alpha = K_\beta - K_\delta$ = net arrest toughness.

[d]Not applicable.

ORNL PHOTO 7402–86

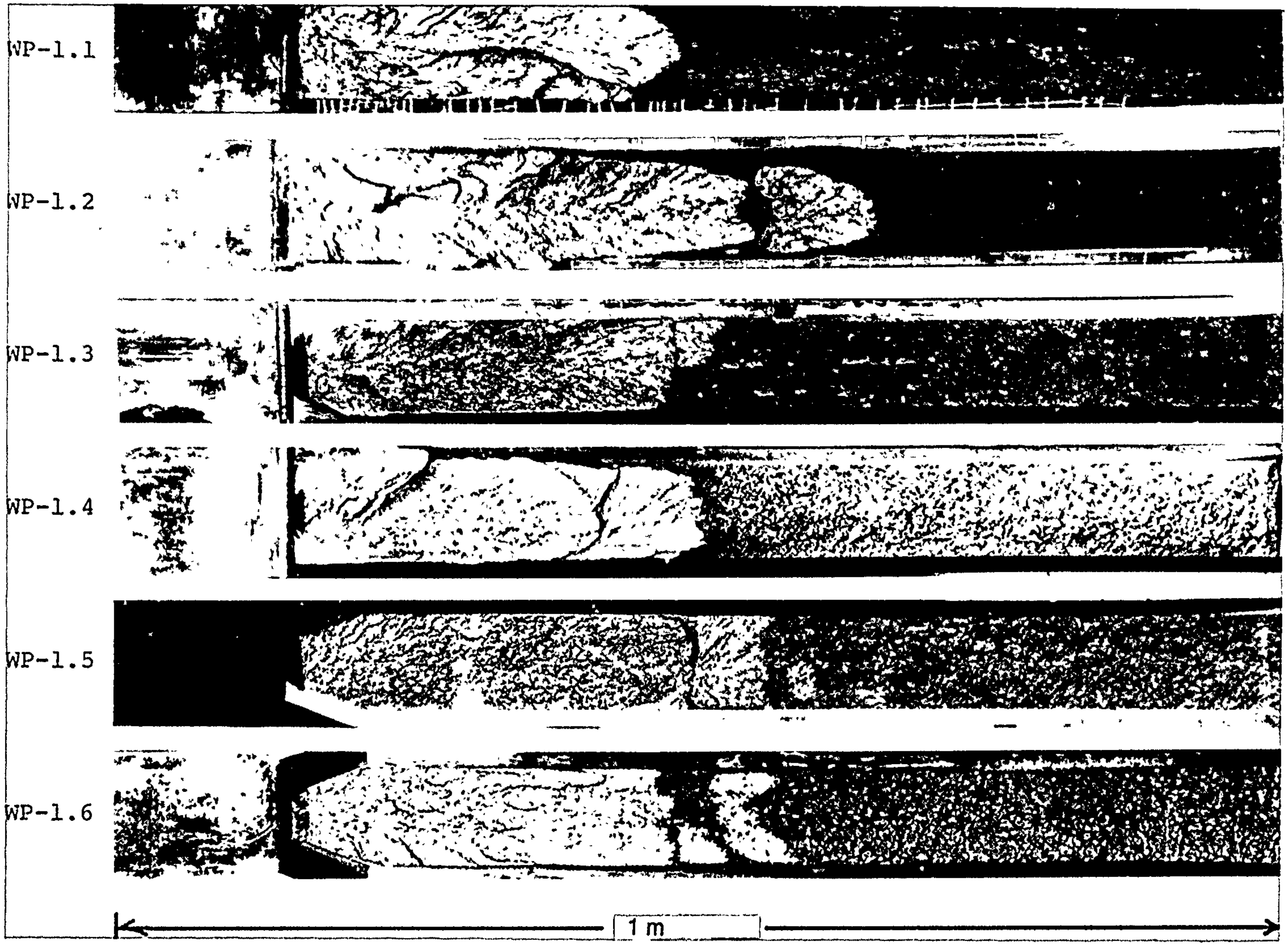

Fig. C.6. Fracture surface of WP-1 series specimens.

tunneling effects; the tunneling corrections for events WP-1.2B and -1.4A now equal only ~10 and 20%, respectively, of the uncorrected arrest toughnesses.

The variation with temperature of arrest toughness including the restraining effect of tunneling is illustrated in Fig. C.7. The corrected data based on Smith's approach lie between the uncorrected values and the corrected values from Popelar's approach in all cases. None of the Smith-corrected data points lies below the ASME reference curve. For both tunneling corrections, the trends in the data clearly show increasing toughness with temperature, continuing significantly above the cut-off in the ASME reference curve. This trend is more pronounced for data corrected using the Smith approach.

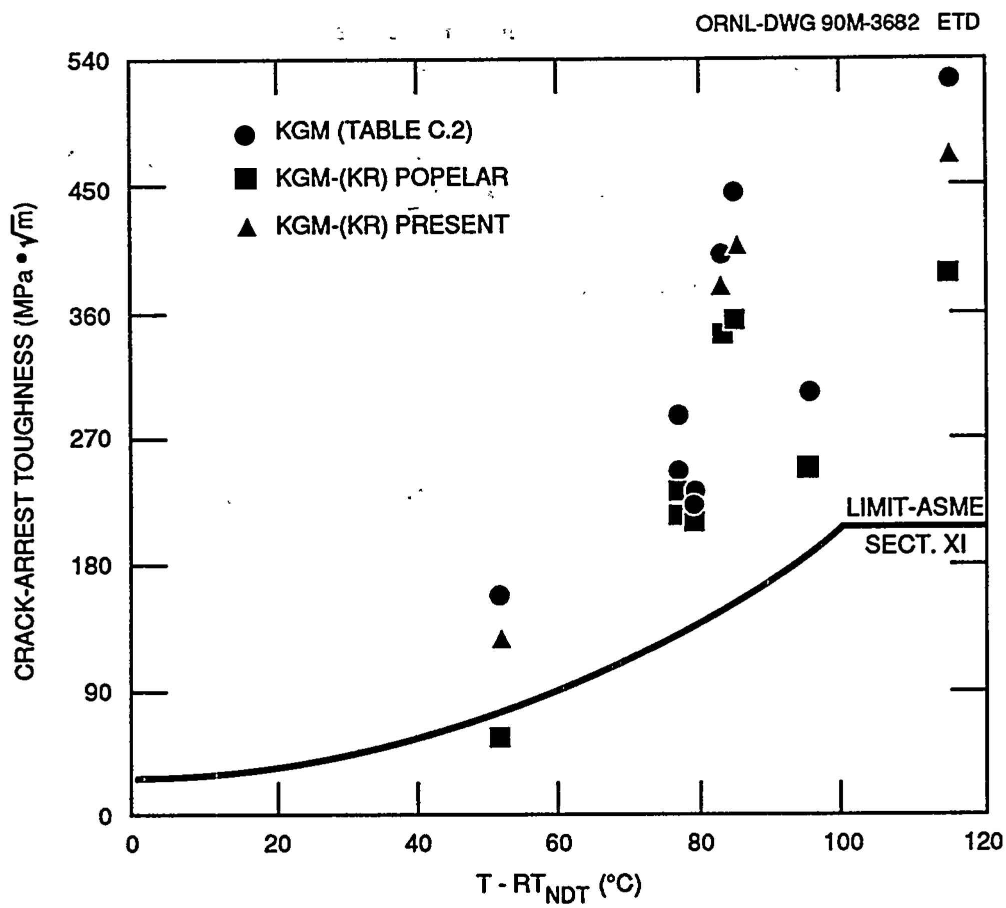

Fig. C.7. Corrected crack-arrest toughness vs temperature for WP-1 test series.

REFERENCES

1. C. H. Popelar, "Tunneling Effects on Crack-Arrest Toughness Calculations," Paper E, Session IV, *Constitutive Equation and Fracture-Model Developments*, Third Annual HSST Workshop on Dynamic-Fracture and Crack-Arrest Technology, National Bureau of Standards, Gaithersburg, Md., May 13–15, 1987.

2. D. J. Naus et al., Martin Marietta Energy Systems, Inc., Oak Ridge Natl. Lab., *Crack-Arrest Behavior in SEN Wide Plates of Quenched and Tempered A 533 Grade B Steel Tested Under Nonisothermal Conditions*, USNRC Report NUREG/CR-4930 (ORNL-6388), August 1987.*

3. C. H. Popelar, "A Quasi-Three-Dimensional Model for Crack Propagation in Materials that Exhibits Extensive Crack Tunneling," pp. 753–66 in *Proceedings of the 4th International Conference on Numerical Methods in Fracture Mechanics*, San Antonio, Tex., March 1987.†

4. E. Smith, "The Restraining Effect of Ductile Ligaments on Plane Strain Crack Propagation and Arrest in Ferritic Steels," *Eng. Frac. Mech.* 19(4), 601–4, 1984.†

5. H. Tada et al., *The Stress Analysis of Cracks Handbook*, Del Research Corp., Hellertown, Pa., 1973.†

---

*Available for purchase for National Technical Information Service, Springfield, VA 22161.

†Available in public technical libraries.

NUREG/CR-5451
ORNL/TM-6584
Dist. Category RF

Internal Distribution

1. D. J. Alexander
2-3. B. R. Bass
4. S. H. Buechler
5. R. D. Cheverton
6. J. M. Corum
7. W. R. Corwin
8. T. L. Dickson
9. F. M. Haggag
10-11. S. K. Iskander
12. J. E. Jones Jr.
13-14. J. Keeney-Walker
15. W. J. McAfee
16. J. G. Merkle
17. R. K. Nanstad
18-22. D. J. Naus
23. C. B. Oland
24-26. W. E. Pennell
27. C. E. Pugh
28. G. C. Robinson
29. D. K. Shum
30. T. J. Theiss
31. ORNL Patent Section
32. Central Research Library
33. Document Reference Section
34-35. Laboratory Records Department
36. Laboratory Records (RC)

External Distribution

37. C. Z. Serpan, Division of Engineering, Nuclear Regulatory Commission, Washington, DC 20555
38-39. M. E. Mayfield, Division of Engineering, Nuclear Regulatory Commission, Washington, DC 20555
40. M. Vagins, Division of Engineering, Nuclear Regulatory Commission, Washington, DC 20555
41-43. R. J. Fields, Fracture and Deformation Division, National Institute of Standards and Technology, Gaithersburg, MD 20899
44. G. R. Irwin, Department of Mechanical Engineering, University of Maryland, College Park, MD 20742
45. C. W. Schwartz, Department of Mechanical Engineering, University of Maryland, College Park, MD 20742
46. W. L. Fourney, Department of Mechanical Engineering, University of Maryland, College Park, MD 20742
47. J. W. Hutchinson, Division of Applied Science, Pierce Hall, Harvard University, Cambridge, MA 02138
48. F. A. Leckie, University of California, Santa Barbara, CA 93106
49. R. J. Dexter, Engineering and Material Science Division, Southwest Research Institute, San Antonio, TX 78284
50. Office of Assistant Manager for Energy Research and Development, Department of Energy, Oak Ridge Operations Office, Oak Ridge, TN 37831
51-52. Office of Scientific and Technical Information, P.O. Box 62, Oak Ridge, TN 37831
53-302. Given distribution as shown in category RF (NTIS-10)

NRC FORM 335 (2-89) NRCM 1102, 3201, 3202

U.S. NUCLEAR REGULATORY COMMISSION

BIBLIOGRAPHIC DATA SHEET

(See instructions on the reverse)

1. REPORT NUMBER (Assigned by NRC, Add Vol., Supp., Rev., and Addendum Numbers, if any.)

NUREG/CR-5451
ORNL-6584

2. TITLE AND SUBTITLE

Crack-Arrest Behavior in SEN Wide Plates of Low-Upper-Shelf Base Metal Tested Under Nonisothermal Conditions: WP-2 Series

3. DATE REPORT PUBLISHED

MONTH	YEAR
August	1990

4. FIN OR GRANT NUMBER

B0119

5. AUTHOR(S)

D. J. Naus, J. Keeney-Walker, B. R. Bass, G. C. Robinson, Jr., S. K. Iskander, R. J. Fields, R. deWit, S. R. Low, C. W. Schwartz, D. J. Alexander, and I.-B. Johansson

6. TYPE OF REPORT

Technical

7. PERIOD COVERED *(Inclusive Dates)*

8. PERFORMING ORGANIZATION – NAME AND ADDRESS *(If NRC, provide Division, Office or Region, U.S. Nuclear Regulatory Commission, and mailing address; if contractor, provide name and mailing address.)*

Oak Ridge National Laboratory
P.O. Box 2008
Oak Ridge, TN 37831

9. SPONSORING ORGANIZATION – NAME AND ADDRESS *(If NRC, type "Same as above"; if contractor, provide NRC Division, Office or Region, U.S. Nuclear Regulatory Commission, and mailing address.)*

Division of Engineering
Office of Nuclear Regulatory Research
U.S. Nuclear Regulatory Commission
Washington, DC 20555

10. SUPPLEMENTARY NOTES

11. ABSTRACT *(200 words or less)*

Six wide-plate crack-arrest tests (WP-2 Series) are discussed in this report. Each test utilized either a $1 \times 1 \times 0.1$-m or a $1 \times 1 \times 0.15$-m thick single-edge notch specimen ($a/w = 0.2$), fabricated from a low-upper-shelf base material, that was subjected to a linear thermal gradient along the plane of crack propagation. The tests were conducted at the National Institute of Standards and Technology and were designed to provide fracture-toughness measurements at temperatures approaching or above the onset of the Charpy upper-shelf regime, in a rising toughness region, and with an increasing driving force. Results obtained from these tests have produced crack-arrest toughness values well above the limit recognized by the current ASME guidelines (220 MPa$\cdot\sqrt{m}$) with arrests occurring at up to 102°C above the material DW_{NDT} (60°C). The fracture data support: (1) use of fracture mechanics concepts to analyze cleavage run-arrest events, (2) treatment of cleavage and ductile fracture modes as separate events, and (3) fact that cleavage arrest occurs above the ASME limit.

12. KEY WORDS/DESCRIPTORS *(List words or phrases that will assist researchers in locating the report.)*

Cleavage fracture
Crack-arrest toughness
Ductile tearing
Fracture mechanics
LWR pressure vessels
Safety assessment
Wide-plate testing

13. AVAILABILITY STATEMENT

Unlimited

14. SECURITY CLASSIFICATION

(This Page) Unclassified

(This Report) Unclassified

15. NUMBER OF PAGES

16. PRICE